Enhancing Real-Time Data Acquisition from Embedded Road Structural Health Monitoring Systems

by

Matea Ceric

A thesis

presented to the University of Waterloo

in fulfillment of the

thesis requirement for the degree of

Master of Applied Science

in

Civil Engineering

Waterloo, Ontario, Canada, 2024

© Matea Ceric 2024

Author's Declaration

This thesis consists of material all of which I authored or co-authored: see Statement of Contributions included in the thesis. This is a true copy of the thesis, including any required final revisions, as accepted by my examiners.

I understand that my thesis may be made electronically available to the public.

Statement of Contributions

This thesis contains sections that have been previously incorporated in conference proceedings, noted below:

1. Ceric, M., Oyeyi, A. G., Wang, S., Tavassoti, P., Baaj, H., Maadani, O., & Shafiee, M., "Monitoring the post Construction Structural and Environmental behaviours of an Instrumented Smart Pavement Section", Transportation Association of Canada Conference, September 24-27, Ottawa, Canada, 2023. https://www.tac-atc.ca/en/conference/papers/monitoring-post-construction-structural-and-environmental-behaviours-instrumented-smart-pavement
    - This paper was published on TAC's website, TAC's Library and also in the Transportation Research International Database. I am the primary author on this paper, and Dr. Oyeyi, Dr. Wang, Dr. Tavassoti, Dr. Baaj, Dr. Maadani and Dr. Shafiee co-authored the paper and provided their edits and inputs.
    - Chapter 1: Introduction: Some of the references and ideas used in this paper have been incorporated into the thesis.
    - Chapter 3: Trial Section Design and Construction: Some of the pavement top and profile diagrams have been incorporated into the thesis.
    - Chapter 5: Truck Testing Evaluation and Results: The concept and charts of the truck testing results, and environmental trends have been incorporated into the thesis, expanded on and edited for error mitigation. Some of the references and ideas used in this paper have been incorporated into the thesis.
2. Ceric, M., Wang, S., Tavassoti, P., Baaj, H., Ghafurian, M., Maadani, O., & Shafiee, M., "Instrumentation and Field Construction for a Smart Flexible Pavement", Artificial Intelligence for Logistics (AI4L) Conference, May 17-18, Ottawa, Canada, 2023.
    - This presentation was presented at the conference, and abstracts of the presentations were gathered, and physical copies were provided to conference attendees. I am the primary author on this paper, and Dr. Wang, Dr. Tavassoti, Dr. Baaj, Dr. Ghafurian, Dr. Maadani and Dr. Shafiee co-authored the paper and provided their edits and inputs.
    - Chapter 1: Introduction: Some of the references and ideas used in this paper have been incorporated into the thesis.
    - Chapter 3: Trial Section Design and Construction: Some of the pavement cross-section diagram concepts, as well as some of the photos highlighting the construction process were incorporated into the thesis.

3. Ceric, M., Oyeyi, A., Tavassoti, P., Baaj, H., Ghafurian, M., Maadani, O., Shafiee, S., "Towards the Development of Pavement Structural Health Monitoring Systems with AI", Artificial Intelligence for Logistics (AI4L) Conference, May 17-18, Ottawa, Canada, 2023.
    - This presentation was presented at the conference, and abstracts of the presentations were gathered, and physical copies were provided to conference attendees. I am the primary author on this paper, and Dr. Oyeyi, Dr. Tavassoti, Dr. Baaj, Dr. Ghafurian, Dr. Maadani and Dr. Shafiee co-authored the paper and provided their edits and inputs.
    - Chapter 5: Truck Testing Evaluation and Results: The concept and charts of the truck testing results, and environmental trends have been incorporated into the thesis, expanded on and edited for error mitigation.
    - Chapter 9: Database Development: The preliminary concept of the database was further expanded upon in the thesis.
4. Ceric, M.,Tavassoti, P., Baaj, H., Oyeyi, A, Maadani, O., "Analyzing Environmental and Traffic Load Trends in an Instrumented Pavement Test Section, Kitchener, Ontario", MairePav 2024 - 10th International Conference on Maintenance and Rehabilitation of Pavements, July 24-26, 2024.
    - To-date, this paper has been submitted to the conference and has been accepted. All accepted papers will be published in Springer Lecture Notes in Civil Engineering, indexed in Scopus, Ei-Compendex and Web of Science.
    - Chapter 8: In-Service Pavement Performance Trends: The trends charts from the thesis were used within this paper. Some of the references and ideas used in this paper have been incorporated into the thesis.

Abstract

Roadways are crucial for Canada's economy, serving as the primary mode of transportation. However, the country faces challenges in managing its pavement assets due to past cuts in infrastructure spending. To safeguard the economy and optimize road conditions, there's a pressing need for the development and implementation of a pavement management system (PMS) to efficiently allocate resources across the network. The conventional method for assessing pavements within a PMS relies on monitoring surface conditions, which is time-consuming, costly, and limited by long intervals between assessments. In response, in situ condition monitoring has emerged as a promising alternative, providing continuous data collection and addressing time and expertise constraints. This approach aligns with the development of "smart" pavements, incorporating advanced technologies like Artificial Intelligence (AI) and machine learning (ML) to extend service life, enhance performance, and improve safety.

This thesis forms a part of the Smart Pavements project at the University of Waterloo. The project aims to assess the responses of a flexible instrumented pavement section on Courtland Avenue in Kitchener, Ontario, Canada, through data collection and preliminary assessments using sensory systems. These efforts seek to understand how the pavement reacts to different loads, environmental factors, and seasonal variations. The thesis successfully integrates advanced monitoring and predictive technologies, such as embedded sensors, within an instrumented test section, yielding favorable results. Ultimately, this work is expected to advance the integration of AI/ML-aided predictive modeling for predicting pavement performance and climate change impacts across various instrumented test sections.

Previous research has identified several gaps in the literature, including a lack of consideration for sensor response results during construction, limited data collection periods with sensory systems over various seasons, inadequate exploration of long-term pavement response trends, understanding the impacts of vehicle wander on pavement response, and a scarcity of comparative studies between static and dynamic pavement response simulation methods. Additionally, there is a need for scalability and cost-benefit analysis of implementing pavement sensor technologies on a wider scale over decades. This thesis addresses the first five gaps while identifying scalability and cost-benefit analysis as a future research topic.

The instrumentation and testing processes for the pavement section were documented, covering design, sensor types, construction, hydro connection, and material sampling. Challenges included weather-related delays, with recommendations for scheduling installations during favorable weather and allowing time for sensor calibration to address discrepancies. Other issues highlighted included installation planning, sensor placement accuracy, vibration impact, and data security.

Material testing procedures during construction were outlined, including field tests like truck and LWD testing and lab tests evaluating layer properties. Dynamic modulus and Proctor tests were

employed on HMA and granular layers, respectively. Recommendations for future studies include regular testing, expanding tests to characterize various pavement layers, such as FWD testing, and adopting a structured approach to enhance insights into material properties and trend assessments.

One of the major assessment phases of this research focused on truck testing. Truck tests involved a standard 14-wheeler truck traversing the section at varying speeds and temperatures, analyzing the impact of speed, temperature, moisture, axle load, and traffic on layer strain and pressure. Conducted five times across seasons, the tests aimed to capture diverse data, revealing variations across speeds and sensor arrays, emphasizing the importance of environmental factors and traffic conditions in interpreting sensor data. Key findings include longitudinally higher strain responses, clearer signals at slower speeds, and seasonal variations in sensor responsiveness.

Following the truck testing, the assessment of the impact of vehicle wander on pavement behavior by correlating tire position with pavement response was performed. Wander tests involved the truck traversing different trajectories at 10 km/h, collecting sensor data. Polynomial expressions were developed to quantify the relationship between strain or pressure responses and lateral deviations, accurately representing strain responses but showing some skewness for pressure responses. Future studies should conduct more wander tests to refine baseline responses for validating truck test outcomes and identifying outliers, crucial for constructing a national database. Integration of similar relationships into data filtering algorithms can assess the accuracy of truck test results, indicating the need for retesting if necessary.

The study compared KENPAVE and 3D-Move software results from truck tests across different seasons with field measurements to assess their accuracy in modeling pavement damage. Initial tests showed disparities, but subsequent experiments demonstrated improvements likely due to stabilized properties and tire-pavement interactions. 3D-Move proved superior in estimating pavement stress, especially in in-service scenarios, and facilitated dynamic response curve generation. Challenges with 3D-Move emerged before summer conditions testing, suggesting ongoing research and validation are necessary to enhance predictive capabilities in pavement engineering during construction. Future assessments should explore alternative software options for improved usability while comparing results across temperatures and speeds.

The analysis explored detailed strain, pressure, and moisture trends spanning approximately nine months across various seasons, aiming to evaluate sensor functionality. It unveiled correlations between seasonal variations and sensor responses, with clear and consistent trend data. However, high-speed data analysis yielded ambiguous outcomes in some cases, posing challenges in visualization due to data volume. Future studies should integrate live and high-speed data for improved sensitivity in trend assessments and extend the duration of assessment beyond the initial nine-month period to offer a yearly perspective and more comprehensive insights for pavement engineering applications.

Finally, the thesis introduced a basic database for organizing and sharing data from the instrumented test section, proposing preliminary charts and data collection methods adaptable to databases using tools like SQL. The goal is to efficiently capture, store, and filter project data and potentially data from similar projects. Continued development of this concept is recommended, starting with preliminary tests and establishing a basic database state to assess functionality and identify areas for improvement before extending to other similar projects. This iterative approach aims to create a robust tool for managing and analyzing instrumented test section data, facilitating decision-making in pavement engineering.

This study provided an understanding in pavement instrumentation by conducting controlled truck tests immediately after laying Hot Mix Asphalt (HMA) layers, providing comprehensive data on pavement structural responses. It advanced understanding by subjecting an instrumented test section to rigorous testing across various seasons, offering insights into how heavy vehicle loads affect strain and pressure responses in freshly placed asphalt. Additionally, it delved into long-term trends and assessments of load and environmental factors, addressing the existing gap in understanding long-term pavement behavior. Furthermore, the study explored the impact of vehicle wander on pavement sensor responses and compared the efficacy of static and dynamic pavement response simulation methods across different seasons and speeds, enhancing their utility in predicting real-world pavement behavior.

The thesis suggests several recommendations for future work to advance understanding of instrumented pavement sections from a pavement management perspective. These include integrating artificial intelligence and machine learning algorithms to enhance prediction models, prioritizing long-term data collection to evaluate climate change impacts, replicating test sections on other roads for a broader dataset, completing and implementing a national database for sharing data, developing standardized guidelines for sensor implementation and testing, and assessing the scalability and feasibility of the technology from both a lifecycle and economic standpoint. These efforts aim to improve pavement management practices and enhance the effectiveness of pavement performance assessment and modeling on a broader scale.

Acknowledgements

I would like to express my sincere gratitude to the following individuals and organizations who have supported me throughout my Master's journey:

First and foremost, I extend my deepest appreciation to my thesis supervisors, Professor Hassan Baaj and Professor Pejoohan Tavassoti. Their guidance and encouragement over the past five years have been invaluable to me. Our relationship began in 2019 when they welcomed me into the CPATT family as a co-op student with limited experience and skills. From the outset, they recognized potential in me that I hadn't seen in myself, instilling in me the confidence to pursue my academic and life goals. What I particularly admire about them is their ability to provide exceptional mentorship while also considering my individual needs and aspirations. Their expertise, patience, and constructive feedback have not only shaped this thesis but have also played a substantial role in my personal and academic growth. I am truly grateful for their support throughout my academic journey.

I am grateful to the members of my thesis committee, Professor Chul Min Yeum and Professor Christian Bachmann and Professor Baaj, for their insightful comments, suggestions, and expertise that enriched the quality of this work.

My heartfelt thanks to the Department of Civil and Environmental Engineering staff and technical support, in particular Peter Volcic, Richard Morrison, Victor Lewis, Mark Hummel, Shannon Cary, Robert Kaptein, Jaimee Kropf, Mark Merlau, Kevin Rampersad, Mark Sobon, Tia Sgarbossa, Shirley Springall. Your support and guidance, whether directly or indirectly connected to my thesis work, have been indispensable and greatly appreciated.

I would like to thank the Centre for Pavement and Transportation Technology at the University of Waterloo for providing the resources and facilities necessary for conducting this research. Additionally, I acknowledge the financial support received through the National Research Council of Canada (NRC), and my direct advisors through this organization, Dr. Omran Maadani and Dr. Mohammad Shafiee who have provided plenty of support through our encounters at conferences, and at various milestones throughout my degree.

I would like to extend my gratitude to the Region of Waterloo for their support in providing a suitable location for the instrumented pavement test section. A special acknowledgment goes to Luke Misurka and Karolina Krol, project managers whose efforts were pivotal in facilitating our testing and construction processes. I am also indebted to Carlos Muzlera and Matthew Gray, as well as the entire Capital Paving team. Their invaluable support during sensor installation and implementation was instrumental to our success. Furthermore, thank you to Steed and Evans for their unwavering support throughout the truck testing phase post-construction. Their consistent assistance, positive attitudes, and enthusiasm made the testing process all the more enjoyable.

I am immensely grateful to all the professors and colleagues at CPATT, both past and present, who have not only provided tremendous support for my research but also offered emotional support and assistance with laboratory and field work. Among them, I would like to extend special thanks to Grace Oyeyi, Shenglin Wang, Robert Aurilio, Peggie Wang, Aditi Sharma, Saeid Salehiashani, Adam Schneider, Tianshu Zhang, Hana Hailu, Anahita Diyanoush, and Leila Miri as current students, as well as Paula Barbi, Edward Abreu, Ata Nahidi, Abdulrahman Hamid and Taher Moghaddam as former students. Your contributions have been invaluable to my academic journey, and I deeply appreciate all of the wonderful conversations we've had.

I want to thank all of my graduate student friends and peers that I have worked with in various clubs and teams throughout the years, and who have always been a source of interesting conversations, good memories and excellent advice.

I wanted to thank all of my colleagues at Boxfish Infrastructure Group, who, beyond accepting my journey to pursue a master's degree in conjunction with working part time, have taken an active interest in my research work. These include my direct colleagues, Aleks Trpkovic, Darius Keung, Zhenyu Niu, Fitra Hartono, Rebecca Chung, Megan Lee, Mark Batten-Carrew, Karl Junkin and Felipe Camargo as well as my other colleagues at BIG, notably Jon Lomow and Vedrana Petrovic. Thank you so much for the accommodation and the support these past few years, it means more than you know.

Lastly, but certainly not least, I want to express my deepest gratitude to my family. You have been my rock and my backbone, providing monumental support without which I could not have achieved even half of what I have accomplished. My mama Anita, tata Emir and my sestra Adriana, as well as my tetka Boška, my late striko Borko and grandparents, the late baka Mirjana and late dedo Antun, as well as the late baka Sunčica and dedo Fuad who have provided unconditional love and care throughout my life and have encouraged me to always dream big. I love you all.

Dedication

To my wonderful and loving parents, Anita and Emir, and my beautiful and strong sister, Adriana

Table of Contents

Author's Declaration ii

Statement of Contributions iii

Abstract v

Acknowledgements viii

Dedication x

List of Figures xvii

List of Tables xxix

Chapter 1 Introduction 1

1.1 Problem Statement 3

1.2 Research Objectives & Methodology 6

1.3 Thesis Structure 8

Chapter 2 Literature Review 10

2.1 Pavement Distresses 10

2.1.1 Common Types of Flexible Pavement Distresses 11

2.1.2 Critical Response Points within Pavements 14

2.1.3 Pavement Distress Impact on Pavement Performance 16

2.2 Current Pavement Monitoring Practices and Limitations 17

2.2.1 Condition Surveys 17

2.2.2 Destructive Testing Methods for Structural Capacity Assessment 18

2.2.3 Non-Destructive Testing Methods for Structural Capacity Assessment 19

2.3 Pavement Monitoring and Instrumentation 21

2.3.1 Sensors used within Instrumented Test Sections 22

2.3.2 Previous Examples of Pavement Instrumentation 27
2.4 Applications of Pavement Performance Monitoring 29
2.4.1 Pavement Performance Prediction Models 30
2.4.2 Consideration of Climate Change Effects in Pavement Performance Prediction 32
2.5 Research Gaps 33
Chapter 3 Trial Section Design and Construction 35
3.1 Project Overview 35
3.2 Project Site Description 35
3.3 Trial Section Design 37
3.4 Instrumentation Background and Installation 38
3.4.1 Dataloggers 38
3.4.2 Horizontal and Vertical Asphalt Strain Gauges 39
3.4.3 Temperature Sensors and Temperature Probes 39
3.4.4 Moisture Probes 40
3.4.5 Total Earth Pressure Cells 40
3.4.6 Sensor Installation Plans 40
3.4.7 Sensor Labelling Methodology 47
3.5 Construction Activities 51
3.5.1 Confirmation of concrete base location (August 24th, 2022) 51
3.5.2 Determining the position of sensors (September 29th, 2022) 52
3.5.3 Sensor installation Day 1– Installation of sensors on the subgrade, subbase, and base (September 30th, 2022) 53
3.5.4 Pouring of Concrete Pad (October 5th, 2022) 59

3.5.5 Arrangement of the base/asphalt concrete sensors (October 11th, 2022) 60
3.5.6 Sensor Installation Day 2– Installation of sensors on the base and asphalt concrete (October 12th, 2022) 61
3.5.7 Hydro Connection – hydro line installation and grounding (December 21, 2022) 65
3.5.8 Material Sampling 66
3.6 Construction Challenges 67
Chapter 4 Testing of Materials 69
4.1 Post-Construction Field Testing 69
4.1.1 Truck Testing 69
4.1.2 LWD Testing 69
4.2 Lab Testing 72
4.2.1 Asphalt: Dynamic Modulus Testing 72
4.2.2 Base and Subbase: Optimum Moisture Content Determination 75
Chapter 5 Truck Testing Evaluation and Results 86
5.1 Description of Truck Testing Procedure 86
5.1.1 Data Presentation 89
5.2 Truck Test #1: Fall Conditions and First HMA Lift Construction Analysis 90
5.2.1 Method for Strain and Pressure Data Analysis 91
5.2.2 Impact of Speed on Layer Strain & Pressure 91
5.2.3 Impact of Temperature/moisture on Layer Strain & Pressure 99
5.2.4 Comparison of Pressure in the Pavement Structure during Construction 102
5.3 Truck Test #2: Early Spring Conditions 103
5.3.1 Impact of Speed on Longitudinal & Transverse Strain 104

5.3.2 Impact of Speed on Pressure in the Base, Subbase and Subgrade 106
5.4 Truck Test #3: Summer Conditions 109
5.4.1 Impact of Speed on Longitudinal & Transverse Strain 110
5.4.2 Impact of Speed on Pressure in the Base, Subbase and Subgrade 113
5.5 Truck Test #4: Summer Conditions and Second HMA Lift Construction Analysis 115
5.5.1 Impact of Speed on Longitudinal & Transverse Strain 116
5.5.2 Impact of Speed on Pressure in the Base, Subbase and Subgrade 118
5.6 Truck Test #5: Late Fall Conditions and Construction 120
5.6.1 Impact of Speed on Longitudinal & Transverse Strain 120
5.6.2 Impact of Speed on Pressure in the Base, Subbase and Subgrade 122
5.7 Strain and Pressure Comparison 124
5.7.1 Strain and Pressure Comparison Between the Right and Left Sensor Arrays 124
5.7.2 Maximum Pressure and Strain Comparison 130
Chapter 6 Quality Control for Data Analysis 142
6.1 Description of Wander Test Procedure 142
6.2 Wander Test Results 145
6.2.1 Visual Assessment of Video Pass Results 145
6.2.2 Strain Sensor Assessment 150
6.2.3 Pressure Sensor Assessment 162
6.2.4 Comparison of the Results 168
Chapter 7 Pavement Section Modelling 173
7.1 Introduction 173
7.2 Input Parameters 174

7.2.1 Determination of HMA Dynamic Moduli 174
7.2.2 Determination of Layer Elastic Moduli 174
7.2.3 Summary of Input Parameters 176
7.3 Results and Discussion 191
7.3.1 KENPAVE Results 191
7.3.2 3D-Move Results 193
7.4 Key Takeaways 197
Chapter 8 In-Service Pavement Performance Trends 198
8.1 Environmental Load Data Analysis 198
8.1.1 Temperature - Layer Profile Over Time 199
8.1.2 Moisture - Layer Profile Over time 207
8.2 Traffic Load Data Analysis 210
8.2.1 Pressure 211
8.2.2 Strain 218
Chapter 9 Database Development 222
9.1 Background 222
9.2 Database Development 223
9.2.1 Current Data Setup 223
9.2.2 Proposed Database Concept for Smart Pavement Project 230
Chapter 10 Conclusions and Recommendations 243
10.1 Summary of Work Performed 243
10.2 Contributions of the Research 245
10.3 Recommendations for Future Work 246

References 249

Appendices 261

Appendix A Calibration Sheets for RST and BDI Sensors 262

Appendix B Schematics of DAC Setup 307

Appendix C Data Cleaning Scripts 322

List of Figures

Figure 1.1 Map of the National Highway System in Canada, and its connection to the National Airport System, another important transportation mode [2]. 1
Figure 1.2 Framework for the implementation of a self-operating data gathering platform [19]. 5
Figure 2.1 Factors affecting pavement performance and the interactions between those factors [23]. 11
Figure 2.2 Examples of Mix Rutting (left), Subgrade Rutting (middle), and Densification (right) [24]. 12
Figure 2.3 Example of a transverse crack across the surface of a pavement structure [25]. 12
Figure 2.4 An example of longitudinal cracking [26]. 13
Figure 2.5 An example of how to properly pave a roadway to minimize the appearance of longitudinal cracks [26]. 13
Figure 2.6 An example of fatigue cracking [27]. 14
Figure 2.7 An example of a pothole [28]..... 14
Figure 2.8 Critical response points in a flexible pavement structure [29]. 15
Figure 2.9 General pavement deterioration curve as a function of pavement condition and age [30]. 16
Figure 2.10 Images showing the trenching process; cutting a trench (left) and the visible trench layers (right) [32]. 19
Figure 2.11 The coring of a pavement section using a core rig [32]. 19
Figure 2.12 How an FWD functions [17]. 20
Figure 2.13 How a GPR functions [17]. 21
Figure 2.14 Wheatstone bridge schematic [17]. 23
Figure 2.15 Typical locations of common sensor types located in a pavement structure [17]. 27
Figure 2.16 Plan view of the pavement instrumentation setup for this project [41]..... 29
Figure 2.17 Pavement performance deterioration curve, showing how prediction of future deterioration and proposed rehabilitation actions will affect the pavement condition [43]. 30
Figure 2.18 Steps in the development of a pavement performance prediction model using machine learning [42]. 32
Figure 3.1 Location of the instrumented test section in relation to Highway 8, Overland Drive and Walton Avenue in Kitchener, Ontario [49]. The instrumented test section is highlighted in red. 36

Figure 3.2 Closer view of lane selected as instrumented test section in relation to the surrounding land uses [49]. 36
Figure 3.3 Street view look at the approximate location of the instrumented test section [49]. 37
Figure 3.4 Site plan drawing produced by the Region of Waterloo, including the location for the instrumented test section in red [50]. 37
Figure 3.5 Typical cross-sectional view of the roadway near the instrumented pavement section, produced by the Region of Waterloo [50]. 38
Figure 3.6 Sensors and other equipment installed at the instrumented section on Courtland Avenue. 42
Figure 3.7 Moisture tree through which all sensors were threaded. 43
Figure 3.8 Image showcasing how all the sensors were threaded through the moisture tree. 43
Figure 3.9 Data Acquisition System for the instrumented section. 43
Figure 3.10 Schematic (plan view) showcasing the sensor instrumentation layout. 45
Figure 3.11 Section view of the instrumentation. 45
Figure 3.12 Top view of the instrumented section setup, showcasing the concrete base and the hydro pole. 46
Figure 3.13 Plan view of the instrumented section setup, showcasing the location of the PVC conduit relative to the pavement structure 46
Figure 3.14 Additional plan view of the instrumented section setup, showcasing the location of the PVC conduit relative to the hydro pole. 47
Figure 3.15 Naming convention for the horizontal asphalt strain gauges. 48
Figure 3.16 Naming convention for the vertical asphalt strain gauges. 48
Figure 3.17 Naming convention for the temperature thermistors 49
Figure 3.18 Naming convention for the temperature probes. 49
Figure 3.19 Naming convention for the temperature probes for each sensor. 49
Figure 3.20 Naming convention for the moisture probe sensors. 50
Figure 3.21 Naming convention for the total earth pressure cell sensors. 50
Figure 3.22 Summary of the construction activities and the dates of occurrence. 51
Figure 3.23 Location of the proposed concrete pad (right). The white painted marking denotes the proposed location. Position of proposed concrete pad relative to the hydro pole is also shown (left). 52

Figure 3.24 Exposed subgrade where the sensors are to be laid (left) and markings denoting the edge of pavement and wheel path (right). 52
Figure 3.25 Orange markings showcasing the southbound outermost lane in which the sensors will be laid as well as the chosen wheel path (lines closest to the curb and sidewalk. A trench for the location of the PVC pipes, which will carry the wires from the moisture tree to the DAC can also be seen near the person. 53
Figure 3.26 Subgrade condition the day of inspection (left) and the measuring and marking of sensor positions on the subgrade (right). 53
Figure 3.27 Packaged sensors brought on site (left) and bundling of sensors to place through PVC pipe (right). 54
Figure 3.28 Placement of the black PVC pipe over the bundled wire(right) and the completed L-shaped PVC structure guiding all sensor wires from the subgrade to the DAC (left). 54
Figure 3.29 Installation of the moisture tree within the subgrade. 55
Figure 3.30 Find sand being placed around subgrade soil pressure sensors (right) and box protecting the group of sensors during backfilling procedure (left). 56
Figure 3.31 Both the (left) and (right) images show the backfilling of the Granular B material. 56
Figure 3.32 Compaction roller (right) and hand compactor (left) to flatten the subbase soil..... 57
Figure 3.33 Implementation of the pressure sensors on the top of the subbase (left) and images of the backfilling procedure of Granular A with the wooden box present as protection to the moisture tree (right). 57
Figure 3.34 Removal of the protective box around the sensors (left) and image of the moisture tree with sensors (right). 58
Figure 3.35 Exposed temperature probe sensor tops (left) and hand compaction of the soil adjacent to the sensors (right). 59
Figure 3.36 Protected sensors. 59
Figure 3.37 Installation of the concrete base pad for the data acquisition system. 60
Figure 3.38 Two views of the implementation of the asphalt strain gauges and the pressure sensors on site. 61
Figure 3.39 View of the pressure sensor installation to the left and the asphalt strain gauge installation to the right. 61

Figure 3.40 Covering of the sensor wires with asphalt concrete to protect them. 62
Figure 3.41 Targeted pouring of asphalt concrete over the instrumented section. 62
Figure 3.42 Instrumented section with targeted pouring complete. 63
Figure 3.43 Asphalt concrete being poured onto the instrumented section (right), and compaction roller compacting the asphalt pavement section (left). 63
Figure 3.44 Identification of the temperature probe sensor 64
Figure 3.45 Comparison of the initial(left) and final (right) installation plans for the temperature probes. 64
Figure 3.46 Hydro wire connection and box on the adjacent utility pole 65
Figure 3.47 Ground wire, hydro wire and plug box setup. 65
Figure 3.48 Closeups of the plug box and hydro wire. 66
Figure 3.49 Sampling of the Granular B material. 66
Figure 4.1 Light Weight Deflectometer (LWD) testing. 70
Figure 4.2 Shift factor for test data. 73
Figure 4.3 Master curve. 75
Figure 4.4 Moisture content vs. dry unit weight plot [59]. 76
Figure 4.5 Drying of subgrade soil setup. 76
Figure 4.6 Container for mixing and adding moisture to each of the Gran. A, Gran. B and subgrade soil samples (left). Wrapping of the samples within the moulds to prevent moisture loss for use on site (right). 79
Figure 4.7 All 11 samples prepared for moisture sensor calibration. 79
Figure 4.8 Extruded and cut samples of soil from each of the 11 samples, with two cups per sample for a total of 22 cups. 80
Figure 4.9 Moisture content vs. dry unit weight plot for the Version 1 material/soil samples. 83
Figure 4.10 Moisture content vs. dry unit weight plot for the Version 2 material/soil samples. 83
Figure 5.1 Image depiction of the map showing the path that the truck takes during truck testing (in red brown) in relation to nearby intersections. 87
Figure 5.2 An image of a standard axle configuration of a truck used for truck testing, with a steering axle, single axle with dual tire “lift axle” and tandem axle with dual tires. 87

Figure 5.3 Trucks aimed to pass directly over the right sensor array during each truck test. Done by spray-painting the array position on the pavement to guide the driver. 88
Figure 5.4 Standard configuration of testing truck with axle measurements. 88
Figure 5.5 Comparison of the transverse (top) and longitudinal (bottom) strain responses at 72°C for a truck running at 45 km/h. 92
Figure 5.6 Strain response at 72°C at 30 km/h, showcasing the lack of clear sensor signals at this testing speed. 92
Figure 5.7 This is a 4-panel figure, describing the comparison of strain in the transverse direction in the right wheel path: a) at 51°C at various speeds. b) at 51°C at various speeds, focused analysis of front tandem axle. c) at 43°C at various speeds. d) at 43°C at various speeds, focused analysis of front tandem axle..... 94
Figure 5.8 Comparison of the raw strain response in the transverse direction in the right wheel path at 51°C (a) and 43°C (b), at various speeds. 95
Figure 5.9 This is a 6-panel figure of the comparison of the pressure response in the base (a and b), subbase (c and d) and subgrade (e and f) layers at 51°C (a,c,e) and 43°C (b,d,f) at various speeds.... 96
Figure 5.10 This is a 3-panel figure, which depicts the comparison of the raw pressure response at 51°C at various speeds in the base (a), subbase (b) and subgrade (c). 97
Figure 5.11 This is a 6-panel figure, depicting the comparison of the raw pressure response in the base (a and b), subbase (c and d) and subgrade (e and f) layers at 43°C at various speeds. 98
Figure 5.12 This a 3-panel figure, depicting the comparison of the transverse strain responses at 45 km/h at various temperatures (a), a comparison of the steering axle transverse strain responses at 45 km/h (b) and a comparison of the transverse strain responses at 30 km/h at various speeds (c)..... 100
Figure 5.13 This is a 4-panel figure, depicting the comparison of the pressure response at 45 km/h in the base (ta), subbase (b), and subgrade (c); further analysis for the front tandem axle responses at 45km/h in subbase layer (d). 101
Figure 5.14 This is a 4-panel figure, depicting the comparison of the pressure response at 30 km/h in the subbase (a) and subgrade (b) and 10 km/h in the subbase (c) and subgrade (d)..... 101
Figure 5.15 Pressure depth profile indicating changes in pressure during the construction phase at 51°C and 43°C..... 103

Figure 5.16 The setup for the early spring truck test. The orange spray paint on the pavement surface demarcates the right array of sensors to guide the truck during the different speeds. 104
Figure 5.17 This is a 6-panel figure demonstrating the comparison of the impact of longitudinal (a,c,e) and transverse (b,d,f) strain at 5km/h and 10, 20 and 50 km/h. 105
Figure 5.18 This is a 6-panel figure demonstrating the comparison of the impact of raw longitudinal (a,c,e) and transverse (b,d,f) strain at 5km/h and 10, 20 and 50 km/h. 107
Figure 5.19 This is a 9-panel figure depicting the comparison of the impact of the pressure in the base (a,b,c), subbase (d,e,f), and subgrade (g,h,i) at 5km/h and 10, 30 and 50 km/h. 108
Figure 5.20 Comparison of the impact of the raw pressure in the base (a,b,c), subbase (d,e,f), and subgrade (g,h,i) at 5km/h and 10, 30 and 50 km/h. 109
Figure 5.21 Drawing of guideline 0.7 metres from the edge of pavement to guide the truck during truck testing. 110
Figure 5.22 Summer truck testing setup - data collection and truck passing over sensor arrays. 110
Figure 5.23 This is a 6-panel figure demonstrating the comparison of the impact of longitudinal (a,c,e) and transverse (b,d,f) strain at 5km/h and 10, 20 and 50 km/h. 111
Figure 5.24 This is a 6-panel figure demonstrating the comparison of the impact of raw longitudinal (a,c,e) and transverse (b,d,f) strain at 5km/h and 10, 20 and 50 km/h. 112
Figure 5.25 Comparison of the impact of the pressure in the base (a,b,c), subbase (d,e,f), and subgrade (g,h,i) at 5km/h and 10, 30 and 50 km/h. 114
Figure 5.26 Comparison of the impact of the raw pressure in the base (a,b,c), subbase (d,e,f), and subgrade (g,h,i) at 5km/h and 10, 30 and 50 km/h. 115
Figure 5.27 This is a 6-panel figure demonstrating the comparison of the impact of longitudinal (a,c,e) and transverse (b,d,f) strain at 5km/h and 10, 20 and 50 km/h. 116
Figure 5.28 This is a 6-panel figure demonstrating the comparison of the impact of raw longitudinal (a,c,e) and transverse (b,d,f) strain at 5km/h and 10, 20 and 50 km/h. 117
Figure 5.29 Comparison of the impact of the pressure in the base (a,b,c), subbase (d,e,f), and subgrade (g,h,i) at 5km/h and 10, 30 and 50 km/h. 118
Figure 5.30 Comparison of the impact of the raw pressure in the base (a,b,c), subbase (d,e,f), and subgrade (g,h,i) at 5km/h and 10, 30 and 50 km/h. 119

Figure 5.31 This is a 6-panel figure demonstrating the comparison of the impact of longitudinal (a,c,e) and transverse (b,d,f) strain at 5km/h and 10, 20 and 50 km/h. 121
Figure 5.32 This is a 6-panel figure demonstrating the comparison of the impact of raw longitudinal (a,c,e) and transverse (b,d,f) strain at 5km/h and 10, 20 and 50 km/h. 122
Figure 5.33 Comparison of the impact of the pressure in the base (a,b,c), subbase (d,e,f), and subgrade (g,h,i) at 5km/h and 10, 30 and 50 km/h. 123
Figure 5.34 Comparison of the impact of the raw pressure in the base (a,b,c), subbase (d,e,f), and subgrade (g,h,i) at 5km/h and 10, 30 and 50 km/h. 124
Figure 5.35 Comparing speed impact on pavement strain response: longitudinal and transverse sensors in left and right arrays. Y-axis: Strain (με), X-axis: Time (s) for all plots. 127
Figure 5.36 Comparison of speed impact on pavement pressure response for sensors in base, subbase, and subgrade within the right array. Y-axis: Pressure (kPa), X-axis: Time (s) for all plots. 128
Figure 5.37 Comparison of the speed impact on pavement pressure response for sensors in the base, subbase and subgrade in the left array. Y-axis: Pressure (kPa), X-axis: Time (s) for all plots. 129
Figure 5.38 Maximum strain and pressure results captured for various sensors during Truck Test #1 (Fall conditions) at various temperatures. 130
Figure 5.39 Maximum strain results captured for various sensors during Truck Test #2 to #5 across tested sensors for all tested speeds. 131
Figure 5.40 Maximum pressure results captured for various sensors during Truck Test #2 to #5 across tested sensors for all tested speeds. 133
Figure 5.41 Comparison of the maximum pressure responses during all five truck tests, including the load of the truck when passing over the sensors. 136
Figure 5.42 Comparison of the maximum strain response in both the longitudinal and transverse directions during all five truck tests, including the loads of the truck when passing over the sensors 139
Figure 5.43 Pressure depth profile showing changes in pressure during the construction phase (43°C) and 5 months after (6°C). 141
Figure 6.1 Theoretical change in longitudinal strain magnitude because of lateral wander [68]. 142
Figure 6.2 Plan showcasing the trajectories that the truck passed over during each round of the wander test. 144

Figure 6.3 Truck trajectory step-by-step for Round #1, Attempt 1. 146
Figure 6.4 Truck trajectory step-by-step for Round #1, Attempt 2. 147
Figure 6.5 Truck trajectory step-by-step for Round #2, first attempt. The wheel passed more on the curb than over the pavement-curb interface. 148
Figure 6.6 Truck trajectory step-by-step for Round #2, second attempt. The wheel passed more on the pavement-curb interface. 149
Figure 6.7 Truck trajectory step-by-step for Round #3, first attempt. The wheel passes directly over the right sensor array. 150
Figure 6.8 Truck trajectory step-by-step for Round #3, second attempt. The wheel also passes directly over the right sensor array. 151
Figure 6.9 Strain results for both truck testing attempts for sensor AS-LO-R-1 (longitudinal, right array). Note: labels are provided and are the same for similar figures. 152
Figure 6.10 Strain results for both truck testing attempts for sensor AS-LO-R-7 (longitudinal, right array). 152
Figure 6.11 Strain results for both truck testing attempts for sensor AS-TR-R-3 (transverse, right array). 154
Figure 6.12 Strain results for both truck testing attempts for sensor AS-TR-R-5 (transverse, right array). 154
Figure 6.13 Strain results for both truck testing attempts for sensor AS-LO-L-2 (longitudinal, left array). 155
Figure 6.14 Strain results for both truck testing attempts for sensor AS-LO-L-8 (longitudinal, left array). 155
Figure 6.15 Strain results for both truck testing attempts for sensor AS-TR-L-4 (transverse, left array). 156
Figure 6.16 Strain results for both truck testing attempts for sensor AS-TR-L-6 (transverse, left array). 156
Figure 6.17 This is an 8-panel figure; Strain data that will be used in further analysis. 158
Figure 6.18 Demonstration of raw strain results and the tension and compression portions of the responses highlighted for clarity. Responses are for sensor AS-LO-R-7 (Longitudinal, Right Array). 160

Figure 6.19 Raw strain responses for data that will be used in further analysis. 161
Figure 6.20 Pressure results for Attempt 2 for sensor PC-BA-R-1 (Base, Right Array). 163
Figure 6.21 Pressure results for Attempt 2 for sensor PC-BA-R-5 (Base, Right Array). Note: labels are provided and are the same for similar figures. 163
Figure 6.22 Pressure results for Attempt 2 for sensor PC-BA-L-2 (Base, Left Array). 164
Figure 6.23 Pressure results for Attempt 2 for sensor PC-BA-L-6 (Base, Left Array). 164
Figure 6.24 Pressure results for Attempt 2 for sensor PC-SB-R-3 (Subbase, Right Array). 165
Figure 6.25 Pressure results for Attempt 2 for sensor PC-SB-L-4 (Subbase, Right Array). 165
Figure 6.26 Pressure results for Attempt 2 for sensor PC-SG-R-7 (Subgrade, Right Array). 166
Figure 6.27 Pressure results for Attempt 2 for sensor PC-SG-L-8 (Subgrade, Right Array). 166
Figure 6.28 Raw pressure responses for data that will be used in further analysis. 167
Figure 6.29 Longitudinal strain versus lateral offset relationships for the right and left sensor arrays. 169
Figure 6.30 Transverse strain versus lateral offset relationships for the right and left sensor arrays. 169
Figure 6.31 Measurements between right and left truck tires and the right and left sensor arrays. 170
Figure 6.32 Base pressure response versus lateral offset relationship for the right and left sensor arrays. 171
Figure 6.33 Subbase pressure response versus lateral offset relationship for the right and left sensor arrays. 171
Figure 6.34 Subgrade pressure response versus lateral offset relationship for the right and left sensor arrays. 172
Figure 7.1 General information inputted in KENPAVE. 176
Figure 7.2 Z-coordinates (vertical coordinates) as will be inputted in KENPAVE as points of analysis. 177
Figure 7.3 Z-coordinates inputted in KENPAVE. 177
Figure 7.4 Thickness and Poisson Ratio values for each layer in KENPAVE. 178
Figure 7.5 Modulus input in KENPAVE. 178
Figure 7.6 Load information inputted in KENPAVE. 179
Figure 7.7 Number of coordinates under a single tire to be analyzed. 181
Figure 7.8 Coordinates inputted in KENPAVE 181

Figure 7.9 Setting the dynamic modelling features in 3D-Move. 182
Figure 7.10 Braking coefficient determination (modified from [80]). 183
Figure 7.11 Sample input of the pavement contact stress distribution for 72 C at 45 km/h. 184
Figure 7.12 Sample of the DLC determination in 3D-Move. 185
Figure 7.13 Pavement structure inputs in 3D-Move. 185
Figure 7.14 Input of dynamic modulus values in 3D-Move. 186
Figure 7.15 Input of phase angle and Poisson's Ratio values in 3D-Move. 186
Figure 7.16 Input of HMA Superpave values in 3D-Move. 187
Figure 7.17 Input of unit weight and analysis temperature values in 3D-Move. 187
Figure 7.18 Input of Granular A values in 3D-Move. 188
Figure 7.19 Input of Granular B values in 3D-Move. 188
Figure 7.20 Input of subgrade values in 3D-Move. 189
Figure 7.21 Input of analysis points values in 3D-Move. 189
Figure 7.22 Normal tensile strain and compressive stress results in the field and 3D-Move for 51°C and 45 km/h. 195
Figure 7.23 Normal tensile strain and compressive stress results in the field and 3D-Move for 6°C and 40 km/h. 197
Figure 8.1 Aggregated temperature profile from March 9th, 2023, to March 10th, 2023, including all temperature sensors. 200
Figure 8.2 Aggregated temperature profile from March 9th, 2023, to March 10th, 2023, not including the TEMPS-01 temperature probe for easier visibility of trends. 201
Figure 8.3 Daily temperature variation over two days (midnight March 8th to midnight March 10th, 2023) which shows the typical times for peak asphalt and granular temperatures. 202
Figure 8.4 Daily temperature variations from March 3rd, 2023, to March 15th, 2023, including all temperature sensors. The erratic nature of the TEMPS-01 temperature probe data is visible in this case. 203
Figure 8.5 Daily temperature variations from March 3rd, 2023, to March 15th, 2023, not including the TEMPS-01 temperature probe for easier visibility of trends. Ambient temperature is also plotted. . 204
Figure 8.6 Monthly temperature variations from March 2023 to mid November 2023. The TEMPS-02-3 sensor begins to not function properly. 206

Figure 8.7 Monthly temperature variations from March 2023 to mid November 2023, removing the odd data from the TEMPS-03-3 sensor. 207
Figure 8.8 Moisture profile for the instrumented test section from July 13th, 2023, to November 6th, 2023, in all granular layers as compared to precipitation data from Environment Canada. 208
Figure 8.9 Critical pavement responses due to tire-pavement interaction [91]. 210
Figure 8.10 Pressure profile over time for the instrumented test section, divided into right and left sensor arrays within the base, subbase, and subgrade layers. 214
Figure 8.11 Time-pressure profiles including right and left sensor arrays in base, subbase, and subgrade layers. Y-axis adjusted to highlight average trends, excluding major outliers. 215
Figure 8.12 High-speed pressure profile over a 24-hour period. 217
Figure 8.13 Strain-time profile from March 3rd, 2023, to November 6th, 2023. Includes data in the left and right sensor arrays, and in both the longitudinal and transverse directions. 219
Figure 8.14 High-speed strain profile over a 24-hour period. 220
Figure 8.15 Filtered high-speed strain profile over a 24-hour period. 221
Figure 9.1 LTPP database and information types that can be selected for each section [95]. 223
Figure 9.2 The structure of a TDMS file as per National Instruments [96]. 224
Figure 9.3 View of the remote desktop on-site. 225
Figure 9.4 View of the way data within TDMS files is stored on the on-site desktop. 225
Figure 9.5 File mirroring to transfer files to remote data storage, as seen from the on-site desktop. 226
Figure 9.6 Remote data storage, mirrored with the remote desktop on-site to collect data every 12 hours. 227
Figure 9.7 Within each monthly folder, the data developed is split daily. 227
Figure 9.8 Within each daily folder, the high-speed strain/pressure and low-speed trend data is stored. 228
Figure 9.9 Low-speed, trend data files, general information page. 229
Figure 9.10 Low-speed, trend data files, data collected per sensor. 229
Figure 9.11 High speed data files, data collected per sensor. 230
Figure 9.12 General logic for database development for this project and how it connects to the national database. 231
Figure 9.13 Similar project information from LTPP InfoPave [95]. 232

Figure 9.14 Example of low-speed trend data collected from the TDMS data system. 238
Figure 9.15 Example of high-speed trend data collected from the TDMS data system. 239
Figure 9.16 Trends analyses features within the LTPP database. 240
Figure 9.17 Comparisons analyses within the LTPP database. 240

List of Tables

Table 2.1 Most Common Sensor Types ([15] unless otherwise mentioned) 24
Table 3.1 Sensor Summary 41
Table 3.2 Sensor configuration, location relative to subgrade and sensor name(s) within the moisture tree 44
Table 4.1 Elastic Modulus Results from LWD Testing 71
Table 4.2 Deflection Results for LWD Testing 71
Table 4.3 Specimen testing information derived from the tests. 73
Table 4.4 Dynamic Modulus in MPa 74
Table 4.5 Phase Angle in Degrees 74
Table 4.6 Granular A Material Gradation 77
Table 4.7 Granular B Material Gradation 77
Table 4.8 Subgrade Material Gradation 78
Table 4.9 Mould Weight, Wet Soil Mass, Mould Dimensions, Specimen Volume, and Density for Eleven Mould Specimens prepared for Granular A, Granular B and Subgrade Soil 82
Table 4.10 Version 1: Volumetric Content Determination 82
Table 4.11 Version 2: Volumetric Content Determination 82
Table 4.12 Average Volumetric Moisture Content for the Granular A, Granular B and Subgrade Soil samples 84
Table 5.1 Truck Testing Information 89
Table 7.1 Chosen elastic modulus values for each layer. 175
Table 7.2. KENPAVE Input Parameters Summary 182
Table 7.3 Extracted braking Coefficients for Input into 3D-Move 183
Table 7.4 3D-Move Input Parameters Summary 190
Table 7.5 Average Compressive Stress/Pressure and Strain Results during TT#1 (Fall) 191
Table 7.6 Average Compressive Stress/Pressure and Strain Results during TT#2 (Spring) 192
Table 7.7. Average Compressive Stress/Pressure and Strain Results during TT#3 (Summer) 192
Table 9.1 Legend for Current Naming Convention 233
Table 9.2 Naming Convention, Data Collected and Output Units Produced for each sensor 235
Table 9.3 Calibration Factors related to each Sensor 236

Table 9.4 Examples of Information Included in the General Sensor Information Table, Part 1 237
Table 9.5 Examples of Information Included in the General Sensor Information Table, Part 2 237

Chapter 1
Introduction

Roadways are an undeniably important part of any nation's economy, as they facilitate the movement of people and goods. In Canada specifically, roads play a vital role in bolstering the economy and maintaining its competitiveness and productivity. They serve as the primary mode of transportation, surpassing rail, marine, and air travel as of 2021, according to Transport Canada in terms of usage for freight and passengers [1].

Canada has a combination of paved and unpaved roads (40 and 60%, respectively) that provide economic support and make up the country's vast network [2]. According to Statistics Canada, as of 2018 the nation had "…more than 1.13 million two-lane equivalent lane-kilometres of public road" [2, Sec.2]. In addition, the country includes over 38,075 lane-kilometres of highways as part of the National Highway System, or NHS [2], as seen in Figure 1. That number has likely increased since 2018, making Canada one of the nations with the largest road networks worldwide [3].



Figure 1.1 Map of the National Highway System in Canada, and its connection to the National Airport System, another important transportation mode [2].

Paved roads in Canada offer several advantages over unpaved roads, making them a preferred choice for many high-profile and complex road projects. In Canada's often harsh climates, roads provide a safe and reliable surface, ensuring smooth driving conditions with excellent traction. This enhances driving comfort and minimizes vehicle wear and tear, contributing substantially to road safety and efficiency [4]. This is especially important for long-distance travel and in urban areas with heavy traffic. In addition, well-designed paved roads are built with durability in mind and can withstand the stresses, strains and deflections imposed by heavy truck traffic as compared to unpaved roads which are prone to erosion and degradation [5]. Paved roads also provide an accessible means for people living in remote regions of Canada to access and be accessed by vital services, such as health care, trade, and commerce, as well as education, and make roads usable year-round [6]. Finally, a paved road surface and designed pavement structure protect the soil beneath it from environmental factors, such as freeze-thaw and moisture infiltration [7].

With this knowledge, there must exist the development and implementation of a plan to manage pavement assets within Canada, to firstly safeguard the nation's economy, and secondly to protect and manage the road network, which is in and of itself a very valuable (read: costly) asset.

Unfortunately, Canada is struggling in this regard. As a result of cuts in infrastructure spending in the 1980s and 1990s, the country is experiencing what is known as an "infrastructure deficit", which signifies a reduction in infrastructure spending and leads to delays in developing and maintaining new and existing infrastructure [8]. Although the early 2000s brought a much greater amount of investment than in the "golden years" of the 1960s and 70s, this period of budget cuts has led much of Canada's infrastructure, including its roads and highways, to fall into a state of disrepair [9]. This disrepair is felt even today, as described by the Canadian Infrastructure Report Card [10]. In 2019, the report card found that about 146,000 km of roads (16.4% of the nation's total) were in a "poor" or "very poor" state, while a little over 200,000 km (or 22.6% of the nation's total) were in a "fair" state [10]. A fair rating means that the "asset requires attention" [10, p. 8], since there are deficiencies, a poor rating means the asset is "approaching the end of its service life" [10, p. 8] and a very poor rating means the asset is "unfit for sustained service" [10, p. 8]. The exact values for this infrastructure deficit vary widely depending on the estimator, with an average value ranging between $110 to $270 billion for all infrastructure, with roads constituting a substantial portion [11].

The Core Public Infrastructure Survey, performed in 2020 by Statistics Canada, found that roads have a total replacement value of $894.2 billion, 42.6% of the almost $2.1 trillion in total infrastructure replacement value, excluding affordable housing [12]. This survey also found that roads are the

infrastructure that requires the most replacement from poor and very poor conditions (condition rating defined similarly to the Canadian Infrastructure Report Card).

Based on these statistics provided by both the Canadian Infrastructure Report Card and the Core Public Infrastructure Survey, pavement management and a pavement management system have become imperative to ensure that the conditions of the paved roads over an entire road network (such as that in Canada) are optimized to the best possible state depending on the available budgets and resources. These budgets and resources should be distributed efficiently and effectively across the network to address construction, operating and maintenance needs.

As stated in the 1993 AASHTO Guide for Design of Pavement Structures, pavement management, or PM, "…encompasses all the activities involved in the planning, design, construction, maintenance, evaluation and rehabilitation of the pavement portion of a public works program" [13, pp. I-31]. A pavement management system, or PMS, comes in as "…a set of tools or methods that assist decision-makers in finding optimum strategies for providing, evaluating, and maintaining pavements in a serviceable condition over a period of time" [13, pp. I-31]. A PMS is either a planning/analysis tool or a software program that will allow a practitioner to perform pavement management tasks [14].

The major components of a PMS include [15]:

1. A road network inventory, including road locations and geometries.
2. An assessment of road conditions, including pavement surface roughness, texture, skid resistance and structural properties. This is performed through what is known as a "condition survey".
3. A pavement performance deterioration model to foresee the deterioration rate of a pavement section based on load and environmental factors.
4. Maintenance decision criteria to serve as a baseline for acceptable and unacceptable pavement conditions.
5. A schedule of when maintenance and rehabilitation of the pavement network will occur.

1.1 Problem Statement

It is imperative that the condition of the pavement structure is accurately captured. Without this precision, the resulting data becomes unreliable, compromising the accuracy of assessments. This, in turn, hinders the ability to gather essential insights for the implementation of timely and effective maintenance and rehabilitation strategies, whether at the level of an individual pavement section or for the entire network [15].

Condition surveys currently are performed in one of two ways [15]:

1. Surface Condition Monitoring: investigated manually, through either expert visual inspection, equipped vehicles or equipment that will scan the pavement surface.
2. In-situ Condition Monitoring: investigated using sensing devices, which are embedded in the pavement structure and capture a variety of data types, such as stress, strain, deflection, moisture, temperature, etc.

In the pavement industry, the prevailing method for assessing pavements primarily involves monitoring surface conditions. However, this technique poses several challenges—it is time-consuming, demanding expert practitioners for both execution and data analysis, and incurs substantial costs [15], [16]. The most substantial drawback lies in its inability to offer continuous monitoring, typically occurring at intervals of a few years, which often proves impractical since pavement deterioration, although gradual, has the potential to change from season to season, meaning the assessment rate is limited [15], [16]. In addition, only assessing the pavement conditions at the surface ignores the fact that pavement deterioration could, in fact, begin within the granular layers. When surface distresses indicate the need for substantial or complete rehabilitation, destructive techniques such as coring or trenching need to be performed to understand the impact of damage in each specific layer [14].

In response to these challenges, in situ condition monitoring has emerged as a promising alternative, gaining traction in the literature [15], [16], [17], [18], [19], [20]. This method offers continuous, remote data collection for pavements, addressing the time and expertise constraints associated with surface condition monitoring. Eventually, this technology could enable the simultaneous monitoring of entire networks, where the generated data is automatically logged and seamlessly transferred to a database system, streamlining the overall conditions assessment process [14].

This approach contributes to the evolving field of "smart" pavements, which is typically understood as a road that incorporates advanced materials and technologies for active monitoring and adaptation. It aims to extend the service life, enhance the performance, and improve the safety of existing and new roads [21]. Smart pavements can provide real-time insights into pavement performance characteristics using Artificial Intelligence (AI) [19]. As part of the smart pavements concept, machine learning (ML) algorithms can signal when a specific pavement structure requires maintenance based on the actual structural responses of the pavement, [22]. Additionally, by applying machine learning concepts, environmental data for the section can be gathered to develop pavement degradation models and performance predictions for future climate change scenarios based on current climate and performance data [17], [19]. This is best expressed in the framework expressed in Figure 1.2, developed by Tavassoti

et al. in [19]. It demonstrates how the real-time monitoring of pavements, supported by a self-operating Big-Data gathering platform, could function and integrate AI models.

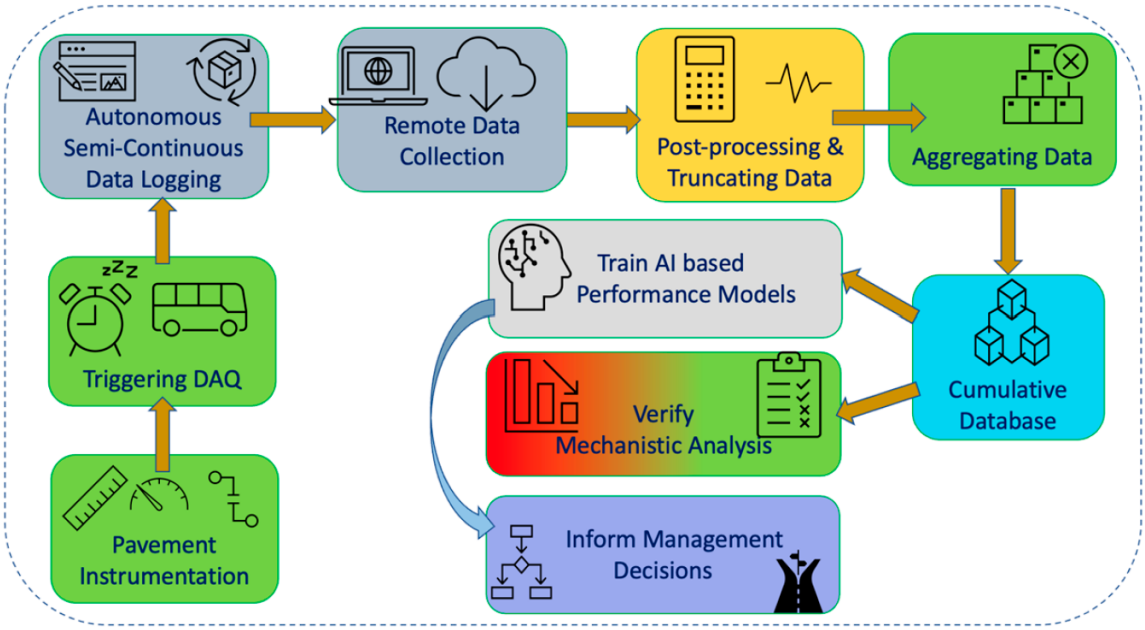


Figure 1.2 Framework for the implementation of a self-operating data gathering platform [19].

This thesis forms a part of the Smart Pavements project at the University of Waterloo, fronted by the work performed by Jianqi Kang [22]. The continuation of the project seeks to construct and assess the responses from an actual flexible pavement instrumented section, located in Southwestern Ontario, Canada. It begins the data collection and cleaning processes and undertake preliminary assessments to gain an initial understanding of the pavement structural response to various loads, environmental conditions, and seasonal variations. This aims to advance work towards the integration of AI/ML-aided predictive modelling within this and other instrumented test sections for pavement performance prediction and climate change impact prediction objectives [19].

Preliminary data assessment work is very important since in the literature, there is a lack of published in-depth assessment on the initial pavement performance and responses of an instrumented pavement section. Heavy vehicles, such as trucks, exert the greatest impact and inflict the greatest damage to pavement structures. Therefore, they are the vehicle of choice during relevant tests in this study.

Through careful screening of the literature, it was found that there is limited research in the following areas:

1. The responses of a pavement structure during the construction phase and what impacts are exerted by heavy vehicles on freshly placed asphalt. This study will address this gap by collecting pavement structural response data using a controlled truck test immediately after the placing of a Hot Mix Asphalt (HMA) layer.
2. In-depth heavy vehicle (truck) testing analysis performed over various seasons overtop an instrumented test section. This gap in research limits a thorough understanding of the relationships between a pavement section's structural responses over various HMA and ambient temperatures. This study will seek to address this gap by undertaking a more extensive assessment compared to that in the existing literature, where truck tests are typically conducted during only one test/day/season.
3. Long-term trends and assessments of load and environmental data collected for an instrumented test section for a busy arterial roadway, and a look into sensor functionality based on these trend results. This study will seek to address this gap through the collection of real-time data from the instrumented test section over multiple months and seasons and assess the trend results.
4. A comparison between the response magnitude and shape of an embedded sensor and the extent of vehicle tire deviation (known as vehicle "wander") as a heavy vehicle attempts to pass over that embedded sensor. In essence, there is a lack of understanding of how vehicle wander impacts the pavement sensor responses. This study will address this gap by deliberately testing sensor responses at various lateral deviations from the sensor arrays and developing correlations.
5. The comparison between static and dynamic pavement response simulation methods, especially over various seasons, and speeds and how it will compare to embedded sensor field results. This study will work to address this gap by modelling the truck testing performed over several seasons in two common static and dynamic pavement software and comparing them to the field results.

Therefore, this thesis will seek to do this work to advance future pavement performance prediction research.

1.2 Research Objectives & Methodology

In the realm of smart pavements, in-situ monitoring offers real-time insights into pavement condition, aiding timely maintenance and averting costly rehabilitation. Unlike traditional methods, it allows proactive interventions, saving both time and resources in pavement management. Furthermore, in-situ

pavement monitoring lessens the need for frequent surface condition checks and invasive borehole analysis. It provides personalized, localized data on the impact of loads and environmental factors on pavement degradation, enabling customized performance predictions at sensor-installed locations. Lastly, when enhanced with AI/ML predictive capabilities, these algorithms could forecast the timing of needed pavement maintenance strategies and continually adjust these predictions in real-time as conditions evolve. With the unpredictable impact of climate change, aging infrastructure, and urban population growth in Canada, integrating advanced monitoring and predictive technologies becomes increasingly vital for effective infrastructure management and sustainability.

This research aims to contribute to the implementation of embedded sensors within pavements as part of an improved national pavement management system. This is done by providing a comprehensive assessment of the implementation, data collection, data analysis and database development processes of an instrumented test section located on Courtland Avenue in Kitchener, Ontario, Canada. This instrumented test section provides a means to assess and test the functionality of an embedded sensor network on an arterial roadway, develop a framework for sensor implementation, collect preliminary sensor data for both traffic loads and environmental responses and describe lessons learned for future projects and applications of this technology.

The following research objectives are addressed in this thesis based on the problems described in the previous section:

1. Synthesize the historical and recent works regarding pavement distresses, current pavement monitoring practices and limitations, examples of sensors and test sections in past studies, applications of pavement performance monitoring and current research gaps.
2. Provide practical documentation of the instrumentation as well as the field and laboratory testing processes for the pavement section selected for analysis. This section describes the construction, materials, and procedures used and performed, as well as presents results and challenges.
3. Conduct a comprehensive, multi-seasonal assessment of the responses received from the instrumented test section. This is attained through a series of controlled truck tests in which pavement data such as strain, stress, moisture, and temperature data at various truck speeds and various pavement temperatures were collected. Assessments are done during various construction conditions, including different seasonal temperatures and pavement structures.
4. Provide detailed strain, pressure and moisture trend results over a period of about nine months over various seasons to assess sensor functionality.

5. Model the results of several truck tests performed over various seasons in KENPAVE and 3D-Move software and validate these results with the field measurements to understand the software's accuracy and reliability in modelling pavement damage under local conditions.
6. Develop correlations between a heavy vehicle's tire position and the pavement response to assess the impact of wander on pavement response.
7. Develop a rudimentary database concept for the organization and dissemination of the data collected at the instrumented test section.

1.3 Thesis Structure

This thesis contains ten chapters:

- Chapter 1: Introduction
  - Presents the thesis context, and provides a statement of the objectives, research and thesis methodology and summary of contributions.
- Chapter 2: Literature Review
  - Presents a review of relevant literature, encompassing topics on common pavement distresses, current pavement monitoring practices and limitations, several key examples of previous instrumented pavement sections, typical sensors used in pavement monitoring, pavement performance prediction models and climate change applications. Research gaps are explored.
- Chapter 3: Trial Section Design and Construction
  - Outlines the design, rationale, and configuration of the instrumented test section. The data gathered plays a crucial role in the subsequent chapters of this thesis, where further analysis and interpretation are detailed.
- Chapter 4: Construction, Field, and Laboratory Testing
  - Outlines the results of the various post-construction/field and laboratory testing actions and procedures undertaken to obtain further information on the properties of the various materials in the pavement structure. This section is divided into two sections: post-construction field testing and laboratory testing.
- Chapter 5: Truck Testing Evaluation and Results
  - Describes the results from the series of controlled truck tests performed on the Courtland Avenue instrumented test section. Various tests are performed over various seasons/temperatures and truck speeds to assess the impact on the pavement response.
- Chapter 6: Quality Control for Data Analysis

- Examines the correlation between truck trajectory and pavement response to establish a link between the truck tire’s lateral movement and the sensor's reaction. These tests use a truck of known weight and axle configuration to traverse the sensor-installed test section at various distances from the sensor arrays.

- Chapter 7: Pavement Section Modelling
  - Compares KENPAVE and 3D-Move software tools for predicting pavement response in the project. It involves modelling truck tests conducted across different seasons in both software programs and validating these results with field measurements to gauge accuracy and reliability. Additionally, it offers lessons learned and acts as an example for future test sections with similar needs for simulating and modelling pavement structures across varying seasons and speeds.
- Chapter 8: In-Service Pavement Performance Trends
  - Focuses on trends observed in environmental and traffic load data collected from the Courtland Avenue instrumented test section since the full deployment of the DAC system, including sensor installation, power supply, and initial calibration. The primary goal is to evaluate sensor effectiveness by analyzing the data for meaningful insights and verifying their reliability. The term “performance” is used as a general term to describe the results obtained from moisture and temperature sensors, and the responses obtained from the load sensors.
- Chapter 9: Database Development
  - Outlines the development of a specialized database for collecting and storing data from this pavement section and comparable projects. The aim is to create a database concept that can incorporate artificial intelligence algorithms and ensure nationwide accessibility, streamlining information dissemination to diverse agencies.
- Chapter 10: Conclusions and Recommendations
  - Provides a summary of the work performed in this project, the contributions of this research and the recommendations for future work.

Chapter 2
Literature Review

This Chapter presents a review of relevant literature, encompassing topics on common pavement distresses, current pavement monitoring practices and limitations, several key examples of previous instrumented pavement sections, typical sensors used in pavement monitoring, pavement performance prediction models and climate change applications. Research gaps are explored.

2.1 Pavement Distresses

The prevalent "poor" or "very poor" condition of the majority of Canada's paved road network can be attributed to a substantial degree of pavement distress. This distress is a natural occurrence in all pavements and is influenced by various factors. These include load-related factors, such as those imparted on the pavement structure from passing heavy vehicles. When the road is under designed for the current traffic Equivalent Single Axle Loads (ESALs), where traffic volume exceeds the design capacity, the rate of deterioration intensifies. In addition, the type of tire, axle position and configuration, as well as the speed of the passing vehicles can also impact the pavement structure [23].

Beyond load factors, environmental elements also exert a substantial impact on the pavement deterioration process. Daily and seasonal temperature fluctuations, coupled with phenomena such as freeze-thaw cycles, pose substantial challenges to the structural integrity of the pavement. The expansion and contraction resulting from temperature variations, especially in regions experiencing extreme climate conditions, contribute to the development of cracks and other distress types. In addition, the moisture and radiation content also contributed to pavement deterioration [23].

Finally, various design and construction-related issues further contribute to pavement distress. Poor drainage practices can lead to water accumulation, compromising the pavement's foundation and accelerating deterioration. Material deficiencies, construction-related lapses, and suboptimal design choices, such as pavement layer thicknesses, types and properties also play pivotal roles in determining the long-term resilience of the pavement structure [23].

Figure 2.1 shows all of these factors visually and the interplay between each of the factors and how they relate to each other. In essence, all of the factors do contribute to each other and all need to be taken into consideration when determining the source of pavement distresses and what maintenance and rehabilitation methods to use.

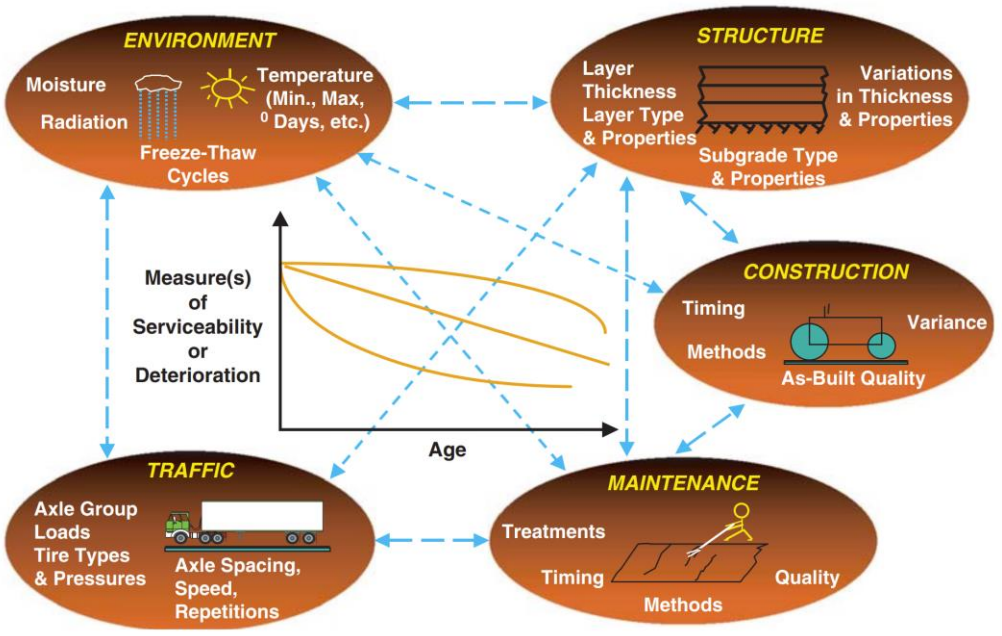


Figure 2.1 Factors affecting pavement performance and the interactions between those factors [23].

2.1.1 Common Types of Flexible Pavement Distresses

There are various kinds of performance distresses that impact both rigid and flexible pavements. These can be classified into several major categories, which include [14]:

1. Cracking: fatigue cracking, block cracking, edge cracking, longitudinal and transverse (thermal) cracking, and reflection cracking at joints.
2. Patching and potholes
3. Surface deformation: rutting and shoving
4. Surface defects: bleeding and raveling

For flexible pavements, some of the most addressed distresses include rutting, transverse and longitudinal cracking, fatigue cracking and potholes [14].

2.1.1.1 Rutting

Rutting typically shows up as a surface depression present within the wheel path [24]. When permanent deformation occurs in any of the pavement layers or subgrade soil, ruts can appear. There are three kinds of ruts that can appear, which include [24]:

1. Mix Rutting: rutting that occurs within the HMA layer, typically because of mix/compaction problems.

2. Subgrade Rutting: rutting that occurs due to consolidation as a result of loading.
3. Densification: rutting that occurs as a result of poor asphalt compaction during construction.

Figure 2.2 shows examples of all three of these rutting types.

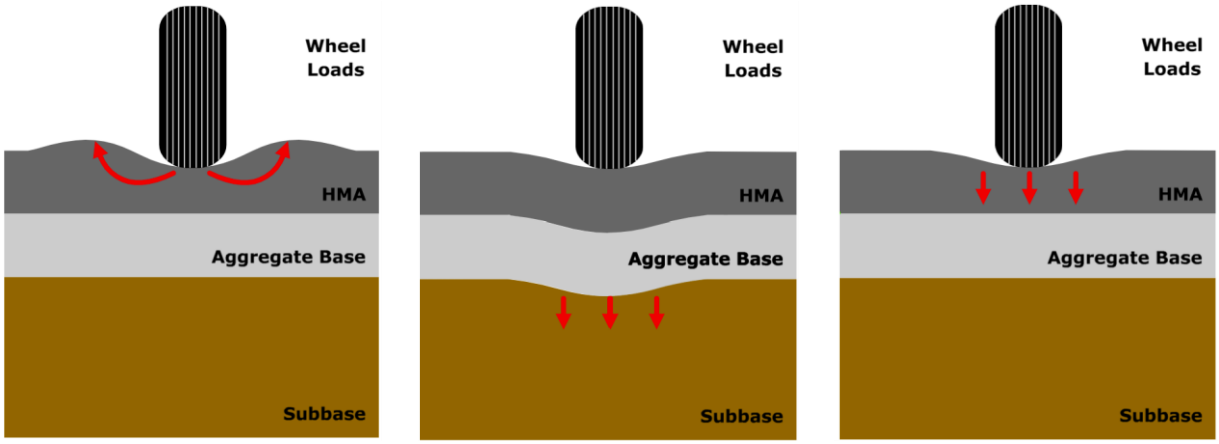


Figure 2.2 Examples of Mix Rutting (left), Subgrade Rutting (middle), and Densification (right) [24].

2.1.1.2 Transverse Cracking

Transverse cracking typically shows up as cracks across the lanes of asphalt, perpendicular to the direction of traffic. This kind of cracking is also called thermal cracking since the main cause of transverse cracking is the shrinkage of the HMA layer under cold weather conditions [25]. Figure 2.3 shows an example of a transverse crack, situated perpendicular to the direction of traffic.

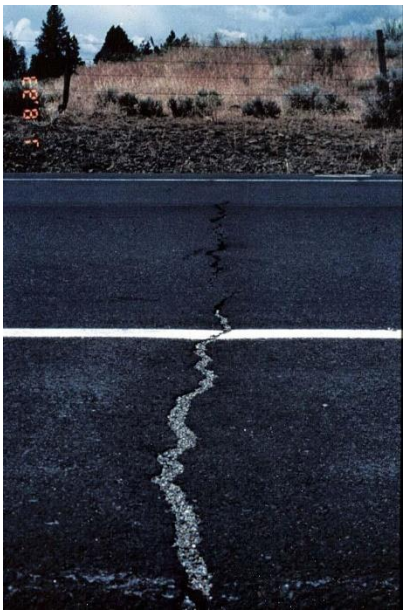


Figure 2.3 Example of a transverse crack across the surface of a pavement structure [25].

2.1.1.3 Longitudinal Cracking

On the other hand, longitudinal cracks typically show up as cracks that are in the same direction as that of the traffic passing on the pavement surface. An example is shown in Figure 2.4. Because pavements are typically constructed by pouring out lanes of pavement (see Figure 2.5), the joints where the lanes of pavement meet become areas sensitive to loads if poorly constructed [26]. Other potential causes include HMA fatigue and top-down cracking [26].



Figure 2.4 An example of longitudinal cracking [26].

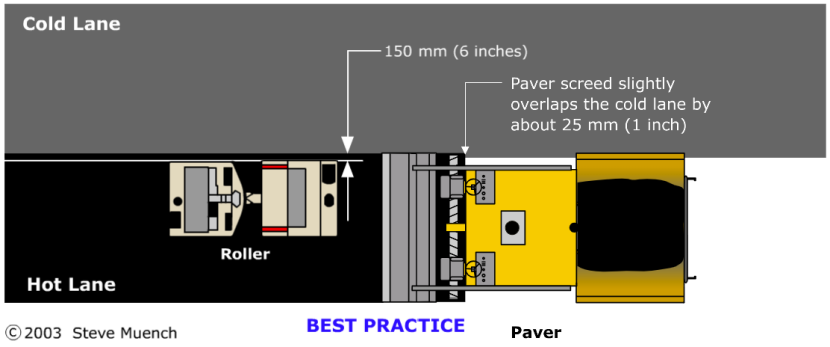


Figure 2.5 An example of how to properly pave a roadway to minimize the appearance of longitudinal cracks [26].

2.1.1.4 Fatigue Cracking

Fatigue cracking, an extension of transverse and longitudinal cracks, manifests as a connected matrix of cracks that are either localized or that span the pavement. Various factors contribute to its occurrence, such as a decline in load support characteristics of the granular layers [27]. Repeated traffic loading or

increased loads beyond pavement design capacity are common triggers [27]. The manifestation of fatigue cracking differs in thin and thick pavement HMA layers. In thin pavements, cracking initiates at the bottom due to heightened tensile stresses, progressing upward—termed bottom-up fatigue cracking. In thick layers, cracks result from repeated pressures by heavy vehicles on the surface, known as top-down fatigue cracking [27]. An example of this distress is shown in Figure 2.6.

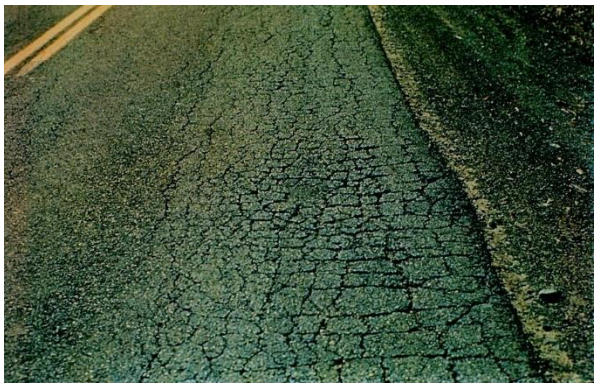


Figure 2.6 An example of fatigue cracking [27].

2.1.1.5 Potholes

Finally, potholes are pavement distresses that appear for the most part because of moisture accumulation and the inability of the HMA layer to support freeze-thaw loads, due to insufficient thickness. An example of this distress is shown in Figure 2.7.

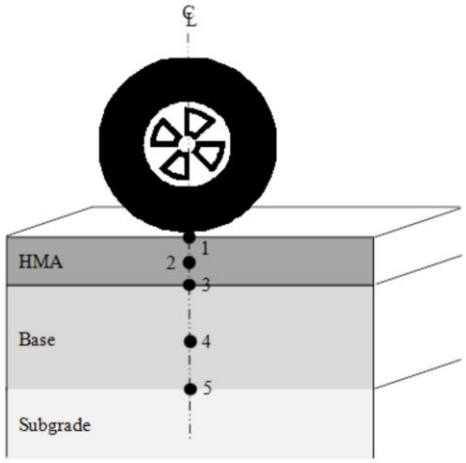


Figure 2.7 An example of a pothole [28].

2.1.2 Critical Response Points within Pavements

To ensure a pavement design minimizes the distresses mentioned earlier, a crucial step involves understanding the critical response points within flexible pavement structures. This understanding is pivotal not only for accurately predicting pavement performance degradation but also for strategically placing instrumentation in instrumented test sections. Figure 2.8 provides a visual representation of a

basic flexible pavement structure, featuring a tire symbolizing the load on the pavement. The diagram illustrates five key points in the pavement structure influenced by applied loads, based on layered elastic theory. It was developed by the FHWA [29].



1. Tensile horizontal strain at top of HMA layer
2. Compressive vertical stress/strain within HMA layer
3. Tensile horizontal strain at bottom of HMA layer
4. Compressive vertical stress/strain within the base/subbase layers
5. Compressive vertical stress/strain at the top of the subgrade

Figure 2.8 Critical response points in a flexible pavement structure [29].

Examining these points, the first and third points on the surface and bottom of the HMA layer, respectively, play a substantial role in determining fatigue cracking. The horizontal tensile strain at these locations is crucial. When a load is applied, the asphalt layer acts like a beam, experiencing tension at the bottom and compression at the top. In flexible pavement, when deflection occurs due to load application, compressive horizontal strain forms at the top and tensile horizontal strain forms at the bottom of the HMA layer. Given the weaker tensile strength of asphalt, the bottom of the asphalt layer becomes particularly critical. In cases of tension-induced issues, cracks are more likely to initiate at the bottom of the asphalt layer than the top. Additionally, attention must be given to deflection in the vertical direction at the top of the pavement layer.

Moving to points two, four, and five, the focus shifts to compressive vertical stress and strain within the HMA layer, vital in assessing rutting failure [29]. The top of the subgrade layer emerges as the most critical point among these, as excessive deformation at the bottom could lead to the appearance of rutting and is closely related to fatigue cracking. Therefore, meticulous consideration of vertical stresses and strains is paramount in pavement design.

2.1.3 Pavement Distress Impact on Pavement Performance

Once a pavement section is constructed, deterioration sets in due to various forces, especially load and environmental factors, leading to pavement distress as discussed in the previous section. Without maintenance and rehabilitation actions integrated into a Pavement Management System (PMS), the pavement structure will degrade over time. Figure 2.9 illustrates the deterioration process of a road, representing it as a function of a condition rating (see Section 2.2.1), and the pavement's age. The condition rating assesses the pavement section on a scale from very good (newly built) to very poor (unusable). As a pavement degrades and goes from very good to very poor, the rate of deterioration increases, and maintenance and rehabilitation actions become more and more necessary. At the same time, the costs of the maintenance and rehabilitation activities will also become more expensive, with initial deterioration requiring minor repairs such as seals, and heavy deterioration requiring actions such as full-depth reclamation or reconstruction.

Pavement deterioration curves play a crucial role in developing and understanding pavement performance prediction models, as is discussed in future section.

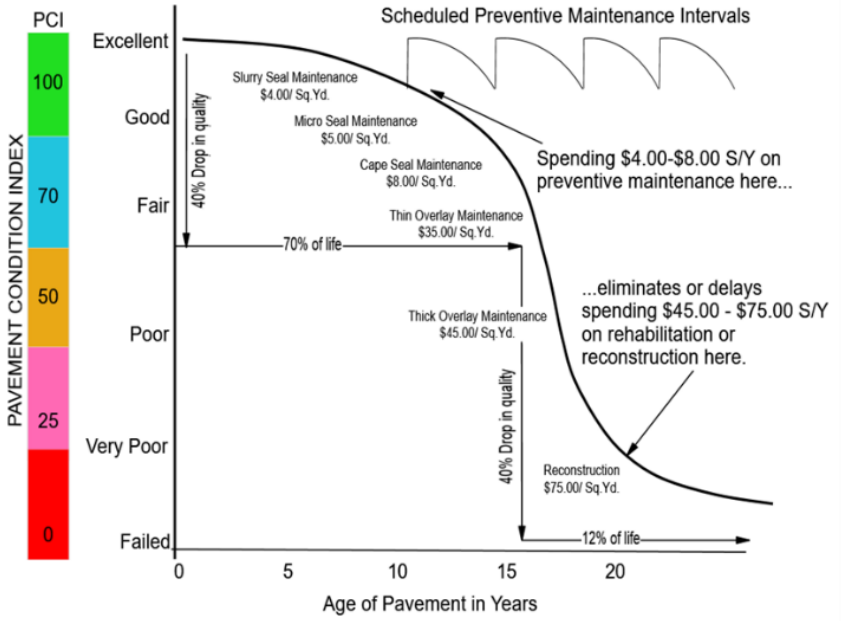


Figure 2.9 General pavement deterioration curve as a function of pavement condition and age [30].

2.2 Current Pavement Monitoring Practices and Limitations

2.2.1 Condition Surveys

At the end of Section 1.1, it is highlighted that a key element of a PMS is the Condition Survey, which involves evaluating current road conditions and recording them for future analysis. Agencies utilize this data to create precise pavement performance deterioration models. Subsequently, they establish thresholds and criteria to identify the allocation of resources within a pavement network.

Two types of pavement condition assessments exist [14]:

1. Project-Level Assessment: concentrate on designated sections of the pavement network, where comprehensive lab and field data are collected during scheduled projects. These assessments include technical and economic analyses of project alternatives, leading to the selection of options, detailed quantities, and the development of costs and schedules. Essentially, a project level investigation scrutinizes the specifics of deterioration within a small section of the pavement network.
2. Network-Level Assessment: cover a broader scope than project level surveys, encompassing more roadway in their evaluation. These surveys involve creating a comprehensive database of historical distresses and conditions across the network to develop performance prediction models. Alternatives are identified at a more general level, and priority programs are established in this context.

Typically, the type of pavement condition data collected includes [14]:

1. Distress Data: assessing the visible distresses present on the surface of the pavement.
2. Structural Capacity: assessing the pavement's ability to withstand currently applied traffic loads.
3. Surface Characteristics: assessing the pavement's smoothness and surface texture. Some condition indices that follow from this include [31]:
    a. Pavement Condition Index (PCI): a method developed to assess the integrity and operational condition of pavements. It uses a numerical scale from 0 (failed) to 100 (perfect) based on visual surveys. The index considers distress type, severity, and density on the sample unit. While ensuring accurate results, the PCI requires precise input data and is influenced by human capacity for distress detection, making it a time-consuming process.

b. International Roughness Index (IRI): a standardized measurement of pavement roughness. It classifies ride quality based on the longitudinal profile of the wheel path. IRI is calculated as, "…the filtered ratio of the accumulated deviation of the vehicle's suspension divided by the traveled distance" [31, p. 5]. Pavement roughness is crucial for ride quality, comfort, and safety. Unit: m/km or in./mi.

c. Present Serviceability Index (PSI): a metric employed to characterize the functional performance of a pavement in terms of ride quality, performed by visual inspection. It assesses the road's capacity to accommodate traffic, considering various factors like slope variation, rut depth, surface cracking, and patched areas. PSI offers a holistic appraisal of pavement conditions, addressing safety and comfort concerns.

Data can be collected through either destructive or non-destructive testing. Destructive testing involves damaging the pavement structure to assess what's underneath, providing insights into material quality, layer thickness, and potential damage. Non-destructive testing uses various technologies or visual surveys to assess pavement condition without damaging the structure. Non-destructive methods are preferred for network-level analysis, while destructive methods are commonly used in project-level analysis [14].

It has been found that the current condition survey assessment process has issues with data quantity, data quality, and data consistency [14]. It is currently quite expensive to collect large quantities of data on a regular basis, therefore agencies need to budget how much data they want to collect. In addition, it is important that the data being collected is accurate otherwise there could be an erosion of confidence in the system of pavement management. Finally, there appears to be a lack of standardization when it comes to pavement performance assessments. This is because there's many approaches to doing this currently, and depending on the agency and equipment being used, the conditions being assessed can vary [14].

2.2.2 Destructive Testing Methods for Structural Capacity Assessment

As this Smart Pavement project specifically focuses on structural response through pavement instrumentation, methods for structural capacity analysis, whether destructive or non-destructive, are discussed to understand current practices.

Destructive testing methods for structural capacity analysis, including trenching, coring, and auguring, are employed by pavement agencies to accurately assess problematic pavements [32]. This allows them to gather materials for subsequent laboratory testing. Non-destructive testing methods, discussed in Section 2.2.3, struggle to differentiate between layers in a pavement structure, making it challenging to pinpoint problematic layers without cutting open the entire structure [32]. The variations in destructive evaluation methods primarily revolve around how the pavement structure is cut, as detailed in the following sections.

2.2.2.1 Trenching

Trenching involves making a rectangular cut into the pavement structure, excavating deep enough to remove the HMA layer and collect samples from the granular layers below [32]. If needed, the trench walls can be further cut to assess underlying layers. Refer to Figure 2.10 for an illustration of the trench cut procedure.



Figure 2.10 Images showing the trenching process; cutting a trench (left) and the visible trench layers (right) [32].

2.2.2.2 Coring

In this procedure a core sample is extracted using a core rig. The cores are typically 4 to 6 inches in diameter and are tested using a Hamburg test or an overlay test if required [32]. An example of coring the pavement structure can be seen in Figure 2.11.



Figure 2.11 The coring of a pavement section using a core rig [32].

2.2.3 Non-Destructive Testing Methods for Structural Capacity Assessment

As compared to destructive testing, non-destructive testing methods are faster, less damaging to the pavement structure, and more cost effective. As mentioned by Karimi and Mallick [17], there are several kinds of NDT's, such as the falling weight deflectometer, lightweight deflectometer, ground penetrating

radar, Benkelman beam deflection, seismic pavement analyzer, dynamic cone penetrometer, road surface analyzer, time domain reflectometry, etc. Two examples are shown in the next sections.

2.2.3.1 Falling-Weight Deflectometers (FWD) and Light-Weight Deflectometers (LWD)

A Falling Weight Deflectometer (FWD) attempts to replicate the loading from a standard truck on the pavement surface. It works by applying an impulse load, ranging from 4.45 to 156 kN, with a pulse and measuring their vertical and deflection responses in a radial fashion from the loading axis [17]. Variations like Light Weight Deflectometer (LWD) and Heavy Weight Deflectometer (HWD) cater to different impact loads [17], with LWD being suitable to be performed by hand and HWD being suitable for airport pavement evaluation. The elastic modulus of pavement layers is determined through an iterative process [17]. A diagram of an FWD is shown in Figure 2.12.

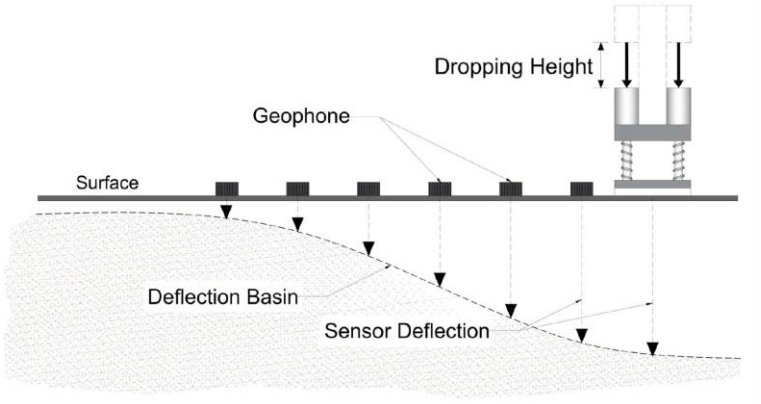


Figure 2.12 How an FWD functions [17].

2.2.3.2 Ground Penetrating Radars (GPR)

Ground-Penetrating Radar (GPR) functions by transmitting high-frequency electromagnetic waves that reflect from boundaries with varying electromagnetic properties. Various material properties, including permittivity, conductivity, and permeability, influence the time and velocity of wave travel, provide information on the depths of reflected interfaces [17]. GPR is widely used for tasks such as measuring pavement layer thicknesses and understanding the objects located beneath the pavement structure. A diagram of a GPR is shown in Figure 2.13.

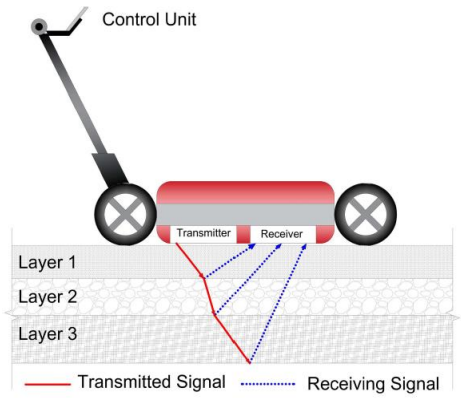


Figure 2.13 How a GPR functions [17].

2.3 Pavement Monitoring and Instrumentation

As was discussed at the beginning of Section 0 and in Section 2.1.3, due to a variety of factors such as traffic loads, environmental conditions, and issues with the design and construction of pavement structures, the formation of various distresses (e.g., rutting and fatigue cracking) can occur, leading to excessive stresses, strains and deflections at the critical response points of a pavement structure. These distresses can accelerate the aging of a specific pavement section within a network, leading to premature failure. This is why concepts such as PM and PMS exist and incorporate ideas such as pavement performance prediction to discern the likely point of failure for a given pavement section based on prevailing traffic and environmental conditions. Being able to better predict the point when a pavement section will fail allows for the timely implementation of maintenance and rehabilitation actions.

As was previously discussed, current methods of pavement condition assessment may not accurately predict pavement responses due to the consistently variable nature of traffic and environmental load changes that most, if not all, pavement sections experience over their service life. Because of this, current condition assessment methods cannot keep up with the changes and may collect inaccurate results. This has been shown in the literature, such as in Tighe, Huen and Haas [23] who acknowledged the "inherent variability of pavement material properties and the lack of precise measuring of traffic load and environmental effects" [23, p. 339] when it comes to the development of performance models and the data that should be included within them. If general calibration factors and performance data are applied and utilized during the design process as is done using the current methods, then it is more likely that a pavement section will experience premature failure [17]. That is why data collected in real-time is extremely important to generate accurate pavement life predictions and to be able to use resources the most effectively in local projects [17].

Implementing in-situ pavement instrumentation offers a valuable means to gather this real-time data on specific pavement sections or networks, enhancing the calibration and performance prediction process [17]. With the implementation of instrumented pavement sections, modern tools like AI and ML can be incorporated as part of pavement performance prediction to automatically predict and notify pavement engineers when certain pavement sections may require mitigation strategies [22].

Beyond predictive maintenance, these instrumented sections can also identify overloaded trucks on pavements, quantify their impact, and promptly notify relevant agencies [17]. Additionally, the system can signal when a road section experiences higher-than-designed real-time traffic and loads [17]. There have also been indications from the literature that the benefits of instrumented pavement sections can contribute to the design of perpetual pavements, which are meant to withstand their design loads for long periods of time, as described in detail by Karimi and Mallick [17]. Pavement instrumentation can help to evaluate the endurance limits of current in-service pavements for a specific geographic location.

And considering the increased concerns regarding climate change and the need for resilience, real time payment response data can help designers understand the effects of environmental stressors like high temperatures, increase the moisture, etc. [19] [17]. As mentioned by Karimi and Mallick, the use of embedded payment instrumentation can lead towards “the construction of genuinely sustainable pavements” [17, pp. 03123001-1].

2.3.1 Sensors used within Instrumented Test Sections

For an instrumented test section, practitioners can choose from a range of sensors based on their specific data collection needs. The literature explores various types, locations, and arrangements of sensors, with the selection depending on the practitioners' requirements [33] [15] [17] [34]. These sensors can measure diverse physical parameters in the pavement structure, including stress, strain, deflection, moisture, and temperature.

Strain sensors are valuable tools for measuring critical strains in pavement structures under dynamic loading, particularly those located at the bottom of the HMA layer. These sensors play a crucial role in assessing fatigue failure, rutting, and permanent deformations in flexible pavements, which often result from high tensile strains at the bottom of the asphalt layer [34]. By monitoring pavement response over time and indicating strain evolution, strain sensors enable practitioners to make predictions related to fatigue and rutting [15]. When it comes to measuring strain in the pavement structure, the choice of sensors depends on whether it is in bonded or unbonded layers. In bonded layers, common strain gauges include foil gauges, H-gauges, and strain coils. On the other hand, for unbonded layers, inductive coils and LVDT-type strain gauges are common [34]. A key concept in many strain gauges is the Wheatstone

bridge, which generates voltage and measures strain. The bridge allows for changes in resistance, altering the voltage of a transducer [17]. When one resistor is unknown, that's where the strain measurement is derived.

The equation of a Wheatstone bridge is [17]:

$$\varepsilon = \frac{\frac{\Delta R}{R}}{G} \tag{1}$$

Where G = gauge factor, ε is the strain, ΔR is the change in strain gauge resistance and R = unstrained resistance of the strain gauge. Figure 2.14 shows a typical schematic of a Wheatstone bridge.

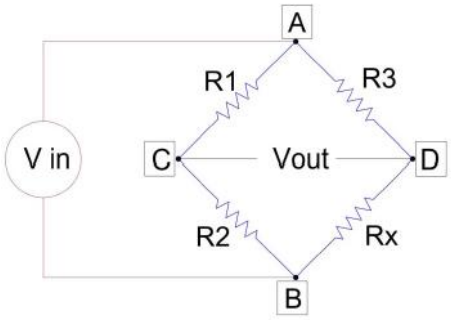


Figure 2.14 Wheatstone bridge schematic [17].

Pressure sensors or pressure cells measure the compressive stress in the road structure, and these are typically placed in the granular layers or unbound layers [15]. There are several kinds of pressure cells and the two most common are hydraulic and diaphragm based [34]. The hydraulic pressure cells have two steel plates filled with a liquid and the pressure is based on the liquid pressure that is measured within the sensor. A diaphragm-based pressure cell has a stiff ring that supports a diaphragm which induces deflection and thus can be translated into a pressure measurement [34].

Deflection sensors play a crucial role in assessing how the pavement structure responds to load. They prove instrumental in determining both the structural layer stiffness and the subgrade resilient modulus. Deflection sensors come in various categories, including acceleration measuring sensors, velocity measuring sensors, and deflection measuring sensors [34]. The first two categories necessitate signal integration before deflection measurement, whereas the last category directly measures deflection [34].

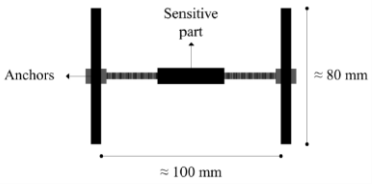
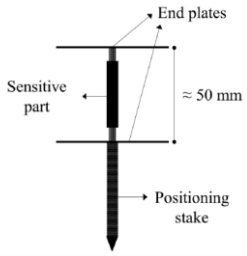
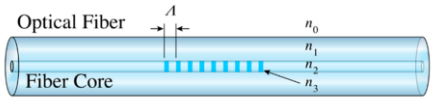
Moisture sensors pick up changes in moisture within the various layers of the pavement structure, typically the granular and other unbound layers. Moisture is a key indicator for water accumulation which is detrimental to the pavement structure. With moisture sensors, the electric pulse is affected by the moisture content. Typically, when there's more moisture, the signal will run more slowly indicating that

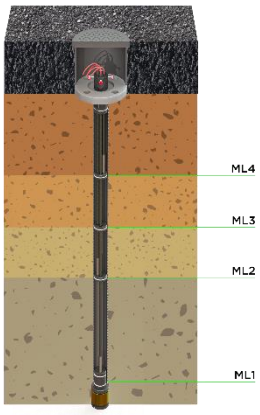
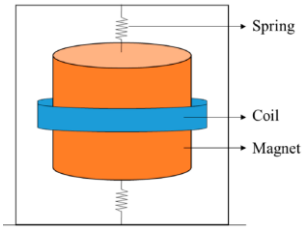
there is a higher moisture content [17]. Therefore, knowing the moisture content of the instrumented test section can provide further insights.

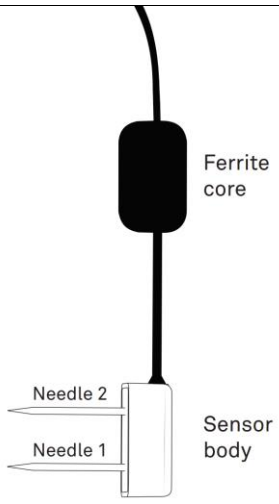
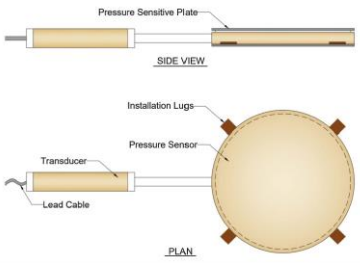
Temperature sensors are instrumental in monitoring the temperature of different layers [15], and their placement substantially influences the data they capture. Temperature plays a pivotal role in structural responses, impacting factors like strain, displacement, and pressure [15]. By gaining insights into the temperature variations within pavement layers, a more comprehensive understanding of the reasons behind specific pavement responses can be achieved.

The most common sensors that are used in an instrumented test section are described in Table 2.1 along with information regarding the sensor and an image to depict what the sensor looks like.

Table 2.1 Most Common Sensor Types ([15] unless otherwise mentioned)

Sensor Name	Sensor Information	Image
Horizontal Asphalt Strain Gauge (HAST)	HASTs, positioned at the bottom of bituminous layers, measure horizontal strain magnitude in pavement under dynamic loading. The sensors' H-shaped design improves anchoring in asphalt. The central bar, comprising one to four active strain gauges in various configurations, contains the sensitive part. Under strain, the anchors elongate the central bar which produces a resistance variation based on the gauge factor (GF), a measure of sensitivity to strain.	
Vertical Asphalt Strain Gauge (VAST)	Like their horizontal counterparts, VASTs consist of a sensitive part held between two circular plates. The bottom plate stabilizes the sensor, while the top plate evenly transfers the load to the central bar. This sensor also includes a sharp stake for insertion into the underlying layer, operating similarly to HASTs. However, VASTs statistically exhibit a lower survival rate compared to their horizontal counterparts.	
Fibre Optic Sensors (FOS)	An FOS employs an optical fiber connected to a light source for detecting specific quantities. These sensors, valued for their small size, flexibility, embeddability, and resistance to electromagnetic interference, provide crucial information about pavement conditions. They enable high-precision local or distributed strain measurements and come in discrete, quasi-distributed, and distributed configurations.	

Linear Variable Differential Transformer (LVDT)	LVDTs measure vertical road pavement deflection by converting relative displacement into voltage. A securely anchored reference rod minimizes surface loading-induced deflection. Options include single layer deflectometers (SLDs) for specific layer measurement and multi-depth deflectometers (MDDs) for assessing deflection at various points in the pavement structure.	 [35]
Accelerometers	An accelerometer measures velocity change in one or multiple directions, allowing for pavement deflection calculation by double integration of the signal. Unlike LVDTs, accelerometers don't require a reference point, as acceleration is an absolute value. The device consists of a mass connected to a spring, experiencing acceleration under applied force, with displacement proportional to acceleration.	 [36]
Geophones	Geophones measure pavement displacement velocity under moving loads, obtaining deflection response through signal integration. Comprising a mass connected to a spring and a coil, geophones induce voltage proportional to displacement velocity. They exhibit nonlinear response and amplitude attenuation below their natural frequency, limiting measurements to frequencies above a minimum threshold.	
Thermocouples	Thermocouples are the most used probes for pavement temperature measurements. They function based on the small voltage generated at the junction of two dissimilar metals, a voltage that varies with temperature. Various types of thermocouples, such as K, E, or T, provide a wide temperature range for measurement, albeit with less accuracy compared to other temperature sensors.	
Thermistors	Thermistors, with resistance dependent on temperature, exhibit greater sensitivity than standard resistors. While they operate within a narrower temperature range than other sensors, they enable more precise measurements.	 [35]

Moisture Probes	TDR probes, the prevalent moisture probes, operate on time domain reflectometry. They send an electric pulse through a waveguide, and its progression reflects the moisture content in the pavement. The reflected pulse, detected at the end of the waveguide, correlates with moisture content. This device achieves a 0-100% water content measurement with 1% accuracy.	 [37]
Pressure Cells	Two main types of pressure cells are hydraulic and diaphragm based. Hydraulic pressure cells consist of two steel plates filled with liquid, and the pressure is determined by measuring the liquid pressure within the sensor. In contrast, a diaphragm-based pressure cell involves a stiff ring supporting a diaphragm, which undergoes deflection, translating into a pressure measurement.	 [17]
Weigh In Motion (WIM) [17]	WI M sensors record of vehicles Axel response and is able to sense the weight of vehicles. It is meant to ensure the weight of vehicles that are using a specific roadway to make sure that they don't exceed the design loads. There are four types of sensors and each one can accommodate various speed Rangers. They're typically applied over the lane in a perpendicular direction to the direction of traffic	 [38]
Data Acquisition System (DAC) [17]	DAC's collect all of the data acquired in a specific sensor configuration. They continuously monitor the sensors for responses collect and store the data as well. They are able to differentiate typically between different sampling frequencies, and it is recommended that sensors collecting environmental data have lower sampling frequency than those that are collecting load responses. Typically, it is installed in a waterproof cabinet.	

A visual representation of previously mentioned sensors within the context of a pavement structure is provided in Figure 2.15. It illustrates the typical placement of sensors relative to layer types. For instance, strain gauges are strategically positioned to capture strain at the bottom of the asphalt layer. Pressure cells find their usual locations in either granular base and subbase layers or in the subgrade layer. Meanwhile,

MDDs span the entire pavement structure, including the subgrade. Incorporating a weather station is crucial for recording ambient temperature, complementing the temperature sensors distributed across asphalt layers. In the absence of an accurate weather system, it is advisable to utilize a specified weather station. Additionally, WIM sensors are commonly situated at the top of the asphalt layer, aligned with the path where axles will traverse.

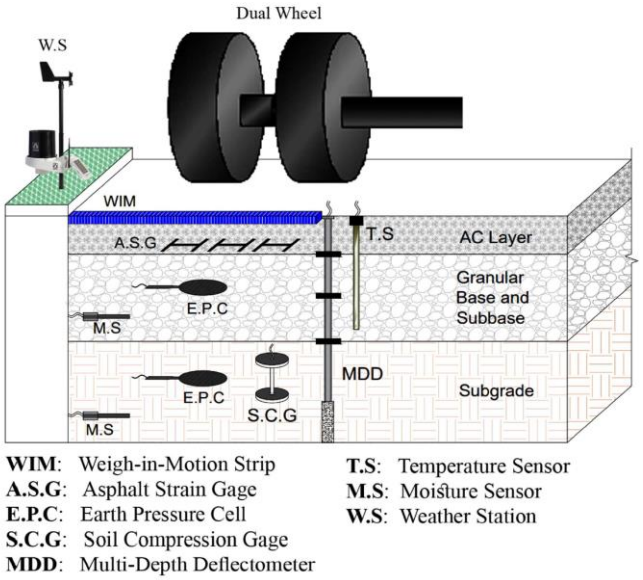


Figure 2.15 Typical locations of common sensor types located in a pavement structure [17].

2.3.2 Previous Examples of Pavement Instrumentation

While early pavement instrumentation research began in the late 1960s, it wasn't until the 1990's that the research really accelerated [17], such as with the review on instrumented sensors presented by Tabatabaee and Sebaaly [34]. The foundational project where many sensors were implemented in a pavement section at the same time was the Virginia Smart Roads project in 2004 [25]. Following this, studies by different authors highlight the application of instrumentation in understanding pavement response to dynamic loads, traffic speed effects, and the validation of finite element models. Various pavement sections are built and involve the use of various sensors and gauges to measure strain, stress, temperature, and moisture in different pavement layers. The following sections will describe three examples of instrumented sections and the results and conclusions that came from them.

2.3.2.1 The Virginia Smart Road

The Virginia Smart Road, conducted by the Virginia Department of Transportation between 1998 and 1999, is one of the first comprehensive instrumented pavement sections [39] [15]. It shows the feasibility of measuring flexible pavement responses to loading. Spanning 3.2 kilometers, the road incorporated 12

monitored sections with various embedded sensors during construction. Strain gauges, pressure cells, thermocouples, TDR probes, and resistivity probes were integrated into the instrumentation, accompanied by a data acquisition system, and specialized software for data acquisition, management, and processing. Data was collected during the compaction process, and during a controlled truck test running at various speeds during various parts of the day [39] [15].

During compaction, the acquisition revealed higher horizontal strains with the presence of compactor vibrations [39]. Subsequent experiments with a loaded truck examined pavement responses under different conditions. Findings indicated an exponential increase in measured vertical stress under the HMA layer with rising temperature. Strain exhibited a similar exponential increase with temperature, and speed affected measured horizontal transverse strain—decreasing speed led to a substantial strain increase [39]. A finite element model, considering effective bonding conditions, was used to predict pavement response, aligning well with experimental results [39].

2.3.2.2 The Instrumentation of the A41N Highway in France

As part of a collaborative research effort, the French highway A41N underwent instrumentation during maintenance operations in 2012 [40] [15]. In this project, two sections of the highway were equipped with 47 strain gauges (horizontal and vertical asphalt strain gauges), 12 temperature probes, and 2 FBGs (type of Fibre Optic sensors) [40]. These sensors were strategically placed at various depths within the road structure to gather information about the wearing, base, and subbase layers. Two rows of sensors are installed, one in the right wheel path and the other in the middle of the right traffic lane [40].

During an on-site measurement campaign with a known loading truck, passages were conducted at speeds of 10 km/h, 50 km/h, and 90 km/h, and along 3 different trajectories ("ΔD") [15]. This aimed to evaluate the structural behavior of the pavement under varied conditions. Notably, no sensor losses were observed during the study [15]. Analysis of the data collected revealed substantial influences of vehicle speed and truck trajectory on measured strains in flexible pavements. For instance, for the testing along three different trajectories, the results indicate that the strains are much higher when the load is directly above the sensors and similar response shapes occur when load axles are overtop the sensors directly [40]. When testing at different speeds, the results concluded that an increase in speed causes a decrease in strain [40].

2.3.2.3 Instrumentation within the US-287 near Mansfield, TX

The location for this instrumented test section was on highway US-287, south of Mansfield, Texas, near the intersection with US-360. In 2018, four longitudinal and four transverse strain gauges were installed

in a straight line along a vehicle's right wheel path, as well as 165 mm to the right of the right wheel path [41]. Figure 2.16 shows the plan view of the instrumented test section used in this project.

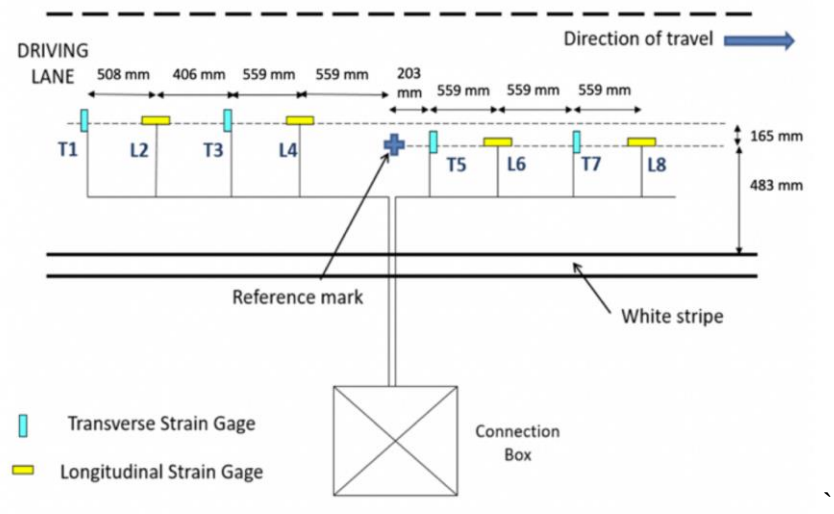


Figure 2.16 Plan view of the pavement instrumentation setup for this project [41].

In order to test the sensors, a truck test took place where seven passes were made at approximately 80 km/h with the FWHA Class 6 truck aiming to position its right wheels over the sensor arrays. Since the lateral position varied between each truck passed, video recordings were taken, and pavement markings were created to determine the truck's lateral position [41]. At the same time HMA temperatures were taken using a thermometer. Strain signals for each test were extracted, and a Finite Element Analysis was performed of the test section to compare to the tested results. Major findings included that longitudinal and transverse strains consistently stayed below 25 με, well below the literature-reported endurance limit of 70 μεs [41]. In addition, transverse strains were slightly larger than longitudinal strains, likely due to axle-induced strain accumulation in the transverse direction, opposite of what was predicted in the FEA. Finally, since no control for wander was made, the authors noted that longitudinal and transverse strain values varied substantially between vehicle passes, attributed to variations in the lateral position of the vehicle relative to the gauge locations [41].

2.4 Applications of Pavement Performance Monitoring

Section 1.1 highlighted several primary applications of integrating sensors and other instrumentation within pavement structures, which not only enhance the efficiency and timeliness of pavement management systems but also introduce advanced functionalities. One notable application involves the utilization of artificial intelligence and machine learning. These technologies facilitate the development of pavement performance prediction models that adapt to changing factors, including age, traffic patterns,

and environmental conditions. These models continuously "learn" from incoming data, ensuring ongoing relevance.

Furthermore, the continuous collection of data holds substantial importance in the context of climate change. Over the years, the accumulation of sufficient data allows the creation of performance prediction models tailored to specific conditions within a pavement network. This proves crucial in forecasting the impact of climate change on pavement structures under various scenarios. These predictive models guide agencies in determining proactive mitigation measures based on anticipated degradation.

The subsequent sections explore these two topics further.

2.4.1 Pavement Performance Prediction Models

A pavement performance prediction model is established based on a correlation between factors like age, traffic load, and material properties to the gradual degradation of the pavement over time [42]. Its primary objective is to forecast future pavement deterioration, encapsulated within an equation representing the evolution of pavement condition. Figure 2.17 from [43] provides a visual representation of this concept, similar to the pavement deterioration curve depicted in Figure 2.9. Notably, the model extends this curve by predicting future deterioration from a point post-construction, labeled “Now”. Acknowledging past deterioration and considering the remaining time within the initial service life, the model forecasts the trajectory towards a minimum acceptable deterioration point, as defined by indices like PSI. The pavement performance model, based on the current level of deterioration, aims to estimate the time until reaching this minimum point and strategically determine when rehabilitation alternatives should be implemented [43].

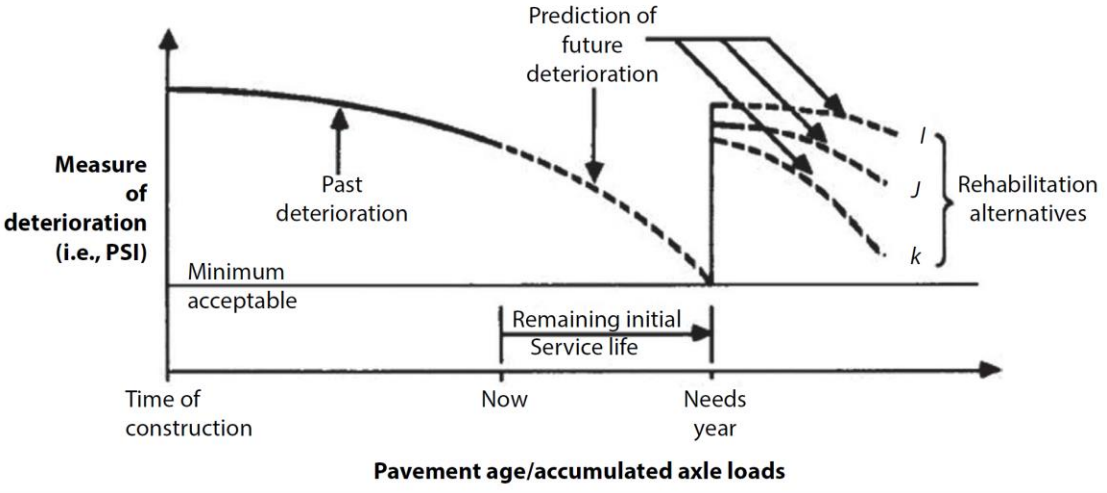


Figure 2.17 Pavement performance deterioration curve, showing how prediction of future deterioration and proposed rehabilitation actions will affect the pavement condition [43].

As mentioned in the AASHTO pavement management guide, a pavement performance model is going to predict one of three things. These include either the distress severity/extent - typically some structural distress like fatigue cracking or running. It can also predict the individual pavement condition indices, such as the IRI. Finally, can also predict some composite indices like PCI [14]. All three kinds have their advantages and disadvantages which need to be considered when developing a specific model [14].

Next, the selection of the model type becomes crucial. Four traditional approaches include: deterministic models, probabilistic models, Bayesian models, and subjective models [14]. These categories can be broken down further into mechanistic, mechanistic empirical, or empirical models, depending on whether they are rooted in pavement behavior, experimental results, or a combination of both. In the realm of pavement performance prediction, the preference often leans towards mechanistic empirical models [14].

2.4.1.1 Incorporation of ML and AI

Machine learning techniques and artificial intelligence have become and new method for pavement performance prediction to facilitate the prediction process due to the inherent nature of prediction in machine learning [22]. As mentioned in the work by Kang, using AI and ML can help the prediction models perform better than traditional models [22].

The development of a pavement performance prediction model through machine learning involves five key steps, illustrated in Figure 2.18. The initial step is data collection, achievable through various methods outlined in [42], such as utilizing agencies, public sources like the Long-Term Pavement Performance (LTPP) database, or employing pavement instrumentation. Once data is gathered, the subsequent step is data preprocessing. This involves techniques to ensure a complete, clean dataset suitable for the learning process, including time series preprocessing, sampling, addressing missing data, and cleaning to eliminate inconsistencies.

Following data preprocessing, the modelling step ensues, utilizing diverse algorithms like random forests, decision trees, support vector regression, and nearest neighbor regression. These algorithms effectively capture the relationship between input factors and pavement degradation performance. The subsequent step is evaluation, involving an assessment of model results to identify potential issues and enhancements. This may entail gathering more data, improving data quality, or adjusting algorithm parameters to better reflect model properties.

Upon completion of these steps, the final model is obtained. Subsequent input of training data and new data into this model enables the prediction of pavement deterioration.

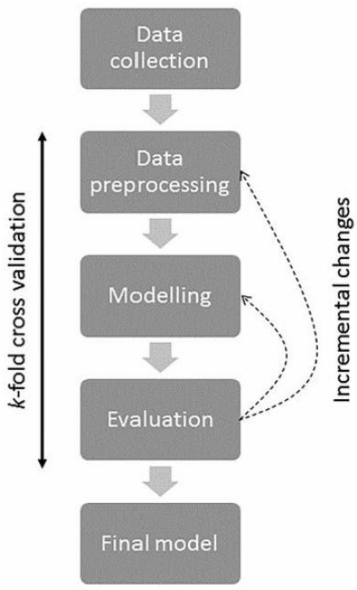


Figure 2.18 Steps in the development of a pavement performance prediction model using machine learning [42].

2.4.2 Consideration of Climate Change Effects in Pavement Performance Prediction

As stated in a study by Maadani et al. in [44], climate change is already causing issues for the transportation sector. The areas of most concern include increased rutting and bleeding due to high temperatures, increased deformation due to freeze-thaw cycles and increased depressions due to precipitation and flooding [44].

Engineers now rely on advanced mechanistic design tools like the Mechanistic-Empirical Pavement Design Guide, or MEPDG, to incorporate climatic data and design parameters into road performance assessments. The Enhanced Integrated Climate Model (EICM) within MEPDG mandates at least one year of actual weather station data, including hourly parameters such as air temperature, wind speed, precipitation, sunshine percentage, and relative humidity throughout the road's design life. Solar radiation and relative humidity are indirectly or directly obtained from climate models [44].

However, a substantial limitation identified in the study by Maadani et al. in [44] is that the road design life often exceeds the available weather time series for performance prediction. This leads to the recycling of the same period weather history, raising concerns about the accuracy of predictions. To address this, currently the Long-term Pavement Performance (LTPP) is used to gather hourly weather data from stations across the United States and Canada, spanning over 10 years. There are still issues with this strategy, however, as occasional gaps and errors in the data pose challenges when used as inputs for MEPDG weather assessments [44].

Effectively utilizing available MEPDG climate data files remain challenging, primarily because weather station data typically lacks the required hourly time intervals for climatic loading parameters. The paper highlights that some literature uses shorter time intervals, but even this may not be enough in some cases [44]. Here, the use of continuous climatic data collected for a specific section would be ideal, likely improving prediction accuracy.

Moreover, this study expresses that there exists a critical gap in understanding how to account for local conditions, materials, construction quality, traffic characteristics, and seasonal fluctuations in moisture and temperature within road layers [44]. The impact of these factors on road response remains unclear, emphasizing the need for a more comprehensive approach that considers the interplay of various variables for accurate road performance assessments [44].

2.5 Research Gaps

The literature review reveals that embedded instrumentation for monitoring pavement conditions has been an established practice for decades. However, recent advancements in state-of-the-art technologies like artificial intelligence, machine learning, and big data have reignited interest in this area. These tools offer easier access to understanding the potential benefits of using embedded sensors to collect and process pavement performance data on a large scale and in real-time. Despite this progress, the research area still faces limitations and gaps, some of which is addressed in this thesis, while others remain topics for future investigation.

For example, none of the previous projects in this literature review accounted for the effects and responses of sensors during the construction phase and sensor installation. This omission largely stems from the fact that most projects incorporated sensors into existing pavements. Unlike these projects, this study integrates sensor implementation as part of the roadway reconstruction process, and the evaluation of sensor responses while the pavement immediately after installation was planned and considered, allowing for data collection during this critical phase. Comparing this construction phase data with other tests conducted in various seasons will help shed light on how loads impact the pavement structure during this phase compared to cooler seasonal conditions. This study addresses this gap by collecting pavement structural response data using a controlled truck test immediately after the pouring of the initial HMA layer. In addition, the literature typically only presents sensor response data gathered over a short period, such as one or a few days. This gap in research limits a thorough understanding of the relationships between a pavement section's structural responses over various HMA and ambient temperatures. This study will seek to address this gap by undertaking a more extensive assessment compared to that in the existing literature, where truck tests are typically conducted during only one test/day/season. To do this,

an in-depth heavy vehicle (truck) testing analysis is performed over various seasons overtop the instrumented test section. Also, there is currently not much research exploring the long-term trends and assessments of load and environmental data collected for an instrumented test section for a busy arterial roadway, and a look into sensor functionality based on these trend results. This study will seek to address this gap through the collection of real-time data from the instrumented test section over multiple months and seasons and assess the trend results.

Next, there is a lack of understanding of how vehicle wander impacts the pavement sensor responses. This study will seek to address this gap by deliberately testing sensor responses at various lateral deviations from the sensor arrays and developing correlations. To do this, a comparison between the response magnitude and shape of an embedded sensor and the extent of vehicle tire deviation (known as vehicle "wander") as a heavy vehicle attempts to pass over that embedded sensor. Also, there is very little exploring the comparison between static and dynamic pavement response simulation methods, especially over various seasons and speeds and how it will compare to embedded sensor field results. This study will work to address this gap by modelling the truck testing performed over several seasons in two common static and dynamic pavement software (namely, KENPAVE and 3D-Move) and compare them to the field results.

One of the primary obstacles facing the integration of this technology into existing pavement management systems is its scalability. While both current literature and ongoing projects have mainly focused on the use of this technology for small instrumented sections (such as the one described in this project) or more rural roads, there are currently no published studies that have looked at the implementation of this technology on a wider scale and the cost-benefit analysis of this method over several decades as compared to the costs of traditional pavement condition monitoring methods [45]. While this thesis does not delve into this aspect, the pursuit of cheaper, more cost-effective sensors to facilitate the broader implementation of these technologies represents a vital avenue for future research.

Chapter 3
Trial Section Design and Construction

This Chapter outlines the design, rationale, and configuration of the instrumented test section. The data gathered plays a crucial role in the subsequent chapters of this thesis, where further analysis and interpretation are detailed.

3.1 Project Overview

The instrumented test section was designed with the explicit goal of capturing real-time data from a specific local road segment. This data encompasses crucial factors like structural elements (stress and pressure) and environmental conditions (temperature and moisture). The selection of this test section was strategic, as it coincided with an active road reconstruction project led by the Region of Waterloo. This intentional choice streamlined the sensor installation process, enabling the research team to precisely align sensor placement with each layer of the pavement structure during the ongoing road reconstruction.

Moreover, the test section's strategic location provides a distinct advantage by enabling the real-time capture of data from continuous live traffic on an urban roadway. This sets the approach of this project apart from others in the existing literature, which often conduct similar testing on roads with limited traffic or controlled-access roadways featuring specific types of vehicles [46], [15], [39], [47], [48]. The dynamic nature of this arterial roadway provides a more representative and diverse dataset for analysis.

3.2 Project Site Description

The instrumented test section location is located on Courtland Avenue East in the City of Kitchener, Ontario. This road is a major arterial roadway that passes underneath and connects to Highway 8 through several onramps and offramps. The instrumented section is situated in the right lane of a two-lane, two-way roadway. From Figure 3.1, the instrumented test section is situated between the intersections of Overland Drive and Courtland Avenue East, as well as Walton Avenue and Courtland Avenue East, and is about 10 meters in length. Figure 3.2 provides a closer look at the location of the test section in relation to the surrounding land uses. It is situated near several business and retail asphalt driveways, and there is pedestrian access through a multi-use trail adjacent to the lane selected for the instrumented test section. Finally, Figure 3.3 provides a view at the street level of the location where the test section is situated with relation to the roadway, a hydro line, the multi-use trail, and other site features.

The red rectangles used to indicate the instrumented test section locations in Figure 3.1, Figure 3.2 and Figure 3.3 indicate the approximate locations and are not drawn to scale.



Figure 3.1 Location of the instrumented test section in relation to Highway 8, Overland Drive and Walton Avenue in Kitchener, Ontario [49]. The instrumented test section is highlighted in red.



Figure 3.2 Closer view of lane selected as instrumented test section in relation to the surrounding land uses [49].

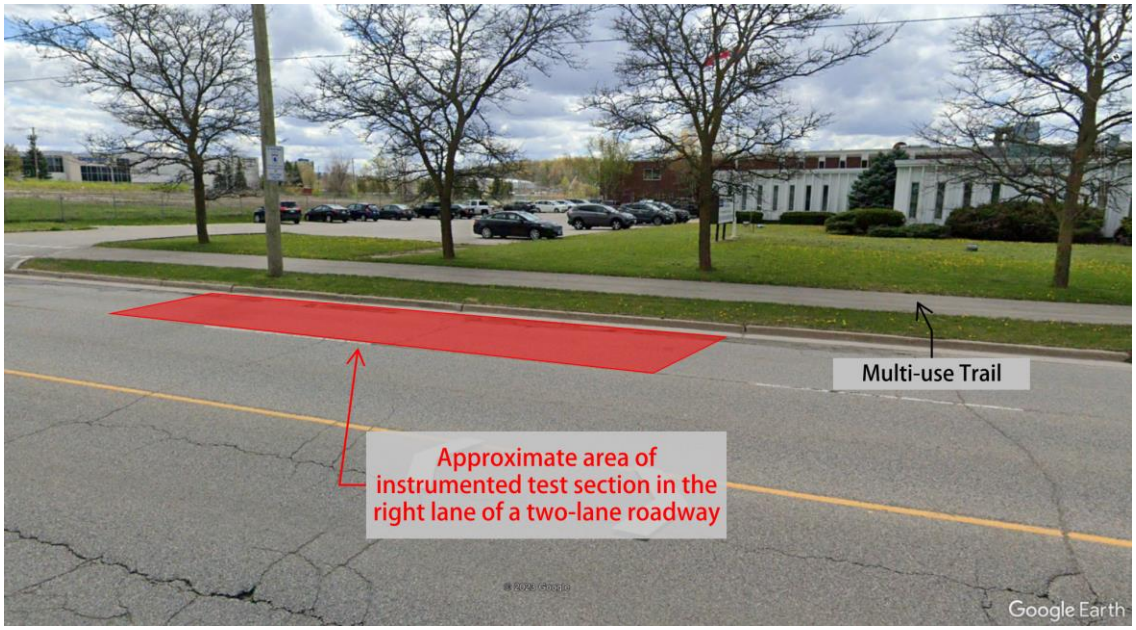


Figure 3.3 Street view look at the approximate location of the instrumented test section [49].

3.3 Trial Section Design

The pavement design was completed by experienced pavement engineers from the Region of Waterloo. The anticipated construction date was meant to be in 2021, however due to the COVID-19 pandemic, construction commenced during 2022, which is the same year the implementation of the instrumented section began. Figure 3.4 shows a portion of the site plan drawings produced by the Region, which includes the location for the test section, situated approximately within stations 10+160 to 10+180.

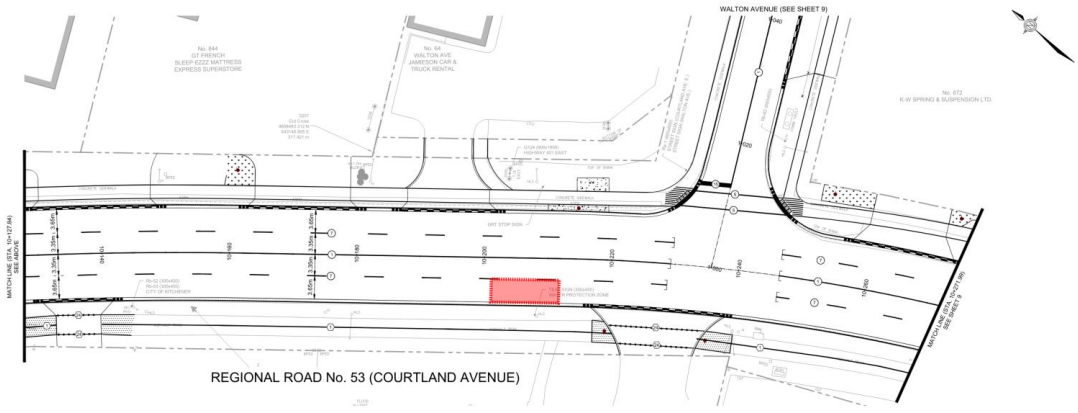


Figure 3.4 Site plan drawing produced by the Region of Waterloo, including the location for the instrumented test section in red [50].

The pavement design is of a typical nature, with an HMA surface course of 195 mm (50 mm of SP 12.5 mm FC2 material which is PGAC 64-28 and 145 mm of SP 19.0 mm material which is PGAC 58-28), a Granular A layer of 150 mm, Granular B Type II layer of 400 mm followed by the natural subgrade soil,

bringing the total structural design depth to 745 mm [51]. Figure 3.5 shows a typical cross-sectional view of the roadway pavement design near the instrumented pavement section, which also describes the layer depths. The drawings were produced by the Region of Waterloo.

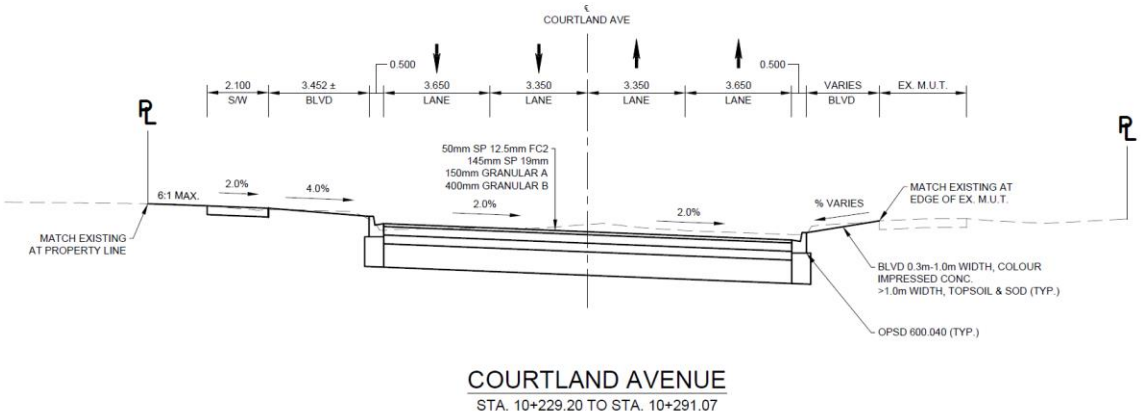


Figure 3.5 Typical cross-sectional view of the roadway near the instrumented pavement section, produced by the Region of Waterloo [50].

In addition, the design traffic values for the portion of Courtland Avenue East containing the instrumented test section are based on values taken directly from a final geotechnical investigation report (Table 6-5) prepared for the Region of Waterloo [51]. For the portion of the road that includes the instrumented test section, the Average Annual Daily Traffic (AADT) was 25,834 vehicles per day in 2015 and 29,093 vehicles per day in 2021, the original construction date. With a commercial vehicle percentage of 6% and a growth rate of 2%, the design ESALs over 20 years was approximately 9.9 million ESALs [51]. However, since at Hayward Avenue the design ESALs over 20 years was the highest along the whole road section of the road reconstruction, at approximately 12.4 million ESALs, this value was what was selected as the design ESALs for the project [51].

3.4 Instrumentation Background and Installation

A variety of sensors were used in the installation of the test section to be able to monitor actual pavement response to various physical and environmental changes. The sensors were sourced from a variety of companies, such as BDI, RST and METER Group. Each of the sensors were calibrated to ensure proper functioning prior to being placed on-site. The following section will describe each component of the sensor equipment in detail.

3.4.1 Dataloggers

The dataloggers used in the instrumented test section data collection were from the company BDI. Specifically, nine of their proprietary STS4-4 Terminal Nodes were used to connect the sensors to the

Core Data Logger, which is the computer designed to process and store all of the incoming sensor information. The terminal nodes, along with the core data logger can pick up data at low and high frequencies for environmental and load data [52].

3.4.2 Horizontal and Vertical Asphalt Strain Gauges

This study implemented both horizontal and vertical gauges, or strain transducers. Both strain gauges were calibrated by BDI. They include a Wheatstone full bridge configuration circuit that has 4 active 1000-ohm strain gauges in order to measure axial strains [35]. The unit of strain measurement produced by these sensors is microstrain (με) based on radiometric to excitation voltage [35]. They are LVDT-type gauges.

The gauge length for the horizontal strain gauges was 8 inches or 233 millimeters, while the plate separation for the vertical strain gauge has a range between 1.375 to 3 inches or 35 to 76 millimeters. As per the BDI specifications, the strain range of these strain gauges are 5000 με, while the temperature range is -45 to 150°C [35].

3.4.3 Temperature Sensors and Temperature Probes

Two types of temperature sensors were used in the instrumented test section. The first type of temperature sensor comes from BDI and is known as a thermistor. The thermistor's functionality comes from a change in resistance, whereby as the temperature increases, the resistance decreases [35]. These were used to gather temperature data throughout the pavement structure granular layers. The temperature range of this sensor is -60°C to 150°C. The non-linear output of the thermistor is represented by the Steinhart-Hart Equation [35]:

$$T_C = \frac{1}{A + B(lnR) + C(lnR)^3} - 273.2 \quad (2)$$

where T is the temperature in degrees Centigrade and R is the resistance in Ohms.

In addition to the temperature sensors, two embedded temperature probes were sourced from BDI. These sensors provide the opportunity to produce thermal measurements which can be used in the development of a thermal gradient to assess the impacts of variations in temperature throughout the pavement structure [35]. In the case of this study, the temperature probe thermistor will be used to understand the effects of thermal differences in the pavement surface (HMA layer). The temperature range of the sensor is -40° to 200 °C [35].

3.4.4 Moisture Probes

The moisture probes used came from the METER Group company, with the model type known as TEROS10. This sensor is designed to be embedded in the porous materials or soils that it will be measuring moisture from. According to the manufacturer, they "use an electromagnetic field to measure the apparent dielectric permittivity (ε_a) of the surrounding medium" [37, p. 12]. The sensor itself produces a raw value based on the substrate permittivity which is then converted to Volumetric Water Content (VWC) [37]. The VWC is the ratio of the volume of water (in m^3) to the volume of soil (also in m^3) [37]. In the field, the TEROS10 moisture probes have been set to produce the data in terms of volts, as they cannot produce data with the units in "relative humidity" as required by BDI. In this way, the data can be converted to VWC through the following calibration equation [37]:

$$\theta\left(\frac{m^3}{m^3}\right) = 4.824 \times 10^{-10} \times mV^3 - 2.278 \times 10^{-6} \times mV^2 + 3.898 \times 10^{-3} \times mV - 2.154 \qquad (3)$$

3.4.5 Total Earth Pressure Cells

The Total Earth Pressure Cell, or TEPC, was provided by the company RST and was also installed throughout all of the granular layers. These pressure sensors are designed to measure stress when laid on flat surfaces. They consist of two stainless steel plates welded together, creating a space filled with deaired glycol (a type of hydraulic fluid) [53]. This cell is connected to a transducer through a stainless-steel tube, forming a closed hydraulic system [53]. The units that are provided to the data logger are in megapascals (MPa).

3.4.6 Sensor Installation Plans

The number and type of sensors, as well as the model type, their labeling methodology, the number of each sensor installed, and the sampling frequency is described in Table 3.1. Images of each of the sensors can be found in Figure 3.6.

In this document, the consistent reference for each sensor will be based on its Sensor Label and not the Model name (see Section 3.4.7 for the sensor labeling methodology). This approach ensures clarity when discussing sensors across different layers or sections of the test area. The sampling frequency is categorized into two types: high-speed (1000 samples/second), primarily used for physical data such as strain and pressure, and low frequency (1 sample/15 minutes), utilized for environmental data like temperature and moisture assessment. However, due to limitations in the BDI frequency configuration, strain and pressure sensors are also included in the low-frequency assessment, which will provide trend data over time (as described in Chapter 8). Initial plans included the installation of two multi-depth deflectometers for in-situ measurement of elastic or permanent deformation in the pavement structure.

Unfortunately, these deflectometers were not installed due to concerns related to construction feasibility. Each of the sensors were calibrated to ensure proper functioning prior to being placed on-site. The calibration sheets for the RST and BDI sensors can be found in the **Error! Reference source not found.**.

Table 3.1 Sensor Summary

Sensor Type	Model	Sensor Label	Sensor Measurements	Number of Sensors Installed	Sampling Frequency
Horizontal asphalt strain gauge	AST1000	AS-XX-Y-#	Strain (με)	8	1000 samp. /sec. & 1 samp. /15 min.*
Vertical asphalt strain gauge	VAST1000	VAS-Y-#	Strain (με)	4	1000 samp. /sec & 1 samp. /15 min.
Temperature sensor (thermistor)	N/A (simply BDI thermistor probes)	TM-XX-#	°C	7	1 samp. /15 min.
Moisture probes	TEROS10	MOI-XX-#	Volumetric Water Content (VWC - m^3/m^3)	5	1 samp. /15 min.
Total earth pressure cells (TEPC)	LPTPC-V	PC-XX-Y-#	Pascals (MPa)	8	1000 samp. /sec & 1 samp. /15 min.
Temperature probes (thermistor)	TT-TS-### (thermsitor)	TEMPS-01/02-#	°C	2	1 samp. /15 min.

**Samp. = sample, sec. = seconds and min. = minutes*

To facilitate the installation of sensors, a device known as a "moisture tree" was developed in the laboratory prior to sensor installation on site. This concept of a "moisture tree" was borrowed from previous research work at CPATT [18], where it was used to distribute moisture probes evenly at the required depths within pavement structures. In this project, the moisture tree was used to contain all sensors (not just the moisture probes), enhancing the efficiency of sensor transportation and installation on site.

The moisture tree for this project was constructed using a 4-inch diameter PVC pipe. Figure 3.7 and Figure 3.8 display the moisture tree constructed and utilized by the research team, with Figure 3.8 specifically demonstrating how all sensor wires were threaded through the moisture tree.

In addition, another PVC conduit of 4 inches in diameter will gather all the wires from all of the sensors situated in the moisture tree and carry it to the Data Acquisition system (DAC). The DAC has nine (9) STS4-4 terminal nodes to which all power supply and ground wires from the sensors are connected, as well as the Core Data Logger, which stores all of the sensor data. The DAC setup is shown in both images in Figure 3.9. Schematics of the DAC setup can be found in Appendix B.



a. Horizontal asphalt concrete strain gauges (BDI)



b. Vertical asphalt concrete strain gauges (BDI)



c. Temperature sensors (thermistor) (BDI)



d. Moisture probes (TEROS10)



e. STS4 Core Data Logger (BDI- [52])



f. STS4-4 Terminal Node (BDI)



g. Total Earth Pressure Cell (TEPC) (RST)



h. Temperature probe in asphalt (BDI)

Figure 3.6 Sensors and other equipment installed at the instrumented section on Courtland Avenue

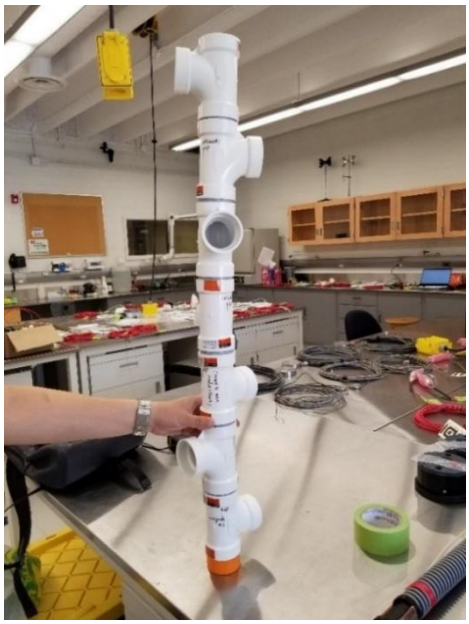


Figure 3.7 Moisture tree through which all sensors were threaded.



Figure 3.8 Image showcasing how all the sensors were threaded through the moisture tree.

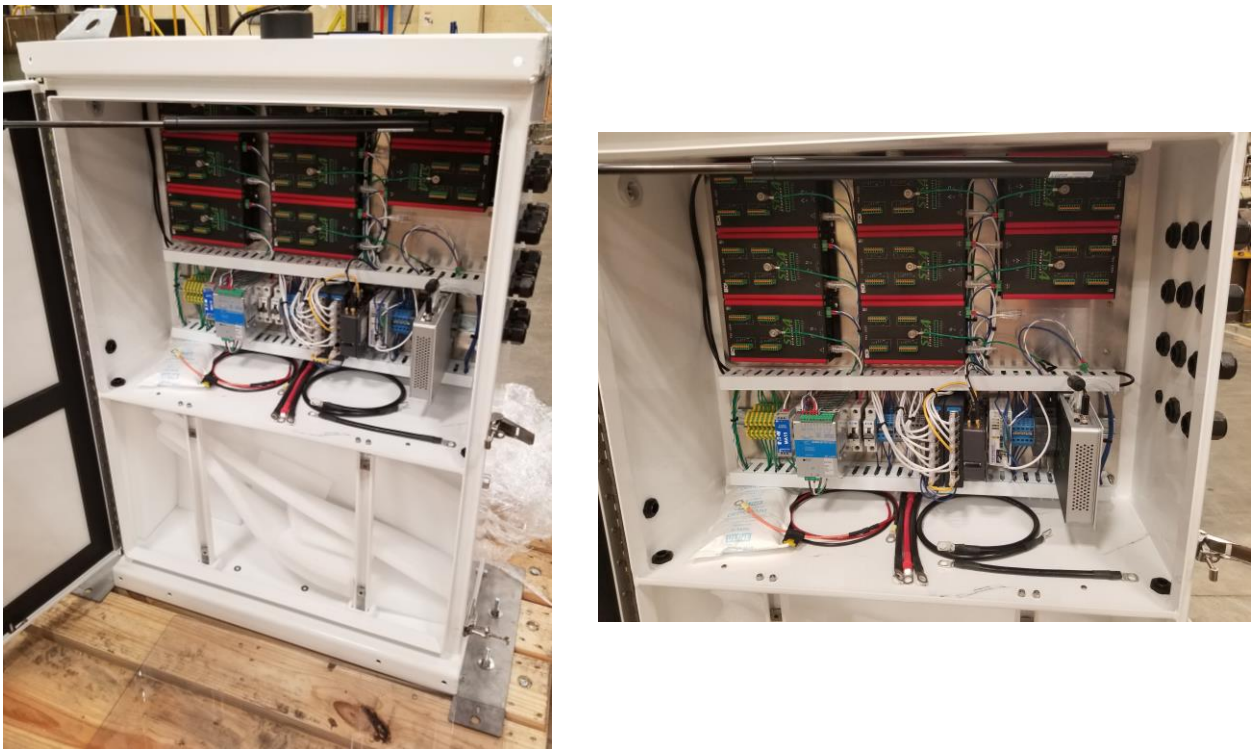


Figure 3.9 Data Acquisition System for the instrumented section.

There are a total of eight openings on the completed moisture tree. Table 3.2 describes the sensors that were installed in each of the openings of the moisture tree. It also shows the relative depth with respect to the subgrade that each of the holes of the moisture tree are situated at (note, these may not necessarily be

the same as the depth of the sensors themselves). For example, Hole 1 is 530 millimeters above the subgrade, while Hole 6 is 70 millimeters below the subgrade. Hole 6 was used as an outlet for all the sensors, so that they all are conveniently gathered in one location.

Table 3.2 Sensor configuration, location relative to subgrade and sensor name(s) within the moisture tree

Opening Number	Location relative to subgrade (mm) (subgrade = 0 mm)	Sensor Name and Location
Hole 1	530	All asphalt strain gauges
Hole 2	480	MOI-BA-1; TM-BA-01; TM-BA-02; PC-BA-R-1; PC-BA-L-2; PC-BA-R-5; PC-BA-L-6
Hole 3	340	MOI-SB-2 ; TM-SB-03 ; TEMPS-01-1/2/3 ; TEMPS-02-1/2/3 ; PC-SB-R-3; PC-SB-L-4
Hole 4	200	MOI-SB-3; TM-SB-04
Hole 5	70	MOI-SB-4; TM-SB-05
Hole 6	-70	Sensor wire outlet
Hole 7	-180	MOI-SG-5; TM-SG-06; PC-SG-L-8; PC-SG-R-7
Hole 8	-340	TM-SG-07

Figure 3.10 shows the plan view of the sensor instrumentation layout. The relative positions and sensor labels are also depicted in the diagram. In a similar manner, Figure 3.11 shows the section view of the instrumentation layout. Note that the diagrams are not to scale.

The installation design comprised two rows of sensors: a right row closest to the pavement edge, aligning closely with the right wheel path of passing vehicles. Additionally, a left row of sensors was positioned 0.7 meters from the right row to capture the tire wander from the right wheel path. They will be referred to as the “right sensor array” and the “left sensor array”, respectively.

Figure 3.12, Figure 3.13 and Figure 3.14 show diagrams for how the concrete base slab, on which the data acquisition system rests, is positioned in relation to the sensor instrumented area. As well, the hydro pole located near the concrete slab, which will serve to provide a constant supply of energy to the sensors and the data acquisition system, is depicted.

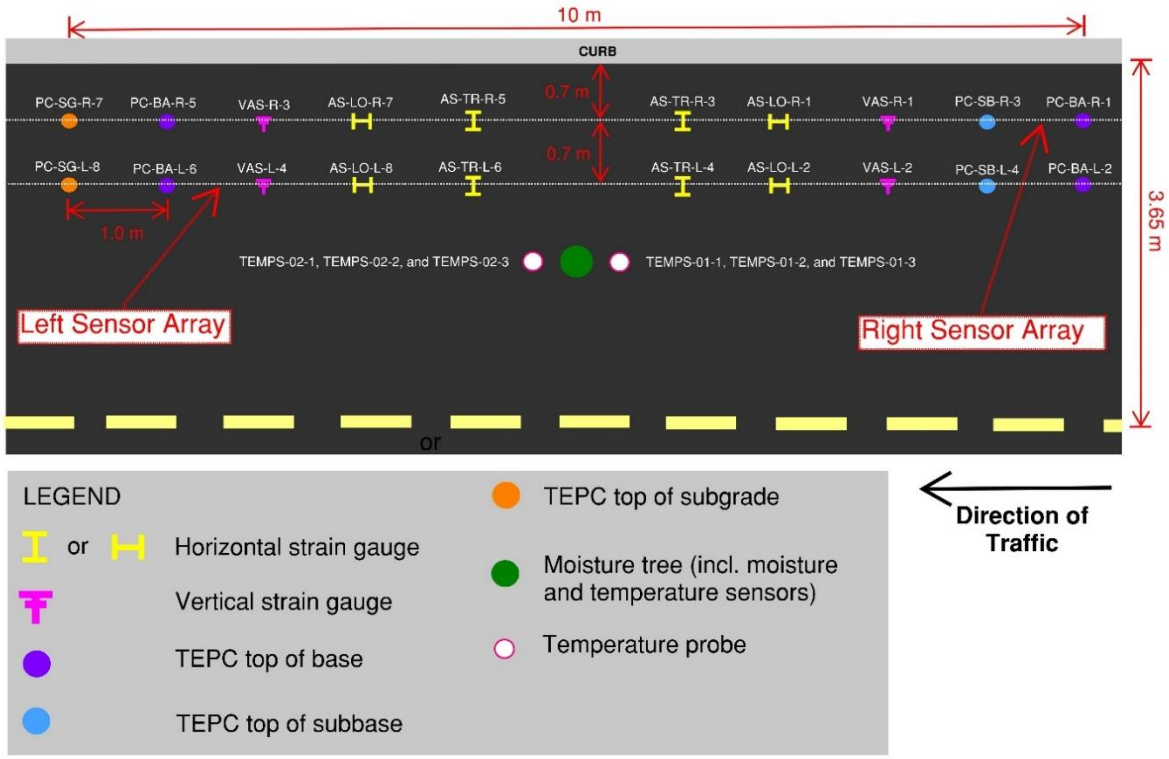


Figure 3.10 Schematic (plan view) showcasing the sensor instrumentation layout.

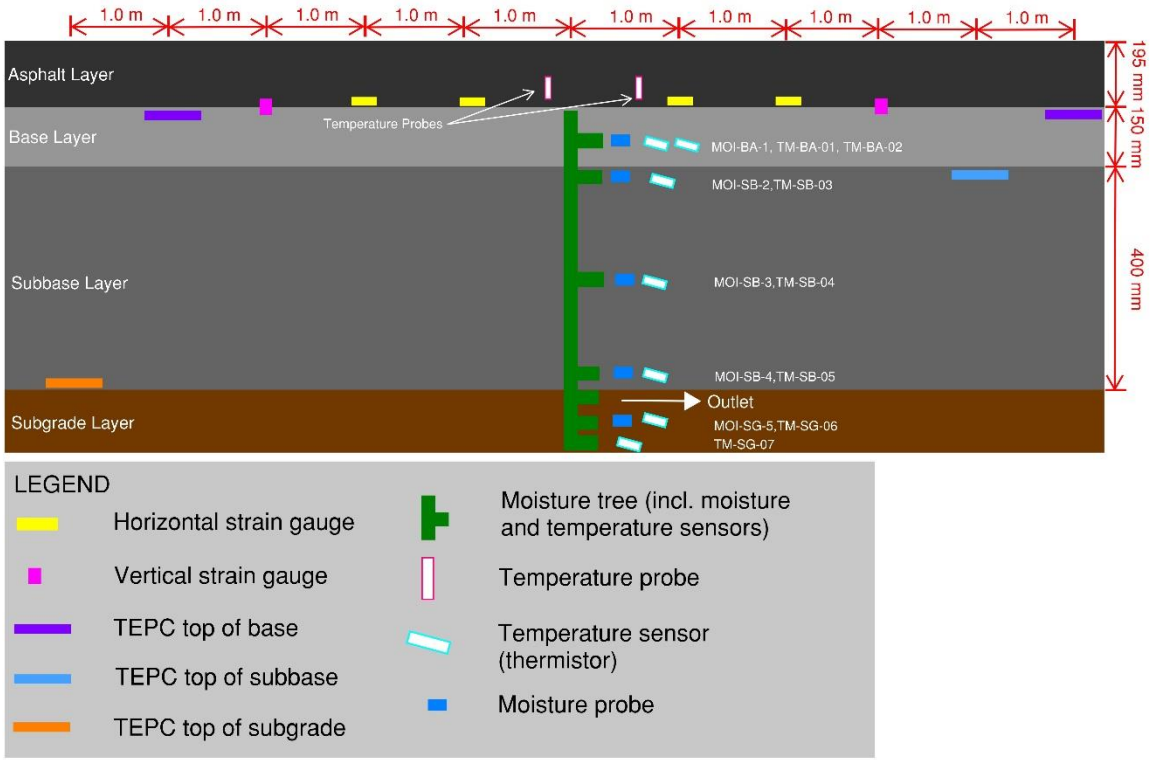


Figure 3.11 Section view of the instrumentation.

In the figures, the HMA layer is expressed as one layer, however, as mentioned previously, the HMA layer is composed of two layers, which includes 50 mm of SP 12.5 mm FC2 and 145 mm of SP 19.0 mm for a total of 195 mm for the surface course.

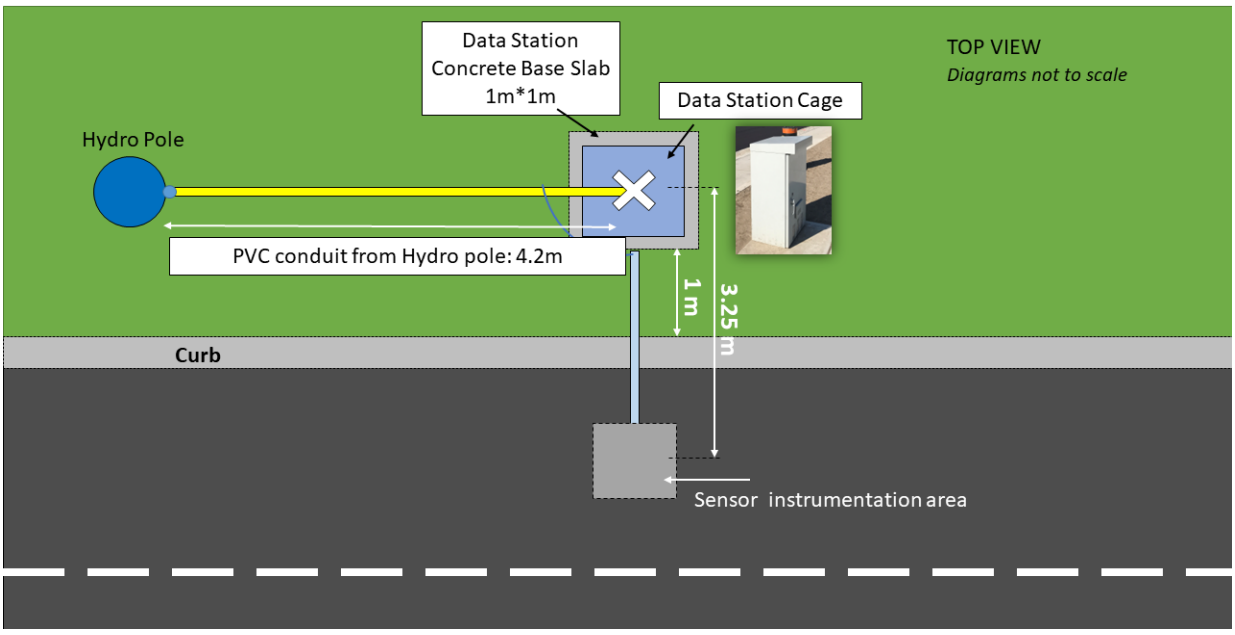


Figure 3.12 Top view of the instrumented section setup, showcasing the concrete base and the hydro pole.

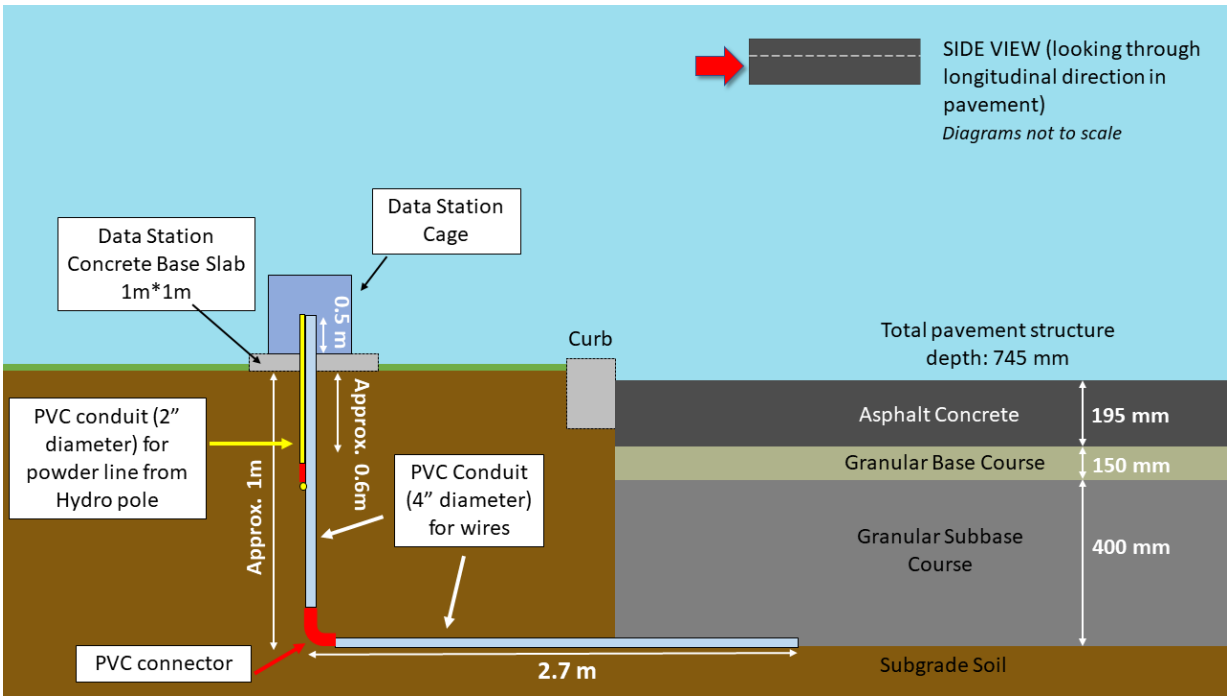


Figure 3.13 Plan view of the instrumented section setup, showcasing the location of the PVC conduit relative to the pavement structure.

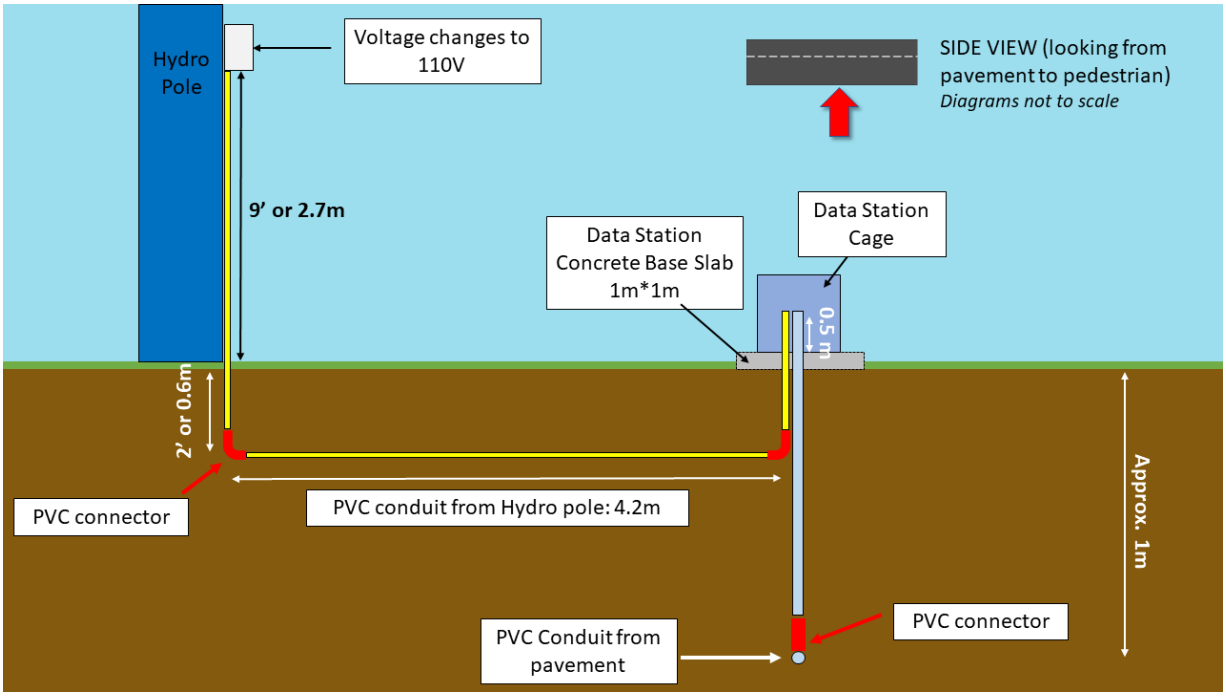


Figure 3.14 Additional plan view of the instrumented section setup, showcasing the location of the PVC conduit relative to the hydro pole.

3.4.7 Sensor Labelling Methodology

To ensure clear and consistent analysis of sensor data, a labeling methodology was implemented to individually identify sensors of each type. The following sections will outline the labeling methodology for each sensor type.

3.4.7.1 Horizontal and Vertical Asphalt Strain Gauges

Horizontal and vertical strain gauges follow the AS-XX-Y-# and VAS-Y-# labeling methodology, respectively. Figure 3.6 illustrates the naming convention for horizontal strain gauges, while Figure 3.7 denotes the naming convention for the vertical strain gauges. The symbol 'AS' designates asphalt strain gauges, followed by two letters indicating longitudinal (LO) or transverse (TR) directions. The subsequent part (Y) specifies the sensor's location in the right or left array; 'R' for the right array and 'L' for the left array. The naming convention concludes with a number indicating the sensor's position along the array, increasing from upstream (e.g., 1) to downstream (e.g., 5). A similar naming convention occurs for the vertical asphalt strain gauges, whereby the 'VAS' designates the sensor as a vertical asphalt strain gauge, the (Y) specifies the sensor's location in the right or left array, and a number that indicates the position of the sensor along the roadway.

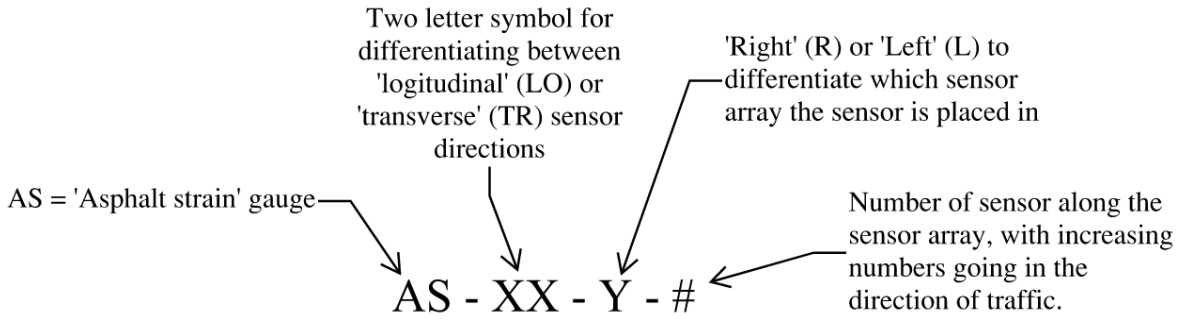


Figure 3.15 Naming convention for the horizontal asphalt strain gauges.

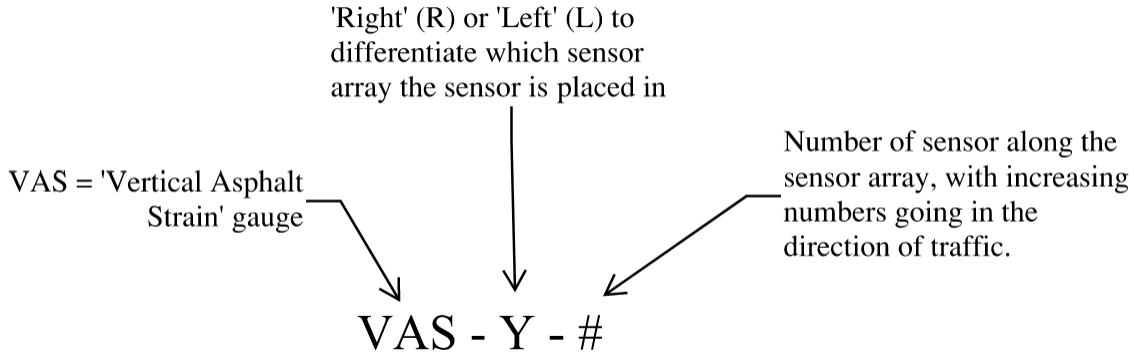


Figure 3.16 Naming convention for the vertical asphalt strain gauges.

3.4.7.2 Temperature Sensors and Temperature Probes

Two different naming conventions were used for both the temperature sensors as well as the temperature probes. This is because the temperature sensors or thermistors only include one sensor while the temperature probes have three sensors per probe.

Figure 3.8 shows the naming convention for the temperature thermistors. They bear the ‘TM’ prefix, followed by a two-letter code denoting layer location (base, subbase, or subgrade). Finally, another number will indicate the position of the sensor within the depth of the pavement structure in relation to the other sensors; an increasing number denotes an increasing depth into the pavement structure.

Figure 3.9 shows the naming convention for the temperature probes. Temperature probes are labeled with a very similar convention as the thermistors but include '01' or '02' to distinguish between the two probes instead of the layer indicator since they are located within the same layer. Figure 3.10 shows the individual sensor labels for the temperature probes for clarity.

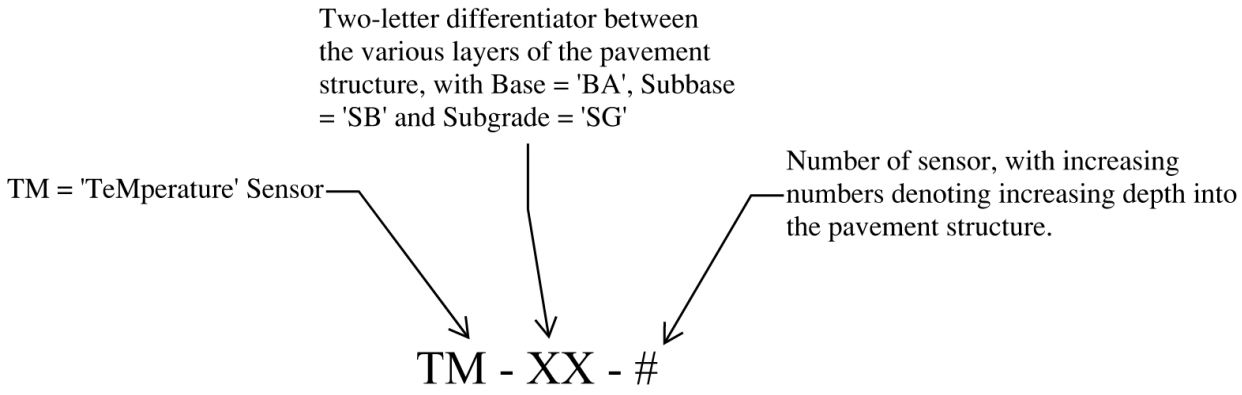


Figure 3.17 Naming convention for the temperature thermistors.

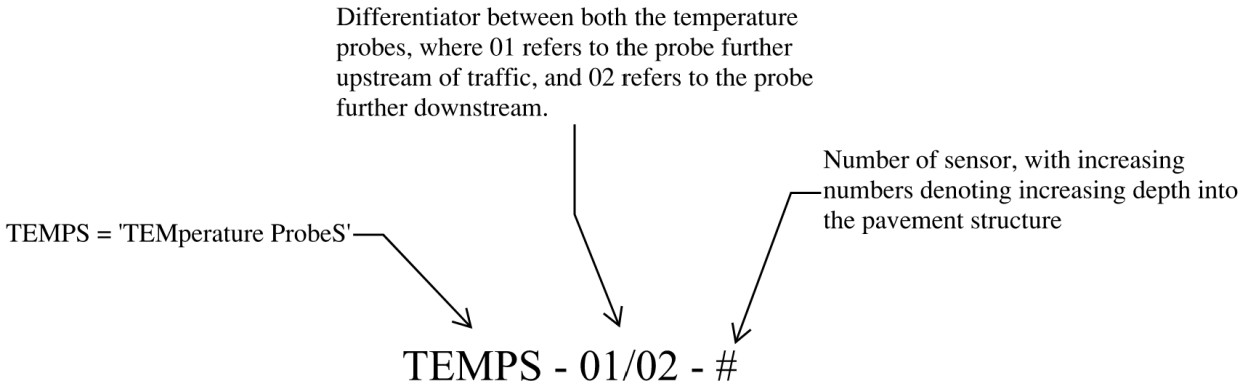


Figure 3.18 Naming convention for the temperature probes.

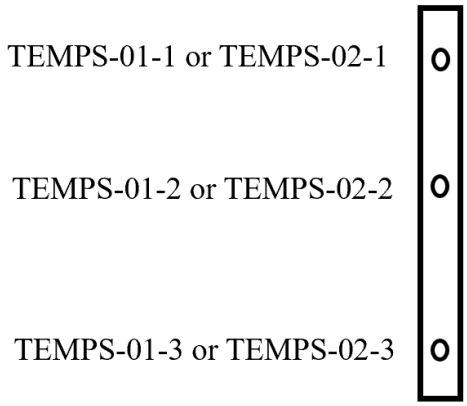


Figure 3.19 Naming convention for the temperature probes for each sensor.

3.4.7.3 Moisture Probes

Moisture probes are labeled very similarly to the thermistors described previously. The prefix begins with the letters ‘MOI’ to denote that it is a moisture sensor, and there is a two-letter differentiator to denote which layer the sensor is located in. Finally, there is a number along the depth of the sensor to show how far into the pavement structure the sensor is located relative to other moisture sensors.

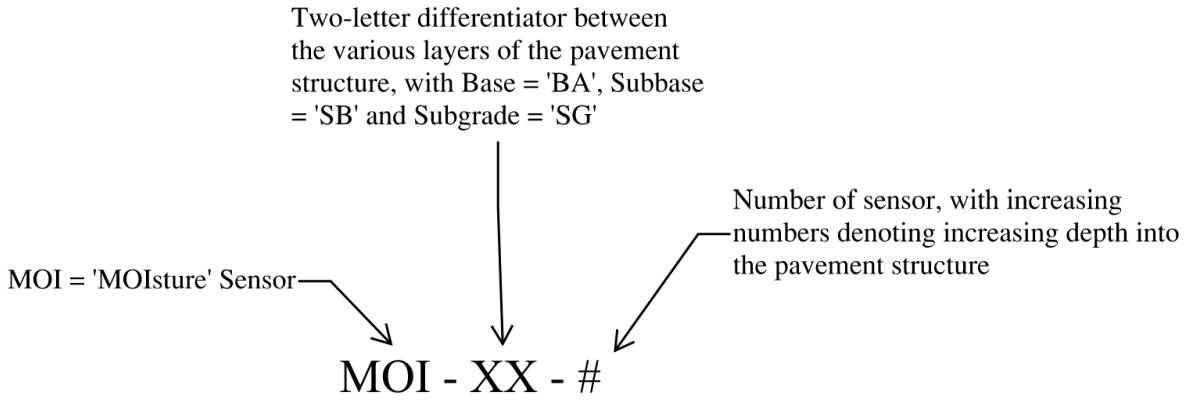


Figure 3.20 Naming convention for the moisture probe sensors.

3.4.7.4 Total Earth Pressure Cells

Total earth pressure cells share a labeling method with asphalt strain gauges, differing mainly in the second part of the naming convention. The prefix 'PC' represents pressure cell, and the letter differentiation indicates the layer of sensor placement, unlike the longitudinal or transverse indication in asphalt strain gauges.

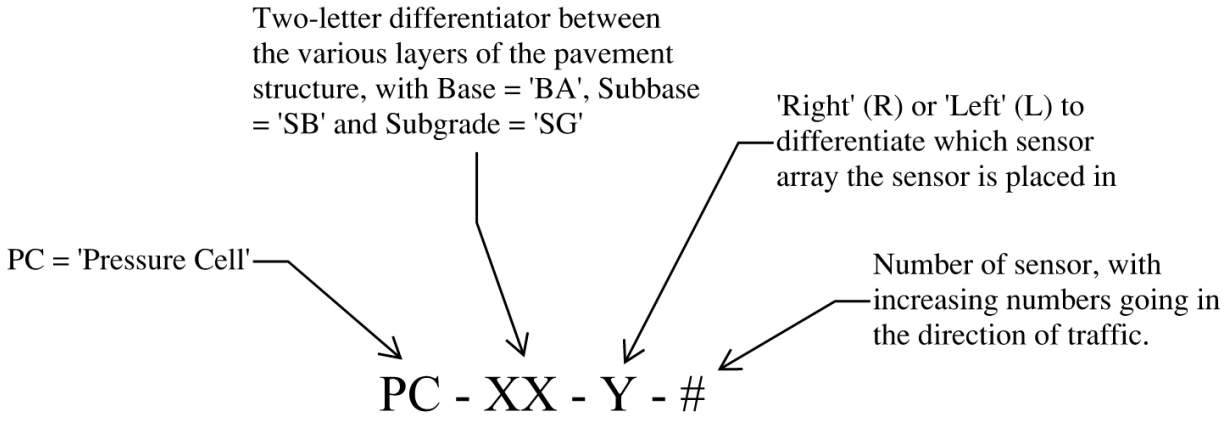


Figure 3.21 Naming convention for the total earth pressure cell sensors.

3.5 Construction Activities

The installation of the sensors on the instrumented pavement section occurred over two days. The dates were September 30th, 2022, for the installation of the sensors in subbase and base layers, as well as October 12th, 2022, for the installation of the sensors that sit below the HMA layer. Other key tasks, such as the calibration of the sensors, took place on other days. There were several key members of the construction team, which included:

1. Capital Paving – the main contractor for the project.
2. Region of Waterloo – overseeing the construction and responsible for the design.
3. National Research Council of Canada (NRC) – provided experienced personnel to support the graduate researchers with the implementation and testing of the sensors.
4. Center for Pavement and Transportation Technology (CPATT) – several graduate and post-doctoral students with their peers participated in the installation of the sensors on-site.

The implementation of the sensors occurred during various stages of the construction of the pavement structure on Courtland Avenue. These include the progressive laying of Granular A, B, and the asphalt concrete. As mentioned in the Project Overview section of this report, the sensors were laid in the southbound outermost lane of Courtland Avenue, and this was the first lane to be reconstructed and re-paved by Capital Paving during the road reconstruction process. In the following sections, the various construction activities that took place will be explained in detail. Figure 3.22 below shows a summary of the timeline for all of the construction activities that will be presented in the following sections.

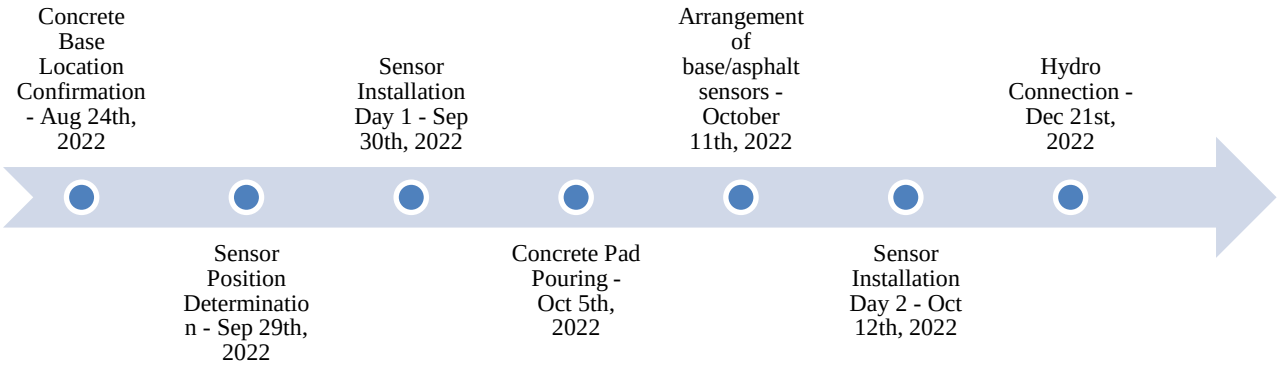


Figure 3.22 Summary of the construction activities and the dates of occurrence.

3.5.1 Confirmation of concrete base location (August 24th, 2022)

The first step of the construction process for the CPATT team included the confirmation of the concrete base location with a representative from the Region of Waterloo. This is depicted in Figure 3.23. The position of the concrete base was chosen so that it was situated 1 metre from the edge of the curb. This

was to ensure adequate distance from the roadway, and also to line up the concrete pad with the hydro pole.



Figure 3.23 Location of the proposed concrete pad (right). The white painted marking denotes the proposed location. Position of proposed concrete pad relative to the hydro pole is also shown (left).

3.5.2 Determining the position of sensors (September 29th, 2022)

The next step in the construction process consisted of confirming the locations of the sensors in the instrumented road section on September 29th, 2022. By this date, the backfilling of the Granular B and Granular A was in progress. However, the construction crew from Capital Paving left the required portion of the subgrade exposed where the sensors needed to be placed to allow for proper sensor placement which was scheduled for September 30th, 2023. This was done to mark the positions of the edge of pavement and the position of the wheel path where the sensors were to be placed. This process can be seen in Figure 3.24 and Figure 3.25.



Figure 3.24 Exposed subgrade where the sensors are to be laid (left) and markings denoting the edge of pavement and wheel path (right).



Figure 3.25 Orange markings showcasing the southbound outermost lane in which the sensors will be laid as well as the chosen wheel path (lines closest to the curb and sidewalk. A trench for the location of the PVC pipes, which will carry the wires from the moisture tree to the DAC can also be seen near the person.

3.5.3 Sensor installation Day 1– Installation of sensors on the subgrade, subbase, and base (September 30th, 2022)

On this day, the graduate and postdoctoral students at the University of Waterloo responsible for this research project, along with several of their peers at CPATT, their faculty advisors and members from NRC were present on site to install the first round of sensors to lie on the subgrade, subbase, and base layers. The weather during the day was sunny with a high of 18 °C and a low of 2 °C, however during the work period, the temperature ranged from 14 to 18 °C.

3.5.3.1 Installation Procedure for Sensors on the Top of Subgrade

The first step in the installation process was demarcating the locations where the sensors will sit along the wheel path on the subgrade surface. This can be seen in Figure 3.26 and the exact locations for the sensors were determined using total station measurements provided by Capital Paving.



Figure 3.26 Subgrade condition the day of inspection (left) and the measuring and marking of sensor positions on the subgrade (right).

Afterwards, the sensors and the moisture tree were brought out onto the subgrade soil and removed from the packaging as can be seen in the left image of Figure 3.27. The next step required the bundling and placement of the sensor wires from the moisture tree through the black PVC conduit which would guide the sensor wires from the subbase to the data acquisition system. The bundling of the sensor wires can also be seen in Figure 3.27 in the right image.

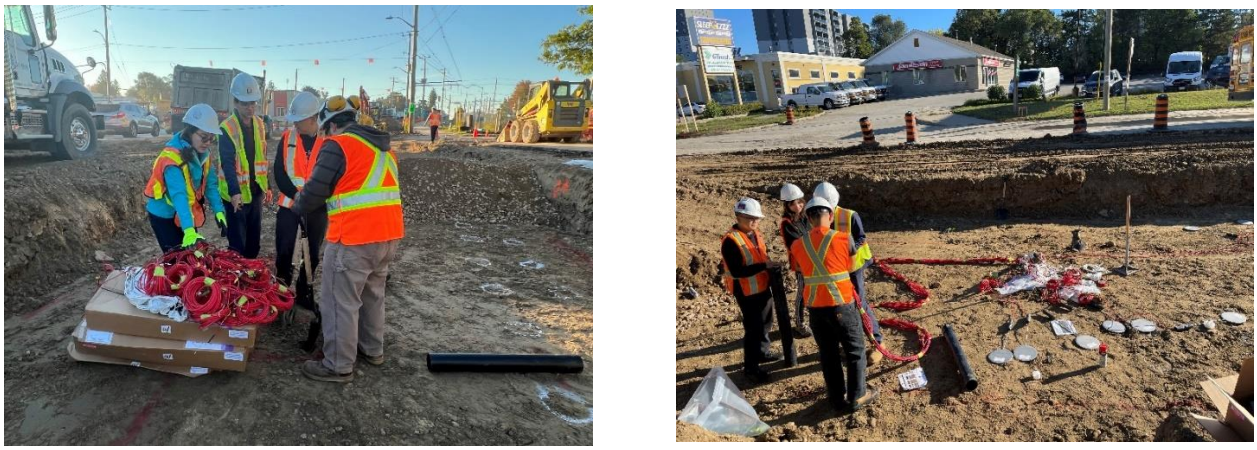


Figure 3.27 Packaged sensors brought on site (left) and bundling of sensors to place through PVC pipe (right).

Once the sensors were properly bundled, the PVC pipes were placed over top of the bundled wires until the required L-shaped structure was built as can be seen in the right image of Figure 3.28.



Figure 3.28 Placement of the black PVC pipe over the bundled wire(right) and the completed L-shaped PVC structure guiding all sensor wires from the subgrade to the DAC (left).

3.5.3.2 Installation Procedure of Moisture and Temperature Sensors

The installation procedure for the moisture and temperature sensors remained consistent throughout the entire construction project, both during the first sensor installation day on September 30th, as well as the next sensor installation day which would occur October 12th (explained in future sections). The first

part of the moisture tree installation consisted of placing the required portion of the moisture tree within the subgrade. As described in Table 3.2, the bottommost hole of the moisture tree, hole 8, is situated 340 millimeters below the top of the subgrade. Once this was in place, the team ensured that as the backfilling of the granular materials occurred that the moisture tree remained in a vertical position.

To install the moisture and temperature sensors, the moisture sensors were embedded into the subgrade or granular material, while the temperature sensors were simply allowed to come into contact with whichever granular material or subbase material it encountered as the backfilling procedure occurred. The temperature sensors were not specifically embedded to obtain accurate temperature measurements. However, each layer, whether it be subgrade, Granular B or Granular A, was hand compacted around the moisture tree after each backfilling procedure in order to maintain the standard level of compaction required for construction. An image of the installation of the moisture tree within the subgrade can be seen in Figure 3.29.

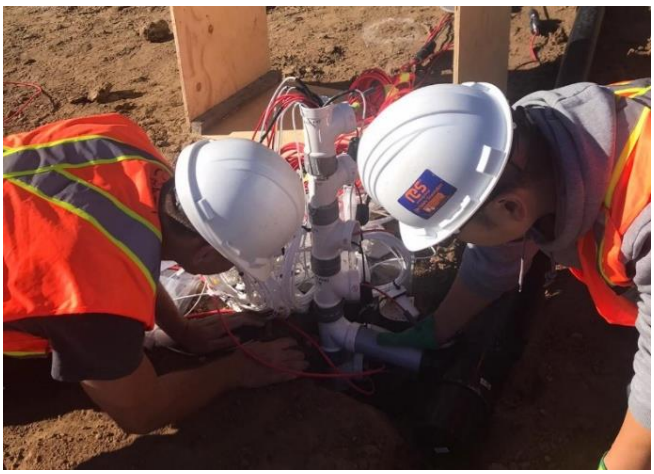


Figure 3.29 Installation of the moisture tree within the subgrade.

Following the initial plan, the pressure sensors intended for placement on the subgrade soil (specifically PC-SG-L-8 and PC-SG-R-7) were positioned. Shallow trenches of soil were dug so the sensor remained level and did not bend, and fine sand material was placed all around the sensors to provide protection and stability. The sensors were placed 180 degrees to the direction of traffic (to accommodate the sensor rods). This can be seen in the right image of Figure 3.30. Then some of the subbase soil was placed over top for protection.

To protect the remaining sensors during the backfilling of the Granular B, a wooden box was placed around the remaining bundle of sensors that were to be placed in other layers. In addition, some black plastic covering was placed over the exposed sensor wires to protect them. This can be seen in Figure 3.30 in the left image.



Figure 3.30 Find sand being placed around subgrade soil pressure sensors (right) and box protecting the group of sensors during backfilling procedure (left).

After this, the backfilling of the Granular B occurred. This can be seen in Figure 3.31 in the left image. Fortunately, the L-shaped PVC structure remained intact, and the wooden box was sufficient to protect the sensors during the backfilling process.



Figure 3.31 Both the (left) and (right) images show the backfilling of the Granular B material.

3.5.3.3 Installation Procedure for Sensors within the Subbase

After the backfilling of the subbase, a compaction roller passed several times over the Granular B soil to make sure that it was properly compressed. During this time, the remaining sensors in the box were supervised to make sure that no damage occurred to them. In addition, Capital Paving performed hand compaction of the soil close to the location of the sensors to be able to compact as much as possible

without potentially compromising any of the sensors or the moisture tree. Both the compaction roller and hand compaction processes can be seen in Figure 3.32.

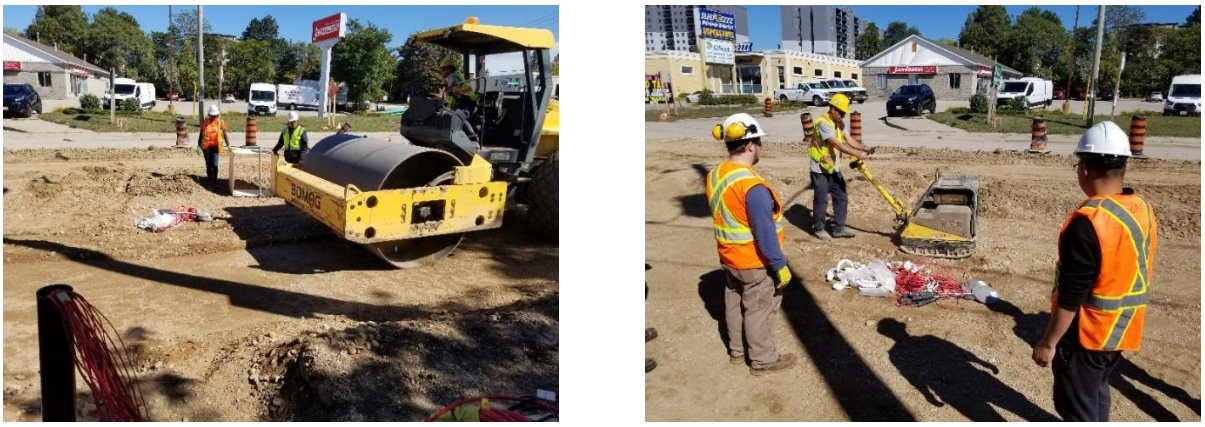


Figure 3.32 Compaction roller (right) and hand compactor (left) to flatten the subbase soil.

The pressure sensors PC-SB-R-3 and PC-SB-L-4 were installed on the top of the subbase as per the plan presented in Figure 3.11. Then Granular A soil was backfilled over the instrumented pavement section and once again, the area was compacted through a compaction roller and also through a hand compactor. In the left image in Figure 3.33, the installation of the two pressure sensors can be seen. Likewise, the right image in Figure 3.33 shows the backfilling and the compaction of the Granular A base material on the subbase. The wooden boxes continued to provide protection to the moisture tree and other sensors while the backfilling process was underway.



Figure 3.33 Implementation of the pressure sensors on the top of the subbase (left) and images of the backfilling procedure of Granular A with the wooden box present as protection to the moisture tree (right).

3.5.3.4 Sensor Installation within and on Top of Base

The next step of the construction process consisted of the implementation of the sensors within the base layer. This correlates to the implementation of the sensors within the Granular A material. As can be seen in Figure 3.34, the wooden box structure was dismantled and removed from the site. This was done by simply breaking off sections of the box and pulling them out from the base and subbase material. Also, in Figure 3.34 an image of the moisture tree within the Granular A material with all the sensors can be seen.



Figure 3.34 Removal of the protective box around the sensors (left) and image of the moisture tree with sensors (right).

Next, the compaction for the base was completed. Care was taken to ensure that none of the sensors would be damaged in the compaction process. This was especially important for the temperature probe sensors since the tops of these sensors would have to remain exposed. This needed to be done since the tops of the temperature probes would measure the temperatures within the HMA layer, to be poured at a future date. An image of the two exposed temperature probe tops can be seen in Figure 3.35.



Figure 3.35 Exposed temperature probe sensor tops (left) and hand compaction of the soil adjacent to the sensors (right).

Finally, the day concluded with wrapping the remaining sensors that were to be placed on the base surface in an additional box with a tarp to protect it from the elements until the asphalt concrete pouring date was confirmed. The protected box setup can be seen in Figure 3.36 below.



Figure 3.36 Protected sensors.

3.5.4 Pouring of Concrete Pad (October 5th, 2022)

Several days after the first sensor installation day, the graduate team from CPATT went out on site to supervise the pouring and installation of the concrete base pad on which the data acquisition system for the sensors will sit. When the team arrived, there was formwork ready to go for the pouring and the

concrete truck was already there. The pouring went very smoothly. In Figure 3.37 the concrete pouring and smoothing process can be seen.



Figure 3.37 Installation of the concrete base pad for the data acquisition system.

3.5.5 Arrangement of the base/asphalt concrete sensors (October 11th, 2022)

During this day, the CPATT graduate team went out on site to arrange the sensors that will sit on the surface of the base layer. These included the pressure sensors PC-BA-R-1, PC-BA-L-2, PC-BA-R-5, and PC-BA-L-6, as well as all the asphalt strain gauges (vertical and horizontal). The team ensured that all of the sensors were installed according to their designated planned locations.

For the pressure sensors, the same installation procedure used as during the construction of the subbase (i.e., a small trench was dug out to ensure the pressure sensor was level, and a fine sandy material was placed underneath and around the sensors to provide support and to ensure no large granular material had a chance of damaging the sensors). The TEPC sensors were placed at 45-degree angles relative to the traffic flow to accommodate the long rods stemming from the sensor. In a similar manner, the asphalt concrete strain gauges were placed into the base layer by digging out a small trench, then placing the fine granular material around the gauges to minimize damage. In addition, the asphalt strain gauges were covered by a small amount of PG 54 - 28 asphalt an order to protect it from the pouring of the HMA that would happen the next day.

Images of the pressure sensors and asphalt strain gauges as they were set up on site can be seen in Figure 3.38 and Figure 3.39.



Figure 3.38 Two views of the implementation of the asphalt strain gauges and the pressure sensors on site.



Figure 3.39 View of the pressure sensor installation to the left and the asphalt strain gauge installation to the right.

3.5.6 Sensor Installation Day 2– Installation of sensors on the base and asphalt concrete (October 12th, 2022)

On this day, the graduate and postdoctoral students at the University of Waterloo responsible for this research project, along with several of their peers at CPATT, their faculty advisors and members from NRC were present on site to install the second round of sensors to lie on the base layer and within the asphalt concrete. The weather during the day was a mix of sun and cloud with a high of 20 °C and a low of 11 °C.

One of the first tasks once the team arrived on site was to cover the external wires from the strain gauges with a layer of asphalt to protect them from direct contact with the hot asphalt paver. This was done by hand as can be seen in Figure 3.40.



Figure 3.40 Covering of the sensor wires with asphalt concrete to protect them.

Next, the asphalt paver came and specifically poured asphalt concrete over the area where the sensors were to provide additional protection. This was done on the part of Capital Paving. Images of the paver covering the area where the sensors are located can be seen in Figure 3.41.



Figure 3.41 Targeted pouring of asphalt concrete over the instrumented section.

Once the paver had finished covering the sensors the instrumented area looked like what is shown in Figure 3.42 below.



Figure 3.42 Instrumented section with targeted pouring complete.

Afterwards, the asphalt paver poured out the first lift of asphalt concrete to form the lane which sits southbound closest to the curb edge. Due to the preliminary pouring of the actual concrete over the instrumented section, there was less of a risk of sensors being moved or damaged while the paver was laying the asphalt in the lane. Next, the compaction roller for the asphalt concrete rolled over the lane. Both the pouring and compaction of the asphalt can be seen in Figure 3.43.



Figure 3.43 Asphalt concrete being poured onto the instrumented section (right), and compaction roller compacting the asphalt pavement section (left).

For most sensors, the installation process concluded with the pouring of the first layer of asphalt concrete over the instrumented test section. However, the temperature probe sensors, being elongated and requiring precise placement in multiple layers of the pavement structure, posed an additional step. As per the original installation plan, the top of the temperature probe sensor needed to protrude from the first

layer of concrete poured, as it had to be situated within the second lift (the topmost layer of AC). Marking the location of the temperature probe was necessary before the asphalt hardened. Figure 3.44 illustrates the team excavating the asphalt surface to locate the temperature probe sensor.



Figure 3.44 Identification of the temperature probe sensor.

Uncertainty regarding the timing of the second asphalt lift, slated for approximately a year later, prompted the team to make a practical decision. To shield the moisture temperature probe sensor from potential exposure to live traffic immediately after paving, the team chose to fully immerse it in the existing first lift of asphalt. This adjustment resulted in a shift of all temperature probe sensors further down than originally planned. Figure 3.45 illustrates the original and current plans for moisture probes, with a switch from in the asphalt layer to slightly within the Granular Base layer for the TEMPS-01-3 and TEMPS-02-3 sensors. This is because the first lift of asphalt is 145 mm, whereas the bottommost sensors in the temperature probes are located 190.5 mm from the top of the sensor. Note that the drawings in the figure are not to scale.

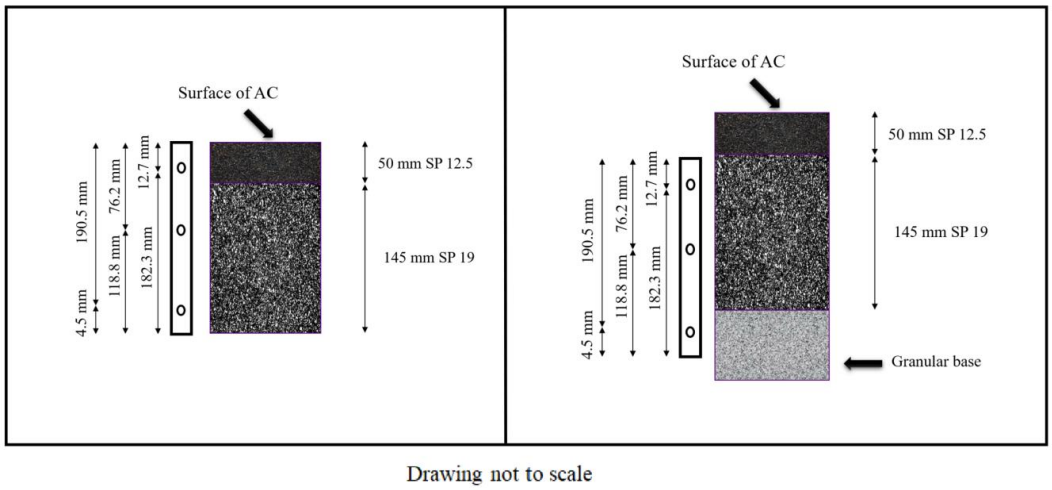


Figure 3.45 Comparison of the initial(left) and final (right) installation plans for the temperature probes.

3.5.7 Hydro Connection – hydro line installation and grounding (December 21, 2022)

To provide constant reliable power to the data acquisition system, a connection to the city hydro line was installed. Representatives from the Region of Waterloo were present on site to assist with the establishment of the hydro connection on the adjacent utility pole. First, a hydro box needed to be installed to the hydro pole, and the hydro wire connection along the utility pole. Both can be seen in Figure 3.46.



Figure 3.46 Hydro wire connection and box on the adjacent utility pole.

Next, the hydro wire was placed into the DAC, to be able to be plugged into a plug box. In addition, a ground wire was also placed in the DAC, and this can be seen in Figure 3.47.

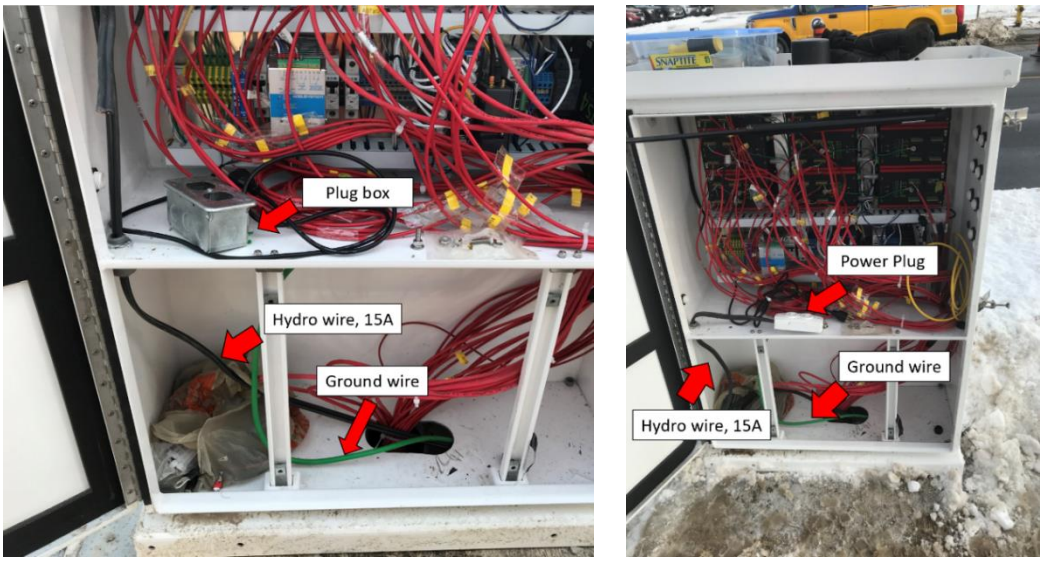


Figure 3.47 Ground wire, hydro wire and plug box setup.

The plug box, along with the power plug will be used as a connection point to be able to connect the hydro wires to the computer and other components of the DAC. Figure 3.48 shows more images of the plug box and the wire setup within the DAC.



Figure 3.48 Closeups of the plug box and hydro wire.

3.5.8 Material Sampling

3.5.8.1 Sampling of base/subbase material

Several bags of both Granular A and Granular B material were collected from the site as the backfilling procedures for each layer occurred. For instance, Figure 3.49 below shows the sampling of the Granular B material.



Figure 3.49 Sampling of the Granular B material.

3.5.8.2 Sampling of asphalt concrete material

In addition, as the concrete was being poured on the lane during the asphalt pouring face, about 30 cardboard boxes of asphalt concrete sample were collected for later materials testing.

3.6 Construction Challenges

There were several construction challenges that were encountered during the sensor instrumentation of the test section, which should be addressed in the future for improved data quality:

1. **Issues Related to Weather Concerns and Construction Schedule Coordination**: The installation process commenced in the fall season, as it was only at this time that the site was available to the graduate team after the works performed by the contractors (watermain/storm/sewer installation, etc.). This limited the amount of time the team had to install the sensors before the winter arrived, and it increased the chances of poor weather conditions affecting the installation process. For future studies, the sensor installation process should, as much as possible, try to be done during warm and sunny periods. However, this all depends on the timelines imposed by the construction crew. Coordinating the sensor installation with the construction crew's schedule is crucial. Delays in one activity may have a domino effect on the overall project timeline.
2. **Time Constraints**: There was a limited amount of time from when the sensors were shipped to the University of Waterloo to the date when the sensors needed to be installed on site, which limited the amount of time available to the graduate team to fully test the sensors in the lab prior to installation. The graduate team did end up calibrating and ensuring that each of the sensors worked prior to construction, however this was done in a short period of time (2 to 3 weeks of full-time work). A longer time is recommended in future projects to ensure that there are no problems with the sensors and that they all are capable of measuring to the ranges specified in their specification sheets. In addition, the data acquisition system box was not delivered to the University of Waterloo on time for the truck testing procedure. This would have permitted for much more preliminary construction data to be collected during crucial tests such as the first track test (explained in Chapter 5). Since there was only one STS4-4 -4 Terminal Node available to the team, which can hold up to four sensors at a time, the sensors were switched to try and capture as much data as possible.
3. **Faulty Equipment**: The LWD machine was broken, and spare parts needed to be acquired which delayed the LWD testing of the subgrade.

4. **Changes in Installation Plans**: As mentioned previously, the moisture probe, which was supposed to be installed partially in the top lift of the asphalt structure is now not installed there due to the delays in the pouring of the top lift. Therefore, the temperatures experienced in the top lift will not be able to be captured. In addition, the multi-depth deflectometer sensors that were planned to be installed during this project were not installed due to complications with the installation process.
5. **Accuracy of Sensor Placement:** Precise placement of sensors is essential for accurate data collection. Challenges may arise in achieving the required accuracy while working in a dynamic construction environment.
6. **Vibration and Impact:** Construction activities, such as heavy machinery and compaction, can generate vibrations and impact the sensors. Implementing measures to protect the sensors from damage is important. An example of this challenge arose when it was discovered shortly after installation that all the vertical asphalt strain gauges were no longer functioning (despite working before installation in the soil). Despite efforts to protect the sensors by covering them with asphalt, it proved insufficient to prevent their breakdown.
7. **Data Security:** With the increasing use of smart infrastructure, ensuring the security of sensor data is crucial. Implementing encryption and secure communication protocols becomes essential to protect sensitive information. The University of Waterloo IT department helped to set up measures for data protection.

Chapter 4
Testing of Materials

This Chapter outlines the results of the various post-construction/field and laboratory testing actions and procedures undertaken to obtain further information on the properties of the various materials in the pavement structure. This section is divided into two sections: post-construction field testing and laboratory testing.

4.1 Post-Construction Field Testing

Various field-testing procedures were conducted both during and after the installation of the sensors. These procedures encompassed sampling materials from both the base and subbase, as well as the asphalt concrete. Additionally, the pavement structure underwent light weight deflectometer (LWD) testing across its various layers. Furthermore, truck testing was carried out on the freshly paved lane, which included the instrumented test section.

4.1.1 Truck Testing

Truck testing was an important testing method used in the months following the construction and installation of the sensors within the test section. This test requires a truck of known weight and axle configuration to run over the row of sensors that are installed in the test section, while the section is closed to live traffic. This kind of test is done to understand the effect of a vehicle of known weight on the sensor responses under a controlled axle load. Throughout the months following the installation of the test section, the truck test was performed five times: the first being right after construction and pouring of the asphalt concrete layer, the second occurring five months after in March 2023, the third occurring during the summer months in July 2023, the third right after the pouring of the top asphalt layer in August of 2023, and the final being done during fall conditions in December of 2023. The results of this test will be presented in Chapter 5 as the analysis associated with the results are extensive. In addition, Chapter 6 will use the data collected in the last truck test for its assessment on the relationship between truck position and sensor response.

4.1.2 LWD Testing

The Lightweight Deflectometer Test (LWD) was performed on September 30th, between 2 to 5 PM by a team of four members from CPATT. This test is performed to determine the pavement modulus or stiffness [18], and it was performed on both the left and right sensor arrays throughout the instrumented test section a total of four times. Because this test is manually performed, it can be subject to human error, thus care was taken to minimize this error by ensuring that at least three drops with consecutively

constant or close outcomes were achieved at any testing point before moving to the next location. Also, care was taken to drop the load properly from the required height. Images of the LWD testing can be seen in Figure 4.1.

The testing for the subbase and base materials was performed as the backfilling and compaction process was underway. For the base and subbase, the tests were performed on compacted material. However, the testing for the subgrade was done on exposed subgrade slightly further away (~15 to 20 m) from the subgrade at the instrumented test section since the LWD machine was broken during the time that the subgrade within the instrumented test section was exposed. The construction process needed to continue, therefore the contractors continued with the backfilling of the Granular B material while the CPATT team attempted to fix the LWD. Therefore, the team needed to perform the LWD testing on the subgrade at a different location, but it is assumed that the properties of the subgrade are the same in both areas since they were situated so close together.

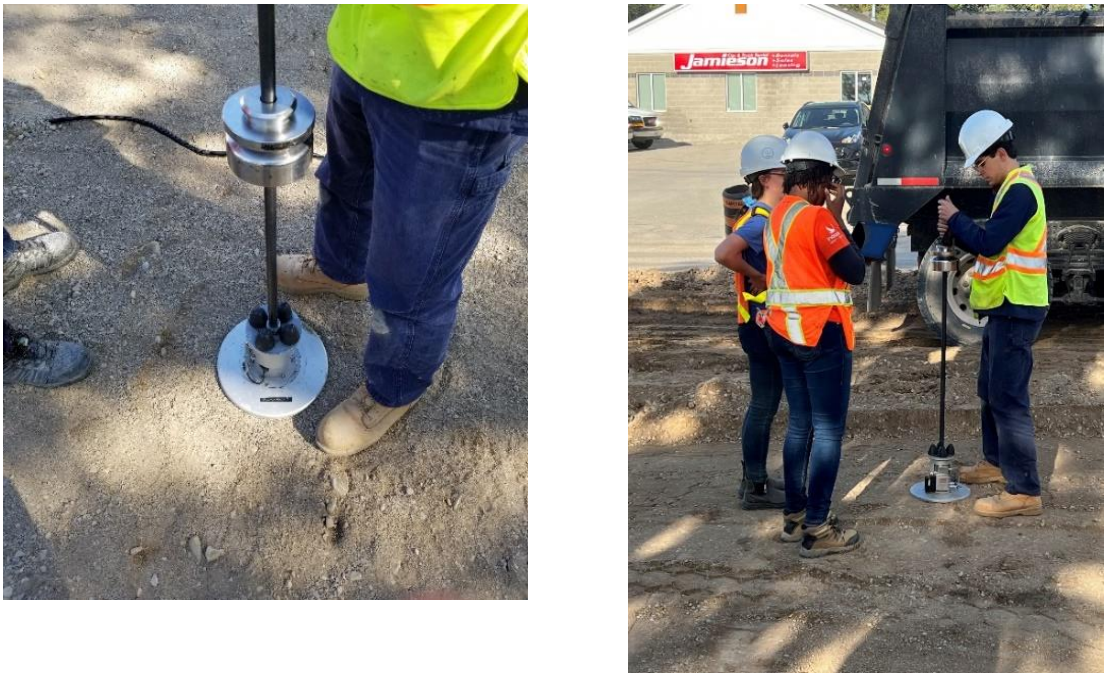


Figure 4.1 Light Weight Deflectometer (LWD) testing.

Table 4.1 Elastic Modulus Results from LWD Testing

Location	Average Eo (MPa)	Standard Deviation of Eo (MPa)
Base (*Granular A****)***		
1	85.67	2.08
2	73.00	1.00
3	80.67	2.52
4	80.00	2.00
Subbase (*Granular B****)***		
Left Array		
1	60.00	5.20
Right Array		
1	53.67	3.51
Subgrade		
1	21.00	1.00

As can be seen from the results, the modulus results decrease as one goes from the base to the subgrade. This makes sense as the asphalt concrete would have a greater modulus than the granular materials to provide additional strength support to the pavement structure.

Table 4.2 Deflection Results for LWD Testing

Location	Average Deflection (µm)	Standard Deviation of Micron (µm)
Base (*Granular A****)***		
1	474.33	12.22
2	540.33	9.29
3	498.33	18.72
4	494.67	10.02
Subbase (*Granular B****)***		
Left Array		
1	671.00	61.54
Right Array		
1	751.00	42.04
Subgrade		
1	816.33	25.77

The results for the deflection indicate that as one goes down from the base to the subgrade, the average deflection increases.

4.2 Lab Testing

4.2.1 Asphalt: Dynamic Modulus Testing

Using samples collected from the post-construction testing, the dynamic modulus of the asphalt was determined for use in the development of a master curve. According to the relevant ASTM standard, the dynamic modulus is defined as "the absolute value of the complex modulus that defines the elastic properties of a linear viscoelastic material subjected to a sinusoidal loading, $|E^*|$" [54, p. 1]. The complex modulus is defined as "a complex number that defines the relationship between stress and strain for a linear viscoelastic material, or E^* or G^*" [54, p. 1]. The complex modulus is a vector, composed of the Elastic/Storage modulus, or G', and the Viscous/Loss modulus, or G''.

The complex modulus better represents the behaviour of asphalt than using either the shear modulus or elastic/Young's modulus due to asphalt behaving like a viscoelastic material. During warm summer months, asphalt pavement displays more viscous behaviour and is more prone to permanent deformation and rutting, while in the cooler winter months, the pavement behaves more like a brittle or rigid material and tends to be prone to low temperature cracking. A modulus master curve demonstrates the changes in the asphalt concrete modulus with changes in temperature and loading frequency. This fundamental property is key for understanding how the material will react overtime based on external factors. According to the relevant ASTM standard, asphalt mixtures with elevated complex shear modulus at a given service temperature are anticipated to show reduced permanent deformation compared to similar mixes with lower complex shear modulus values tested at the same temperature [55].

In order to perform this test, cylindrical specimens of compacted asphalt concrete mixes are created. On these cylindrical specimens, sinusoidal cyclic loading in the compressive direction is applied to the specimens at various temperatures and loading frequencies. Strain is produced and captured by Linear Variable Displacement Transducers (LVDT's), which is then used to calculate the dynamic modulus.

In this project, three specimens were generated and subjected to testing in a gyratory format and a cylindrical format. The ensuing information in Table 4.3 was derived from these tests, where the average of the responses from the tests and the standard deviation of the three samples tested.

For this project, the dynamic modulus test was performed at five different temperatures (-10, 4, 21, 37 and 54 °C) and six different frequencies (25, 10, 5, 1, 0.5 and 0.1 Hz). The test begins from the highest frequency and the lowest temperature. Due to time/temperature superposition, and the master curve reference temperature (which was 21 °C in this case), the data was able to be shifted, and the shift factor for this data can be seen in Figure 4.2.

Table 4.3 Specimen testing information derived from the tests.

	Specimen No.	Average	Standard Deviation
Gyratory Specimen of 150 mm in diameter and 178 mm in height	Mass of Compacted Specimen in Air (gr)	7231.5	6.6
	Saturated Surface Dry Mass of Compacted Specimen in Air (gr)	7286.8	10.9
	Mass of Compacted Specimen in Water (gr)	4201.9	7.9
	Volume (cm^3)	3084.9	7.7
	Maximum Relative Density	2.6	0.0
	Bulk Relative Density	2.3	0.0
	Percent Voids in the Specimen (%)	8.4	0.2
Cylindrical Specimen of 100 mm in diameter and 150 mm in height after coring and cutting	Mass of Specimen in Air (gr)	2863.3	14.3
	Saturated Surface Dry Mass of Specimen in Air (gr)	2865.9	14.3
	Mass of Specimen in Water (gr)	1666.9	11.1
	Volume (cm^3)	1198.9	3.3
	Maximum Relative Density	2.6	0.0
	Bulk Relative Density	2.4	0.0
	Percent Voids in the Specimen (%)	6.7	0.2

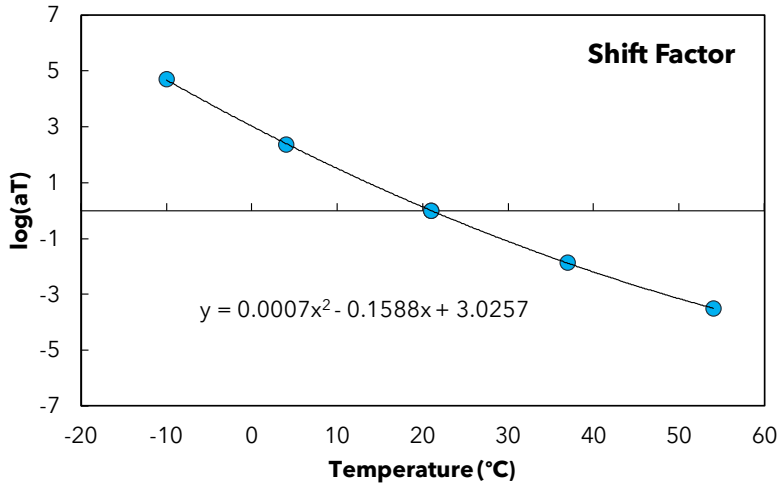


Figure 4.2 Shift factor for test data.

Table 4.3 and Table 4.4 below show the results of the dynamic modulus tests that occurred. The dynamic modulus results in megapascals are shown in Table 4.3, while the phase angle results in degrees are shown in Table 4.4. The master curve can then be developed and will define the relationship between the dynamic modulus and the reduced frequency at the reference temperature. This test was performed on HMA samples that were taken from when the first layer of HMA was poured in October 2022, or SP 19.0 mm SG 58-28 asphalt.

Table 4.4 Dynamic Modulus in MPa

		Testing Frequency (Hz)					
		0.1	**0.5**	**1**	**5**	**10**	**25**
Testing Temp (°C)	**-10**	17432	18817	21097	22573	23604	24876
	4	7452	9224	11249	13539	14872	16574
	21	1605	2427	3246	4983	5998	7471
	37	304	487	698	1231	1618	2329
	54	105	138	172	297	394	627

Table 4.5 Phase Angle in Degrees

		Testing Frequency (Hz)					
		0.1	**0.5**	**1**	**5**	**10**	**25**
Testing Temp (°C)	**-10**	10.2	8.3	6.4	6.2	5.6	5.0
	4	21.4	17.6	16.7	12.2	11.4	10.3
	21	25.7	27.8	23.2	23.4	22.0	20.2
	37	23.5	27.3	34.4	29.9	30.7	30.1
	54	17.7	22.1	21.2	28.9	31.0	32.3

This was done by fitting the data developed in Table 4.3 and Table 4.4 produce a reduced frequency and a fitted dynamic modulus which was then plotted on the master curve. When the error was minimized, the following master curve, shown in Figure 4.3, was produced.

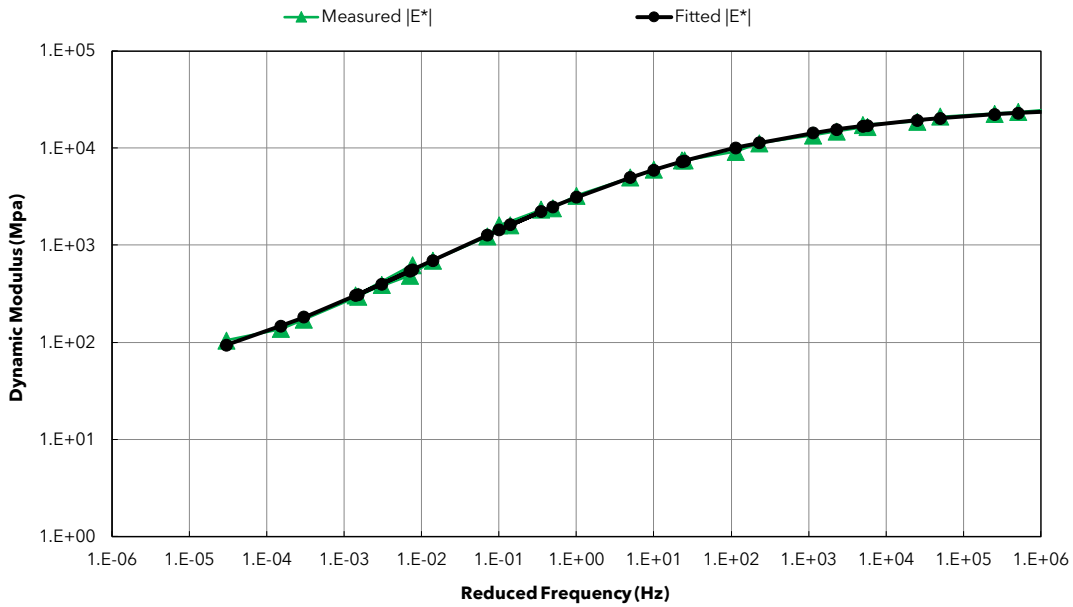


Figure 4.3 Master curve.

4.2.2 Base and Subbase: Optimum Moisture Content Determination

In tandem with the Dynamic Modulus test, a Standard Proctor Test was conducted on granular materials extracted from the instrumented test section site, adhering to ASTM D698-12(2021) guidelines [56]. The decision to employ the Standard Proctor Test stemmed from the need to calibrate moisture sensors, prompted by their initial malfunction, as detailed in Chapter 8. After resolving the moisture sensor issues independently of the Proctor Test results, the test assumed a dual role—serving as a method to discern and enhance understanding of the soil moisture properties directly within the instrumented test section and validating these findings against the geotechnical report [51] prepared for the Region of Waterloo.

The primary advantage of conducting the Proctor Test lies in its ability to ascertain the optimal moisture content essential for compacting soils for diverse applications, including road bases, embankments, and foundations [57]. Soil compaction, facilitated by the Proctor Test, yields several benefits from a construction standpoint, such as establishing more robust surfaces for load-bearing projects like roads, as well as ensuring "satisfactory engineering properties such as, shear strength, compressibility, or permeability" [56, p. 3]. This process not only enhances immediate stability but also ensures the long-term durability of these roads, guaranteeing their ability to withstand and sustain heavy vehicles over time [58]. In essence the Proctor Test procedure that determines the optimal moisture content of the soil being tested [56]. This is done by preparing soil specimens that have progressively more moisture added. The soil is then compacted into moulds with known volumes and weighed. Theoretically, the unit weights of

the moulds will increase with each soil specimen until the optimal moisture content is reached, after which the moisture content will decrease. This is determined by plotting the dry unit weight versus the moisture content, whereby the maximum point on the curve represents the optimal moisture content (w_{opt}) [56]. This plot can be seen in Figure 4.4.

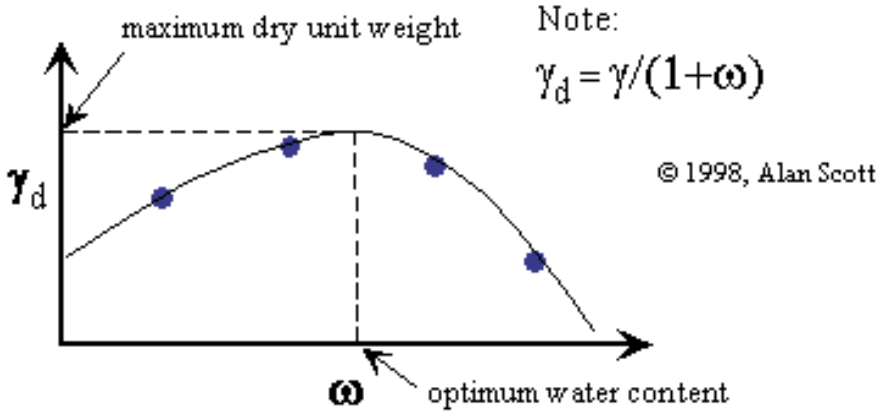


Figure 4.4 Moisture content vs. dry unit weight plot [59].

The first step in the Proctor Test procedure entailed verifying the suitability of all designated samples for testing. While the Granular A and Granular B materials were relatively dry, the subgrade soil presented itself in an inherently agglomerated state, characterized by substantial clumps and larger fragments, which would prevent much of the soil from passing through the sieves. To address this, the subgrade soil was spread out on plastic sheets in a thin layer, allowing it to dry overnight. This deliberate drying process facilitated the escape of moisture and enabled the breaking down of larger soil pieces. The drying process can be seen in Figure 4.5.



Figure 4.5 Drying of subgrade soil setup.

Following sample preparation, the Granular A, Granular B, and subgrade soils were individually allocated to distinct containers and subjected to a drying process within an oven. Notably, the subgrade material underwent drying until it attained a friable state, adhering to the specifications outlined in the ASTM standard [56]. Upon achieving friability, the subgrade material underwent meticulous disintegration to dismantle any soil aggregations.

With the granular layers and subgrade soils appropriately dried and disintegrated, the subsequent phase involved commencing the sieving process. In this instance, the ASTM-prescribed Method A was employed, designating the number four- or 4.75-millimeter sieve as the defining sieve. However, the comprehensive suite of sieves utilized in the assessment comprised the 19-millimeter, 12.5-millimeter, 9.5-millimeter, 4.75-millimeter, 2.36-millimeter, one, and 1.18-millimeter sieves. Notably, any soil passing through the 1.18-millimeter sieve was categorized as “fines”. The sieving process was performed for all of the granular layers and subgrade soil. Table 4.6, Table 4.7, and Table 4.8 show all of the sample weights per sieve for each of the materials/soil types.

Table 4.6 Granular A Material Gradation

Sample Weight: 10169.5 g	
Sieve Size	**Sample Weight per Sieve**
19 mm	270.1 g
12.5 mm	1404.8 g
9.5 mm	886.8 g
4.75 mm	1570.8 g
2.36 mm	1557.2 g
1.18 mm	1343.0 g
Fines	3145.4 g

Table 4.7 Granular B Material Gradation

Sample Weight: 10324.1 g	
Sieve Size	**Sample Weight per Sieve**
19 mm	357.8 g
12.5 mm	594.7 g
9.5 mm	661.4 g
4.75 mm	1118.5 g
2.36 mm	1192.0 g
1.18 mm	1953.3 g
Fines	4440.7 g

Table 4.8 Subgrade Material Gradation

Sample Weight: 10082.9 g	
Sieve Size	**Sample Weight per Sieve**
19 mm	91.6 g
12.5 mm	300.8 g
9.5 mm	796.1 g
4.75 mm	3181.8 g
2.36 mm	2123.6 g
1.18 mm	1187.8 g
Fines	2394.9 g

After the aforementioned procedures, the portions of material from each of the Granular A, Granular B, and subgrade soil, which successfully passed through the 4.75-millimeter sieve, were combined. This amalgamation constituted the composite sample designated for the subsequent Proctor Test.

The Proctor Test consisted of continuously adding moisture to the Granular A, Granular B and subgrade soil samples, and then filling 11 compaction moulds with the ever-increasing moisture samples, with 3 moulds being filled with Granular A, four moulds being filled with Granular B and four moulds being filled with the subgrade soil.

The Proctor Test procedure entailed a progressive addition of moisture to the samples of Granular A, Granular B, and subgrade soil. Then, eleven (11) compaction mould were filled, with three moulds dedicated to Granular A, four moulds dedicated to Granular B, and four moulds dedicated to the subgrade soil. Notably, each mold designated for Granular A, Granular B, and subgrade soil witnessed a progressive augmentation in moisture content during the filling process. This was done in a container as shown in the left image of Figure 4.6. Within each mould, the soil was compacted in three layers using a manual rammer, with each layer being compacted in 25 blows [56]. The compacted specimens were trimmed with a straightedge to flatten the tops of the moulds.

During the compaction process, each mould, encompassing both the mould structure and the soil within, was enveloped in plastic wrap. This is shown in the right image in Figure 4.6, as well as Figure 4.7. This precautionary measure was implemented to curtail moisture loss from the moulds. Originally, this step was devised with the intention of transporting the samples to the site for utilizing a moisture sensor, on loan from BDI, to calibrate the pavement structure's existing moisture sensors. However, upon discovering that the issue with the moisture sensors was unrelated to calibration but rather stemmed from certain sensor settings, the samples were promptly returned. Subsequently, the Proctor Test proceeded to its subsequent stages for determining the moisture contents of the samples.



Figure 4.6 Container for mixing and adding moisture to each of the Gran. A, Gran. B and subgrade soil samples (left). Wrapping of the samples within the moulds to prevent moisture loss for use on site (right).



Figure 4.7 All 11 samples prepared for moisture sensor calibration.

Portions from the top and bottom of the extruded material/samples from the moulds were transferred to coffee cups. Two coffee cups were used for each of the 11 samples, which resulted in 22 cups being prepared, as depicted in Figure 4.8.



Figure 4.8 Extruded and cut samples of soil from each of the 11 samples, with two cups per sample for a total of 22 cups.

Each of these samples was then placed in the oven to dry 24 hours before recording the dry unit weights.

Table 4.9, Table 4.10, and Table 4.11 display the results of volumetric moisture content calculations for all 22 cups sourced from the 11 samples. In Table 4.6, the initial phase of the Proctor Test is outlined, where the weights of the moulds, the moulds plus the wet soil, the wet soil alone, as well as the specimen's volume and density were determined following ASTM requirements. This comprehensive data allowed for the calculation of both moisture content and volumetric moisture content for each sample version—each version corresponding to one of the two coffee cups used for each of the 11 samples.

The subsequent equations detail the computations for various parameters featured in Table 4.9 to Table 4.11, covering calculations for moisture content, volumetric water content, and other relevant parameters. The calculation for moisture content by weight is as follows, along with the density of the specimen:

$$w = \frac{M_w}{M_s}$$

$$\rho_{total} = \frac{M_{total}}{V_{total}} = \frac{M_w + M_s}{V_{total}}$$

Then, for each specimen:

$$M_s = \frac{M_{total}}{1 + w}$$

$$M_w = \frac{M_{total}}{1+w} \times w$$

Therefore,

$$\theta = \frac{V_w}{V_{total}} = \frac{M_w/\rho_w}{V_{total}} = \frac{\frac{M_{total}}{1+w} \times w/\rho_w}{V_{total}}$$

Where, θ = Volumetric moisture content [dimensionless]

w= Moisture content by weight [%]

V_w, M_w, ρ_w = volume [L^3], mass [M], and density of water [M/L^3]

V_s, M_s, G_s (≈2.65) = volume, mass, and specific gravity [dimensionless] of soil

V_{total}, M_{total} = volume, mass for soil + water + air (wet soil)

Table 4.9 Mould Weight, Wet Soil Mass, Mould Dimensions, Specimen Volume, and Density for Eleven Mould Specimens prepared for Granular A, Granular B and Subgrade Soil

	Specimen #	Weight of mold (g)	Weight of mold+wet soil (g)	Weight of wet soil Mtotal(g)	Diameter of specimen (cm)	Height of specimen (cm)	Volume of specimen Vtotal (cm3)	Density of specimen (g/cm3)
Granular A	1	2482.4	3753.8	1271.4	10.08	7.87	628.04	2.02
	2	2333.3	3668.9	1335.6	10.08	8.12	647.99	2.06
	3	2339.1	3714.4	1375.3	10.08	7.87	628.04	2.19
Granular B	4	2354.9	3604.4	1249.5	10.08	7.87	628.04	1.99
	5	2348.7	3583.3	1234.6	10.08	7.87	628.04	1.97
	6	2326.6	3564.9	1238.3	10.08	7.87	628.04	1.97
	7	2342.7	3589.4	1246.7	10.08	7.87	628.04	1.99
Subgrade	8	2338.4	3489.3	1150.9	10.08	7.87	628.04	1.83
	9	2494.3	3725.8	1231.5	10.08	8.12	647.99	1.90
	10	2256.2	3631	1374.8	10.08	7.87	628.04	2.19
	11	2261.1	3653.1	1392	10.08	7.87	628.04	2.22

Table 4.10 Version 1: Volumetric Content Determination

	Specimen #	Weight of Soil Sample with Water (g)	Dry Weight of Soil Sample (g)	Moisture content by weight/w (%)	Dry Density of specimen (g/cm3)	Volumetric content/θ (%)
Granular A	1-1	111.40	105.50	5.592	1.9172	10.72
	2-1	119.70	111.30	7.547	1.9165	14.46
	3-1	102.10	95.50	6.911	2.0483	14.16
Granular B	4-1	92.60	88.90	4.162	1.9100	7.95
	5-1	79.00	75.40	4.775	1.8762	8.96
	6-1	105.50	99.00	6.566	1.8502	12.15
	7-1	108.40	100.40	7.968	1.8386	14.65
Subgrade	8-1	85.70	81.60	5.025	1.7449	8.77
	9-1	82.20	76.80	7.031	1.7756	12.49
	10-1	102.60	91.60	12.009	1.9543	23.47
	11-1	104.40	87.80	18.907	1.8640	35.24

Table 4.11 Version 2: Volumetric Content Determination

	Specimen #	Weight of Soil Sample with Water (g) Version 2	Dry Weight of Soil Sample (g) Version 2	Moisture content by weight/w (%)	Dry Density of specimen (g/cm3)	Volumetric content/θ (%)
Granular A	1-2	103.90	97.70	6.346	1.9036	12.08
	2-2	119.60	111.00	7.748	1.9129	14.82
	3-2	95.40	89.40	6.711	2.0521	13.77
Granular B	4-2	87.30	83.90	4.052	1.9120	7.75
	5-2	85.50	81.40	5.037	1.8715	9.43
	6-2	94.30	88.70	6.313	1.8546	11.71
	7-2	105.30	97.50	8.000	1.8380	14.70
Subgrade	8-2	75.90	70.40	7.813	1.6997	13.28
	9-2	81.10	75.50	7.417	1.7693	13.12
	10-2	107.30	95.80	12.004	1.9544	23.46
	11-2	112.80	95.00	18.737	1.8667	34.98

After determining the parameters, the subsequent step involved preparing the compaction curves for each of Version 1 and Version 2. Figure 4.9 illustrates the compaction curve for version one, while Figure 4.10 illustrates the compaction curve for version two. These figures depict the optimal moisture content based on the provided data. Only the data for the subgrade was plotted, as it presented the most comprehensible trends. The Granular A and Granular B materials did not exhibit clear trends; hence, only the subgrade layer data was considered.

As depicted in Figure 4.9, the optimal moisture content for version one is 13.84%, while for version two, as indicated in Figure 4.10, it is 14.42%. Averaging these values yields an overall optimal moisture content for the subgrade of 14.13%.

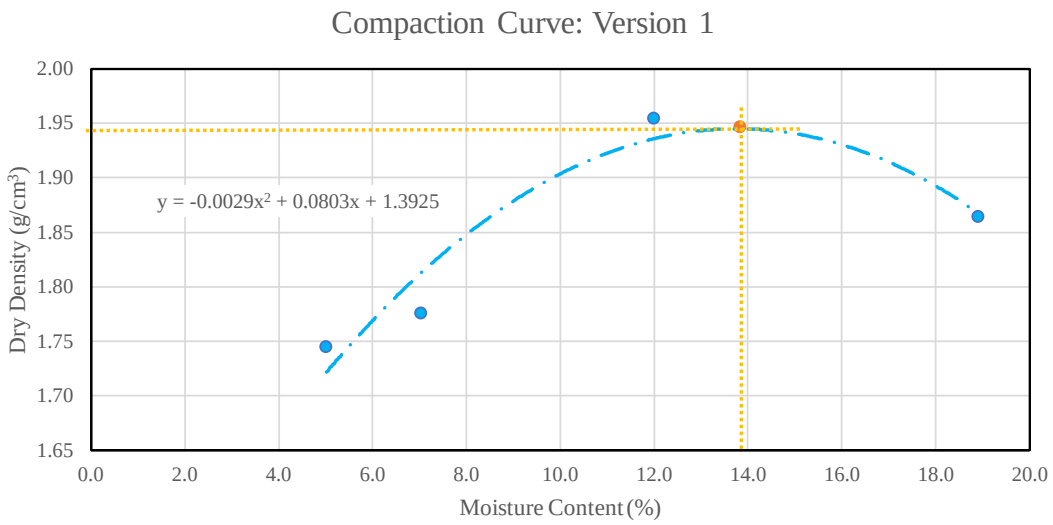


Figure 4.9 Moisture content vs. dry unit weight plot for the Version 1 material/soil samples.

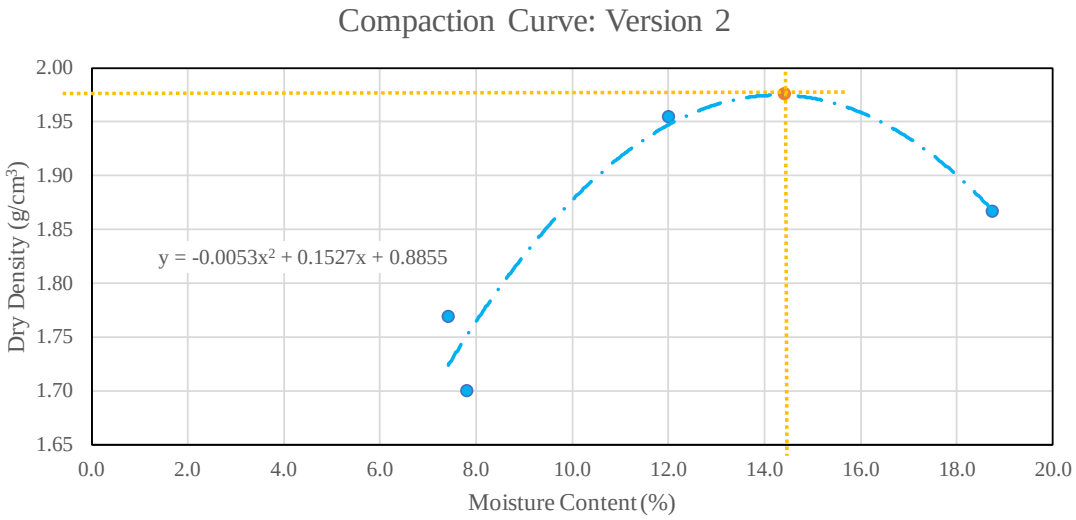


Figure 4.10 Moisture content vs. dry unit weight plot for the Version 2 material/soil samples.

In addition, the average volumetric moisture content was determined based on the results of the volumetric contents obtained for the version one and version two samples. The results can be seen in Table 4.12. As can be seen from the table, the lowest volumetric moisture content was determined to be in Granular B with a value of 7.85%, while the largest moisture content is found in the subgrade at 35.11%. In addition, if we look at the average volumetric content per layer, we get a result of 13.34% for the Granular A layer, 10.91% for the Granular Belayer and 20.6% for the subgrade layer. This means that the average volumetric content for the Granular A layer is higher than that of the Granular B layer, but both are lower than the subgrade layer.

Table 4.12 Average Volumetric Moisture Content for the Granular A, Granular B and Subgrade Soil samples

	Specimen #	**Volumetric content/θ (%) Version 1**	**Volumetric content/θ (%) Version 2**	**Average Volumetric Content (%)**
Granular A	1	10.72	12.08	11.40
	2	14.46	14.82	14.64
	3	14.16	13.77	13.96
Granular B	4	7.95	7.75	7.85
	5	8.96	9.43	9.19
	6	12.15	11.71	11.93
	7	14.65	14.70	14.68
Subgrade	8	8.77	13.28	11.02
	9	12.49	13.12	12.80
	10	23.47	23.46	23.47
	11	35.24	34.98	35.11

4.2.2.1 Results from the Geotechnical Report Prepared for the Region of Waterloo

The geotechnical fieldwork in the region involved the examination of five boreholes, varying in depth from 6.7 to 8.2 meters, conducted between January 28th and 30th, 2020 [51]. Two of these boreholes were installed for groundwater monitoring, sampling, and dewatering assessment, accomplished by the placement of monitoring wells. In each borehole, six soil samples were collected for subsequent analysis [51].

Upon finalizing the results of the soil sampling, it became evident that the soil profile predominantly comprised fill soils, encompassing sand and gravel, sandy silt, and sand beneath the asphalt surface layer. Specifically, three out of the five samples revealed a foundation of sandy silt beneath the asphalt material, one exhibited sandy material, and the last one featured native silt material. Consequently, the moisture content of these samples varied between 3% and 23% [51].

Third-party contractors, commissioned by the Region of Waterloo, conducted smooth steel drum roller tests to roll the exposed subgrade soil without vibration. The subgrade material was identified as a silty

sand with trace gravel material, a determination consistent with findings presented in the final geotechnical report prepared for the Region [51].

The comparison between the results obtained from the Proctor Test and the geotechnical findings in the report reveals a notable correspondence and similarity in the data. The moisture content ranges observed in various layers and boreholes during the Proctor Test closely align with the moisture content and volumetric content obtained by the Region. Specifically, the moisture contents for the Granular A, Granular B, and subgrade layers fall within the range of about 4% to 18%, which aligns closely with the range of 3% to 23% reported by the Region of Waterloo. Similarly, the volumetric content exhibits a comparable range, spanning from 7% to 35%.

This consistency underscores the success of the Proctor Test. However, it is essential to recognize that while the geotechnical report provides information for the entire road section under investigation, the Proctor Test offers a more specific geotechnical analysis of the soil within the immediate region of the instrumented pavement section. This precision is crucial, considering that geotechnical properties of soil can exhibit substantial variations over short distances. Obtaining precise data is imperative for a thorough understanding.

Furthermore, the Proctor Test not only validates but also enhances the visual representation of the soil observed during testing. For example, the Proctor Test shown the subgrade soil was able to achieve a very stiff and clayey state, which aligns with the geotechnical report's observations of trace clay or some clay in many borehole samples. This alignment justifies the procedural approach. Such information is pivotal in interpreting the moisture results to be elucidated in Chapter 8 contributing to a comprehensive assessment of trends over time.

Chapter 5
Truck Testing Evaluation and Results

This Chapter describes the results from the series of controlled truck tests performed on the Courtland Avenue instrumented test section. Various tests are performed over various seasons/temperatures and truck speeds to assess the impact on the pavement response.

5.1 Description of Truck Testing Procedure

Each truck test involved a standardized process, whereby a truck with known load, axle configuration, and axle weight traveled over a specific route on Courtland Avenue East in the lane containing the instrumented test section. Each truck was typically filled with granular material, (except for the first truck test – to be elaborated in Section 5.2), and was not equipped with any sensors of its own as all of the data was meant to be captured by the sensors embedded in the instrumented test section. Testing was conducted under typical urban conditions, with variations in weather conditions monitored closely. All tests were performed during calm weather conditions to minimize external factors affecting truck performance. Finally, testing sessions were scheduled during daylight hours to ensure optimal visibility.

The objective was to capture sensor pressure and strain responses at various speeds during each run, as the truck aimed to pass over the right sensor array directly. Furthermore, for one of the five truck tests (Truck Test #1), its objective extended to capturing sensor responses at various asphalt pavement temperatures. This focus was particularly crucial during the times when the asphalt surface application occurred, which unfolded in two distinct phases to separate the pouring of the first and second lifts of HMA. This means that the first three truck tests occurred while the asphalt pavement only had one layer, while the last two tests occurred when the second layer of pavement was poured.

The designated route covered a substantial portion of Courtland Avenue East (approximately 220 m) between the intersections of Courtland Avenue and Hwy. 8 towards the intersection of Courtland Avenue and Hayward Avenue. The route that the truck took during each run of the truck test is depicted in Figure 5.1. For safety and data accuracy, the lane with the instrumented test section was closed to live traffic during each test, ensuring that the captured data solely reflected the responses of the known load of the truck undergoing the test.

The truck model and type were the same throughout each of the tests (although the trucks themselves were not identical). A typical truck resembles the truck presented in Figure 5.2, whereby there is a front steering single axle with single tires, a middle/lift axle which was a single axle with dual tires, and a rear tandem axle with dual tires. As mentioned previously, each structuring the truck tests aims to pass over

the right sensor array directly for consistency, and this is shown in Figure 5.3. In addition, a truck configuration plan showcasing the spacing between tires and axles (measured by researchers) is shown in Figure 5.4.



Figure 5.1 Image depiction of the map showing the path that the truck takes during truck testing (in red brown) in relation to nearby intersections.



Figure 5.2 An image of a standard axle configuration of a truck used for truck testing, with a steering axle, single axle with dual tire “lift axle” and tandem axle with dual tires.



Figure 5.3 Trucks aimed to pass directly over the right sensor array during each truck test. Done by spray-painting the array position on the pavement to guide the driver.

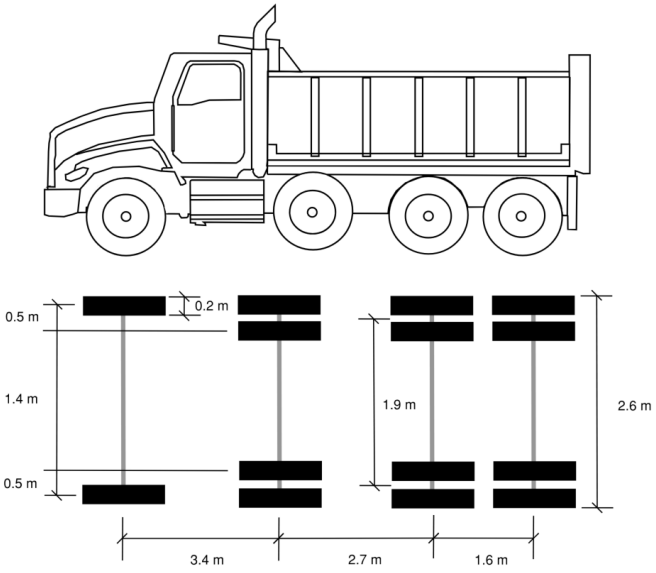


Figure 5.4 Standard configuration of testing truck with axle measurements.

As mentioned, five truck tests have been performed to assess the impact of a known load on the sensor response. Table 5.1 below explains details of each truck test conducted, including the date of the test, how many sensors were tested, the speeds tested during the truck test, the temperatures of the HMA during testing and finally the load of the truck and the individual axles if applicable.

In terms of analysis, three major aspects were looked at for each test [33]:

1. The effect of speed on layer strain and pressure.
2. The effect of temperature/moisture on layer strain and pressure (during construction tests).
3. The effect of axle load/traffic on layer strain and pressure.

These will be completed through several comparisons of the truck test data.

Table 5.1 Truck Testing Information

Truck Testing #	Date of Test	Sensors Tested	Speeds Tested (km/h)	Asphalt Concrete Temp. (°C)	Truck Test Load (kN)	Axle Loads for steering, lift and each of the tandems (kN)
1	12-Oct-22	Several sensors	10, 30, and 45	72, 51, and 43	140 (unloaded - gross)	N/A
2	22-Mar-23	All sensors	5, 10, 20, 30, 40, 50, 60, and 70	6	348 (loaded - gross) & 134 (tare)	67, 61, and 105
3	20-Jul-23	All sensors	5, 10, 20, 30, 40, 50, 60, and 70	25	353 (loaded - gross) & 138 (tare)	68, 78, and 102
4	28-Aug-23	All sensors	5, 10, 20, 30, 40, 50, 60, and 70	23	337 (loaded - gross) & 138 (tare)	55, 70, and 102
5	11-Dec-23	All sensors	5, 10, 20, 30, 40, and 50	5	348 (loaded gross) & 154 (tare)	74, 76, and 100

5.1.1 Data Presentation

Over the next several sections, various data will be graphically presented in the form of pressure and strain responses, illustrating the impact of different pressures and truck tests across various seasons on the pavement structure, considering different layers and sections of the instrumented test section. it is essential to differentiate between two types of data presentations—change in strain or pressure responses and raw strain or pressure responses.

The first type, involving change in strain or pressure responses, is crucial for assessment as it provides an indication of the actual response of the pavement structure to climate or traffic conditions. This presentation excludes additional stresses and strains induced within the pavement structure itself, preventing misleading magnitude results due to external factors [18]. It helps establish a clearer relationship between the applied load and pavement response. The change in strain or pressure is calculated by taking the difference between the preceding data point and current data point produced by the data acquisition system (effectively Δstrain and Δpressure) overtime.

The second type of response involves raw strain and/or pressure responses. While it may not provide a clear, filtered result in terms of magnitude regarding the truck impact on the sensor and pavement, raw results are important for accurately depicting the shape of pressure and strain responses. They allow for a comparison of magnitudes between compression and tension portions of strain/pressure in a more precise

manner than the change in pressure and strain responses. Raw results are valuable for understanding the accurate shapes of the responses. As with all other strain gauge responses, positive values indicate tensile strain and negative values indicate compressive strain. As with all other pressure cell responses described in this thesis, positive values indicate compression, and negative values indicate tension.

Therefore, while the change in pressure and strain focuses on accurate magnitudes, the raw pressure results emphasize precise shapes of pressure and strain responses. The stress and pressure magnitudes will, in many cases, be higher in raw data, as it includes stress and strain beyond the truck's effect based on temperature and load. Literature has included both raw (for example [60] [61] and [20]) and change (for example, [18]) in pressure and strain responses, emphasizing the importance of incorporating both types of analyses for a comprehensive understanding.

5.2 Truck Test #1: Fall Conditions and First HMA Lift Construction Analysis

The first truck test took place in October 2022 and represented conditions immediately after pouring the first lift of asphalt pavement, with only a limited number of sensors available for testing as outlined in Table 5.1. This limitation arose because the DAC was not accessible to the research team at that time due to shipping delays, resulting in a restricted availability of testing equipment. Consequently, a specific set of sensors, including some longitudinal and transverse strain gauges, as well as pressure cells from different depths, had to be chosen for the first truck test. These sensors included: AS-LO-R-1, AS-TR-R-3, AS-TR-L-4, AS-TR-L-6, AS-LO-R-7, AS-LO-L-8, PC-BA-R-5, PC-SB-R-3, and PC-SG-L-8. This selection was made to accommodate the testing on the only STS4-4 Terminal Node available to the research team, able to test up to four sensors simultaneously. No temperature or moisture sensors were used in this first truck test but will be available for future truck tests.

Because the testing was performed immediately after pouring the first lift of asphalt pavement, the asphalt was initially at high temperatures and cooled over a period of about an hour post-pouring. The interest lay in capturing data as the truck traversed the instrumented test section at high HMA temperatures, in order to examine the correlation between temperature and pavement response. During this construction phase, the truck test was conducted at HMA temperatures of 72°C, 51°C, and 43°C. For most temperatures, the speeds tested include 45 km/h, 30 km/h, and 10 km/h. The truck used for testing was also unloaded and had a gross weight of 140 kN. During testing, the ambient temperature was about 16°C and sunny. The testing occurred between 4:02 PM to 5:30 PM.

Unforeseen challenges arose as the construction crew, concurrently working on asphalt pouring in other lanes of Courtland Avenue East, needed access to the lane with the instrumented test section for their construction equipment and vehicles. This lane was the only one poured at that point, impacting the

number of temperatures tested, which fell short of the initial expectations. Nevertheless, data at the three temperatures mentioned previously were successfully captured. In addition, for this initial truck test, only an unloaded truck was available. This limitation can also be attributed to the constraints in truck availability and the need for coordination with the construction crew.

Therefore, to enhance the impact on the pavement structure and obtain clearer responses, future truck tests employed a loaded truck. In addition, future truck tests will also include the weights of individual axles for better analysis, however this truck test was not able to capture that data.

5.2.1 Method for Strain and Pressure Data Analysis

Throughout this chapter, the emphasis is on analyzing the change in pressure and strain responses over raw responses when evaluating pavement behavior. The core objective is to gain insights into how pavements truly react to external influences such as climate and traffic load. Instead of delving into the complexities associated with raw signal responses, the focus shifts to the calculated *change* in strain responses. This method provides a more nuanced understanding of the pavement's dynamic reaction to traffic conditions over specific time intervals. The correlation established between load intensity and pavement response becomes more evident through this approach. While raw responses are included as supplementary information for context, the primary analytical focus is on the differentiation in strain and pressure responses. This shift aims to isolate the genuine impact of vehicular loads, offering a clearer depiction of how the pavement authentically responds to varying traffic conditions. This also makes the analysis clearer as the raw values from the strain and pressure sensors were not zeroed during their calibration by BDI.

5.2.2 Impact of Speed on Layer Strain & Pressure

As mentioned previously, one of the three major aspects being considered for this analysis was the effect of speed on layer strain and pressure. Therefore, strain and pressure variations at the different testing speeds (45 km/h, 30 km/h, and 10 km/h) were considered if the sensor responses were clear and accurate. This assessment was conducted across all testing temperatures (72°C, 51°C, and 43°C) for strain and only some temperatures (51°C, and 43°C) for pressure due to the aforementioned testing limitations.

5.2.2.1 Impact of Speed on AC Layer Strain at 72°C

Figure 5.5 illustrates strain results at 72°C and 45 km/h in both the longitudinal and transverse directions. The figure delineates distinct signal responses from various axles as the truck traverses the instrumented test section. Notably, responses from the steering axle, lift axle, and tandem axle are clearly discernible in the sensor signals. The analysis prioritizes the information derived from examining longitudinal and

transverse strain at a speed of 45 km/h, as data from other speeds was excluded due to the ambiguous sensor readings produced, exemplified in Figure 5.6. Both sensors selected for this analysis are situated in the right sensor array.

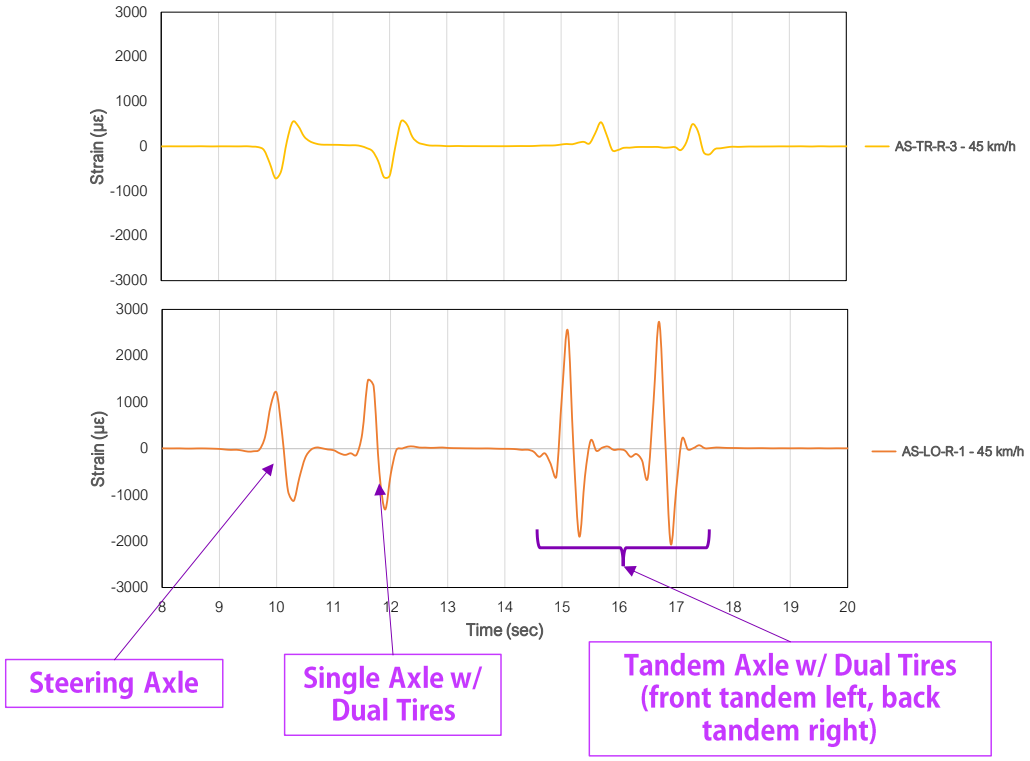


Figure 5.5 Comparison of the transverse (top) and longitudinal (bottom) strain responses at 72°C for a truck running at 45 km/h.

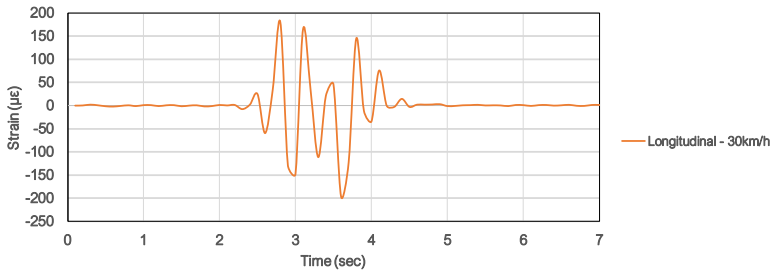


Figure 5.6 Strain response at 72°C at 30 km/h, showcasing the lack of clear sensor signals at this testing speed.

Notably, the maximum or peak longitudinal strain response of the front tandem axle at 45 km/h (2534.51 με) is 4.7 times greater than that of the transverse strain at 537.13 με. This is a decrease of about 79%. Additionally, the tandem axle exerts the most substantial influence on the longitudinal strain, while in the transverse direction the impacts of the steering or lift axles are greater than the tandem axles.

This difference in magnitude between the longitudinal and transverse strains is expected and can be attributed to the anisotropic nature of asphalt. Anisotropy is a material property whereby the modulus and strength properties of a material vary in the vertical, longitudinal, and horizontal directions [62]. This characteristic holds significance in pavement design, especially when considering that traffic loading in longitudinal directions induces substantial anisotropy in relation to the transverse direction [62]. This may mean that the variations in modulus and strength properties across different directions could lead to uneven load distribution on the pavement and result in localized stress concentrations, potentially leading to cracks, rutting, or other forms of distress.

5.2.2.2 Impact of Speed on AC Layer Strain at 51°C and 43°C

The influence of speed on strain was examined at 51°C and 43°C using transverse strain gauges, as illustrated in Figure 5.7. The results of the truck test at speeds of 45 km/h and 30 km/h were those that resulted in the clearest responses; therefore, they will be assessed. For similar reasons, the transverse strain is assessed.

At 51°C, a 28% decrease in strain magnitude is observed for the front tandem axle when comparing results at 45 km/h (583.92 με at peak magnitude) versus 30 km/h (423.32 με). This shows that the transverse strain magnitude for the tandem axle decreases with decreasing speed. In contrast, for the steering axle and lift axle, the strain response magnitude at 30 km/h surpasses that at 45 km/h.

Transitioning to 43°C, a discrepancy surfaces in the peak strain magnitude between speeds of 45 km/h and 30 km/h. Importantly, at 45 km/h, the response peaks in the positive sense, indicating tension according to the BDI asphalt strain gauge manuals and datasheets, while at 30 km/h, it peaks in the negative direction, denoting compression within the layers. Even without delving into this compression-tension difference, the magnitudes of the strain response at 45 km/h (458.41 με at peak magnitude) far exceed those experienced at 30 km/h (-179.57 με). This is a 139% decrease in strain magnitude.

In typical cases, one would anticipate longer wavelengths between axles at lower speeds, with peaks of axle responses further apart and larger magnitudes of pressure response for all axles [63]. This expectation arises from the extended time it takes for the axles to pass over any given sensor at lower speeds as compared to higher speeds. However, an intriguing departure from this norm was observed for the tandem axles. This observation suggests that material properties at higher temperatures may be influencing the results. Alternatively, it is plausible that at 45 km/h, the truck consistently traversed the right sensor array more directly, with reduced deviations to the sides compared to its movement at 30 km/h, thereby reducing the wander effect.

When contrasting results between temperatures of 51°C and 43°C, a notable difference in strain magnitude severity emerges, with 51°C exhibiting higher magnitudes. Specifically, strain magnitudes at 51°C reach nearly 600 με, for the front tandem axle, while a range of 400 to 500 με is observed at 43°C for the front tandem axle. This discrepancy can be attributed to the heightened stiffness of the HMA layer at cooler temperatures. This increased stiffness enhances the pavement's resistance to loads, consequently leading to lower strain values at 43°C [63].

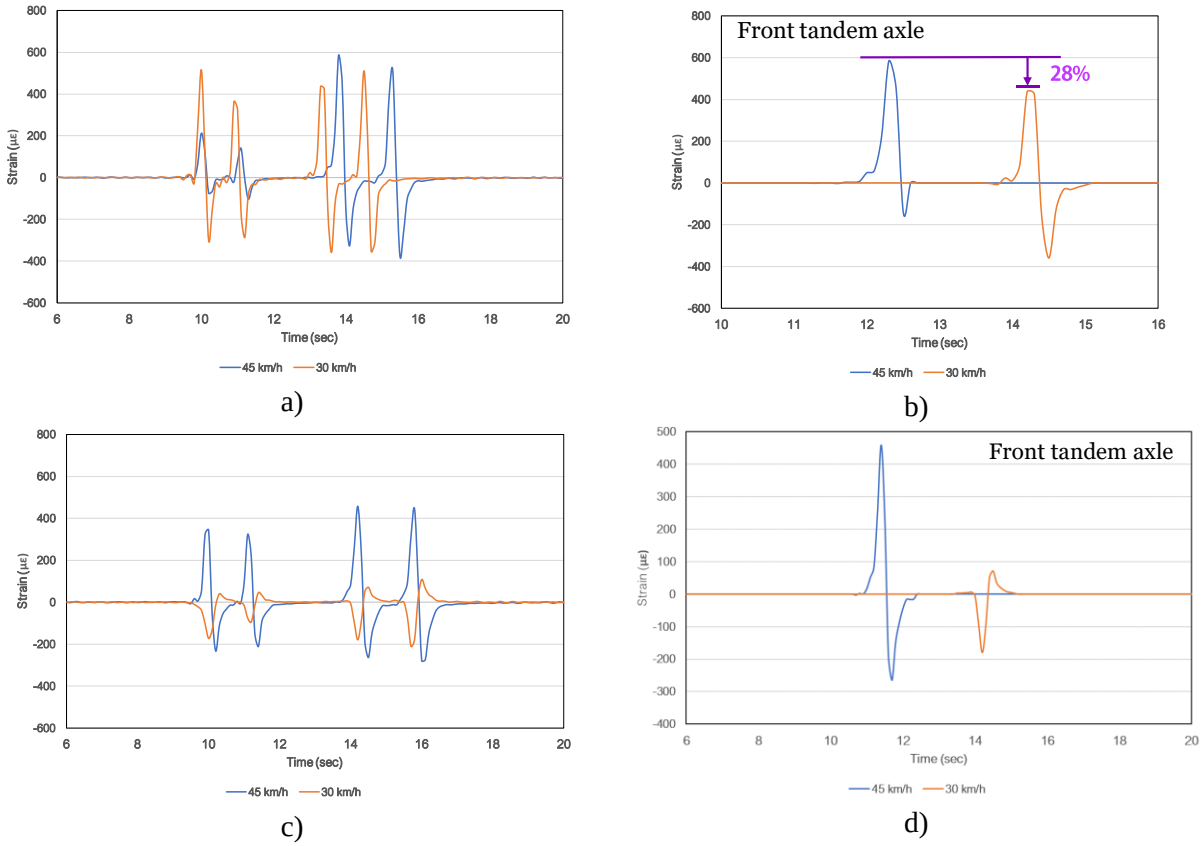


Figure 5.7 This is a 4-panel figure, describing the comparison of strain in the transverse direction in the right wheel path: a) at 51°C at various speeds. b) at 51°C at various speeds, focused analysis of front tandem axle. c) at 43°C at various speeds. d) at 43°C at various speeds, focused analysis of front tandem axle.

Figure 5.8 below presents the same strain signals as demonstrated in Figure 5.7, but these are the raw strain responses. Although the strain gauges and pressure cells were calibrated by the supplier with limited time for recalibration, differences between actual axle responses and non-responses are discernible.

The main difference immediately noticeable between the change in strain response captured in Figure 5.7 and the raw strain response in figure 5.8 is the shape of the response. The raw strain response more accurately depicts what the axles of the truck are imparting onto the pavement structure in terms of compression and tension. For instance, at speeds of 45 and 30 km/h, the general shape of the strain

response indicates the initial impact by the steering and lift axles, followed by a gap, and then the tandem axles at the end, typically in the form of a pair. Notably, the strain response from the tandem axles does not immediately return to the initial strain response before picking up the strain response from the second tandem axle after the truck has passed over the sensor. The strain response takes some time to return to the neutral position, suggesting that the pavement structure may be holding onto some residual strain. Illustratively, consider the comparison of the raw strain results in the transverse direction at 51°C. At a speed of 45 km/h, the strain response's neutral strain is -3000 με. As the truck passes over the sensor, after the tandem axle has left the sensor, the strain response does not promptly revert to -3000 με. This phenomenon is not typically observed in the raw strain results of future truck tests, as will be seen in future sections.

While determining the magnitude of raw strain responses might lead to potential misinterpretations, the observed trends align with those identified in the changing strain and changing pressure responses presented in Figure 5.7. Notably, there is a slight increase in net magnitudes at faster speeds, contrary to expectations based on existing literature. Additionally, the strain response at 30 km/h in the chart depicting strain at 43°C shows a compression trend rather than tension, as observed in the change in strain chart in Figure 5.7's bottom left corner. This negative response could suggest a potential instance of wander, where the truck may not fully cross over the specific sensor at this particular time.

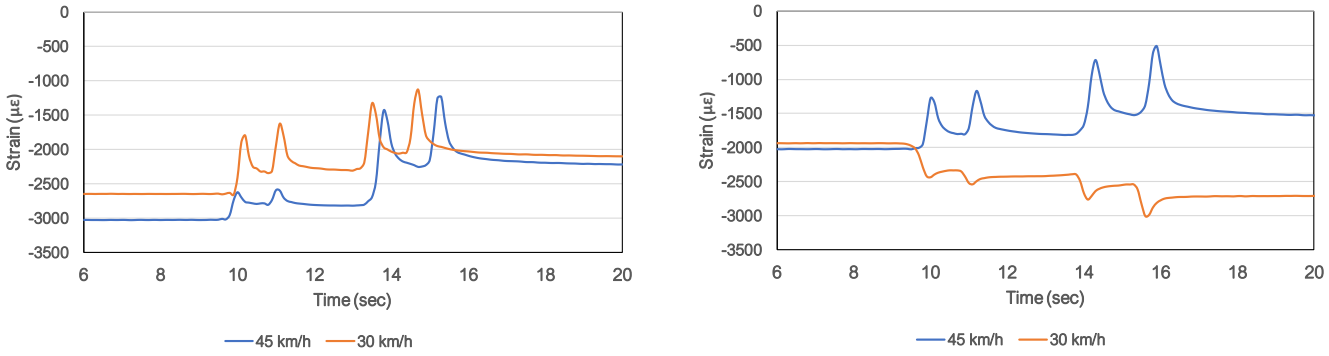


Figure 5.8 Comparison of the raw strain response in the transverse direction in the right wheel path at 51°C (a) and 43°C (b), at various speeds.

5.2.2.3 Impact of Speed on Layer Pressure at 51°C and 43°C

Along with determining the impact of speed on layer strain, the impact of speed on layer pressure was also performed at various temperatures. At both 51°C and 43°C, the study examined the pressure variation in all layers, and extracted relevant trends. The results of this analysis are given in Figure 5.9.

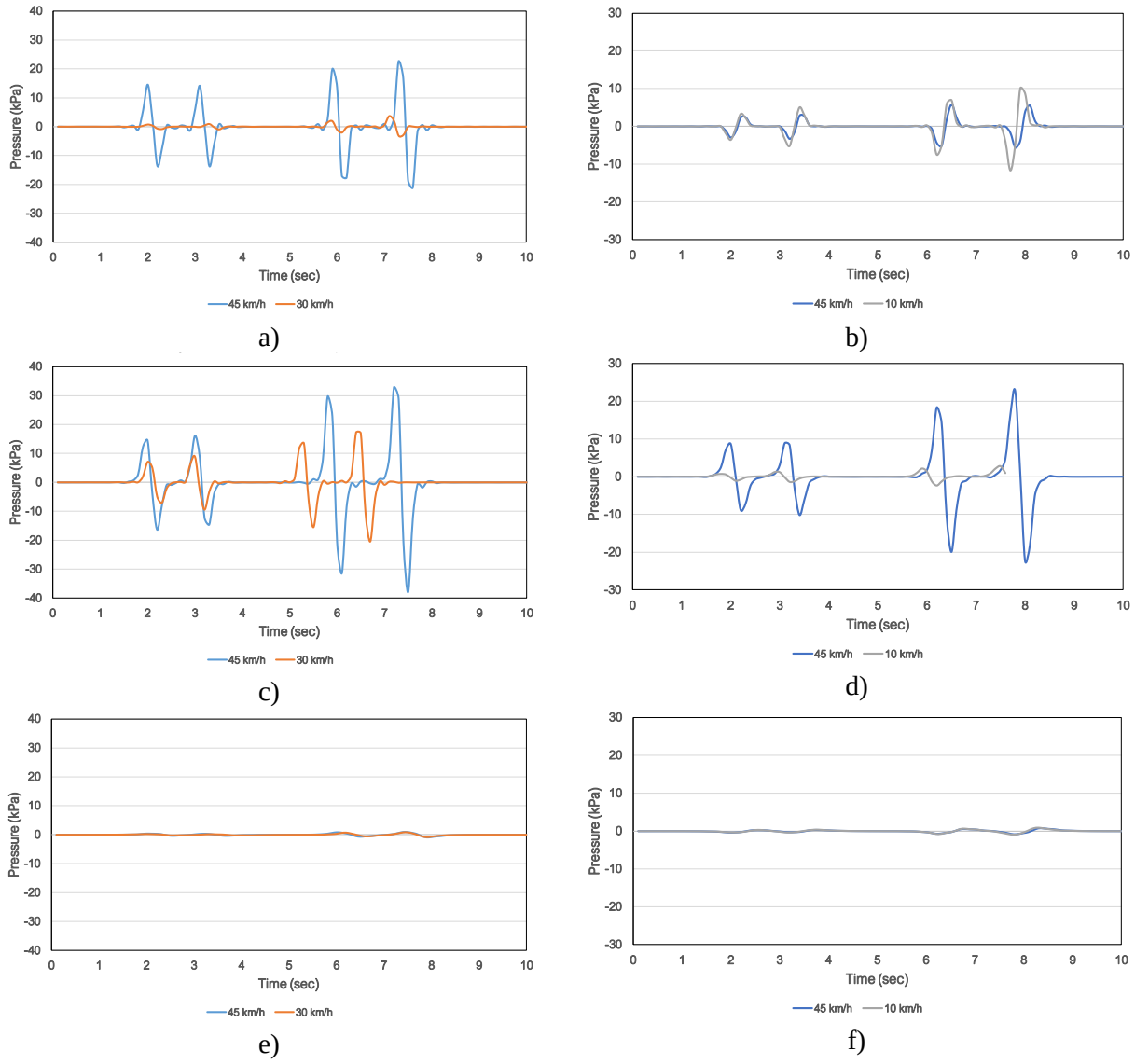
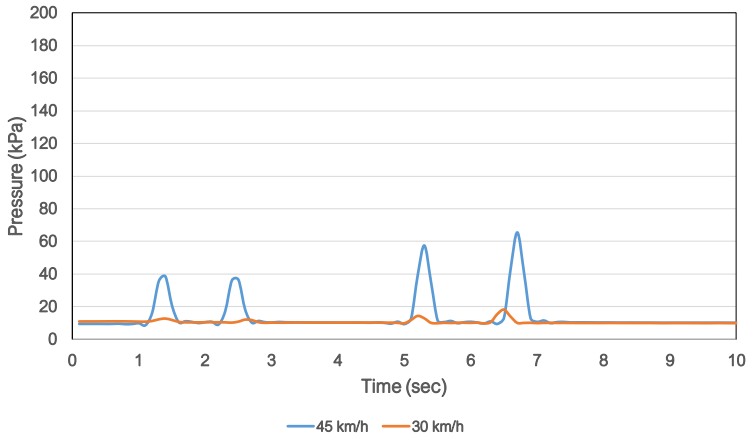
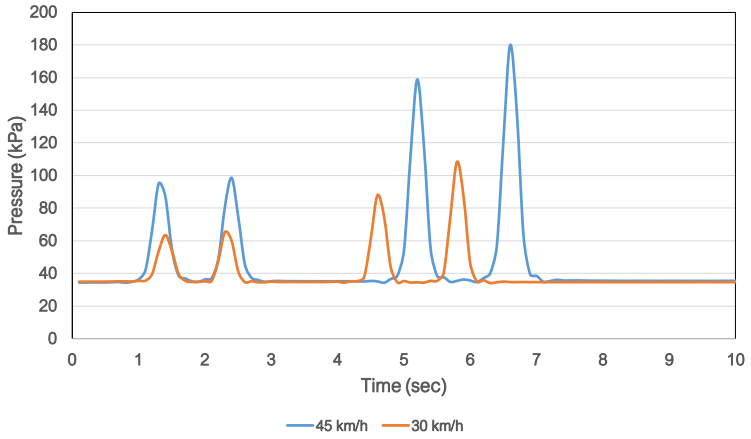


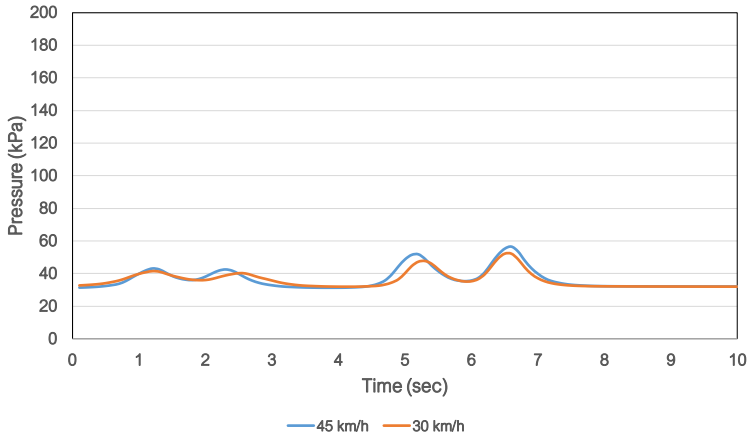
Figure 5.9 This is a 6-panel figure of the comparison of the pressure response in the base (a and b), subbase (c and d) and subgrade (e and f) layers at 51°C (a,c,e) and 43°C (b,d,f) at various speeds.



a)



b)



c)

Figure 5.10 This is a 3-panel figure, which depicts the comparison of the raw pressure response at 51°C at various speeds in the base (a), subbase (b) and subgrade (c).

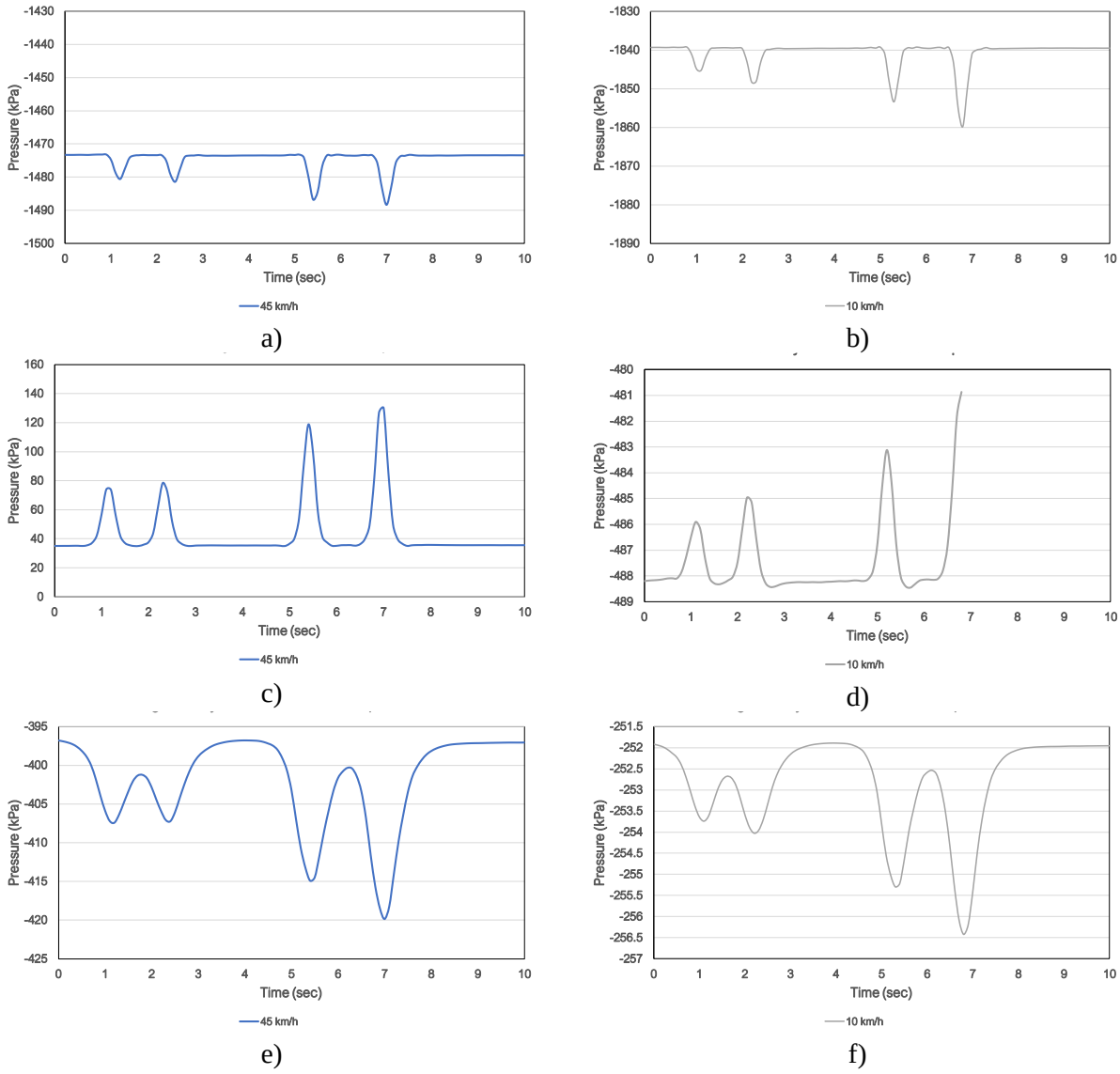


Figure 5.11 This is a 6-panel figure, depicting the comparison of the raw pressure response in the base (a and b), subbase (c and d) and subgrade (e and f) layers at 43°C at various speeds.

The predominant trend identified is a reduction in the magnitude of the pressure impact generated by the passing truck at slower speeds. This trend is particularly evident in the base and subbase layers, as well as across all axles. For example, in the subbase layer for the front tandem axle, at 45 km/h, the pressure response is 29.72 kPa while at 30 km/h the response is 13.39 kPa. Again, this is opposite to what is expected, as typically a decrease in vehicle speed would result in an increase in the elastic surface response (i.e., deflection) and therefore an increase in the pressure applied to each layer [64]. This has been shown to be the case in several studies, such as those in [65]. However, there is also the possibility that there could be small but substantial cooling of the pavement structure in between each tested speed, which could then impact the pressure results. In the subgrade layer, the impact at both speeds is very

similar, suggesting that at high temperatures, the damage imparted on the subgrade layer at various speeds will be similar.

In addition, as one goes down the pavement layers, there is a noticeable variation in the magnitude range of the pressures. For instance, in the base, the maximum pressure impact is around 20 kPa. In the subbase, the impact is about 30 kPa, while in the subgrade, the impact decreases to around 1 kPa. This observation underscores a notable reduction in subgrade pressure in comparison to the regions closer to the surface, such as those below the AC layer [66].

The raw pressure results are illustrated in Figure 5.10 and Figure 5.11. Figure 5.10 displays the raw pressure results for all layers at 51°C, while Figure 5.11 presents the pressure responses for all layers at 43°C. Figure 5.10 includes both speeds in the same charts, as the sensors had the same neutral axis during those runs. However, for the runs at 43°C, the neutral axis for these pressure cells varied, requiring the charts to be split into two: one for 45 kilometers per hour and the other for 10 kilometers per hour. Examining Figure 5.10, similar trends to those observed in the changing pressure results in Figure 5.9 are evident when comparing pressure results between 45 and 30 kilometers per hour.

The focus here is on the shape of the pressure results, which predominantly exhibit positive pressure responses, consistent with the literature [20]. As noted in Figure 5.9, the subbase demonstrates the largest response, followed by the base and then the subgrade. This pattern persists even in the raw results. The results presented in Figure 5.11 show some differences. There are pressure results in the negative direction, indicating a likely deviation from the main sensor array which would result in some tension results. Only the subbase responses show compression, meaning the responses are in the positive direction, while the responses in the negative direction indicate tension being captured.

5.2.3 Impact of Temperature/moisture on Layer Strain & Pressure

Given that the truck test took place during a construction phase involving the pouring of the first lift of the HMA, the evaluation will specifically focus on assessing the influence of temperature and moisture on layer strain and pressure.

5.2.3.1 Impact of Temperature on Layer Strain at 45 km/h, 30 km/h and 10 km/h

To commence the analysis, the examination of temperature's impact on layer strain was conducted at speeds of 45 km/h, 30 km/h, and 10 km/h to discern potential trends. Figure 5.12 visually presents the strain impacts at various temperatures on a transverse sensor at 45 km/h and 30 km/h.

A key observation is the consistent trend in which, at higher temperatures, the magnitude of horizontal strain tends to be larger compared to at lower temperatures. For instance, at 45 km/h, the strain magnitude

decreases by approximately 61% from 72°C (543.14 kPa) to 51°C (211.5 kPa), and around 37% from 72°C to 43°C (344.60 kPa) for the steering axle. The peak horizontal strain is evident at an asphalt concrete temperature of 72°C, aligning with expectations that at higher HMA temperatures, the strain response will be higher since the AC layer tends to be softer under these conditions and the material is more prone to deformation or strain under load [63].

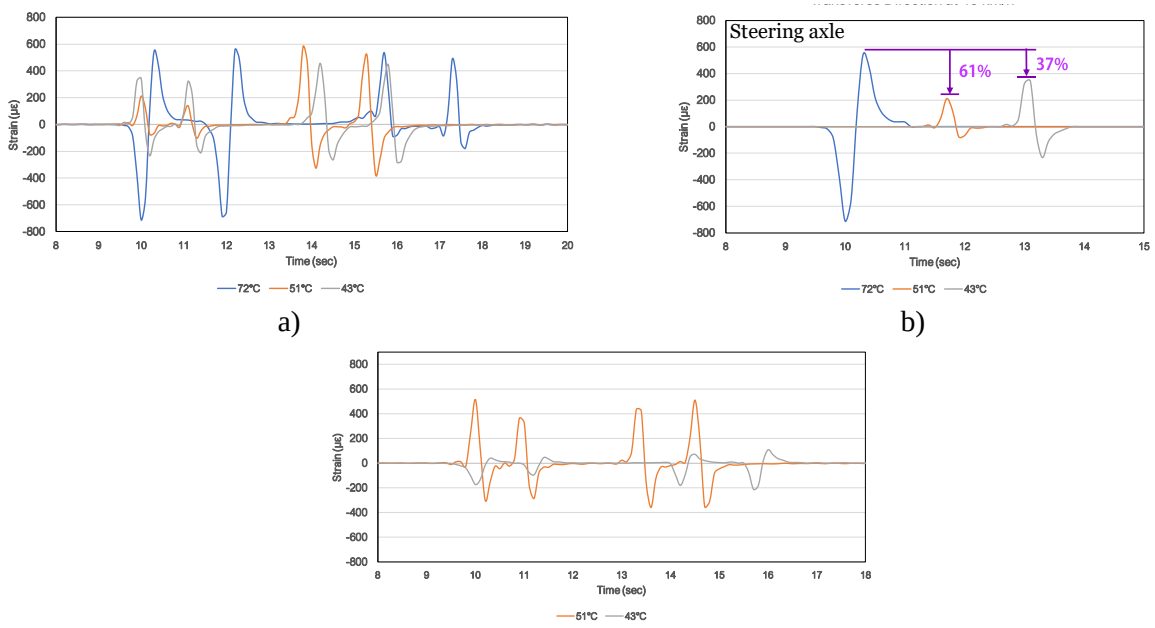


Figure 5.12 This a 3-panel figure, depicting the comparison of the transverse strain responses at 45 km/h at various temperatures (a), a comparison of the steering axle transverse strain responses at 45 km/h (b) and a comparison of the transverse strain responses at 30 km/h at various speeds (c).

5.2.3.2 Impact of Temperature on Layer Pressure at 45 km/h, 30 km/h and 10 km/h

The impact of temperature on layer pressure was also examined for speeds of 45 km/h, 30 km/h, and 10 km/h. Figure 5.13 and Figure 5.14 display the results of this analysis, where the former shows the results for all layers at 45 km/h, including a close-up of the results of the front tandem axle in the subbase, while the latter shows the results for the subbase and subgrade only for 30 km/h and 10 km/h.

The primary trend observed is that, generally, the pressure impact at higher temperatures is larger as compared to lower temperatures. This trend is consistent across all tested speeds, except for the response of the tandem axle in the subgrade layer at 10km/h (Figure 5.14). This trend is also consistent with the results of similar tests, such as those of [20].

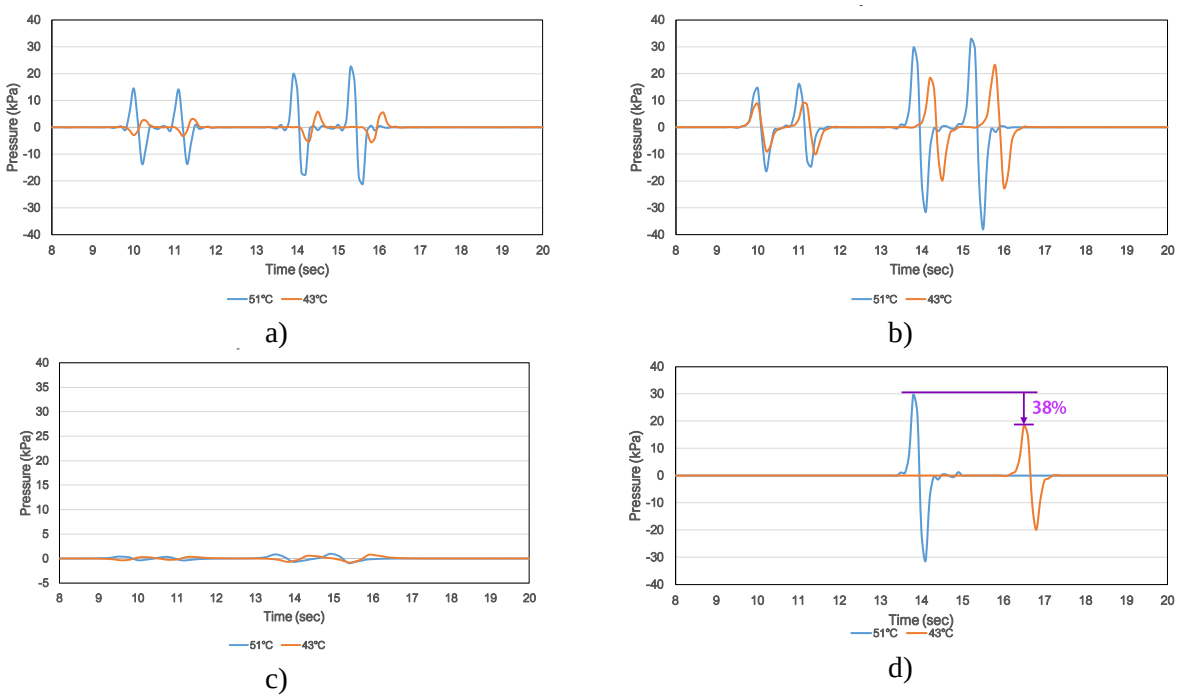


Figure 5.13 This is a 4-panel figure, depicting the comparison of the pressure response at 45 km/h in the base (ta), subbase (b), and subgrade (c); further analysis for the front tandem axle responses at 45km/h in subbase layer (d).

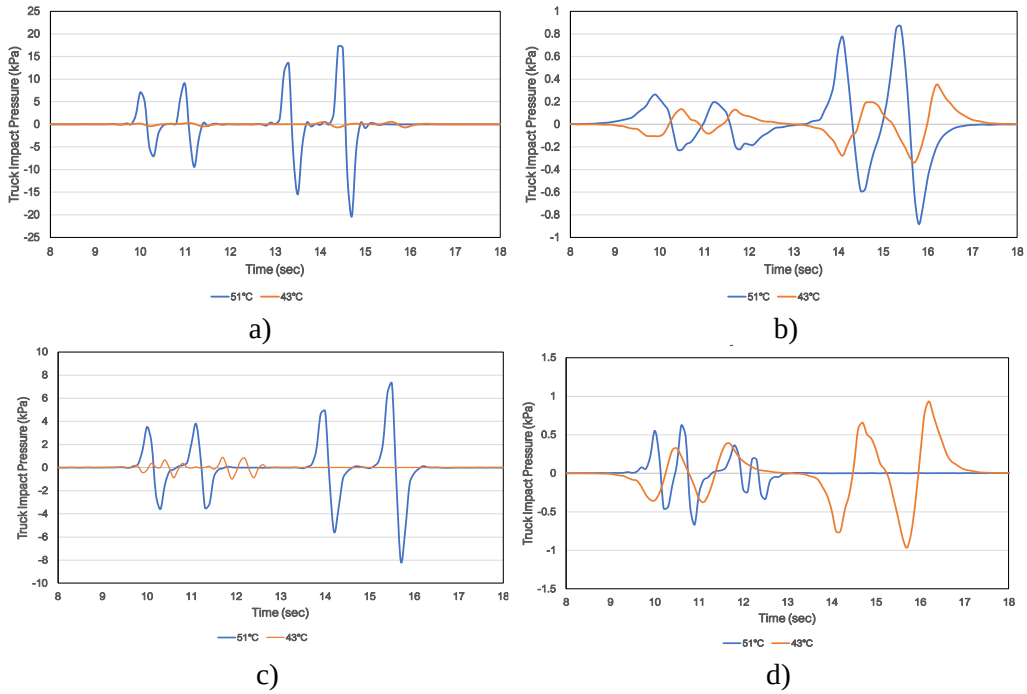


Figure 5.14 This is a 4-panel figure, depicting the comparison of the pressure response at 30 km/h in the subbase (a) and subgrade (b) and 10 km/h in the subbase (c) and subgrade (d).

Like what was described in Section 5.2.2.3, when analyzing the pressure response at different temperatures, the magnitude of the pressure impact varies within each layer. For instance, the maximum

pressure impact in the base layer is approximately 20 to 25 kPa at 45 km/h. In the subbase layer, the maximum impact ranges from 30 to 35 kPa at 45 km/h to 17 kPa at 30 km/h and around 7 to 8 kPa at 10 km/h. These pressure results are much lower than some other studies [20], however this could be a result of the materials and design of the pavement structure (as the test section in the study is situated in Los Angeles, CA), the weight of the vehicle used for testing, wander, etc.

5.2.4 Comparison of Pressure in the Pavement Structure during Construction

In Figure 5.15, a pressure profile is presented, outlining the pressure response for this truck test at various depths within the pavement structure. This profile is generated for temperatures of 51 °C and 43 °C while comparing the same sensor at both temperatures for consistency. It reveals that pressure has a diminished impact on the pavement structure at lower temperatures. For example, at 51 °C, the pressure in the base layer is 50% higher than at 43 °C.

While temperature notably influences the magnitude of pressure impact in the base and subbase layers, the subgrade layer exhibits negligible change. The pressure impact in the subgrade layer remains consistently low, irrespective of the temperature of the HMA layer. This suggests that, during construction, the subgrade undergoes minimal impact, and its behavior is not substantially affected by the temperature variations in the HMA layer.

A significant trend evident in this figure is the unexpected observation that the pressure responses in the subbase layer are larger than those in the base layer. Previous studies typically indicate that pressure results in the base layer should surpass those in the subbase layer, with the subgrade layer exhibiting the smallest response [20].

There are several potential explanations for this deviation. It could stem from construction variability, where variations in material placement, compaction, or other construction practices may lead to localized differences in pressure responses. Uneven construction practices could influence the pressure distribution within the pavement layers. In addition, the material properties of the subbase and base layers, such as stiffness or compaction characteristics, could result in varying pressure responses. Sensor placement could be another factor, where the exact placement of sensors within the pavement layers could introduce discrepancies. If sensors are not uniformly positioned or are affected by irregularities in layer thickness, it may impact the recorded pressures. Finally, it could stem from issues with sensor calibration, however this is avoided with regular calibration checks. Unfortunately, these sensors were not calibrated by the research team but by a third party, and there was not enough time to verify the calibration process between when the sensors were received and when they needed to be installed in the instrumented test section, therefore it is difficult to determine whether the calibration was correctly performed.

To validate and understand this anomaly, it becomes crucial to consult trends across various truck tests, especially those conducted under different conditions. If this pattern persists across multiple tests, it may point towards a miscalibration in the pressure sensors. This factor will warrant careful consideration during future analyses, emphasizing the need for meticulous calibration and interpretation of pressure sensor data in upcoming assessments.

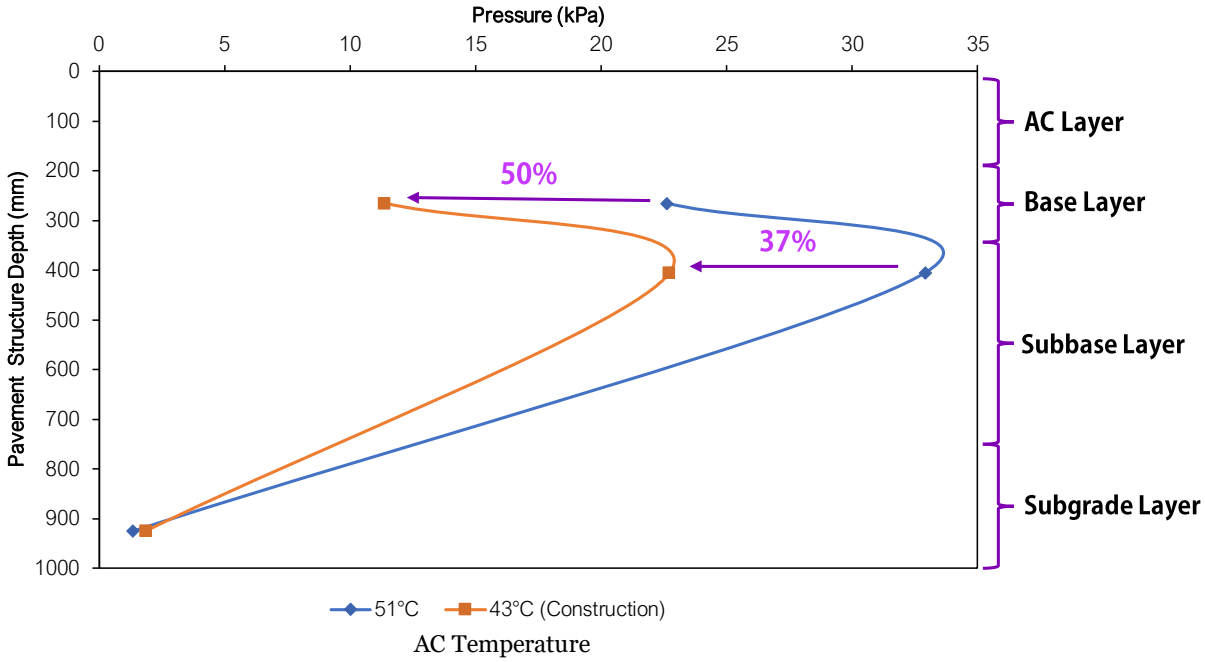


Figure 5.15 Pressure depth profile indicating changes in pressure during the construction phase at 51°C and 43°C.

5.3 Truck Test #2: Early Spring Conditions

The second truck testing occurred on March 22nd, 2023, approximately five months after the initial construction truck testing, between 11:00 AM to 12:00 PM. During this truck testing session, all sensors were successfully tested as the DAC was operational at that time. Various speeds were examined, including 5, 10, 20, 30, 40, 50, 60, and 70 km/h at an asphalt temperature of 6 °C, while the ambient temperature was about 3 °C, with cloudy weather conditions. During this truck test, the truck was loaded and had a gross loading weight of 348 kN, and a tare weight of 134 kN. In addition, the weights of the individual axles were also captured, and they were: 67 kN for the steering axle, 61 kN for the lift axle, and 105 kN each for the tandem axles. These were provided weights by the contractor, and it is recognized that there is a 10 kN gap between the sum of the individual axles and the gross weight.

Figure 5.16 shows the set up for the early spring truck test. To guide the truck along the right sensor array, a spray-painted line was applied on the pavement surface 0.7 meters away from the curb.

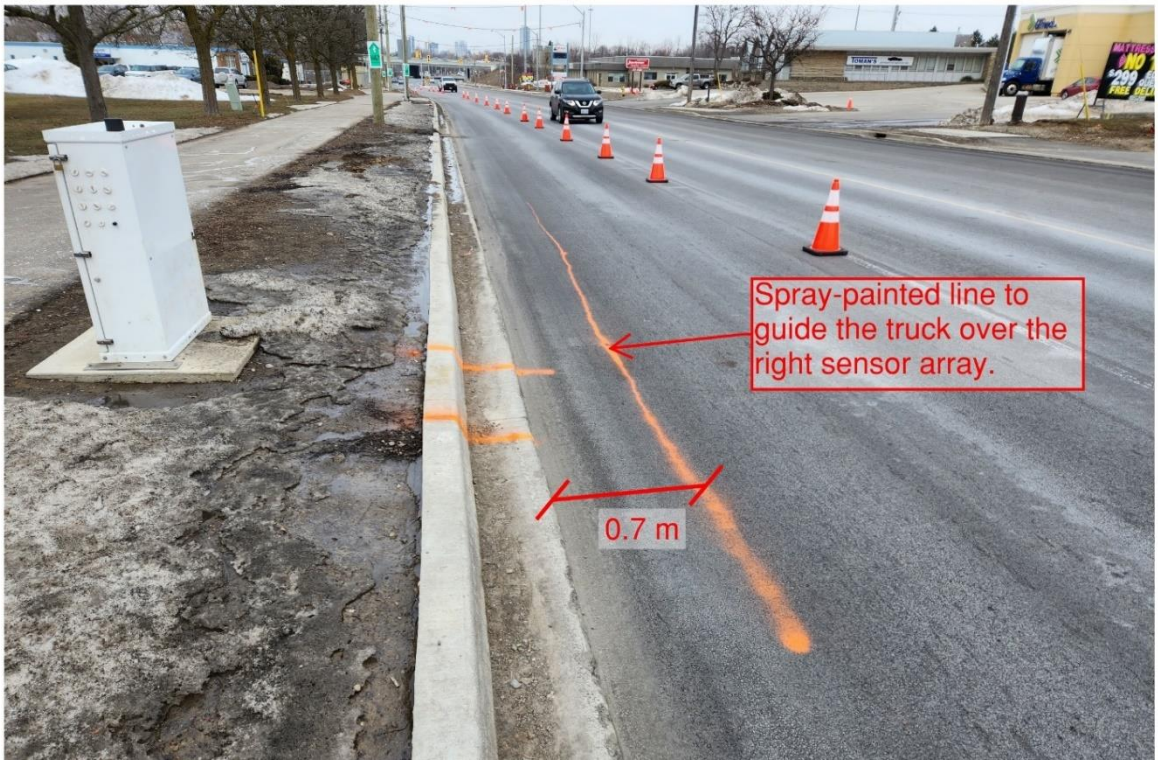


Figure 5.16 The setup for the early spring truck test. The orange spray paint on the pavement surface demarcates the right array of sensors to guide the truck during the different speeds.

5.3.1 Impact of Speed on Longitudinal & Transverse Strain

One focus of the analysis for the truck testing conducted during early spring conditions was to examine the effect of speed on pressure and strain. Figure 5.17 illustrates a selection of the results of the truck testing at various speeds for both longitudinal and transverse strain. These include 5, 10, 20 and 50 km/h.

A significant trend emerges when analyzing the longitudinal strain: the strain decreases with increasing speed. As the speed of the truck rises, the amplitudes between the axle peak responses shorten, and the magnitudes of the strain diminish. This trend is expected because when a truck travels at higher speeds over a pavement structure, the impact that each tire has on each sensor decreases. Additionally, all axles pass over a specific sensor more quickly. This result is corroborated by [65], [64] and [33].

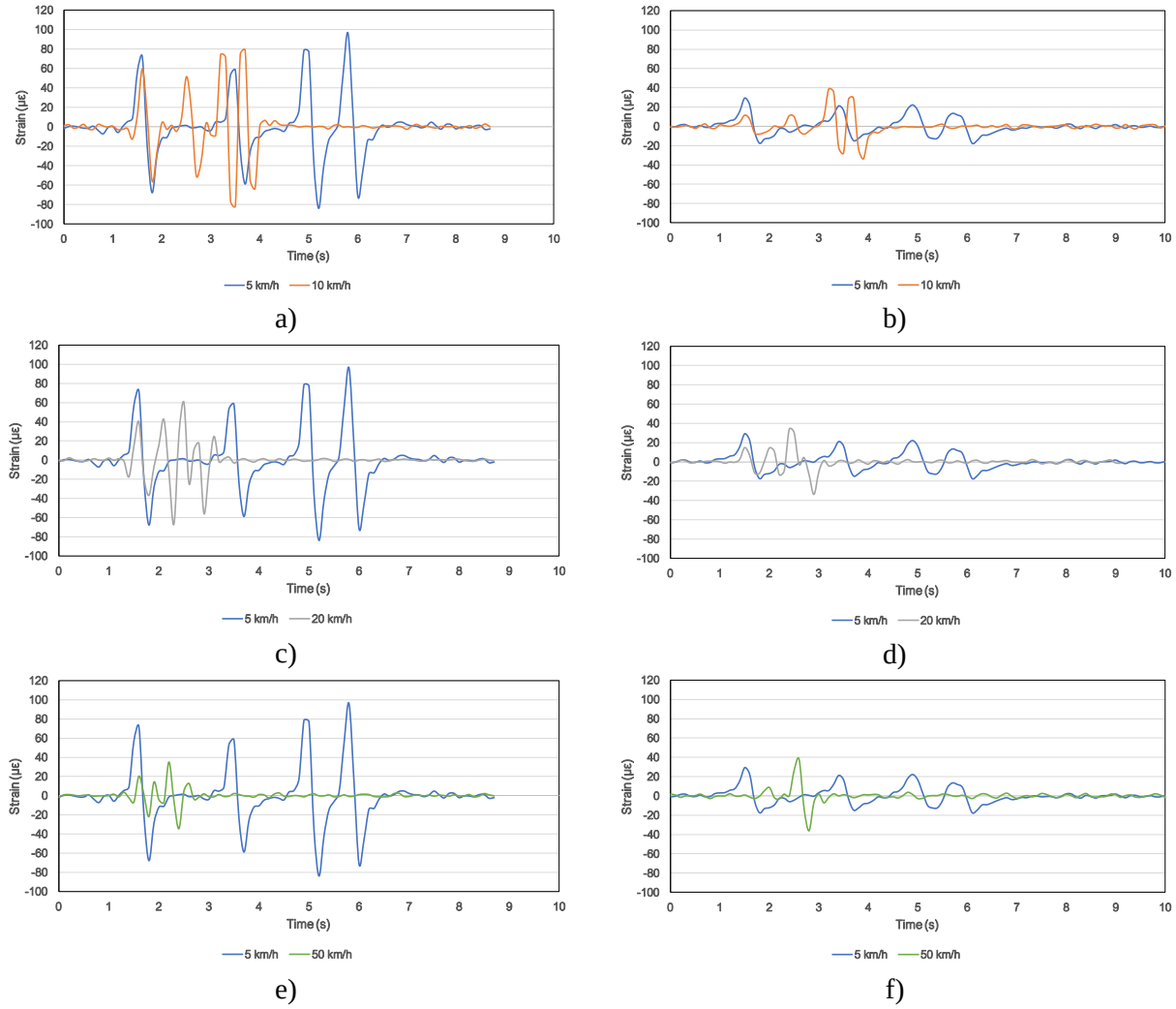


Figure 5.17 This is a 6-panel figure demonstrating the comparison of the impact of longitudinal (a,c,e) and transverse (b,d,f) strain at 5km/h and 10, 20 and 50 km/h.

In contrast, a different trend is observed in the transverse direction. As the speed increases, the amplitude between the axle peaks still diminishes due to the truck running at a faster speed, causing all axles to pass over a specific sensor more quickly. However, the magnitude of the strain response increases as the speed rises. This finding also aligns with what was observed in the construction data (see Section 5.2.2.2) but contrasts what is shown in the literature, such as the transverse strain data at various speeds plotted by [65].

Observing the raw strain results in Figure 5.18 reveals intriguing details about the strain gauge responses in their unprocessed state. In contrast to the change in strain results in Figure 5.17, the raw strain results allow for the examination of the true shape of the strain as a truck passes over each sensor. The distinctive pattern for a tire passing over a strain gauge is its characteristic four-peak shape, with each peak representing the steering axle, lift axle, and the two peaks at the end (furthest to the right of any

presented chart) representing the tandem axle. In some cases, particularly in the transverse direction, the tandem axle response appears as a single response cleaved in two, as the response does not return to a neutral position before the second tandem axle passes over the same sensor. However, in the longitudinal direction, all strain responses are well-defined and clear.

Like the trends observed in the change in strain results in Figure 5.17, the same magnitude trends are apparent here. Firstly, the longitudinal strain responses generally have larger magnitudes than the transverse strain responses. Additionally, the effect of speed aligns with what was observed in the change in strain response; as the speed increases, the time it takes for the truck axles to pass over a particular strain gauge decreases, resulting in a shorter total response length in terms of time at higher speeds. Moreover, the magnitude of the strain response is typically higher at lower speeds compared to higher speeds.

The unique value of observing the raw results, as opposed to just the change in strain response, lies in the clarity with which one can see the tension and compression of the axles on the pavement structure. The raw results vividly depict the raw effect of tension and compression, where tension is represented as a positive response and compression as negative. In the change in strain response, positive and negative responses do not necessarily represent tension and compression, as it primarily demonstrates a change in strain. Hence, the raw results offer valuable insights for comparison purposes.

5.3.2 Impact of Speed on Pressure in the Base, Subbase and Subgrade

Figure 5.19 illustrates the impact of speed on the pressure experienced in the base layer, subbase layer, and subgrade layer of the pavement structure. Overall, a consistent trend is observed across all three layers: as the speed increases, the magnitude of the pressure decreases, and the time between peak pressure magnitudes for each axle decreases. However, variations within each layer exist that warrant further analysis.

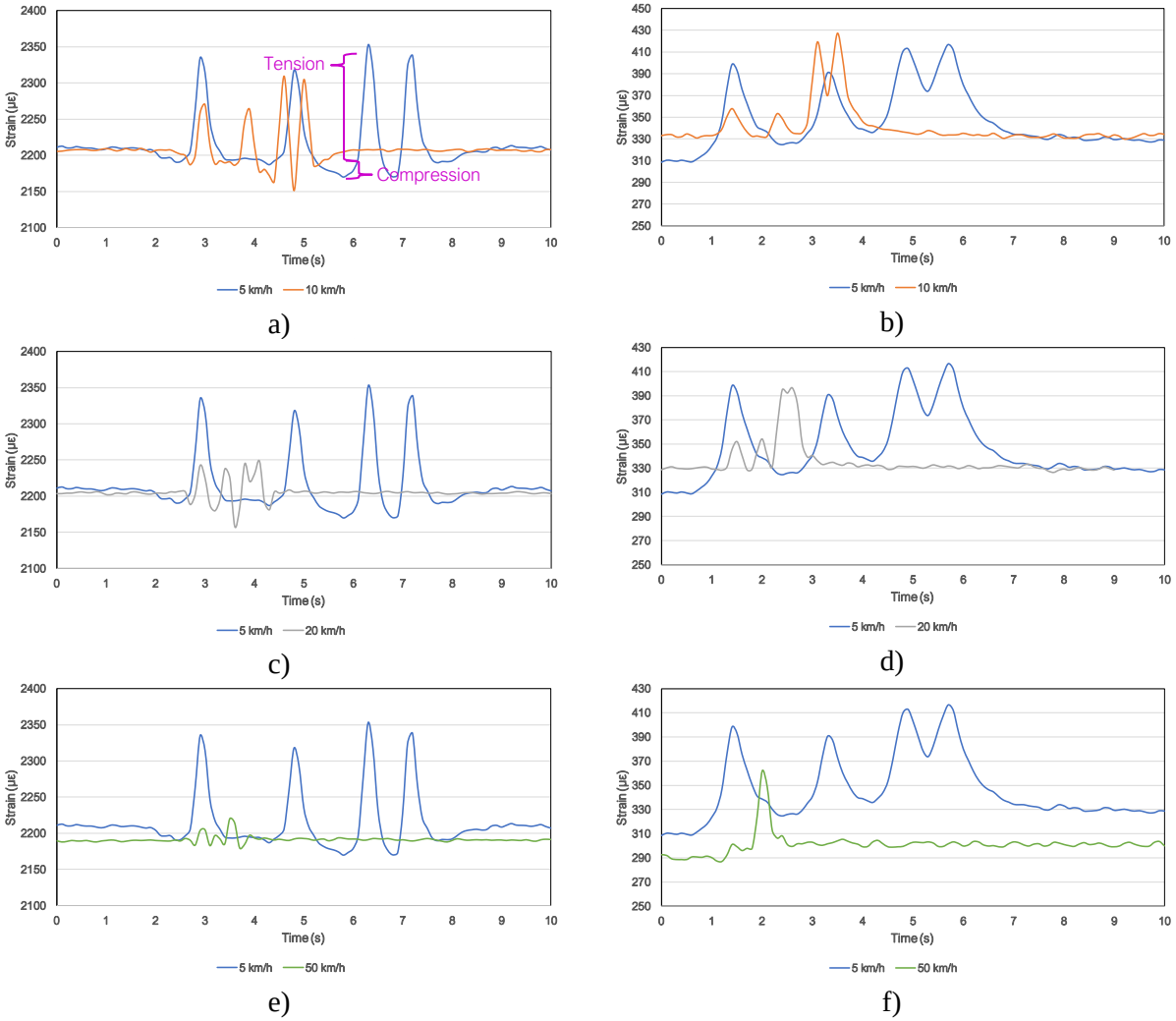


Figure 5.18 This is a 6-panel figure demonstrating the comparison of the impact of raw longitudinal (a,c,e) and transverse (b,d,f) strain at 5km/h and 10, 20 and 50 km/h.

In the base layer, there are instances where the pressure magnitude at certain speeds (e.g., 20 km/h) is higher than at the lowest tested speed of 5 km/h. For example, the magnitude of the front axle pressure at 5 km/h is approximately 17.6 kPa, whereas, at 20 km/h, it is around 30.1 kPa. This suggests that the impact of the load on the base layer results in larger pressure magnitudes for some axles, especially the tandem axle. Or tire wander was likely variable between 5 km/h and 20 km/h, even if care was taken to ensure that the truck was running over the same sensor array path each time.

The subbase layer exhibits a similar trend to the base layer. In addition to this, however, the magnitudes of the pressure responses in the subbase layer are slightly larger than those in the base layer. This indicates that loads have a greater impact on the subbase layer than the base layer but raises questions (see 5.2.4).

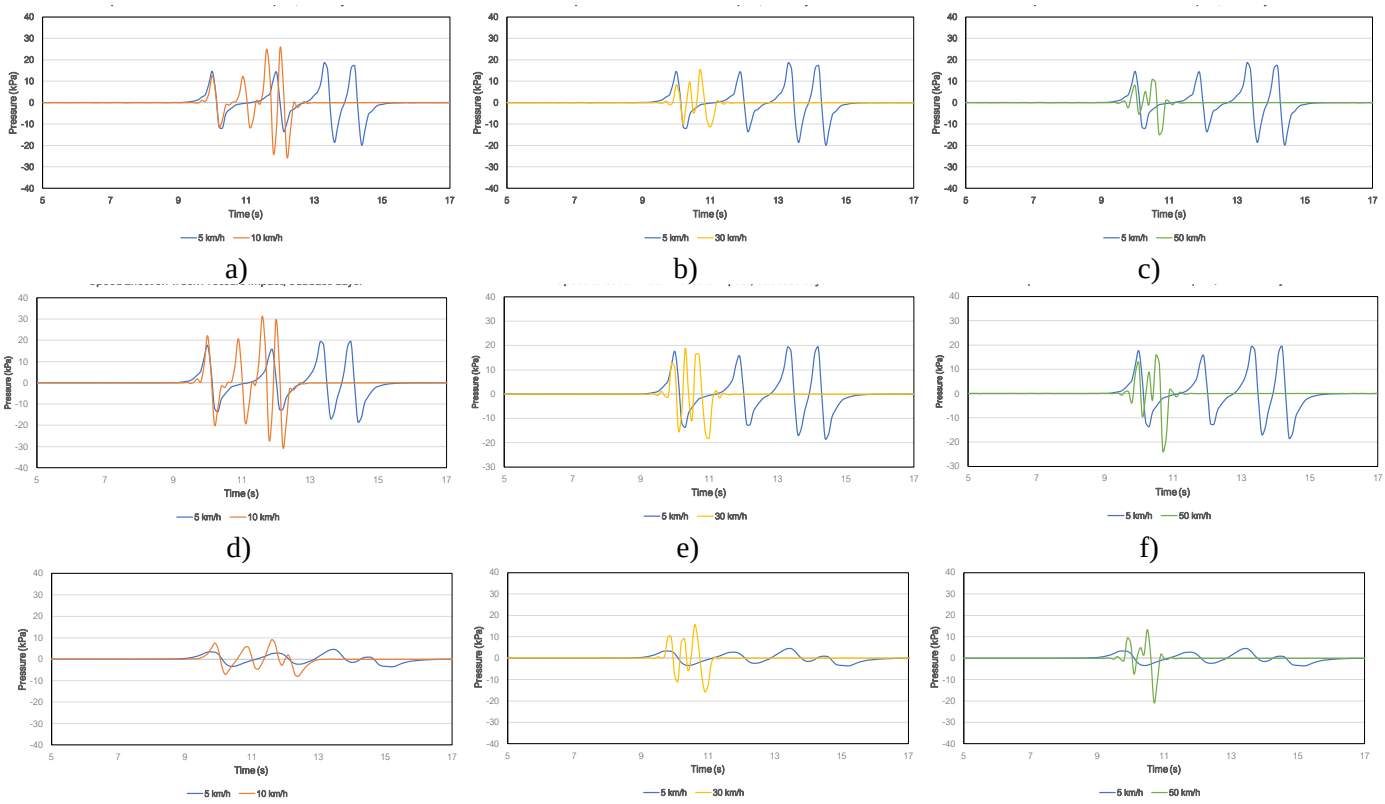


Figure 5.19 This is a 9-panel figure depicting the comparison of the impact of the pressure in the base (a,b,c), subbase (d,e,f), and subgrade (g,h,i) at 5km/h and 10, 30 and 50 km/h.

Finally, the subgrade layer follows a similar trend as demonstrated in the previous two layers, with pressure magnitudes sometimes increasing as speed increases. In addition, the overall magnitudes of the pressure responses in the subgrade layer are lower as compared to the base and subbase layers. This is expected since the sensors in the subgrade layer are located furthest away from the applied load.

The raw pressure results are illustrated in Figure 5.20. Like the raw strain results depicted in Figure 5.18, the shapes of the raw pressure results reflect the way the truck passes over the sensors and the types of axles situated on the sensors. There is a clear representation of a steering axle, lift axle, and a tandem axle, which appears as a single response but cleaved. The magnitudes of the pressure responses vary from layer to layer, with the base and subbase exhibiting higher responses than the subgrade. The signal responses are notably clearer in the base and subbase, characterized by more pointed and defined responses, while in the subgrade layer, the responses are more curved, indicating that the subgrade pressure cells are situated deep within the pavement structure and may not be capturing the full pressure response.

Once again, the trends observed in previous sections, such as the relationship between speed and pressure magnitude, as well as speed and response length, are evident. In general, these trends align logically and provide clear and sensible results.

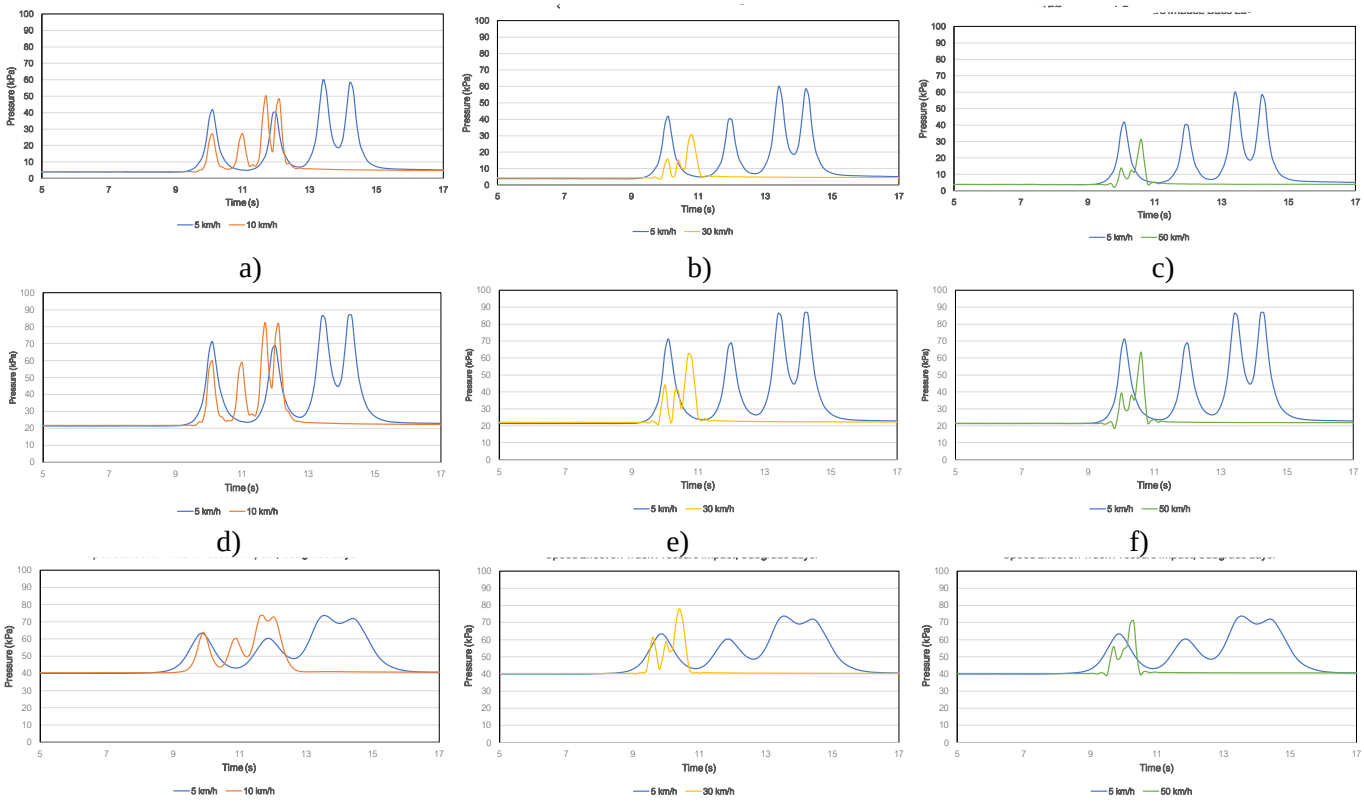


Figure 5.20 Comparison of the impact of the raw pressure in the base (a,b,c), subbase (d,e,f), and subgrade (g,h,i) at 5km/h and 10, 30 and 50 km/h.

5.4 Truck Test #3: Summer Conditions

The third truck test occurred on July 20th, 2023, during warm summer conditions between 11:00 AM and 1:00 PM. During this truck testing session, all sensors were successfully tested as the DAC was operational at that time. Various speeds were examined, including 5, 10, 20, 30, 40, 50, 60, and 70 km/h at an asphalt temperature of 25 °C, while the ambient temperature was about 20 °C, with a mix of sun and cloud weather conditions. During this truck test, the truck was loaded and had a gross loading weight of 353 kN, and a tare weight of 138 kN. In addition, the weights of the individual axles were also captured, and they were: 68 kN for the steering axle, 78 kN for the lift axle, and 102 kN each for the tandem axles. These were provided weights by the contractor, and it is recognized that there is a 3 kN gap between the sum of the individual axles and the gross weight.



Figure 5.21 Drawing of guideline 0.7 metres from the edge of pavement to guide the truck during truck testing.



Figure 5.22 Summer truck testing setup - data collection and truck passing over sensor arrays.

5.4.1 Impact of Speed on Longitudinal & Transverse Strain

Figure 5.21 shows a selection of the results of the truck testing at various speeds for both longitudinal and transverse strain. These include speeds of 5, 10, 20 and 50 km/h.

It is apparent that for both the longitudinal and transverse strain directions, the strain magnitude decreases with increasing speed. In some cases, such as 5 km/h and 10 km/h, the magnitudes are very similar as the speed difference is not very large, but as the speed increases, such as to 20 or 50 km/h, the difference in magnitude becomes apparent. The strain magnitude trends in the transverse direction are opposite to those that appeared in the early spring conditions assessment, however now the results generally follow what is described in the literature, such as in [65], [64] and [33].

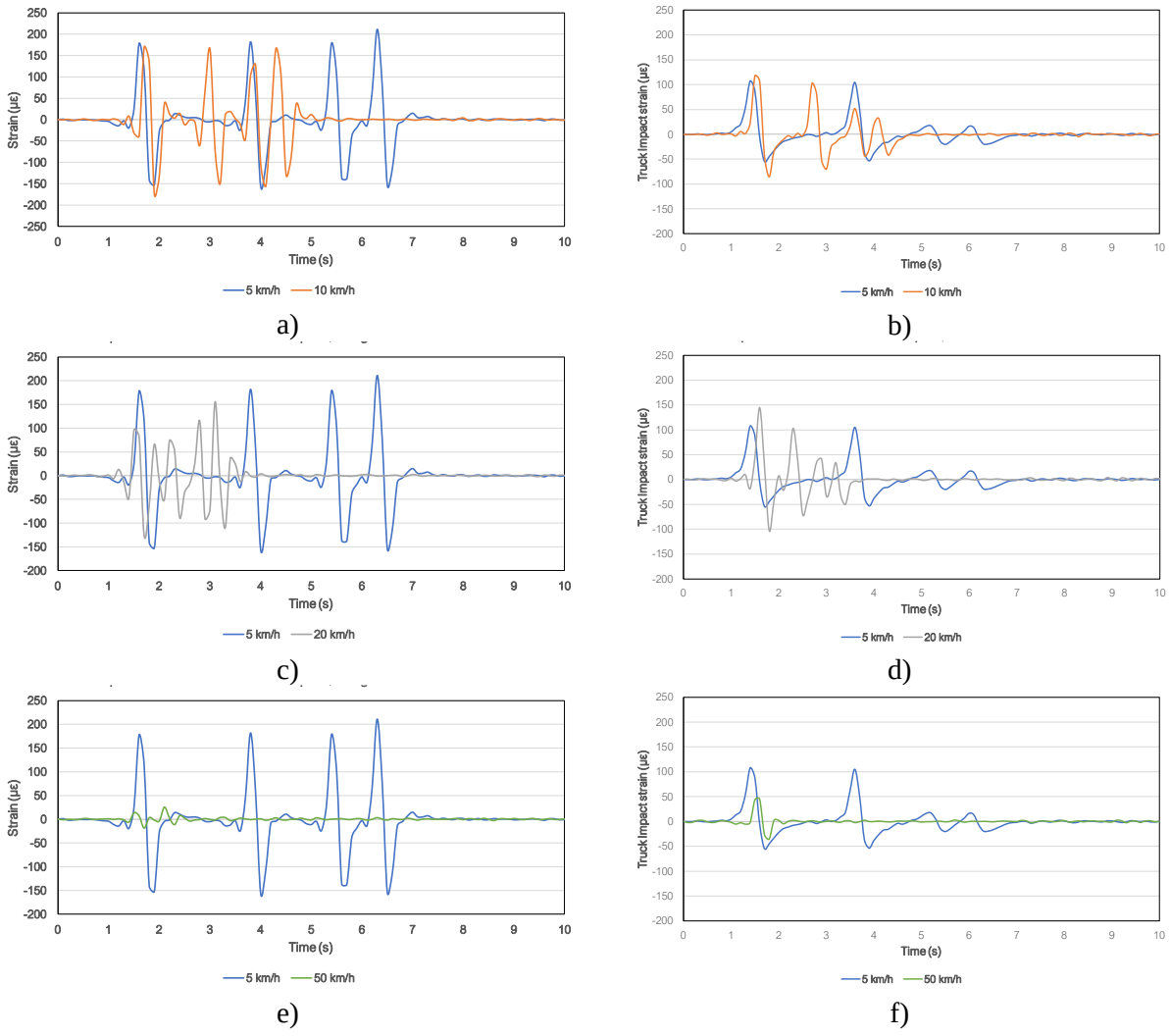


Figure 5.23 This is a 6-panel figure demonstrating the comparison of the impact of longitudinal (a,c,e) and transverse (b,d,f) strain at 5km/h and 10, 20 and 50 km/h.

It is apparent that for both the longitudinal and transverse strain directions, the strain magnitude decreases with increasing speed. In some cases, such as 5 km/h and 10 km/h, the magnitudes are very similar as the speed difference is not very large, but as the speed increases, such as to 20 or 50 km/h, the difference in magnitude becomes apparent. The strain magnitude trends in the transverse direction are opposite to those that appeared in the early spring conditions assessment, however now the results generally follow what is described in the literature, such as in [65], [64] and [33].

When comparing the strain responses in early spring and summer conditions, it becomes evident that the strain experienced during summer is consistently higher. Take for example the front tandem axle at 5 km/h: in winter conditions, the strain magnitude is 80 kN, while in summer, it surges to 180 kN. This discrepancy can be attributed to the higher average asphalt pavement temperature during the truck test in

summer compared to the early spring test. The elevated temperature renders the asphalt softer, making the material more susceptible to deformation and strain, thus resulting in a heightened strain response [63].

Similarly, to the previous observations, as the truck's speed increases, the intervals between axle peak responses shorten, and the strain magnitudes decrease—both in the longitudinal and transverse directions. When comparing the overall length of signal responses between this and the previous tests, no noticeable change emerges when contrasting winter and summer conditions. For instance, at 5 km/h, the total signal response length in summer is approximately 5.5 seconds, whereas in early spring, it hovers around 5.7 seconds. Confirming this trend requires additional data, but this is a positive preliminary assessment since it indicates that the trucks in both tests ran at relatively similar speeds.

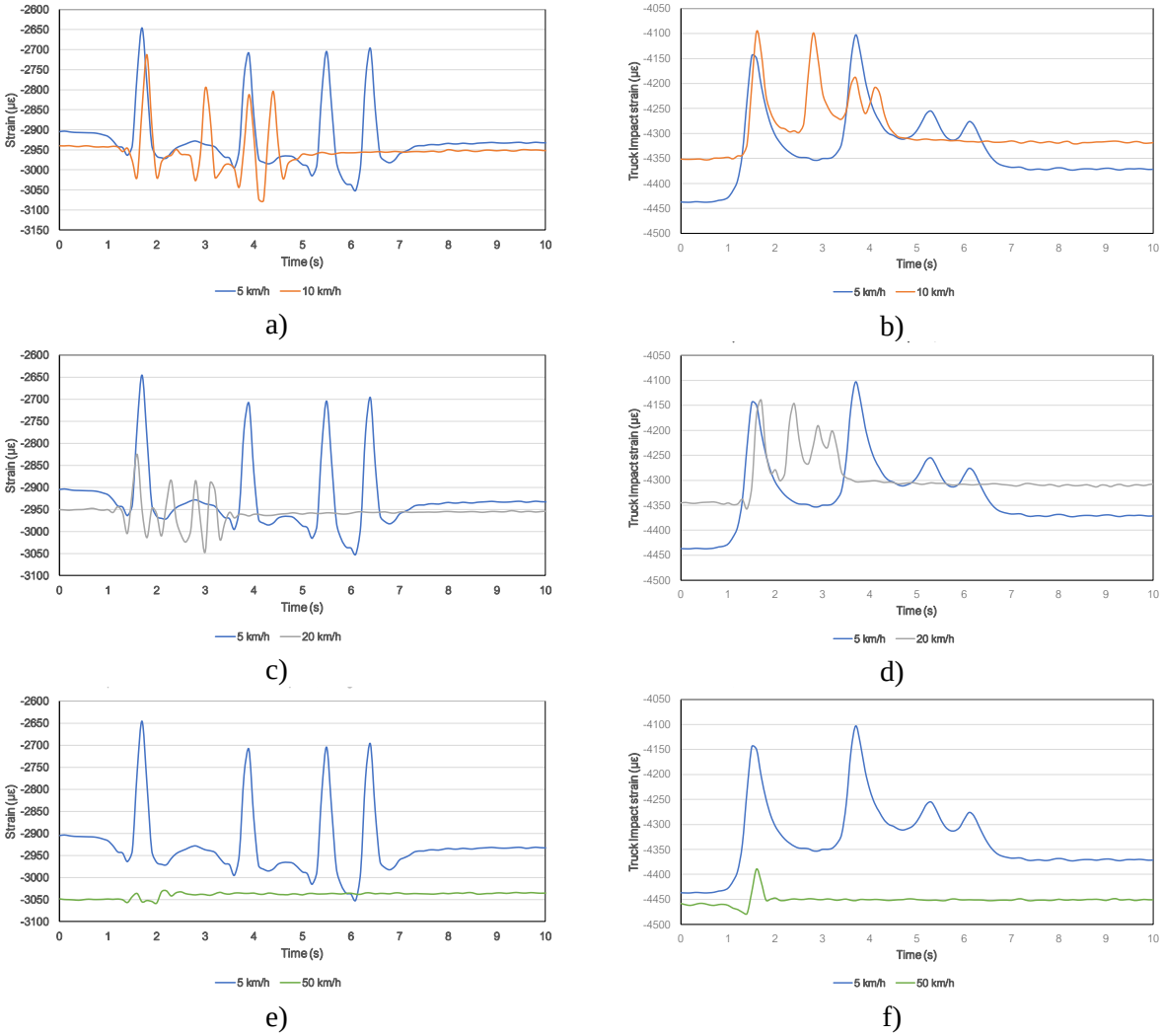


Figure 5.24 This is a 6-panel figure demonstrating the comparison of the impact of raw longitudinal (a,c,e) and transverse (b,d,f) strain at 5km/h and 10, 20 and 50 km/h.

The raw longitudinal and transverse strain results are depicted in Figure 5.24. This figure reveals both similarities and variations when comparing the strain from this test to that of test #2. One similarity is the

clear and well-defined nature of both signals, with all axles distinctly represented in the responses, especially at slower speeds. The trends in both the transverse and longitudinal strain gauges remain consistent, indicating that as speed increases, the magnitudes decrease, and the time it takes for the truck to pass over the sensors shortens, resulting in shorter and more condensed sensor responses at higher speeds.

However, differences emerge in the shapes of the responses, particularly in the transverse direction. In the longitudinal direction, the patterns are relatively like those observed in the previous truck test, with well-defined responses. Yet, in the transverse direction, the steering axle and lift axle exhibit the highest magnitudes, while the tandem axle does not show a large response in the transverse direction.

5.4.2 Impact of Speed on Pressure in the Base, Subbase and Subgrade

Figure 5.25 illustrates the impact of speed on the pressure experienced in the base layer, subbase layer, and subgrade layer of the pavement structure during the summer truck test. Overall, a consistent trend is observed across all three layers: as the speed increases, the magnitude of the pressure decreases, and the time between peak pressure magnitudes for each axle decreases.

The trends presented within the context of this figure are like those that were experienced in the early spring conditions. The pressures in the base and subbase are much higher than those experienced in the subgrade layer, and the layer with the greatest pressure response is the subbase layer. In all layers, the higher the speed, the smaller the gap between the peak pressure loads for the different axles. In some cases, especially for speeds that are like and close to 5 km/h, such as those like 10 km/h, the magnitudes could actually be higher than those at 5 km/h.

When comparing pressure responses in summer and early spring conditions, variations in signal shape and strain magnitude become apparent. In early spring, the tandem axles exhibit the highest pressure response, followed by the steering and lift axles. In contrast, summer conditions reveal a different hierarchy, with the steering axle registering the greatest response, followed by the lift axle and then the tandem axle. This discrepancy raises the possibility of tire wander discrepancies over the sensor arrays, resulting in diverse signal responses.

Additionally, there's a notable disparity in pressure magnitudes between the seasons. For instance, comparing the steering axle, pressure magnitudes range from 10 kPa to 20 kPa in early spring, whereas in summer, they span from 5 kPa to 75 kPa.

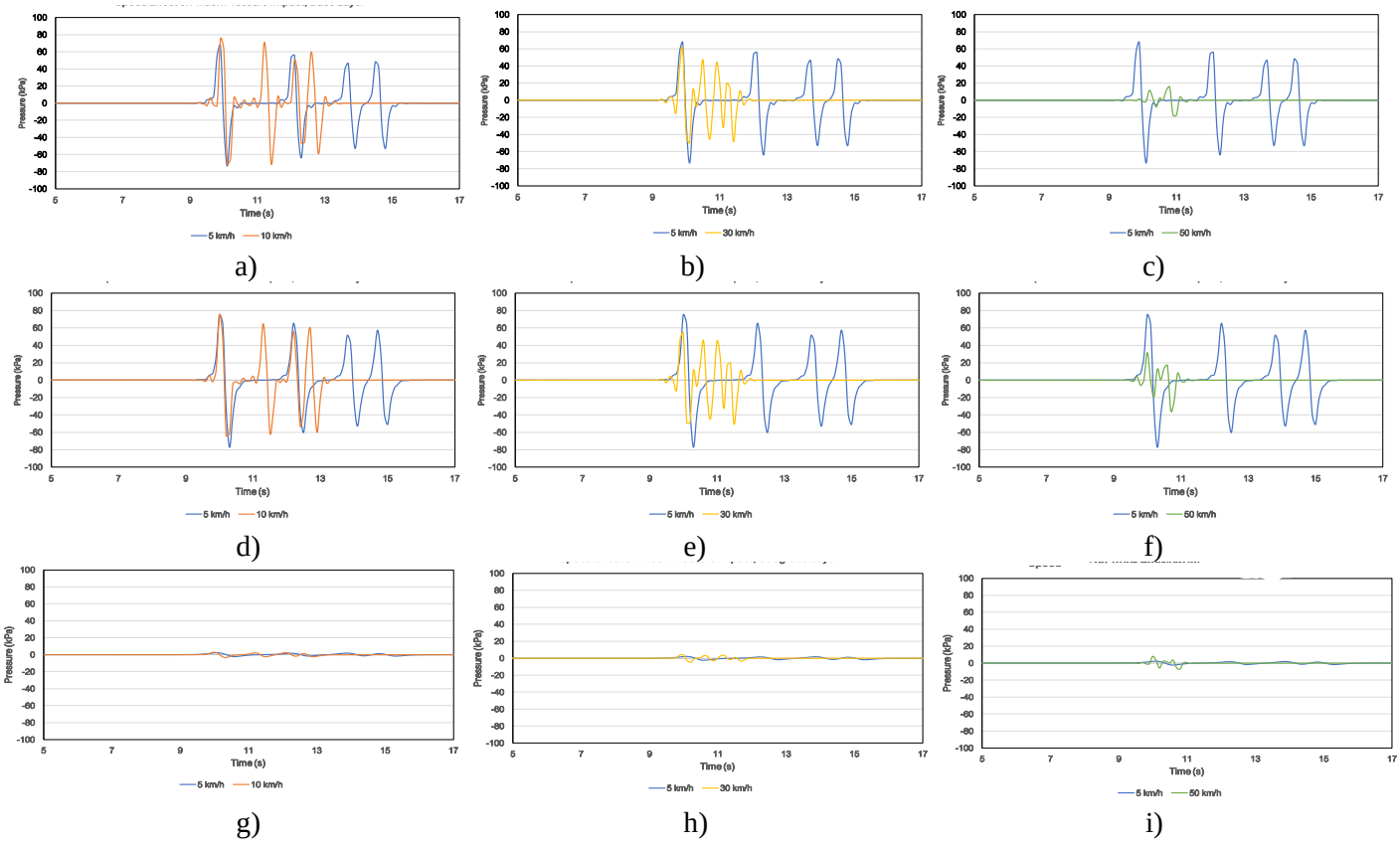


Figure 5.25 Comparison of the impact of the pressure in the base (a,b,c), subbase (d,e,f), and subgrade (g,h,i) at 5km/h and 10, 30 and 50 km/h.

The raw pressure results are presented in Figure 5.26 below. The shapes of the signal responses indicate a higher pressure impact from the steering and lift axles compared to the tandem axles. In this case, the signals are very clear and exhibit higher magnitudes than the raw pressure responses from the previous test. This is likely a result of the higher asphalt pavement temperature, creating warmer conditions that are more susceptible to pressure and strain responses.

It is evident, even in the raw pressure responses that the subgrade pressure response is significantly lower than that experienced in the base and subbase layers. This contrast was not as pronounced in the previous truck test, where the subgrade response was less than the base and subbase responses as well, but the difference in the pressure response was not as drastic. This could be attributed to variations in moisture content and temperature between truck TT#2 and truck TT#3. Changes in moisture content within layers, for example, can influence the mechanical behavior of the pavement structure, affecting the stiffness and strength of materials, especially in cases of subgrades with high clay or silt content that can absorb a lot of moisture. Given that the subgrade in this case is silty, these variations in response may be attributed to differences in moisture and temperature between early spring and summer.

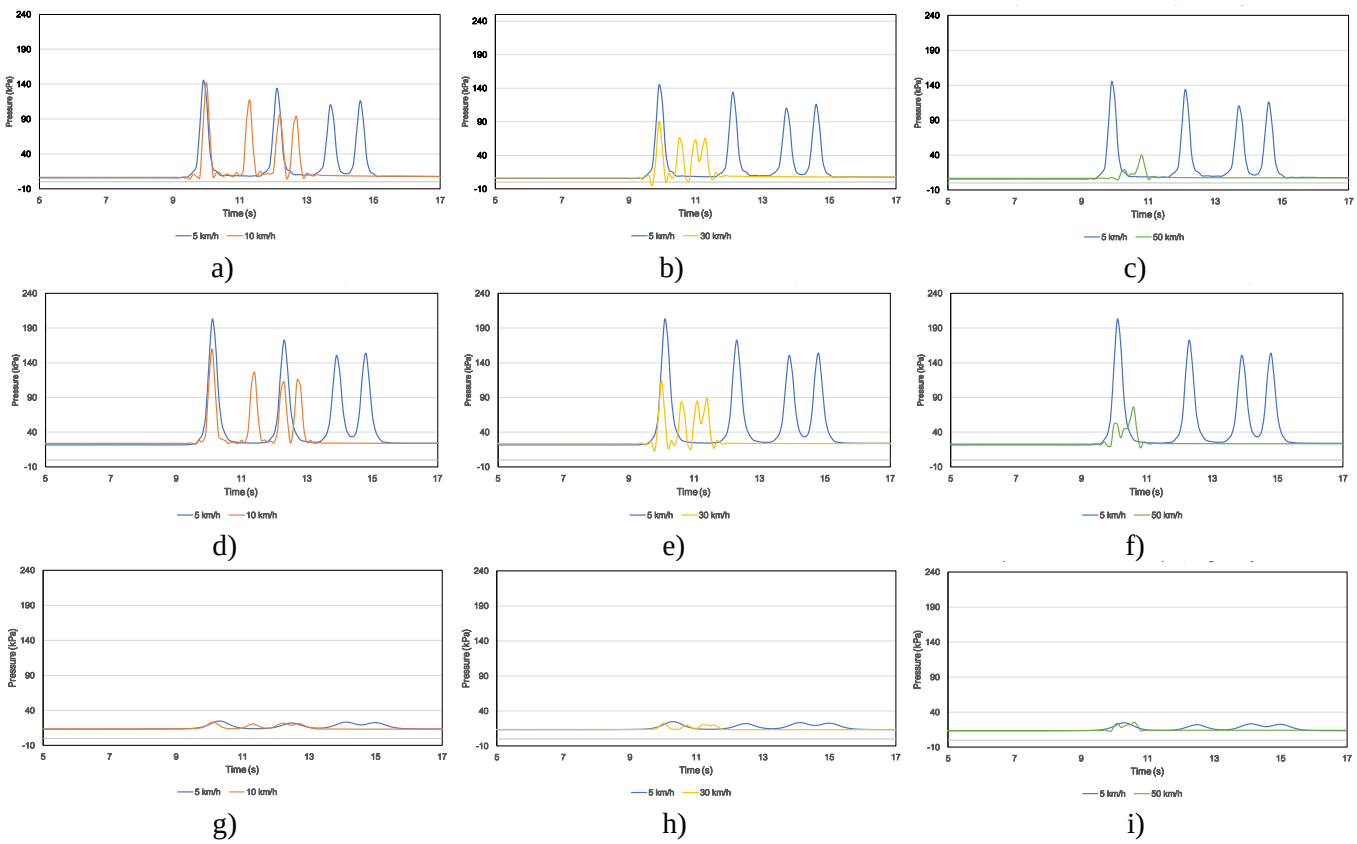


Figure 5.26 Comparison of the impact of the raw pressure in the base (a,b,c), subbase (d,e,f), and subgrade (g,h,i) at 5km/h and 10, 30 and 50 km/h.

5.5 Truck Test #4: Summer Conditions and Second HMA Lift Construction Analysis

The fourth truck testing occurred on August 28th, 2023, during warm summer conditions between 10:45 and 11:30 AM. The difference between this test and the previous test during the summer was that this test occurred four days after the pouring of the second lift of asphalt pavement. The first three tests occurred while the pavement structure only had the first layer of asphalt poured. During this truck testing session, all sensors were successfully tested as the DAC was operational at that time. Various speeds were examined, including 5, 10, 20, 30, 40, 50, 60, and 70 km/h at an asphalt temperature of 23 °C, while the ambient temperature was about 20 °C, with a mix of sun and cloud weather conditions. During this truck test, the truck was loaded and had a gross loading weight of 337 kN, and a tare weight of 138 kN. In addition, the weights of the individual axles were also captured, and they were: 55 kN for the steering axle, 70 kN for the lift axle, and 102 kN each for the tandem axles. These were provided weights by the contractor, and it is recognized that there is an 8 kN gap between the sum of the individual axles and the gross weight.

5.5.1 Impact of Speed on Longitudinal & Transverse Strain

Figure 5.28 shows a selection of the results of the truck testing at various speeds for both longitudinal and transverse strain. These include speeds of 5, 10, 20 and 50 km/h.

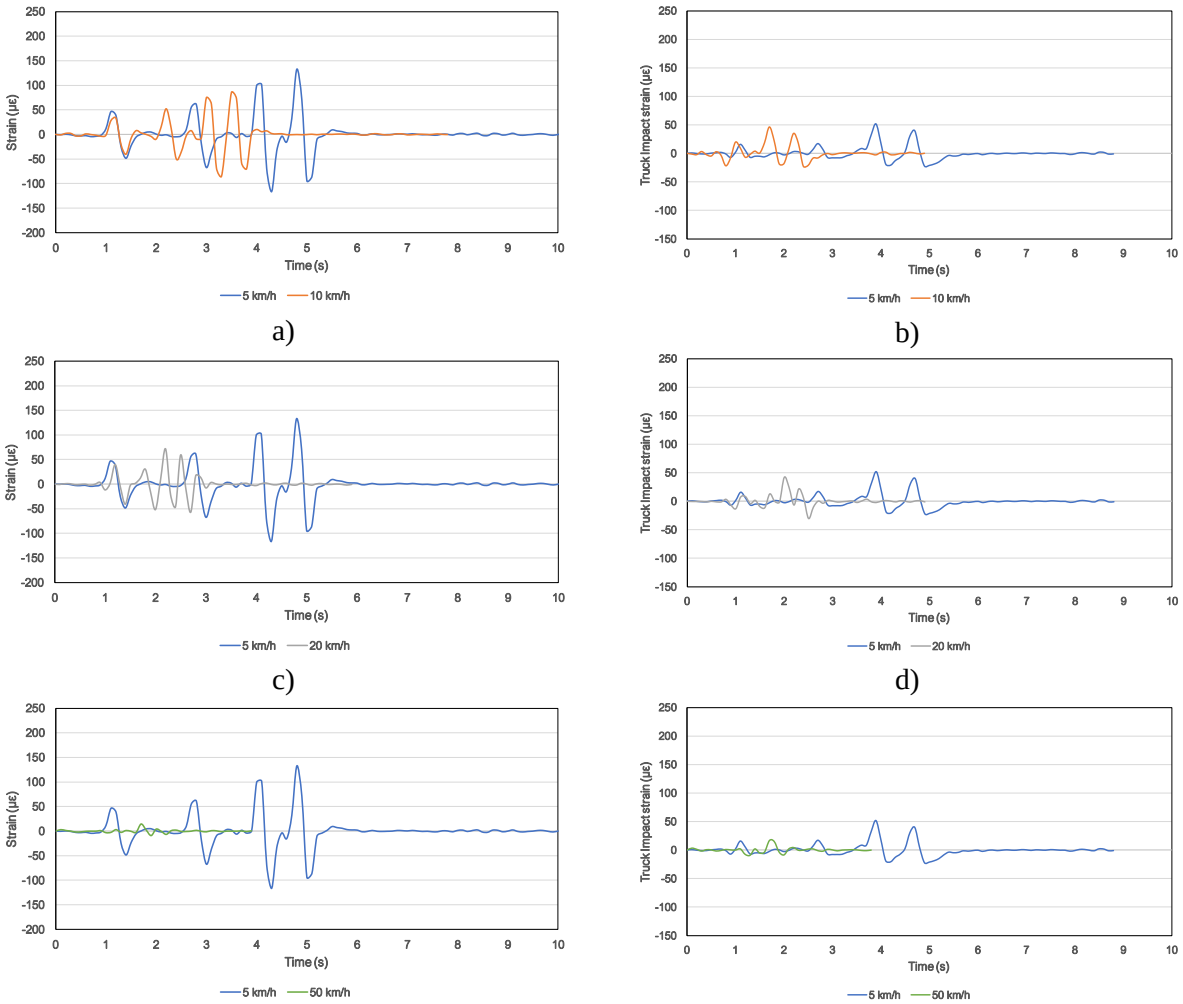


Figure 5.27 This is a 6-panel figure demonstrating the comparison of the impact of longitudinal (a,c,e) and transverse (b,d,f) strain at 5km/h and 10, 20 and 50 km/h.

As with the previous tests, the strain trends from the figure indicate that as the trucks speed increases, the intervals between the axle peak responses shorten and the strain magnitudes decrease in both the longitudinal and transverse directions.

In comparison to the strain responses in early spring and the first summer test conditions, where for the front tandem axle at 5 km/h the strain magnitude was 80 kN in the early spring conditions and 180 kN in the first summer truck test conditions, in this case the front end and axle strain magnitude peaks at about 100 kN. This falls in line with the results obtained previously, as once again the tests are conducted during warmer summer months which causes the actual material to be softer and have a higher strain

response. In addition, the truck is running on relatively freshly paved asphalt at this point meaning that the asphalt could potentially be more susceptible to damage. However, it is not as high as the first summer truck test because of the additional asphalt layer which is providing additional support to the granular and subbase layers. In essence, the pavement structure is thicker.

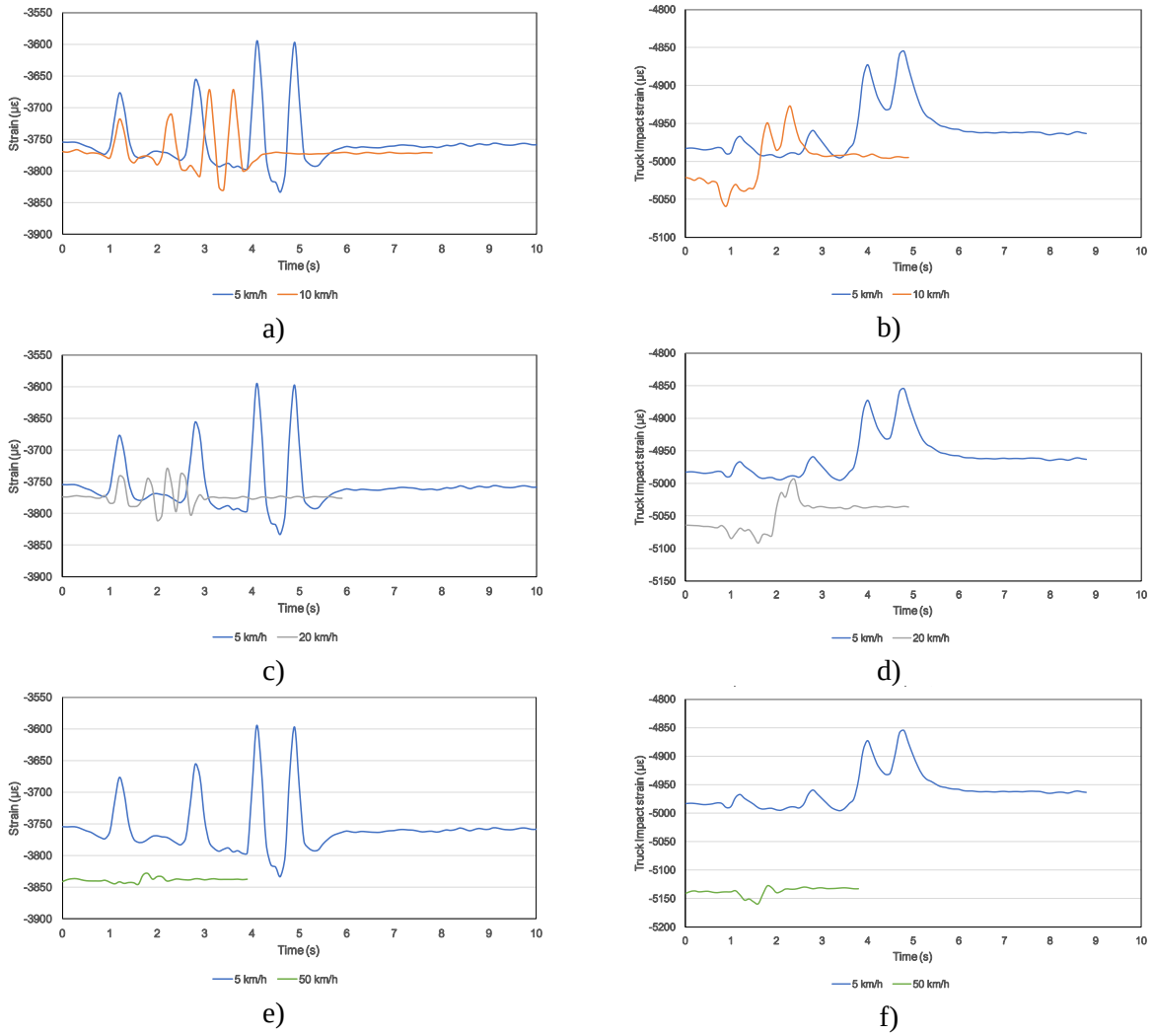


Figure 5.28 This is a 6-panel figure demonstrating the comparison of the impact of raw longitudinal (a,c,e) and transverse (b,d,f) strain at 5km/h and 10, 20 and 50 km/h.

Contrasting the strain responses from early spring and the initial summer test, where the front tandem axle at 5 km/h exhibited a strain magnitude of 80 kN in early spring and 180 kN in the first summer test, the current scenario sees the front end and axle strain peaking at around 100 kN. This aligns with previous findings, as the tests continue to be conducted in warmer summer months, resulting in a softer HMA material and heightened strain responses. Furthermore, the truck traverses relatively freshly paved asphalt at this point. The strain magnitude, although not reaching the levels observed in the first summer test, is

moderated by an additional asphalt layer that provides extra support to the granular and subbase layers, effectively thickening the pavement structure.

When comparing the overall length of signal responses between this and the previous tests, no noticeable change emerges when contrasting winter and summer conditions. For instance, at 5 km/h, the total signal response length in the first summer test is approximately 5.5 seconds, whereas in early spring, it hovers around 5.7 seconds. This second summer test also has a signal response length of about 5.5 seconds.

Figure 5.28 shows the raw longitudinal and transverse strains for this truck test. In the longitudinal strain, it is noticeable that the tandem axles produce the highest magnitude strain, which is larger than the strain from the steering and lift axles. Similarly, in the transverse strain, the tandem axle demonstrates the largest response compared to the steering and lift axles.

5.5.2 Impact of Speed on Pressure in the Base, Subbase and Subgrade

Figure 5.29 illustrates the impact of speed on the pressure experienced in the base layer, subbase layer, and subgrade layer of the pavement structure during the second summer truck test.

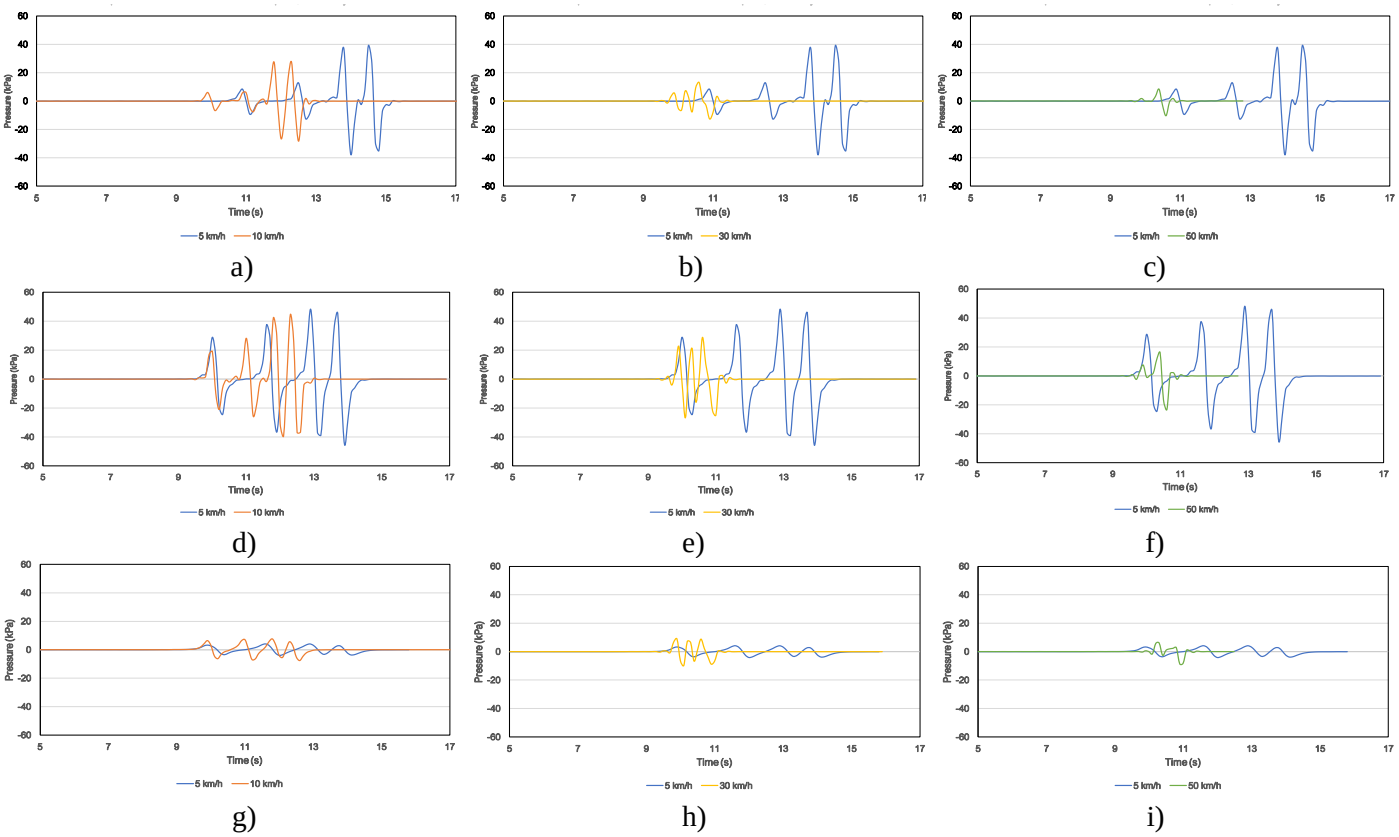


Figure 5.29 Comparison of the impact of the pressure in the base (a,b,c), subbase (d,e,f), and subgrade (g,h,i) at 5km/h and 10, 30 and 50 km/h.

Again, a consistent trend is observed across all three layers: as the speed increases, the magnitude of the pressure decreases, and the time between peak pressure magnitudes for each axle decreases. As with the two previous truck tests, the trends presented within the context of this figure are like those that were experienced. The pressures in the base and subbase are much higher than those experienced in the subgrade layer, and the layer with the greatest pressure response is the subbase layer. In all layers, the higher the speed, the smaller the gap between the peak pressure loads for the different axles.

Comparing pressure responses from early spring, the first summer test, and the current summer test, the results from this round of summer testing closely resemble those from early spring in terms of shape—where the tandem axles produce a greater response than the lift and steering axles. In terms of magnitude, the current summer test aligns more with the first summer truck test. For example, considering the front tandem axle in the base layer at 5 km/h, the early spring response is 20 kPa, the first summer truck test registers 40 kPa, and the latest summer truck test also records 40 kPa at the same speed.

Figure 5.29 shows the raw pressure results for this test period. In this case, the tandem axles have the largest response, typically in comparison to the steering and lift axles, which is opposite to the previous summer test.

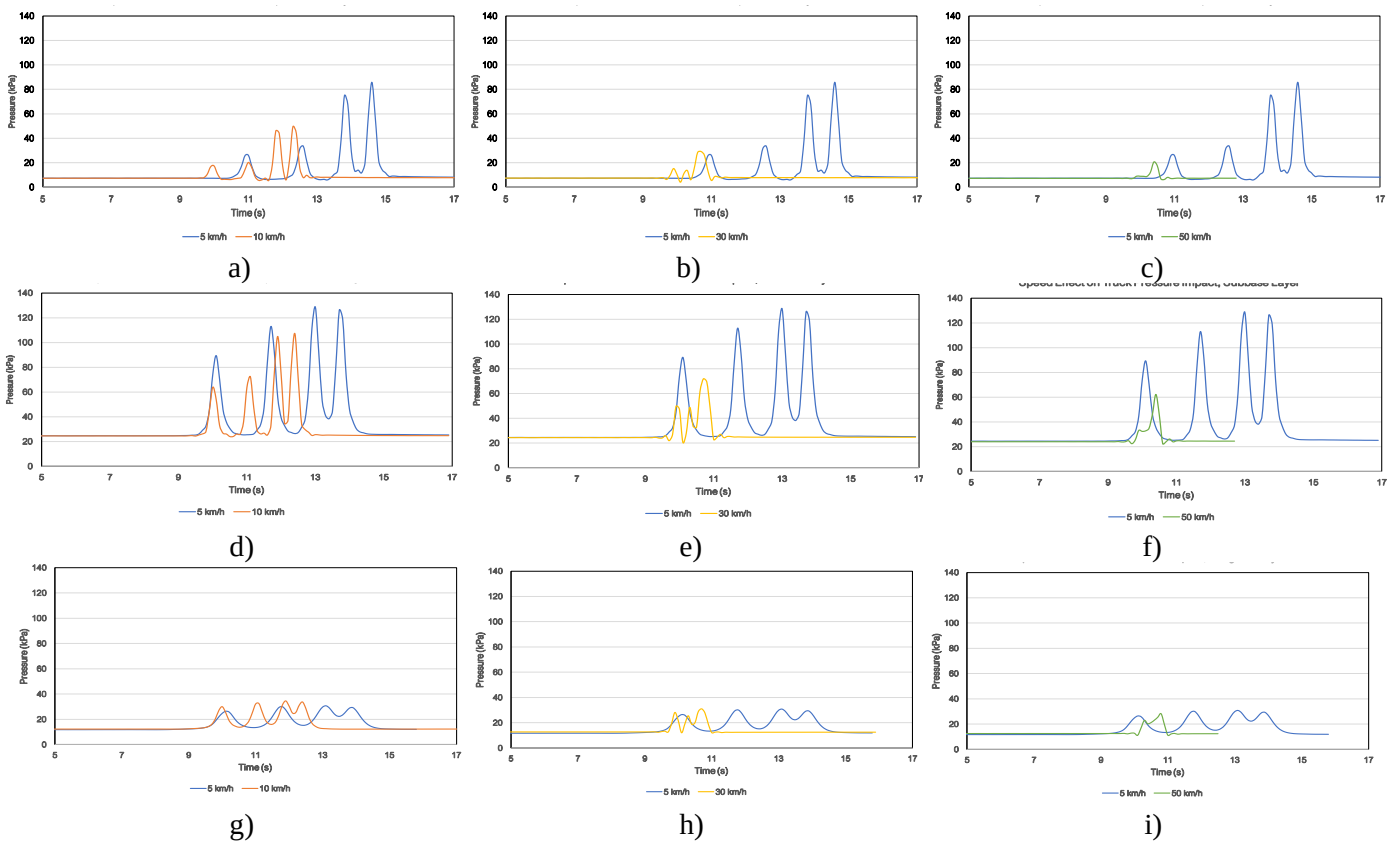


Figure 5.30 Comparison of the impact of the raw pressure in the base (a,b,c), subbase (d,e,f), and subgrade (g,h,i) at 5km/h and 10, 30 and 50 km/h.

5.6 Truck Test #5: Late Fall Conditions and Construction

The fifth and final truck testing occurred on December 11th, 2023, during warm summer conditions between 10:00 and 10:30 AM. During this truck testing session, all sensors were successfully tested as the DAC was operational at that time. Various speeds were examined, including 5, 10, 20, 30, 40, and 50 km/h (due to inclement weather conditions and safety concerns, 60 and 70 km/h were not able to be tested). The asphalt temperature was 5 °C, while the ambient temperature was about 1 °C, with some flurries and some sunny weather conditions. During this truck test, the truck was loaded and had a gross loading weight of 348 kN, and a tare weight of 154 kN. In addition, the weights of the individual axles were also captured, and they were: 74 kN for the steering axle, 76 kN for the lift axle, and 100 kN each for the tandem axles. These were provided weights by the contractor, and it is recognized that there is a 2 kN gap between the sum of the individual axles and the gross weight.

5.6.1 Impact of Speed on Longitudinal & Transverse Strain

Figure 5.31 shows a selection of the results of the truck testing at various speeds for both longitudinal and transverse strain. These include speeds of 5, 10, 20 and 50 km/h.

Compared to the strain results in previous tests, the first thing that stands out in this figure is the significantly smaller magnitudes in both the longitudinal and transverse directions. This could be attributed to a couple of factors. The first one being the fact that at this point in the year, the temperature is cooler therefore the magnitudes of the strain are smaller [63]. Additionally, the thicker AC layer now in place distributes the strain more evenly among the sensors, revealing why the results in this truck test exhibit smaller magnitudes compared to truck test number two conducted in early spring conditions.

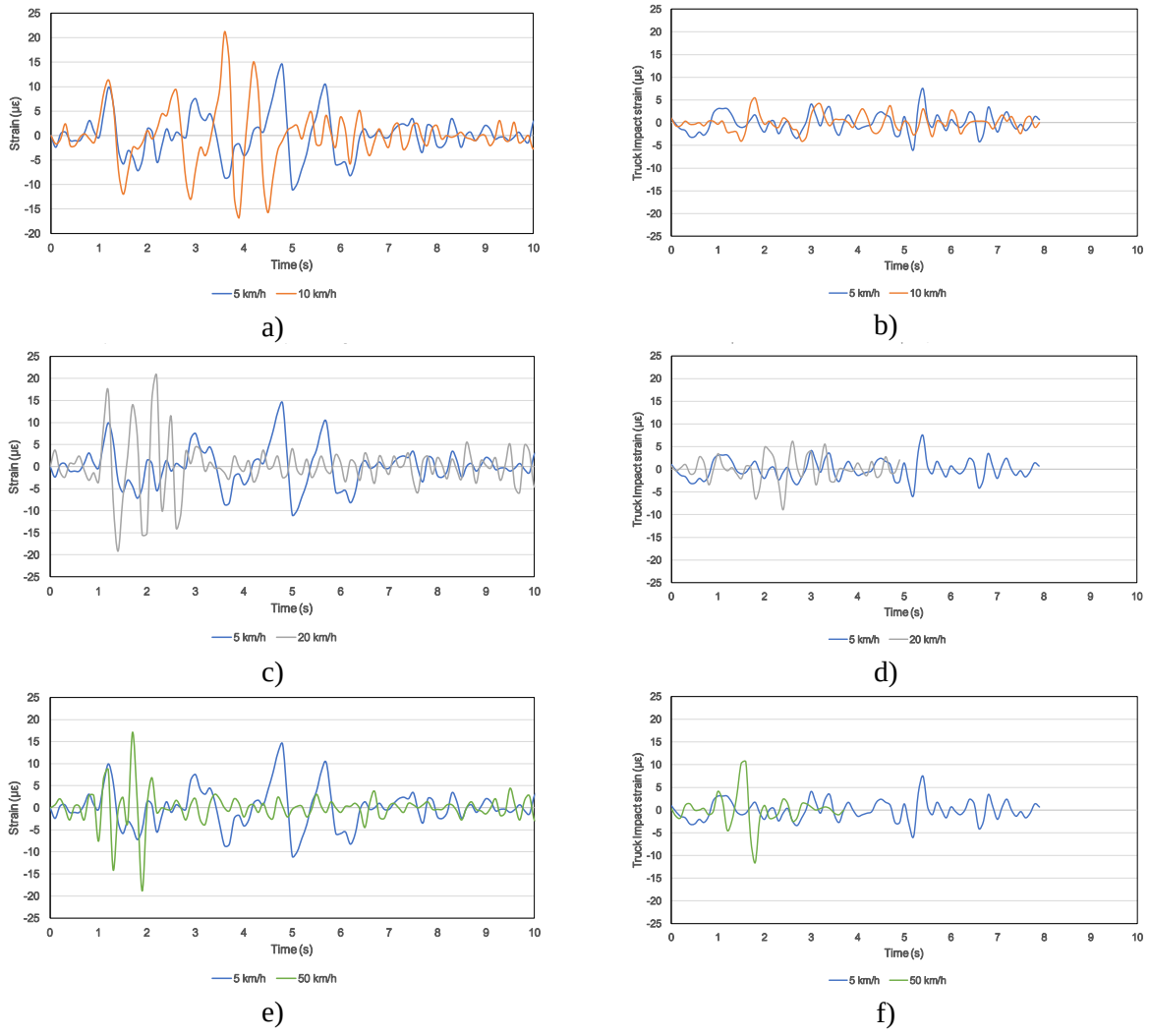


Figure 5.31 This is a 6-panel figure demonstrating the comparison of the impact of longitudinal (a,c,e) and transverse (b,d,f) strain at 5km/h and 10, 20 and 50 km/h.

The reduced magnitudes also impact the clarity of the signal, introducing more variation and making it less pristine compared to previous tests. Consequently, it becomes challenging to discern typical trends, such as the expected patterns for longitudinal and transverse strains. Despite the diminished clarity, some trends persist, like those observed in the longitudinal strain. However, these trends deviate from expectations; for instance, instead of the anticipated decrease in strain magnitude with increasing truck speed, cases where the magnitude is larger is observed.

Figure 5.31 shows the longitudinal and transverse strain results for this final truck test period. Compared to the previous truck tests, one can observe that the responses are much less clear, likely due to the overall smaller magnitude of strain produced at this asphalt and ambient temperature. In the longitudinal direction, especially at lower speeds like 5 to 10 km/h, the axles are clearly defined, allowing one to see

the shape of the signal response. However, in the transverse direction, the signal response is less pronounced and not very clear, likely influenced by the effect of these lower temperatures.

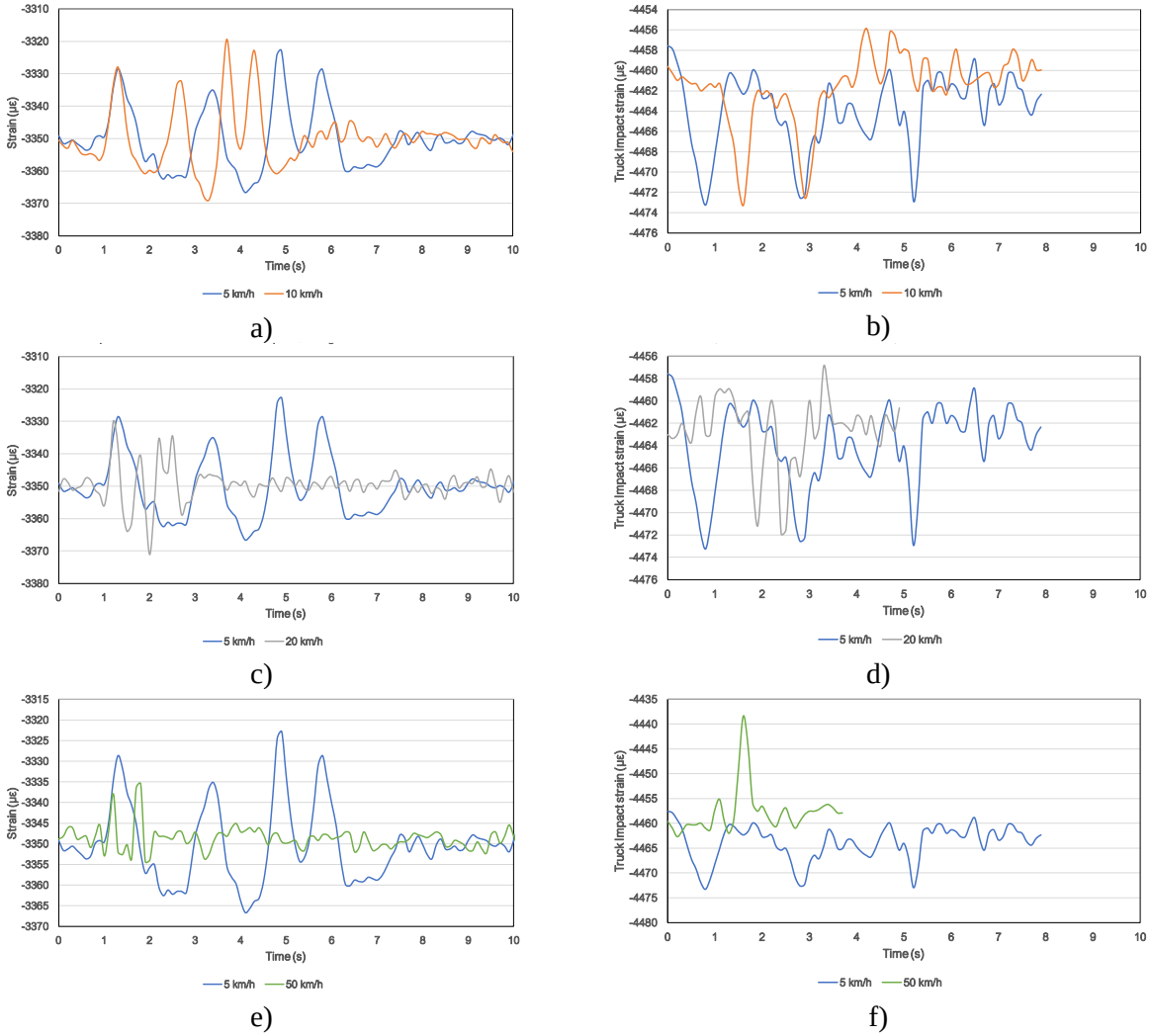


Figure 5.32 This is a 6-panel figure demonstrating the comparison of the impact of raw longitudinal (a,c,e) and transverse (b,d,f) strain at 5km/h and 10, 20 and 50 km/h.

5.6.2 Impact of Speed on Pressure in the Base, Subbase and Subgrade

The observed trends in Figure 5.33 for pressure closely parallel those identified in strain patterns but exhibit slight deviations from trends observed in prior tests. Notably, an increase in speed corresponds to sharper and less dispersed signal responses. However, a noteworthy departure from the expected norm is observed in the pressure magnitudes, with higher speeds consistently yielding higher pressure magnitudes than those recorded at lower speeds consistently surpass the pressure magnitudes observed at 5 km/h. This contrasts with the findings of the three preceding truck tests, where signals rarely exceeded the pressure magnitudes recorded at 5 km/h. Moreover, the pressure magnitudes in this truck test are consistently lower than those observed in previous truck tests, especially as compared to the early spring test.

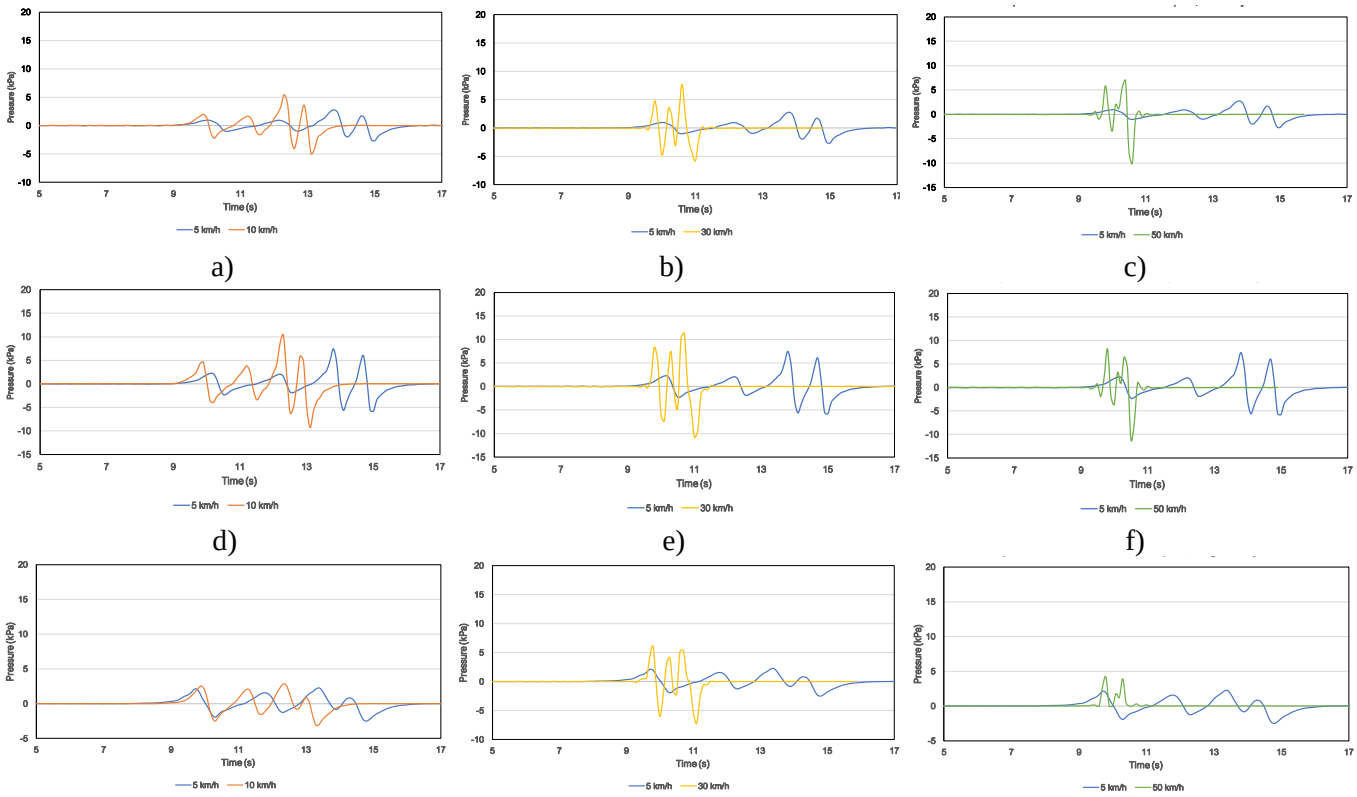


Figure 5.33 Comparison of the impact of the pressure in the base (a,b,c), subbase (d,e,f), and subgrade (g,h,i) at 5km/h and 10, 30 and 50 km/h.

Finally, Figure 5.35 shows the raw pressure results for this final truck test. At slower speeds, the axles are quite distinguished, and one can differentiate between all the various types. Previous trends noted before are again present, such as the fact that at higher speeds, the signal responses become more condensed both in magnitude and in time. The effect of ambient and asphalt temperatures is quite apparent in this case, as the magnitude of the pressure here is much less than the ones calculated in the previous tests. All these tests have demonstrated the influence of seasons on the magnitude and shape of the signal response. This insight is valuable for further developments in climate and artificial intelligence-related research to better understand future data and provide more accurate predictions and outcomes.

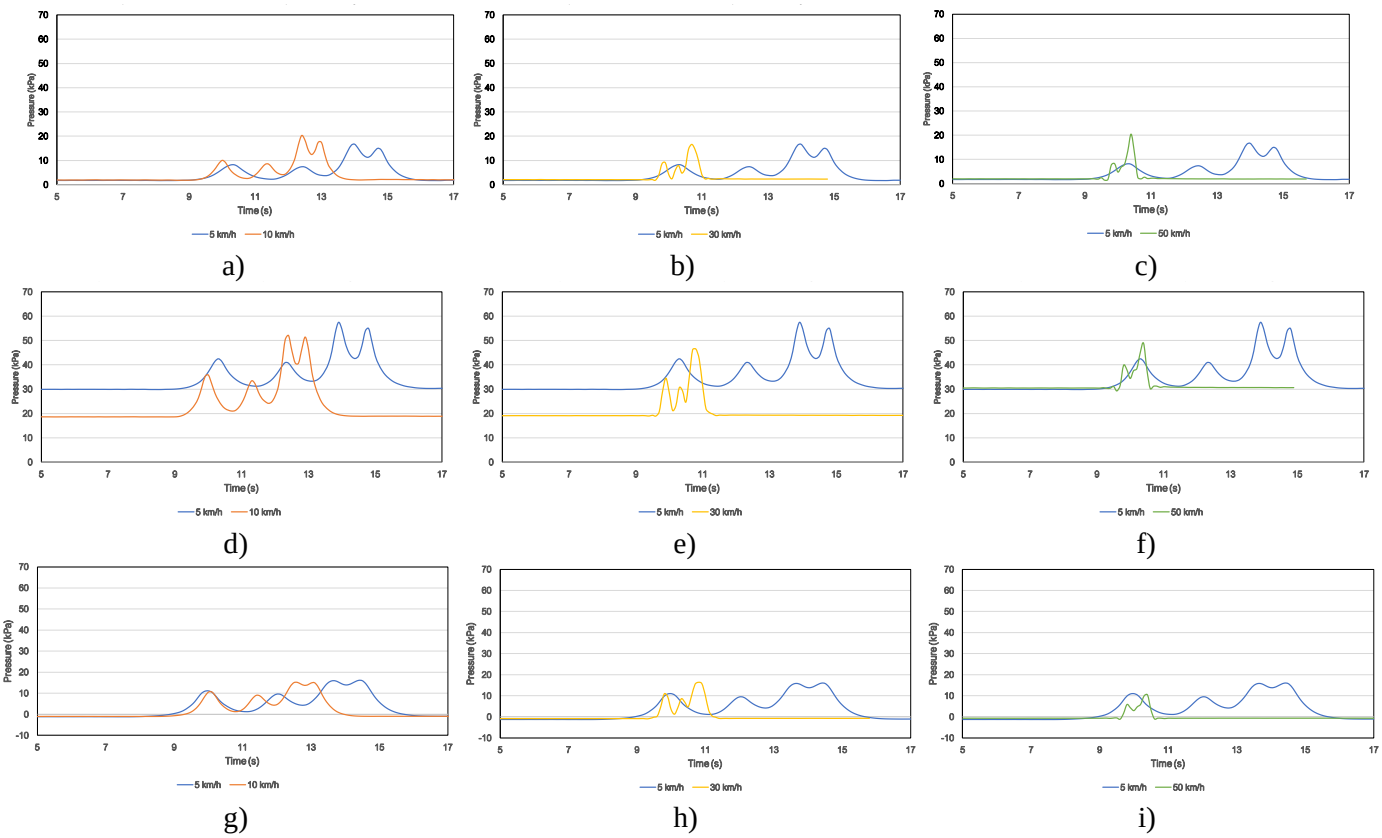


Figure 5.34 Comparison of the impact of the raw pressure in the base (a,b,c), subbase (d,e,f), and subgrade (g,h,i) at 5km/h and 10, 30 and 50 km/h.

5.7 Strain and Pressure Comparison

This section aims to establish comprehensive comparisons between the pressure and strain data gathered across all five truck tests. The initial focus involves evaluating the strain and pressure distinctions between the right and left sensor arrays, utilizing a single test as an illustrative example. Subsequently, the analysis extends to comparisons between the maximum strain and maximum pressure observed in the various tests, first as a function of truck speed and sensor, then more generally in terms of the sensor location and orientation. This comparative exploration is designed to offer a swift and straightforward visualization of how signal responses vary among the diverse sensors, shedding light on potential comparisons and anomalies within the dataset.

5.7.1 Strain and Pressure Comparison Between the Right and Left Sensor Arrays

The first assessment performed was focused on comparing strain and pressure responses between the right and left sensor arrays, covering both longitudinal and transverse directions for the strain gauges, as well as spanning various layers of the pavement structure for the pressure cells. Truck Test #2 was used for this comparison. During this test, intriguing variations emerged in the magnitude and signal type of

responses between the two sensor arrays for both strain and pressure. Efforts were made to ensure the alignment of all sensor signal data, facilitating an accurate comparison of signal responses.

5.7.1.1 Strain Signal Comparison

In Figure 5.35, a comparison of the strain response in microstrain (με) are illustrated in terms of truck speed, sensor orientation and sensor array. Each column of charts within this figure represents results obtained from a single sensor.

Notably, the right sensor array exhibits more distinct and higher-magnitude strain signals than the left sensor array in both longitudinal and transverse directions. For example, at 5 km/h, the clarity of signal responses in the right array surpasses those in the left array, regardless of direction. "Clear" in this context refers to the visibility of all axles in the signal response; is it possible to discern the steering axle, lift axle and tandem axle in the signal response? In addition, the overall magnitude of strain responses in the right array is consistently larger than that in the left array, with for instance, at 5 km/h, values approaching 100 με for the back tandem axle in the longitudinal direction and 23 με for the steering axle in the transverse direction. These values are much larger than those in the left sensor array, which peak at about 10 to 12 με for the front tandem axle as described by the longitudinal left sensor array.

Interestingly, beyond 30 km/h, the signal becomes unclear for most sensors in all directions and arrays, making it challenging to discern axles. Despite this, it is evident that as speed increases, the signal response time shortens, indicating the quicker passage of truck axles over a specific sensor. Additionally, the strain magnitude generally decreases as truck speed increases. An intriguing observation arises when comparing longitudinal and transverse sensors in the same sensor array. At speeds exceeding 30 km/h, the magnitudes of the signal responses appear quite similar between the longitudinal and transverse directions in the right array. A similar pattern is observed in the left array, but this time, magnitudes seem comparable across all speeds regardless of strain gauge direction, not just speeds exceeding 30 km/h.

5.7.1.2 Pressure Signal Comparison

In addition to the strain signal comparison, a comparison of the pressure responses showcasing differences between the responses in the right and left arrays, as well as between whether the sensor is located in the base, subbase and subgrade layers is displayed in Figure 5.36 and Figure 5.37.

The analysis revealed that, generally, an increase in the speed of testing during the truck tests correlates with a decrease in the magnitude of the pressure response. However, exceptions were observed; at 5 km/h, the responses were unexpectedly lower than those at 10 and 20 km/h. This anomaly might be

attributed to the truck tires passing more directly over the sensor array at 10 and 20 km/h compared to 5 km/h.

Furthermore, the subgrade response consistently exhibited much lower values as compared to both the base and subbase responses. This trend aligns with observations from previous assessments, emphasizing the substantial decrease in the pressure impact response in the subgrade when contrasted with the base and subbase.

In addition, the clarity of axles diminishes around 20 to 30 km/h, making individual axles challenging to discern beyond this speed range.

In a broader context, the subbase responses consistently surpass those of the base, a phenomenon observed at all speeds. This suggests a heightened receptivity of the subbase sensor compared to the base sensor, and is the same phenomenon noticed as the analysis in Section 5.2.4.

Comparing responses between the right and left sensor arrays, the right array consistently produces higher-magnitude responses than the left array. However, a noteworthy observation in the left array is that responses in the subgrade tend to be generally higher across all speeds than either the base or subbase responses. This deviates from the anticipated trends discussed previously, and deviates from the trends in the right sensor array. By 70 km/h, the subgrade response in both the right and left sensor arrays becomes barely noticeable and can hardly be picked up by the pressure cells.

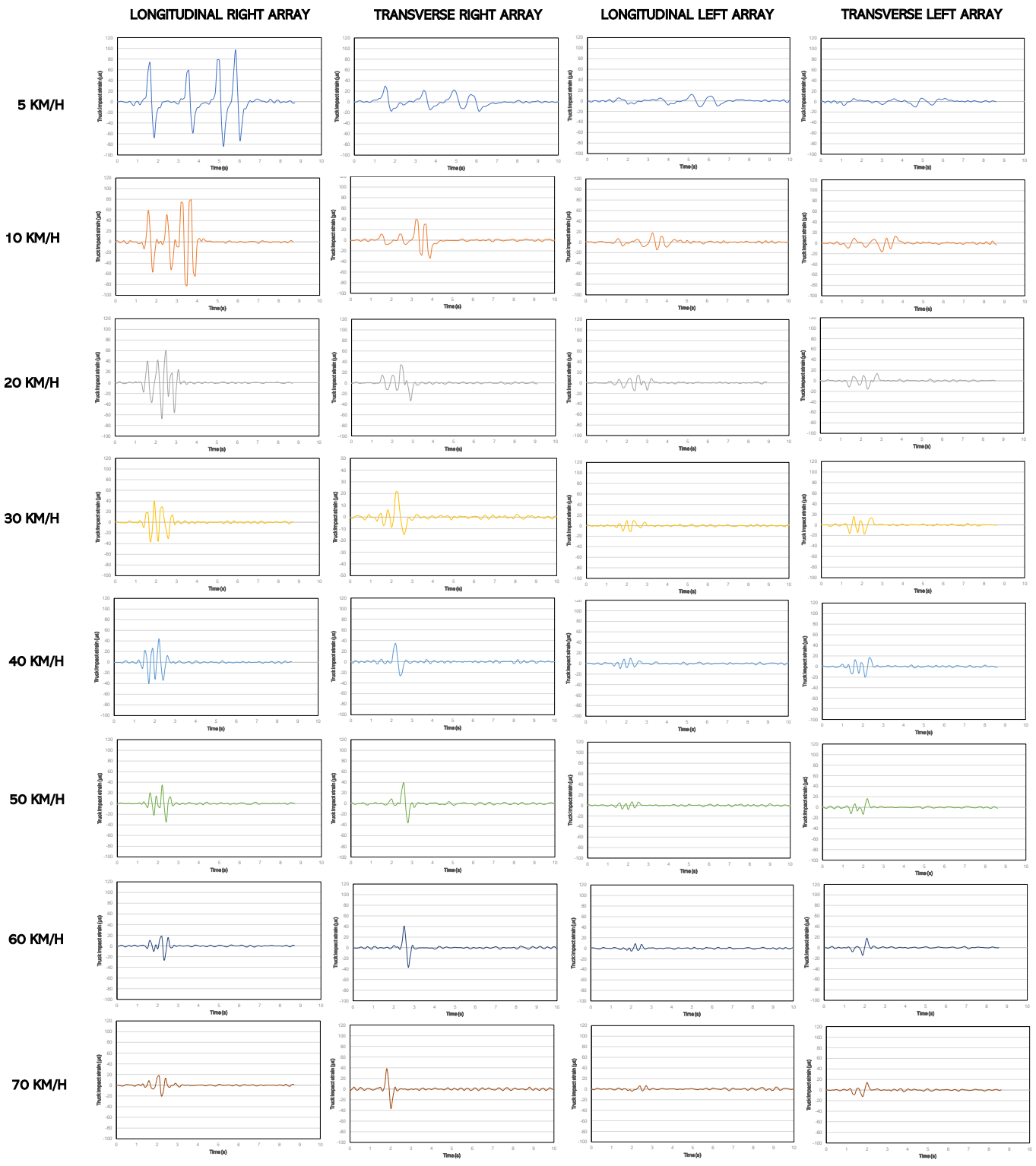


Figure 5.35 Comparing speed impact on pavement strain response: longitudinal and transverse sensors in left and right arrays. Y-axis: Strain (με), X-axis: Time (s) for all plots.

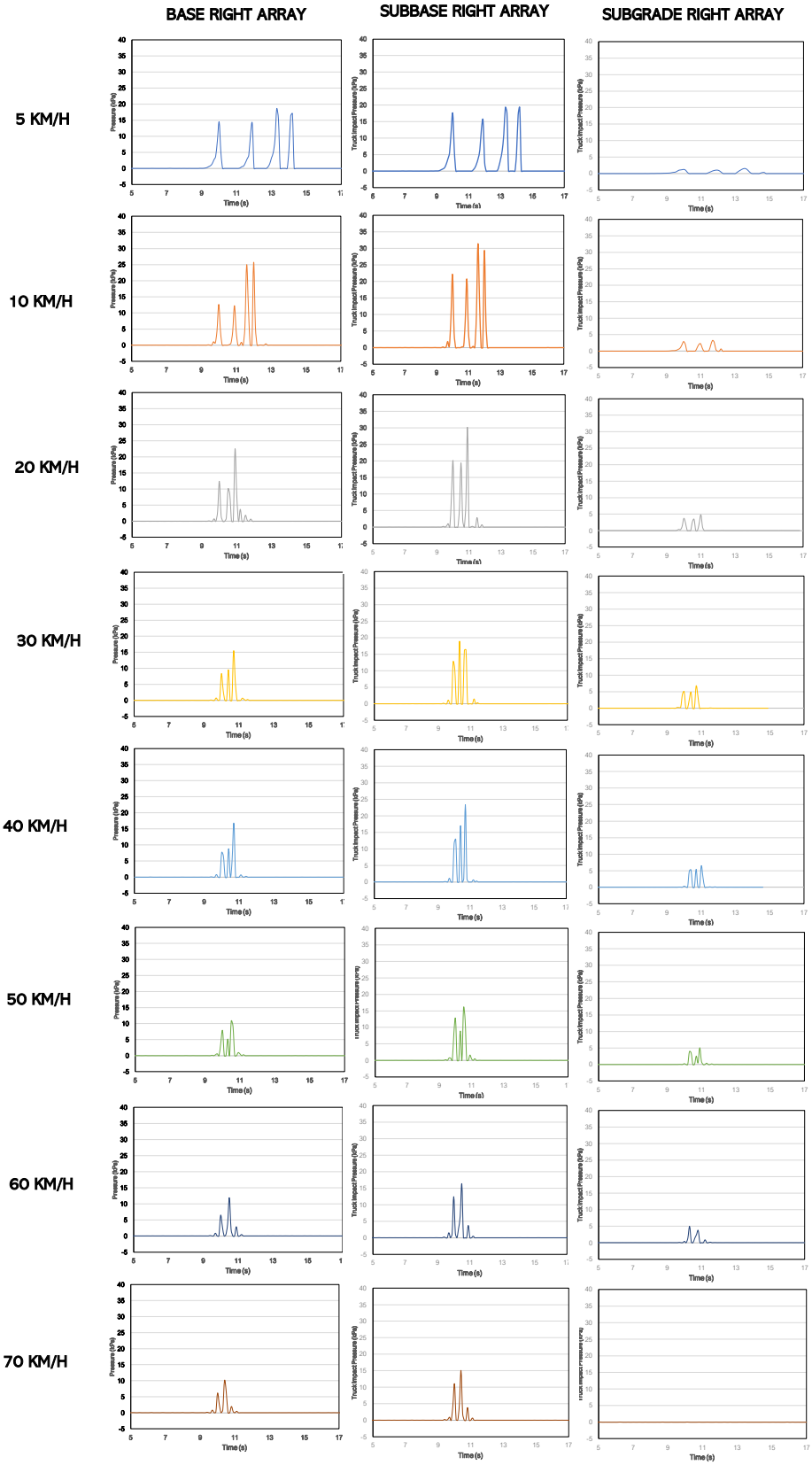


Figure 5.36 Comparison of speed impact on pavement pressure response for sensors in base, subbase, and subgrade within the right array. Y-axis: Pressure (kPa), X-axis: Time (s) for all plots.

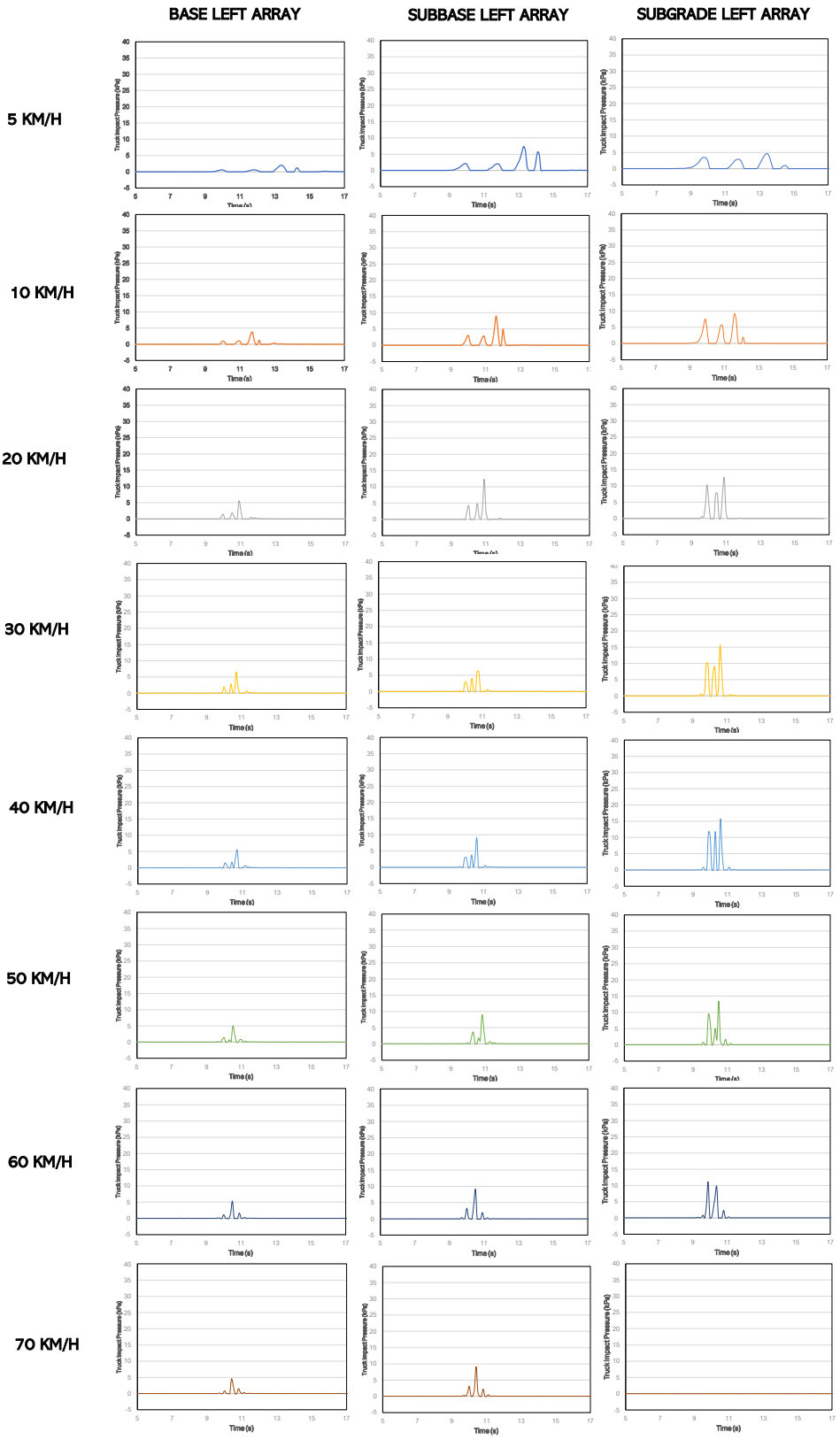


Figure 5.37 Comparison of the speed impact on pavement pressure response for sensors in the base, subbase and subgrade in the left array. Y-axis: Pressure (kPa), X-axis: Time (s) for all plots.

5.7.2 Maximum Pressure and Strain Comparison

To facilitate a more comprehensive comparison between the impact of loads on the pavement structure throughout all five truck tests, the maximum pressure and strain for each test will be compared to develop conclusions. The maximum pressure and strain values were determined to irrespective of axle type.

5.7.2.1 Pressure and Strain Comparison for Individual Sensors

Figure 5.38 depicts the maximum strain and pressure results captured for various sensors during truck test #1 (fall conditions) at various temperatures for the various sensors used during that test. Figure 5.39 and Figure 5.40 show, for truck tests 2 to 4, the maximum strain and pressure magnitudes across all tested speeds and sensors.

Notably, sensors AS-LO-R-1 and AS-LO-R-7 consistently exhibit the highest strain responses, irrespective of seasonal variations, temperature fluctuations, or testing speeds (for the most part – with higher speed does come greater variability in wander therefore the high-speed results may not be higher than longitudinal left array or transverse right array sensors). This alignment with expectations can be attributed to the longitudinal orientation of both sensors and their placement within the right sensor array.

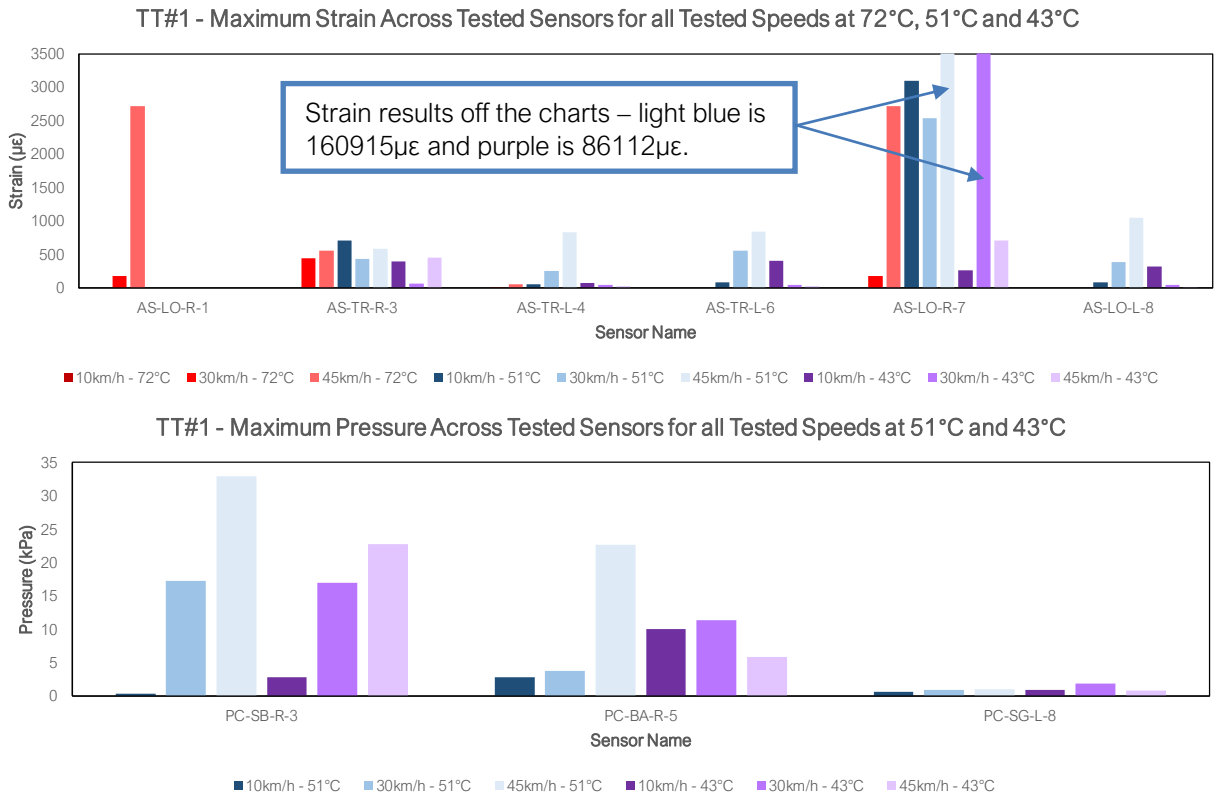


Figure 5.38 Maximum strain and pressure results captured for various sensors during Truck Test #1 (Fall conditions) at various temperatures.

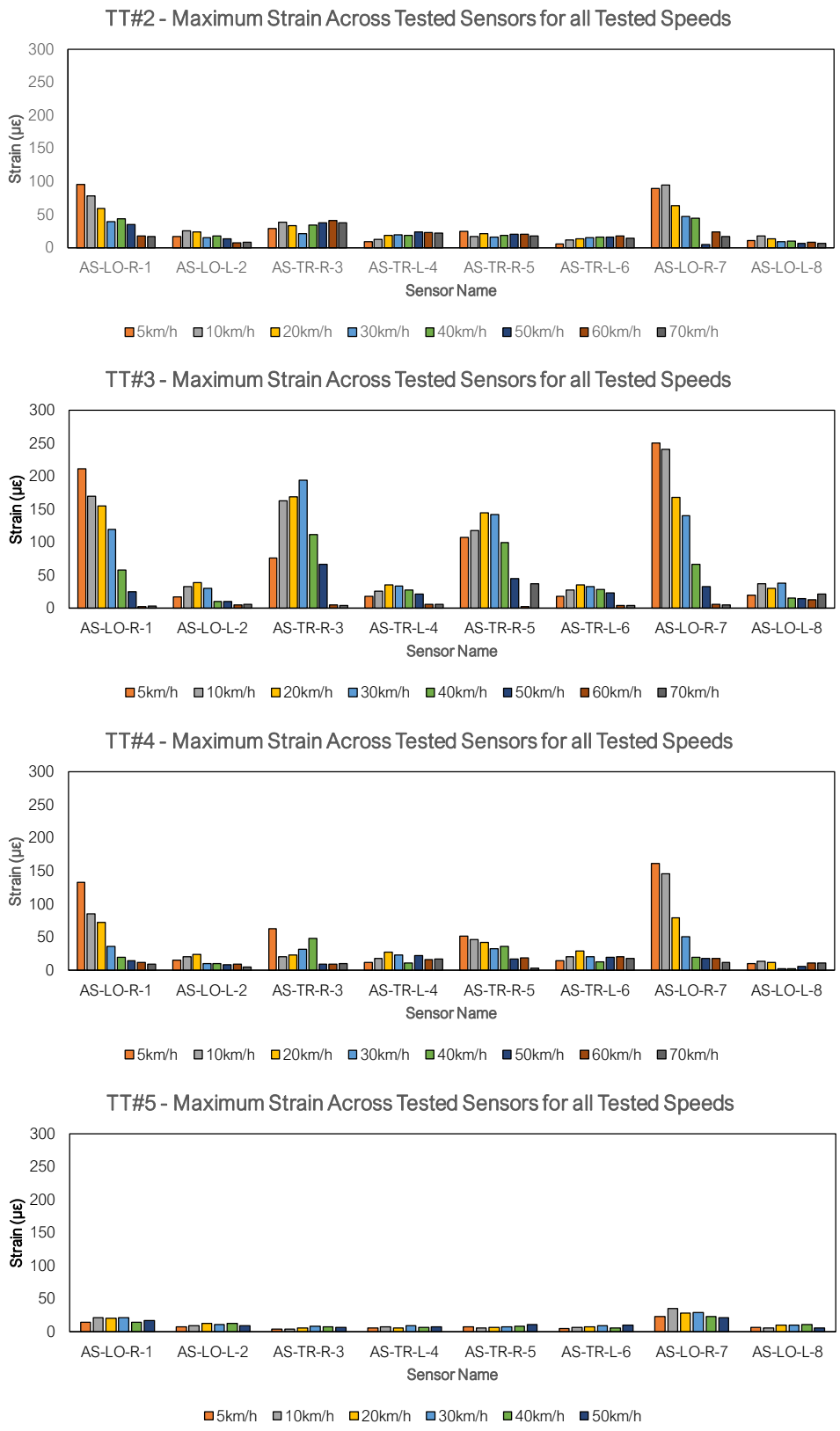


Figure 5.39 Maximum strain results captured for various sensors during Truck Test #2 to #5 across tested sensors for all tested speeds.

In addition, transverse strain gauges in the right sensor array also exhibit elevated strain responses. While the magnitudes are not as pronounced as the longitudinal, right array sensors, this also aligns with the idea that the responses in the right array should be higher on average than a comparable sensor in the left array. These trends are most clearly visible in TT#3 in Figure 5.39, where at some speeds the strain magnitude can reach values of 150 to 250 με in the longitudinal direction, and 150 to 200 με in the transverse direction. This is likely due to TT#3 taking place in the warm summer months, where asphalt temperatures are high which amplifies the strain responses in the longitudinal and transverse directions. In contrast, during other truck tests in different seasons where the ambient and HMA temperatures are lower, the impact from the transverse strain gauges in the right array is less pronounced, but still visible.

Additionally, results from truck tests with a second layer of asphalt are notably lower than those with only one layer, particularly evident in TT#2 and TT#3 compared to TT#4 and TT#5. This observation is intriguing, considering that tests two and five share similar ambient temperatures, as do tests three and four. The addition of an extra asphalt layer likely alters the strain distribution in the sense that the strain is more distributed, contributing to the observed differences.

Consistent with earlier sections, the trends observed when assessing full signal responses for each test persist here. Generally, an increase in speed correlates with a decrease in strain response; however, numerous exceptions challenge this pattern. Notably, in the case of transverse strain gauges, speeds of 20-30 and 40 km/h can yield higher strain results than those at 5-10 or 60-70 km/h, forming a speed hump contrary to the expected trend. This deviation can be attributed to wander, especially in the left sensor array, where the array may not receive the full force of the truck load due to lateral movement impacting the strain results. The most pronounced adherence to the expected trend—higher strain response at lower speeds and lower response at higher speeds—is observed in the longitudinal strain gauges located in the right sensor array, across all seasons.

Returning to Figure 5.25, it is evident that construction conditions (extremely high temperatures) play a pivotal role in the expressed strain response magnitudes. Several cases exhibit significantly higher strain responses than those in TT#2-TT#5. Clearly, the high temperatures impact the collected responses of the sensors which is not seen when the pavement structure cools.

Figure 5.40 show is similar results set up as Figure 5.39, except now it is showing the maximum pressure results captured from TT#2 to TT#5 across all tested sensors for all tested speeds. Unlike the strain results, construction conditions do not exhibit as pronounced an impact on the pressure results. Pressure results show a moderate variation ranging from 4 to 35 kPa, which is within a reasonable range and notably lower than several pressure results observed in subsequent tests.

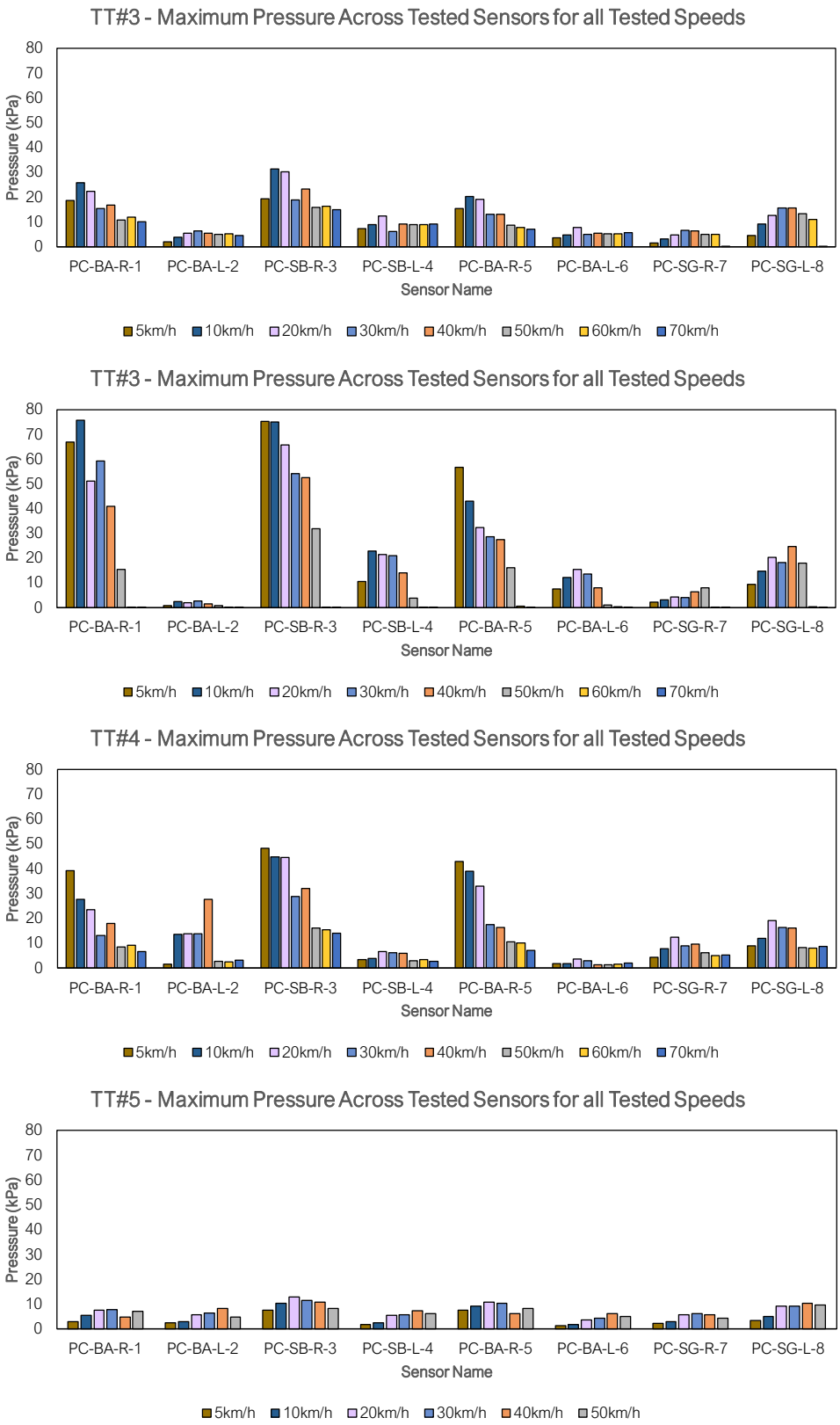


Figure 5.40 Maximum pressure results captured for various sensors during Truck Test #2 to #5 across tested sensors for all tested speeds.

This difference may stem from the positioning of the pressure cells, which are not embedded in the asphalt layer— the material subjected to high temperatures. Consequently, the pressure results do not manifest the same level of dramatic fluctuations.

Much like the strain sensors, certain pressure cells consistently yield maximum pressure results irrespective of season, ambient temperature, and test speeds. Notably, PC-BA-R-1, PC-SB-R-3, PC-BA-R-5, and PC-SG-L-8 emerge as the primary contributors to the largest responses in each test. These pressure sensors are predominantly located in the right wheel array, apart from PC-SG-L-8 situated in the subgrade within the left sensor array.

In line with expectations, the pressure cells generally adhere to the theoretical pattern of decreasing pressure response with increasing speed. This trend is particularly evident for sensors in the right sensor array, regardless of depth. However, deviations from this pattern are not uncommon. In certain instances, a counterintuitive scenario unfolds where pressure appears to increase with higher speeds or a distinctive pressure bump is observed, with speeds in the midrange generating the most substantial pressure response for a specific sensor.

5.7.2.2 Overall Maximum Pressure and Strain Comparison

Figure 5.41 and Figure 5.42 visually represent the maximum longitudinal and transverse strains, as well as the maximum pressures observed in each truck test. Notably, these charts feature the single highest strain and/or pressure value selected, regardless of axle type and speed. The same sensor responses were compared, namely sensor AS-LO-R-7 for the longitudinal right array data and AS-LO-L-8 for the longitudinal left array. Sensors AS-TR-R-3 and AS-TR-L-4 were used for the transverse right and left sensor data respectively. Sensors PC-SB-R-3, PC-BA-R-5 and PC-SG-L-8 were used for the pressure data in all layers.

In Figure 5.41, the maximum pressure across all seasons, truck tests, and layers— including the top of the base, top of subbase, and top of subgrade—is depicted. The pressure trends remain consistent across all layers of the pavement structure, with the subbase layer consistently exhibiting the highest pressure regardless of the specific test conducted. This was discussed in previous sections of this thesis chapter but is very clearly demonstrated here. As was mentioned previously, this deviation from the expected norm prompts questions and considerations. Typically, one would anticipate higher pressure in the base layer compared to the subbase layer, with both surpassing the pressure experienced in the subgrade layer. This anomaly, while deviating from the expected norm, is a noteworthy aspect discerned from the collected sensor data. Potential explanations include construction variability, material placement, compaction

results, construction uniformity, material properties such as stiffness affecting pressure responses, sensor placement, and the possibility of sensor calibration issues.

Examining each test independently, in the fall maximum pressure chart positioned in the top left corner of Figure 5.28, the pressure results obtained by the pressure sensors undergo substantial fluctuations during construction conditions. These variations span from approximately 1 to 2 kPa in the subgrade layer to exceeding 30 kPa in the subbase layer. This notable contrast underscores the distinct pressure levels encountered by each layer, emphasizing that, during construction, the subgrade layer experiences lower pressure compared to the base and subbase layers.

On the flip side, during the second truck test in early spring, the maximum pressure distribution reveals a more evenly spread load across the pavement structure. Although the subgrade layer continues to bear the lowest pressure, averaging around 16 kPa, the difference in load impact between the subgrade layer and the subbase and base layers is noticeably reduced. This implies that as the pavement undergoes cooling and hardening post-construction, the load is more efficiently transmitted to the subgrade layer.

The third truck test conducted during the summer months reveals significantly higher pressure levels across all layers, particularly in the base and subbase layers. While the maximum pressure in the subgrade layer did increase from 16 kPa in early spring to 25 kPa in summer—an increase of approximately 56% or a 9 kPa difference—the subbase layer experienced a more substantial increase from 31 kPa to 75 kPa, marking a 141% increase or a 44 kPa difference. Similarly, the base layer pressure rose from 20 kPa to 57 kPa, indicating an increase of 185% or 37 kPa. This underscores the notable pressure fluctuations experienced by the base and subbase layers.

The fourth truck test, conducted during the summer and incorporating responses with the pavement structure's second lift of asphalt pavement, reveals a more subdued pressure response compared to the previous summer truck test. This observation, previously discussed in other sections of this chapter, is reaffirmed here through a simplified representation of the maximum responses in all layers. Notably, the responses in the base and subbase exhibit substantial reduction, while the pressure in the subgrade experiences a reduction, it is not as pronounced as that observed in the base and subbase layers. This illustrates that the additional pavement layer provides enhanced protection to the base and subbase against tire and vehicle loads, resulting in decreased pressure responses in these layers as well as in the subgrade layer.

Concluding with the late fall truck test, the influence of the second lift of pavement becomes evident once more. This test exhibits a subdued response, with the base, subbase, and subgrade layers all showing very similar maximum pavement responses, differing only by a few kPa. Ambient temperature and pavement

temperature certainly play a role, but the substantial impact is likely attributed to the presence of the second pavement layer, offering additional protection to the base and subbase layers.

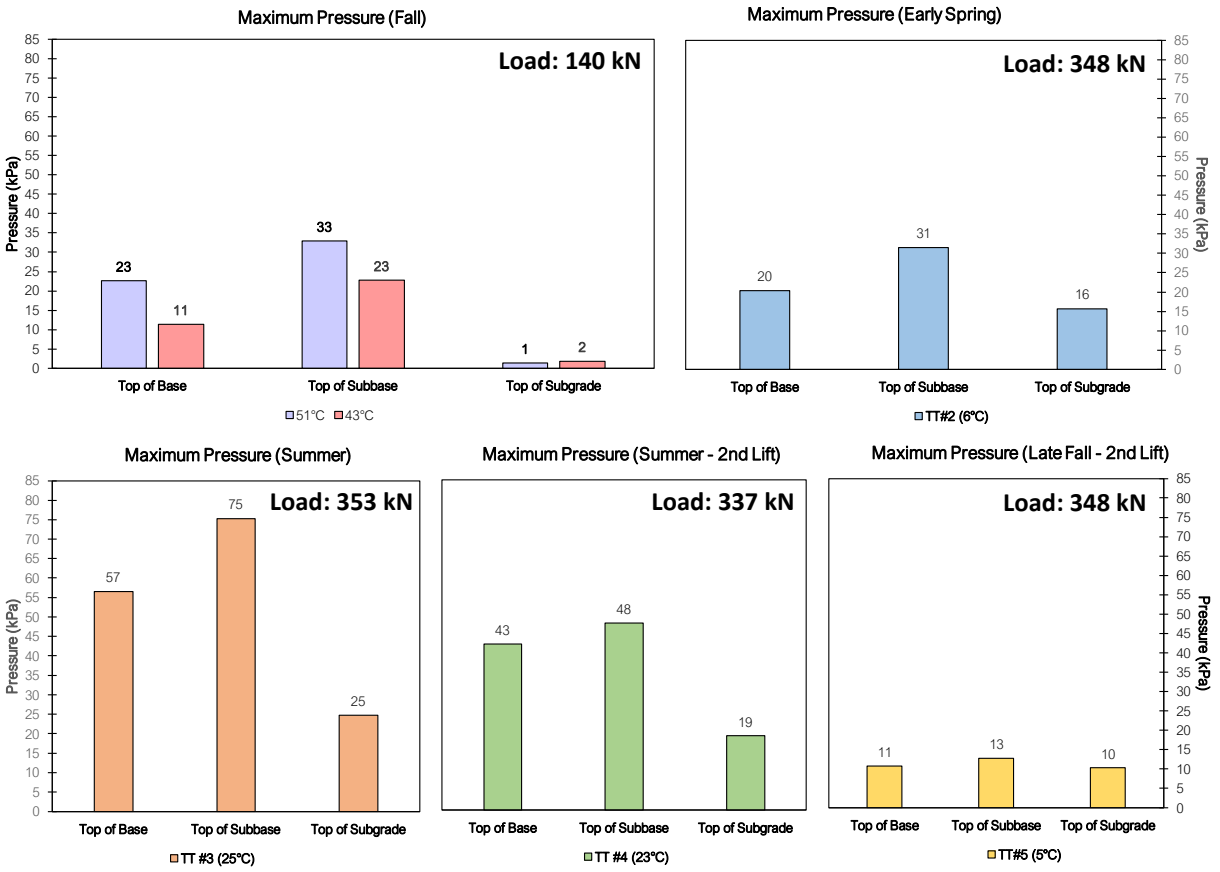


Figure 5.41 Comparison of the maximum pressure responses during all five truck tests, including the load of the truck when passing over the sensors.

In Figure 5.42, the maximum strain across all seasons, truck tests and in both the transverse and longitudinal directions is depicted. Again, there appears to be a consistent trend amongst the strain results throughout most of the tests. This is that the right sensor array has significantly greater results than the left sensor array. In the longitudinal direction, this trend applies to all tests and all temperatures, even during construction. In the transverse direction there are two instances when this trend is broken, one is when the construction testing occurs at 51°C and the second is during the last late fall truck testing where the ambient temperature is about 6°C. This is likely due to wander and slight deviations in the truck position during testing.

Looking at the results for the first truck test more closely, one major trend is that the strain response at 72°C is lower than that at 51°C and 43°C. One would expect that if the measurement at 51°C yields 714 με, then at 72°C, it should read higher, perhaps aRound 1000 or 1100 με. This suggests the possibility

that the path of the truck's wheels passing over the sensors deviated slightly from directly aligning with the sensors due to wander. It is essential to investigate the relationship between the tire's position and the sensor's response further.

The most notable observation is that the pavement structure experiences substantial strain impacts during construction. For instance, the maximum longitudinal strain, particularly in the right sensor array, exceeds 160,000 με. In contrast, the measurements obtained in the second truck test indicate an average maximum strain of approximately 96 με. This indicates a significant difference between the response conditions during construction and post-construction. Furthermore, it highlights the inconsistency in the data obtained during construction, particularly in comparing the right and left sensor arrays. This indicates variability in the state of the HMA during construction, resulting in high magnitudes of strain. These higher strains imply that elevated strains may be induced immediately after construction, which is detrimental to the fatigue performance of the pavement [46].

The subsequent truck tests demonstrate similar trends in magnitude to the pressure results. The second truck test during early spring stands out for its notably smaller strain results compared to the first construction testing, marked by erratic temperature variations. In the early spring test, strain exhibits a higher level of consistency. Noteworthy in these results is the larger strain response in the right sensor array in the longitudinal direction, while for the left sensor array, the transverse direction yields larger results.

Moving to the third truck test during summer, the strain responses in the right sensor array are significantly larger than those observed in early spring conditions. A consistent trend persists, with larger longitudinal strain results in the right sensor array, and with the response in the left sensor array being larger in the transverse direction compared to the longitudinal direction.

Examining the strain results for the fourth and fifth truck tests, conducted with the second lift of asphalt pavement installed, reveals subdued strain responses, mirroring the previously explored pressure results. The addition of this second pavement layer diminishes the impact of strain on the surface of the base layer or the bottom of the asphalt layer where the sensors are positioned. This aligns with expectations for typical pavement responses [46].

Strain values exceeding about 100 με are considerably higher than the endurance limit demonstrated in certain studies [67] for conventional HMA. This observation raises concerns regarding the road's ability to withstand consistent heavy truck loads. The conventional asphalt used for this arterial roadway may face challenges, particularly in terms of bottom-up cracking and fatigue cracking induced by excessive longitudinal strains impacting the pavement structure. This vulnerability is particularly pronounced during

the summer months when the road experiences heightened strains from heavy vehicle traffic, posing a potential risk to the overall integrity and longevity of the pavement structure.

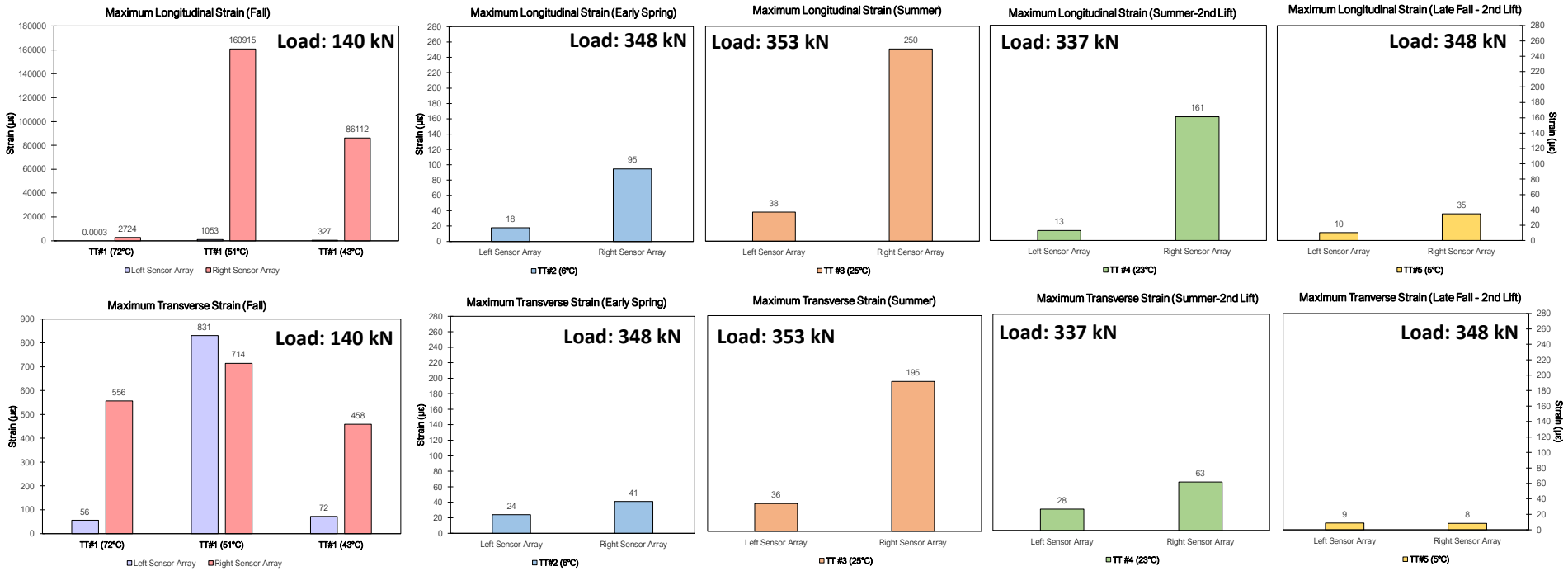


Figure 5.42 Comparison of the maximum strain response in both the longitudinal and transverse directions during all five truck tests, including the loads of the truck when passing over the sensors

5.7.2.3 Maximum Pressure Comparison with Depth

In Figure 5.43, the pressure depth profile compares the pressure response in kPa for the same sensors across all five truck tests. This profile illustrates the pressure variation across different layers of the pavement structure relative to the pavement depth in millimeters.

The most prominent observation from the figure is the atypical shapes of the pressure profiles. Conventionally, pressure profiles should exhibit higher pressure in the upper layers, gradually decreasing in the deeper layers of the pavement structure. This has been shown in the literature, such as in [20] and [61]. Ideally, the base layer should register the highest pressure response, followed by the subbase layer, and finally the subgrade layer. However, this anticipated pattern is not reflected in the data. This inconsistency has been noted in both the raw sensor data responses and the maximum pressure analysis conducted in earlier sections of this chapter.

These anomalies are distinct and pervasive, occurring consistently across all truck tests that encompass diverse temperatures and pavement states, ranging from construction to non-construction, and involving variations like single-layer asphalt to a complete layer with two layers. This consistent occurrence strongly suggests potential miscalibrations in the sensors, particularly in capturing greater subbase responses. Unfortunately, rectifying this issue is challenging, as the pressure cells are calibrated by the manufacturer prior to delivery.

Despite these challenges, some general trends emerge. Truck tests conducted at higher temperatures, such as Truck Test #3 and Truck Test #4, exhibit overall greater pressure responses, positioning their pressure profiles to the right on the chart. Conversely, as temperatures decrease, pressure profile values also decrease, as observed in Truck Test #2 and Truck Test #5. Notably, anomalies are identified during construction temperatures; despite the elevated temperatures, responses in Truck Test #1 are relatively low, indicating potential anomalies in data collection during construction conditions.

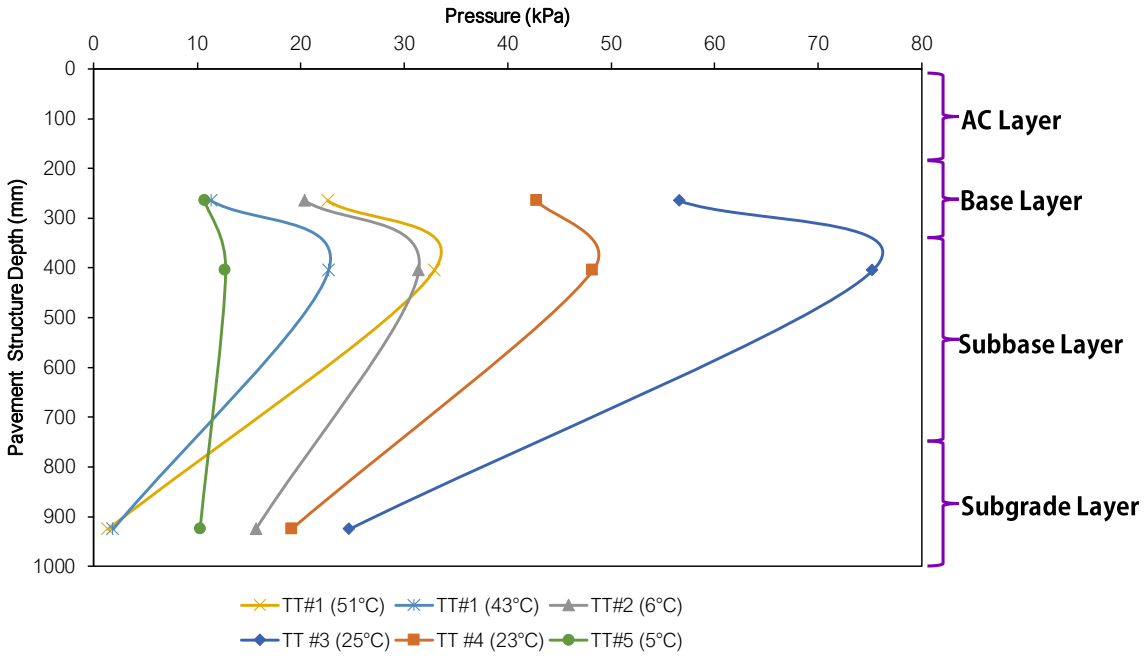


Figure 5.43 Pressure depth profile showing changes in pressure during the construction phase (43°C) and 5 months after (6°C).

Chapter 6
Quality Control for Data Analysis

This Chapter examines the correlation between truck trajectory and pavement response to establish a link between the truck tire's lateral movement and the sensor's reaction. These tests use a truck of known weight and axle configuration to traverse the sensor-installed test section at various distances from the sensor arrays.

6.1 Description of Wander Test Procedure

As mentioned in a study by Timm and Priest in [68], as trucks and other vehicles drive along a road section, they don't always drive along the same trajectory in the same straight line; there is some lateral deviation and variability as to where the tires are located along the roadway. There are a variety of factors that contribute to the occurrence of lateral tire wander as vehicles are driving, which include: driver behaviour, lane width, vehicle speed and width, weather conditions and the size of axles [68]. Predicting vehicle wander poses a degree of complexity, attributed to the fact that the likelihood of a given wander distance deviating from a reference point aligns with a normal distribution. In addition, even when the position of the tire is known, the magnitude of the strain response in relation to the tire position follows a curve shape as shown in Figure 6.1. Regardless of the complexity, vehicle wander helps to decrease the deterioration and loads experienced in any one point of a pavement wheel path, minimizing the damage imparted in any one area [68].

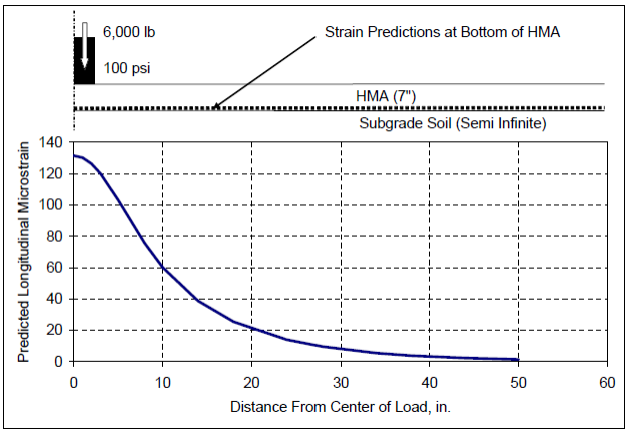


Figure 6.1 Theoretical change in longitudinal strain magnitude because of lateral wander [68].

In the literature, there are a few studies that are focused on vehicle wander on pavement response. They typically focus on the impacts of WIM sensors, such as in [69] and [70], which are not captured in this study. Several studies have looked at this topic in varying levels of detail using sensors used in this study, such as [40], [64], [68], [71], [72] and [73]. A notable gap in existing studies lies in their predominant

focus on determining wander impacts exclusively concerning horizontal strain responses at the base of the HMA layers. One study [64], using an MDD, looks at structural response impacts in granular layers, and only one of the studies assessed wander using pressure cells [61].

Assessing vehicle wander in a controlled setting is crucial for understanding and evaluating the quality of data presented earlier in this thesis, particularly in Chapter 5 when discussing truck testing results. Given the lack of specific control over wander in those truck tests, observed deviations from anticipated patterns in strain and pressure could potentially be attributed to wander. Consequently, it is crucial to grasp how wander influences the form and intensity of strain and pressure responses, to improve the accuracy of predictions during truck testing. Originally, the study envisioned installing a camera to monitor traffic traversing the instrumented test section, to offer a visual assessment of wandering concerning diverse truck trajectories. However, this wasn't feasible, making this study even more vital as researchers lack visual information about the passage of vehicle axles and tires in relation to the sensor arrays.

The wander test coincided with the final truck test held on December 11th, 2023. The same truck employed in the final truck test, as detailed in Chapter 5, was used for the wander test - refer to Section 5.6 for more information regarding this test.

During the wander test, the truck traversed three different trajectories at 10 km/h, illustrated in Figure 6.2 in relation to the sensor arrays. Each trajectory is referred to as a “Round” and each Round was passed over twice by the truck. In the first set of passes (i.e., Round 1, or R1.1 and R1.2 for the first and second pass attempts, respectively), involved the truck passing between the right sensor array and the lane edge. Given the 0.7 m distance from the edge of the lane to the first sensor array, the trajectory for Round 1 was positioned 0.35 m to the right of the right sensor array, considering the direction of truck traffic. The next round of testing (Round 2, or R2.1 and R2.2) involved the truck running at the interface of the pavement and the curb. Given the 0.7 m distance from the edge of the lane to the first sensor array, the trajectory for Round 2 was positioned 0.7 m to the right of the right sensor array. In the final test (Round 3, or R3.1 and R3.2), the truck precisely crossed over the right sensor array, with 0 m deviation.

The initial plan for the wander test included one final trajectory whereby the truck would pass between the two sensor arrays. However, the presence of fast-moving and live traffic adjacent to the truck testing site prompted a modification in the research team's approach. Safety concerns with regards to the adjacent lane led to a decision to avoid running the truck close to the high-speed traffic, necessitating the removal of that trajectory from the research plan. Additionally, the placement of cones to separate traffic further limited the available width for testing.

Using three vertical arrows, Figure 6.2 illustrates the relationship between the placement of the right and left tires of the truck across different rounds of testing. As highlighted in Chapter 5, the total width of the truck is 2.4 meters. The vertical lines depicted for each round indicate the relative positions of the truck width in relation to the left sensor array during the passage over various trajectories. For instance, in Round 1 (light blue trajectory), the right tires and axles of the truck pass between the right sensor array and the pavement edge, while the left tires of the axles pass 1.35 meters away from the left sensor array. Similar variations in the proximity of the left tires to the left sensor array occur in Rounds 2 and 3, influencing the forthcoming results sections.

In each test, the steering axle aimed to pass over this sensor array, while the subsequent axles followed suit. In essence, the steering axle tire was used as the guiding tire over each of the trajectories. In each round, the truck ran over the sensor array in the same direction as was done in tests performed in Chapter 5 and is indicated in Figure 6.2. Refer to Figure 3.10 for the diagram with full sensor names.

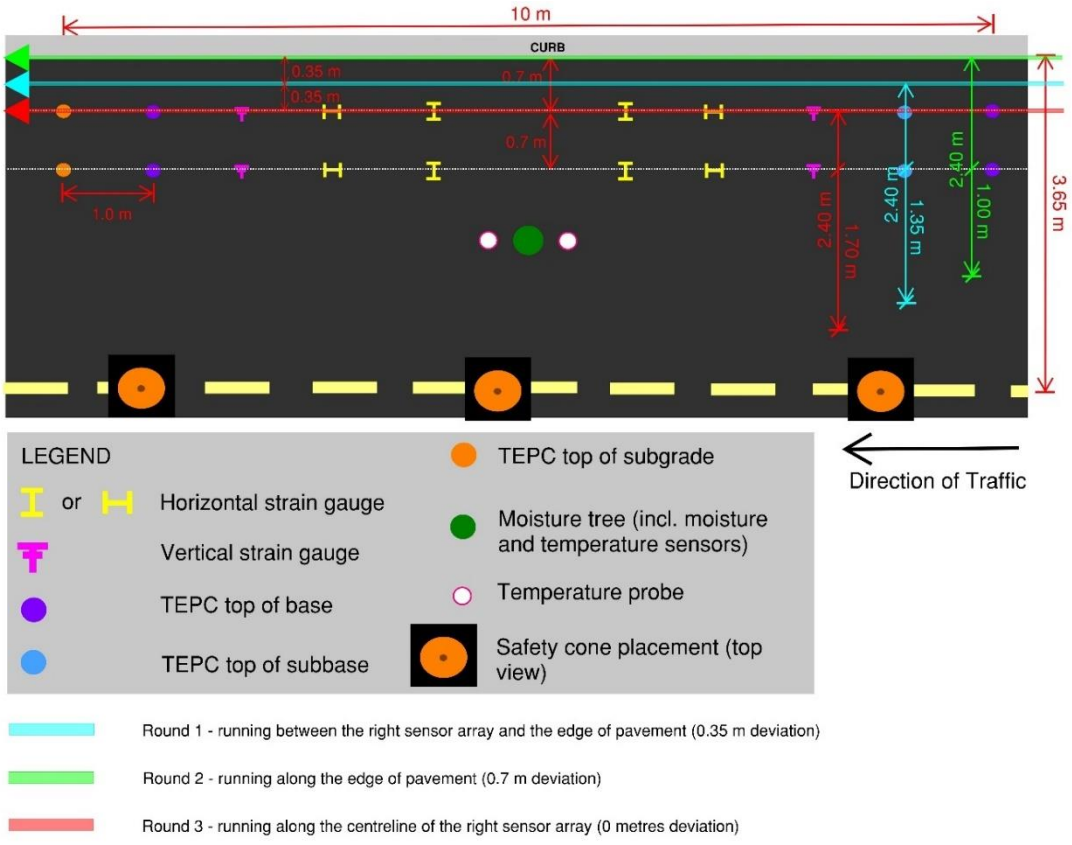


Figure 6.2 Plan showcasing the trajectories that the truck passed over during each round of the wander test.

6.2 Wander Test Results

The following section will present the results of the wander tests. During each round of testing, the results of each run were captured both using the sensors, as well as through video recording to assess their proximity to the required trajectory. Snapshots from the video passes over the right sensor array will be provided to validate the graphical findings.

6.2.1 Visual Assessment of Video Pass Results

Each round of testing was conducted twice at 10 km/h, as mentioned earlier. It was important to determine which of the two attempts provided the best results in terms of signal clarity and magnitude. This determination, performed by assessing the video captures of the test runs, was vital for subsequent assessments, as only one pass from each round would be considered for comparison, simplifying the analysis.

6.2.1.1 Round #1 – Running between Right Sensor Array and the Edge of Pavement (0.35m deviation)

In the first round of the wander test, the truck's right wheels deviated 0.35 m to the right of the right sensor array as they passed between the right array and the edge of the pavement.

Starting with Round 1's two attempts, both attempts are presented in Figure 6.3 and Figure 6.4, capturing six key moments in the videos for each attempt. These snapshots highlight instances when the steering axle, lift axle, and tandem axles are clearly visible, indicating their proximity to the demarcated line.

Figure 6.3 suggests that the truck accurately passed over the guideline in the first attempt, with the remaining tires closely following the steering axle. This suggests that the data from this attempt can be considered for the response assessment.

Similarly, Attempt 2 in Figure 6.4 also depicts an accurate pass over the guideline. Based on the video results, as well as the six snapshots presented in both figures, in both cases the truck passed over the demarcated trajectory relatively well. There is not one trajectory that is clearly more accurate than the other from the visual inspection. In this case then the attempts for Round 1 will be assessed based on the graphical responses that are produced to determine which of the results appear to be clearer to carry those on for further analysis.



a)



b)



c)



d)



e)



f)

Figure 6.3 Truck trajectory step-by-step for Round #1, Attempt 1.



a) b) c) d) e) f)

Figure 6.4 Truck trajectory step-by-step for Round #1, Attempt 2.

6.2.1.2 Round #2 – Running along the Edge of Pavement (0.7 m deviation)

During Round 2 of the wander test, the trucks right wheels passed along the edge of pavement interface. Therefore, this is a 0.70 m deviation to the right of the right sensor array. Attempt 1 is displayed in Figure 6.5 and Attempt 2 is displayed in Figure 6.6.

Figure 6.4 shows that during the video assessment, the tires came really close to the curb edge and grazed the curb. It is improbable for this road, known for high-speed traffic, that vehicles would normally operate under such conditions, where their tires graze the curb face. Even in situations where drivers may need to stop for emergency vehicles or move to the side of the road, it is expected that they would steer their vehicles away from the curb to safeguard their tires. In essence, this trajectory is not typical for this roadway.



a) b)

c) d)

e) f)

Figure 6.5 Truck trajectory step-by-step for Round #2, first attempt. The wheel passed more on the curb than over the pavement-curb interface.

However, Figure 6.6 presents a more plausible representation of how drivers would navigate this trajectory. The truck passes along the pavement curb interface more directly, without grazing the curb face on its path. Consequently, in this scenario, the test results from the second attempt will be considered for more in-depth assessment.



a) b)

c) d)

e) f)

Figure 6.6 Truck trajectory step-by-step for Round #2, second attempt. The wheel passed more on the pavement-curb interface.

6.2.1.3 Round #3 - Running along the Right Sensor Array (0m deviation)

During Round 3 of the wander test, the trucks right wheels passed directly over the right sensor array. Therefore, this is an attempted 0.0 m deviation to the right of the right sensor array. Attempt 1 is displayed in Figure 6.7 and Attempt 2 is displayed in Figure 6.8.

Upon reviewing the results in both figures, it is evident that all axles and tires passed directly over the sensor array in a similar manner for both attempts. The visual assessment from the figures does not distinctly indicate one attempt providing superior results over the other. Consequently, similar to the approach taken for Round 1, the results will be thoroughly assessed in conjunction with the sensor signal responses to determine which attempt will be selected for further analysis.



a) b)

c) d)

e) f)

Figure 6.7 Truck trajectory step-by-step for Round #3, first attempt. The wheel passes directly over the right sensor array.

6.2.2 Strain Sensor Assessment

The upcoming section will present the results obtained from the strain gauges during the wander test. These results will serve as the basis for determining the preferred attempt for each round during the final assessment of Rounds 1 and 3. Despite this focus, the results for all rounds and both attempts will be systematically displayed and discussed to maintain consistency throughout the analysis.

6.2.2.1 Longitudinal Strain, Right Sensor Array

There are two dedicated sensors for measuring the longitudinal strain in the right array, namely sensors AS-LO-R-1 and AS-LO-R-7. The strain responses are graphically represented in Figure 6.9 and Figure 6.10, respectively. Attempt 1 for both sensors for all Rounds is shown in the first row of charts. For

example, R1.1 means Round 1, Attempt 1, and R3.1, means Round 3, Attempt 1. On the other hand, Attempt 2 for both sensors are shown in the second row of charts.



Figure 6.8 Truck trajectory step-by-step for Round #3, second attempt. The wheel also passes directly over the right sensor array.

There are some patterns that appear with a general assessment of both the magnitudes and shapes of the strain responses in Figure 6.9 and Figure 6.10. Firstly, based on the trajectory of the truck and where it is positioned relative to the right sensor array, the magnitude of the sensor response will differ. For example, Round 3, which was done directly over the right sensor array has the largest magnitudes, which makes sense as the sensors are receiving the full pressure load of the tires. The next largest magnitudes occur in Round 1, when the tire trajectory had a 0.35 m deviation from the right sensor array. Looking at the response of the steering axle in both Rounds 1 and 3 for sensor AS-LO-R-1, there is a 61.8% decrease in strain magnitude in Attempt 1 (dropping from 37.7 με in Round 3 to 14.4 με in Round 1) and a 69.0%

decrease in strain magnitude in Attempt 2 (dropping from 41.1 με in Round 3 to 12.7 με in Round 1). The decrease becomes even more apparent when comparing Round 3 with Round 2, which had the truck run at a deviation of 0.7 m from the right sensor array. For example, for Attempt 1 for sensor AS-LO-R-1, there is a 94.5% decrease in strain magnitude (dropping from 37.7 με to 2.06 με).

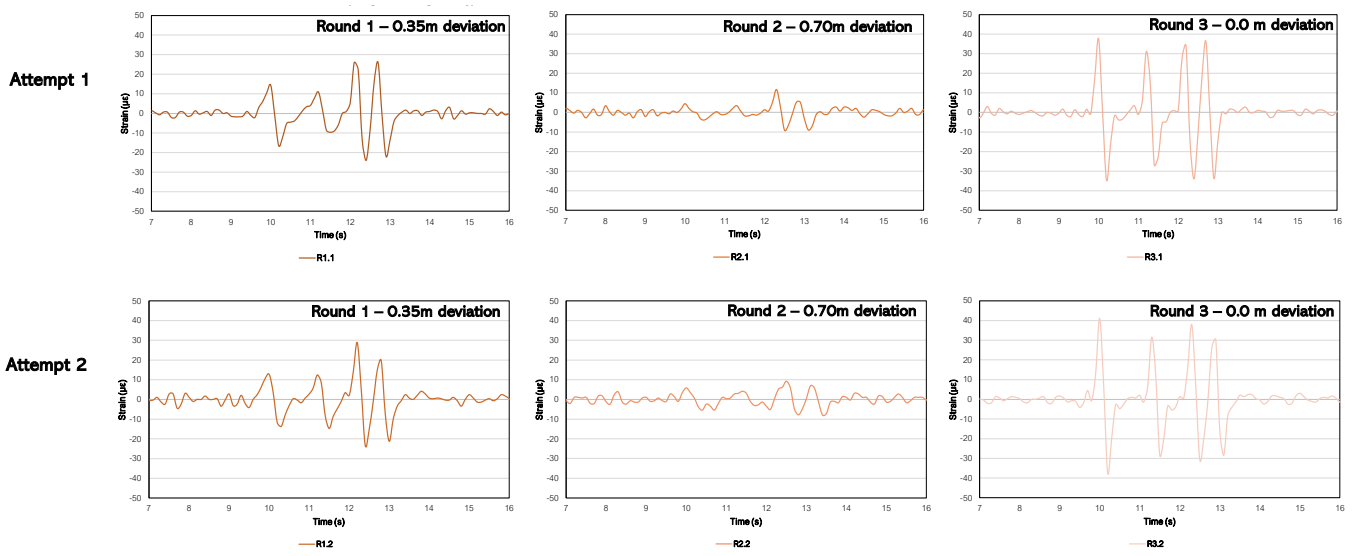


Figure 6.9 Strain results for both truck testing attempts for sensor AS-LO-R-1 (longitudinal, right array). Note: labels are provided and are the same for similar figures.

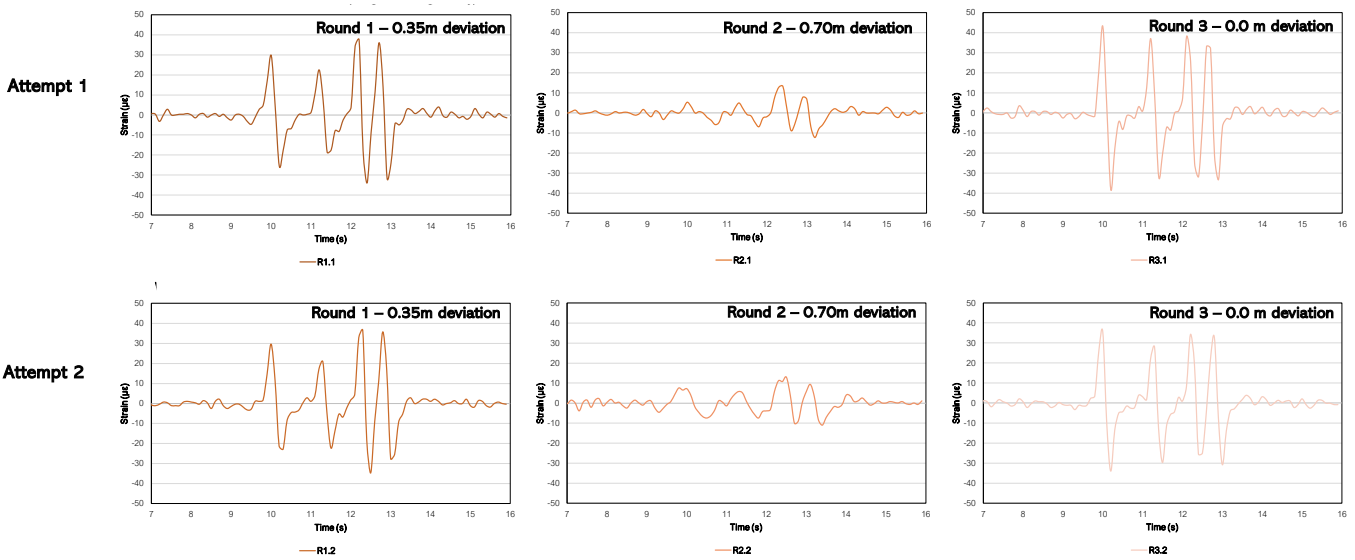


Figure 6.10 Strain results for both truck testing attempts for sensor AS-LO-R-7 (longitudinal, right array).

These results are significant, since they show that even a slight deviation of about 35 cm from the sensor array can cause a significant decrease in the strain magnitude response that will be captured by the sensors. This is important when looking at truck test results since it shows that care must be taken to ensure that the tires are running over the sensor array directly to be able to capture the full extent of the

sensor response and to be able to accurately compare responses at different speeds. This trend of the sensor magnitude decreasing with greater lateral deviation from the centerline of the sensor array is also corroborated by several studies, such as [40] and [68].

The variations in the truck's trajectory in the longitudinal right sensor array sensors also influence the shape of the sensor response. In Round 3, when the truck is directly over the right sensor array, the strain response magnitude exhibits the steering axle with the largest response, followed by smaller responses from the steering and tandem axles. This contrasts with the responses observed during Rounds 1 and 2, where the strain response shape indicates that both the steering and lift axles have smaller magnitudes than the tandem axle.

The similarity in magnitudes between both sensors of AS-LO-R-1 and AS-LO-R-7 suggests that both sensors are likely to yield comparable results across all wander cases.

6.2.2.2 Transverse Strain, Right Sensor Array

As with the previous section, there are two sensors that are dedicated to measuring the transverse strain in the right sensor array, and those are AS-TR-R-3 and AS-TR-R-5, for which the graphical results are shown in Figure 6.11 and Figure 6.12, respectively.

Examining the magnitudes of the strain responses in the transverse direction in the right sensor array reveals several notable trends, mirroring observations made for the longitudinal right sensor array sensors. Notably, the responses presented in Round 3 for both sensors exhibit the highest magnitude and clarity in terms of their shape. In Round 3, all axles are distinctly defined, with the steering axle displaying a much larger response compared to the lift and tandem axles. This consistent pattern is observed across both sensors and attempts, indicating that this signal response is indicative of the truck directly traversing the sensor array.

Regarding magnitudes, the disparity between Round 3 and the other two rounds (rounds one and two) is substantial. Even in Round 1, the axles are not as clearly delineated as seen in the longitudinal strain results for the right sensor array. This implies that even a relatively small deviation, such as 35 centimeters, results in a significant reduction in the magnitude of the strain response in the transverse direction. Quantifying this difference, the decrease for the steering axle between Round 3 and Round 1 for sensor AS-TR-R-3, Attempt 1 is 81.7% (falling from 22.1 με to 4.05 με).

When comparing the magnitudes between the two sensors, it is evident that the magnitude for sensor AS-TR-R-3 tends to be higher than that for AS-TR-R-5. This trend is particularly pronounced in the results of Round 3 for both attempts and sensors. This discrepancy could suggest that AS-TR-R-3 is more responsive than the other due to differences in the variations in the road surface above both sensors.

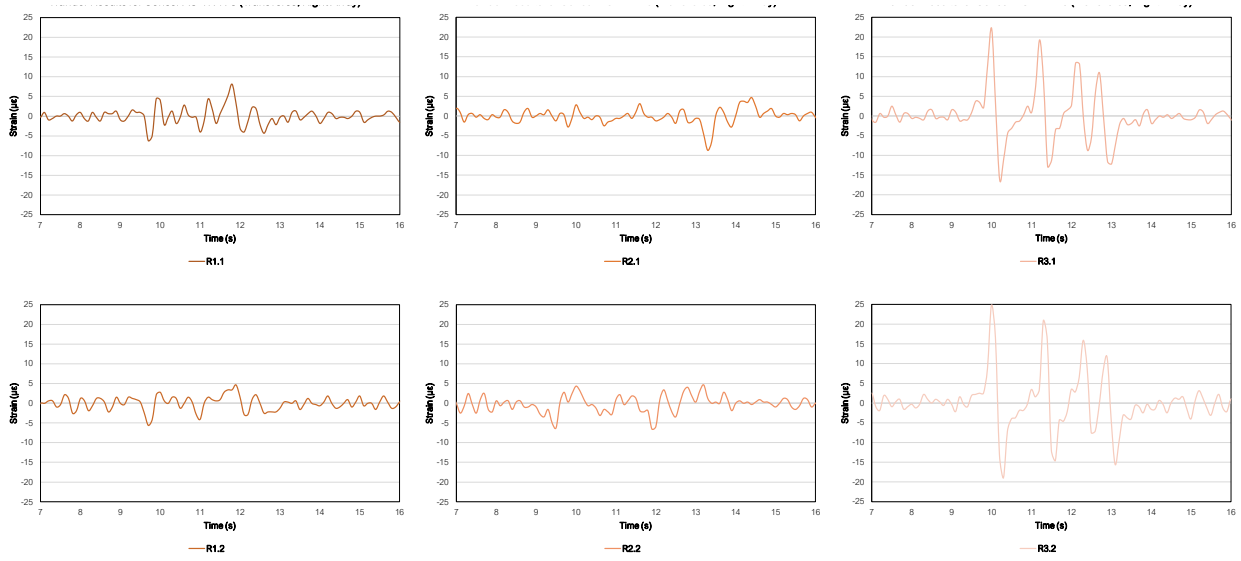


Figure 6.11 Strain results for both truck testing attempts for sensor AS-TR-R-3 (transverse, right array).

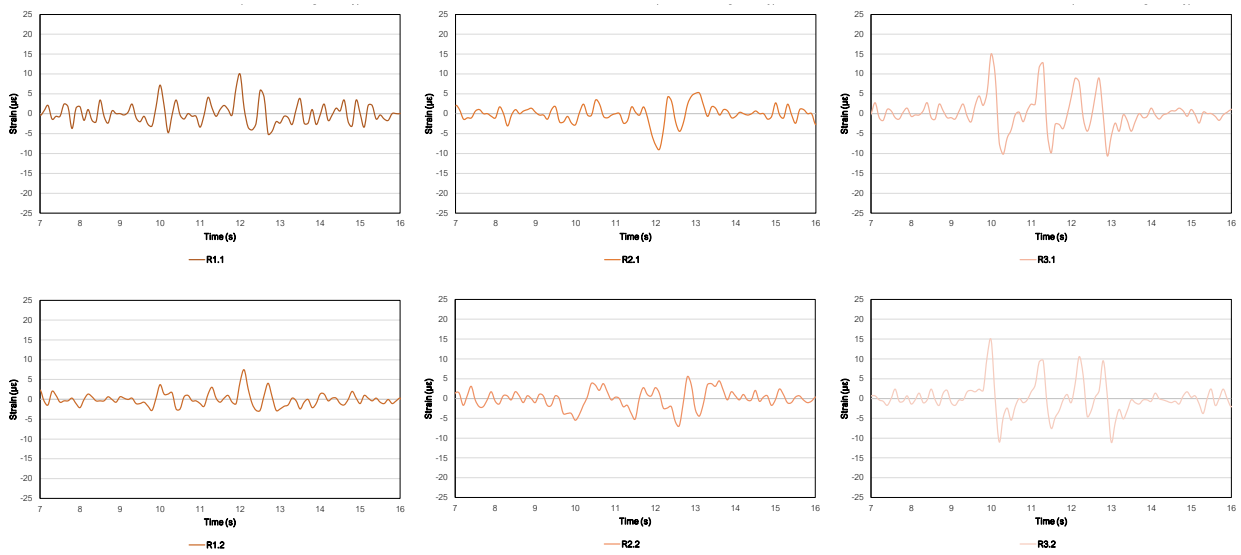


Figure 6.12 Strain results for both truck testing attempts for sensor AS-TR-R-5 (transverse, right array).

6.2.2.3 Longitudinal Strain, Left Sensor Array

There are two sensors that are dedicated to measuring the longitudinal strain in the left sensor array and those are AS-LO-L-2 and AS-LO-L-8, for which the graphical results are shown in Figure 6.13 and Figure 6.14, respectively.

Upon scrutinizing the magnitudes in both sensors and both attempts, it is evident that, in this case, the responses from Round 2 of the wander test are the most substantial compared to Rounds 1 and 3. This aligns logically, given that in Round 2 the left tires of the truck are in closest proximity to the left sensor array.

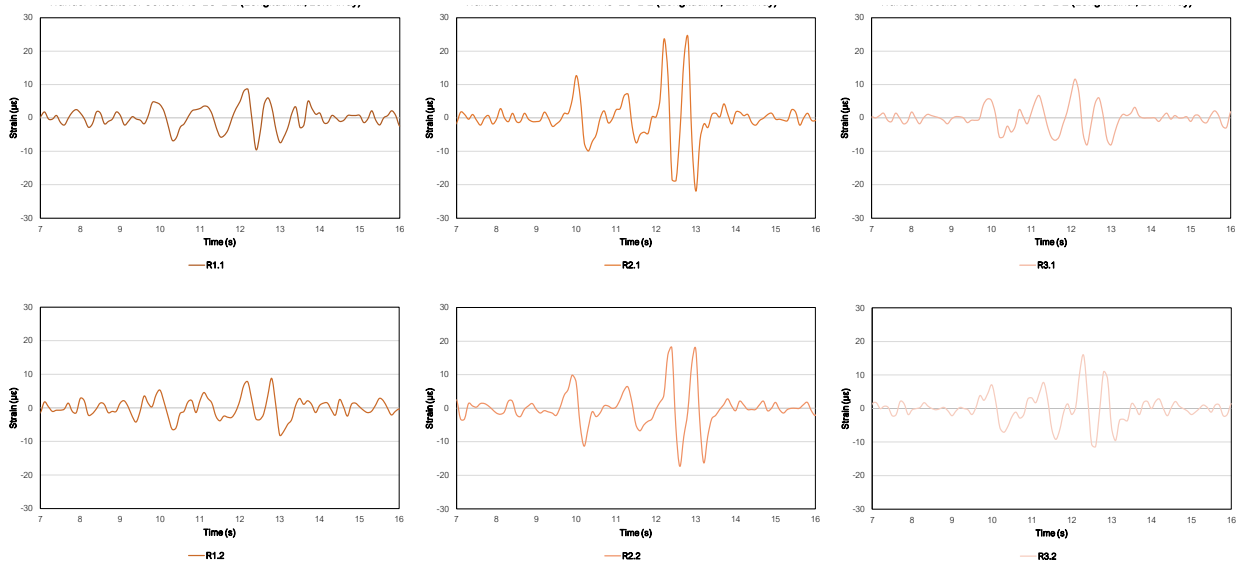


Figure 6.13 Strain results for both truck testing attempts for sensor AS-LO-L-2 (longitudinal, left array).

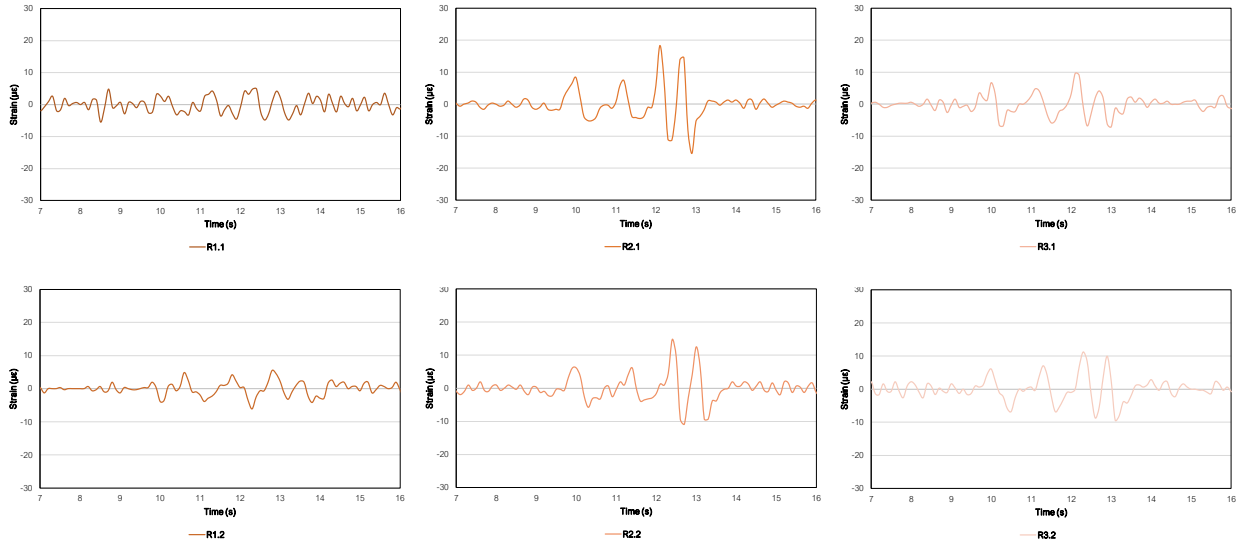


Figure 6.14 Strain results for both truck testing attempts for sensor AS-LO-L-8 (longitudinal, left array).

Notably, the magnitudes of the responses for Rounds 1 and 3 are quite similar, exhibiting no significant difference between them. For instance, comparing the steering axle from Round 1 and Round 3 in Attempt 1 for sensor AS-LO-L-2, the magnitudes are 4.6 με and 5.6 με, respectively. The decrease in strain between Round 2 and Round 1 in Attempt 1 for this same sensor is 63.8%, with the magnitude dropping from 12.7 με to 4.6 με. Again, this is a significant decrease in strain response being captured by the sensors.

In terms of the shape of the strain responses in the longitudinal direction, it appears that the standardized shape across all rounds and attempts is that the tandem axle produces a larger magnitude than the steering and lift axles. This pattern is reminiscent of the longitudinal sensors in the right sensor

array that were 0.35 m deviated from the right sensor array. This alignment in response patterns is logical since, in all cases, the axles in the left tires, when compared to the left sensor array, deviate from the left sensor. There isn't a scenario where the tires precisely align with the left sensor array.

6.2.2.4 Transverse Strain, Left Sensor Array

Finally, there are two sensors that are dedicated to measuring the transverse strain in the left sensor array and those are AS-TR-L-4 and AS-TR-L-6, for which the graphical results are shown in Figure 6.15 and Figure 6.16, respectively.

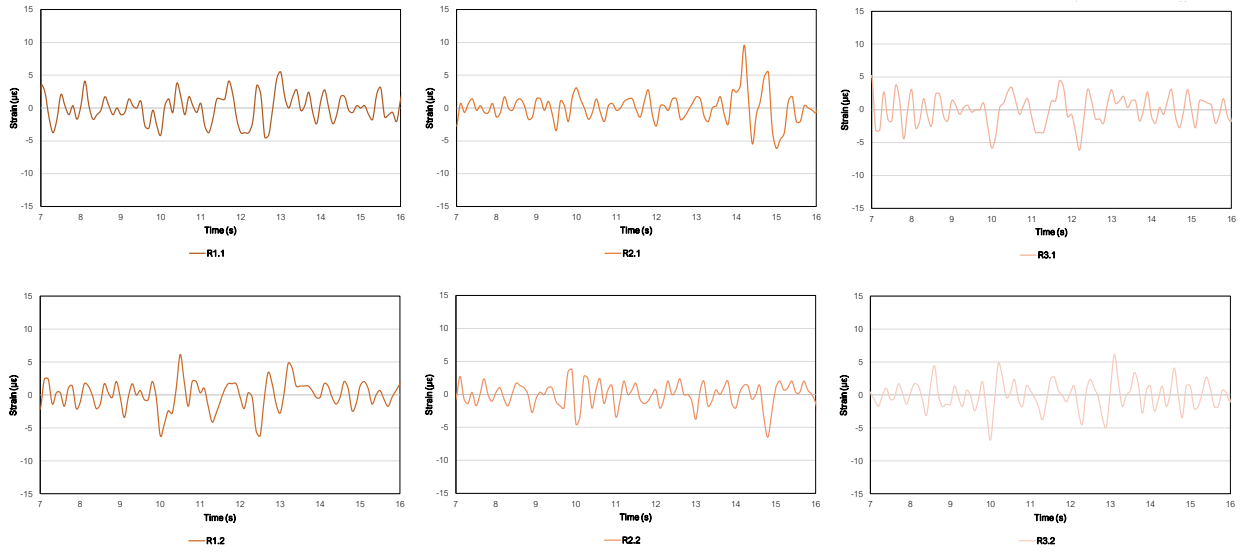


Figure 6.15 Strain results for both truck testing attempts for sensor AS-TR-L-4 (transverse, left array).

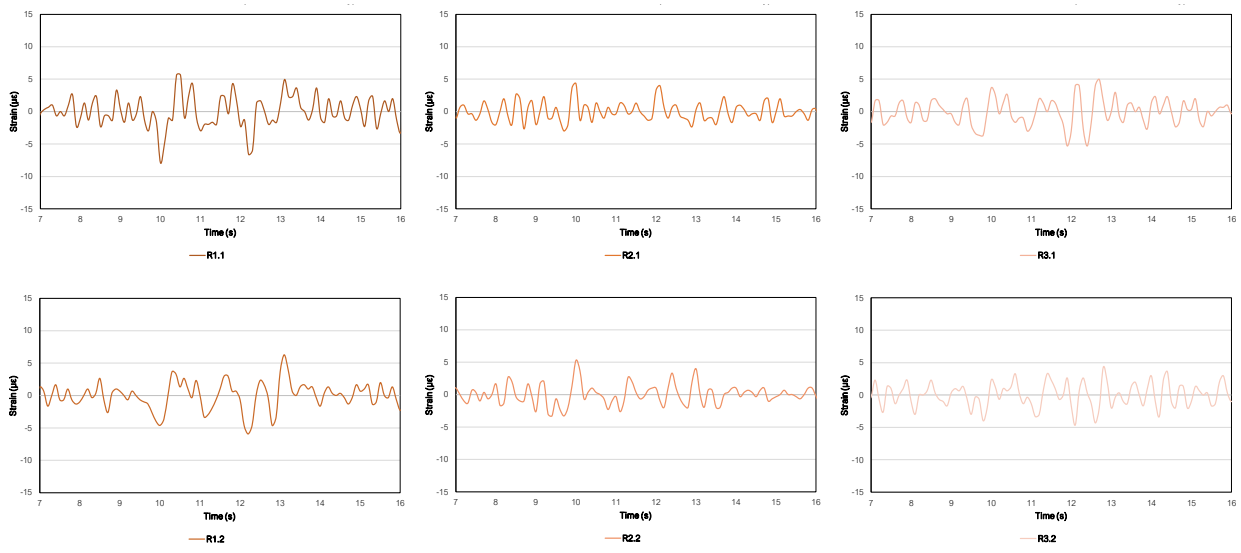


Figure 6.16 Strain results for both truck testing attempts for sensor AS-TR-L-6 (transverse, left array).

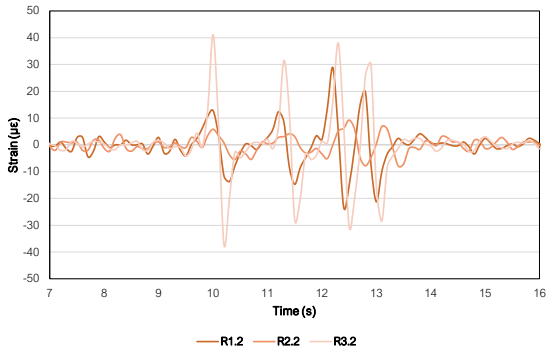
Assessing the magnitudes and shapes of the strain responses for both sensors in the transverse direction in the left sensor array, it is clear that the shapes of the strain responses are not very well-defined, for any sensor, round or attempt.

This finding is corroborated with discussions in Chapter 5, which also indicated that the magnitudes of the responses from the sensors that are situated in the left sensor array in the transverse direction are the lowest of the four possibilities of strain gauge arrangement.

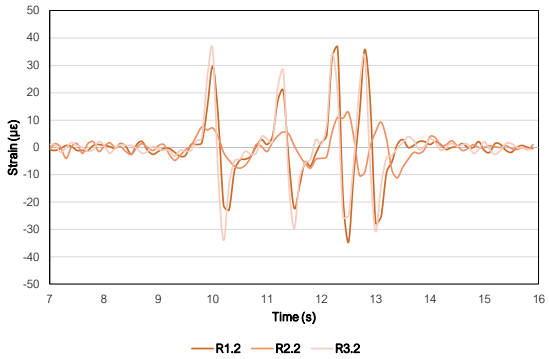
6.2.2.5 Attempt Selection for Round 1 and Round 3

It is already established from Subsection 6.2.1.2 that the second attempt will be selected for further analysis of Round 2 data. Regarding Round 3, although the video for both attempts for this truck test appeared to demonstrate that both attempts passed directly over the right sensor array, the results for Attempt 2 typically appear to show clearer signal for both longitudinal and transverse responses, therefore it will be selected for further analysis. In a similar manner, the second attempt will be selected for Round 1 data. While both the first and second attempts for this round are very similar, the second attempt has objectively crisper signal responses.

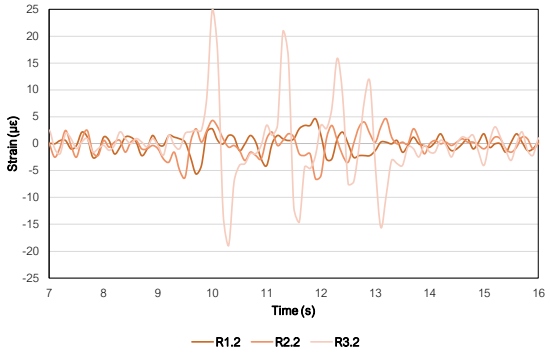
Figure 6.17 presents a comprehensive view of the selected responses for further analysis. The graph displays all Rounds for Attempt 2 for each sensor, facilitating a straightforward comparison of magnitudes and shapes. The signal responses align exactly with those discussed earlier, reinforcing the previously identified trends.



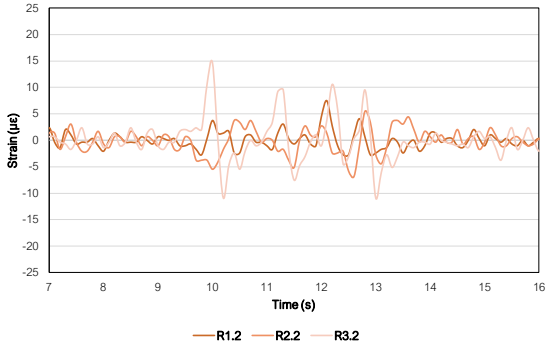
a) AS-LO-R-1 (Longitudinal, Right Array)



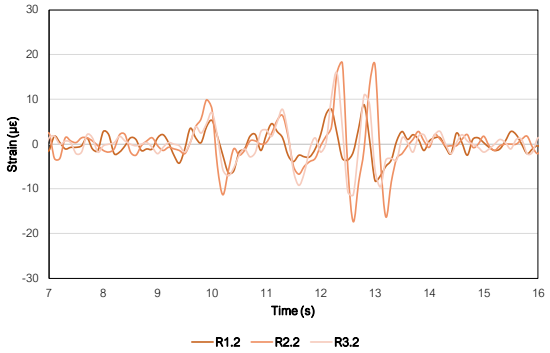
b) AS-LO-R-7 (Longitudinal, Right Array)



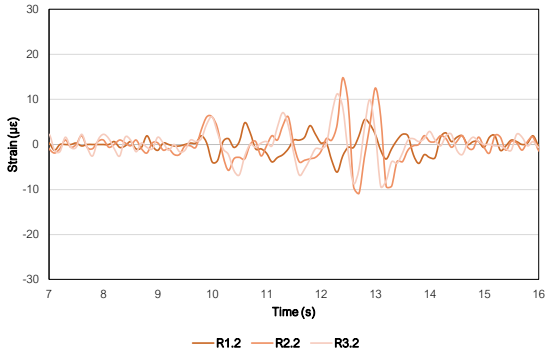
c) AS-TR-R-3 (Transverse, Left Array)



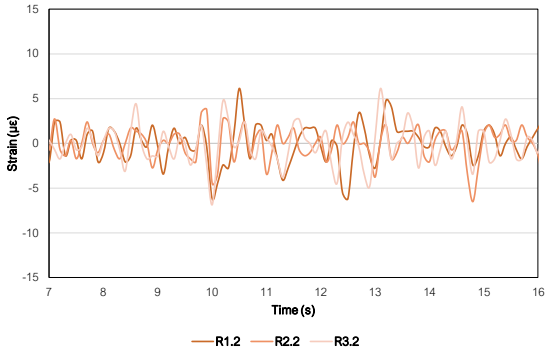
d) AS-TR-R-5 (Transverse, Right Array)



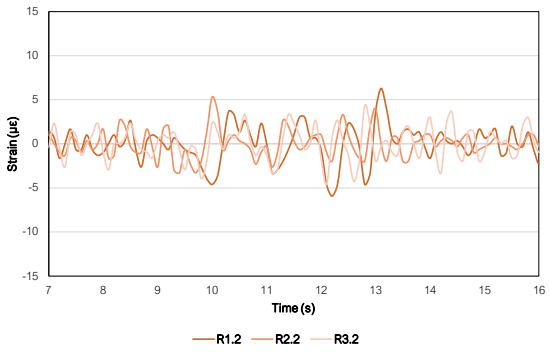
e) AS-LO-L-2 (Longitudinal, Left Array)



f) AS-LO-L-8 (Longitudinal, Left Array)



g) AS-TR-L-4 (Transverse, Left Array)



h) AS-TR-L-6 (Transverse, Left Array)

Figure 6.17 This is an 8-panel figure; Strain data that will be used in further analysis.

For instance, for the wander results for the longitudinal and transverse sensors located in the right sensor array, the Round 3 data exhibits the highest magnitudes, corresponding to the tires passing directly over the right sensor array. Similarly, the responses for the longitudinal and transverse sensors in the left sensor array show a predominant trend where the Round 2 data has the largest magnitudes, coinciding with the left tires being closest to the left sensor array.

These charts provide valuable benchmarks for future truck tests, offering insights into strain magnitudes and shapes. These magnitudes are specific to tests conducted at 10 km/h. Further tests at different speeds and seasons are recommended to capture wander results throughout the year, ensuring a more comprehensive assessment.

6.2.2.6 Raw Strain Results for all Strain Sensors

Figure 6.19 depicts the raw sensor data for all strain gauges presented in Figure 6.17. As with all other strain gauge responses, positive values indicate tensile strain and negative values indicate compressive strain. This is expressed in Figure 6.18.

As outlined in Chapter 5, the strain gauge responses as the truck passed over each gauge revealed distinct patterns for the steering axle, lift axle, and both axles in the tandem axle. The usual shape of the strain response depicts the steering axle with values similar to or sometimes higher than the tandem axle, accompanied by a lower lift axle magnitude. The tandem axle response typically exhibits two peaks—one for each axle. Before the strain response returns to the neutral position, it briefly ascends, indicating the second axle's response in the tandem axle.

Although the strain gauges and pressure cells were calibrated by the supplier with limited time for recalibration, differences between actual axle responses and non-responses are discernible. The strain magnitude can be computed by measuring the difference in signal response between the maximum strain for each axle and the neutral position strain.

However as mentioned in Chapter 5, the rationale behind calculating the difference in strain and pressure responses lies in the need to assess the actual strain/pressure response of the pavement structure based on climate, traffic, and other factors, without the additional stress and strain responses originating from the pavement itself. The change in strain response offers a more accurate representation of the actual response to the traffic load during a specific time period, aiding in establishing a correlation between load magnitude and pavement response. Taking raw strain and pressure values introduces complexities in the assessment, requiring consideration of various factors such as the weight of the pavement structure above the sensors. By calculating the difference in strain responses, the focus shifts to isolating the impact of the truck's load, providing a clearer understanding of the pavement's genuine response to traffic conditions.

The typical shape of the strain response describes the passing of the tires over the specific sensor. In many instances, as the truck approaches the sensor, compressive strain is produced before registering tensile strain after each tire from each axle passes over the gauge. Notably, no compressive strain was observed for the tandem axle in between both tandem axles as it traversed the strain gauge. Similar responses are observed in [61].

As across all charts illustrating the differences in strain response, consistent trends emerge. Longitudinal strain gauges in the right sensor array consistently exhibit higher magnitudes and clearer responses, while those in the left sensor array or the transverse direction indicate lower strain magnitudes and unclear strain responses. Additionally, certain responses show changes in compression more prominently than changes in tension, particularly evident in the transverse strain gauges located in the left sensor array.

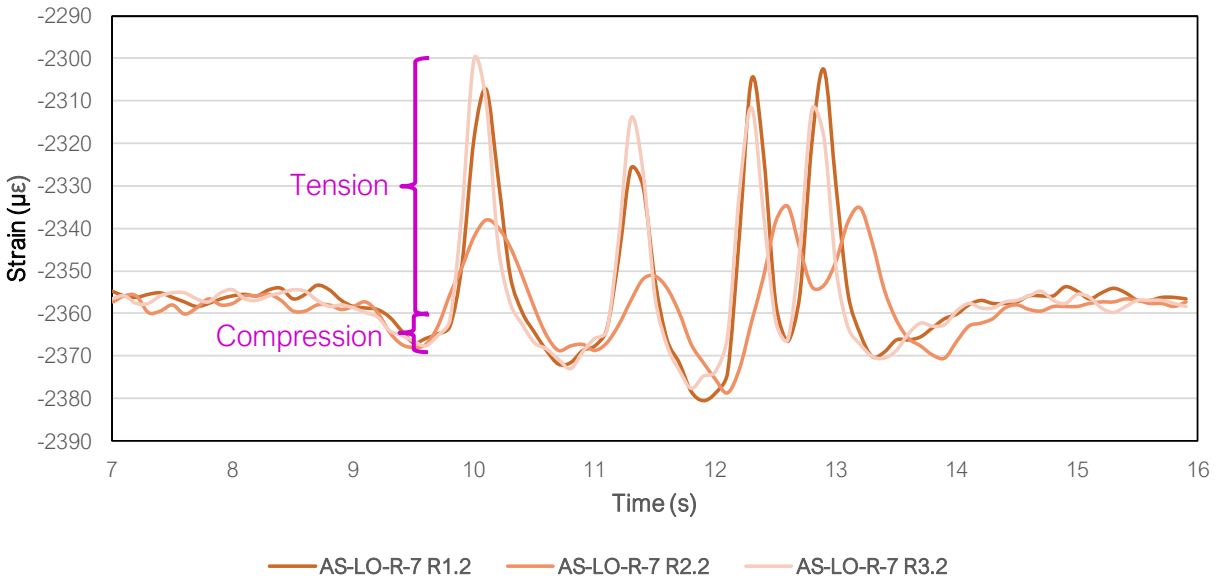
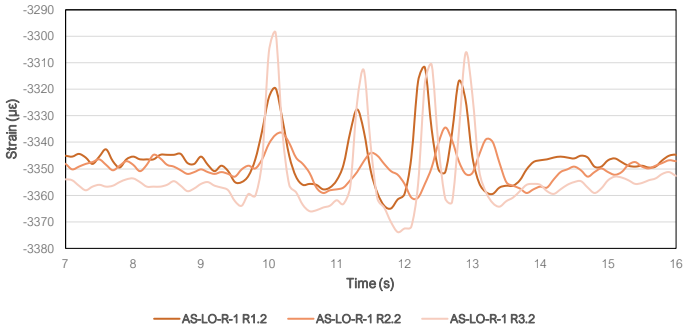
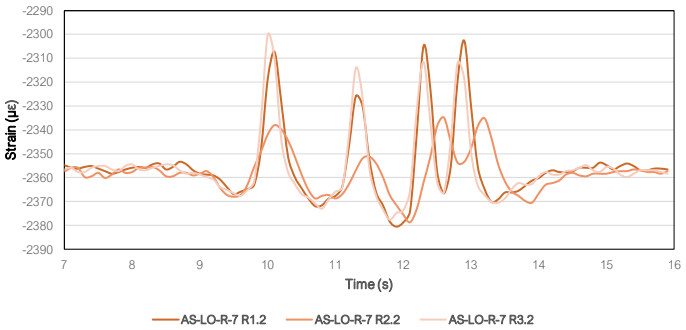


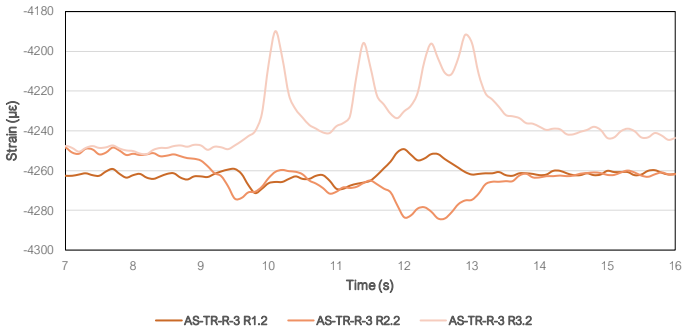
Figure 6.18 Demonstration of raw strain results and the tension and compression portions of the responses highlighted for clarity. Responses are for sensor AS-LO-R-7 (Longitudinal, Right Array).



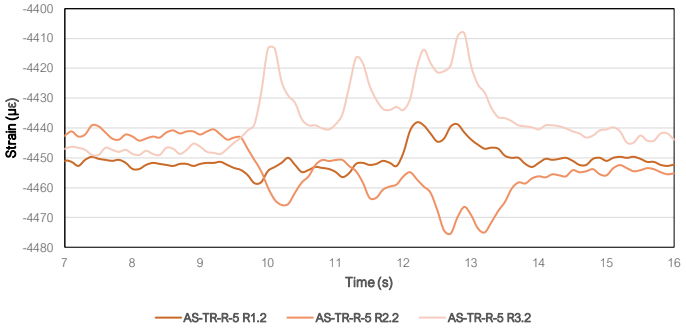
a) AS-LO-R-1 (Longitudinal, Right Array)



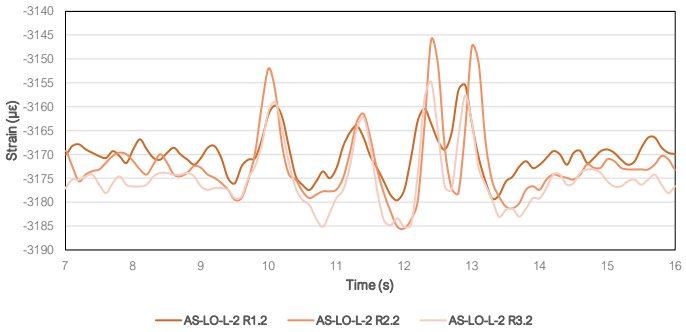
b) AS-LO-R-7 (Longitudinal, Right Array)



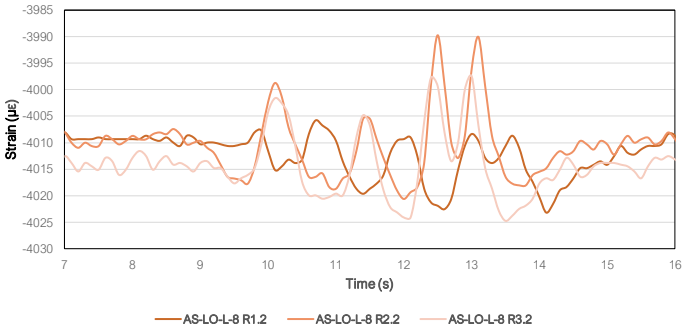
c) AS-TR-R-3 (Transverse, Left Array)



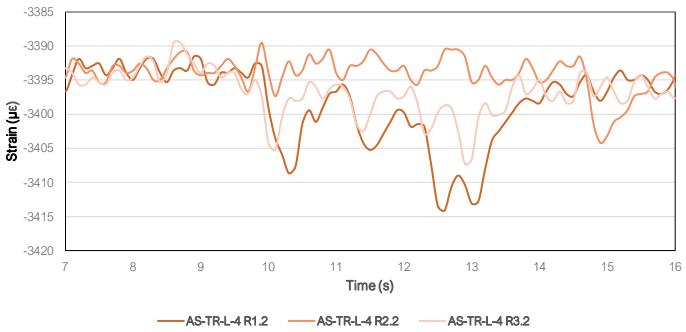
d) AS-TR-R-5 (Transverse, Right Array)



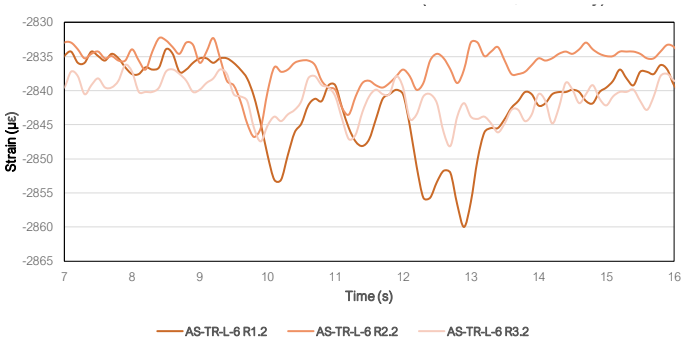
e) AS-LO-L-2 (Longitudinal, Left Array)



f) AS-LO-L-8 (Longitudinal, Left Array)



g) AS-TR-L-4 (Transverse, Left Array)



h) AS-TR-L-6 (Transverse, Left Array)

Figure 6.19 Raw strain responses for data that will be used in further analysis.

6.2.3 Pressure Sensor Assessment

In the upcoming section, the results derived from the pressure cell responses during the wander test will be presented. With the determination from the previous section in this chapter that Attempt 2 for all rounds yields the clearest responses, only the data from Attempt 2 will be shown and compared in the pressure response analysis. The emphasis of the analysis will be on comparing the responses within the base, subbase, and subgrade pressure cells.

6.2.3.1 Base Pressure Cell Responses

Figure 6.19 to Figure 6.22 present the pressure cell responses from the base array, focusing on sensors in both the right and left sensor arrays during the wander test. The included sensors in the base array are PC-BA-R-1 and PC-BA-R-5 in the right sensor array, as well as PC-BA-L-2 and PC-BA-L-6 in the left sensor array.

Analyzing the trends evident in the figures, the right sensor array pressure responses, illustrated in Figure 6.19 and Figure 6.20, exhibit similar response shapes to those observed in the longitudinal right sensor array strain responses. In Round 3, the signals are most distinct, clearly defining the axle responses for the steering axle, lift axle, and tandem axle. As deviations in tire lateral position occur, such as in Round 1 with a 0.35m deviation from the right sensor array centreline, the magnitude decreases, and the shape changes, with the lift and steering axles appearing smaller than the tandem axle and less clearly defined.

In the presentation of Round 2 data, the actual responses are notably unclear, and the magnitude is minimal. Comparing magnitudes between sensor PC-BA-R-1 and PC-BA-R-5, PC-BA-R-1 demonstrates higher pressure responses in Round 3 and smaller pressure responses in Round 1. This observation is intriguing, as one might expect a sensor producing lower results to consistently do so across all rounds. However, this is not the case in this instance.

For example, for the steering axle change in response for sensor PC-BA-R-1 between Round 3 and Round 1, the pressure magnitude decreases by 77.5% (from 10.14 kPa to 2.28 kPa from Round 3 to Round 1), and for the same sensor, between Round 3 and Round 2, the pressure magnitude decreased by 95.2% (from 10.14 kPa to 0.49 kPa from Round 3 to Round 2). Once more, this underscores the immense importance of the lateral position of the tires concerning the sensor array. It emphasizes the necessity for precise control tests on the sensor array, highlighting the considerable impact on pressure responses when the tire deviates even slightly from the sensor array.

.

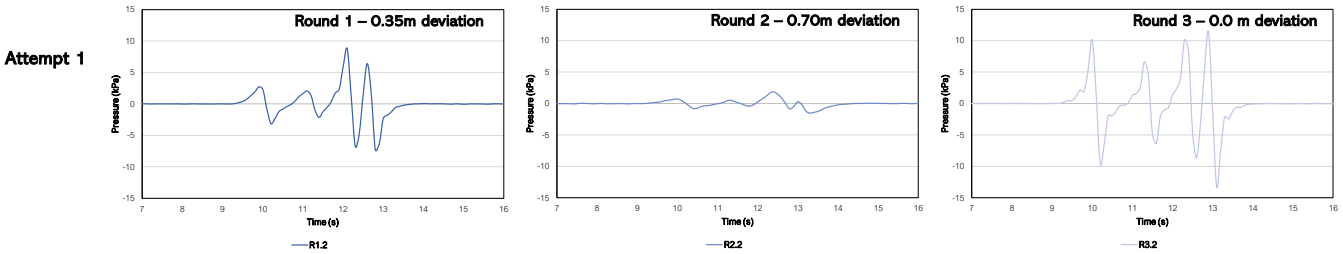


Figure 6.20 Pressure results for Attempt 2 for sensor PC-BA-R-1 (Base, Right Array).

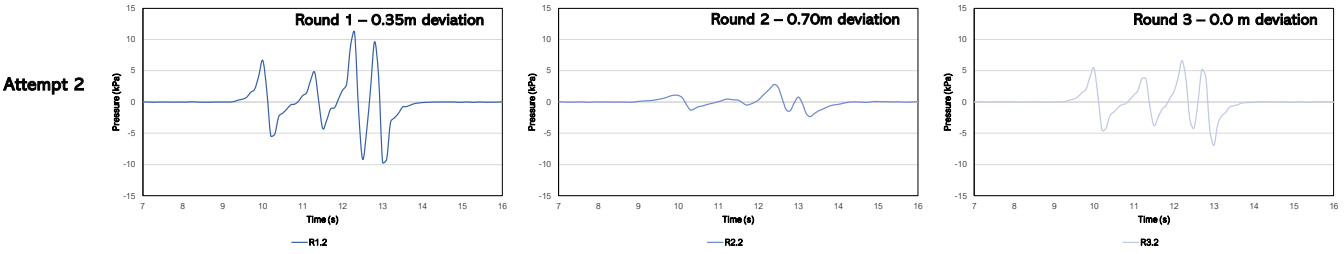


Figure 6.21 Pressure results for Attempt 2 for sensor PC-BA-R-5 (Base, Right Array). Note: labels are provided and are the same for similar figures.

Moving to the left sensor array, illustrated in Figure 6.22 and Figure 6.23, the responses closely mirror the patterns observed in the strain responses for the same array. Specifically, sensor PC-BA-L-2 exemplifies the trend well, with Round 2 producing the highest pressure response since the left tires of the truck axles are closest to the left sensor array during this round. Intriguingly, this trend does not appear as consistently for PC-BA-L-6, which could be attributed to testing method inconsistencies or potential limitations in data recording for this sensor. It might be worthwhile to scrutinize the data from PC-BA-L-6 more closely and assess its reliability in comparison to PC-BA-L-2.

For example, for the steering axle change in response for sensor PC-BA-L-2 between Round 2 and Round 1, the pressure magnitude decreases by 71.2% (from 4.27 kPa to 1.23 kPa from Round 3 to Round 1), and for the same sensor, between Round 2 and Round 3, the pressure magnitude decreased by 67.2% (from 10.14 kPa to 1.40 kPa from Round 3 to Round 2).

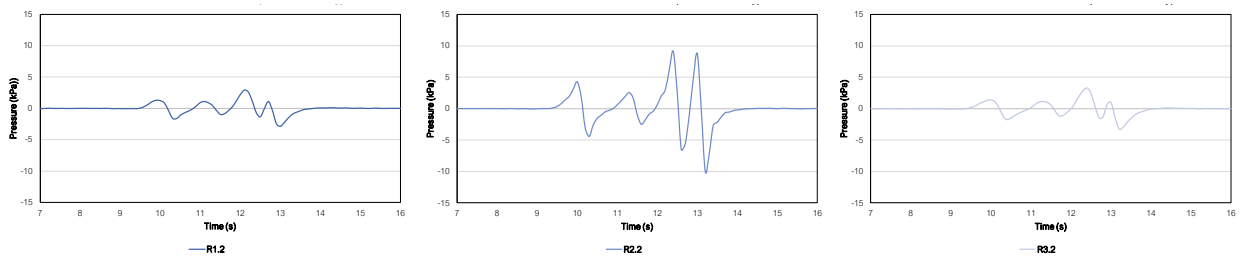


Figure 6.22 Pressure results for Attempt 2 for sensor PC-BA-L-2 (Base, Left Array).

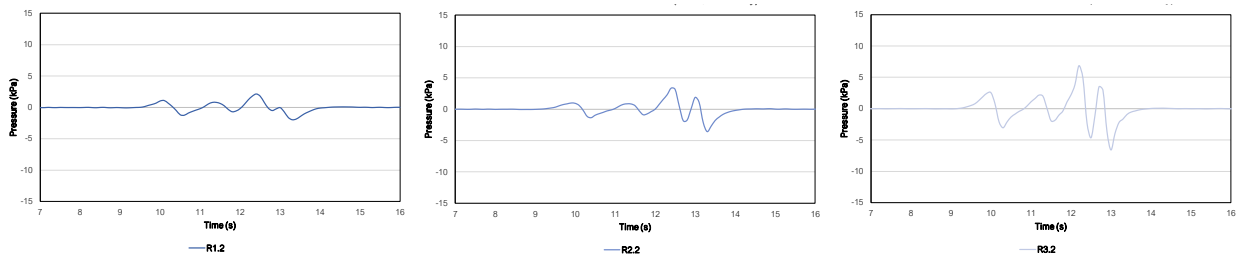


Figure 6.23 Pressure results for Attempt 2 for sensor PC-BA-L-6 (Base, Left Array).

6.2.3.2 Subbase Pressure Cell Responses

Transitioning to the subbase pressure cell responses, the clarity of data from the right and left sensor arrays, as depicted in Figure 6.24 and Figure 6.25 respectively, unveils intriguing trends. In the right sensor array, the responses remain distinctly clear; however, a noteworthy observation is that the magnitude of Round 1 data is slightly higher than that of Round 3. This discrepancy may suggest that, in this particular instance, the tires in round three did not pass over the sensors as effectively as they did in Round 1. As seen in the previous section with the base sensors, the magnitudes in the left sensor array are smaller than those in the right sensor array. Furthermore, in the left sensor array, it is noteworthy that Round 3 consistently yields the highest pressure responses, contrary to Round 2, which typically produces the highest pressure responses in other arrays. Perhaps the pressure sensors being situated deeper into the pavement structure is having an effect on the pressure response.

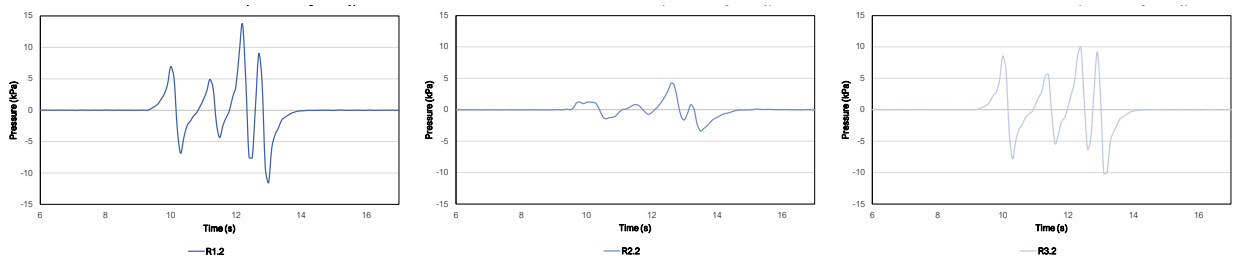


Figure 6.24 Pressure results for Attempt 2 for sensor PC-SB-R-3 (Subbase, Right Array).

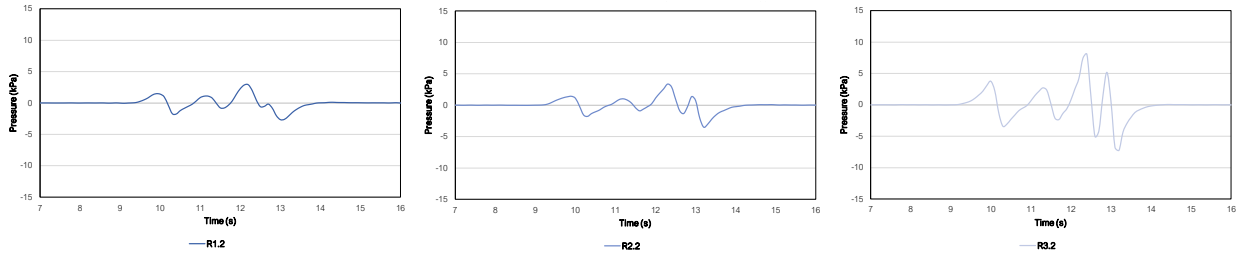


Figure 6.25 Pressure results for Attempt 2 for sensor PC-SB-L-4 (Subbase, Right Array).

6.2.3.3 Subgrade Pressure Cell Responses

Finally, Figure 6.25 and Figure 6.26 unveil the pressure results for attempt two for sensor PC-SG-R-7 and PC-SG-L-8 in both the right and left sensor arrays, respectively. Interestingly, the trends observed in the base layer pressure cells and strain gauges do not align as strongly in the subgrade responses, a pattern also noticed in the subbase trend responses.

In this case, the sensor responses appear quite similar across all three Rounds in terms of magnitude and shape, with magnitudes in Rounds 1 and 2 higher than those in Round 3. This could be attributed to the spreading effect of the load applied by a tire on the pavement structure, a function designed to distribute loads in the HMA layer. Consequently, the magnitudes are not as high directly underneath the tire response, as the load is dispersed outward and the sensor is situated quite far into the pavement structure.

In the right sensor array, the response shapes differ from those found in the base layer and even in the subbase layer. In the subgrade response, the axle peaks are rounder and less crisp, making it more difficult to identify the general areas of the steering, lift, and tandem axles in the signal than in the previous layers. This shape trend is also evident in the left sensor array's pressure response in the subgrade.

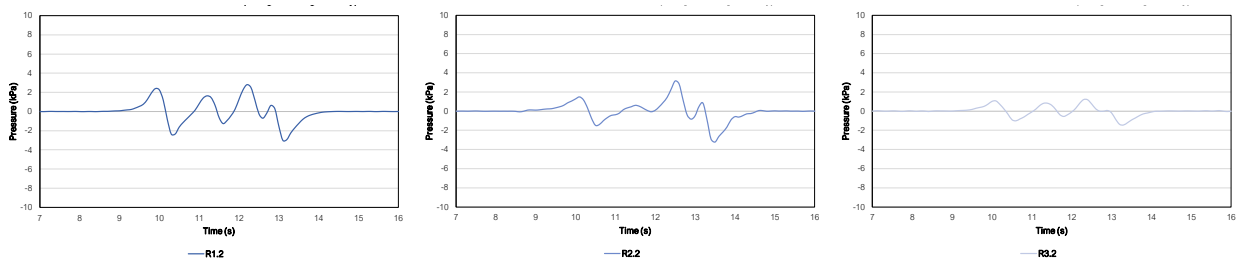


Figure 6.26 Pressure results for Attempt 2 for sensor PC-SG-R-7 (Subgrade, Right Array).

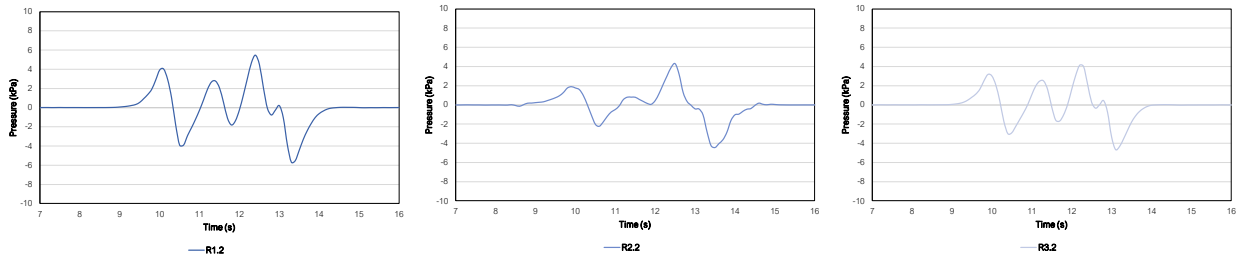
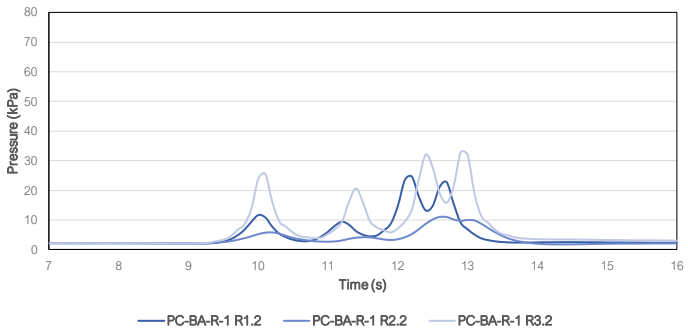


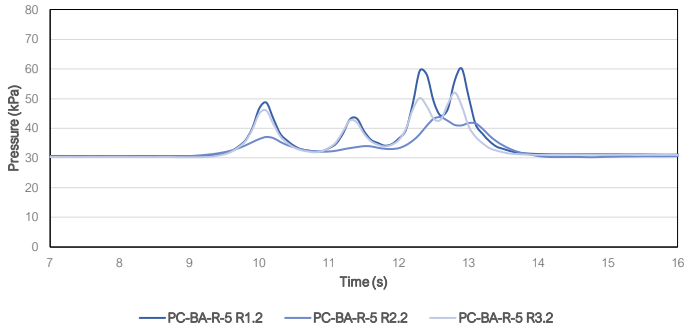
Figure 6.27 Pressure results for Attempt 2 for sensor PC-SG-L-8 (Subgrade, Right Array).

6.2.3.4 Raw Pressure Results for all Sensors

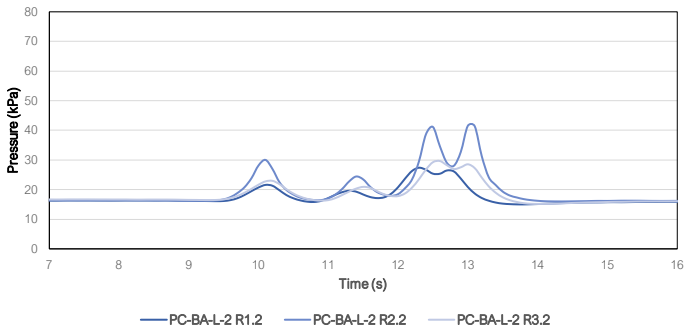
Figure 6.28 shows the raw pressure data for all pressure cells. As with all other pressure cell responses described in this thesis, positive values indicate compression, and negative values indicate tension.



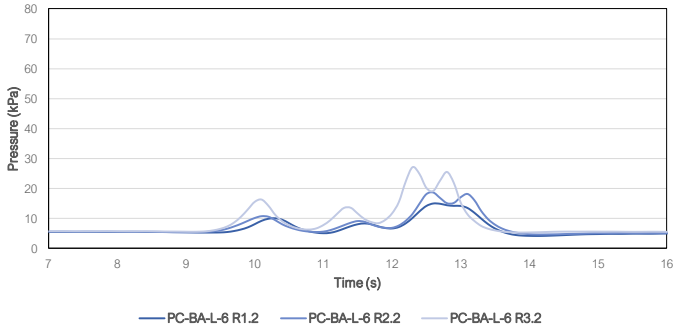
a) PC-BA-R-1 (Base, Right Array)



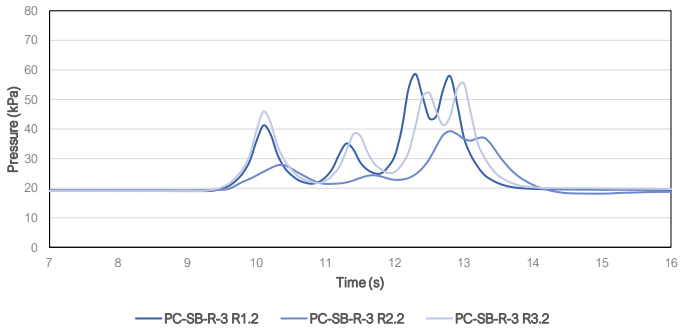
b) PC-BA-R-5 (Base, Right Array)



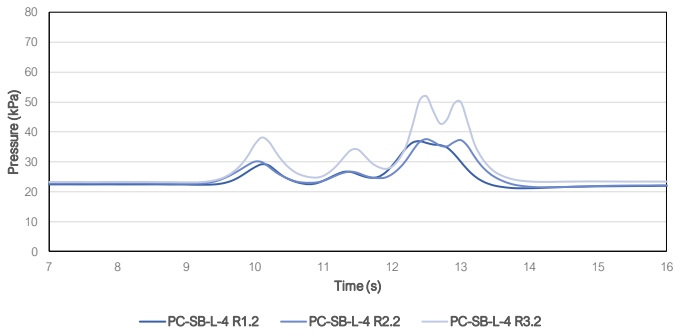
c) PC-BA-L-2 (Base, Left Array)



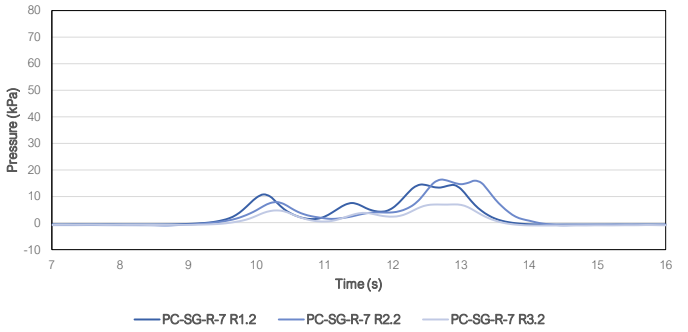
d) PC-BA-L-6 (Base, Left Array)



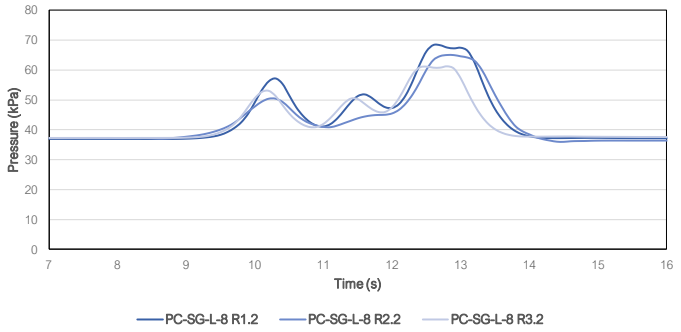
e) PC-SB-R-3 (Subbase, Right Array)



f) PC-SB-L-4 (Subbase, Left Array)



g) PC-SG-R-7 (Subgrade, Right Array)



h) PC-SG-L-8 (Subgrade, Left Array)

Figure 6.28 Raw pressure responses for data that will be used in further analysis.

Similar to what was illustrated in Chapter 5, the pressure cell responses during the truck's passage over each pressure cell unveil distinct patterns corresponding to each axle of the truck. The shapes for each pass are typically clear, highlighting the steering axle, lift axle, and the tandem axle, with both axles in the tandem axle being individually expressed for the most part. The only exception to this pattern is observed

in the subgrade responses. This deviation is likely because subgrade sensors are situated far below the pavement surface, making them less easily expressed compared to those located in the base layer and subbase layers.

6.2.4 Comparison of the Results

This section will outline the quantification of the relationship between either the measured strain or the measured pressure responses and the offsets, which are the lateral wander deviations used in the previous sections of testing. These relationships between the dynamic response and the wander will provide a fundamental baseline that will allow for the determination of patterns and trends within the data and ensure that in future testing, the prediction of the strain and pressure response can be performed based on the relationships determined in the analysis. This means that future test results can be compared to these baselines validate the accuracy of new tests and filter out outliers.

Typically, the relationship that expressed the correlation between the response and wander the best was a second order polynomial, which is also has been found to express the relationship between the response and offset in other studies [68]. Relationships were developed for the strain response, further divided into relationships for longitudinal and transverse strain gauges as well as the pressure responses, divided into base subbase and subgrade relationships. In each of these divisions, relationships were developed for the right array and the left array.

6.2.4.1 Strain vs. Lateral Offset Relationship

Figure 6.29 and Figure 6.30 display the strain versus wander distance for the longitudinal and transverse sensors, respectively. Beginning with Figure 6.28, the relationships for the right array and the left array are distinctly different in shape. Notably, the right array relationship is a concave down second-order polynomial, while the left array exhibits a concave up second-order polynomial. This accurately characterizes the observed relationships in the longitudinal sensors, where an increase in wander distance or offset from the right sensor array centerline corresponds to a decrease in strain response in the right sensor array.

Moving to the left sensor array responses, they present an interesting yet logical pattern. During Round 3, when the right axle tires pass directly over the right sensor array, the distance between the right tires and the left sensor array is 0.7 meters, whereas the distance between the left axle tires and the left sensor array is 1.7 meters. Conversely, when the deviation from the right sensor array is 0.35 meters in Round 1, the right tires are located 1.05 meters away from the left sensor array, and the left tires are positioned 1.35 meters away from the left sensor array. Finally, in the case of a 0.7-meter deviation from the right sensor array in Round 2, the distance from the left sensor array to the right tires of the truck is 1.4 meters, while

the distance from the left tires to the left sensor array is only 1 meter. This is expressed visually in Figure 6.31.

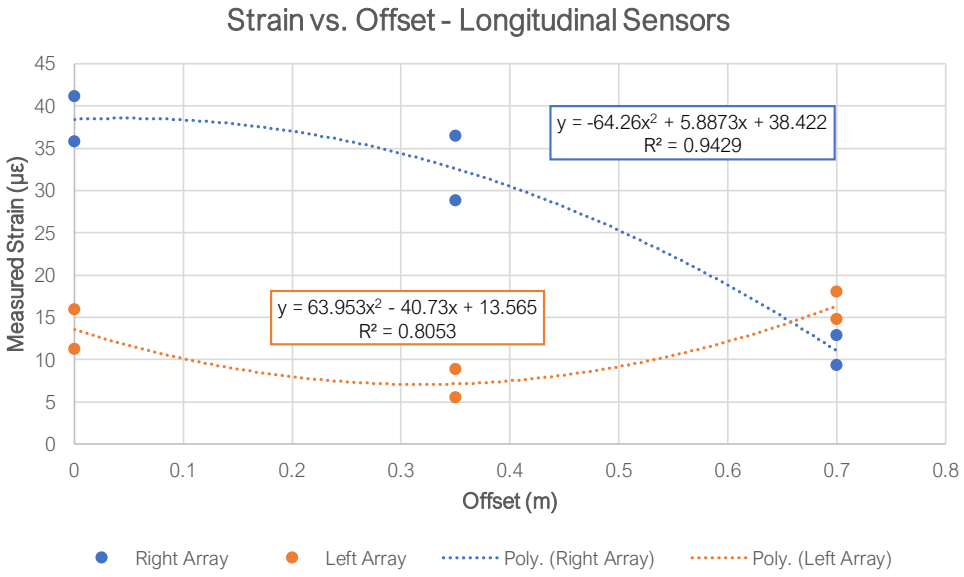


Figure 6.29 Longitudinal strain versus lateral offset relationships for the right and left sensor arrays.

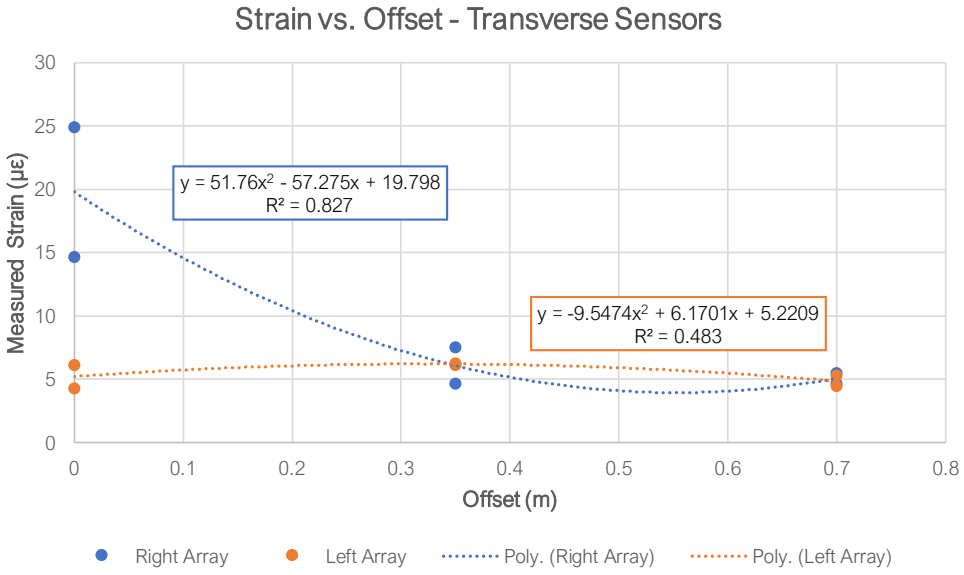


Figure 6.30 Transverse strain versus lateral offset relationships for the right and left sensor arrays.

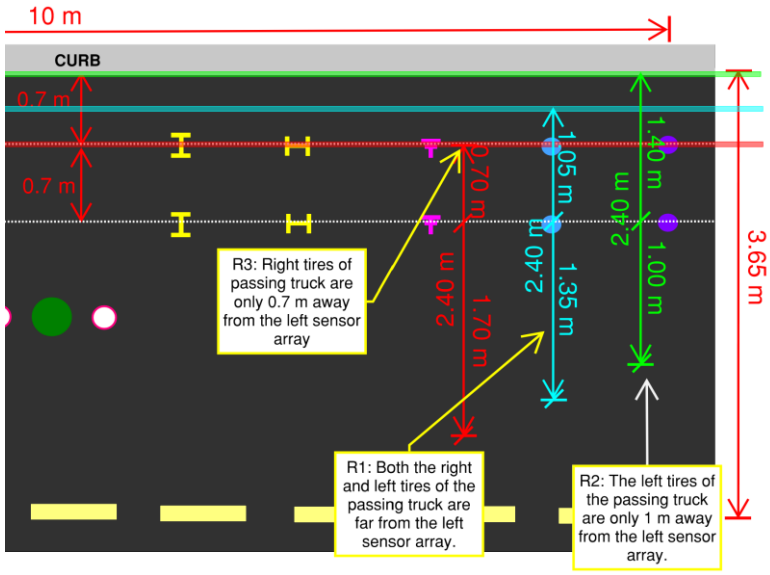


Figure 6.31 Measurements between right and left truck tires and the right and left sensor arrays.

In essence, when the tires are 0.35 meters deviated from the right sensor array, both rows of tires are farthest away from the left sensor array. This contributes to a decrease in response, as neither the right tires nor the left tires are as close to the left sensor array as in the cases of Round 3 and Round 2 positioning. Therefore, they cannot contribute to a higher strain response as observed in Round 3 and Round 2 data.

In contrast, examining the relationships for the transverse sensors reveals a flip in concavity. Specifically, for the right sensor array, the concavity becomes concave up in the second-order polynomial, whereas for the left sensor array, the concavity becomes slightly concave down.

In both cases, it appears that the equation for the relationships indicates that at the zero offset point, the maximum longitudinal and transverse strain occurs in the right sensor array, and moving further away from the Your array will cause a decrease in the strain response. This has been corroborated by some studies, such as [68]. However, here is no relationship development in the literature for transverse strain gauges, an especially transverse strain gauges and longitudinal strain gauges in the left sensor arrays.

6.2.4.2 Pressure vs. Lateral Offset Relationship

As mentioned earlier, the pressure relationship development concerning lateral offset was explored for the base, subbase, and subgrade layers. This exploration aimed to investigate potential differences in relationships between the various layers. Commencing with the base sensor relationship development, as depicted in Figure 6.32, the patterns for the right and left sensor arrays closely resemble those observed in the longitudinal and transverse strain responses. This consistency was also noted in the individual sensor response measurements in previous sections.

However, a notable difference is that the peak of the second-order polynomials does not align with the 0-meter deviation point, as observed in both the transverse and longitudinal strain gauges. In this case, the maximum occurs at approximately 0.2 m deviation. This shift suggests that these sensors may have moved, warranting a reassessment and confirmation of their locations.

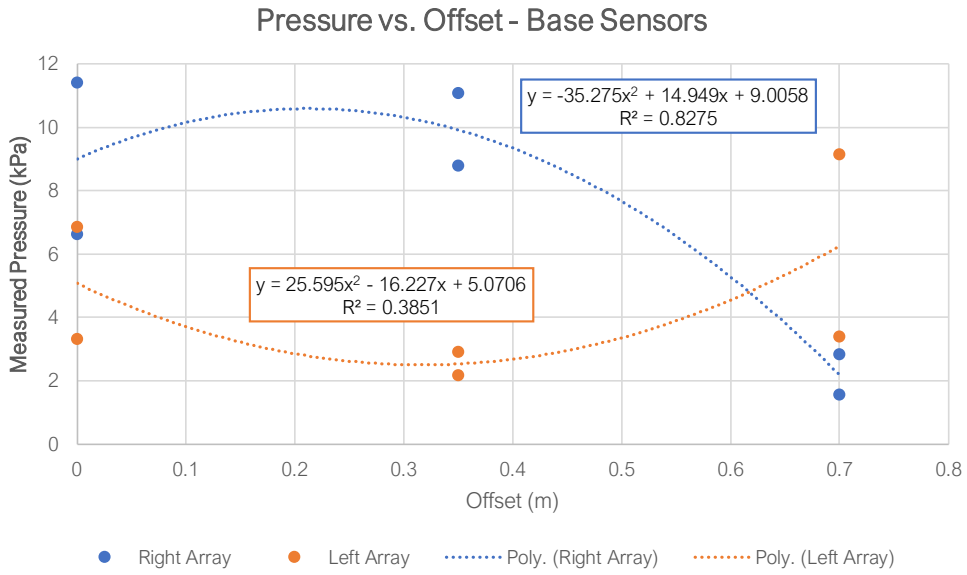


Figure 6.32 Base pressure response versus lateral offset relationship for the right and left sensor arrays.

The primary distinction evident in the base sensor relationships compared to the subbase sensor relationships, as illustrated in Figure 6.33, is simply the magnitude of the subbase sensor responses, which is larger than the base responses.

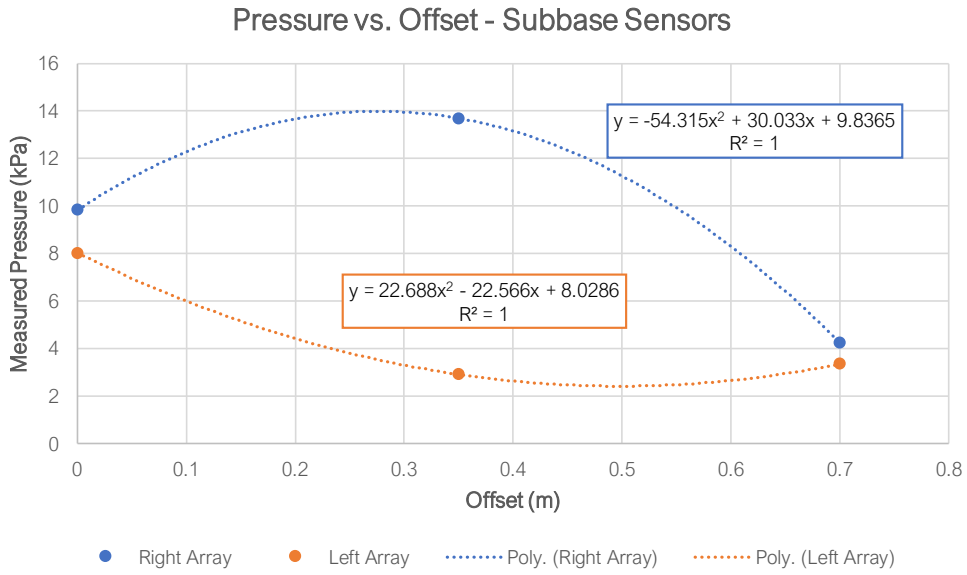


Figure 6.33 Subbase pressure response versus lateral offset relationship for the right and left sensor arrays.

Finally, Figure 6.34 presents the relationship between the lateral offset and the measured pressure response for the subgrade layer. In this case, the relationship is the most unusual among the three layers. The second-order polynomial predicts that the maximum longitudinal pressure response will occur at 0.7 meters deviation from the right sensor array mark, while the transverse pressure maximum will occur at 0.35 meters deviation from the right sensor array mark. Both cases exhibit a concave-down shape, and the right array magnitudes are consistently lower than those of the left array.

Given the deviation from the patterns observed in the other layers, it is advisable to repeat the test for the subgrade response to confirm and understand the impact of the offset on the measured pressure in the subgrade.

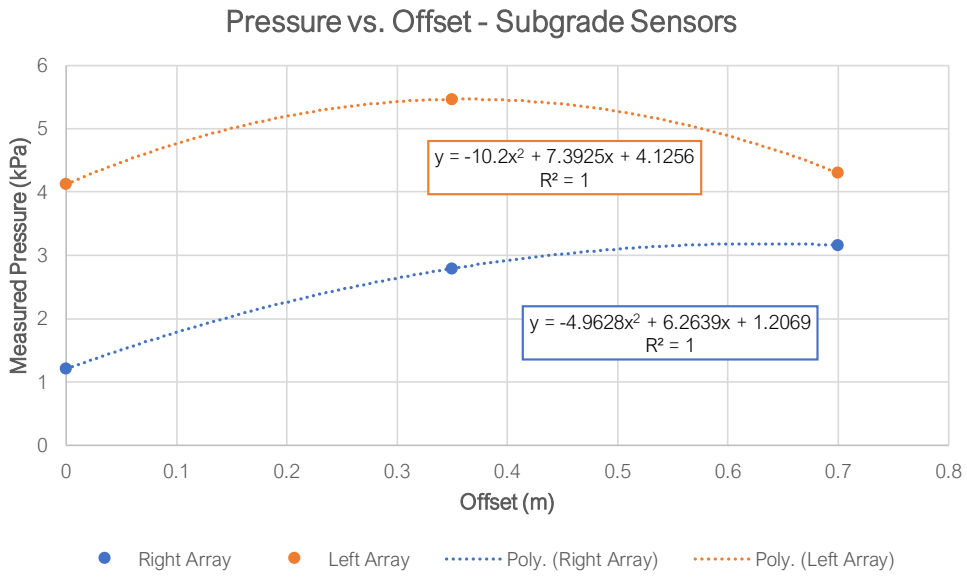


Figure 6.34 Subgrade pressure response versus lateral offset relationship for the right and left sensor arrays.

Previously mentioned, establishing this fundamental baseline serves a crucial purpose: validating the accuracy of forthcoming truck test outcomes and eliminating data outliers. This validation is vital for constructing a national database (see Chapter 9), which will involve extensive data inputting and necessitate an efficient and automated data filtering mechanism. If similar relationships, as those developed in this chapter, are established for various speeds commonly executed during truck tests and integrated into the national database as filters, algorithms designed for data cleaning can leverage these fundamental baselines to determine the accuracy of truck test results, thus indicating whether retesting is necessary.

Chapter 7
Pavement Section Modelling

This Chapter compares KENPAVE and 3D-Move software tools for predicting pavement response in the project. It involves modelling truck tests conducted across different seasons in both software programs and validating these results with field measurements to gauge accuracy and reliability. Additionally, it offers lessons learned and acts as an example for future test sections with similar needs for simulating and modelling pavement structures across varying seasons and speeds.

7.1 Introduction

As mentioned in previous sections of this thesis, being able to investigate the initial stages of deterioration within the various layers of a pavement structure, as well as the reasons entailing this deterioration, are valuable to implementing maintenance and rehabilitation methods at the right time. Key responses include tensile horizontal strains at the bottom of the HMA layer, compressive vertical stresses and strains within the HMA and the base/subbase layers, as well as compressive vertical stresses/strains at the top of the subgrade (see Figure 2.8).

Advancements in technology have led to the development of various software tools for predicting pavement response under different loading conditions. KENPAVE and 3D-Move are examples of such tools that can be used to analyze pavement responses, such as stress, strain, and deflection under a given loading configuration.

KENPAVE is a computer software developed by Yang H. Huang, to consider static loads and to model typical flexible and rigid pavement structures and assess stresses, strains, and deformations [74]. The entire KENPAVE software is a combination of four individual software that are used to calculate pavement responses for both flexible and rigid layers, and they are LAYERINP, KENLAYER, SLABSINP and KENSLABS [74]. It is based on the multi-layer elastic theory [75]. This software cannot distinguish between temperature variations (thermal stresses) and dynamic changes in load, unless moduli from different seasons are inputted separately every time a new simulation is run [76].

On the other hand, 3D-Move, developed at the University of Nevada Reno, uses what is known as a “continuum-based finite-layer approach” to simulate dynamic pavement responses [77]. The FE model associated with this software efficiently addresses factors such as 3D contact stress, vehicle speed, and the viscoelastic properties of pavement layers, which allows for the examination of pavement responses under varying vehicle speeds [77]. Here, temperature can be considered, which means the seasonal differences in testing can be accommodated.

Although pavement analysis tools can provide valuable insights about the pavement responses under various loading conditions, it is essential to validate the analytically calculated responses with their real in-situ counterparts. Literature in the Canadian context examining the comparison between these software tools and real-life data indicates a gap regarding the responses from axial loads at different speeds and temperatures. Some of the limited relevant literature related to this topic includes that of Shafiee et al., who have also used both KENPAVE and 3D-Move along with 2D FEM modelling to validate FWD responses collected from their test track in Edmonton, Alberta over various seasons [75].

To this end, KENPAVE and 3D-Move software packages were utilized in this study to compare the theoretical with real-life pavement strain and pressure response data obtained from an instrumented pavement section in Canada. The study by Shafiee et al. [75] has proven that the use of these two software, when provided with similar inputs, will produce similar output, therefore making them suitable for comparison purposes. The study will compare 3 scenarios, namely 51°C at 45 km/h during TT#1, 6°C at 40 km/h for TT#2 and 25°C at 45 km/h for TT#3. The entire investigation will be based on the results of the lift (middle) axle of the trucks which are single axles with dual tires.

Such investigations are vital to validate and understand the software's accuracy and reliability in modelling pavement damage under local conditions and is a step towards implementing a framework for smart pavements in Canada [19].

7.2 Input Parameters

7.2.1 Determination of HMA Dynamic Moduli

In 3D-Move, the dynamic modulus is required to simulate the dynamic nature of the loads that are being applied to the pavement structure. As was mentioned in subsection 4.2.1, dynamic modulus tests were performed, and a master curve was developed for the HMA samples. From this master curve, the HMA dynamic modulus can be determined at any temperature.

In addition, a singular value of the dynamic modulus at a specific temperature and frequency can be selected for use in KENPAVE for static load modelling.

7.2.2 Determination of Layer Elastic Moduli

Similar to what was done in [75], to be able to accurately model the pavement structure in KENPAVE, the elastic moduli of the various layers of the pavement structure could be determined using the LWD data that was collected as per subsection 4.1.2. However, there are several problems with this. The LWD test is not the most accurate collection method for the elastic modulus of certain layers. This is because it is not certain that the deflection induced by the LWD is penetrating throughout the entire layer it is

supposed to measure when the deflection basin is created to obtain and accurate modulus value. The deflection basin, or the phenomena developed by tools such as the LWD and FWD when the apparatus strikes the surface that it is measuring and is created by the deflection produced in the surrounding layers, may not reach the throughout the entire layer during an LWD test. An FWD is more suitable for this but was not used in the collection process. In addition, when performing the LWD test on layers above the subgrade (e.g. surface of base), the test is not simply collecting the deflection data of that specific layer but also the layers below. Therefore, the most accurate layer is that of the subgrade where it is certain that the data being collected is that of the subgrade only. Because of these reasons, elastic modulus values from the studies performed by Oyeyi et al. in [78] will be referred to as required, as the test sections in their study are the closest geographically to that assessed in this project.

For reference, the Layer Elastic Moduli to be used in this assessment are as follows in Table 7.1:

Table 7.1 Chosen elastic modulus values for each layer.

Layer	**Elastic Modulus (MPa)**
HMA	4983
Granular A (Base) [78]	226
Granular B (Subbase) [78]	145
Subgrade	21

The modulus for the HMA layer was determined as described in subsection 7.2.1. This modulus was based on the average testing frequency and testing temperature, or 21°C and 5 Hz. The moduli for the Granular A and B layers were obtain from the study in [78] because both studies are conducted within the same municipality, with similar material sources and classifications. It is understood that, when compared to the results in [75] and [78], the modulus results for the unbound materials obtained from the LWD testing are relatively low, and likely do not reflect the actual moduli for each layer fully and separately from the others. Finally, the modulus for the subgrade was selected from the LWD testing as was mentioned previously.

As mentioned in subsection 4.2.1, the dynamic modulus tests were performed on HMA samples that were taken from when the first layer of HMA was poured in October 2022, or SP 19.0 mm SG 58-28 asphalt. These details correspond to the pavement structure conditions during the first three truck tests out of the total five. In those initial tests, conducted in Fall, Early Spring, and Summer, the first layer of the two-layer HMA was poured using only SP19 material, resulting in a total HMA thickness of 145mm at that time. Therefore, it is more appropriate to focus on the first three truck tests and model them for the assessment.

7.2.3 Summary of Input Parameters

As mentioned, the truck tests in the Fall, Early spring and Summer (TT#1, TT#2, and TT#3) will be modeled/simulated in KENPAVE and 3D-Move using a 4-layer pavement structure.

7.2.3.1 KENPAVE

The initial inputs in the KENPAVE software pertain to general information, as depicted in Figure 7.1. This includes selecting linear material (MATL), modelling four layers (NL), specifying six Z-coordinates for analysis (NZ), and opting for SI units (NUNIT).

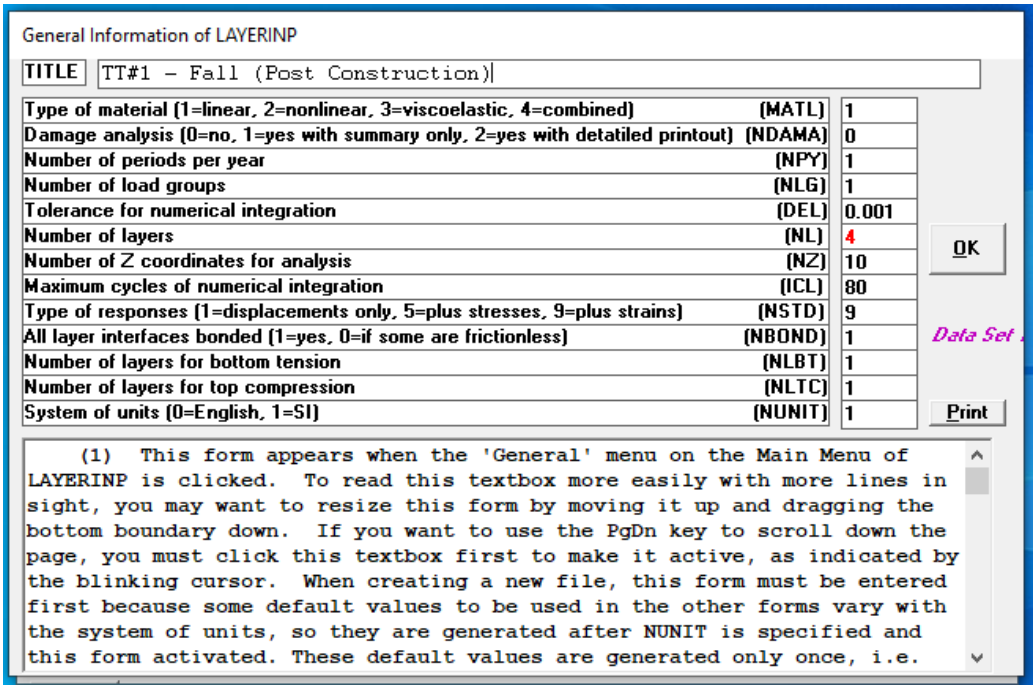


Figure 7.1 General information inputted in KENPAVE.

Vertical coordinates, known as Z-coordinates in KENPAVE, are those that indicate the points of analysis where stress, strain and deflection will be determined. Figure 7.2 shows the six Z-coordinates that will be inputted into the software, represented with red circles with white interiors. The Z-coord. selected for analysis included the bottom of the AC layer, the top and bottom of the base layer, the top and bottom of the subbase layer as well as the top of the subgrade layer to correspond to the sensor locations.



Figure 7.2 Z-coordinates (vertical coordinates) as will be inputted in KENPAVE as points of analysis.

Figure 7.3 are the Z-coordinates (ZC) within the KENPAVE software.

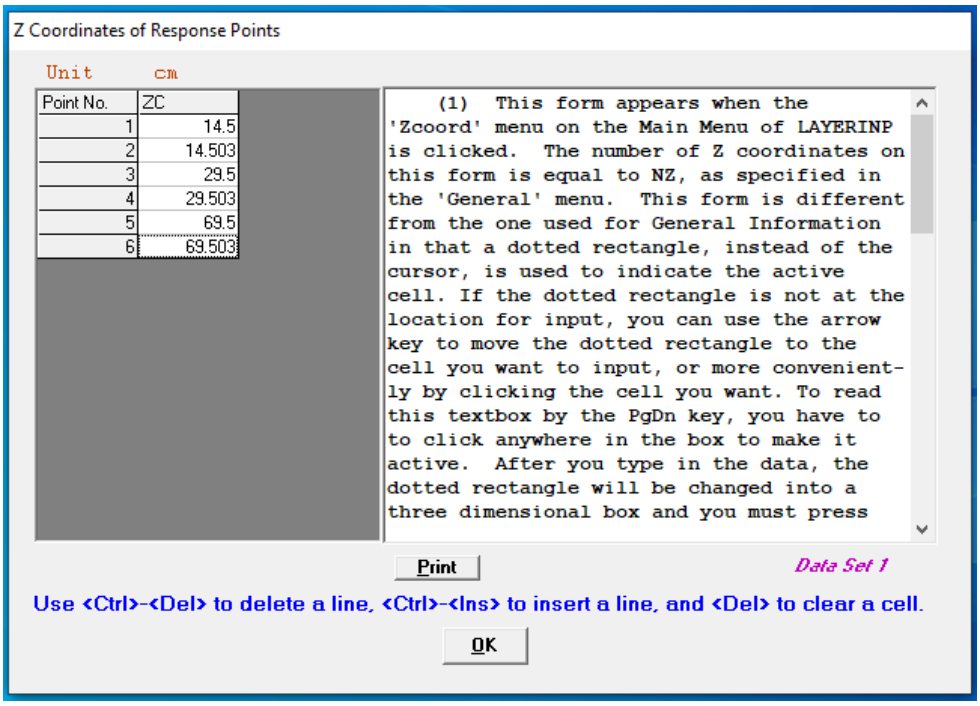


Figure 7.3 Z-coordinates inputted in KENPAVE.

The next inputs consisted of outlining the thicknesses (TH) of each of the layers as well as their Poisson's Ratios (PR). To determine the latter, the *Ontario's Default Parameters for AASHTOWare Pavement ME Design* report from 2019 were consulted [79]. This is represented in Figure 7.4.

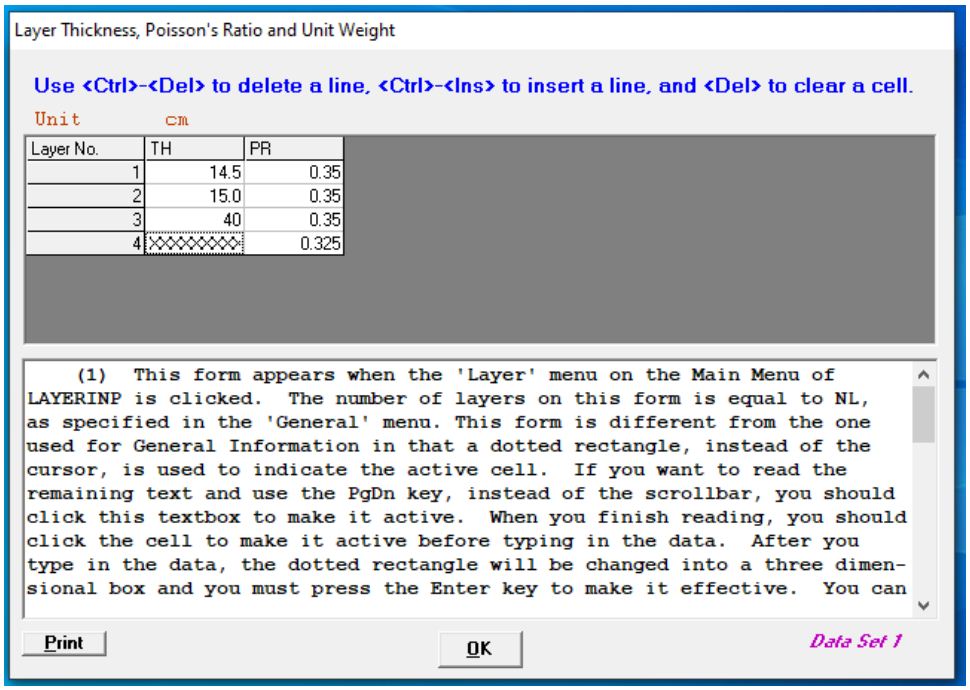


Figure 7.4 Thickness and Poisson Ratio values for each layer in KENPAVE.

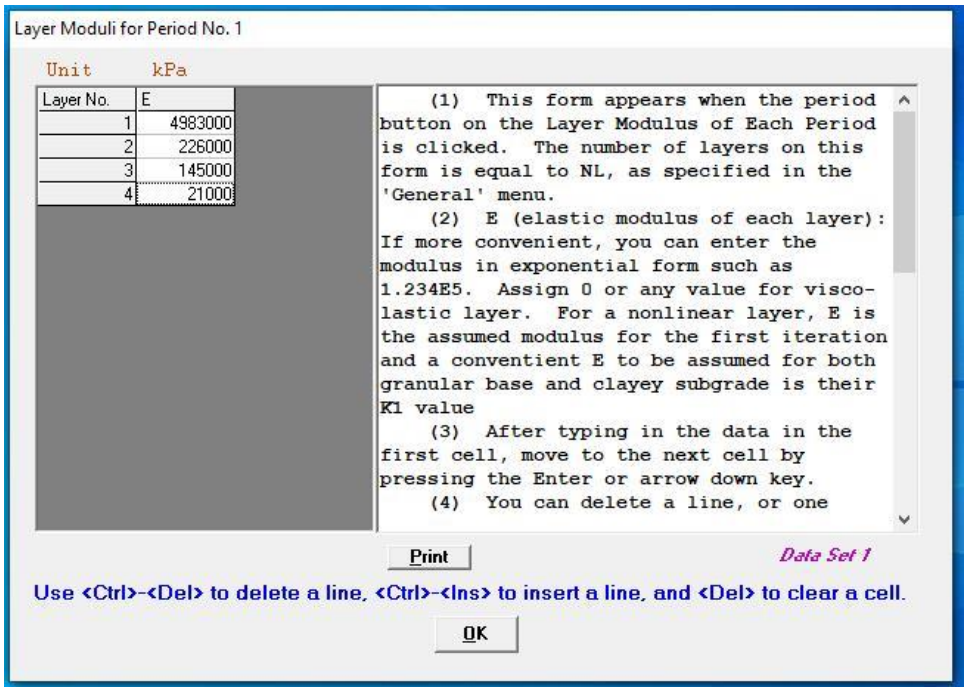


Figure 7.5 Modulus input in KENPAVE.

The modulus values, as described in Table 7.1, were inputted into the software as shown in Figure 7.5. Note that the inputted modulus values are in kPa.

The next step consisted of determining the various load information inputs. This is shown in Figure 7.6.

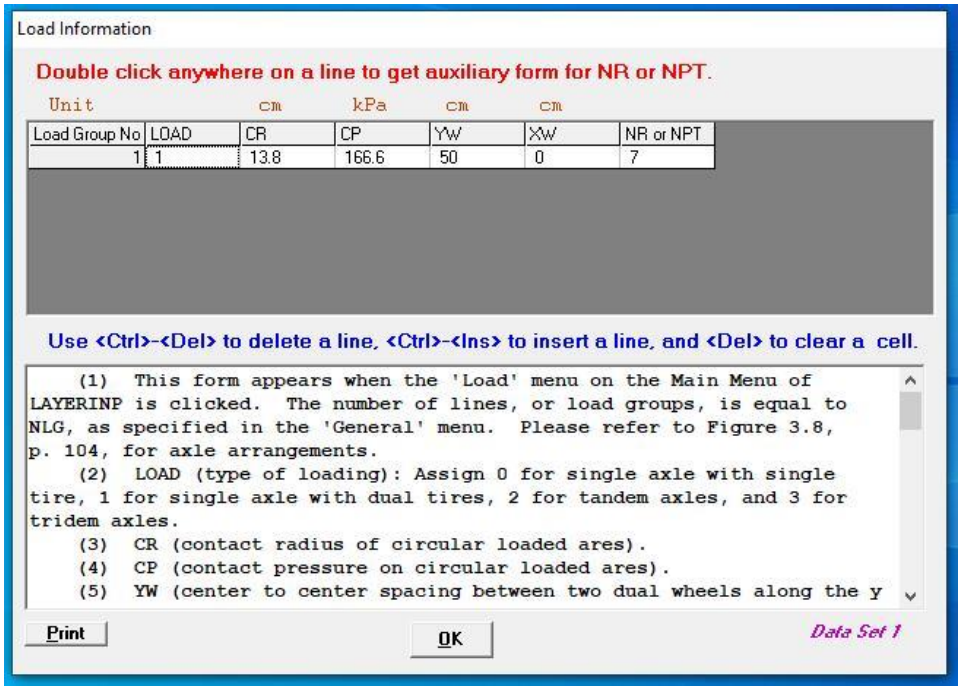


Figure 7.6 Load information inputted in KENPAVE.

Under the "LOAD" input, the value of 1 was inputted as the reference axle that was assessed included the single axle with dual tires. The value of "CR" is the contact radius of the tires in cm. Since this was not explicitly calculated for each tire in the current project, the tire-pavement interface will be taken from another study that used a very similar truck configuration in their truck tests. This study from Oyeyi [18] determined the interface to be 0.06m^2. Assuming a circular tire-pavement interface as per the KENPAVE program, the contact radius is:

$$A = \pi r^2$$

$$r = \sqrt{\frac{A}{\pi}}$$

$$\text{r} = \sqrt{\frac{0.06\text{m}^2}{\pi}} = 0.138 \text{ m}$$

To convert this radius from meters to centimeters, multiply by 100:

$$Radius\ in\ centimetres = 0.138\,m\ \times 100\,\frac{cm}{m} = 13.8\,cm$$

Therefore, the contact radius is approximately 13.8 centimetres.

Next, the contact pressure, defined by the letters "CP" needs to be determined. This will be calculated based on the weights of the trucks measured for each truck test (see Table 5.1).

TT#1 – Fall Test & Construction Conditions

Since the truck load for this test is 140 kN (unloaded), and each truck has 14 tires and specific axle weights were not measured by the construction company, the tire pressure is:

$$Pressure = \frac{\frac{140\ kN}{14\ tires}}{0.06m^2} = 166.6\ kPa\ per\ tire$$

TT#2 – Early Spring Test

Since the truck load for this test is 348 kN (loaded), there are 14 tires and the lift axle containing 4 tires weighs 61 kN:

$$Pressure = \frac{\frac{61\ kN}{4\ tires}}{0.06m^2} = 254.2\ kPa\ per\ tire$$

TT#3 – Summer Test

Since the truck load for this test is 353 kN (loaded), there are 14 tires and the lift axle containing 4 tires weighs 78 kN:

$$Pressure = \frac{\frac{78\ kN}{4\ tires}}{0.06m^2} = 325\ kPa\ per\ tire$$

Next, the letters "YW" represent the spacing between two dual wheels, which will be 50 cm as per Figure 5.4. The letters "XW" represents the spacing between two axles. Since in this case, the axle being modeled is a single axle with dual tires, this section will be left as a value of zero. Finally, NR or NPT refers to the number of radial coordinates to be analyzed under a single wheel or the number of points in x and y coordinates to be analyzed under multiple wheels, respectively. For this assessment, 7 points were chosen, as demonstrated in Figure 7.7, and inputted in KENPAVE as shown in Figure 7.8.

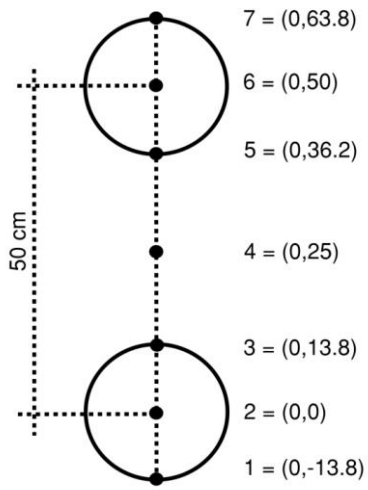


Figure 7.7 Number of coordinates under a single tire to be analyzed.

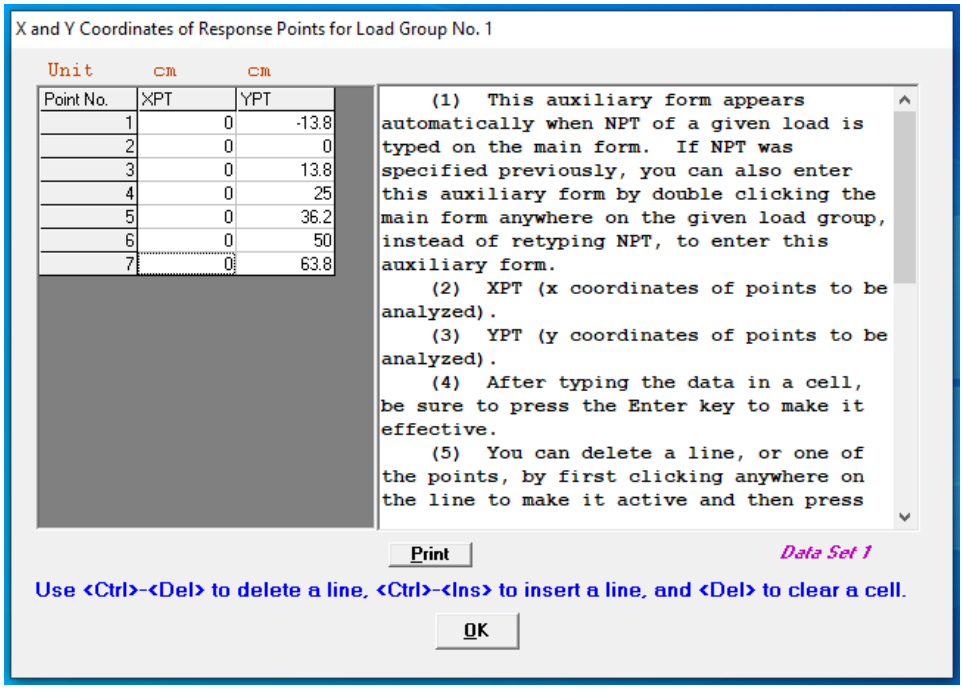


Figure 7.8 Coordinates inputted in KENPAVE.

A summary of all of the input parameters for the KENPAVE program can be seen in Table 7.2. These are some of the main inputs for each of the drug tests. The only difference is the load based on the contact pressure that's applied to each of the tires. The KENPAVE testing will occur three times; one for each of the truck tests.

Table 7.2. KENPAVE Input Parameters Summary

Parameter	TT#1 Fall Conditions	TT#2 Early Spring Conditions	TT#3 Summer Conditions
General	Linear Material (MATL), 4 layers (NL), 6 Z-coords (NZ)		
Zcoord. (cm)	14.5, 14.503, 29.5, 29.503, 69.5, 69.503		
Layers	HMA, Base, Subbase		
Layer Thicknesses (cm)	14.5, 15, 40		
Modulus	(Layer No., E in MPa)		
	HMA: 4983 at 21°C Gran. A: 226 at 21°C Gran. B: 145 at 21°C Subgrade: 21 at 19°C		
Load	Contact radius = 13.8 cm, Contact Pressure (lift axle) = 166.6 kPa	Contact radius = 13.8 cm, Contact Pressure (lift axle) = 254.2 kPa	Contact radius = 13.8 cm, Contact Pressure (lift axle) = 325 kPa

7.2.3.2 3D-Move

Using 3D-Move, three combinations of speeds and temperatures were modeled across TT#1, TT#2 and TT#3. These include 51 °C at 45 km/h for TT#1, 6 °C at 40 km/h for TT#2 and 25 °C at 40 km/h for TT#3.

The following few paragraphs will detail sample inputs for 72 °C and 45 km/h (of which the results will not be shown). 3D-Move has the option to model the pavement structure statically or dynamically. For the purposes of this assessment, dynamic modelling will be employed, as shown in Figure 7.9.

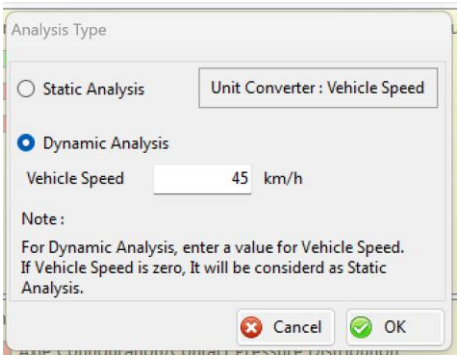


Figure 7.9 Setting the dynamic modelling features in 3D-Move.

One of the major inputs for 3D-Move is the pavement contact stress distribution type. There are several options provided in the software, and the one that was selected was “Option B: User-Selected Pre-Defined

Axle/Tire Configuration (Uniform Pressure)". This was selected since it will be able to use similar inputs to that in KENPAVE, and also it was the option that could accommodate this specific truck testing scenario the best.

One of the key inputs in this section is looking for the breaking friction coefficient. A study by Liu et al. [80], was referred to as they provided braking friction coefficients for dry and wet asphalt concrete as a function of various sliding velocities or speeds. Figure 7.10 shows braking friction coefficients for 40 km/h and 45 km/h as per the chart. The final extracted braking coefficient values can be seen in Table 7.3.

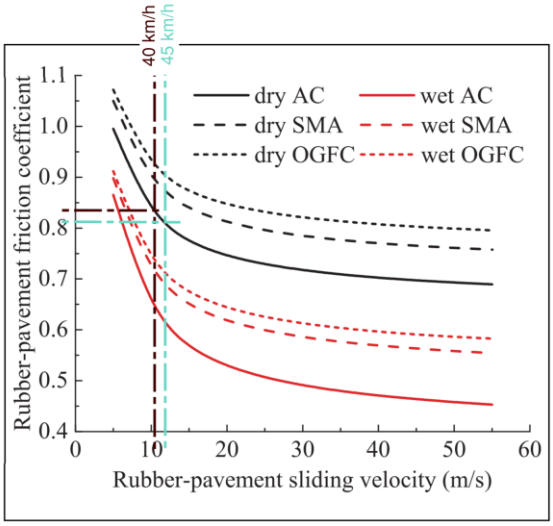


Figure 7.10 Braking coefficient determination (modified from [80]).

Table 7.3 Extracted braking Coefficients for Input into 3D-Move

Speed (km/h)	Braking Coefficient
40	0.84
45	0.82

Other inputs in this section include the tire pressure, the tire load (calculated by dividing the truck/axle weights by the number of tires) and also the axle spacing. An example of the completed inputs can be seen in Figure 7.11 for the left axle example at 72 °C at 45 km/h.

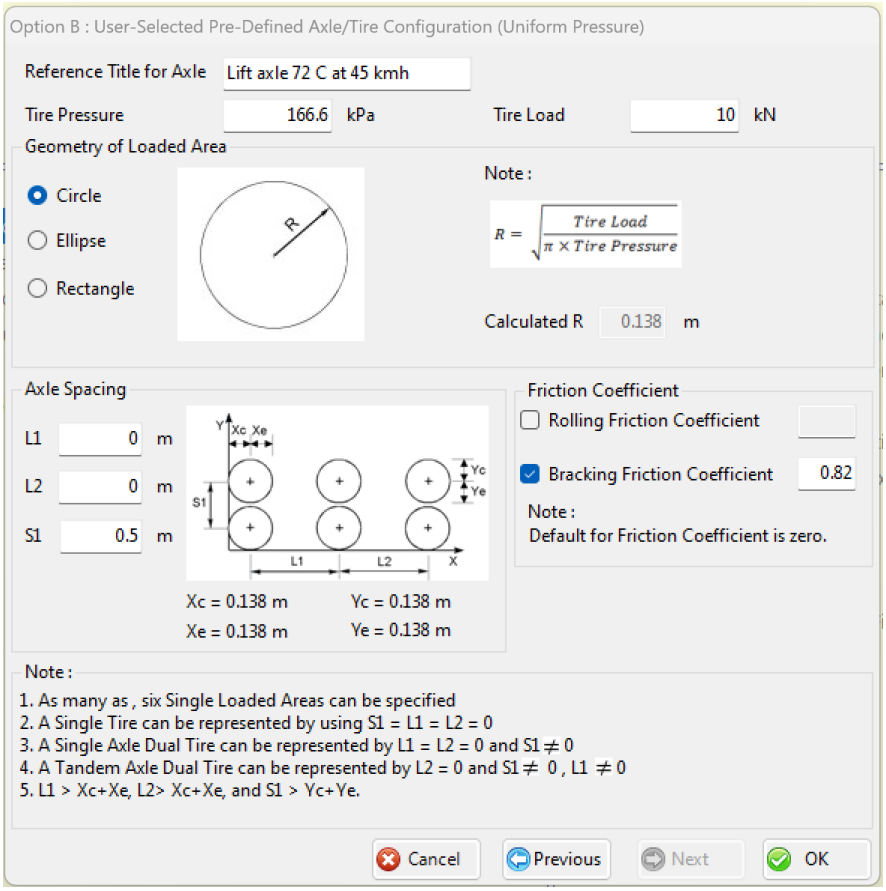


Figure 7.11 Sample input of the pavement contact stress distribution for 72 C at 45 km/h.

The next input parameters are those for vehicle suspension and road roughness. The 3D-Move software utilizes a metric known as the Dynamic Load Coefficient, or DLC. The DLC is a common metric for characterizing the dynamic loads generated by axles, indicating the magnitude of dynamic variation in axle load for specific combinations of road roughness and speed. Average values for the DLC range between 0.05 to 0.3 and smaller values indicate a smoother road, as mentioned in Buhari et al. [81].

Within 3D-Move, an airbag suspension was selected since it seemed to correspond the closest to the suspension type of the trucks used in the truck test. The data source selected was Woodrooffe and LeBlanc (1986, 1995) and road roughness will be selected as smooth for TT#1 and average for TT#2 and TT#3. This is expressed in the 3D-Move software as shown in Figure 7.12.

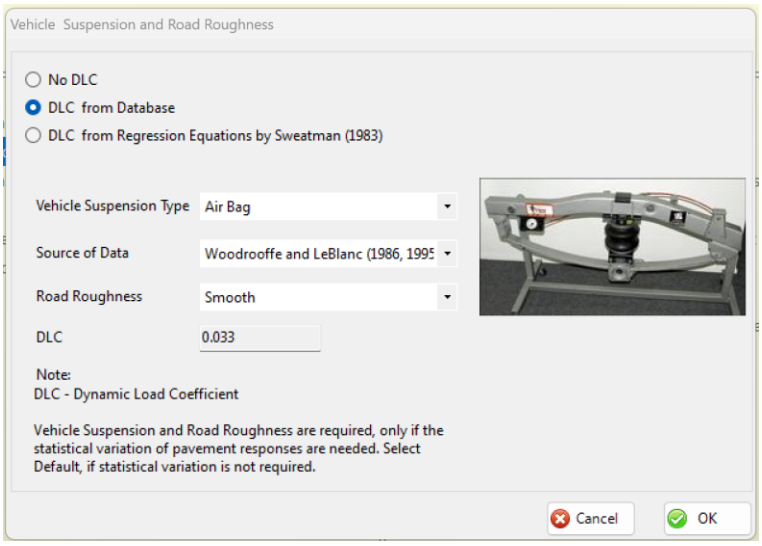


Figure 7.12 Sample of the DLC determination in 3D-Move.

The pavement structure was inputted as shown in Figure 7.13.

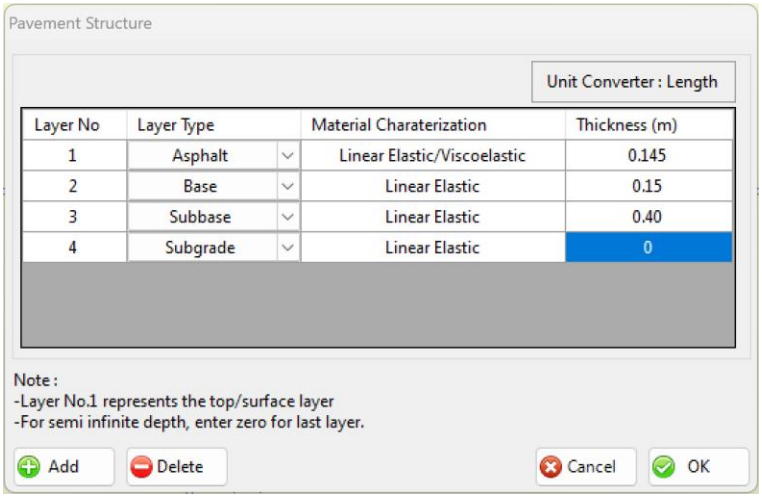


Figure 7.13 Pavement structure inputs in 3D-Move.

The following steps consist of inputting the parameters for the various layers. Figure 7.14 to Figure 7.17 show the inputs for the HMA layer. Key inputs include the implementation of the dynamic modulus values and the phase angles as obtained from the dynamic modulus test. The Poisson's ratio is also implemented from the MTO's Default Parameters for MEPDG [79]. Next, the binder properties are able to be inputted in a variety of formats. Since the Superpave information for the HMA layer was available, Input 2 was used, and the PG 58-28 grade was inputted. Finally, the unit weight of the material was inputted, which was obtained from [79]. After some experimentation with the software, the reference temperature in Figure 7.14 was determined to be 72 ℃ and the analysis temperature in Figure 7.17 was determined to be 21 ℃.

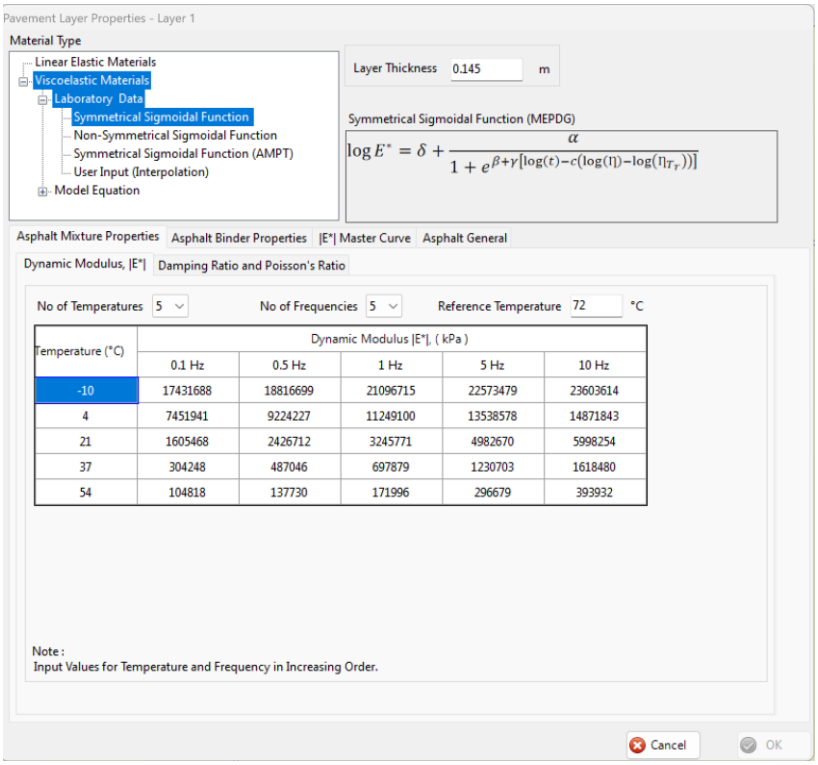


Figure 7.14 Input of dynamic modulus values in 3D-Move.

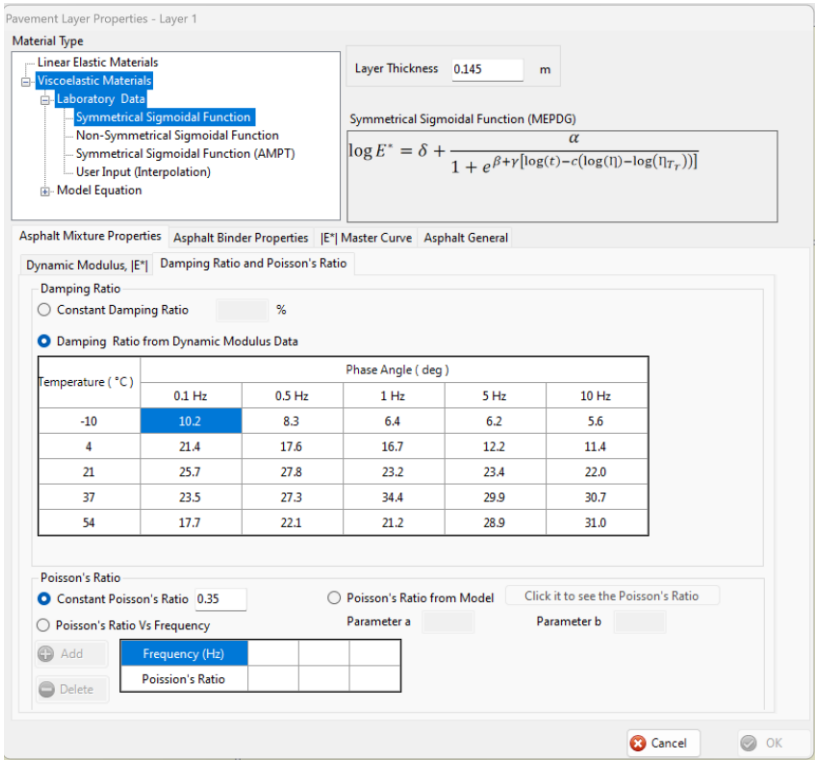


Figure 7.15 Input of phase angle and Poisson's Ratio values in 3D-Move.

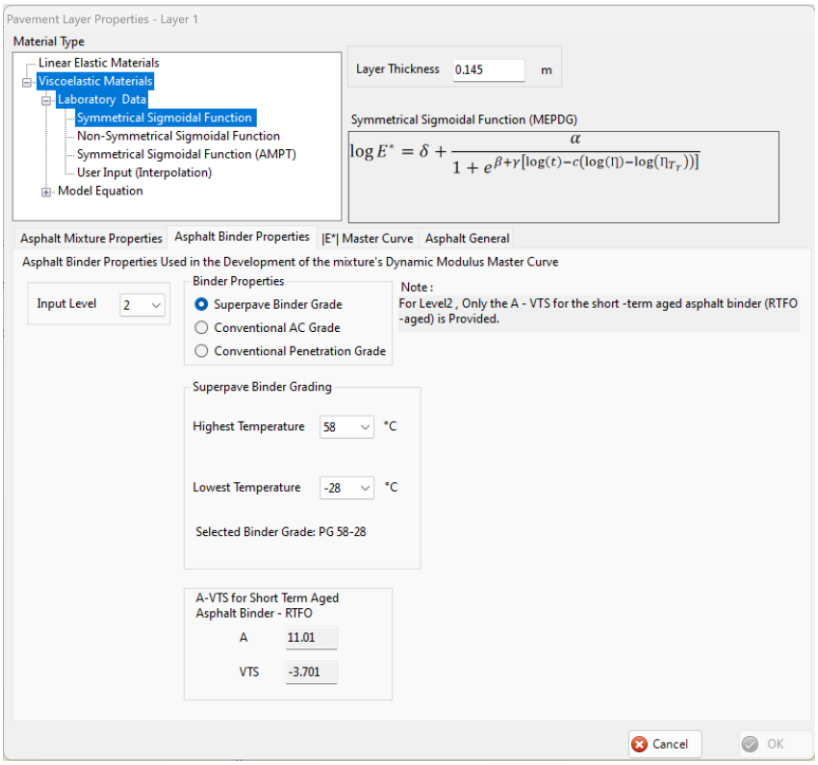


Figure 7.16 Input of HMA Superpave values in 3D-Move.

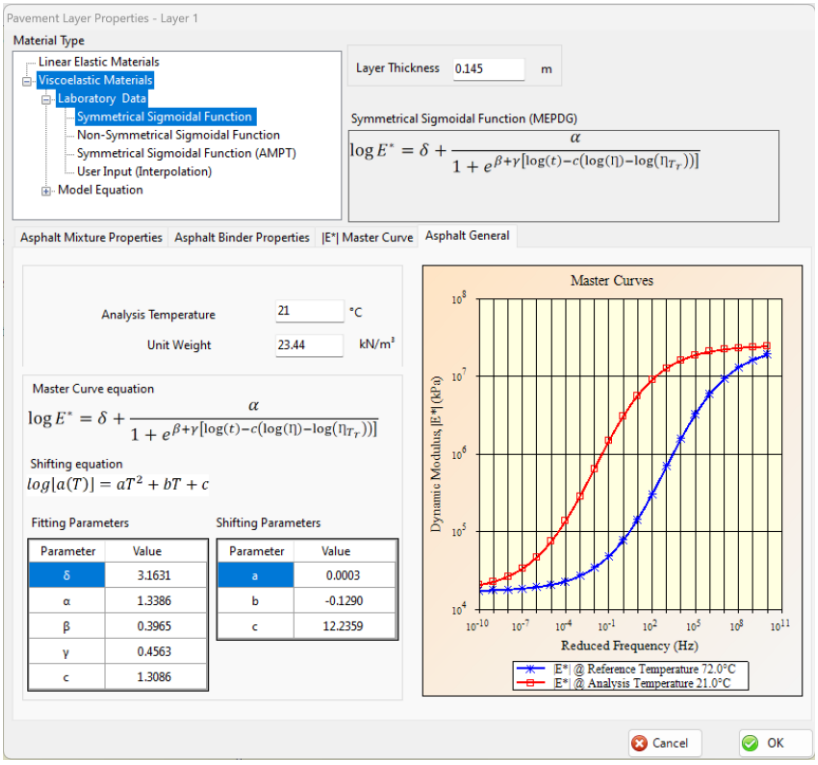


Figure 7.17 Input of unit weight and analysis temperature values in 3D-Move.

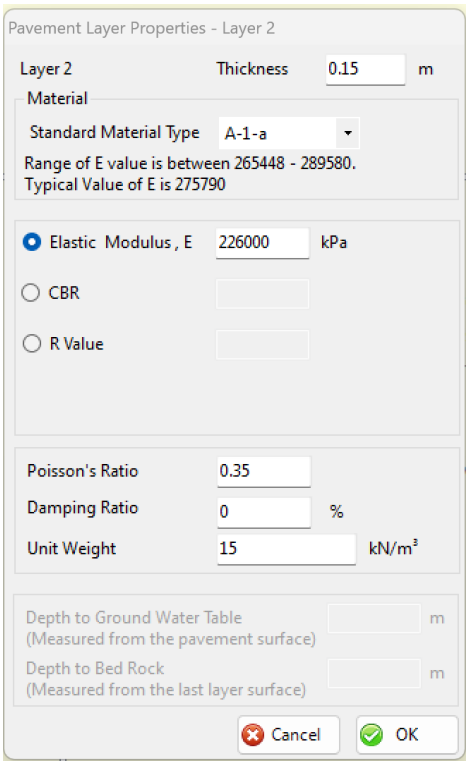


Figure 7.18 Input of Granular A values in 3D-Move.

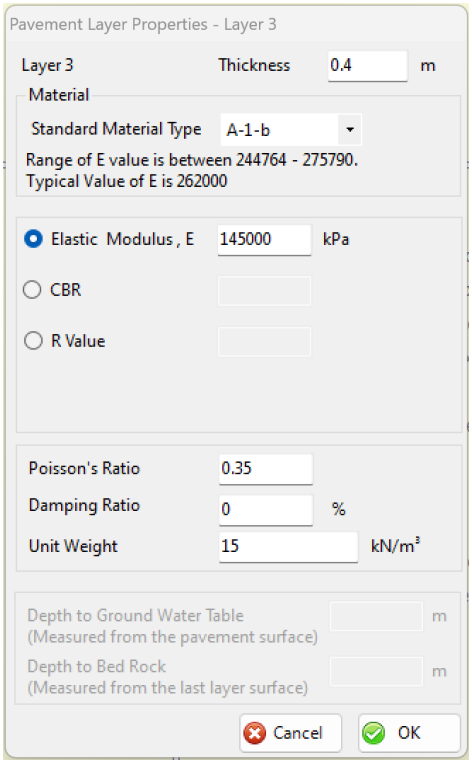


Figure 7.19 Input of Granular B values in 3D-Move.

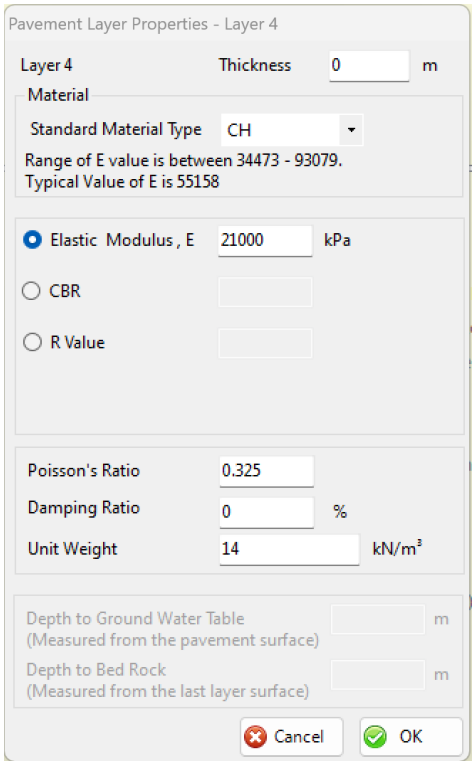


Figure 7.20 Input of subgrade values in 3D-Move.

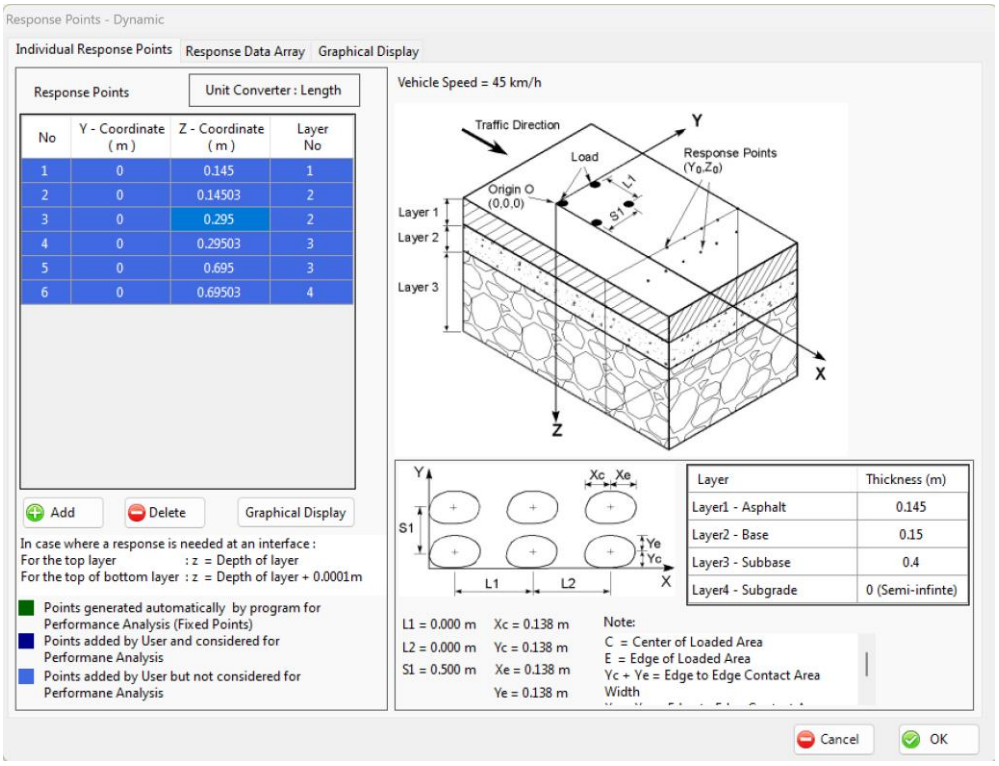


Figure 7.21 Input of analysis points values in 3D-Move.

Figure 7.18 to Figure 7.20 show the inputs for the base, subbase and subgrade layers, which are the same as inputs for the KENPAVE simulation. The standard material types were determined from [79], such as the CH designation (medium to high plasticity clays) for the subgrade. The unit weights for the various layers were determined from database values from [82]. Finally, as shown in Figure 7.21, the various analysis points were inputted into the software.

A summary of the input parameters for 3D-Move can be seen in Table 7.4.

Table 7.4 3D-Move Input Parameters Summary

Parameter	**TT#1 Fall Conditions**	**TT#2 Early Spring Conditions**	**TT#3 Summer Conditions**
Speed	45 km/h	40 km/h	40 km/h
Load Type	Option B: Uniform Pressure		
Tire Pressure (kPa)	166.6	254.2	325
Tire Load (kN/tire)	10	15.25	19.5
Axle Spacing	L1 = 0, L2 = 0, S1 = 0.5 m		
Braking Friction Coefficient	Varies based on speed (e.g., 0.82) → see Table 7.3		
Geometry of Loaded Area	Circle		
Vehicle Suspension and Road Roughness			
Type	Air Bag		
Source of Data	Woodrooffe and LeBlanc (1986, 1995)		
Road Roughness	Smooth		
DLC	0.033	0.04	
Layers	Asphalt, Base, Subbase, Subgrade		
Layer Thickness (m)	Asphalt: 0.145; Base: 0.150; Subbase: 0.40; Subgrade: 0		
Asphalt Layer Properties	Unit Weight = 2390 kg/m3 (23.44 kN/ m^3) [79], Reference Temp = 21°C Asphalt Binder=Input Level 2, PG58-28		
Analysis Temp (°C)	51	6	25
Base Layer Properties	A-1-a, E=226000 kPa, Poisson's Ratio = 0.35, Unit Weight = 15 kN/m^3 [82]		
Subbase Layer Properties	A-1-b, E=145000 kPa, Poisson's Ratio = 0.35, Unit Weight = 15 kN/m^3 [82]		
Subgrade Layer Properties	CH, E=21000 kPa, Poisson's Ratio = 0.325, Unit Weight = 14 kN/m^3 [82]		
Response Points – Dynamic (m)	Y-coord. = 0; X-coord. = 0.145, 0.14503, 0.295, 0.29503, 0.695, 0.69503		

7.3 Results and Discussion

Using the previously presented loading information, material properties, and axle configurations, results from both KENPAVE and 3D-Move software were utilized to compare:

1) asphalt tensile strains measured by the asphalt strain gauges at the bottom of the HMA layer with minor principal strain results in KENPAVE and normal strain in the Y-Y direction at the bottom of the asphalt layer in 3D-Move, and

2) the pressure measured by TEPCs in the top of base, subbase, and subgrade layers to vertical stress results in KENPAVE and normal stress in the Z-Z direction within each of the base, subbase, and subgrade layers in 3D-Move.

7.3.1 KENPAVE Results

With respect to the static nature of the analysis in KENPAVE, numerical output values (obtained from the points directly beneath the centre of the tire, or point 2 from Figure 7.7) were compared to maximum values extracted from dynamic pressure and strain behaviours obtained from the field based on the lift axle results at 40 or 45 km/h depending on the truck test/season.

Table 7.5 to Table 7.7 demonstrate the results of the stress and strain for each of the truck tests. Comparing the simulated KENPAVE results to the field results, there are several key observations that are noticeable.

Table 7.5 Average Compressive Stress/Pressure and Strain Results during TT#1 (Fall)

Metric	Field	KENPAVE	Percent Error
Compressive Stress/Pressure Top of Base (δ_c) [kPa]	25.90	31.650	18.2%
Compressive Stress/Pressure Top of Subbase (δ_c) [kPa]	63.51	15.915	-299.1%
Compressive Stress/Pressure Top of Subgrade (δ_c) [kPa]	9.76	3.631	-168.8%
Tensile Strain Bottom of Surface Layer (ε_t) [με]	139.74	-0.0000557	100%

Table 7.6 Average Compressive Stress/Pressure and Strain Results during TT#2 (Spring)

Metric	Field	KENPAVE	Percent Error
Compressive Stress/Pressure Top of Base (δ_c) [kPa]	11.37	48.292	76.5%
Compressive Stress/Pressure Top of Subbase (δ_c) [kPa]	21.21	24.283	12.7%
Compressive Stress/Pressure Top of Subgrade (δ_c) [kPa]	16.18	5.540	-192.1%
Tensile Strain Bottom of Surface Layer (ε_t) [με]	25.36	-0.000085	100%

Table 7.7. Average Compressive Stress/Pressure and Strain Results during TT#3 (Summer)

Metric	Field	KENPAVE	Percent Error
Compressive Stress/Pressure Top of Base (δ_c) [kPa]	42.27	61.742	31.5%
Compressive Stress/Pressure Top of Subbase (δ_c) [kPa]	50.39	31.046	-62.3%
Compressive Stress/Pressure Top of Subgrade (δ_c) [kPa]	5.49	7.083	22.5%
Tensile Strain Bottom of Surface Layer (ε_t) [με]	46.95	-0.000109	100%

Looking at the results for TT#1, it can be recognized that KENPAVE's pressure and strain results underestimate the in-situ results at the presumed contact pressures. While the results of the base are relatively similar, the deviations really begin to occur in the subbase layer, where the field measurements are significantly larger than the KENPAVE predications. In actuality, the KENPAVE results make sense theoretically since the pressure impact should decrease going deeper within a pavement structure, however this anomaly has been recognized in several other Chapters of this thesis, therefore the field results here are not surprising. In any case, the field results are elevated, especially the tensile strain field measurement. Such discrepancy can be attributed to several factors including the non-uniform temperature gradient of the newly compacted HMA layer (immediately post-construction), changes in the tire-pavement interaction and footprint at elevated temperatures while the matt was cooling down from the compaction temperature, and the inherent adjustment of instrumentation right after installation in the pavement structure.

Similar conclusions can be developed from the results from TT#2, however, in this case the base field results are overestimated in KENPAVE, while the subbase and subgrade are underestimated. This is interesting and could point to a measurement discrepancy in the field results. However, TT#2 does take place in early spring conditions, which would result in lower pressure results as confirmed in previous

sections of this thesis, along with a relatively high pressure applied to the subgrade layer. KENPAVE cannot take this temperature gradient into consideration if the material properties are not accommodated to seasonal variations. Therefore, it makes sense why the software might assume a higher value for the base pressure estimate.

Finally, TT#3 presents similar trends to TT#2, but in general the results are greater than those in TT#2 since these results are captured during warm summer months. In general, KENPAVE provides a good reference point for comparison of field data to see how it compares to a theoretically derived set of material responses in the various layers of the pavement structure. However, for this particular project, the software under- or over-estimates values and does not take the multitude of other factors that result in the strain/pressure results that are obtained in the field, such as weather, material property fluctuations, moisture, etc.

7.3.2 3D-Move Results

3D-Move can generate the dynamic response curves, and hence results could be directly compared with the measured dynamic responses from the field experiments.

Figure 7.22 and Figure 7.23 show some of the results of this assessment, both for 51°C at 45 km/h and 6 C at 40 km/h. The software ceased to function prior to the results for the summer test were obtained.

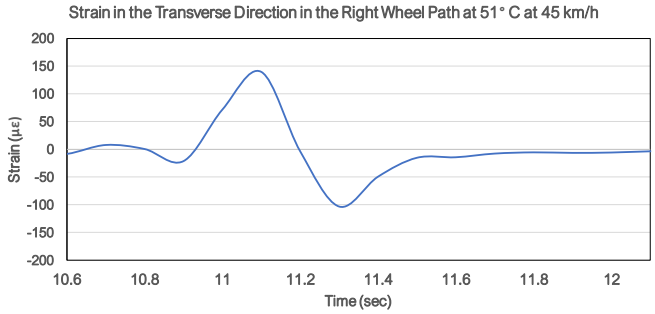
Looking first at Figure 7.22, there are some comparisons that can be made with regards to the shape and the magnitude of the responses within 3D-Move in comparison to the field results. The software underestimates the fall/construction-related dynamic strain responses at 51°C. For instance, in the field, the tensile strain in the field was measured to have a maximum value of almost 140 με, while the 3D-Move response peaks at about -15 με for the Y-Y normal strain response. In the base layer, the field pressure response peaks at about 26 kPa, while that simulated by 3D-Move peaks at 20 kPa. The subbase layer is underestimated by the software, with the field results being around 63 kPa, and the response by 3D-Move peaks at approximately 12 kPa. Finally, the subgrade response in the field is about 10 kPa while the response in 3D-Move peaks at about 3.3 kPa.

It is clear that the dynamic response magnitudes to not accurately model the responses obtained in the field. The shapes of the responses are generally similar, except for the responses for tensile strains in the field as compared to the response obtained in 3D-Move.

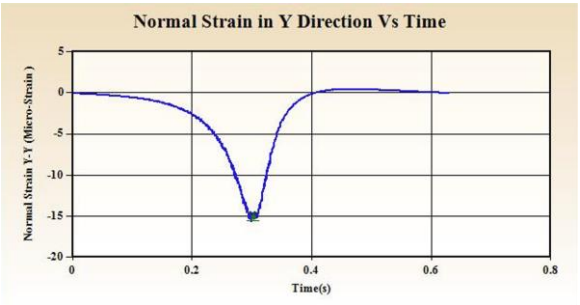
However, the pressure magnitudes obtained between 3D-Move and KENPAVE are comparable, with the responses being: 26 kPa vs 32 kPa, 12 kPa vs 16 kPa, and 3 kPa vs. 4 kPa, in the base, subbase and subgrade, respectively. The strain magnitudes are not comparable between the two software, and 3D-

Move predicts strain magnitudes more realistically than KENPAVE, likely as a result of its ability to consider dynamic load factors.

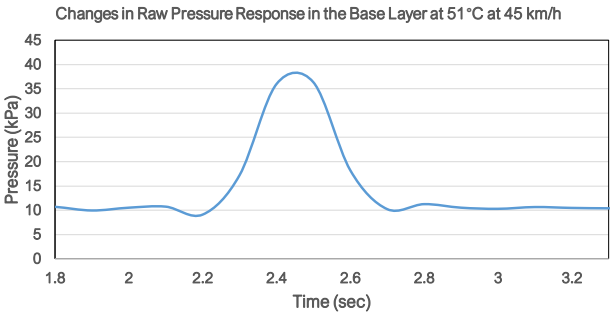
Field Dynamic Response	3D-Move Dynamic Response



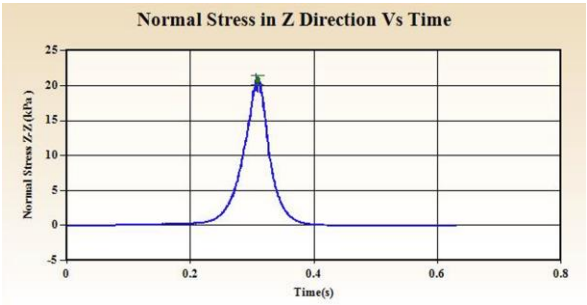
d) Field strain results at the bottom of the HMA layer based on 51 °C at 45 km/h.



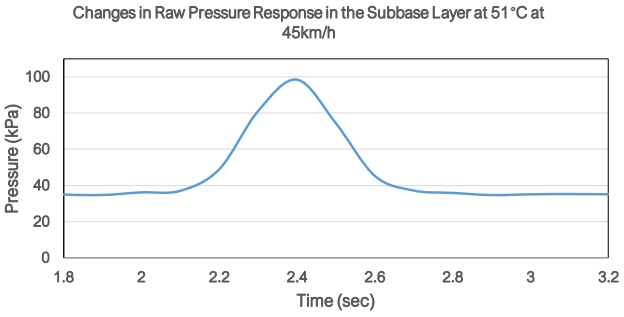
b) 3D-Move normal strain response in the Y-Y direction based on 51 °C at 45 km/h.



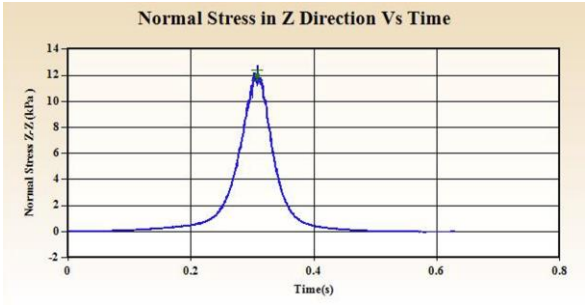
c) Field pressure results at the top of the base layer based on 51 °C at 45 km/h.



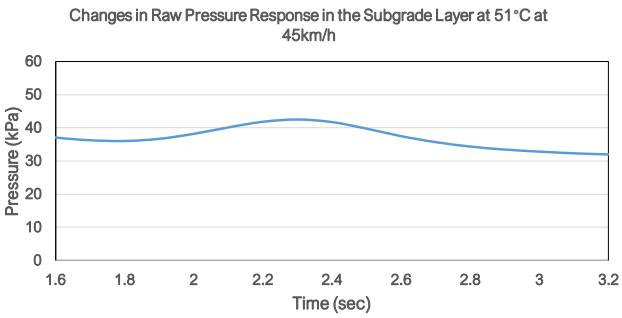
d) 3D-Move normal stress response in the Z-Z direction in the base layer based on 51 °C at 45 km/h.



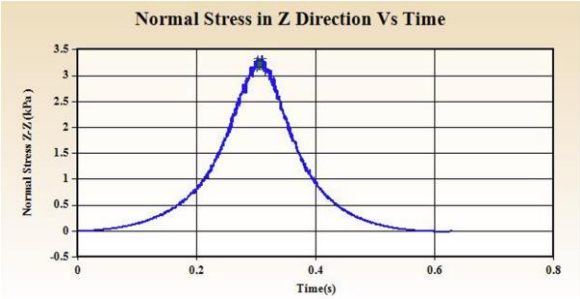
e) Field pressure results at the top of the subbase layer based on 51 °C at 45 km/h.



f) 3D-Move normal stress response in the Z-Z direction in the subbase layer based on 51 °C at 45 km/h.



g) Field pressure results at the top of subgrade based on 51 °C at 45 km/h.



h) 3D-Move normal stress response in the Z-Z direction in the subgrade layer based on 51 °C at 45 km/h.

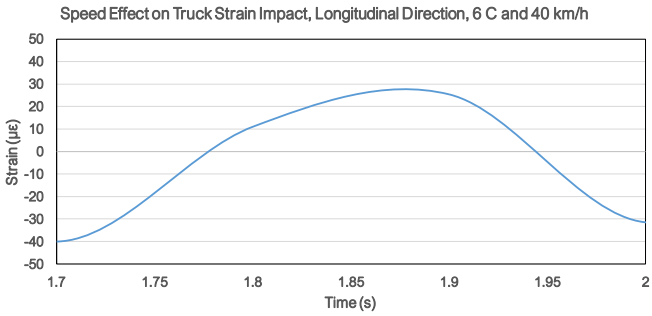
Figure 7.22 Normal tensile strain and compressive stress results in the field and 3D-Move for 51°C and 45 km/h.

Looking at Figure 7.23, there are some similar and varying trends that appear within this data. The tensile strain in the field was measured to have a maximum value of about 25 με, which is similar to the almost 30 με simulated by 3D-Move. In this case, the shape of the strain response is also simulated in the same direction, which indicates similar tensile/compressive response estimation by 3D-Move, although it still overestimates the field response. In the base layer, the field response was about 11.37 kPa, compared to a peak response of about 18 kPa from 3D-Move, again, an overestimate. The field response for the subbase layer is about 21 kPa and the response from 3D-Move is about 12 kPa. In this case, the response was underestimated by the software. Finally, the field response for the subgrade is about 6 kPa, compared to 16 kPa estimated by 3D-Move.

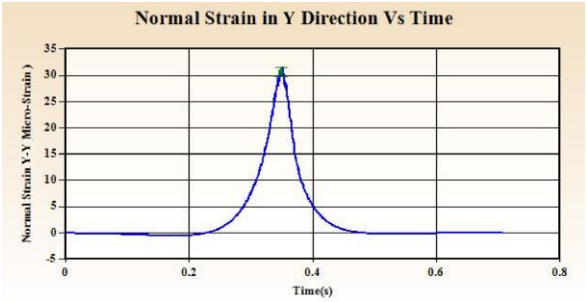
The dynamic response magnitudes better model the responses obtained in the field as compared to the responses obtained for TT#1 since they are modelling more reasonable temperatures (not construction conditions). The shapes of all of the responses are generally similar.

Again, the pressure magnitudes obtained between 3D-Move and KENPAVE are comparable, with the responses being: 18 kPa vs 48 kPa, 12 kPa vs 24 kPa, and 5 kPa vs. 5.5 kPa, in the base, subbase and subgrade, respectively. Again, the strain magnitudes are not comparable between the two software, and 3D-Move predicts strain magnitudes more realistically than KENPAVE, likely as a result of its ability to consider dynamic load factors.

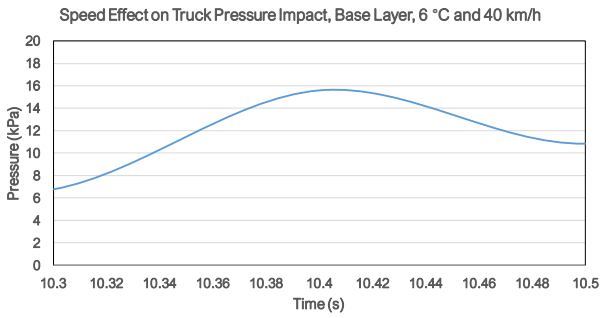
Field Dynamic Response	3D-Move Dynamic Response



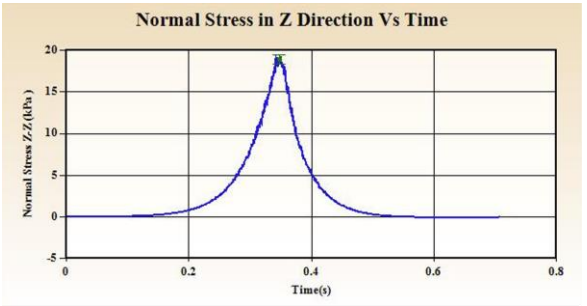
e) Field strain results at the bottom of the HMA layer based on 6 °C at 40 km/h.



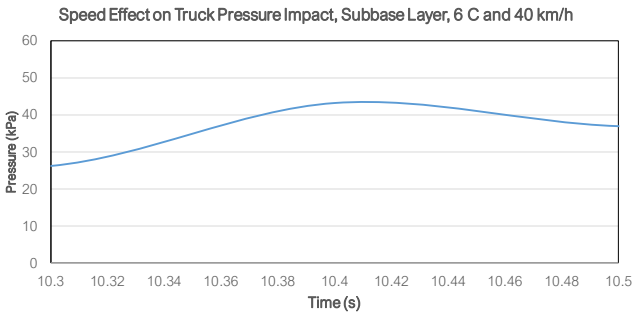
b) 3D-Move normal strain result in the Y-Y direction based on 6 °C at 40 km/h.



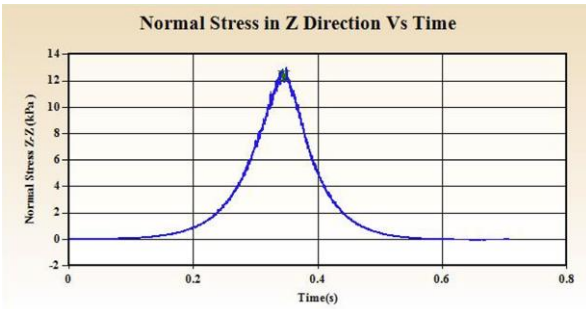
d) Field pressure results at the top of the base layer based on 6 °C at 40 km/h.



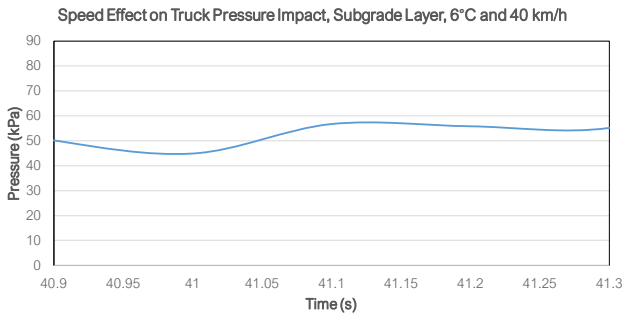
d) 3D-Move normal stress result in the Z-Z direction in the base layer based on 6 °C at 40 km/h.



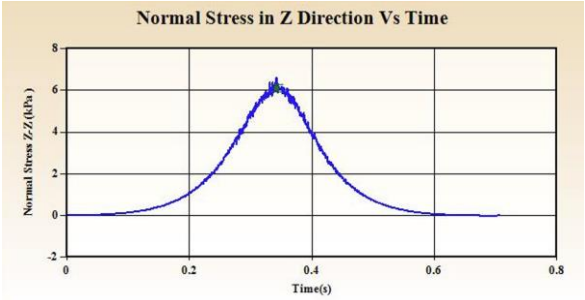
f) Field pressure results at the top of the subbase layer based on 6 °C at 40 km/h.



f) 3D-Move normal stress result in the Z-Z direction in the subbase layer based on 6 °C at 40 km/h.



h) Field pressure results at the top of subgrade based on 6 °C at 40 km/h.



h) 3D-Move normal stress result in the Z-Z direction in the subgrade layer based on 6 °C at 40 km/h.

Figure 7.23 Normal tensile strain and compressive stress results in the field and 3D-Move for 6°C and 40 km/h.

7.4 Key Takeaways

This study compares static and dynamic pavement analysis methods by correlating simulation results with real in-situ measurements from an instrumented pavement section, utilizing KENPAVE and 3D-Move software. The first set of truck tests (TT#1) provided a unique insight about the pavement responses right after construction. In terms of analysis, considerable discrepancies were observed between the software results and field data. Both tools showed improved accuracy after five months experiments (TT#2), possibly due to more stable and uniform viscoelastic properties as well as tire-pavement interactions that were closer to the conventional assumptions. However, 3D-Move demonstrated better precision in estimating pavement stress when field conditions resembled in-service scenarios. This approach is also capable of generating the dynamic pavement response curves which can be directly compared with the ones gathered in the field using truck testing. It is unclear what cause d the issues with the 3D-Move software prior to the testing of the summer conditions of TT#3. Continued research and validation should enhance predictive capabilities of these tools for improved pavement engineering, particularly during construction.

Chapter 8

In-Service Pavement Performance Trends

This Chapter focuses on trends observed in environmental and traffic load data collected from the Courtland Avenue instrumented test section since the full deployment of the DAC system, including sensor installation, power supply, and initial calibration. The primary goal is to evaluate sensor effectiveness by analyzing the data for meaningful insights and verifying their reliability. The term "performance" is used as a general term to describe the results obtained from moisture and temperature sensors, and the responses obtained from the load sensors.

8.1 Environmental Load Data Analysis

Temperature and moisture are critical factors affecting a pavement section's load-bearing capacity and structural integrity [18] [83] [63]. A pavement structure is susceptible to dynamic changes in temperature and moisture even within a period of 24 hours [84]. Fluctuations can arise from changes in moisture content, often induced by rainfall, as well as temperature gradients experienced throughout the day. Additionally, variations in the water table level, daily temperature changes, and the impacts of freeze-thaw cycles all play substantial roles in contributing to the dynamic responses and performance of the pavement structure [84]. These environmental and climatic influences can collectively impact the mechanical properties and performance of the pavement structure over short or long time frames [84].

For example, the interplay of moisture and traffic loading, particularly on wet pavement, reduces the pavement dynamic modulus [63]. Furthermore, fluctuations in asphalt temperature exert a substantial influence on the stiffness of both bound and unbound layers. Higher asphalt temperatures, for instance, lead to a softening of the asphalt material, contributing to increased horizontal strains at the bottom of the asphalt layers [63], a key location for fatigue cracking to begin and propagate. Changes in moisture content in the base and subgrade soils impact the stiffness of these pavement components. Excessive moisture reduces the resilient modulus of unbound layers, leading to increased strains in the asphalt bound layers due to poorer support [63]. This strain is particularly substantial in cold regions where pavements often become saturated during spring thaw, causing a decrease in stiffness modulus in granular layers [63]. Therefore, it is essential to assess the impact of these environmental variables across the various layers of the pavement structure, as doing so can provide insights into how these variables will contribute to pavement degradation over time.

As outlined in Chapter 3, temperature and moisture sensors have been strategically placed at various depths throughout all pavement layers. The asphalt layer is equipped with two temperature probes to

measure its temperature at three different depths (12.7 mm, 76.2 mm, and 190.5 mm below the first lift of asphalt pavement which is a 145 mm thick SP 19 layer). Note that although the bottommost sensors of the temperature probes are technically within the base layer, their proximity to the asphalt layer and integration into the probes categorize them as part of the asphalt layer measurements. In addition to the temperature probes, the base layer incorporates two temperature thermistors, while the subbase layer and subgrade layer each have three and two, respectively. Similarly, there is one moisture sensor in the base layer, three in the subbase layer, and one in the subgrade layer. This comprehensive sensor deployment enables the evaluation of temperature and moisture effects across the entire pavement structure.

The following two sections will describe the temperature and moisture trends from the past several months.

8.1.1 Temperature - Layer Profile Over Time

The temperature profiles for the test section are expressed from Figure 8.1 to Figure 8.7. Each successive figure illustrates temperature trends over progressively longer time spans, starting from one day and extending to several months.

Firstly, Figure 8.1 shows the aggregated temperature profile over a period of 24 hours, from midnight of March 9th, 2023, to midnight of March 10th, 2023. Initially, trend data for all sensors was aggregated to every 5 minutes until June 2023, after which it was aggregated to every 15 minutes to streamline the volume of data. Within Figure 8.1, separate charts are dedicated to the sensors in each layer, including asphalt pavement (HMA) layer temperatures, base layer temperatures, subbase layer temperatures, and subgrade layer temperatures. In the case of this figure, all of the temperature sensors are included to observe the trends.

Looking at the figure, it appears that the sensors in the TEMP-01 temperature probe produce erratic temperature measurements, as they range between approximately -40 °C to about 80 °C. Comparing these readings with those from other sensors, especially the other temperature probe, suggests that TEMPS-01 might be malfunctioning, providing inaccurate temperature results. It is quite unlikely that ambient temperatures during March in Ontario would reach these extremes as per Canadian historical climate data [85]. Consequently, this sensor was removed to assess whether the temperature trends would improve. Temperature trends for this sensor will continue to be monitored over longer time spans to observe whether the erratic trends persist.

The outcomes, as depicted in Figure 8.2, show more coherent temperature data. In this scenario, temperatures fall within a reasonable range of 0 °C to 10 °C. Notably, the trends within various layers are clearer and more sensible and align well with ambient data. The ambient temperature data is sourced from

Environment Canada's historical climate data repository [85]. For example, in the HMA layer, temperature fluctuations are more pronounced than in other layers and decrease as one moves deeper into the pavement structure. Upon reaching the subgrade layer, temperature fluctuations over a 24-hour period are minimal, in line with the expectation that changes in ambient temperature would require more time to influence the subgrade temperature [86].

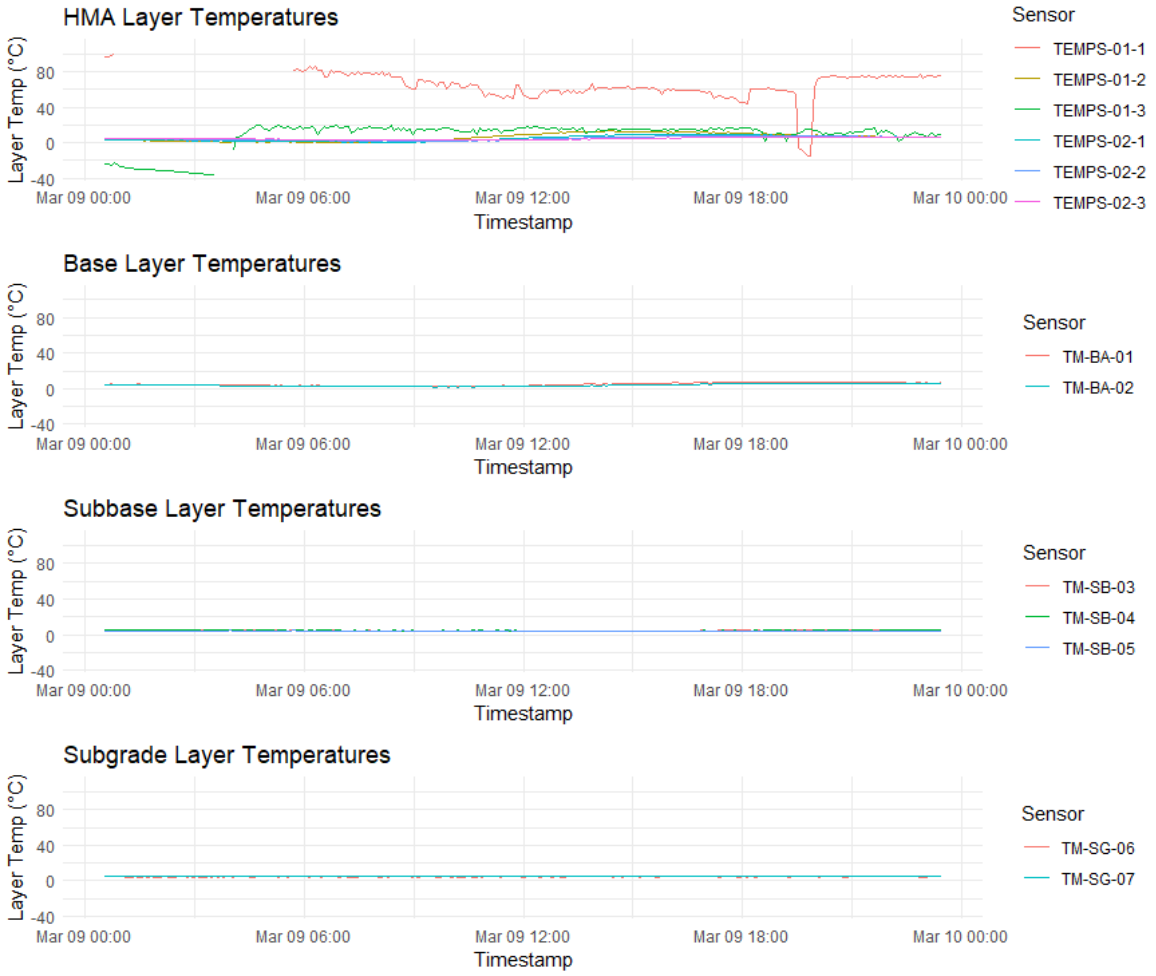


Figure 8.1 Aggregated temperature profile from March 9th, 2023, to March 10th, 2023, including all temperature sensors.

Examining the HMA layer reveals that TEMPS-02-1, positioned closest to the asphalt surface, experiences the greatest temperature fluctuation (ranging between 0 °C to 10 °C). On the other hand, TEMPS-02-2 and TEMPS-02-3 show progressively smaller fluctuations, indicating that as one moves deeper into the HMA layer, the temperature change decreases and there is not as much fluctuation. Within the base layer, the temperature fluctuation ranges between approximately 2.5 °C to approximately 7 or 8 °C, a narrower range compared to the HMA layer. Technically, the thermistors within this layer were installed at the same depth. However, TM-BA-01 records slightly higher temperatures than TM-BA-02,

suggesting a potential difference in sensor depth. Confirmation would require excavation or other methods to precisely determine sensor positions. In the subbase layer, all three thermistors exhibit temperatures within the range of 4 to 6 °C. This consistency is intriguing, considering the substantial thickness of the subbase layer at 400 mm and the separation of the moisture sensors from each other. Despite being further apart, the sensors display a uniform temperature fluctuation trend for the entire layer. Lastly, the subgrade layer displays minimal variation in temperature over a 24-hour period. Both thermistors fluctuate around 5 °C, indicating limited change during this timeframe.

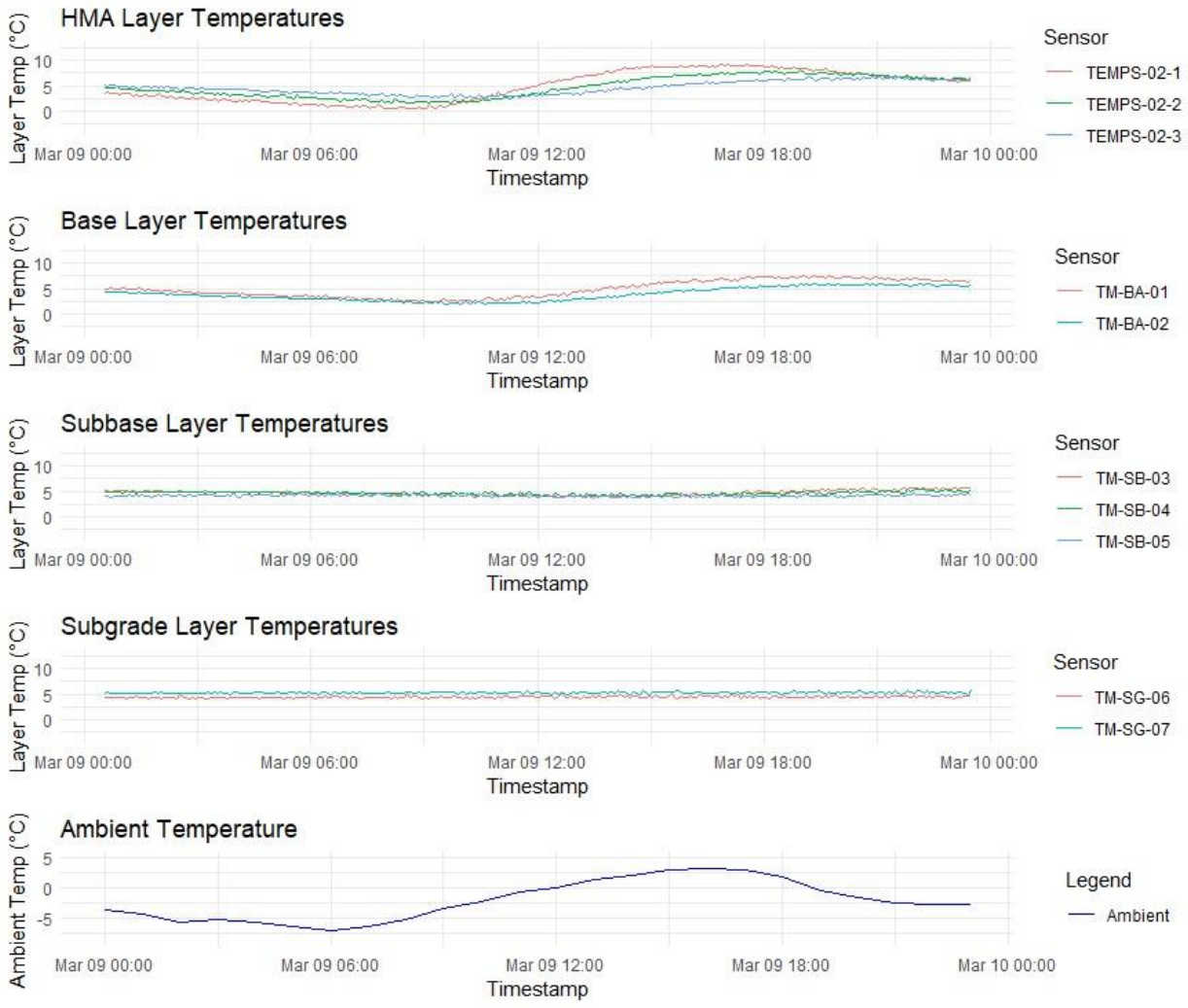


Figure 8.2 Aggregated temperature profile from March 9th, 2023, to March 10th, 2023, not including the TEMPS-01 temperature probe for easier visibility of trends.

In Figure 8.3, the temperature variations over a 48-hour period, specifically from midnight on March 8th, 2023, to midnight on March 10th, 2023, are illustrated. Since the data for TEMPS-01 was still erratic, it was excluded from this time duration, so only TEMPS-02 is plotted over 48 hours. Figure 8.3 confirms many of the trends observed in the 24-hour plots from Figure 6.2, simply expanded over two days.

Notably, the HMA layers exhibit greater temperature fluctuations compared to the lower granular layers and the subgrade layer, that has very minimal fluctuations.

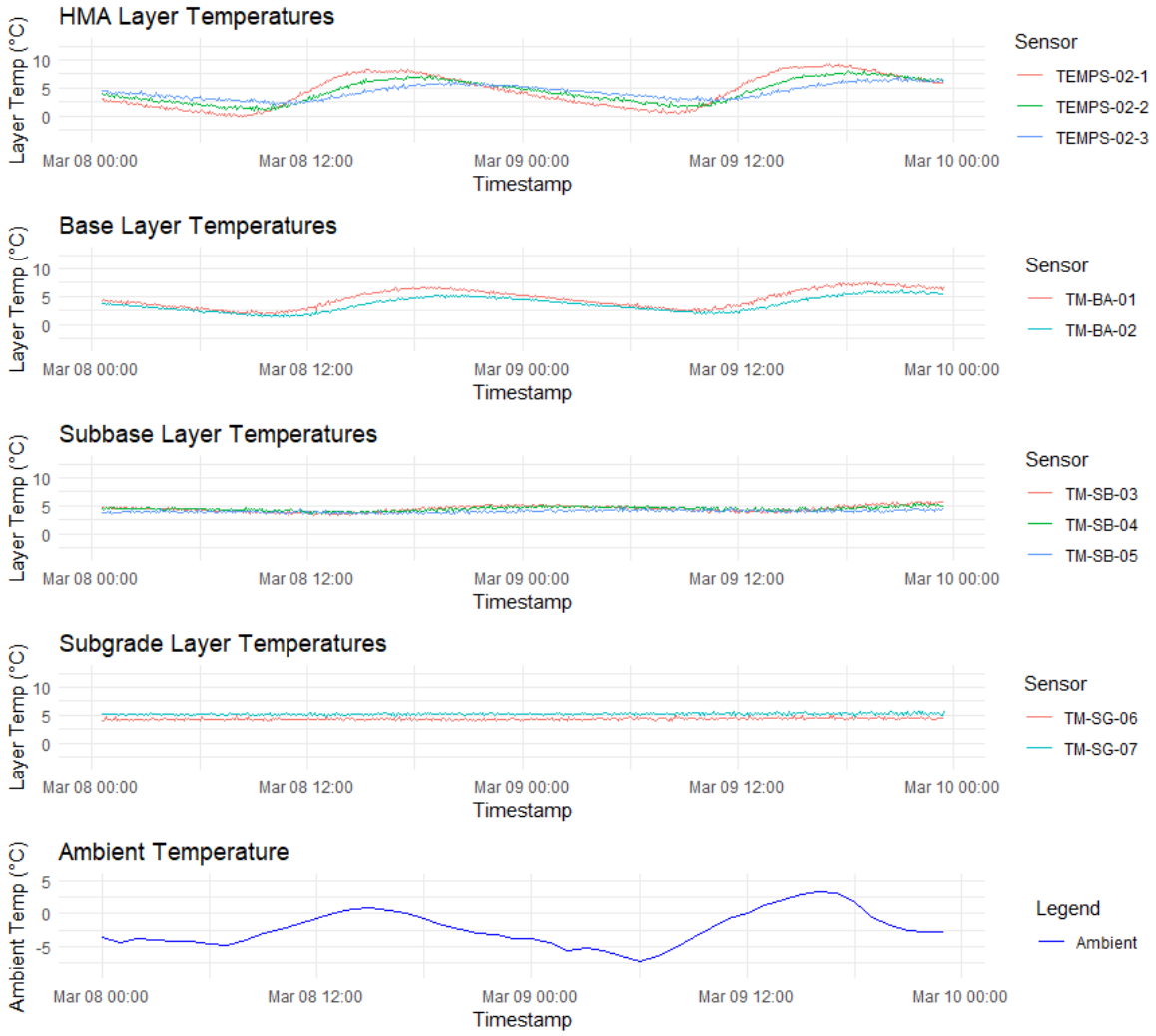


Figure 8.3 Daily temperature variation over two days (midnight March 8th to midnight March 10th, 2023) which shows the typical times for peak asphalt and granular temperatures.

The plot offers valuable insights into the temperature variations in both the asphalt and granular layers. Typically, the asphalt reaches its highest temperature in the afternoon, peaking between noon and 4:00 or 5:00 PM, while the coolest times are generally observed between 6:00 and 10:00 AM. Figure 8.3 also includes four charts illustrating the temperatures in each layer, along with the ambient temperature over the same timeframe The ambient temperature closely mirrors the sensor-recorded temperatures, indicating that the sensors effectively capture temperature fluctuations during peak and off-peak times. It is worth mentioning that, during the period from midnight on March 8th, 2023, to midnight on March 10th, 2023, the ambient temperature ranged from a maximum of 3.3 °C to a minimum of -7.2 °C.

Since the ambient temperature is slightly lower than those of the asphalt layer, it is crucial to consider that asphalt layers typically store heat, resulting in them being generally warmer than ambient temperatures [87]. It is also important to note that the temperature fluctuations in these layers may not precisely synchronize with changes in ambient temperature. This discrepancy is attributed to a delay in the layers' process of storing and releasing heat [18] [87].

Figure 8.4 shows daily temperature variations from March 3rd, 2023, to March 15th, 2023, displaying the temperature data for all of the sensors, including TEMPS-01 temperature probe. The data from the TEMPS-01 probe appears highly erratic and lacks correlation with both ambient temperature results and the data from other sensors. Unfortunately, the sensor continues to malfunction, and the discrepancies noticed in Figure 8.1 translate over longer periods of time. In this way, we can exclude the temperature data from the TEMPS-01 sensor from the analysis from this point forward and we can conclude that this temperature probe does not function as expected.

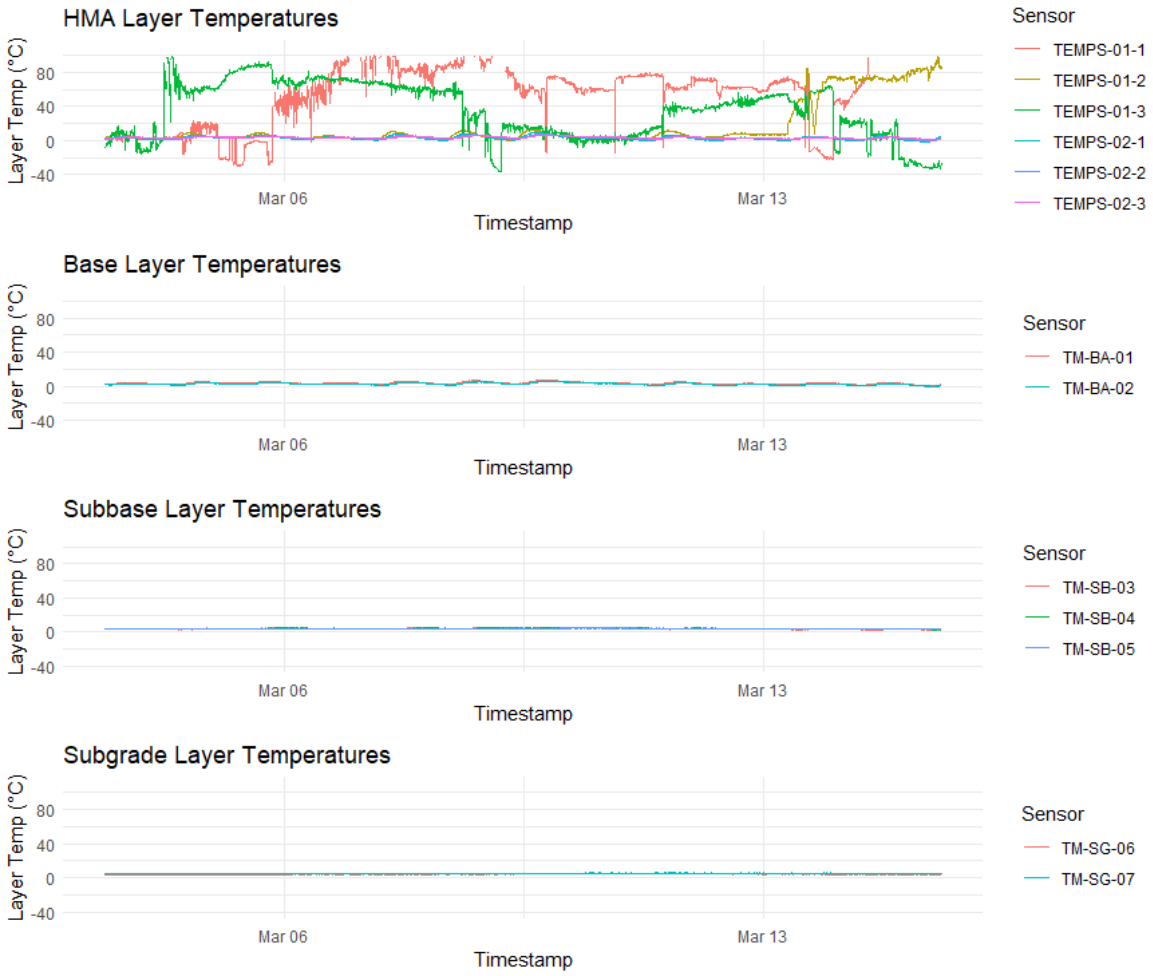


Figure 8.4 Daily temperature variations from March 3rd, 2023, to March 15th, 2023, including all temperature sensors. The erratic nature of the TEMPS-01 temperature probe data is visible in this case.

Figure 8.5 shows data within the same timeframe as Figure 8.4, but without the TEMPS-01 sensor. This timeframe allows us to discern trends in temperature over several days, and daily peaking trends are much more visible. Like Figure 8.3, the temperature data is juxtaposed against ambient temperature data sourced from Environment Canada [85].

Broadly, the temperature results from the sensors consistently align with the ambient temperature, affirming the reliable performance of the sensors over an extended period. As observed in earlier charts, the HMA layer displays the most substantial temperature fluctuations. Conversely, the base layer exhibits some variation, especially during periods of heightened temperature changes, as evident on March 9th and 10th. In contrast, the subbase and subgrade layers demonstrate comparatively minor variations, consistent with trends observed in the 24-hour and 48-hour analyses.

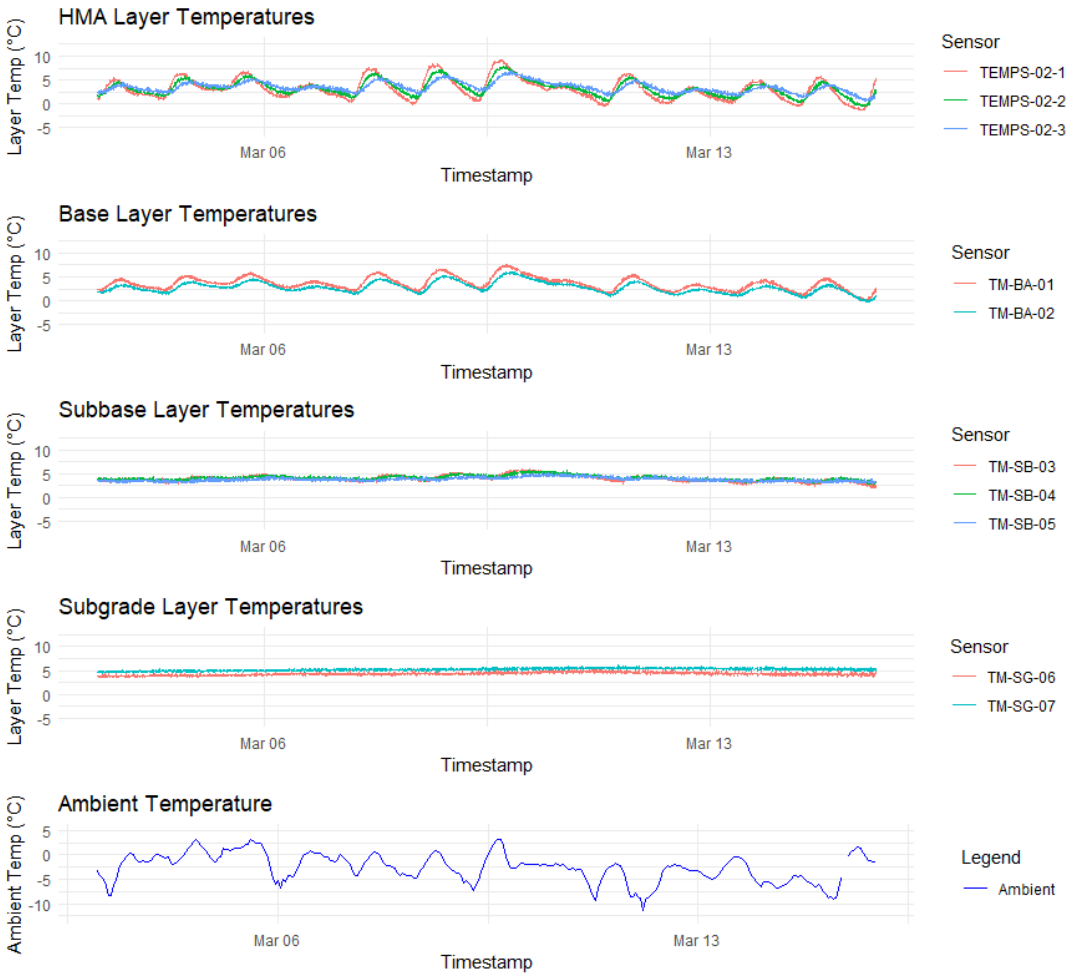


Figure 8.5 Daily temperature variations from March 3rd, 2023, to March 15th, 2023, not including the TEMPS-01 temperature probe for easier visibility of trends. Ambient temperature is also plotted.

The temperature variations throughout the entire period covered by this thesis are illustrated in the last charts in Figure 8.6 and Figure 8.7, spanning from March 3rd, 2023, to November 6th, 2023. Figure 6.6 serves as an example showcasing these fluctuations. Observing the diagrams, it is evident that all sensors performed well, consistently collecting data in alignment with the ambient temperature until approximately mid-July 2023. However, an anomaly arises around this time, specifically with TEMPS-02-3, as it begins to yield erratic results starting on July 11th around 4:30 PM. There is no clear indication of the underlying cause. The moisture sensors were updated on July 13th, and there was no evidence of the system being manipulated or turned on/off on that day. This suggests that the malfunction in TEMPS-02-3 occurred independently of external interference, leading to the conclusion that the sensor began to malfunction at this specific point in time. Fortunately, it is noteworthy that only one of the temperature probe sensors was affected, with the other two continuing to function normally.

Sensor TM-SB-04 started showing irregular results around mid-October, like the previously mentioned case. Despite thorough investigation, there is no evidence of tampering with the data acquisition system during this period. This suggests that the sensor might be malfunctioning on its own. However, a more in-depth analysis is needed to confirm this conclusion.

With this being the case, the temperature results without the impact of the erratic sensor on the temperature probe were observed. After removing this data, a re-plotting was performed, yielding the representation in Figure 8.7. The revised figure visually emphasizes the correlation between the temperatures recorded by the temperature sensors and the ambient temperature. The ambient temperature proves to be a reliable benchmark for evaluating the accuracy of the temperature data collected by all the sensors.

Figure 8.7 also serves to illustrate the temperature variations across different seasons. Seasons will be defined as per the definition from the National Research Council of Canada. This means that Spring goes from March 20th to June 21st, Summer goes from June 21st to September 23rd, Autumn goes from September 23rd to December 22nd and Winter goes from December 22nd to March 20th of the following year [88]. In the late winter to spring, spanning from March to mid-May, instances were observed where the temperature of the HMA and base layers dropped below 0 °C. However, as spring progressed into April and May, temperatures consistently increased, reaching a plateau from mid to late June through July, officially during the summer season. During this period, consistently high temperatures with substantial day-to-day fluctuations were noted. Finally, the fall season elicits a decrease in temperature.

These temperature shifts from late winter, through spring, to summer offer insights into the evolving conditions experienced by the various layers. Of note is the substantial temperature variation in the

subgrade layer. Given that the subgrade is particularly susceptible to moisture and temperature fluctuations, the temperature fluctuations ranging between five and almost 30 °C underscore the wide range in temperatures that this layer undergoes across various seasons [86]. Such variability in subgrade temperature has implications for the layer's properties, potentially substantially influencing the overall strength and integrity of the pavement structure [83]. The subsequent sections will delve into these implications further, particularly in the context of trends in pressure and strain over the same time period.

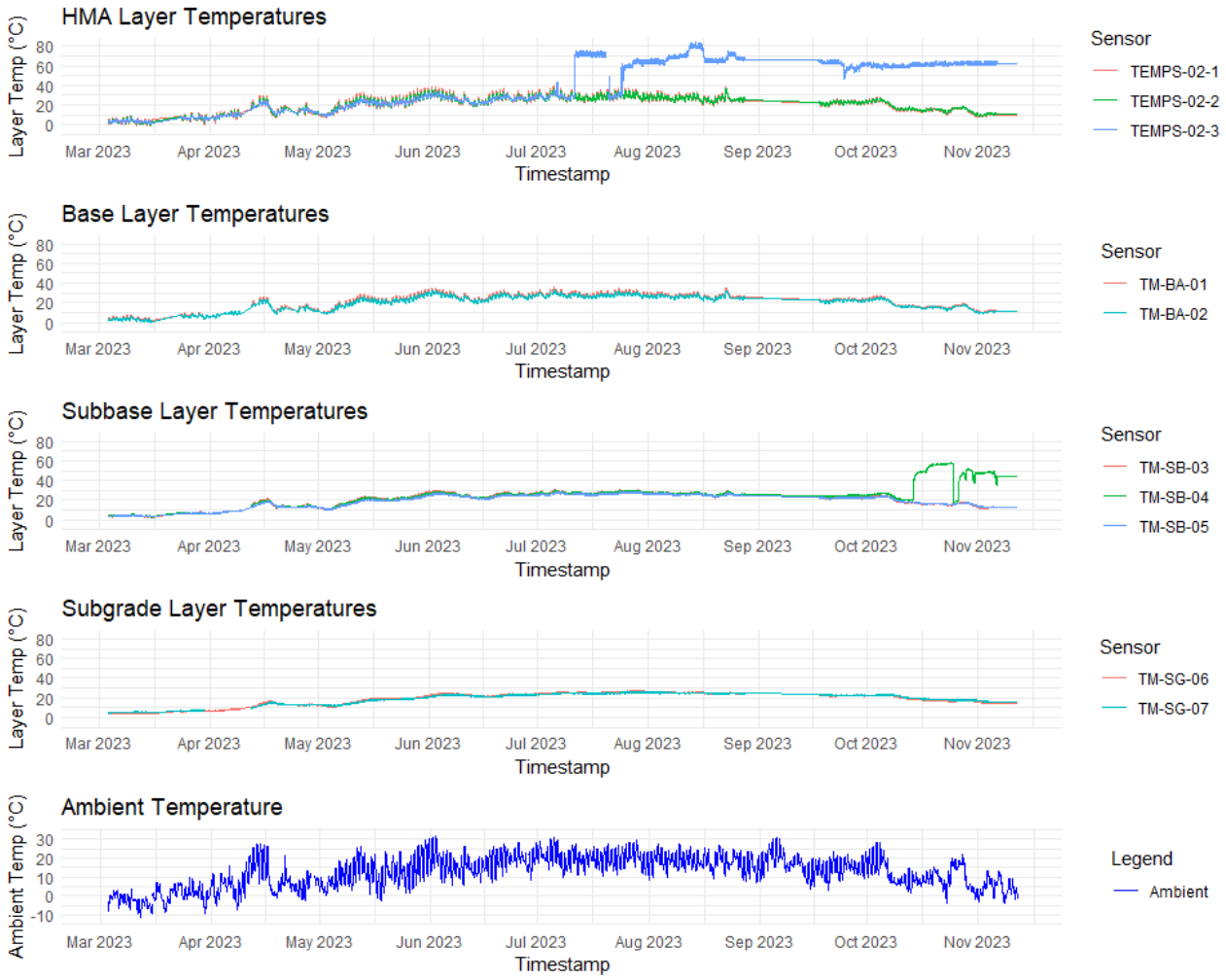


Figure 8.6 Monthly temperature variations from March 2023 to mid November 2023. The TEMPS-02-3 sensor begins to not function properly.

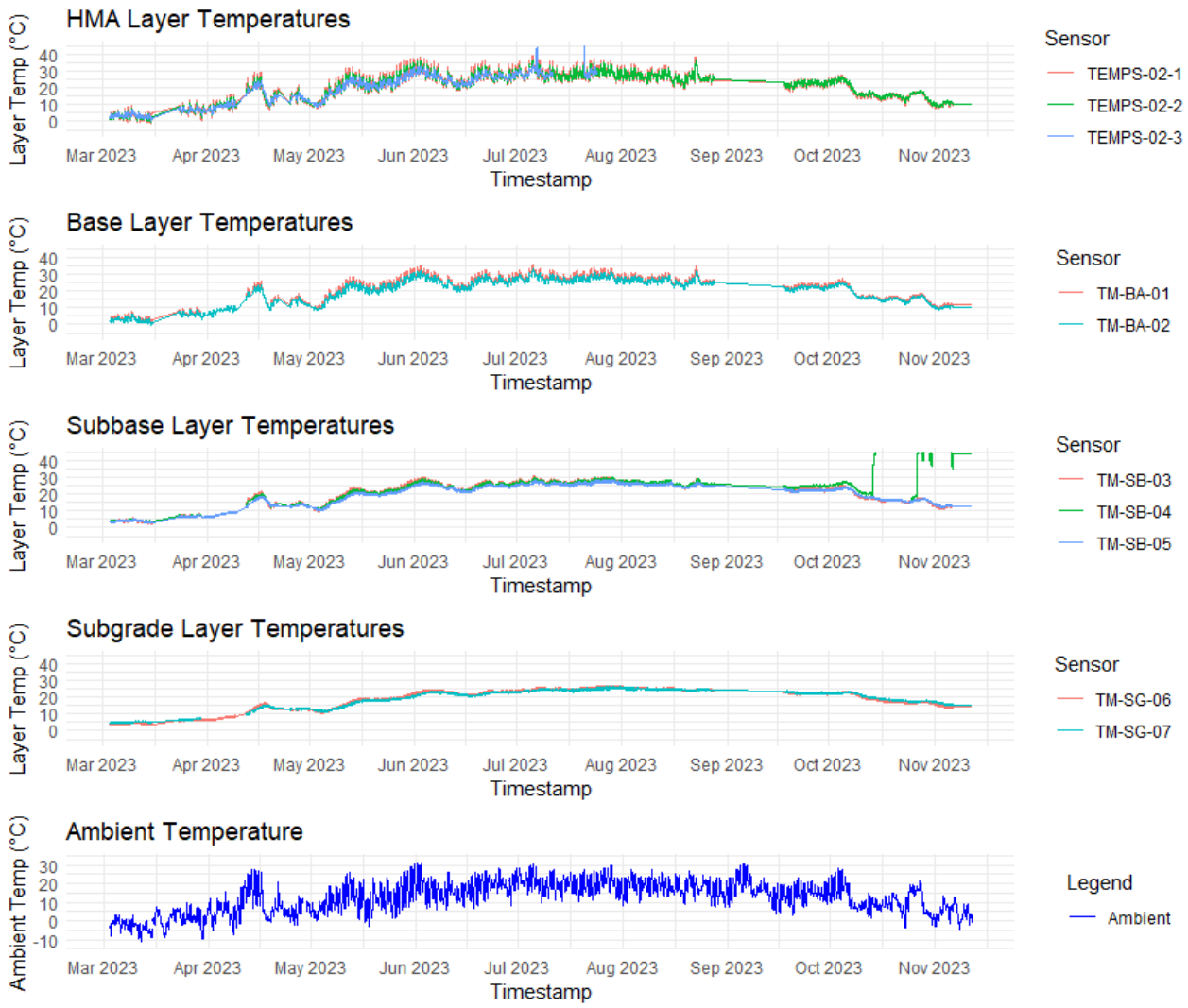


Figure 8.7 Monthly temperature variations from March 2023 to mid November 2023, removing the odd data from the TEMPS-03-3 sensor.

8.1.2 Moisture - Layer Profile Over time

As mentioned previously, moisture sensors were strategically placed in various layers of the granular structure—specifically, one in the base layer, three in the subbase layer, and one in the subgrade layer.

To analyze moisture trends, the comparison was made between sensor data and daily precipitation records for Kitchener-Waterloo obtained from Environment Canada [85]. The resulting trends were graphically represented in Figure 8.8 in the form of a bar chart along with the moisture results separated by granular layer. Reliable moisture data begins only from July 13th, 2023. Prior to this date, technical issues with the sensors resulted in unreadable data from March 2023 to mid-July 2023. These issues were attributed to inaccurate sensor settings, affecting the proper transmission of signals to the VWC unit of measurement.

The moisture sensors collect data in the unit of VWC which was explained in Chapter 3. According to the TEROS10 manual, for mineral soils, the VWC range that should be expected is between 0.00 and 0.64 m^3/m^3 [37]. The equation provided in Chapter 3 in Section 3.4.4 has a maximum limit of 0.77 m^3/m^3 in pure water, meaning that lower readings around 0.00 m^3/m^3 indicate unsaturated conditions, while higher readings suggest greater saturation within the respective layer [37].

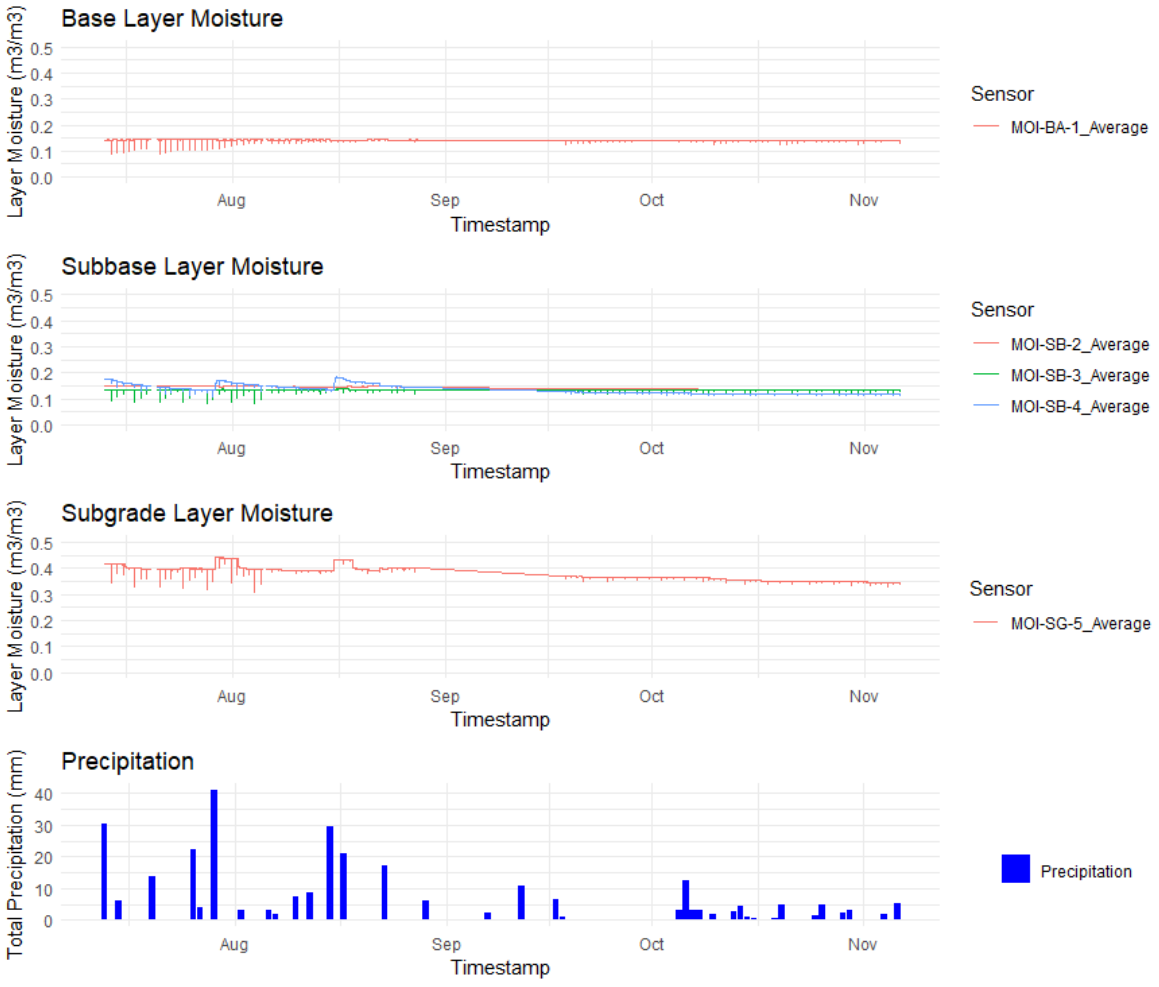


Figure 8.8 Moisture profile for the instrumented test section from July 13th, 2023, to November 6th, 2023, in all granular layers as compared to precipitation data from Environment Canada.

As can be seen from Figure 8.8, the moisture levels tend to closely follow periods of increase and decrease in precipitation. This can also be confirmed as occurring in previous studies [18]. This is most clearly visible in the subgrade, where when there has been larger than average amounts of rainfall, such as a rainfall of about 40 mm near the end of July, the VWC of the subgrade increases from 0.4 m^3/m^3 to 0.45 m^3/m^3. A similar situation also occurs around mid-August.

Furthermore, a general observation reveals that the subgrade consistently exhibits higher saturation levels compared to the subbase and base layers. The moisture content in the subbase layer falls within the range of 0.1 to 0.2 m^3/m^3, while in the base layer, it hovers around 0.15 m^3/m^3. This observation aligns with expectations, considering that Granular A, employed in the base layer, is more permeable than Granular B, used in the subbase layer. Both granular materials demonstrate higher permeability than standard subgrade materials, which would retain more moisture due to presence of larger amounts of fine particles like silt or clay. This is consistent with the findings of other works [18] [89].

These findings confirm those established in Chapter 4, where the volumetric moisture content was analyzed. The analysis revealed that the Granular A layer had a slightly higher average volumetric moisture content compared to Granular B, although the values were still quite similar. Specifically, Granular A recorded an average volumetric moisture content of 13.34%, while Granular B registered at 10.91%. However, both layers exhibited lower average volumetric moisture contents than the subgrade, thereby aligning with the observed moisture trends as illustrated in the trend data presented in Figure 8.8.

Additional patterns emerge when examining the seasonal impact of moisture over the several months. During the warm summer months, moisture levels remain consistently stable across all layers. This appears to be particularly important within the subgrade layer which seems to have the greatest variation amongst all of the granular layers. Aside from occasional spikes due to higher precipitation, the results remain relatively steady. However, come September, a noticeable shift occurs, especially in the subgrade, where the moisture content gradually drops from an average of 0.4 m^3/m^3 to around 0.3 m^3/m^3. Similar observations have been documented in another study which has also stated that during the warm summer months the moisture in the subgrade layer is very stable [86]. In addition, the paper demonstrates that during colder months, this stability will be lost as the moisture content begins to decline [86], which seems likely to occur in the case of the data collected around Kitchener as well. While this suggests a potential trend, it is essential to collect data throughout the winter months to confirm this pattern in the context of the data gathered in Kitchener.

While moisture trends exhibit good consistency across layers, there are periodic dips in moisture levels within each layer over time. Analysis of DAC-produced data indicates that these sporadic moisture dips occur occasionally before resuming the upward trajectory of the moisture trend.

8.2 Traffic Load Data Analysis

Traffic loads, such as pressure and strain, are important response factors in the understanding of pavement performance over time as these forces impact the pavement structure. Repeated traffic loads result in the development of pavement distresses over time which impacts the modulus of the asphalt and granular layers [90].

When it comes to pavements, critical pavement responses are concentrated in three major areas, each playing a crucial role in understanding how loads impact the pavement structure. These include the top and bottom of the asphalt layer as well as the top of the subgrade layer. All of these areas are shown in Figure 8.9 [91].

The first critical response is situated at the bottom of the asphalt layer. Here, the primary focus lies in identifying tensile stresses and strains. This occurs as a wheel approaches and traverses a specific point on the asphalt surface, such as a sensor embedded at the bottom of the asphalt layer, as implemented in this study. This phenomenon is akin to the behaviour of a beam, which exhibits tensile stresses at the bottom and compressive stresses at the top as it deforms under a point load. Asphalt pavements, functioning similarly to beams, undergo the same kind of deflection despite having support beneath the structure, defining them as “flexible pavements”. Figure 8.9 illustrates this, depicting compression ("C") on the surface directly under the tire and tension ("T") at the bottom of the asphalt layer. At the same time, on the sides of the tire (not directly under the tire’s point load), the asphalt pavement layer experiences tension and compression, but now with tension on the surface and compression at the bottom of the asphalt layer [91]. In this context, the critical parameter to assess is the maximum tensile strain at the bottom of the HMA layer, since, like many engineering materials, asphalt demonstrates weakness in tension. The point load induces maximum tensile strain at the bottom of the asphalt layer, leading to the initiation and propagation of cracks that eventually manifest as failure distresses on the surface—examples of which include fatigue cracking [41].

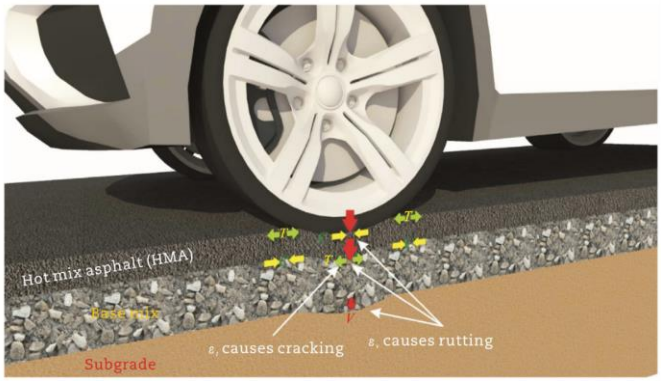


Figure 8.9 Critical pavement responses due to tire-pavement interaction [91].

The second critical response is situated at the bottom of the subgrade layer. Here, the primary emphasis is on compressive strains and stresses, which have the potential to induce permanent deformation. This deformation can arise from excessive creep in the HMA layers or from deformations occurring in the granular layers. Consolidation in the soil and granular materials beneath the vehicle tires plays a substantial role. This consolidation process reduces the air void content, contributing to the formation of ruts—a manifestation of permanent deformation in the pavement structure [91] [92]. In Figure 8.9, the propagation of vertical compressive strains and stresses is illustrated by the red arrows pointing downward into the subgrade, which signify the forces that will instigate rutting [91]. These downward forces are instrumental in inducing the permanent deformation observed in the pavement structure. In this study, the compressive strains and stresses will be captured by the total earth pressure cells installed in the various layers of the pavement structure.

The final critical response is the deflection that occurs on the pavement surface. Introducing a load, such as a wheel tire, onto the pavement surface results in the application of a force that induces deflection in the vertical direction. While the deflection is not specifically captured in this study, the impacts of deflection should be noted as the results are analyzed.

As mentioned in Chapter 3, the asphalt strain gauges are primarily situated at the bottom of the asphalt surface layer, comprising horizontal (two longitudinal and two transverse) and two vertical strain gauges in each of the left and right sensor arrays. On the other hand, the total earth pressure cells are distributed across all granular layers, specifically at the top of the base, the top of the subbase, and the top of the subgrade. In each layer, a pair of total earth pressure cells is present—one in the right sensor array and the other in the left array.

This section will describe both the layer pressure profiles as well as the layer strain profiles over short and long timeframes throughout both the various arrays and pavement layers.

8.2.1 Pressure

8.2.1.1 Layer Pressure Profile Over Time

Figure 8.10 and Figure 8.11 display the pressure profiles over time for all pressure sensors, segmented across the base, subbase, and subgrade layers, as well as across the right and left sensor arrays. The data in both figures is aggregated at 15-minute intervals, and the absolute pressure is shown to compare the pressure magnitudes more easily. The key distinction between the two figures lies in the Y-axis scale.

In Figure 8.10, instances of high pressure are observed, notably around July and August 2023 in the base right array. This surge is attributed mainly to sensor PC-BA-R-5, although this is reciprocated as

well by sensor PC-BA-R-1, albeit not to such a large degree. The likely explanation for the excessive pressure results is the fact that they coincide with increased construction activity during the second phase of the Courtland Avenue Road reconstruction, which includes the use of heavy trucks and machinery, leading to elevated pressure responses. Apart from the excessive peaks, most of the pressure data seems relatively stable compared to ambient temperature. This could imply that either ambient temperature has minimal influence on pressure or that the data is overshadowed by the extreme pressure responses. Filtering out these excessive peaks is essential for an accurate assessment of regular pressure trends, enabling a clearer visualization of average aggregated patterns over the months.

The pressure trends in Figure 8.11 captures trends while filtering out extraneous values using a 50 kPa Y-axis threshold. The trends observed in this figure reveal several patterns. In the base layer, both the right and left sensor arrays generally show similar pressure magnitudes, ranging between 5 and 25 kPa. However, an exception is noted for PC-BA-R-5 in the right array, consistently recording higher average pressures between 25 to 30 kPa. This discrepancy can be attributed to its location in the right wheel path of passing vehicles, suggesting that this sensor is experiencing consistently heavier loads compared to others in the array. Another potential factor could be a higher baseline pressure and different calibration when compared to PC-BA-R-1. In any case, the pressure values recorded by this sensor are nearly three times larger than those from the other sensor in the right wheel path (PC-BA-R-1). The investigation into these disparities is essential to accurately interpret and reconcile the pressure data obtained from these sensors. In the left sensor array, base layer sensors show comparable pressure magnitudes over time, with PC-BA-L-2 slightly higher than PC-BA-L-6, possibly for reasons similar to those in the right array.

Transitioning to the subbase layer, both the right and left arrays consistently generate pressures averaging around 15 to 35 kPa. This observation raises intrigue, particularly in the left array, which is not directly positioned in any vehicle wheel path. The similarity in magnitudes, and the slightly higher average pressures, suggests a notable impact of wander in this context.

In contrast to the subbase trends, notable differences appear in the subgrade. The left sensor array shows a notably higher average pressure trend compared to the right sensor array. This difference could stem from varying sensor calibration, or the sensor being placed in a specific soil patch more prone to pressure response.

In evaluating the results across the base, subbase, and subgrade layers, alongside the comparison between right and left sensor arrays, a notable observation emerges: ambient temperature exhibits no substantial impact on the pressure response. The pressure responses generally remain consistent from March to November. As temperatures rise, particularly from May 2023 onwards, a subtle increase in the frequency of pressure variations becomes apparent. This phenomenon is likely attributed to heightened

heavy vehicle activity during the spring and summer seasons but not the ambient temperature. This has also been shown in the finding of Oyeyi [18], who's pavement sections also experienced minimal average trend pressure fluctuations over a period of several months. Likely, with lower temperatures, and lower moisture content in the pavement layers, the pressure trends will reduce [18] – but this will need to be assessed over a period of several years.

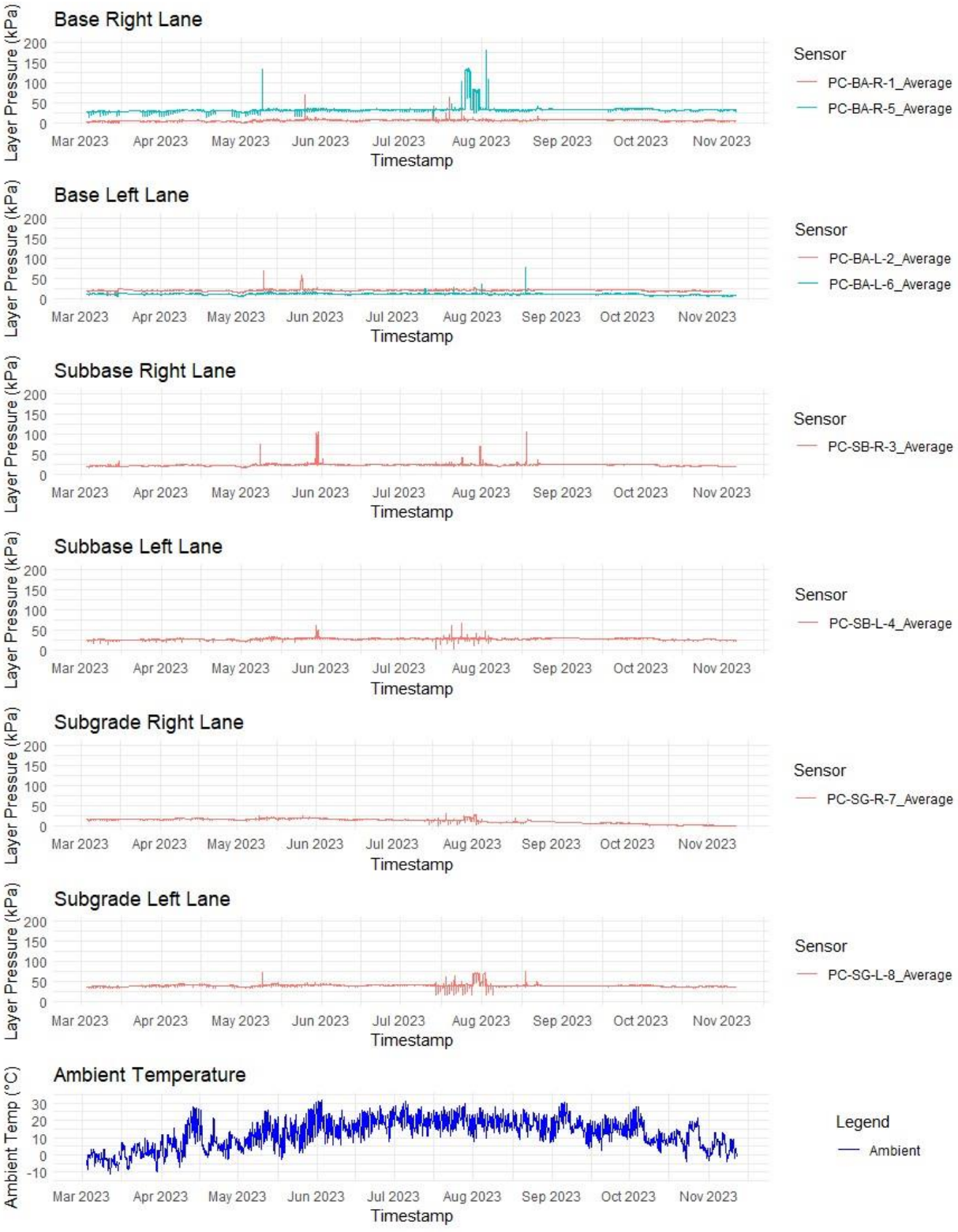


Figure 8.10 Pressure profile over time for the instrumented test section, divided into right and left sensor arrays within the base, subbase, and subgrade layers.

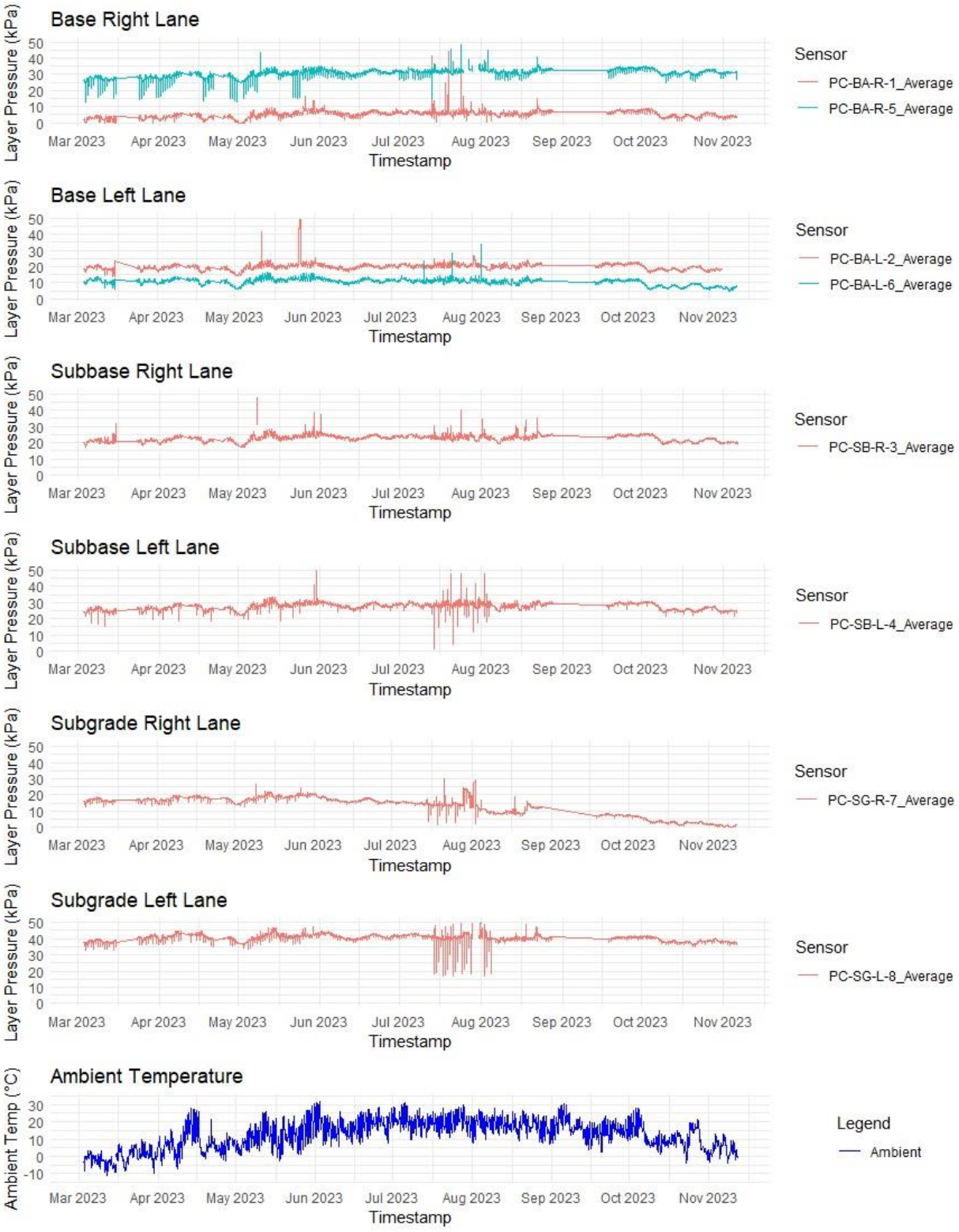


Figure 8.11 Time-pressure profiles including right and left sensor arrays in base, subbase, and subgrade layers. Y-axis adjusted to highlight average trends, excluding major outliers.

8.2.1.2 High-Speed Pressure Trends

Figure 8.11 provides a snapshot of high-speed pressure data captured from June 2nd, 2023, to June 3rd, 2023, over a period of 24 hours. The data is selectively filtered to show positive pressure results, given the absence of physical significance in negative pressure outcomes [20]. In addition, only data within a 24-hour period is selected, as the amount of data is very large.

The continuous data stream of pressure results in the base layer, regardless of the sensor array, suggest that the sensors consistently capture pressure almost continuously over a 24-hour period, with periodic instances of higher-pressure data occurring once or twice every 6 hours. In contrast, the subbase and subgrade layers only exhibit these periodic positive pressure results and no continuous data streams, likely corresponding to instances of heightened pressure from passing vehicles systematically recorded by the sensors. This could be explained by the fact that during these periods of increased pressure, the force is able to be transferred to the lower layers, whereas low-pressure periods in the base layer do not register as positive pressure in the subbase and subgrade.

The disparities in pressure magnitude across different pavement layers are significant. In the base layer, instances of high-pressure data ranging from 100 to 200 kPa are observed. Similarly, in the subbase layer, the right array records high-pressure impacts between 100 and 200 kPa. However, the left array in the subbase layer exhibits a lower pressure impact between 25 to 50 kPa, suggesting it may experience fewer vehicle loads, possibly due to its location outside of a direct vehicle wheel path and being less affected by vehicle tire wander.

In the subgrade layer, pressure results are generally lower, also ranging between 25 to 100 kPa between both arrays. Both the right and left sensor arrays show similarity, although the left array produces slightly higher-pressure results. Notably, this pressure range aligns with findings in a previous study [18], where sensors in the subgrade layer recorded pressures within a similar range. This observation is crucial for comparing subgrade responses, particularly since this pressure correlates with the compressive stresses and strains that substantially influence the performance of the pavement structure [63].

The variations in pressure responses observed throughout the day over a 24-hour period are intriguing. High-pressure responses are more prevalent between 6:00 AM and 6:00 PM, coinciding with higher temperatures. In contrast, during the low-temperature period from midnight to 6:00 AM, the pressure response captured by the sensors is at its lowest. This correlation may be attributed to reduced vehicle activity during that time and/or the association of lower temperatures with lower pressure.

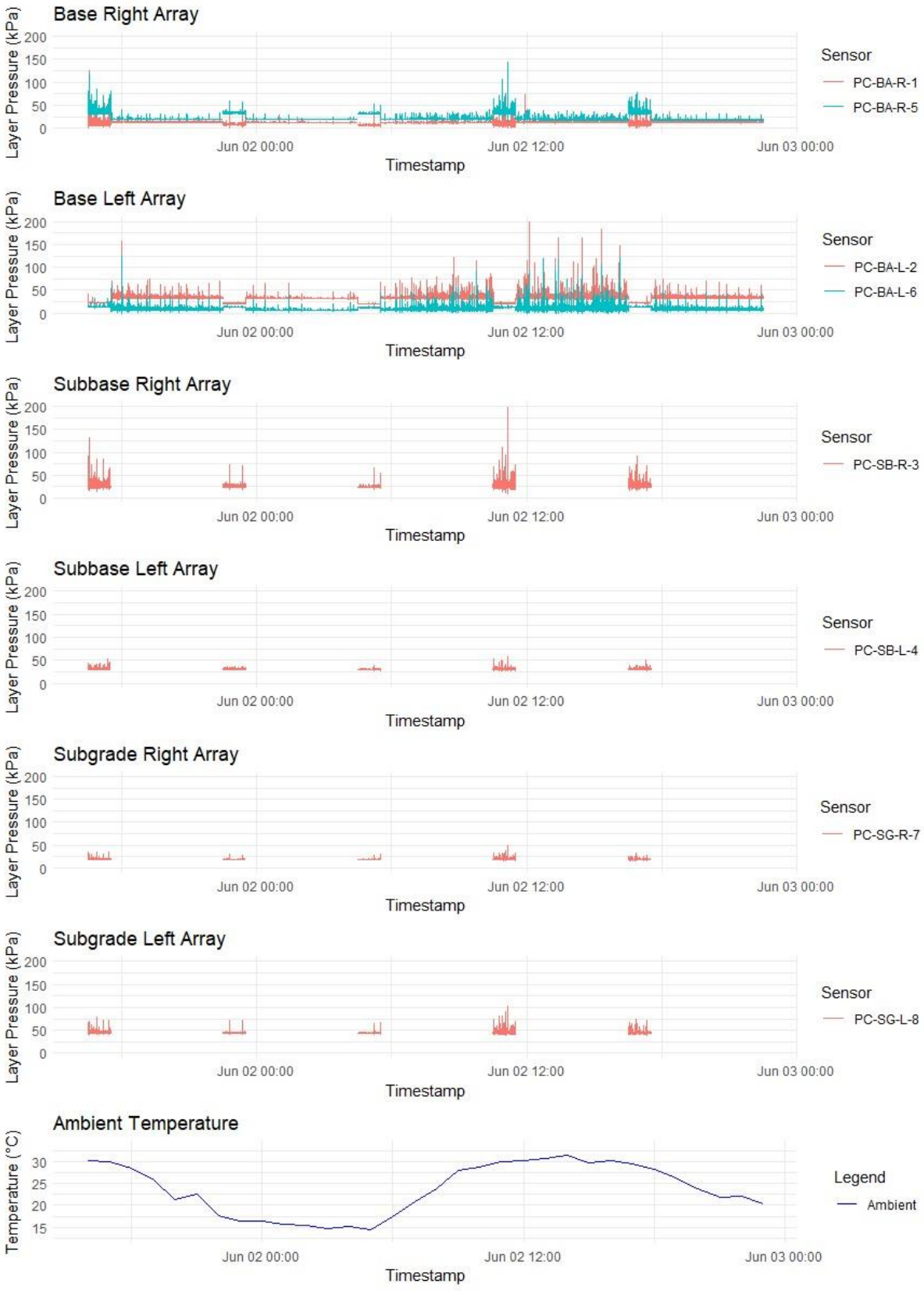


Figure 8.12 High-speed pressure profile over a 24-hour period.

8.2.2 Strain

8.2.2.1 Layer Strain Profile Over Time

Figure 8.13 illustrates the strain profile over time for all strain gauges in both the right and left sensor arrays, specifying their longitudinal and transverse orientation, and data aggregated to 1 point every 15 minutes is plotted. According to the BDI asphalt strain gauge manuals and datasheets, positive strain indicates tension, while negative strain denotes compression within the layers. Unfortunately, it was determined very early in the sensor installation process that the vertical strain gauges were malfunctioning and we're producing incorrect results, therefore there are no results for the vertical strain gauges. The data reveals that in the cooler months, longitudinal strain results are positive, and as the ambient temperature increases, such as during the summer months, the strain results become more negative.

The sensors in this study have been calibrated by the manufacturer to show that positive strain indicates tension, and a negative strain denotes compression. This is the opposite to the geomechanics/soil mechanics convention, where positive strain results indicate compression and negative strain results indicate tension. In the case of the study by [18], their strain gauges recorded positive strain as compression and negative strain as tension, as they were following geomechanics conventions. Therefore, when this is considered, the trend results obtained make sense and will simply be the opposite to the regular geomechanics convention. As stated at the beginning of this chapter, rising asphalt temperatures soften the asphalt material, causing increased horizontal strains at the bottom of the asphalt layer and promoting the propagation of fatigue cracks. In this case, the results show that in warmer summer months, the magnitude of the strain is larger, which follows this trend. In addition, when the soil is saturated during spring thaw in colder regions or in colder temperatures, the excessive moisture will reduce the resilient modulus of the unbound layers which will lead to an increase in the strain that the asphalt layer experiences, again in line with standard pavement strain conventions [63].

The variations in strain magnitudes over time seem to align closely with the findings in [18]. In the data from Figure 6.13, all sensors initially start around 1000 to 3000 με, followed by a dip below 0 με, reaching as low as -5000 με. This aligns with the strain profile observed by Oyeyi in their Notre Dame Drive study, where the strain typically ranged between 4000 and -4000 με, occasionally dipping as low as approximately -7000 με [18].

It is intriguing to observe that regardless of the sensor array, type or the orientation of sensors—be it longitudinal or transverse—a consistent downward trend emerges, albeit with slight variations in magnitudes. There was an expectation that sensors in the right arrays, especially in the longitudinal direction, would show higher strain magnitude trends than those in the left or transverse directions.

However, the agglomeration of data over time may mask individual sensor trends. A closer examination of each sensor type on a shorter time frame is necessary to determine if there are any trends related to longitudinal or transverse strains in either the right or left sensor arrays.

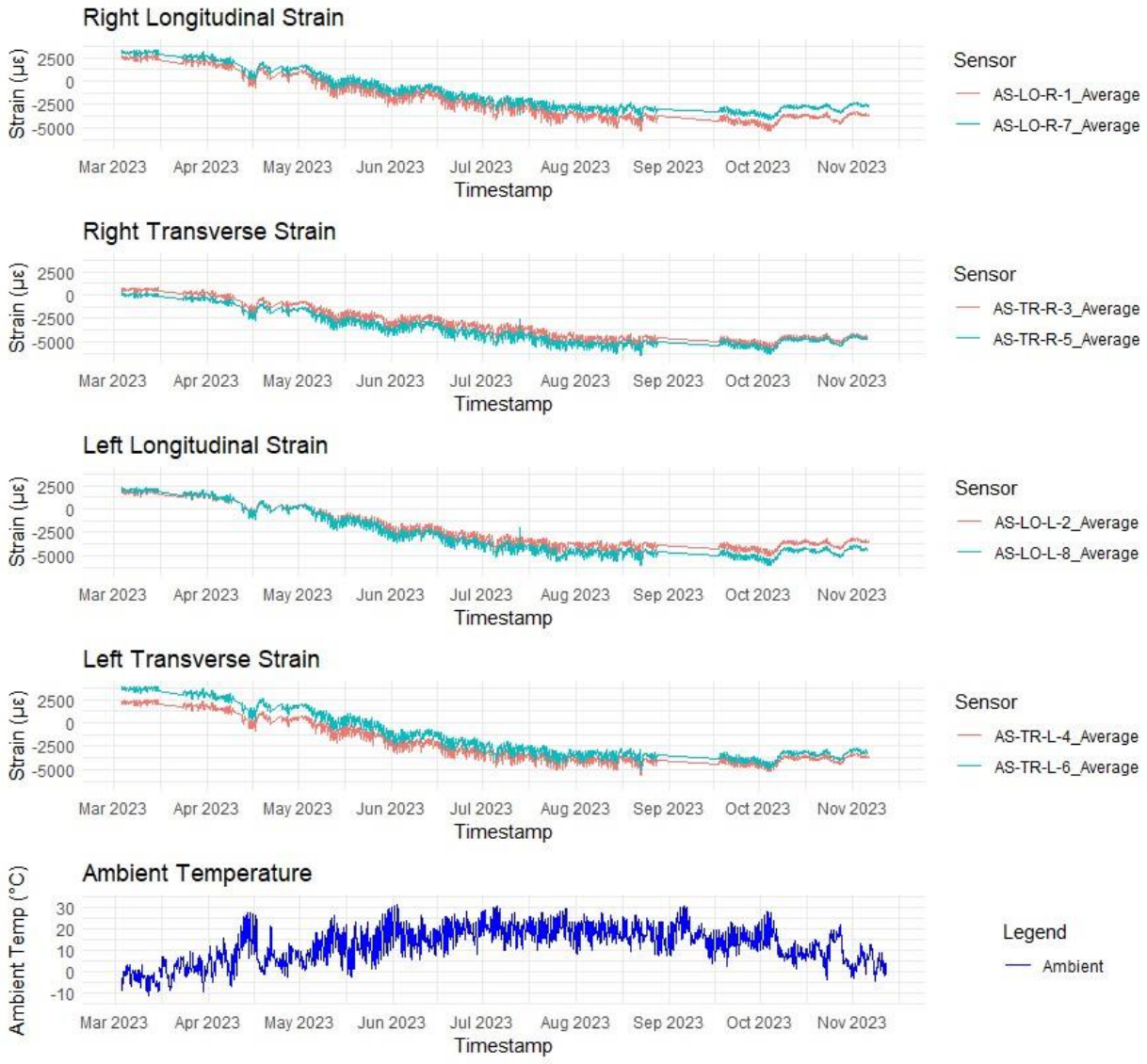


Figure 8.13 Strain-time profile from March 3rd, 2023, to November 6th, 2023. Includes data in the left and right sensor arrays, and in both the longitudinal and transverse directions.

8.2.2.2 High-Speed Strain Trends

Figure 8.14 and Figure 8.15 provide insights into high-speed strain results observed over the same 24-hour period depicted in the high-speed pressure results in Figure 8.13. Figure 8.14 displays the complete high-speed dataset without any filtering, whereas Figure 8.15 presents the data after filtering.

In the right sensor array, both in the longitudinal and transverse directions, the asphalt strain gauges consistently register strain within a narrow range. This is evident in Figure 6.14, where the data essentially forms a straight line. Conversely, within the left sensor array, particularly in sensor AS-LO-L-8 and to a lesser extent in sensor AS-LO-L-2, there is a noticeable and regular decrease in strain in the longitudinal direction. In the transverse direction of the left array, there is not as much deviation.

Upon thorough examination of various 24-hour periods, this consistent trend in the left, longitudinal sensors appear to persist continuously. Consequently, to accurately comprehend the trends in the right array and the transverse direction, it becomes imperative to filter out this outlier data.

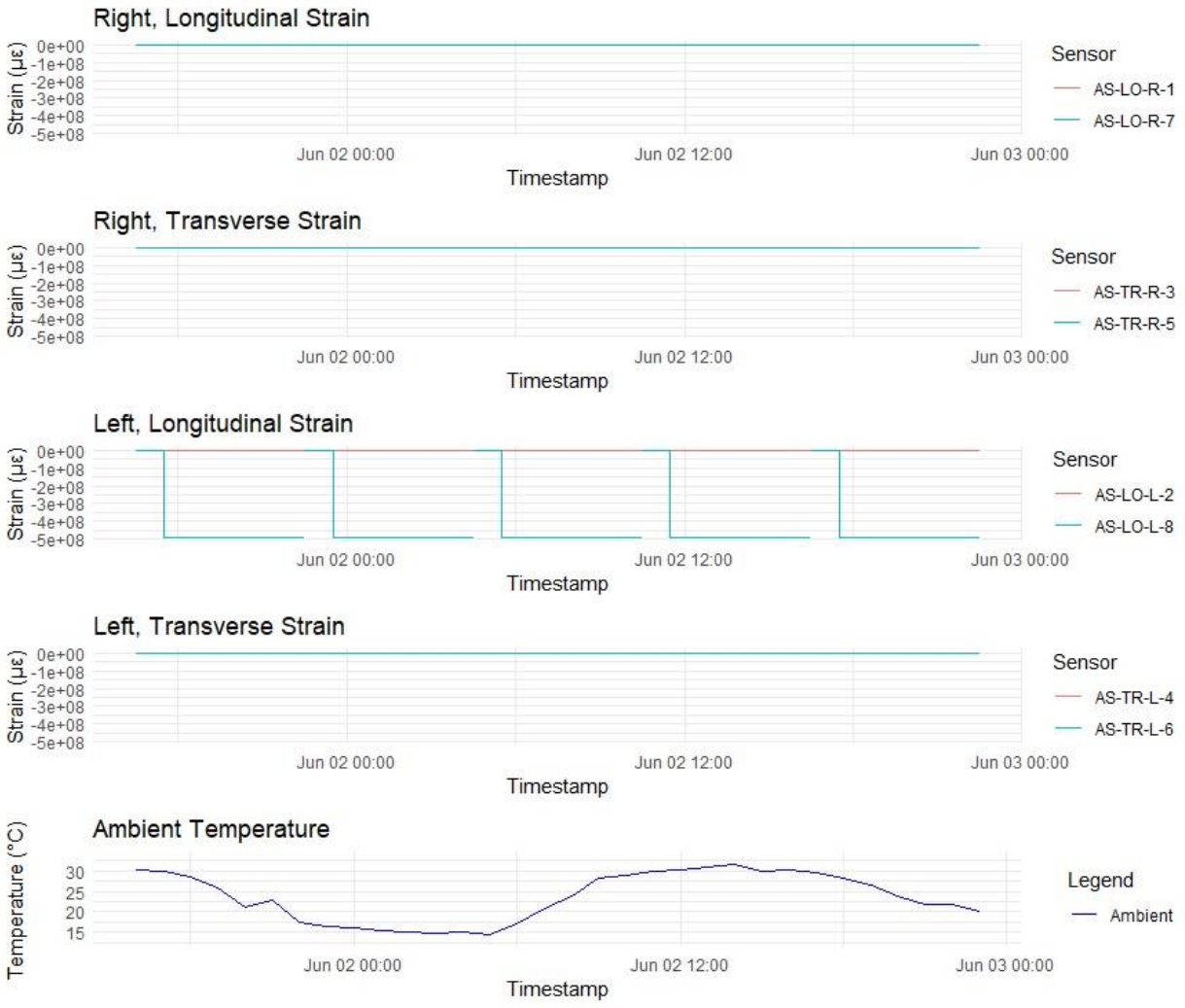


Figure 8.14 High-speed strain profile over a 24-hour period.

By excluding outlier data, Figure 8.15 reveals clear trends in both the right and left arrays, both longitudinally and transversely. For example, in the longitudinal strain of the right sensor array, we see

strain values fluctuating between -3500 με and 1500 με, with periodic dips at regular intervals. The transverse strain in the right sensor array shows fluctuations between -4000 and -2000 με. Notably, there's a clear correlation between strain fluctuations and ambient temperature—lower temperatures coincide with increased strain values, and higher temperatures correspond to decreased strain values. This pattern aligns with trends observed in Figure 8.13 but on a shorter time frame.

Shifting focus to the left sensor array, in the longitudinal direction, the data now only displays points where the right sensor array had dips. Despite the non-continuous data, the trend of higher strain values at lower temperatures remains visible. As for the left transverse strain data, the values range from -4000 to -1000 με, and once again, temperature changes induce fluctuations in strain values, similar to the right transverse strain data.

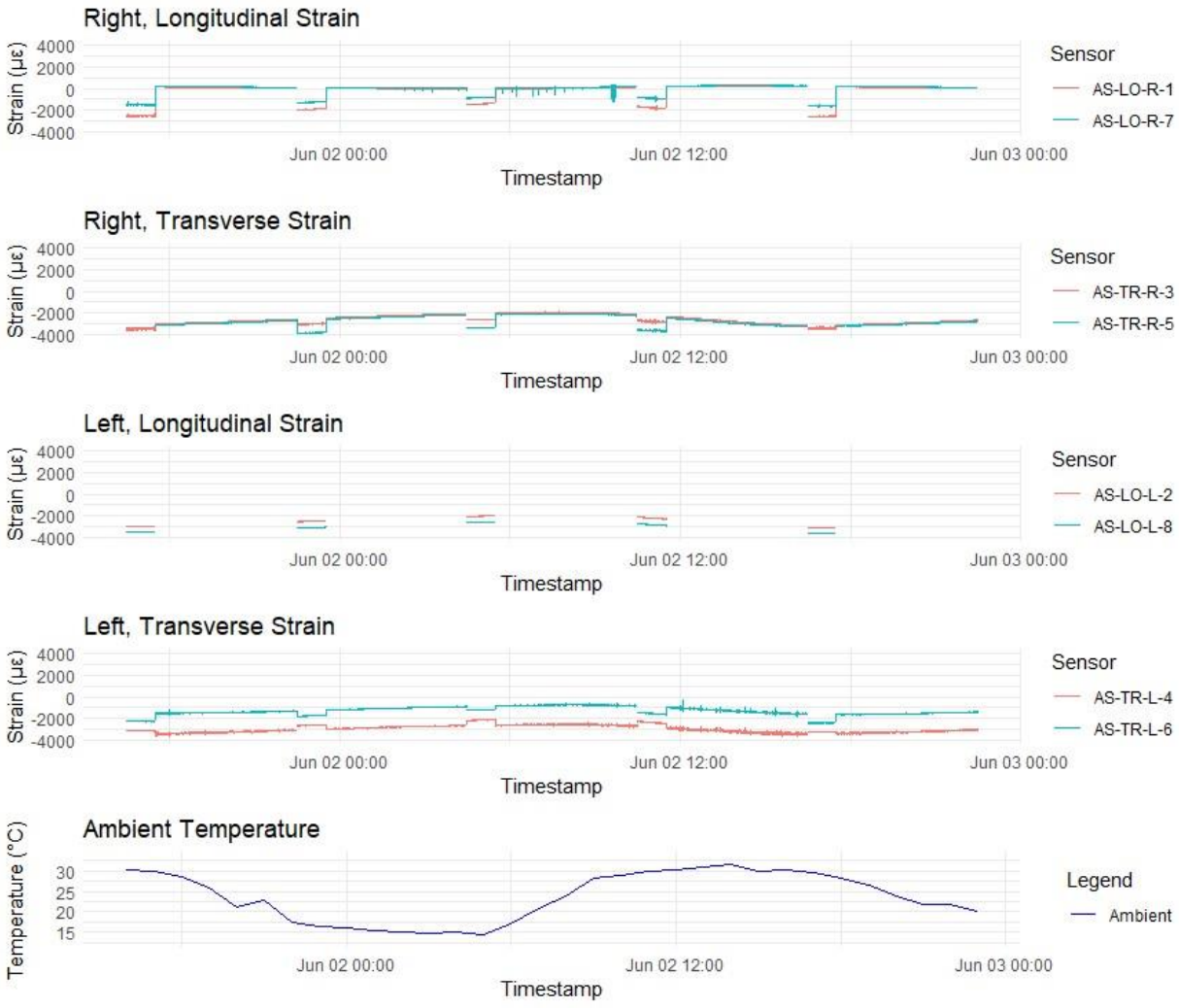


Figure 8.15 Filtered high-speed strain profile over a 24-hour period.

Chapter 9
Database Development

This Chapter outlines the development of a specialized database for collecting and storing data from this pavement section and comparable projects. The aim is to create a database concept that can incorporate artificial intelligence algorithms and ensure nationwide accessibility, streamlining information dissemination to diverse agencies.

9.1 Background

Currently, there is not one nationwide database that describes the performance and conditions of the pavement network in Canada. From the literature, it appears that pavement management systems are developed on a regional basis and can vary from agency to agency [93]. In addition, research has shown that regional agencies tend to lack the required funds to have accurate and up-to-date pavement management systems [93]. Therefore, implementing a national pavement management system not only enables regional agencies to consolidate their funds and establish frameworks for provincial and regional entities but also establishes a standardized method for recording pavement performance data, facilitating easier comparisons between pavement sections on a national scale.

One of the most popular databases that stores information on a variety of active and inactive pavement sections in the US and Canada is called the Long-Term Pavement Performance database, or LTPP database. It was established by the U.S. Department of Transportation's Federal Highway Administration, or FHWA, to provide information on all these sites [94]. The information is classified within 7 modules which include topics like maintenance, traffic, and monitoring of distresses [94].

Figure 9.1 presents a screenshot of the LTPP InfoPave database, illustrating the diverse range of information that can be extracted for each pavement section [95]. This encompasses General Information, covering details such as age, construction year, monitoring status, treatment and preservation type, and location. The database also provides insights into structural aspects like surface type and base type. Climatic information, encompassing freezing index, precipitation, and temperature, is available for each section. Traffic-related details, including average annual daily traffic (AADT) and average annual daily truck traffic (AADTT), are also accessible. Additionally, performance information, detailing aspects like cracking and faulting, is provided for each study.

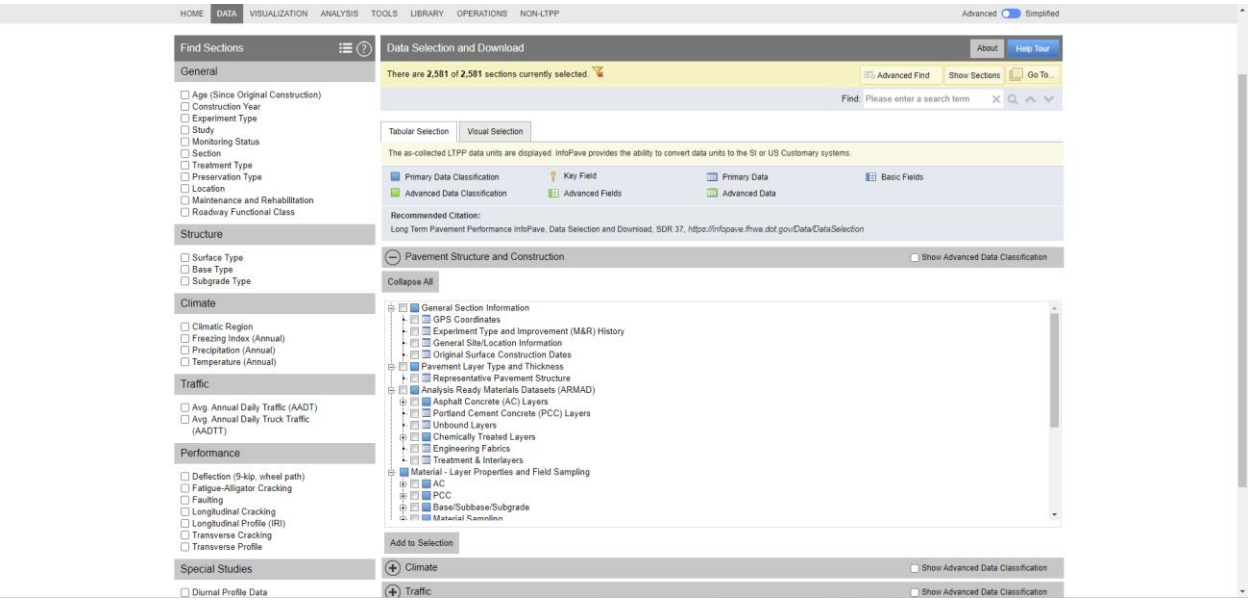


Figure 9.1 LTPP database and information types that can be selected for each section [95].

The components covered in the LTPP database align with the principles outlined in the literature regarding essential components of a pavement management system database and framework [93]. The database serves as a crucial repository for collecting data, which is subsequently utilized in performance prediction models. These models, discussed in earlier sections of this thesis, are designed to forecast the deterioration of pavement structures over time. Whether deterministic or probabilistic, these performance prediction models rely on the comprehensive data stored within these databases.

AI algorithms play a critical role in managing extensive datasets like these, aiding in the streamlined refinement of results by automatically identifying and correcting inaccuracies. They can flag inputs that deviate from common value ranges, ensuring data quality. Moreover, AI algorithms enhance predictive capabilities, leveraging existing data to make more accurate projections. Over time, these algorithms can learn from new data additions, continuously improving their performance and adaptability within the database.

9.2 Database Development

9.2.1 Current Data Setup

To establish a comprehensive database consolidating data from various similar nationwide projects in Canada, it is essential to understand the nature and origin of the collected data. The data acquired by the data acquisition system on-site is stored in TDMS (Technical Data Management Solution) files [96]. TDMS is a file format developed by National Instruments (NI) to accurately represent data collected by its equipment [96]. NI claims that their TDMS file type is easy to share and manipulate since it has a

small file size relative to other types of database files and is also exchangeable, searchable, and is capable of high-speed streaming, and is conducive to database creation [96].

The file structure of a TDMS file can be expressed as in Figure 9.2. Each file typically includes a file description section providing details such as title and author. Then it will go into each of the channel groups, describing information such as the UUTs, procedure test fixtures, etc. Then there are the individual channels themselves. In the context of this project, channels correspond to each of the four channels on each of the nine STS-4 nodes within the data acquisition system (see Figure 3.6, part f). Each channel can accommodate one or two sensors, establishing the connection between the sensor and the computer while storing all relevant information [96].

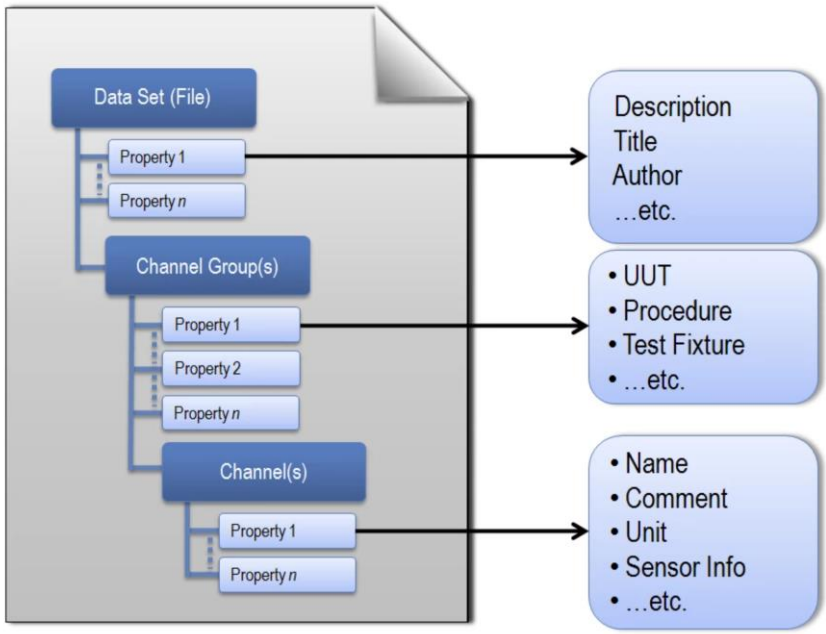


Figure 9.2 The structure of a TDMS file as per National Instruments [96].

The data is then stored on the on-site computer, which collects data on an hourly basis, produces TDMS files, and then aggregates them on a per day and then per month basis in a file folder system. Figure 9.3 shows the remote desktop on site. The grey dialog box shows the connection to the testing capabilities of the system, whereby tests can be started and stopped and other information relating to the amount of data that's collected at a certain time can also be viewed. To access the TDMS files, one navigates to a designated data folder, arranged by month and date (see Figure 9.4), and can transfer these files to the desktop, or any other database system as needed. In this project, the research data was primarily collected and transferred directly to the researcher's desktop using TeamViewer's file transfer capabilities and then converted to Excel files for manipulation, graphing, and storage.

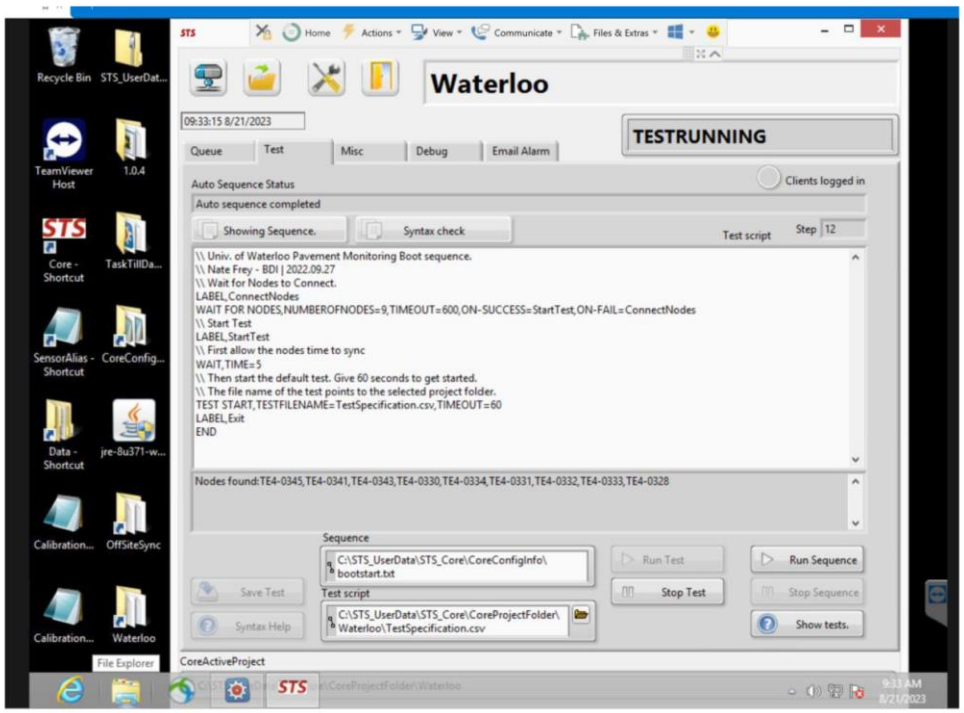


Figure 9.3 View of the remote desktop on-site.

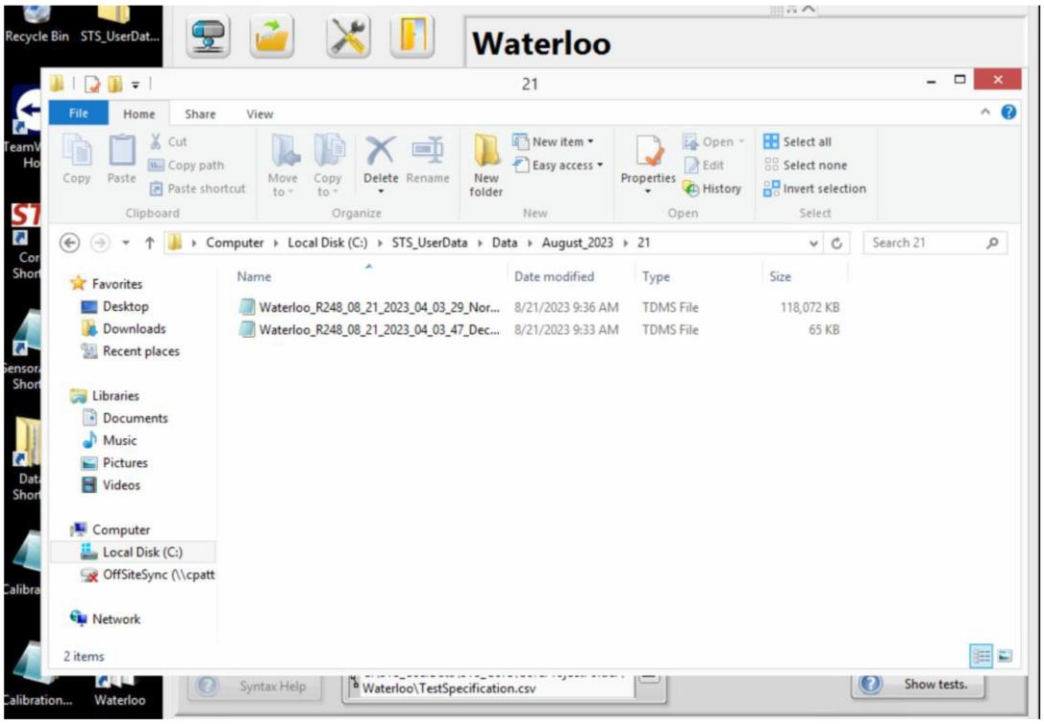


Figure 9.4 View of the way data within TDMS files is stored on the on-site desktop.

In addition, a public database between researchers was used (called the “CPATT Server”) to store all the data for backup purposes and to not use all of the data storage capabilities of the on-site computer.

This is accessed through a Windows Remote Desktop platform and is easily accessible by the whole research team. The file transfer includes a file mirroring process, where the university's IT department set up a mirroring system to automatically synchronize on-site computer data with the CPATT Server every 12 hours. This was performed with a free task scheduler called Task Till Dawn, developed by Oliver Matuschin [97], and visible in Figure 9.5.

For example, in Figure 9.6, one can see that the data that has been stored to date is stored by month and year. Within each of these folders, the data is then stored by day for each month, as shown in Figure 9.7 . Then, in Figure 9.8, the data stored per day can be viewed as TDMS files, and this includes both the high speed and low speed load and environmental data. In this way the data is stored externally and can easily be viewed.

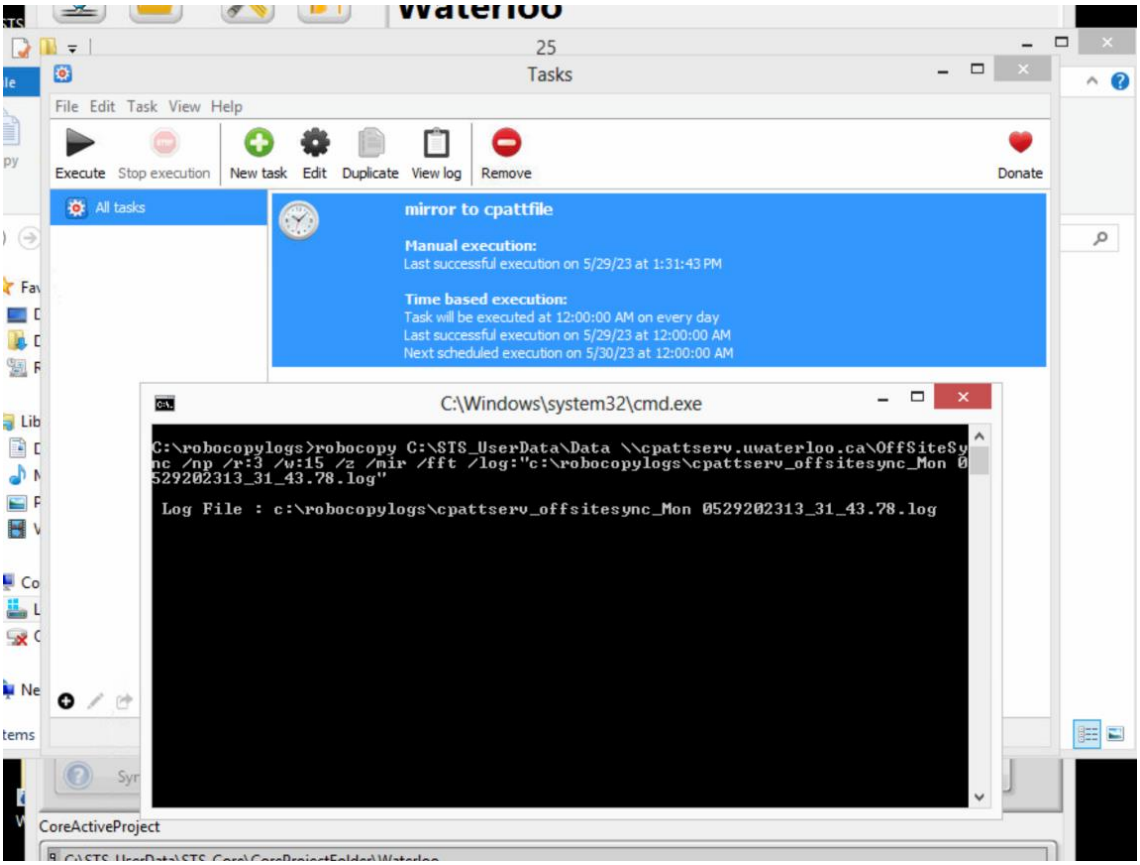


Figure 9.5 File mirroring to transfer files to remote data storage, as seen from the on-site desktop.

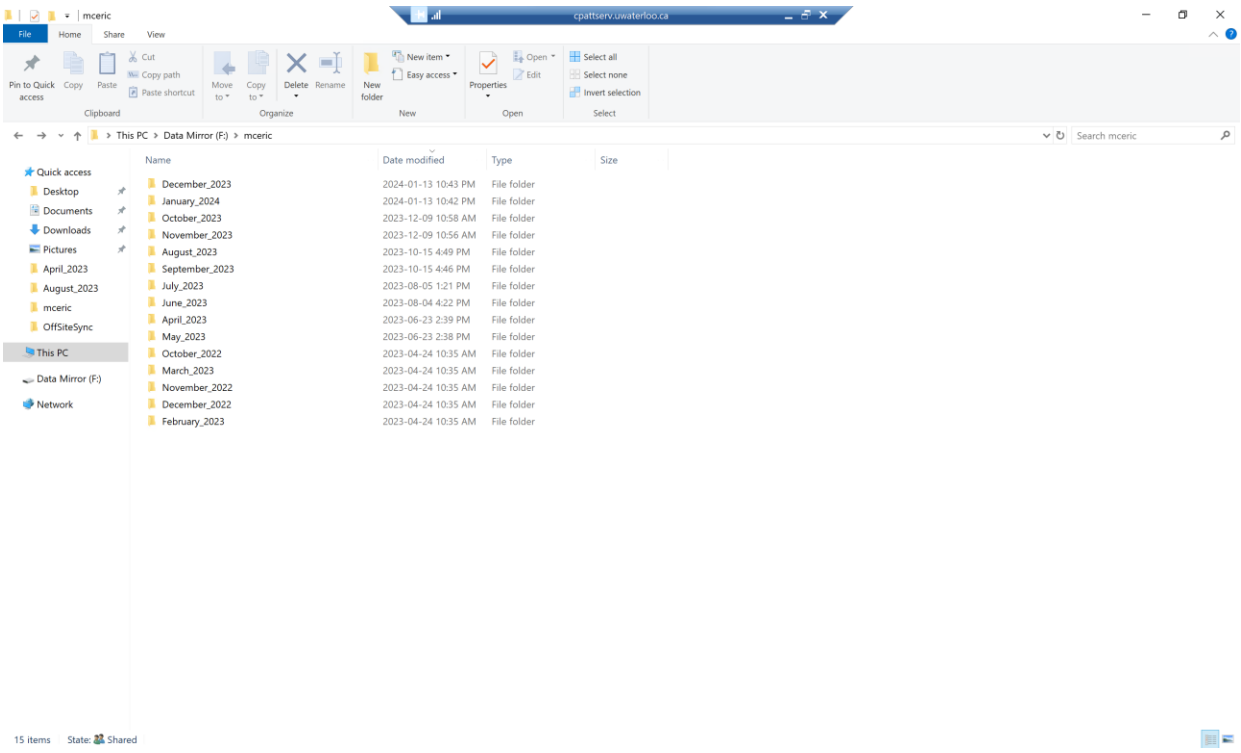


Figure 9.6 Remote data storage, mirrored with the remote desktop on-site to collect data every 12 hours.

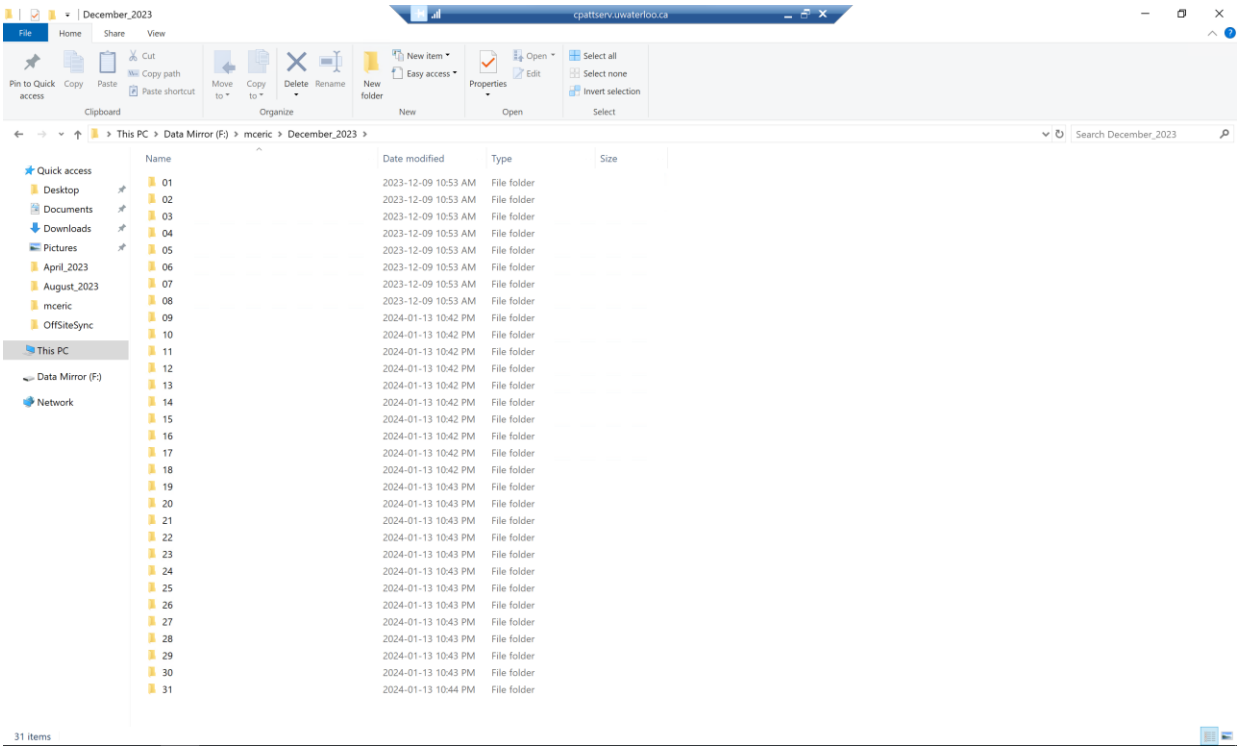


Figure 9.7 Within each monthly folder, the data developed is split daily.

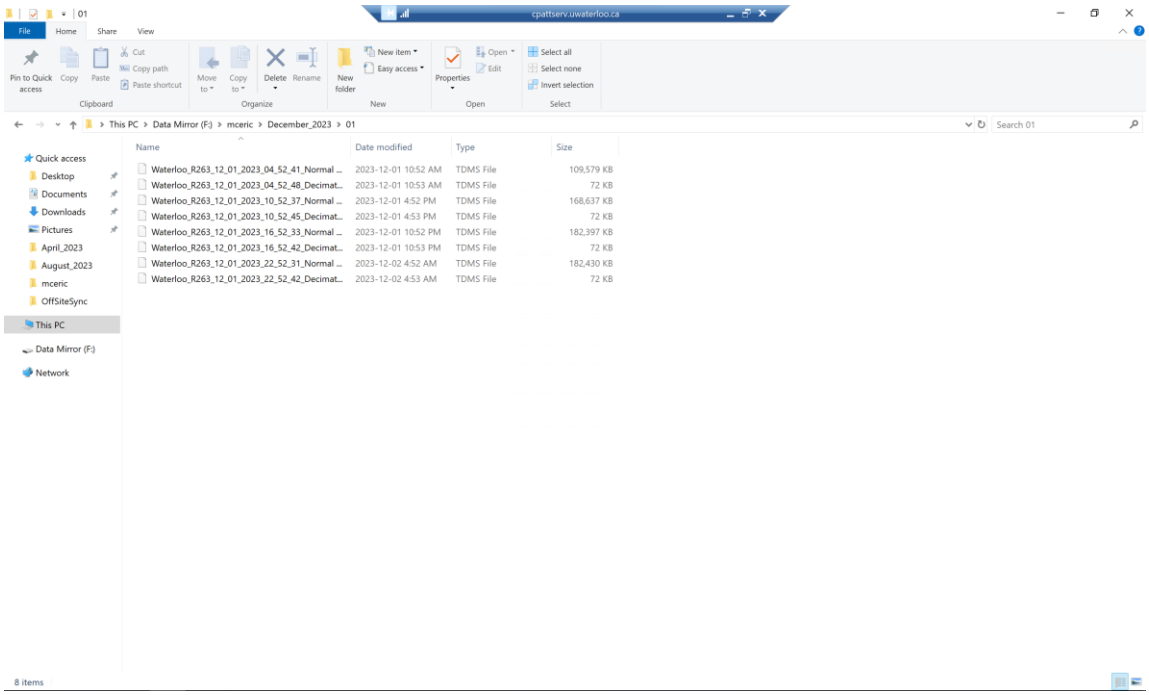


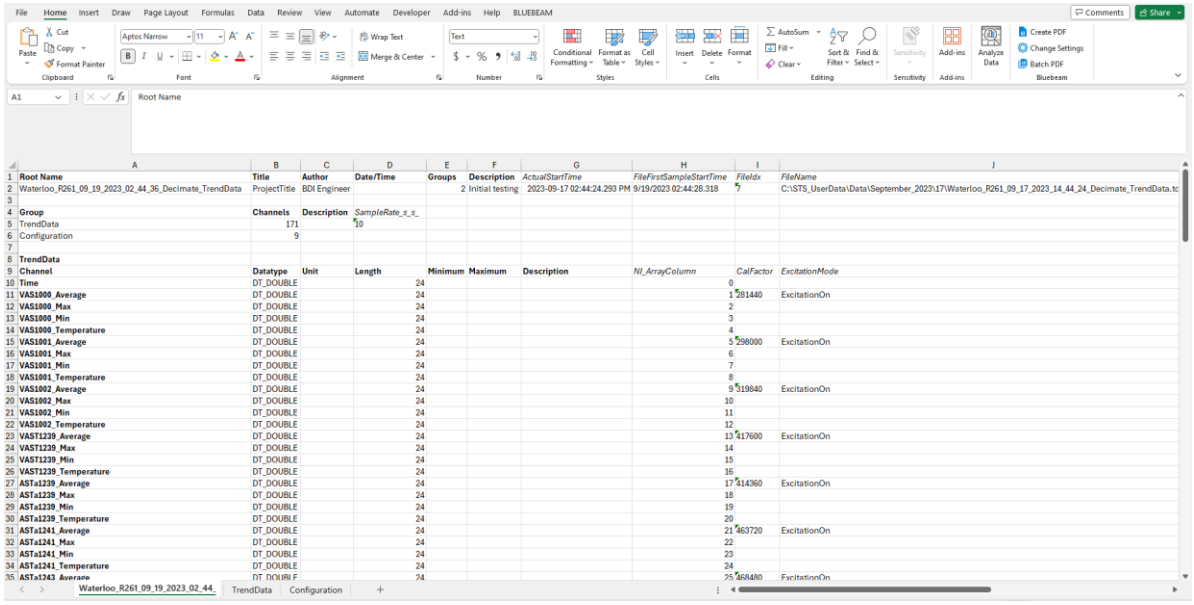
Figure 9.8 Within each daily folder, the high-speed strain/pressure and low-speed trend data is stored.

Examining each of the TDMS data files provides insights into the contents depicted in Figure 9.9 to Figure 9.11. To facilitate the viewing of TDMS files, the researchers opted for a TDMS-to-Excel file converter developed by NI, enabling the automatic opening of all TDMS files in Excel for further data analysis. Figure 9.9 shows the first page of the Excel worksheet for each TDMS file produced. This worksheet is applicable for both low speed and high-speed data collection files for both the load and environmental data, respectively. On this page, information about all of the sensors for which the data is being collected is provided along with project, date, and start time details.

The start time is particularly crucial as it is utilized to create a timestamp to indicate the time and date a row of data is produced, a feature not automatically included in the data files produced. The timestamp that was used comes from a column called *TestStart_Time*. To create the timestamp, an Excel VBA formula was created whereby the *TestStart_Time* was added to the "Time" in seconds columns on subsequent worksheets where the raw or trend data is stored. The *TestStart_Time* signifies the time of file creation, and each instance of manually initiating a new file (by starting or stopping the DAC) generates a fresh *TestStart_Time*. The same *TestStart_Time* is replicated in new files if the DAC test remains unchanged.

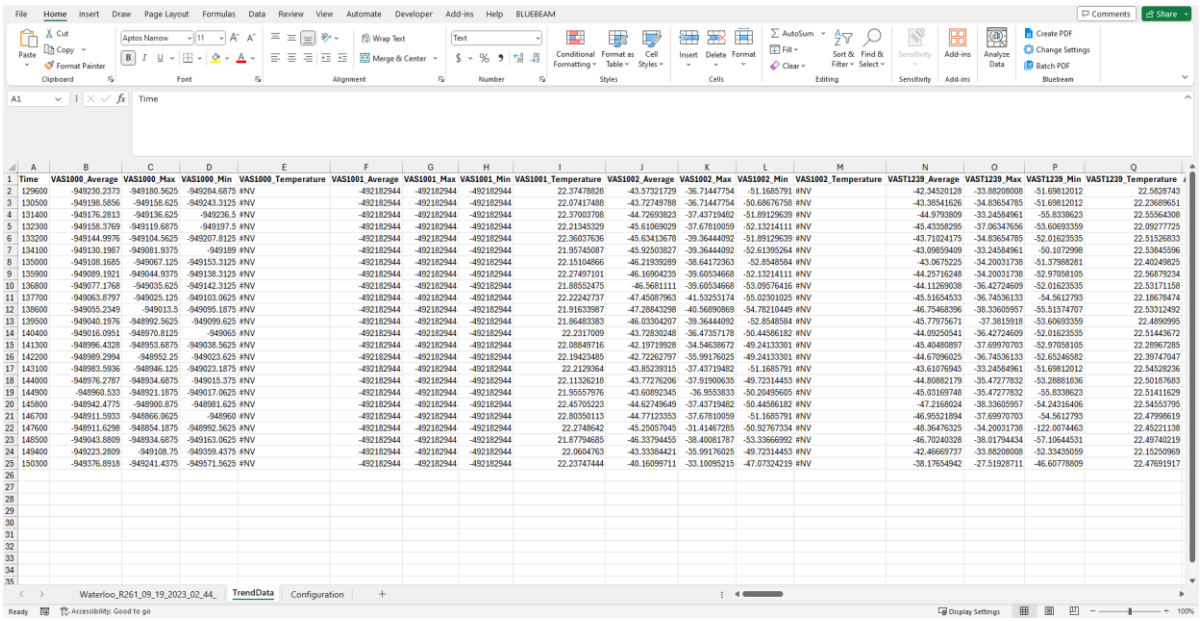
Next, each data file contains either a trend data or a high-speed data worksheet as its subsequent sheet. Within the trend data tab, as shown in Figure 9.10, the data of the sensors is typically aggregated to 15 minutes, although earlier files do have smaller aggregation times due to decisions made to increase

intervals as data collection progressed. Within each trend file, the data for each sensor is presented as an average, maximum value, and minimum value, each in its respective column. This format is valuable for assessing the average, maximum, and minimum response that a sensor produces within a specific timeframe without needing the high-speed information. Furthermore, these trend data files encompass environmental sensors such as moisture and temperature sensors since these metrics change at a slower pace and don't need to be captured at such high speeds as load data. Pressure and strain trend data is also captured for reference purposes.



	A	B	C	D	E	F	G	H	I	J
1	**Root Name**	**Title**	**Author**	**Date/Time**	**Groups**	**Description**	*ActualStartTime*	*FileFirstSampleStartTime*	*FileIdx*	*FileName*
2	Waterloo_R261_09_19_2023_02_44_36_Decimate_TrendData	ProjectTitle	BDI Engineer		2	Initial testing	2023-09-17 02:44:24.293 PM	9/19/2023 02:44:28.318		C:\STS_UserData\Data\September_2023\17\Waterloo_R261_09_17_2023_14_44_24_Decimate_TrendData.tc
3										
4	**Group**	**Channels**	**Description**	*SampleRate_s_s_*						
5	TrendData	171		10						
6	Configuration	9								
7										
8	**TrendData**									
9	**Channel**	**Datatype**	**Unit**	**Length**	**Minimum**	**Maximum**	**Description**	*NI_ArrayColumn*	*CalFactor*	*ExcitationMode*
10	**Time**	DT_DOUBLE		24				0		
11	**VAS1000_Average**	DT_DOUBLE		24				1	281440	ExcitationOn
12	**VAS1000_Max**	DT_DOUBLE		24				2		
13	**VAS1000_Min**	DT_DOUBLE		24				3		
14	**VAS1000_Temperature**	DT_DOUBLE		24				4		
15	**VAS1001_Average**	DT_DOUBLE		24				5	298000	ExcitationOn
16	**VAS1001_Max**	DT_DOUBLE		24				6		
17	**VAS1001_Min**	DT_DOUBLE		24				7		
18	**VAS1001_Temperature**	DT_DOUBLE		24				8		
19	**VAS1002_Average**	DT_DOUBLE		24				9	319840	ExcitationOn
20	**VAS1002_Max**	DT_DOUBLE		24				10		
21	**VAS1002_Min**	DT_DOUBLE		24				11		
22	**VAS1002_Temperature**	DT_DOUBLE		24				12		
23	**VAST1239_Average**	DT_DOUBLE		24				13	417600	ExcitationOn
24	**VAST1239_Max**	DT_DOUBLE		24				14		
25	**VAST1239_Min**	DT_DOUBLE		24				15		
26	**VAST1239_Temperature**	DT_DOUBLE		24				16		
27	**ASTa1239_Average**	DT_DOUBLE		24				17	414360	ExcitationOn
28	**ASTa1239_Max**	DT_DOUBLE		24				18		
29	**ASTa1239_Min**	DT_DOUBLE		24				19		
30	**ASTa1239_Temperature**	DT_DOUBLE		24				20		
31	**ASTa1241_Average**	DT_DOUBLE		24				21	463720	ExcitationOn
32	**ASTa1241_Max**	DT_DOUBLE		24				22		
33	**ASTa1241_Min**	DT_DOUBLE		24				23		
34	**ASTa1241_Temperature**	DT_DOUBLE		24				24		
35	**ASTa1243_Average**	DT_DOUBLE		24				25	468480	ExcitationOn

Figure 9.9 Low-speed, trend data files, general information page.



	A	B	C	D	E	F	G	H	I	J	K	L	M	N	O	P	Q
1	**Time**	**VAS1000_Average**	**VAS1000_Max**	**VAS1000_Min**	**VAS1000_Temperature**	**VAS1001_Average**	**VAS1001_Max**	**VAS1001_Min**	**VAS1001_Temperature**	**VAS1002_Average**	**VAS1002_Max**	**VAS1002_Min**	**VAS1002_Temperature**	**VAST1239_Average**	**VAST1239_Max**	**VAST1239_Min**	**VAST1239_Temperature**
2	129600	-949230.2373	-949180.5625	-949284.6875	#NV	-492182944	-492182944	-492182944	22.37478828	-43.57321729	-36.71447754	-51.1685791	#NV	-42.34501228	-33.88208008	-51.69812012	22.5828743
3	130500	-949198.5856	-949158.625	-949243.3125	#NV	-492182944	-492182944	-492182944	22.07417488	-43.72749788	-36.71447754	-50.68676758	#NV	-43.38541626	-34.83654785	-51.69812012	22.23689651
4	131400	-949176.2813	-949136.625	-949236.5	#NV	-492182944	-492182944	-492182944	22.37003708	-44.72693823	-37.43719482	-51.89129639	#NV	-44.9793809	-33.24584961	-55.8338623	22.55564308
5	132300	-949158.3769	-949119.6875	-949197.5	#NV	-492182944	-492182944	-492182944	22.21345329	-45.61069029	-37.67810059	-52.13214111	#NV	-45.43358295	-37.06347656	-53.60693359	22.09277725
6	133200	-949144.9976	-949104.5625	-949207.8125	#NV	-492182944	-492182944	-492182944	22.36037636	-45.63413678	-39.36444092	-51.89129639	#NV	-43.71024175	-34.83654785	-52.01623535	22.51526833
7	134100	-949130.1987	-949081.9375	-949189	#NV	-492182944	-492182944	-492182944	21.95745087	-45.92503827	-39.36444092	-52.61395264	#NV	-43.09859409	-33.24584961	-50.1072998	22.53845596
8	135000	-949186.1685	-949067.125	-949153.3125	#NV	-492182944	-492182944	-492182944	22.15104666	-46.21939289	-38.64172363	-52.8548584	#NV	-43.0675225	-34.20031738	-51.37988281	22.40249825
9	135900	-949089.1921	-949044.9375	-949138.3125	#NV	-492182944	-492182944	-492182944	22.27497101	-46.16904235	-39.60534668	-52.13214111	#NV	-44.25716248	-34.20031738	-52.97058105	22.56879234
10	136800	-949077.1768	-949035.625	-949142.3125	#NV	-492182944	-492182944	-492182944	21.88552475	-46.5681111	-39.60534668	-53.09576416	#NV	-44.11269038	-36.42724609	-52.01623535	22.53171158
11	137700	-949063.8797	-949025.125	-949103.0625	#NV	-492182944	-492182944	-492182944	22.22242737	-47.45087963	-41.53253174	-55.02301025	#NV	-45.51654533	-36.74536133	-54.5612793	22.18678474
12	138600	-949055.2349	-949013.5	-949095.1875	#NV	-492182944	-492182944	-492182944	21.91633987	-47.28843298	-40.56890869	-54.78210449	#NV	-46.75468396	-38.33605957	-55.51574707	22.53312492
13	139500	-949040.1976	-948992.5625	-949099.625	#NV	-492182944	-492182944	-492182944	21.86483383	-46.03304207	-39.36444092	-52.8548584	#NV	-45.77975671	-37.3815918	-53.60693359	22.4890995
14	140400	-949016.0951	-948970.8125	-949065	#NV	-492182944	-492182944	-492182944	22.2317009	-43.72830248	-36.47357178	-50.44586182	#NV	-44.09250541	-36.42724609	-52.01623535	22.51443672
15	141300	-948986.4328	-948953.6875	-949038.5625	#NV	-492182944	-492182944	-492182944	22.08849716	-42.1971928	-34.54638672	-49.24133301	#NV	-45.40480897	-37.69970703	-52.97058105	22.28967285
16	142200	-948989.2994	-948952.25	-949023.625	#NV	-492182944	-492182944	-492182944	22.19423485	-42.72262797	-35.99176025	-49.24133301	#NV	-44.67096025	-36.74536133	-52.65246582	22.39747047
17	143100	-948983.5936	-948946.125	-949023.1875	#NV	-492182944	-492182944	-492182944	22.2129364	-43.85239315	-37.43719482	-51.1685791	#NV	-43.61076945	-33.24584961	-51.69812012	22.54528236
18	144000	-948976.2787	-948934.6875	-949015.375	#NV	-492182944	-492182944	-492182944	22.11326218	-43.77276206	-37.91900635	-49.72314453	#NV	-44.80882179	-35.47277832	-53.28881836	22.50187683
19	144900	-948960.533	-948921.1875	-949017.0625	#NV	-492182944	-492182944	-492182944	21.95557976	-43.60892345	-36.9553833	-50.20495605	#NV	-45.03169748	-35.47277832	-55.8338623	22.51411629
20	145800	-948942.4775	-948900.875	-948981.625	#NV	-492182944	-492182944	-492182944	22.45705223	-44.62749649	-37.43719482	-50.44586182	#NV	-47.2168024	-38.33605957	-54.24316406	22.54553795
21	146700	-948911.5933	-948866.9625	-948960	#NV	-492182944	-492182944	-492182944	22.80350113	-44.7723353	-37.67810059	-51.1685791	#NV	-46.95521894	-37.69970703	-54.5612793	22.47998619
22	147600	-948911.6298	-948854.1875	-948992.5625	#NV	-492182944	-492182944	-492182944	22.2748642	-45.25057045	-31.41467285	-50.92767334	#NV	-48.36476325	-34.20031738	-122.0074463	22.45221138
23	148500	-949043.8809	-948934.6875	-949163.0625	#NV	-492182944	-492182944	-492182944	21.87794685	-46.33794455	-38.40081787	-53.33666992	#NV	-46.70240328	-38.01794434	-57.10644531	22.49740219
24	149400	-949223.2809	-949108.75	-949359.4375	#NV	-492182944	-492182944	-492182944	22.0604763	-43.33384421	-35.99176025	-49.72314453	#NV	-42.46669737	-33.88208008	-52.33435059	22.15250969
25	150300	-949376.8918	-949241.4375	-949571.5625	#NV	-492182944	-492182944	-492182944	22.23747444	-40.16099711	-33.10095215	-47.07324219	#NV	-38.17654942	-27.51928711	-46.60778809	22.47691917

Figure 9.10 Low-speed, trend data files, data collected per sensor.

The second type is the high-speed data, of which an example is shown in Figure 9.11. It provides information on select sensors, mainly those that require high-speed data collection, such as strain and pressure. They do not capture environmental data. These high-speed files tend to be much larger in size than trend data files and require greater manipulation.

Regardless of the data collection speed type, the data required cleaning to ensure its utility for subsequent analysis. This step is crucial, especially when preparing data for a national database, as it needs to be accurately organized, collected, and cleaned to support meaningful data analysis and avoid any inaccuracies or misleading information.

A variety of tools were used for this purpose, such as Excel Visual Basic, Python, and R in order to develop scripts that will take this data, convert headers and clean unnecessary columns that are not collecting data, flag up inconsistencies, etc. All the major scripts that were used in the data cleaning process can be found in Appendix C.

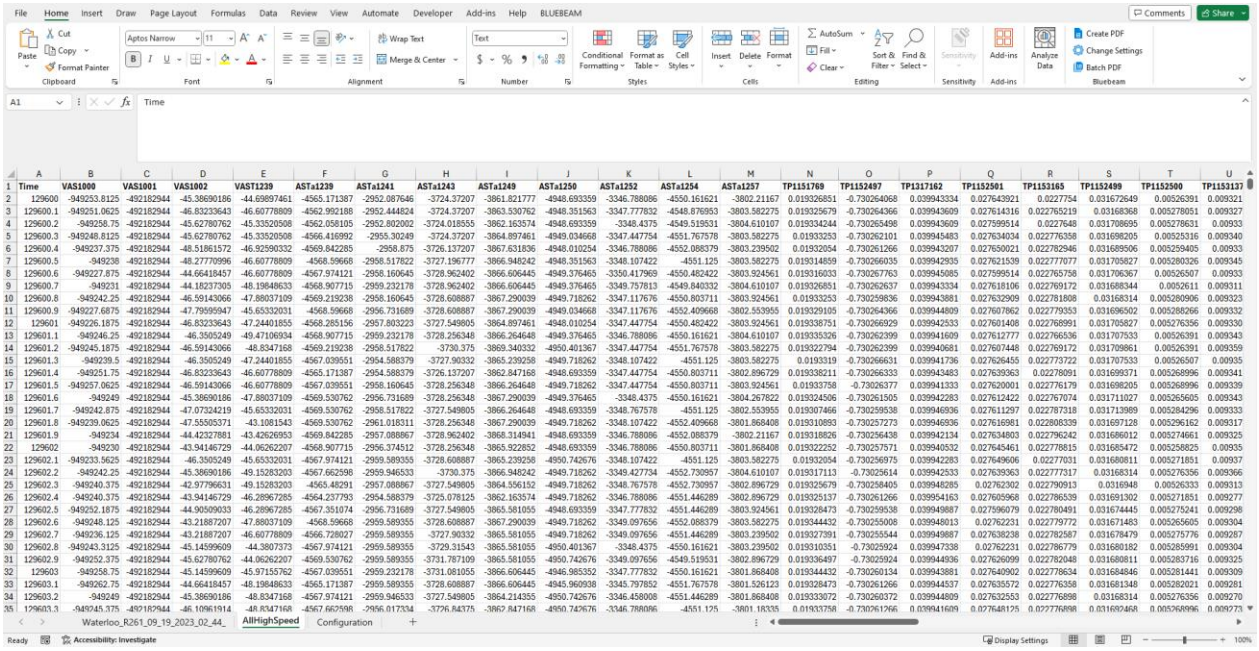


Figure 9.11 High speed data files, data collected per sensor.

9.2.2 Proposed Database Concept for Smart Pavement Project

With this amount of data that's produced, a database would be an excellent way in to store and share this data not only for this project but for all similar projects. This will then contribute towards the implementation and set up of a national database whereby similar pavement sections such as these collecting similar information can be consolidated for use and analysis by Canadian scientists and engineers. Essentially, the logic that it will be proposed for this database follows the LTPP structure in a

similar manner, as much of the linkage and setup of the database is inspired by the LTPP database. This is because the LTPP database has key factors that are critical for database success.

The proposed database concept is displayed in Figure 9.12.

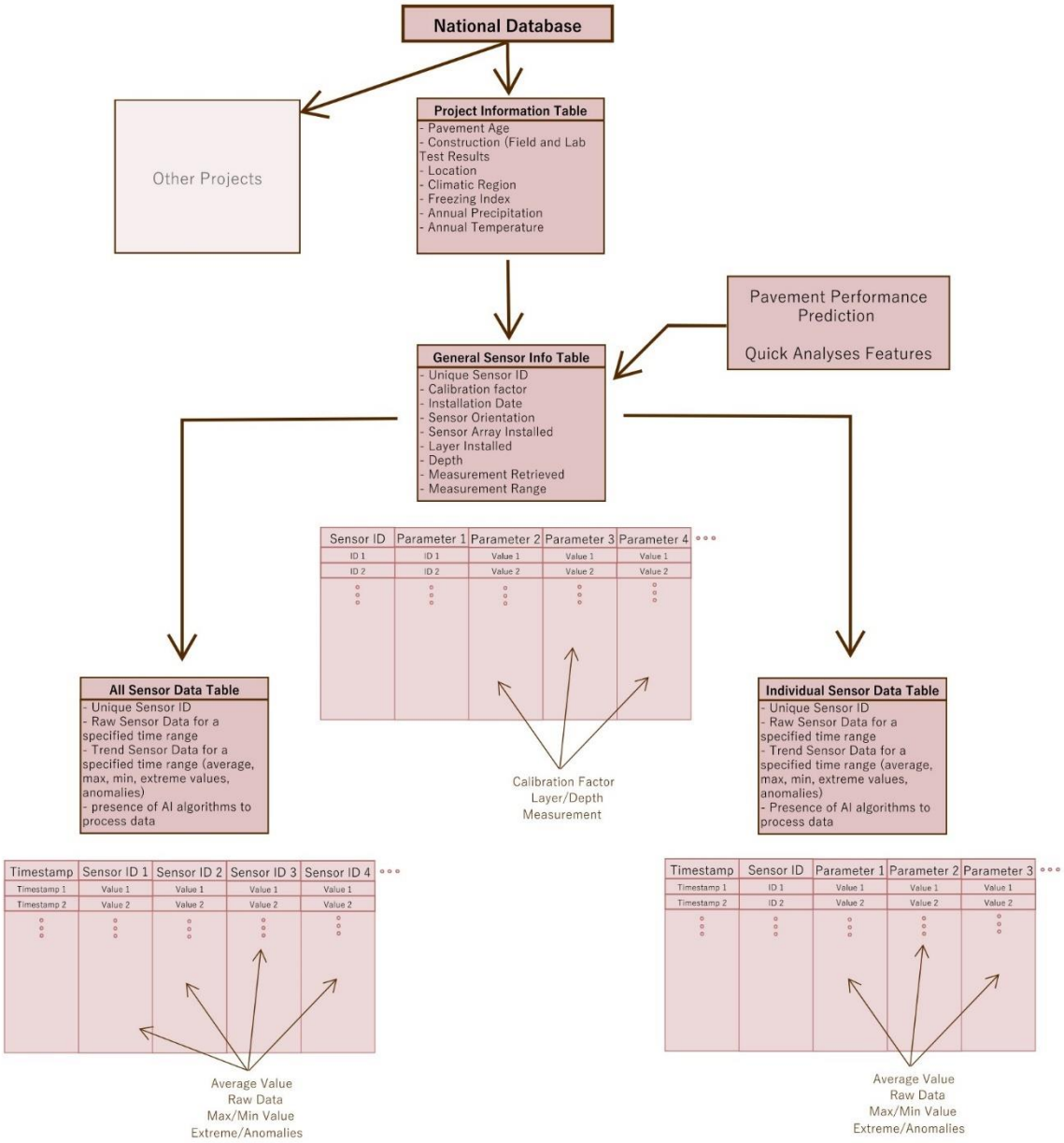


Figure 9.12 General logic for database development for this project and how it connects to the national database.

9.2.2.1 Project Information within the National Database

Observing Figure 9.12, the overarching idea revolves around the establishment of a national database. This database is designed to aggregate data from a diverse range of projects originating from different pavement sections across Canada. The primary objective is to create a comprehensive repository, consolidating data from various projects into a single, centralized database. This overarching concept serves as the guiding principle for the intended direction of the research.

Within the national database, each project will be equipped with its own set of project information, systematically organized into project information tables. These tables will feature various project descriptors, offering insights into specific aspects such as the pavement age at the time of construction, lab and field test results, project location, sensor calibration factor information, project soil properties, climate regions, and details on freezing, precipitation, and temperature will be encapsulated within these project information tables. This categorization approach allows projects to be systematically grouped based on their unique characteristics, which could permit for easy filtering of project information by users. The LTPP database provides similar information which can be used as a reference, which is expressed in Figure 9.13.

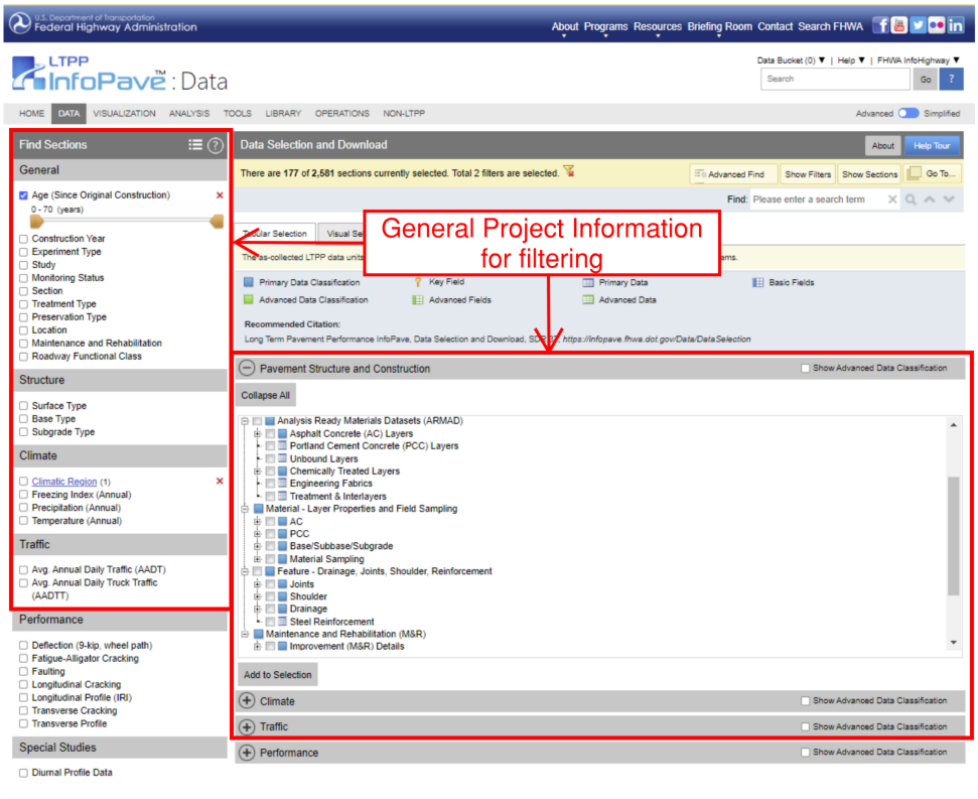


Figure 9.13 Similar project information from LTPP InfoPave [95].

9.2.2.2 General Sensor Information Table

Within each project, users should be able to extract various sensor details through the associated “General Sensor Information Table”. The sensor table’s role should be to outline information on all sensors utilized in a specific project, assigning each a unique sensor ID.

For this project, the sensor ID system should be designed to clearly represent each individual sensor through distinct and easily distinguishable names. These names should convey specific information, such as the type of sensor, the layer or depth it is situated in if applicable, its longitudinal or transverse positioning if relevant, and whether it is installed to the right or left sensor array. For other projects, other naming conventions should be used that reflect the specific conditions of that project (while also providing some unifying labels throughout the projects). The current naming system for this project incorporates these features. For instance, an asphalt strain gauge is identified by the letters “AS”, while the directional orientation is denoted by “LO” for longitudinal and “TR” for transverse positioning. Additionally, the letters R and L indicate whether the sensor is in the right or left array, respectively. Lastly, a numerical value is assigned to indicate the sensor's position when viewed in the direction of traffic or in terms of depth within the pavement structure. A legend that explains the various meanings of the current labelling system is expressed in Table 9.1.

Table 9.1 Legend for Current Naming Convention

Abbreviation	Meaning
R	right sensor array
L	left sensor array
BA	base
SB	subbase
SG	subgrade
TR	transverse
LO	longitudinal
AS	asphalt strain gauge
VAS	vertical asphalt strain gauge
MOI	moisture sensor
PC	pressure cell
TEMP	thermistor
TM	temperature probe

A revision in the current naming convention may need to occur to reflect a more precise way of labeling each individual sensor that has been used. For instance, it may be challenging to accurately determine the exact depth measurement of each sensor solely from its name. To address this, a potential improvement could involve incorporating depth information directly into the naming convention. Alternatively, creating a dedicated column in the sensor information tables to explicitly describe the depth of each

sensor would offer a more organized and accessible way for users to retrieve this information from the database. This adjustment would streamline the naming convention, making it more informative and user-friendly.

In addition to the sensor ID, the general sensor information table should encompass crucial details, including the units generated by each sensor during data collection, the type of data gathered (e.g., strain, moisture content, pressure, temperature), and the calibration factors specific to each sensor. This information serves as a valuable resource for users, aiding in the interpretation of raw and trend data. In the event of any data discrepancies, users can utilize this information, particularly the calibration factors, to verify and make necessary adjustments.

For example, Table 9.2 presents several of these pertinent details for this project. The first column features the manufacturer names of the sensors received by the research team upon acquisition. The second column provides the sensor ID, employing the unique names established earlier. The third column outlines the types of data collected, such as longitudinal or transverse strain for asphalt strain gauges and volumetric water content (VWC) for moisture sensors. The last column specifies the output units produced when data is collected, aiding users in accurately interpreting the stored database information.

Moving on to Table 9.3, this table highlights essential calibration factors corresponding to each sensor. The first column expresses the sensor ID, while the second column shows the relevant calibration factors. For asphalt strain gauges, calibration was generally conducted by the manufacturer, BDI, with specific calibration factor values not explicitly determined. However, for other sensors like moisture sensors and pressure cells, the relevant calibration factor equations are presented in the table. This detailed calibration information enhances the database's utility for users seeking precise and reliable data interpretation.

After inputting all the relevant information into the general sensor information table, it will resemble the format shown in both Table 9.4 and

Table 9.5. These tables provide a preliminary structure for the expression of the general sensor information. While Table 9.4 and

Table 9.5 are conceptually one table, they are presented across two tables for ease of reference and readability in this report.

For instance, in these tables, the sensor types are organized by sensor ID. Additionally, information such as sensor orientation within the sensor array, along with pertinent details like position coordinates and the potential range of collected data, should be incorporated into this comprehensive table.

Table 9.2 Naming Convention, Data Collected and Output Units Produced for each sensor

Manufacturer Name	Sensor ID	Data Collected	Output Produced Units
ASTa1257	AS-LO-R-1	longitudinal strain	με
ASTa1243	AS-LO-L-2	longitudinal strain	με
ASTa1239	AS-TR-R-3	transverse strain	με
ASTa1249	AS-TR-L-4	transverse strain	με
ASTa1250	AS-TR-R-5	transverse strain	με
ASTa1252	AS-TR-L-6	transverse strain	με
ASTa1241	AS-LO-R-7	longitudinal strain	με
ASTa1254	AS-LO-L-8	longitudinal strain	με
VAS1002	VAS-R-1	vertical strain	με
VAS1001	VAS-L-2	vertical strain	με
VAS1000	VAS-R-3	vertical strain	με
VAST1239	VAS-L-4	vertical strain	με
TEROS10_1	MOI-BA-1	VWC (m^3/m^3)	mV
TEROS10_2	MOI-SB-2	VWC (m^3/m^3)	mV
TEROS10_3	MOI-SB-3	VWC (m^3/m^3)	mV
TEROS10_4	MOI-SB-4	VWC (m^3/m^3)	mV
TEROS10_5	MOI-SG-5	VWC (m^3/m^3)	mV
TP1152500	PC-BA-R-1	Pressure	MPa
TP1151769	PC-BA-L-2	Pressure	MPa
TP1153165	PC-SB-R-3	Pressure	MPa
TP1152501	PC-SB-L-4	Pressure	MPa
TP1152499	PC-BA-R-5	Pressure	MPa
TP1153137	PC-BA-L-6	Pressure	MPa
TP1317164	PC-SG-R-7	Pressure	MPa
TP1317162	PC-SG-L-8	Pressure	MPa
ASTa1249_Temperature	TEMPS-02-1	Temperature	°C
ASTa1257_Temperature	TEMPS-01-1	Temperature	°C
ASTa1241_Temperature	TEMPS-02-2	Temperature	°C
ASTa1252_Temperature	TEMPS-01-2	Temperature	°C
ASTa1239_Temperature	TEMPS-02-3	Temperature	°C
ASTa1250_Temperature	TEMPS-01-3	Temperature	°C
TEROS10_4_Temperature	TM-BA-01	Temperature	°C
TEROS10_1_Temperature	TM-BA-02	Temperature	°C
TEROS10_5_Temperature	TM-SB-03	Temperature	°C
TEROS10_2_Temperature	TM-SB-04	Temperature	°C
VAS1001_Temperature	TM-SB-05	Temperature	°C
VAST1239_Temperature	TM-SG-06	Temperature	°C
TEROS10_3_Temperature	TM-SG-07	Temperature	°C

Table 9.3 Calibration Factors related to each Sensor

Sensor ID	Calibration Factors
AS-LO-R-1	Used calibration from BDI
AS-LO-L-2	Used calibration from BDI
AS-TR-R-3	Used calibration from BDI
AS-TR-L-4	Used calibration from BDI
AS-TR-R-5	Used calibration from BDI
AS-TR-L-6	Used calibration from BDI
AS-LO-R-7	Used calibration from BDI
AS-LO-L-8	Used calibration from BDI
VAS-R-1	Used calibration from BDI
VAS-L-2	Used calibration from BDI
VAS-R-3	Used calibration from BDI
VAS-L-4	Used calibration from BDI
MOI-BA-1	Θ = 4.824×10−10×mV 3−2.278×10−6×mV 2 +3.898×10−3×mV −2.154
MOI-SB-2	Θ = 4.824×10−10×mV 3−2.278×10−6×mV 2 +3.898×10−3×mV −2.155
MOI-SB-3	Θ = 4.824×10−10×mV 3−2.278×10−6×mV 2 +3.898×10−3×mV −2.156
MOI-SB-4	Θ = 4.824×10−10×mV 3−2.278×10−6×mV 2 +3.898×10−3×mV −2.157
MOI-SG-5	Θ = 4.824×10−10×mV 3−2.278×10−6×mV 2 +3.898×10−3×mV −2.158
PC-BA-R-1	y=0.7484x-0.7417
PC-BA-L-2	y=0.7563x+0.7594
PC-SB-R-3	y=0.5024x+0.5056
PC-SB-L-4	y=0.4967x-0.4995
PC-BA-R-5	y=0.7522x-0.731
PC-BA-L-6	y=0.7679x-0.7715
PC-SG-R-7	y=1818x-0.18820
PC-SG-L-8	y=0.1767x-0.1818
TEMPS-02-1	No calibration factor
TEMPS-01-1	No calibration factor
TEMPS-02-2	No calibration factor
TEMPS-01-2	No calibration factor
TEMPS-02-3	No calibration factor
TEMPS-01-3	No calibration factor
TM-BA-01	No calibration factor
TM-BA-02	No calibration factor
TM-SB-03	No calibration factor
TM-SB-04	No calibration factor
TM-SB-05	No calibration factor
TM-SG-06	No calibration factor
TM-SG-07	No calibration factor

Table 9.4 Examples of Information Included in the General Sensor Information Table, Part 1

Sensor Type	Sensor Orientation	Wheel Path Position	Sensor Orientation			Sensor Plane Position Coordinates
Asphalt Strain Gauge	Longitudinal	Right	x	y	N/A	Should be collected with GPS to produce GPS coordinates.
		Left				
	Transverse	Right	x	y	N/A	
		Left				
	Vertical	Right	N/A	N/A	z	
		Left				
Pressure Cell	N/A	Right	N/A	N/A	z	
		Left				
Moisture Sensor	N/A	N/A	N/A	N/A	z	
Temperature Sensor	N/A	N/A	N/A	N/A	z	
Temperature Tree	N/A	N/A	N/A	N/A	z	

Table 9.5 Examples of Information Included in the General Sensor Information Table, Part 2

Sensor Type	Sensor Depth from Asphalt Surface (Range)		Physical Quantity Measured	Output Units	Range of Data Collected by Sensor		Data Type	Data Collection Rate	
	Min (mm)	Max (mm)			Min	Max		LIVE MODE	TREND MODE
Asphalt Strain Gauge	0	195	Longitudinal/transverse/vertical strain	με	-5000	5000	real	1000 s/s	Aggregated 1 data point every 15 minutes
Pressure Cell	195	745	Pressure	MPa	(-) 0.7 MPa, 2.0MPa, 3.0MPa	0.7 MPa, 2.0MPa, 3.0MPa	real		
Moisture Sensor	195	745	Volumetric Water Content (m3/m3)	mV	0	0.64 m3/m3	real	N/A	
Temp Sensor	195	745	Temperature	°C	-40	100	real		
Temp Tree	72.7	245	Temperature	°C	-40	100	real		

9.2.2.3 Individual Sensor Data Table

A sensor table should then serve as a gateway for users to access additional or specific information about a sensor. An example includes sorting all raw or trend data collected by the data acquisition system based on sensor type, in a type of "Individual Sensor Data Table". To do this, users can click on each of the individual sensors for more details, since these sensors will be linked to the low-speed and high-speed data gathered on them. For instance, if a user wants to view information from one or more environmental data sensors, like a moisture sensor, they can do so through the individual sensor data table.

Within this individual sensor data table, various parameters for each specific sensor type can be extracted and compared. This includes average values, maximum and minimum values, detection of extremes or anomalies within the specified timestamp range for both low-speed trend and high-speed raw data collection. Notably, the individual sensor data table accommodates both raw and trend data.

9.2.2.4 All Sensor Data Table

Furthermore, the sensor table should guide users to an all-sensor data table, mirroring the current presentation of data already present in TDMS files, and visible when data is converted from a TDMS file to an Excel spreadsheet. This table, based on the selected date-time stamp range, displays sensor data for all sensors within that specific timeframe. It offers the flexibility to present data in low speed or high speed, environmental or load data, facilitating additional avenues for comparison. This is where the TDMS files collected daily could be uploaded and managed within the database system.

For example, Figure 9.14 and Figure 9.15 show the data-cleaned versions of both the low-speed trend and high-speed raw data collected from the TDMS files. In each case, the timestamp has been added and each column presents data from each sensor.

	A	B	C	D	E	F	G	H	I	J	K	L
1	Time	Timestamp	AS-LO-L-2_Average	AS-LO-L-2_Max	AS-LO-L-2_Min	AS-LO-L-8_Average	AS-LO-L-8_Max	AS-LO-L-8_Min	AS-LO-R-1_Average	AS-LO-R-1_Max	AS-LO-R-1_Mir	AS-LO-R-7_Ave A
2	1771200	2023-10-08 2:44	-3721.763542	-3712.366211	-3730.728027	-4555.305949	-4547.271484	-4562.365723	-3871.475717	-3863.895752	-3878.631592	-2958.869661
3	1772100	2023-10-08 2:59	-3714.336978	-3703.185547	-3723.665527	-4546.893737	-4539.241699	-4554.657715	-3863.12226	-3855.328369	-3870.406982	-2951.763844
4	1773000	2023-10-08 3:14	-3706.955457	-3696.476563	-3717.310059	-4538.5106	-4532.176758	-4545.665039	-3855.055239	-3847.789307	-3862.182373	-2944.529932
5	1773900	2023-10-08 3:29	-3699.65431	-3689.767578	-3708.835449	-4531.091186	-4523.826172	-4538.278809	-3847.955241	-3841.278076	-3854.986084	-2937.709946
6	1774800	2023-10-08 3:44	-3692.367594	-3683.058594	-3701.066895	-4522.911406	-4515.797363	-4530.570313	-3840.125951	-3833.39624	-3847.446533	-2930.992975
7	1775700	2023-10-08 3:59	-3685.385901	-3677.40918	-3695.770508	-4516.221246	-4510.337891	-4522.862793	-3834.388468	-3828.598877	-3839.907471	-2924.494572
8	1776600	2023-10-08 4:14	-3679.504778	-3671.405762	-3687.648926	-4508.995117	-4501.987305	-4516.760742	-3829.62294	-3823.115479	-3835.795166	-2918.668892
9	1777500	2023-10-08 4:29	-3674.135541	-3666.109375	-3683.058594	-4502.655229	-4495.885254	-4509.052734	-3824.447218	-3817.974854	-3831.340088	-2912.466999
10	1778400	2023-10-08 4:44	-3668.249297	-3660.106445	-3675.996094	-4496.99439	-4490.74707	-4503.271973	-3818.669967	-3811.806885	-3825.171631	-2906.165172
11	1779300	2023-10-08 4:59	-3663.750792	-3654.103516	-3672.112305	-4491.367035	-4485.929199	-4496.848633	-3813.563912	-3808.036865	-3819.003174	-2900.794578
12	1780200	2023-10-08 5:14	-3659.51482	-3651.984863	-3667.875	-4486.089116	-4480.469238	-4492.995117	-3809.147481	-3803.582275	-3814.548096	-2895.945566
13	1781100	2023-10-08 5:29	-3655.951337	-3648.454102	-3663.284668	-4481.445532	-4474.367188	-4489.140625	-3805.603314	-3798.784424	-3811.121338	-2891.623125
14	1782000	2023-10-08 5:44	-3652.308757	-3644.922852	-3659.400391	-4475.853383	-4462.163574	-4481.433105	-3801.534033	-3795.357666	-3807.009033	-2886.88213
15	1782900	2023-10-08 5:59	-3649.133097	-3640.33252	-3657.281738	-4470.022286	-4463.769043	-4475.652344	-3797.523815	-3791.930908	-3802.896729	-2882.462432
16	1783800	2023-10-08 6:14	-3645.016116	-3637.154785	-3652.338379	-4465.645426	-4460.236328	-4472.119141	-3793.349642	-3787.47583	-3800.155518	-2877.847754
17	1784700	2023-10-08 6:29	-3640.327401	-3632.563965	-3648.101074	-4461.872328	-4456.382324	-4466.659668	-3789.801505	-3783.705811	-3795.699951	-2873.051573
18	1785600	2023-10-08 6:44	-3636.571379	-3628.327148	-3645.276367	-4457.183721	-4451.244141	-4463.126465	-3785.723828	-3779.251221	-3791.587646	-2869.162419
19	1786500	2023-10-08 6:59	-3632.377414	-3624.796387	-3639.979492	-4453.275319	-4447.068848	-4463.126465	-3781.679836	-3772.397217	-3790.217041	-2864.991548
20	1787400	2023-10-08 7:14	-3628.227648	-3621.265137	-3636.801758	-4448.643698	-4442.893555	-4453.492188	-3777.60728	-3772.397217	-3782.677979	-2860.292979
21	1788300	2023-10-08 7:29	-3624.59656	-3616.321289	-3632.211426	-4443.454827	-4437.112793	-4449.638184	-3772.998568	-3766.22876	-3779.593506	-2855.944867
22	1789200	2023-10-08 7:44	-3621.19003	-3613.143555	-3629.739746	-4438.982256	-4432.29541	-4444.820801	-3768.688566	-3763.144775	-3774.110596	-2851.846973
23	1790100	2023-10-08 7:59	-3617.111791	-3609.259277	-3625.148926	-4434.632591	-4429.083496	-4440.324219	-3764.864092	-3755.605713	-3770.341064	-2847.320958
24	1791000	2023-10-08 8:14	-3614.955619	-3607.140625	-3621.265137	-4432.076418	-4427.156738	-4437.112793	-3763.411496	-3758.689697	-3768.627686	-2844.068861
25	1791900	2023-10-08 8:29	-3611.9031	-3600.785156	-3618.792969	-4429.308043	-4423.944824	-4433.901367	-3761.322901	-3745.324951	-3768.627686	-2840.416228

Figure 9.14 Example of low-speed trend data collected from the TDMS data system.

	A	B	C	D	E	F	G	H	I	J	K	L	M	N	O	
1	Time	Timestamp	AS-LO-L-2	AS-LO-L-8	AS-LO-R-1	AS-LO-R-7	AS-TR-L-4	AS-TR-L-6	AS-TR-R-3	AS-TR-R-5	PC-BA-L-2	PC-BA-L-6	PC-BA-R-1	PC-BA-R-5	PC-SB-L-4	PC-S
2	1792796.6	2023-10-08 8:43	-3608.552734	-4428.4414	-3760.060303	-2839.206055	-3713.504395	-3231.279297	-4495.11377	-4789.533203	0.01681505	0.006440378	0.003106707	0.029750051	0.025204122	0.
3	1792796.6	2023-10-08 8:43	-3607.493652	-4428.1201	-3761.088623	-2839.92041	-3713.162598	-3231.939453	-4494.802734	-4789.191406	0.016823614	0.006441568	0.003117457	0.029739022	0.025205661	0.
4	1792796.6	2023-10-08 8:43	-3607.493652	-4427.478	-3760.403076	-2839.563232	-3714.187988	-3233.589355	-4495.425293	-4791.582031	0.016844081	0.006446237	0.003085205	0.029751217	0.025200333	0.
5	1792796.6	2023-10-08 8:43	-3608.90625	-4428.4414	-3758.346924	-2839.563232	-3713.846191	-3232.599121	-4496.670898	-4791.240234	0.016837317	0.006435801	0.00308293	0.029749515	0.025195774	0.
6	1792796.6	2023-10-08 8:43	-3608.552734	-4430.0474	-3758.689697	-2840.635254	-3714.529297	-3231.279297	-4496.981934	-4788.849609	0.016834434	0.006434062	0.003077845	0.029723331	0.025189733	0.
7	1792796.6	2023-10-08 8:43	-3607.847168	-4429.0835	-3760.74585	-2840.992432	-3715.213379	-3230.949219	-4496.359375	-4788.166504	0.016841285	0.006434062	0.00308012	0.029738395	0.025181325	0.
8	1792796.6	2023-10-08 8:43	-3610.318848	-4428.7622	-3761.430908	-2840.635254	-3712.820801	-3232.269043	-4496.359375	-4789.874512	0.016841827	0.006424267	0.00308351	0.029748349	0.025193524	0.
9	1792796.6	2023-10-08 8:43	-3613.143555	-4428.4414	-3760.403076	-2840.277588	-3710.770508	-3234.249023	-4496.359375	-4790.557617	0.016840653	0.006428844	0.003077265	0.029732566	0.02521022	0.
10	1792796.6	2023-10-08 8:43	-3613.143555	-4427.1567	-3759.374756	-2839.563232	-3711.795898	-3233.589355	-4495.11377	-4790.216309	0.016833261	0.006433513	0.003101041	0.029740188	0.025194649	0.
11	1792796.6	2023-10-08 8:43	-3613.496582	-4428.7622	-3760.403076	-2839.563232	-3712.479492	-3231.609375	-4494.802734	-4789.533203	0.016824156	0.006424816	0.003111212	0.029751217	0.025183635	0.
12	1792796.6	2023-10-08 8:43	-3613.143555	-4429.0835	-3760.74585	-2838.134521	-3712.479492	-3231.609375	-4495.425293	-4789.191406	0.01683272	0.006424267	0.003081815	0.029755253	0.025198853	0.
13	1792796.6	2023-10-08 8:43	-3611.024902	-4427.478	-3759.032471	-2837.7771	-3711.795898	-3232.599121	-4495.425293	-4789.533203	0.016838942	0.006414472	0.003081815	0.029755881	0.025202228	0.
14	1792796.6	2023-10-08 8:43	-3611.37793	-4429.0835	-3758.346924	-2837.062744	-3711.453613	-3232.599121	-4496.359375	-4789.874512	0.016823074	0.006406966	0.003096536	0.029741893	0.025198853	0.
15	1792796.6	2023-10-08 8:43	-3613.496582	-4430.0474	-3759.374756	-2837.062744	-3712.820801	-3231.939453	-4496.359375	-4791.582031	0.016819106	0.006424816	0.00306879	0.029734898	0.025202997	0.
16	1792796.6	2023-10-08 8:43	-3613.496582	-4427.1567	-3761.088623	-2838.491699	-3712.820801	-3231.609375	-4495.425293	-4791.92334	0.016833261	0.006427745	0.003069905	0.029743684	0.025199562	0.
17	1792796.6	2023-10-08 8:43	-3611.730957	-4426.8354	-3761.088623	-2837.7771	-3712.479492	-3230.949219	-4495.11377	-4789.874512	0.01683786	0.006414472	0.003105591	0.029748349	0.025197668	0.
18	1792796.6	2023-10-08 8:43	-3609.612305	-4429.0835	-3759.718018	-2835.634033	-3714.529297	-3230.949219	-4494.179688	-4790.898926	0.016833261	0.006426556	0.00307673	0.029740188	0.025198083	0.
19	1792796.6	2023-10-08 8:43	-3608.552734	-4428.4414	-3758.346924	-2837.062744	-3714.529297	-3230.949219	-4494.179688	-4790.557617	0.016829295	0.006432322	0.003048984	0.029737856	0.02518707	0.
20	1792796.6	2023-10-08 8:43	-3608.90625	-4427.478	-3760.060303	-2838.491699	-3714.871582	-3231.279297	-4495.11377	-4787.825195	0.01683272	0.006416211	0.003081235	0.029736064	0.025189733	0.
21	1792796.6	2023-10-08 8:43	-3608.90625	-4428.4414	-3761.430908	-2838.491699	-3716.238281	-3232.599121	-4494.802734	-4788.508301	0.016836688	0.0064185	0.003099926	0.029732028	0.025215905	(
22	1792796.6	2023-10-08 8:43	-3609.259277	-4429.0835	-3759.718018	-2839.92041	-3715.896484	-3231.279297	-4495.736816	-4789.874512	0.016840653	0.00643873	0.003096536	0.029743057	0.025222773	0.
23	1792796.6	2023-10-08 8:43	-3609.96582	-4427.7993	-3759.718018	-2839.563232	-3714.187988	-3230.619141	-4497.293457	-4789.533203	0.016846335	0.006448525	0.003102156	0.029752383	0.025201103	0.
24	1792796.6	2023-10-08 8:43	-3608.90625	-4427.1567	-3761.088623	-2837.062744	-3713.504395	-3232.599121	-4496.981934	-4788.849609	0.016835606	0.006447884	0.003103316	0.029747183	0.025191629	0.
25	1792796.6	2023-10-08 8:43	-3607.847168	-4428.7622	-3759.374756	-2838.491699	-3714.187988	-3232.929199	-4495.736816	-4789.874512	0.016824786	0.006444497	0.003099346	0.029747721	0.025198437	0.
26	1792796.6	2023-10-08 8:43	-3608.200195	-4430.6895	-3759.374756	-2838.134521	-3714.529297	-3232.929199	-4495.11377	-4790.898926	0.016829925	0.006435801	0.003097651	0.029748349	0.025206432	0.
27	1792796.6	2023-10-08 8:43	-3609.259277	-4428.7622	-3760.74585	-2835.991211	-3713.504395	-3232.269043	-4494.491211	-4791.240234	0.016828753	0.006431224	0.003091406	0.029737229	0.025201457	0.
28	1792796.6	2023-10-08 8:43	-3611.37793	-4426.5142	-3759.032471	-2838.134521	-3711.795898	-3228.96875	-4494.802734	-4790.898926	0.016829295	0.006440378	0.003080655	0.029737856	0.025180615	0.
29	1792796.6	2023-10-08 8:43	-3610.671875	-4428.1201	-3756.976318	-2838.491699	-3711.795898	-3229.628906	-4497.60498	-4789.874512	0.016831007	0.006435252	0.003093101	0.029756417	0.025181741	0.
30	1792796.6	2023-10-08 8:43	-3607.847168	-4429.7261	-3758.689697	-2836.348389	-3714.871582	-3232.929199	-4499.161621	-4790.898926	0.016822442	0.006415571	0.003109517	0.029760543	0.025197668	0.
31	1792796.6	2023-10-08 8:43	-3608.90625	-4427.1567	-3761.088623	-2838.491699	-3716.580078	-3231.279297	-4496.359375	-4790.898926	0.016820189	0.006421978	0.003069905	0.029743684	0.025194293	0.
32	1792796.6	2023-10-08 8:43	-3610.318848	-4426.1929	-3761.430908	-2840.992432	-3715.555176	-3230.949219	-4493.868652	-4787.825195	0.016829295	0.006431224	0.003030873	0.02974252	0.025189733	0.
33	1792796.6	2023-10-08 8:43	-3608.552734	-4428.1201	-3760.74585	-2839.92041	-3715.555176	-3232.599121	-4494.802734	-4788.508301	0.016839573	0.006420239	0.003062009	0.029763412	0.025196899	0.
34	1792796.6	2023-10-08 8:43	-3608.552734	-4429.7261	-3760.74585	-2838.848877	-3715.896484	-3231.279297	-4495.736816	-4790.216309	0.016836688	0.006424267	0.003105011	0.029762875	0.025196899	0.
35	1792796.6	2023-10-08 8:43	-3609.259277	-4428.7622	-3759.374756	-2840.277588	-3714.871582	-3231.609375	-4494.802734	-4788.508301	0.01682136	0.006431773	0.003110097	0.029741354	0.025188195	0.

Figure 9.15 Example of high-speed trend data collected from the TDMS data system.

In essence, this multi-layered approach ensures that data is presented to users in various accessible formats, making it easy to view, download, and analyze for specific needs.

9.2.2.5 Pavement Performance Prediction and Quick Analyses Features

In addition to the structured presentation of data, a crucial aspect of this database is the incorporation of advanced analysis features and pavement performance prediction capabilities. The implementation of AI algorithms within the database can provide automated data analysis, offering an additional benefit to users.

A good example of this approach is within the current LTPP database which provides accessible high-level analyses in the form of trends analyses and comparisons, facilitating easy assessments between various pavement sections or within specific sections. For the Canadian National database being proposed in this chapter, a similar feature set should be implemented using AI and pavement performance prediction models. These advanced analytical tools can offer quick insights and comparisons, enhancing the database's utility for agencies and stakeholders. This would involve employing templates that allow agencies to upload their data or use the data in the database, which can then be monitored and filtered through the implemented algorithms and by third-party stakeholders.

The LTPP database currently has analyses already incorporated within their system that uses the information uploaded to the database. The first type is a trend analyses system (Figure 9.16) that will plot various physical parameters of selected pavement sections together overtime. The second type is a

comparisons analysis (Figure 9.17) that will display the correlation between selected parameters for selected pavement sections.

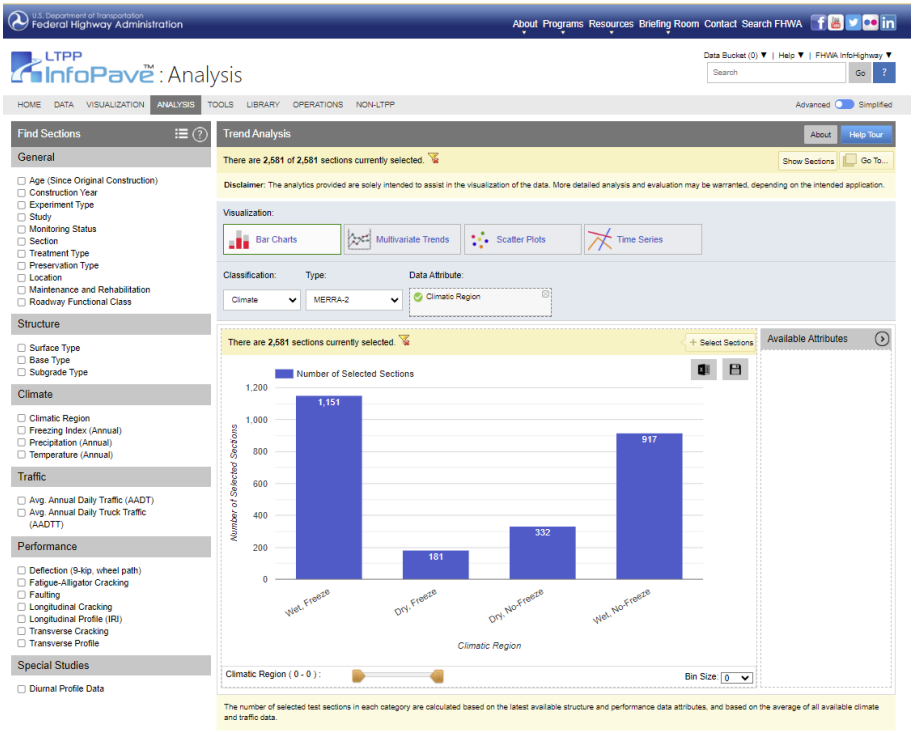


Figure 9.16 Trends analyses features within the LTPP database.

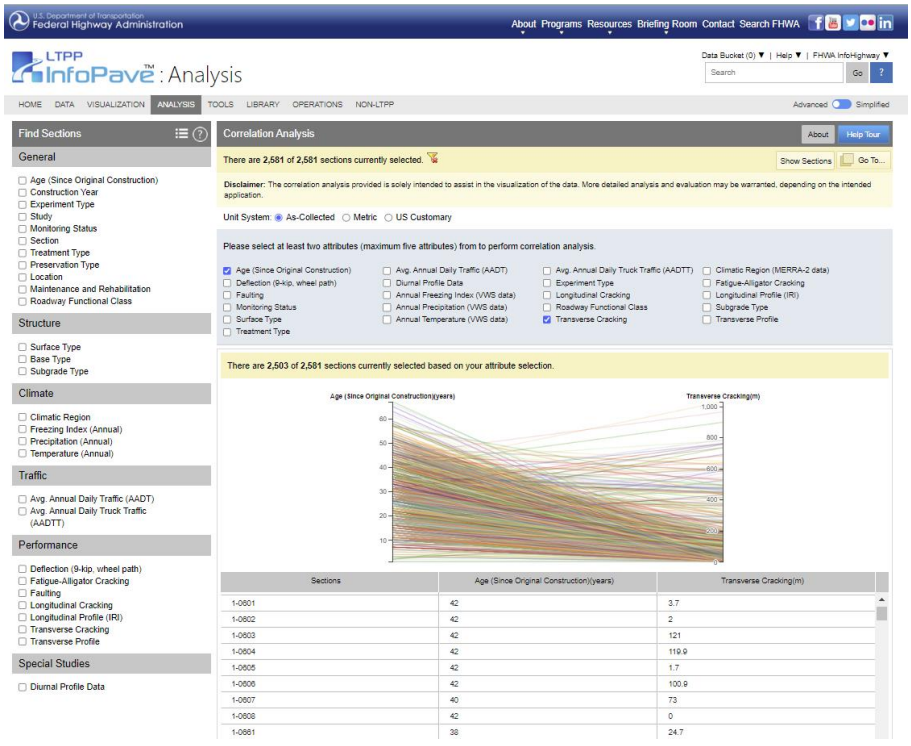


Figure 9.17 Comparisons analyses within the LTPP database.

On a national level, the database would house similar comprehensive information for a diverse array of projects. Agencies can adopt standardized templates for data upload, ensuring consistency across the national database. The application of AI algorithms not only streamlines data analysis but also enhances the ability to predict pavement performance trends.

9.2.2.6 Database Key Features

In order to ensure that the national database is successful, it should be efficient, easily searchable and should allow users to quickly find the data that they need. The setup should be that the database is not too simple nor too complex.

Central to this efficiency is the establishment of robust connections between different sets of data. In both the LTPP database and the proposed database, the integration of a systematic identification method for sensors is crucial. This method serves to describe and link various tables of sensor information, facilitating seamless access and retrieval for users.

The need for such identification becomes apparent at different levels, be it at a project level (for linking sensor information within a specific project) or, in the broader context of a national database, where distinct identification for each pavement section is imperative. Drawing inspiration from the LTPP database, which employs unique identifiers for States and sections of pavement on the same roadway [95], the proposed database for this project focuses on developing a strategy to link sensors and sensor information efficiently. The goal is to contribute to a broader national system that interconnects sensors from diverse projects.

To achieve this seamless linking of sensor information, the database should utilize a database-focused program, such as SQL. SQL, or Structured Query Language, designed specifically for database development and sharing, proves to be an ideal tool for this purpose. Its capabilities include creating and maintaining databases, data entry and modification, and extraction of large datasets [98]. The program's functionalities extend to providing clear identifications and facilitating the combination of data, making it a powerful and versatile tool for the successful implementation of the proposed database project. [98]

Another key feature of this database will be the ability to ensure clear data that is not redundant or duplicated. Of course, when it comes to linking data together in different tables, such as between the General Information table and an individual sensor table, there will be a bridge, such as the Sensor ID. However, minimizing redundant information, such as describing calibration factors in every table instead of just one, will be crucial to minimize the already large amount of input data that will be included in the database. It would be beneficial to explore the use of AI for this purpose.

Finally, the database should be easy to maintain, be secure from outside interference and have multiple backups. These will ensure that the data is not lost or tampered with, which will ensure accuracy for users and agencies.

Chapter 10

Conclusions and Recommendations

10.1 Summary of Work Performed

The primary goal of this thesis was to further the knowledge and understanding of incorporating advanced monitoring and predictive technologies, or embedded sensors, within an instrumented test section. In this regard, the research has succeeded in producing favorable results.

In Chapter 2, a synthesis of the historical and recent works regarding pavement distresses, current pavement monitoring practices and limitations, examples of sensors and test sections in past studies, applications of pavement performance monitoring and current research gaps was presented. Research gaps identified include:

1. Lack of consideration for sensor effects during construction phase and installation.
2. Limited data collection periods for sensor response analysis.
3. Insufficient exploration of long-term trends and load/environmental data assessment.
4. Inadequate understanding of the impact of vehicle wander on pavement sensor responses.
5. Scarcity of comparative studies between static and dynamic pavement response simulation methods.
6. Lack of studies on the scalability and cost-benefit analysis of implementing pavement sensor technologies on a wider scale over decades.

Research gaps 1 – 5 have been addressed in this thesis, while the 6th gap is a topic for future research.

Chapter 3 provided practical documentation of the instrumentation as well as the field and laboratory testing processes for the pavement section, covering design, sensor types, construction processes, hydro connection, and material sampling. Despite successful installation and data acquisition, challenges arose, notably weather-related delays. Recommendations include scheduling installations during favorable weather and allowing ample time for sensor calibration in the lab to address unexpected issues like sensor discrepancies observed in the field. Other issues such as installation planning, sensor placement accuracy, vibration impact, and data security were also noted.

Chapter 4 detailed material testing procedures conducted during the construction phase, encompassing field tests like truck and LWD testing, and lab tests evaluating layer properties following relevant standards. Tests such as dynamic modulus and Proctor tests were employed on the HMA and granular layers, respectively. Recommendations for future studies include implementing regular or scheduled

testing, expanding tests to characterize different pavement layers (e.g., FWD testing), and adopting a structured testing approach to enhance insights into material properties and trend assessments.

Chapter 5 marked the commencement of major assessment phase of the research for the instrumented test section, with the truck test being the primary focus. This test, detailed in the chapter, involved a standard 14-wheeler truck traversing the instrumented test section at varying speeds and, in some instances, temperatures. The analysis primarily centered around exploring the impact of speed, temperature, moisture, axle load, and traffic on layer strain and pressure. Conducted five times across different seasons, the truck tests aimed to capture a broad spectrum of data, providing insights into sensor functionality and performance nuances under diverse conditions. The results, depicted graphically for clarity and comparison, revealed intriguing variations across speeds and within different sensor arrays, shedding light on the dynamic responses of strain and pressure sensors. Key findings from this chapter include observations such as longitudinally higher strain responses compared to transverse directions, with slower speeds yielding greater magnitudes and clearer sensor signals. Seasonal variations were also noted, highlighting differences in sensor responsiveness and performance under construction conditions versus when the pavement cooled down. These insights underscored the importance of considering environmental factors and traffic conditions when interpreting sensor data.

Chapter 6 centered on assessing the impact of vehicle wander on pavement behavior by correlating tire position with pavement response. Wander tests involved the truck traversing different trajectories at 10 kilometers per hour, with sensor data collected for each case. Polynomial expressions were developed to quantify the relationship between strain or pressure responses and lateral deviations. The expressions accurately represented strain responses but showed some skewness for pressure responses. Future studies should conduct more wander tests to refine baseline responses crucial for validating truck test outcomes and identifying outliers. This validation process is integral to constructing a national database, as outlined in Chapter 9. By integrating similar relationships into data filtering algorithms, the accuracy of truck test results can be assessed, indicating the need for retesting if necessary.

Chapter 7 focused on modeling results from truck tests conducted across seasons using KENPAVE and 3D-Move software. The goal was to validate software-generated results against field measurements, assessing their accuracy in modeling pavement damage. Initial tests (TT#1) showed disparities between software and field data, but both tools improved in subsequent experiments (TT#2), likely due to stabilized properties and tire-pavement interactions. 3D-Move demonstrated superior precision in estimating pavement stress, especially in in-service scenarios, and facilitated dynamic response curve generation. Challenges with 3D-Move arose before testing summer conditions in TT#3, suggesting the need for ongoing research and validation to enhance predictive capabilities for pavement engineering

during construction. Future assessments should expand on this, comparing results across temperatures and speeds, while exploring alternative software options for improved ease of use.

Chapter 8 delved into detailed strain, pressure, and moisture trend results spanning approximately nine months across various seasons, aimed at evaluating sensor functionality. The trend analysis unveiled fluctuations in temperature, moisture, pressure, and strain, highlighting the correlation between seasonal variations and sensor responses. While the trend data provided clear and consistent results, the analysis of high-speed data yielded intriguing yet ambiguous outcomes in certain cases. Furthermore, the sheer volume of data made it challenging to effectively visualize in a single chart. Hence, it is recommended that future studies explore methods to integrate live and high-speed data to capture subtle changes in pressure and strain responses, thereby enhancing the sensitivity of trend assessments. Additionally, extending the duration of trend assessment beyond the nine-month period covered in this thesis project is advised. This would offer a yearly perspective on trend data, particularly during winter months, which may not have been entirely captured in the initial assessment. Acquiring data over one or multiple years would enable more accurate and comprehensive trend assessments, providing valuable insights for pavement engineering applications.

Finally, Chapter 9 introduced a basic database concept for organizing and sharing data from the instrumented test section. It proposed preliminary charts and data collection methods adaptable to databases using tools like SQL. These databases would efficiently capture, store, and filter project data and potentially data from similar projects. Continued development of this concept is recommended, expanding to include preliminary tests and establishing a basic database state. This iterative approach allows for assessing functionality and identifying areas for improvement before extending to other similar projects. By gradually refining and expanding, the database can become a robust tool for managing and analyzing instrumented test section data, aiding decision-making in pavement engineering.

10.2 Contributions of the Research

Chapter 1 outlined several research gaps in the literature with regards to pavement instrumentation. This thesis has been able to address all of these gaps to a certain extent.

This study successfully filled the void in understanding the responses of pavement structures during the critical construction phase, particularly regarding the impact of heavy vehicles on freshly laid asphalt. By conducting controlled truck tests immediately after the placement of Hot Mix Asphalt (HMA) layers, comprehensive data on pavement structural responses were meticulously collected and analyzed. This initiative provided invaluable insights into the behavior of pavement under real-world construction

conditions, thereby enhancing our understanding of how heavy vehicle loads influenced strain and pressure responses in freshly placed asphalt.

This study advanced the understanding of the relationships between pavement structural responses, HMA temperatures, and ambient conditions through in-depth heavy vehicle (truck) testing conducted across various seasons. Unlike existing literature, which often confined assessments to single tests per day or season, the research embraced a more exhaustive approach. By subjecting an instrumented test section to rigorous testing across different seasons, it provided a more nuanced understanding of pavement responses to heavy vehicle loads under varying environmental conditions, filling a critical gap in current knowledge.

Utilizing real-time data collected over multiple months and seasons from an instrumented test section on a bustling arterial roadway, the study delved into long-term trends and assessments of load and environmental factors. Through meticulous analysis of these trends, it gleaned insights into sensor functionality and performance, providing a comprehensive view of how pavement structures responded to prolonged exposure to heavy traffic and varying weather conditions. This holistic approach substantially contributed to addressing the existing gap in understanding long-term pavement behavior.

The study addressed the gap in understanding the impact of vehicle wander on pavement sensor responses through deliberate tests at various lateral deviations from embedded sensor arrays. By comparing the response magnitude and shape of embedded sensors with the extent of vehicle tire deviation, crucial correlations were established. These correlations shed light on the relationship between vehicle wander and pavement sensor responses, providing valuable insights into factors influencing sensor accuracy and reliability under real-world traffic conditions.

Through rigorous modeling and analysis, the study addressed the gap in understanding the comparative efficacy of static and dynamic pavement response simulation methods across different seasons and speeds. By modeling truck testing performed over several seasons using two common static and dynamic pavement software, the study meticulously compared the results with field data. This comprehensive approach facilitated a deeper understanding of the strengths and limitations of simulation methods, thereby enhancing their utility in predicting real-world pavement behavior across diverse conditions.

10.3 Recommendations for Future Work

Based on the research conducted in this thesis, several recommendations for future work emerge, aimed at advancing the understanding of instrumented pavement sections from a pavement management perspective.

As outlined in Chapter 1, a key objective of such research in the future is the integration of artificial intelligence (AI) and machine learning (ML) algorithms. These algorithms can leverage the extensive data generated by instrumented test pavement sections to enhance prediction models for pavement performance over time. These models hold potential utility across various domains including government agencies, academic research, and practical applications. The work presented in this thesis represents an initial step towards this objective. It involved the implementation of instrumented test sections, optimization of data generation and interpretation, and identification of trends crucial for discerning meaningful data responses. By establishing criteria for distinguishing between relevant and irrelevant data, this groundwork sets the stage for the automatic filtering and exclusion of unnecessary data within a national database framework. Such processes are integral for the effective utilization of AI and ML algorithms in pavement management.

Furthermore, future endeavors should prioritize the long-term collection of data spanning several years or more. This extended duration is essential for evaluating the impacts of climate change by consistently monitoring trends. For instance, assessments of freeze-thaw cycles, temperature fluctuations, and other relevant factors can be conducted and correlated with ongoing climate change patterns or established temperature norms. This approach allows for a deeper understanding of how climate change influences pavement sections, particularly in the context of southeastern Ontario.

Moreover, future endeavors should explore the possibility of replicating similar test sections on other arterial roads or highly trafficked road sections in Kitchener and neighboring municipalities. This expansion would enable the continuous enrichment of the national database, offering agencies a diverse range of data from various locations with similar conditions. This broader dataset is crucial for enhancing the effectiveness of artificial intelligence models and their applicability in pavement management.

Another recommendation for future work involves the completion and implementation of the national database. This database would serve as a repository for the data currently being generated, employing algorithms to filter and organize it effectively. Once established, this database could facilitate the sharing of information on a national and international scale, fostering collaboration and enhancing the accessibility of valuable pavement management data.

Future work should also focus on the development of standardized guidelines for the implementation and testing of sensors within pavement structures, considering various conditions such as during construction, non-construction periods, and different seasons. As highlighted in the thesis, each of these time periods entails distinct requirements and timelines. If the insights and methodologies derived from this thesis can contribute to the formulation of such guidelines, it would provide substantial value. By establishing standardized protocols, future researchers can learn from past experiences and ensure the

accurate testing, monitoring, and installation of sensors in pavement structures. This approach will foster consistency and reliability in data collection and analysis across different research endeavors.

Lastly, addressing the research gaps highlighted in the study, it is imperative to assess the scalability and feasibility of this technology from both a lifecycle and economic standpoint. Implementing and maintaining such sensory systems can be prohibitively expensive, necessitating either more time or the development of cost-effective alternatives and sensors to capture comparable data. Evaluating the feasibility of such projects on a larger scale will determine whether this technology is viable for widespread implementation, as envisioned for pavement performance assessment and modeling, or if alternative approaches need to be explored. This assessment will be crucial in determining the practicality and sustainability of adopting this technology on a broader scale.

References

[1] Transport Canada, "Transportation in Canada 2021 - Road System," Transport Canada, 2021. [Online]. Available: https://tc.canada.ca/en/corporate-services/transparency/briefing-documents-transport-canada/20191120/overview-canada-s-transportation-sector. [Accessed 24 12 2023].

[2] Statistics Canada, "The Canadian Transportation System," Government of Canada, 13 April 2018. [Online]. Available: https://www144.statcan.gc.ca/tdih-cdit/cts-rtc-eng.htm. [Accessed 24 December 2023].

[3] Central Intelligence Agency, "The World Factbook," Central Intelligence Agency, 2023. [Online]. Available: https://www.cia.gov/the-world-factbook/field/roadways/country-comparison/. [Accessed 24 December 2023].

[4] Ontario Asphalt Pavement Council, "Asphalt is the Smooth Quiet Choice," Ontario Asphalt Pavement Council, 2023. [Online]. Available: http://www.onasphalt.org/asphalt101/whypavewithasphalt/asphalt-is-the-smooth-quiet-choice.html. [Accessed 24 December 2023].

[5] Ontario Asphalt Pavement Council, "Asphalt is the Safe Choice," Ontario Asphalt Pavement Council, 2023. [Online]. Available: http://www.onasphalt.org/asphalt101/whypavewithasphalt/asphalt-is-the-safe-choice.html. [Accessed 24 December 2023].

[6] Government of Canada, "Evaluation of the First Nation Infrastructure Fund," April 2014. [Online]. Available: https://www.rcaanc-cirnac.gc.ca/eng/1414522582745/1537967528936. [Accessed 11 February 2024].

[7] Pavement Interactive, "Environment," 2024. [Online]. Available: https://pavementinteractive.org/reference-desk/design/design-parameters/design-factorsenvironment/. [Accessed 11 February 2024].

[8] M. Khanal, R. Mansell and K. Fellows, "Canadian Competitivness for Infrastructure

Investment," August 2023. [Online]. Available: https://www.policyschool.ca/publications/canadian-competitiveness-for-infrastructure-investment/. [Accessed 24 December 2023].

[9] F. Roy, "From roads to rinks: Government spending on infrastructure in Canada, 1961 to 2005 - ARCHIVED," September 2007. [Online]. Available: https://www150.statcan.gc.ca/n1/en/catalogue/11-010-X200700910332. [Accessed 24 December 2023].

[10] Association of Consulting Engineering Companies; Canadian Construction Association; Canadian Parks and Recreation Association; Canadian Public Works Association; Canadian Society for Civil Engineering; Canadian Urban Transit Association; CNAM; FCM, "2019 Report," 2019. [Online]. Available: http://canadianinfrastructure.ca/en/about.html. [Accessed 24 December 2023].

[11] K. Berz, D. Smith, V. Shandal, W. Lanagan, K. Halliday, N. Abdelmessih, I. Jawa, I. Taylor, H. He, A. Dimov and K. Jamieson, "15 Things to Know About Canadian Infrastructure," 3 January 2020. [Online]. Available: https://www.bcg.com/15-things-to-know-about-canadian-infrastructure. [Accessed 24 December 2023].

[12] Statistics Canada, "Canada's Core Public Infrastructure Survey: Replacement values, 2020," 2020. [Online]. Available: https://www150.statcan.gc.ca/n1/daily-quotidien/230320/dq230320a-eng.htm. [Accessed 24 December 2023].

[13] American Association of State Highway and Transportation Officials (AASHTO), AASHTO Guide for Design of Pavement Structures (4th Edition), Washington: American Association of State Highway and Transportation Officials, 1993.

[14] American Association of State Highway and Transportation Officials, Pavement Management Guide (2nd Edition), American Association of State Highway and Transportation Official, 2012.

[15] M. Barriera, S. Pouget, B. Lebental and J. Van Rompu, "In Situ Pavement Monitoring: A

Review," *Infrastructures,* vol. 5, no. 2, p. 18, 2020.

[16] M. Amândio, M. Parente, J. Neves and P. Fonseca, "Integration of Smart Pavement Data with Decision Support Systems: A Systematic Review," *Buildings,* vol. 11, no. 12, p. 579, 2021.

[17] M. N. Karimi and R. B. Mallick, "Flexible Pavement Instrumentation: A State-of-the-Art Review," *Journal of Transportation Engineering, Part B: Pavements,* vol. 149, no. 2, 2023.

[18] A. G. Oyeyi, "Lightweight Cellular Concrete as Flexible Pavement Subbase Material: Field Performance and Sustainability Study," UWSpace, Waterloo, 2022.

[19] P. Tavassoti, H. Baaj, M. Ghafurian, O. Maadani and M. Shafiee, "A Framework for Smart Pavements in Canada," *Engineering Proceedings,* vol. 36, no. 1, p. 51, 2023.

[20] O. Maadani and A. O. Abd El Halim, "Impact of Asphalt Concrete Temperature and Traffic Loading Speed on Structural Behavior of Flexible Pavement," 2017. [Online]. Available: https://www.tac-atc.ca/sites/default/files/conf_papers/maadanio-impact_of_asphalt_concrete_temperature_traffic_loading_speed_on_structural.pdf.

[21] L. Sun, H. Zhao, H. Tu and Y. Tian, "The Smart Road: Practice and Concept," *Engineering,* vol. 4, no. 4, pp. 436-437, 2018.

[22] J. Kang, "Pavement Performance Prediction Using Machine Learning and Instrumentation in Smart Pavement," *UWSpace,* 2022.

[23] S. Tighe, K. Huen and R. Haas, "Environmental and Traffic Deterioration with Mechanistic–Empirical Pavement Design Model," *Transportation Research Record,* Vols. 1989-2, no. 1, pp. 336-343, 2007.

[24] Pavement Interactive, "Rutting," Pavement Tools Consortium, 2023. [Online]. Available: https://pavementinteractive.org/reference-desk/pavement-management/pavement-distresses/rutting/. [Accessed 25 December 2023].

[25] Pavement Interactive, "Transverse Cracking," Pavement Tools Consortium, 2023. [Online]. Available: https://pavementinteractive.org/reference-desk/pavement-management/pavement-

distresses/transverse-cracking/. [Accessed 25 December 2023].

[26] Pavement Interactive, "Longitudinal Cracking," Pavement Tools Consortium, 2023. [Online]. Available: https://pavementinteractive.org/reference-desk/pavement-management/pavement-distresses/longitudinal-cracking/. [Accessed 25 December 2023].

[27] Pavement Interactive, "Fatigue Cracking," Pavement Tools Consortium, 2023. [Online]. Available: https://pavementinteractive.org/reference-desk/pavement-management/pavement-distresses/fatigue-cracking/. [Accessed 25 December 2023].

[28] Pavement Interactive, "Potholes," Pavement Tools Consortium, 2023. [Online]. Available: https://pavementinteractive.org/reference-desk/pavement-management/pavement-distresses/potholes/. [Accessed 25 December 2023].

[29] L. Pierce, J. Bruinsma, K. Smith, M. Wade, K. Chatti and J. Vandenbossche, "Using Falling Weight Deflectometer Data With Mechanistic-Empirical Design and Analysis, Volume III: Guidelines for Deflection Testing, Analysis, and Interpretation," December 2017. [Online]. Available: https://www.fhwa.dot.gov/publications/research/infrastructure/pavements/16011/index.cfm. [Accessed 27 December 2023].

[30] City of Sacremento, "Pavement Management," City of Sacremento, 2023. [Online]. Available: https://www.cityofsacramento.org/Public-Works/Maintenance-Services/Street-Maintenance/Pavement-Mgmt. [Accessed 26 December 2023].

[31] A. Ragnoli, M. De Blasiis and A. Di Benedetto, "Pavement Distress Detection Methods: A Review," *Infrastructures*, vol. 3, no. 4, p. 58, 2018.

[32] J. Stevenson, "Texas Department of Transportation - Pavement Maual," 2021. [Online]. Available: http://onlinemanuals.txdot.gov/TxDOTOnlineManuals/TxDOTManuals/pdm/pdm.pdf. [Accessed 26 December 2023].

[33] O. Maadani, A. O. Abd El Halim and N. Mostafa, "Instrumentation for Monitoring Pavement Performance in Cold Regions," *Journal of Cold Regions Engineering,* vol. 29, no. 4, p. 04014017, 2015.

[34] N. Tabatabaee and P. Sebaaly, "State-of-the-art pavement instrumentation.," *Transportation Reserach Record* , no. 1260, pp. 246-255, 1990.

[35] BDI, "Sensors," BDI, 2023. [Online]. Available: https://bditest.com/product-category/hardware/sensors/. [Accessed 29 October 2023].

[36] N. Bahrani, J. Blanc, P. Hornych and F. Menant, "Alternate Method of Pavement Assessment Using Geophones and Accelerometers for Measuring the Pavement Response," *Infrastructures,* vol. 5, no. 3, p. 25, 2020.

[37] METER Group, Inc., "TEROS10 Simple Water Content Sensor," 2023. [Online]. Available: https://publications.metergroup.com/Manuals/20788_TEROS10_Manual_Web.pdf. [Accessed 2023].

[38] Kistler, "Lineas quartz sensors for Weigh In Motion (WIM) / 9195G," Kistler Group , 2023. [Online]. Available: https://www.kistler.com/DE/en/cp/lineas-quartz-sensors-for-weigh-in-motion-9195g/P0000645. [Accessed 26 December 2023].

[39] I. L. Al-Qadi, A. Loulizi, M. Elseifi and S. Lahouar, "The Virginia Smart Road: The Impact of Pavement Instrumentation on Understanding Pavement Performance," *In Proceedings of the Technology Sessions, AAPT 2004,* pp. 427-465, 8-10 March 2004.

[40] P. Gaborit, C. Sauzéat, H. Di Benedetto, S. Pouget, F. Olard and A. Claude, "Investigation of highway pavements using in-situ strain sensors," *International Conference on Transportation Infrastructure,* vol. 28, p. 331, 2013.

[41] M. Talebsafa, S. Romanoschi, A. T. Papagiannakis and C. Popescu, "Evaluation of Strains at the Bottom of the Asphalt Base Layer of a Semi-Rigid Pavement Under a Class 6 Vehicle," *MATEC web of conferences,* vol. 271, no. 2019, p. 08008, 2019.

[42] P. Marcelino, M. de Lurdes Antunes, E. Fortunato and M. C. Gomes, "Machine learning approach for pavement performance prediction," *International Journal of Pavement Engineering*, vol. 22, no. 3, pp. 341-354, 2019.

[43] R. Haas, W. Hudson and L. Falls, Pavement Asset Management, Salem, Massachusetts: Scrivener Publishing ; Hoboken, New Jersey, 2015.

[44] O. Maadani, M. Shafiee and I. Egorov, "Climate Change Challenges for Flexible Pavement in Canada: An Overview," *Journal of Cold Regions Engineering,* vol. 35, no. 4, 2021.

[45] A. Di Graziano, V. Marchetta and S. Cafiso, "Structural health monitoring of asphalt pavements using smart sensor networks: A comprehensive review," *Journal of Traffic and Transportation Engineering (English Edition),* vol. 7, no. 5, pp. 639-651, 2020.

[46] Y. Huang, M. M. Nojumi, S. Ansari, L. Hashemian and A. Bayat, "Evaluating the use of machine learning for moisture content prediction in base and subgrade layers," *Road Materials and Pavement Design,* vol. 24, no. 12, pp. 2910-2928, 2023.

[47] L. Swett, R. B. Mallick and D. N. Humphrey, "A study of temperature and traffic load related response in different layers in an instrumented flexible pavement," *International Journal of Pavement Engineering,* vol. 9, no. 5, pp. 303-316, 2008.

[48] J. Blanc, P. Hornych, N. S. Duong, J.-Y. Blanchard and P. Nicollet, "Monitoring of an experimental motorway section," *Road Materials and Pavement Design,* vol. 20, no. 1, pp. 74-89, 2017.

[49] Google Earth, "Google Earth," 2023. [Online]. Available: https://earth.google.com/.

[50] K. Redman and T. Schmidt, *REGIONAL ROAD No. 53 (COURTLAND AVE) RECONSTRUCTION HAYWARD AVE TO HWY 7&8 ON-RAMP CITY OF KITCHENER,* City of Kitchener: Region of Waterloo, 2022.

[51] Wood Environment & Infrastructure Solutions;, "Final Geotechnical Investigation Report," Regional Municipality of Waterloo, 2021.

[52] BDI, "Data Acquisition," BDI, 2023. [Online]. Available: https://bditest.com/product-category/hardware/data-acquisition/. [Accessed 29 October 2023].

[53] RST, "Total Earth Pressure Cells," RST, 2023. [Online]. Available: https://rstinstruments.com/product/total-earth-pressure-cells/. [Accessed October 2023].

[54] ASTM International, *Standard Test Method for Dynamic Modulus of Asphalt Mixtures*, ASTM D 3497 – 79: ASTM International, 2009.

[55] ASTM International, *Standard Test Method for Determining the Complex Shear Modulus (G*) of Asphalt Mixtures Using Dynamic Shear Rheometer*, ASTM D7552 − 22: ASTM International, 2023.

[56] ASTM International, *Test Methods for Laboratory Compaction Characteristics of Soil Using Standard Effort (12,400 ft-lbf/ft3 (600 kN-m/m3))*, ASTM D698-12(2021): ASTM International, 2021.

[57] J.-C. Verbrugge and C. Schroeder, Geotechnical Correlations for Soils and Rocks, London & Hoboken, NJ: ISTE Ltd & John Wiley & Sons, Inc, 2018.

[58] S. H. Shivaprakash and A. Sridharan, "Correlation of compaction characteristics of standard and reduced Proctor tests," *Proceedings of the Institution of Civil Engineers - Geotechincal Engineering*, vol. 174, no. 2, pp. 170-180, 2021.

[59] O. Geiger, "The Natural Building Blog," 30 June 2012. [Online]. Available: https://naturalbuildingblog.com/proctor-soil-compaction-test/. [Accessed 3 November 2023].

[60] X. Chen, J. Zhang and X. Wang, "Full-scale field testing on a highway composite pavement dynamic responses," *Transportation Geotechnics*, vol. 4, pp. 13-27, 2015.

[61] J. Zhu, S. Sargand, I. Khoury, D. Tarawneh, T. Ma and F. Chen, "Dynamic load responses of perpetual pavement test roads on U.S. 23: Full-scale instrumentation and evaluation," *Construction and Building Materials*, vol. 331, p. 127326, 2022.

[62] J. Chen, T. Pan and X. Huang, "Numerical investigation into the stiffness anisotropy of asphalt concrete from a microstructural perspective," *Construction and Building Materials,* vol. 25, no. 7, pp. 3059-3065, 2022.

[63] P. Sulejmani, S. Said, S. Agardh and A. Ahmed, "Impact of temperature and moisture on the tensile strain of asphalt concrete layers," *International Journal of Pavement Engineering,* vol. 22, no. 13, pp. 1-9, 2020.

[64] M. R. S. Mshali and W. J. Steyn, "Effect of truck speed on the response of flexible pavement systems to traffic loading," *International Journal of Pavement Engineering,* vol. 23, no. 4, pp. 1-13, 2020.

[65] O. C. Assogba, Y. Tan, Z. Sun, N. Lushinga and Z. Bin, "Effect of vehicle speed and overload on dynamic response of semi-rigid base asphalt pavement," *Road Materials and Pavement Design,* vol. 22, no. 3, pp. 1-31, 2019.

[66] L. An, F. Zhang, Y. Geng and B. Lin, "Field Measurement of Dynamic Compressive Stress Response of Pavement-Subgrade Induced by Moving Heavy-Duty Trucks," *Shock and Vibration,* vol. 2018, pp. 1-12, 2018.

[67] "Preliminary prediction of endurance limit for asphalt rubber mixtures due to healing," *Canadian Journal of Civil Engineering,* vol. 41, no. 11, pp. 964-969, 2014.

[68] D. Timm and A. Priest, "Wheel Wander at the NCAT Test Track," Transportation Research Board, Auburn, AL United States, 2005.

[69] X. Yang, X. Wang, J. Podolsky, Y. Huang and P. Lu, "Assessing Vehicle Wandering Effects on the Accuracy of Weigh-in-Motion Measurement Based on In-Pavement Fiber Bragg Sensors through a Hybrid Sensor-Camera System," *Sensors,* vol. 23, no. 21, p. 8707, 2023.

[70] R. Bajwa, R. Rajagopal, E. Coleri, P. Varaiya and C. Flores, "In-pavement wireless weigh-in-motion," *Information Processing in Sensor Networks,* pp. 103-114, 2013.

[71] M. Shafiee, S. Nassiri and A. Bayat, "Field Investigation of the Effect of Operational Speed and

Lateral Wheel Wander on Flexible Pavement Mechanistic Responses," Transportation Research Board, Ottawa, ON, Canada, 2014.

[72] N. Lajnef, M. Rhimi, K. Chatti, L. Mhamdi and F. Faridazar, "Toward an Integrated Smart Sensing System and Data Interpretation Techniques for Pavement Fatigue Monitoring," *Computer-Aided Civil and Infrastructure Engineering*, vol. 26, no. 7, pp. 513-523, 2011.

[73] P. Leiva-Padilla, J. Blanc, S. Trichet, A. Salgado, F. Hammoum and P. Huard, "Comparison of the response of an instrumented pavement section under individual and platoon truck loading," *International Journal of Pavement Engineering*, vol. 24, no. 2, 2022.

[74] Y. H. Huang, Pavement Analysis and Design, Volume 2, vol. 2, Upper Saddle River, N.J.; London: Pearson; Prentice Hall , 2004.

[75] M. H. Shafiee, L. Hashemian, A. A. Rostami, A. Bayat and N. Tabatabaee, "Field Measurement and Modeling of Vertical and Longitudinal Strains from Falling Weight Deflectometer Testing," *Journal of Transportation Engineering*, vol. 144, no. 1, pp. 04017021-1 - 04017021-9, 2018.

[76] L. P. Ingrassia, S. Spadoni, G. Ferrotti, A. Virgili and F. Canestrari, "Prediction of the Long-Term Performance of an Existing Warm Recycled Motorway Pavement," *Materials*, vol. 16, no. 3, p. 1005, 2023.

[77] ARC-Software, "Free Softwares - 3D-Move Analysis Software (Version 2.1)," Asphalt Research Consortium, 2024. [Online]. Available: http://www.arc.unr.edu/Software.html. [Accessed 23 January 2024].

[78] A. G. Oyeyi, F. M.-W. Ni and S. Tighe, "In-Service Performance Evaluation of Flexible Pavement with Lightweight Cellular Concrete Subbase," *Applied Sciences*, vol. 13, no. 8, p. 4757, 2023.

[79] Ministry of Transportation of Ontario, "Ontario’s Default Parameters for AASHTOWare Pavement ME Design Interim Report - 2019," Material Engineering Research Office,

Downsview, ON, 2019.

[80] X. Liu, Q. Cao, H. Wang, J. Chen and X. Huang, "Evaluation of Vehicle Braking Performance on Wet Pavement Surface using an Integrated Tire-Vehicle Modeling Approach," *Transportation Research Record: Journal of the Transportation Research Board,* vol. 2673, no. 3, pp. 295-307, 2019.

[81] R. Buhari, M. M. Rohani and M. E. Abdullah, "Dynamic Load Coefficient of Tyre Forces from Truck Axles," *Applied Mechanics and Materials,* Vols. 405-408, pp. 1900-1911, 2013.

[82] ABG Creative Geosynthetic Engineering, "Soil Properties: Unit Weight," ABG Geosynthetics, West Yorkshire, UK, 2024.

[83] A. Vaitkus, L. Žalimienė, J. Židanavičiūtė and D. Žilionienė, "Influence of Temperature and Moisture Content on Pavement Bearing Capacity with Improved Subgrade," *Materials,* vol. 12, no. 23, p. 3826, December 2019.

[84] D. Chandra, K. M. Chua and R. L. Lytton, "Effects of Temperature and Moisture on the Load Response of Granular Base Course Material in Thin Pavements," *Transportation Research Record,* no. 1252, pp. 33-41, 1989.

[85] Government of Canada, "Historical Climate Data," Environment Canada, 2023. [Online]. Available: https://climate.weather.gc.ca/index_e.html. [Accessed 28 October 2023].

[86] B. B. Teltayev and E. A. Suppes, "Temperature in pavement and subgrade and its effect on moisture," *Case Studies in Thermal Engineering,* vol. 13, p. 100363, 2019.

[87] M. Shamsaei, A. Carter and M. Vaillancourt, "A review on the heat transfer in asphalt pavements and urban heat island mitigation methods," *Construction and Building Materials,* vol. 359, p. 129350, 2022.

[88] D. Bohlender, "3. When do the seasons start?," National Reserach Council of Canada, 2023. [Online]. Available: https://nrc.canada.ca/en/certifications-evaluations-standards/canadas-official-time/3-when-do-seasons-start. [Accessed 06 November 2023].

[89] D. Čygas, A. Laurinavičius, M. Paliukaitė, A. Motiejūnas, L. Žiliūtė and A. Vaitkus, "Monitoring the Mechanical and Structural Behavior of the Pavement Structure Using Electronic Sensors," *Computer-Aided Civil and Infrastructure Engineering,* vol. 30, no. 4, pp. 317-328, 2014.

[90] L. Xiao and J. Xue, "Effect of spatial variability in asphalt layer on critical pavement strains," *Construction and Building Materials,* vol. 408, p. 133789, 2023.

[91] N. Sudarsanan and Y. R. Kim, "A critical review of the fatigue life prediction of asphalt mixtures and pavements," *Journal of Traffic and Transportation Engineering (English Edition),* vol. 9, no. 5, pp. 808-835, 2022.

[92] Q. Liu and A. Shalaby, "Simulation of pavement response to tire pressure and shape of contact area," *Canadian Journal of Civil Engineering,* vol. 40, no. 3, pp. 236-242, 2013.

[93] S. K. Guha, K. Hossain and M. Lawlor, "An Economic Pavement Management Framework for Extremely Budget- and Resource-Constrained Agencies in Canada," *Transportation Research Record: Journal of the Transportation Research Board,* vol. 2676, no. 8, pp. 554 - 570, 2022.

[94] Federal Highway Administration, "Long-Term Pavement Performance," U.S. DEPARTMENT OF TRANSPORTATION, 2024. [Online]. Available: https://highways.dot.gov/research/long-term-infrastructure-performance/ltpp/long-term-pavement-performance. [Accessed 14 January 2024].

[95] Federal Highway Administration, "LTPP InfoPave," U.S. Department of Transportation, 2024. [Online]. Available: https://infopave.fhwa.dot.gov/. [Accessed 14 January 2024].

[96] National Instruments, "NI TDMS File Format - What is a TDMS File?," National Instruments, 28 March 2023. [Online]. Available: https://www.ni.com/en/support/documentation/supplemental/06/the-ni-tdms-file-format.html. [Accessed 13 January 2024].

[97] O. Matuschin, "Task Till Dawn," Download, July 2017. [Online]. Available: https://download.cnet.com/task-till-dawn/3000-2094_4-75328791.html. [Accessed 14 January

2024].

[98] C. Fehily, SQL Visual QuickStart Guide, 3rd Edition, Sydney: Pearson Education, Limited, 2008.

[100] Pavement Tools Consortium, "Backcalculation – Pavement Interactive," Pavement Tools Consortium, 2024. [Online]. Available: https://pavementinteractive.org/reference-desk/design/structural-design/backcalculation/. [Accessed 27 January 2024].

[101] G. Beltran and M. P. Romo, "Assessing artificial neural network performance in estimating the layer properties of pavements," *Revista Ingenieria e Investigacion*, vol. 34, no. 2, pp. 11-16, 2014.

[102] U.S. Federal Aviation Administration, "BAKFAA 3.4.2," Federal Aviation Administration, 6 June 2023. [Online]. Available: https://www.airporttech.tc.faa.gov/Products/Airport-Safety-Papers-Publications/Airport-Safety-Detail/bakfaa-342-1. [Accessed 27 January 2024].

[103] ASTM International, *Standard Guide for Calculating In Situ Equivalent Elastic Moduli of Pavement*, ASTM D5858 – 96: ASTM International, 2008.

Appendices

Appendix A

Calibration Sheets for RST and BDI Sensors

Monitor with Confidence

RST Instruments Ltd., 11545 Kingston St., Maple Ridge, British Columbia, Canada V2X 0Z5
Tel: 604 540 1100 • Fax: 604 540 1005 • Toll Free: 1 800 665 5599 (North America only)
e-mail: info@rstinstruments.com • Website: www.rstinstruments.com

Calibration Record

Vibrating Wire Total Earth Pressure Cell

Customer:		University of Waterloo
Model:		LPTPC09-S-Q
Serial Number:		**TP1317162**
Mfg Number:		1317162
Range:		0.70 MPa
Date of Calibration:		06-Sep-22
Temperature:		24.6 °C
Sales Order Number:		232556
Cable Length:		20 meters
Cable Colour Code:	Red / Black (Coil)	Green / White (Thermistor)
Cable Type:		EL380004
Thermistor Type:		3 k Ω

Applied Pressure (MPa)	First Reading mA	Applied Pressure (MPa)	Second Reading mA	Average Pressure (MPa)	Average Readings mA	Calculated Linear (MPa)	Linearity F.S. Error (%)	Polynomial Fit (% FS)
0.000	4	0.000	4	0.000	4	0.000	0.00	0.00
0.140	7	0.140	7	0.140	7	0.140	0.01	0.01
0.280	11	0.280	11	0.280	11	0.280	-0.01	0.00
0.420	14	0.420	14	0.420	14	0.420	0.00	0.00
0.560	17	0.560	17	0.560	17	0.560	0.00	0.00
0.700	20	0.700	20	0.700	20	0.700	0.00	0.00
						Max Error (%):	0.01	0.01

Linear Calibration Factor: **C.F.=** **-0.04411950 MPa/mA**
Regression Zero: **At Calibration =** **4.2 mA**

Polynomial Gage Factors **A:** **-6.2582E-07** **B:** **0.04413490** **C:** **-0.1857**

Pressure is calculated with the following equations:
Linear P(MPa) = C.F. x (Li - Lc) + [0.0001 (Bi - Bc)]
Polynomial $P(MPa) = A(Lc)^2+BLc+C-[0.0001(Bc-Bi)]$

	Date (dd/mm/yy)	Scope Readout Pos. B (Li)	Temp (°C)
Shipped Zero Readings:	06-Sep-22	4	24.6

Calibrated using VW2106 readout, S/N: VR0387

Li, Lc = initial (at installation) and current readings
Bi, Bc = initial (at installation) and current barometric pressure, in millibars
0.0001 = constant for MPa / millibar
B units = B scale output of VW 2102, VW 2104, VW 2106 and DT 2011 readouts
B units = Hz^2 / 1000 ie: 1700Hz = 2890 B units

Technician: G.S Date: 06-Sep-22

rst 9/8/2022 DATE NP NAME

This instrument has been calibrated using standards traceable to the NIST in compliance with ANSI Z540-1
Calibrated using VW2106 readout, S/N: VR0387

Document Number.: LPL0030H

Recycled
MIG0106C

Monitor with Confidence

RST Instruments Ltd., 11545 Kingston St., Maple Ridge, British Columbia, Canada V2X 0Z5
Tel: 604 540 1100 • Fax: 604 540 1005 • Toll Free: 1 800 665 5599 (North America only)
e-mail: info@rstinstruments.com • Website: www.rstinstruments.com

Calibration Record

Vibrating Wire Total Earth Pressure Cell

Customer:		University of Waterloo
Model:		LPTPC09-S-Q
Serial Number:		**TP1152501**
Mfg Number:		1152501
Range:		2.00 MPa
Date of Calibration:		08-Sep-22
Temperature:		24.6 °C
Sales Order Number:		232556
Cable Length:		20 meters
Cable Colour Code:	Red / Black (Coil)	Green / White (Thermistor)
Cable Type:		EL380004
Thermistor Type:		3 k Ω

Applied Pressure (MPa)	First Reading mA	Applied Pressure (MPa)	Second Reading mA	Average Pressure (MPa)	Average Readings mA	Calculated Linear (MPa)	Linearity F.S. Error (%)	Polynomial Fit (% FS)
0.000	4.06	0.000	4.06	0.000	4.06	0.000	0.00	0.00
0.400	7.26	0.400	7.25	0.400	7.26	0.400	-0.02	-0.02
0.800	10.46	0.800	10.46	0.800	10.46	0.801	0.03	0.03
1.200	13.65	1.200	13.65	1.200	13.65	1.200	-0.01	-0.01
1.400	15.25	1.400	15.25	1.400	15.25	1.400	0.00	0.00
2.000	20.05	2.000	20.04	2.000	20.05	2.000	0.00	0.00
						Max Error (%):	0.03	0.03

Linear Calibration Factor: **C.F.=** **-0.12511656 MPa/mA**
Regression Zero: **At Calibration =** **4.1 mA**

Polynomial Gage Factors **A:** 3.7183E-06 **B:** 0.12502769 **C:** -0.5076

Pressure is calculated with the following equations:
Linear P(MPa) = C.F. x (Li - Lc) + [0.0001 (Bi - Bc)]
Polynomial $P(MPa) = A(Lc)^2+BLc+C-[0.0001(Bc-Bi)]$

	Date (dd/mm/yy)	Scope Readout Pos. B (Li)	Temp (°C)
Shipped Zero Readings:	06-Sep-22	4	24.6

Calibrated using VW2106 readout, S/N: VR0387

Li, Lc = initial (at installation) and current readings
Bi, Bc = initial (at installation) and current barometric pressure, in millibars
0.0001 = constant for MPa / millibar
B units = B scale output of VW 2102, VW 2104, VW 2106 and DT 2011 readouts
B units = Hz^2 / 1000 ie: 1700Hz = 2890 B units

rst
9/8/2022
DATE
MP
NAME

Technician: G.S Date: 06-Sep-22

This instrument has been calibrated using standards traceable to the NIST in compliance with ANSI Z540-1
Calibrated using VW2106 readout, S/N: VR0387

Monitor with Confidence

RST Instruments Ltd., 11545 Kingston St., Maple Ridge, British Columbia, Canada V2X 0Z5
Tel: 604 540 1100 • Fax: 604 540 1005 • Toll Free: 1 800 665 5599 (North America only)
e-mail: info@rstinstruments.com • Website: www.rstinstruments.com

Calibration Record

Vibrating Wire Total Earth Pressure Cell

Customer:		University of Waterloo
Model:		LPTPC09-S-Q
Serial Number:		**TP11563165**
Mfg Number:		11563165
Range:		2.00 MPa
Date of Calibration:		06-Sep-22
Temperature:		24.6 °C
Sales Order Number:		232556
Cable Length:		20 meters
Cable Colour Code:	Red / Black (Coil)	Green / White (Thermistor)
Cable Type:		EL380004
Thermistor Type:		3 k Ω

Applied Pressure (MPa)	First Reading mA	Applied Pressure (MPa)	Second Reading mA	Average Pressure (MPa)	Average Readings mA	Calculated Linear (MPa)	Linearity F.S. Error (%)	Polynomial Fit (% FS)
0.000	4.06	0.000	4.06	0.000	4.06	0.458	0.02	0.06
400.000	7.21	400.000	7.21	400.000	7.21	398.657	-0.07	-0.07
800.000	10.38	800.000	10.38	800.000	10.38	799.324	-0.03	-0.06
1200.000	13.56	1200.000	13.55	1200.000	13.55	1201.192	0.06	0.03
1600.000	16.73	1600.000	16.73	1600.000	16.73	1602.680	0.13	0.13
2000.000	19.85	2000.000	19.85	2000.000	19.85	1997.654	-0.12	-0.08
						Max Error (%):	0.13	0.13

Linear Calibration Factor: **C.F.= -126.51289625 MPa/mA**
Regression Zero: **At Calibration = 4.1 mA**

Polynomial Gage Factors **A:** 2.2828E-02 **B:** 125.96691736 **C:** -511.0224

Pressure is calculated with the following equations:
Linear P(MPa) = C.F. x (Li - Lc) + [0.0001 (Bi - Bc)]
Polynomial $P(MPa) = A(Lc)^2+BLc+C-[0.0001(Bc-Bi)]$

	Date (dd/mm/yy)	Scope Readout Pos. B (Li)	Temp (°C)
Shipped Zero Readings:	06-Sep-22	4	24.6

Calibrated using VW2106 readout, S/N: VR0387

Li, Lc = initial (at installation) and current readings
Bi, Bc = initial (at installation) and current barometric pressure, in millibars
0.0001 = constant for MPa / millibar
B units = B scale output of VW 2102, VW 2104, VW 2106 and DT 2011 readouts
B units = Hz^2 / 1000 ie: 1700Hz = 2890 B units

rst
9/8/2022
DATE
NP
NAME

Technician: C.S Date: 06-Sep-22

This instrument has been calibrated using standards traceable to the NIST in compliance with ANSI Z540-1
Calibrated using VW2106 readout, S/N: VR0387

Monitor with Confidence

RST Instruments Ltd., 11545 Kingston St., Maple Ridge, British Columbia, Canada V2X 0Z5
Tel: 604 540 1100 • Fax: 604 540 1005 • Toll Free: 1 800 665 5599 (North America only)
e-mail: info@rstinstruments.com • Website: www.rstinstruments.com

Calibration Record

Vibrating Wire Total Earth Pressure Cell

Customer:		University of Waterloo
Model:		LPTPC09-S-Q
Serial Number:		**TP1151769**
Mfg Number:		1151769
Range:		3.00 MPa
Date of Calibration:		06-Sep-22
Temperature:		24.6 °C
Sales Order Number:		232556
Cable Length:		20 meters
Cable Colour Code:	Red / Black (Coil)	Green / White (Thermistor)
Cable Type:		EL380004
Thermistor Type:		3 k Ω

Applied Pressure (MPa)	First Reading mA	Applied Pressure (MPa)	Second Reading mA	Average Pressure (MPa)	Average Readings mA	Calculated Linear (MPa)	Linearity F.S. Error (%)	Polynomial Fit (% FS)
0.000	3.98	0.000	3.97	0.000	3.97	0.000	0.01	-0.02
0.600	7.16	0.600	7.18	0.600	7.17	0.600	0.01	0.03
1.200	10.36	1.200	10.37	1.200	10.37	1.200	-0.01	0.03
1.800	13.56	1.800	13.56	1.800	13.56	1.799	-0.04	-0.02
2.100	15.16	2.100	15.15	2.100	15.16	2.099	-0.05	-0.05
2.500	17.30	2.500	17.31	2.500	17.30	2.502	0.07	0.04
						Max Error (%):	0.07	0.05

Linear Calibration Factor: **C.F.= -0.18766129 MPa/mA**
Regression Zero: **At Calibration = 4.0 mA**

Polynomial Gage Factors **A: -3.5596E-05** **B: 0.18841731** **C: -0.7485**

Pressure is calculated with the following equations:
Linear P(MPa) = C.F. x (Li - Lc) + [0.0001 (Bi - Bc)]
Polynomial $P(MPa) = A(Lc)^2+BLc+C-[0.0001(Bc-Bi)]$

	Date (dd/mm/yy)	Scope Readout Pos. B (Li)	Temp (°C)
Shipped Zero Readings:	06-Sep-22	4	24.6

Calibrated using VW2106 readout, S/N: VR0387

Li, Lc = initial (at installation) and current readings
Bi, Bc = initial (at installation) and current barometric pressure, in millibars
0.0001 = constant for MPa / millibar
B units = B scale output of VW 2102, VW 2104, VW 2106 and DT 2011 readouts
B units = Hz^2 / 1000 ie: 1700Hz = 2890 B units

rst
9/8/2022 DATE
NAME

Technician: C.G Date: 06-Sep-22

This instrument has been calibrated using standards traceable to the NIST in compliance with ANSI Z540-1
Calibrated using VW2106 readout, S/N: VR0387

Document Number.: LPL0030H

Recycled
MIG0106C

Calibration Record

RST Instruments Ltd., 11545 Kingston St., Maple Ridge, British Columbia, Canada V2X 0Z5
Tel: 604 540 1100 • Fax: 604 540 1005 • Toll Free: 1 800 665 5599 (North America only)
e-mail: info@rstinstruments.com • Website: www.rstinstruments.com

Vibrating Wire Total Earth Pressure Cell

Customer:		University of Waterloo
Model:		LPTPC09-S-Q
Serial Number:		**TP1152497**
Mfg Number:		1152497
Range:		3.00 MPa
Date of Calibration:		06-Sep-22
Temperature:		24.6 °C
Sales Order Number:		232556
Cable Length:		20 meters
Cable Colour Code:	Red / Black (Coil)	Green / White (Thermistor)
Cable Type:		EL380004
Thermistor Type:		3 k Ω

Applied Pressure (MPa)	First Reading mA	Applied Pressure (MPa)	Second Reading mA	Average Pressure (MPa)	Average Readings mA	Calculated Linear (MPa)	Linearity F.S. Error (%)	Polynomial Fit (% FS)
0.000	3.92	0.000	3.98	0.000	3.95	0.003	0.12	0.04
0.600	7.11	0.600	7.11	0.600	7.11	0.597	-0.12	-0.08
1.200	10.31	1.200	10.31	1.200	10.31	1.199	-0.06	0.03
1.800	13.50	1.800	13.51	1.800	13.51	1.799	-0.03	0.02
2.100	15.11	2.100	15.11	2.100	15.11	2.101	0.03	0.04
2.500	17.24	2.500	17.24	2.500	17.24	2.501	0.05	-0.04
						Max Error (%):	0.12	0.08

Linear Calibration Factor: **C.F.=** **-0.18797447 MPa/mA**
Regression Zero: **At Calibration =** **3.9 mA**

Polynomial Gage Factors **A:** **-9.4887E-05** **B:** **0.18998177** **C:** **-0.7480**

Pressure is calculated with the following equations:
Linear P(MPa) = C.F. x (Li - Lc) + [0.0001 (Bi - Bc)]
Polynomial $P(MPa) = A(Lc)^2+BLc+C-[0.0001(Bc-Bi)]$

	Date (dd/mm/yy)	Scope Readout Pos. B (Li)	Temp (°C)
Shipped Zero Readings:	06-Sep-22	4	24.6

Calibrated using VW2106 readout, S/N: VR0387

Li, Lc = initial (at installation) and current readings
Bi, Bc = initial (at installation) and current barometric pressure, in millibars
0.0001 = constant for MPa / millibar
B units = B scale output of VW 2102, VW 2104, VW 2106 and DT 2011 readouts
B units = Hz^2 / 1000 ie: 1700Hz = 2890 B units

rst
9/8/2022
DATE
NAME

Technician: C.B Date: 06-Sep-22

This instrument has been calibrated using standards traceable to the NIST in compliance with ANSI Z540-1
Calibrated using VW2106 readout, S/N: VR0387

Monitor with Confidence

RST Instruments Ltd., 11545 Kingston St., Maple Ridge, British Columbia, Canada V2X 0Z5
Tel: 604 540 1100 • Fax: 604 540 1005 • Toll Free: 1 800 665 5599 (North America only)
e-mail: info@rstinstruments.com • Website: www.rstinstruments.com

Calibration Record

Vibrating Wire Total Earth Pressure Cell

Customer:		University of Waterloo
Model:		LPTPC09-S-Q
Serial Number:		**TP1152499**
Mfg Number:		1152499
Range:		3.00 MPa
Date of Calibration:		06-Sep-22
Temperature:		24.6 °C
Sales Order Number:		232556
Cable Length:		20 meters
Cable Colour Code:	Red / Black (Coil)	Green / White (Thermistor)
Cable Type:		EL380004
Thermistor Type:		3 k Ω

Applied Pressure (MPa)	First Reading mA	Applied Pressure (MPa)	Second Reading mA	Average Pressure (MPa)	Average Readings mA	Calculated Linear (MPa)	Linearity F.S. Error (%)	Polynomial Fit (% FS)
0.000	3.92	0.000	3.92	0.000	3.92	0.001	0.02	0.00
0.600	7.11	0.600	7.12	0.600	7.12	0.600	0.00	0.01
1.200	10.31	1.200	10.30	1.200	10.31	1.199	-0.05	-0.03
1.800	13.51	1.800	13.51	1.800	13.51	1.800	0.01	0.02
2.100	15.11	2.100	15.11	2.100	15.11	2.100	0.02	0.02
2.500	17.24	2.500	17.24	2.500	17.24	2.500	0.01	-0.01
						Max Error (%):	0.05	0.03

Linear Calibration Factor: **C.F.= -0.18766001 MPa/mA**
Regression Zero: **At Calibration = 3.9 mA**

Polynomial Gage Factors **A: -2.2096E-05** **B: 0.18812686** **C: -0.7371**

Pressure is calculated with the following equations:
Linear P(MPa) = C.F. x (Li - Lc) + [0.0001 (Bi - Bc)]
Polynomial $P(MPa) = A(Lc)^2+BLc+C-[0.0001(Bc-Bi)]$

	Date (dd/mm/yy)	Scope Readout Pos. B (Li)	Temp (°C)
Shipped Zero Readings:	06-Sep-22	4	24.6

Calibrated using VW2106 readout, S/N: VR0387

Li, Lc = initial (at installation) and current readings
Bi, Bc = initial (at installation) and current barometric pressure, in millibars
0.0001 = constant for MPa / millibar
B units = B scale output of VW 2102, VW 2104, VW 2106 and DT 2011 readouts
B units = Hz^2 / 1000 ie: 1700Hz = 2890 B units

rst
9/6/2022
DATE
NAME

Technician: C.S Date: 06-Sep-22

This instrument has been calibrated using standards traceable to the NIST in compliance with ANSI Z540-1
Calibrated using VW2106 readout, S/N: VR0387

Monitor with Confidence

RST Instruments Ltd., 11545 Kingston St., Maple Ridge, British Columbia, Canada V2X 0Z5
Tel: 604 540 1100 • Fax: 604 540 1005 • Toll Free: 1 800 665 5599 (North America only)
e-mail: info@rstinstruments.com • Website: www.rstinstruments.com

Calibration Record

Vibrating Wire Total Earth Pressure Cell

Customer:		University of Waterloo	
Model:		LPTPC09-S-Q	
Serial Number:		**TP1152500**	
Mfg Number:		1152500	
Range:		3.00	MPa
Date of Calibration:		07-Sep-22	
Temperature:		24.6	°C
Sales Order Number:		232556	
Cable Length:		20	meters
Cable Colour Code:	Red / Black (Coil)	Green / White	(Thermistor)
Cable Type:		EL380004	
Thermistor Type:		3 k Ω	

Applied Pressure (MPa)	First Reading mA	Applied Pressure (MPa)	Second Reading mA	Average Pressure (MPa)	Average Readings mA	Calculated Linear (MPa)	Linearity F.S. Error (%)	Polynomial Fit (% FS)
0.000	3.98	0.000	3.97	0.000	3.97	0.000	0.01	-0.02
0.600	7.16	0.600	7.18	0.600	7.17	0.600	0.01	0.03
1.200	10.36	1.200	10.37	1.200	10.37	1.200	-0.01	0.03
1.800	13.56	1.800	13.56	1.800	13.56	1.799	-0.04	-0.02
2.100	15.16	2.100	15.15	2.100	15.16	2.099	-0.05	-0.05
2.500	17.30	2.500	17.31	2.500	17.30	2.502	0.07	0.04
						Max Error (%):	0.07	0.05

Linear Calibration Factor: **C.F.=** **-0.18766129 MPa/mA**
Regression Zero: **At Calibration =** **4.0 mA**

Polynomial Gage Factors **A:** **-3.5596E-05** **B:** **0.18841731** **C:** **-0.7485**

Pressure is calculated with the following equations:
Linear P(MPa) = C.F. x (Li - Lc) + [0.0001 (Bi - Bc)]
Polynomial $P(MPa) = A(Lc)^2+BLc+C-[0.0001(Bc-Bi)]$

	Date (dd/mm/yy)	Scope Readout Pos. B (Li)	Temp (°C)
Shipped Zero Readings:	06-Sep-22	4	24.6

Calibrated using VW2106 readout, S/N: VR0387

rst
7/6/2022
DATE
NP
NAME

Li, Lc = initial (at installation) and current readings
Bi, Bc = initial (at installation) and current barometric pressure, in millibars
0.0001 = constant for MPa / millibar
B units = B scale output of VW 2102, VW 2104, VW 2106 and DT 2011 readouts
B units = Hz^2 / 1000 ie: 1700Hz = 2890 B units

Technician: C-L Date: 06-Sep-22

This instrument has been calibrated using standards traceable to the NIST in compliance with ANSI Z540-1
Calibrated using VW2106 readout, S/N: VR0387

Document Number.: LPL0030H

Recycled
MIG0106C

Vibrating Wire Total Earth Pressure Cell

Customer:		University of Waterloo	
Model:		LPTPC09-S-Q	
Serial Number:		**TP11563165**	
Mfg Number:		11563165	
Range:		2.00	MPa
Date of Calibration:		06-Sep-22	
Temperature:		24.6	°C
Sales Order Number:		232556	
Cable Length:		20	meters
Cable Colour Code:	Red / Black (Coil)	Green / White	(Thermistor)
Cable Type:		EL380004	
Thermistor Type:		3	k Ω

Applied Pressure (MPa)	First Reading mA	Applied Pressure (MPa)	Second Reading mA	Average Pressure (MPa)	Average Readings mA	Calculated Linear (MPa)	Linearity F.S. Error (%)	Polynomial Fit (% FS)
0.000	4.06	0.000	4.06	0.000	4.06	0.000	0.02	0.06
0.400	7.21	0.400	7.21	0.400	7.21	0.399	-0.07	-0.07
0.800	10.38	0.800	10.38	0.800	10.38	0.799	-0.03	-0.06
1.200	13.56	1.200	13.55	1.200	13.55	1.201	0.06	0.03
1.600	16.73	1.600	16.73	1.600	16.73	1.603	0.13	0.13
2.000	19.85	2.000	19.85	2.000	19.85	1.998	-0.12	-0.08
						Max Error (%):	0.13	0.13

Linear Calibration Factor: **C.F.= -0.12651290 MPa/mA**
Regression Zero: **At Calibration = 4.1 mA**

Polynomial Gage Factors **A: 2.2828E-05** **B: 0.12596692** **C: -0.5110**

Pressure is calculated with the following equations:
Linear P(MPa) = C.F. x (Li - Lc) + [0.0001 (Bi - Bc)]
Polynomial $P(MPa) = A(Lc)^2+BLc+C-[0.0001(Bc-Bi)]$

	Date (dd/mm/yy)	Scope Readout Pos. B (Li)	Temp (°C)
Shipped Zero Readings:	06-Sep-22	4	24.6

Calibrated using VW2106 readout, S/N: VR0387

Li, Lc = initial (at installation) and current readings
Bi, Bc = initial (at installation) and current barometric pressure, in millibars
0.0001 = constant for MPa / millibar
B units = B scale output of VW 2102, VW 2104, VW 2106 and DT 2011 readouts
B units = Hz^2 / 1000 ie: 1700Hz = 2890 B units

Technician: _____ Date: 06-Sep-22

This instrument has been calibrated using standards traceable to the NIST in compliance with ANSI Z540-1
Calibrated using VW2106 readout, S/N: VR0387

740 S PIERCE AVE, UNIT 15
LOUISVILLE, CO 80027
+1.303.494.3230

BDITEST.COM

Certificate of Calibration

Serial Number: **ASTa1239**

Transducer Model: BDI AST350-6
General Gage Factor (με/mV/V$_{exc}$): 1035.9
Initial Offset Voltage (mV/V$_{exc}$): -0.561

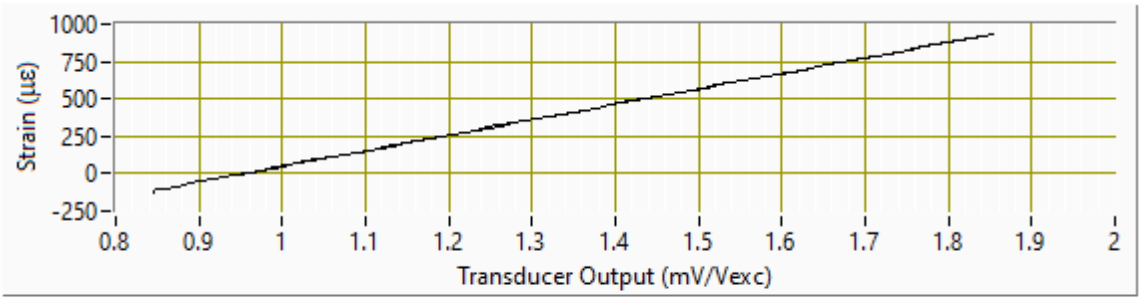
Temperature (C): 25.3
Mean Linear Correlation Coefficient [LCC]: 0.99997
LCC Standard Deviation: 9.123E-6

Table 1: Representative Calibration Data

Strain (micro-strain)	Transducer Output (mV/Vexc.)
-122.755	0.846
-82.792	0.874
-23.124	0.930
37.641	0.989
96.375	1.043
156.695	1.105
216.577	1.164
275.801	1.219
335.806	1.277
394.928	1.337
456.107	1.394
514.564	1.451
575.627	1.509
635.382	1.566
696.825	1.628
756.365	1.684

Strain (micro-strain)	Transducer Output (mV/Vexc.)
816.958	1.741
875.232	1.799
931.895	1.853
892.448	1.815
832.686	1.759
773.056	1.698
711.937	1.642
651.140	1.582
590.409	1.521
530.607	1.465
470.558	1.406
411.845	1.349
351.095	1.292
293.163	1.233
232.599	1.176
173.706	1.122

Calibration Curve



Calibrated By: Connor H.
Date and Time: 6/24/2022 3:09 PM

Signature: _____

Specifications

Automated Strain Transducer Calibration System (ASTCS)

ASTCS Serial Number:	BDI CAL 0001
ASTCS Software Version Number:	2.0.1
ASTCS Independant Verification Date:	12/14/2020 3:47 PM
Transducer Gage Length:	5.25 inches (133.3 mm)
Full Scale Displacement Range:	-0.0000, +0.0062 (inches)
Method for Applying Displacement:	Precision Stepper Motor Connected to Linear Stage
Excitation Voltage for Calibration:	2.5 VDC
Displacement Measurements:	Dual Precision LVDTs, Output Averaged
Displacement Certification:	NIST 274437-07
Linearity Verification Technique:	Linear Correlation Coefficient < 0.9996
Repeatability Verification Technique:	Standard Deviation < 0.5% of mean

ASTCS System Check

Reference Strain Transducer:	5695
Reference General Gage Factor:	317.00 με/mV/V
LVDT #1 Sensitivity (inches/volt):	0.0055
LVDT #2 Sensitivity (inches/volt):	0.0055
System Temperature Status:	Passed
Date/Time of Last System Check:	6/17/2022 9:27 AM

Strain Transducer Connections

Red:	Excitation +
Black:	Excitation -
Green:	Signal +
White:	Signal -
Grey/Bare:	Shield

NIST Reference:

The manufacturer certifies that the supplied ASTCS instrument meets or exceeds published specifications at the time of manufacturing and has been verified using standards and instruments whose accuracies are traceable to the National Institute of Standards and Technology (NIST), an accepted value of a natural physical constant or a ratio calibration technique. Sensor calibrations performed by this instrument are certified by the owner of the ASTCS and are in accordance with the owner's quality assurance program. Measurements and information provided on this report are valid at the time of calibration only.

740 S PIERCE AVE, UNIT 15
LOUISVILLE, CO 80027
+1.303.494.3230

BDITEST.COM

Certificate of Calibration

Serial Number: ASTa1241

Transducer Model: BDI AST350-6
General Gage Factor (με/mV/V$_{exc}$): 1159.3
Initial Offset Voltage (mV/V$_{exc}$): -0.376

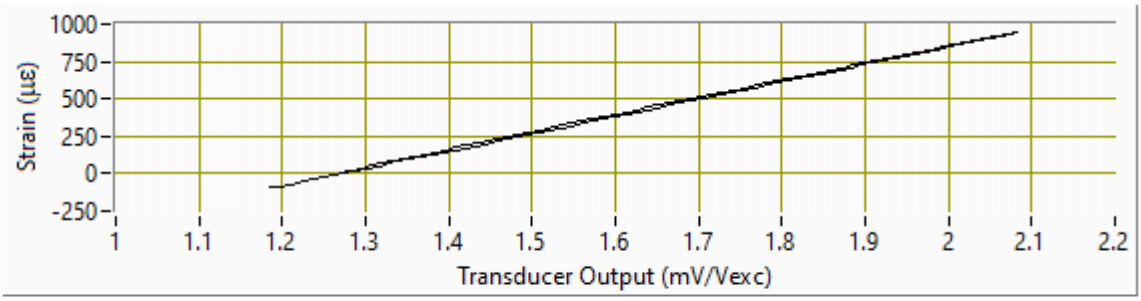
Temperature (C): 25.7
Mean Linear Correlation Coefficient [LCC]: 0.99979
LCC Standard Deviation: 2.452E-5

Table 1: Representative Calibration Data

Strain (micro-strain)	Transducer Output (mV/Vexc.)
-94.933	1.186
-39.076	1.237
22.083	1.288
81.520	1.340
141.848	1.394
199.886	1.445
261.204	1.495
320.701	1.548
381.639	1.600
440.303	1.651
502.302	1.705
560.938	1.753
621.619	1.807
680.369	1.860
740.706	1.909
800.615	1.959

Strain (micro-strain)	Transducer Output (mV/Vexc.)
860.568	2.014
921.103	2.063
921.506	2.059
862.293	2.007
800.730	1.950
742.060	1.900
680.694	1.848
621.365	1.795
561.338	1.743
501.514	1.691
442.421	1.639
381.656	1.589
322.959	1.537
261.561	1.483
203.794	1.436
143.150	1.384

Calibration Curve



Calibrated By: Connor H.
Date and Time: 6/24/2022 3:41 PM

Signature: _____

Specifications

Automated Strain Transducer Calibration System (ASTCS)

ASTCS Serial Number:	BDI CAL 0001
ASTCS Software Version Number:	2.0.1
ASTCS Independant Verification Date:	12/14/2020 3:47 PM
Transducer Gage Length:	5.25 inches (133.3 mm)
Full Scale Displacement Range:	-0.0000, +0.0062 (inches)
Method for Applying Displacement:	Precision Stepper Motor Connected to Linear Stage
Excitation Voltage for Calibration:	2.5 VDC
Displacement Measurements:	Dual Precision LVDTs, Output Averaged
Displacement Certification:	NIST 274437-07
Linearity Verification Technique:	Linear Correlation Coefficient < 0.9996
Repeatability Verification Technique:	Standard Deviation < 0.5% of mean

ASTCS System Check

Reference Strain Transducer:	5695
Reference General Gage Factor:	317.00 με/mV/V
LVDT #1 Sensitivity (inches/volt):	0.0055
LVDT #2 Sensitivity (inches/volt):	0.0055
System Temperature Status:	Passed
Date/Time of Last System Check:	6/17/2022 9:27 AM

Strain Transducer Connections

Red:	Excitation +
Black:	Excitation -
Green:	Signal +
White:	Signal -
Grey/Bare:	Shield

NIST Reference:

The manufacturer certifies that the supplied ASTCS instrument meets or exceeds published specifications at the time of manufacturing and has been verified using standards and instruments whose accuracies are traceable to the National Institute of Standards and Technology (NIST), an accepted value of a natural physical constant or a ratio calibration technique. Sensor calibrations performed by this instrument are certified by the owner of the ASTCS and are in accordance with the owner's quality assurance program. Measurements and information provided on this report are valid at the time of calibration only.

740 S PIERCE AVE, UNIT 15
LOUISVILLE, CO 80027
+1.303.494.3230

BDITEST.COM

Certificate of Calibration

Serial Number: ASTa1243

Transducer Model: BDI AST350-6
General Gage Factor (με/mV/V_{exc}): 1171.2
Initial Offset Voltage (mV/V_{exc}): -0.217

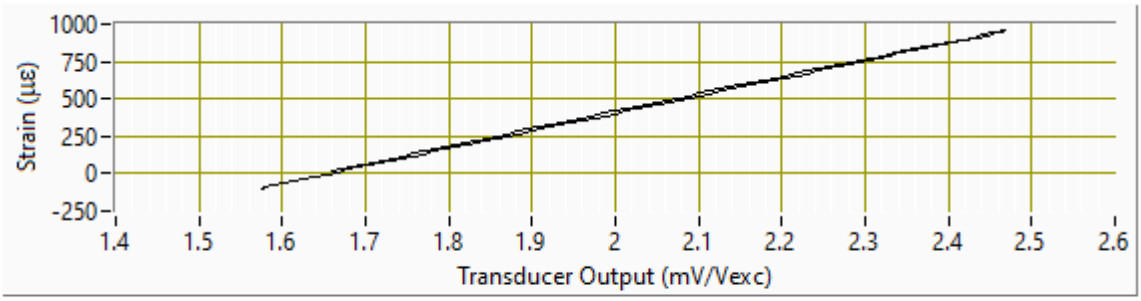
Temperature (C): 25.7
Mean Linear Correlation Coefficient [LCC]: 0.99970
LCC Standard Deviation: 2.177E-5

Table 1: Representative Calibration Data

Strain (micro-strain)	Transducer Output (mV/Vexc.)
-104.361	1.577
-77.513	1.590
-18.077	1.640
42.721	1.691
101.252	1.744
161.611	1.796
220.181	1.845
281.026	1.898
340.950	1.947
401.146	2.001
461.111	2.053
521.056	2.100
581.224	2.152
640.595	2.205
701.411	2.254
759.913	2.305

Strain (micro-strain)	Transducer Output (mV/Vexc.)
821.235	2.356
880.091	2.407
940.370	2.459
926.479	2.443
866.587	2.389
806.119	2.335
746.469	2.283
686.034	2.231
626.107	2.180
566.588	2.125
506.731	2.076
448.172	2.026
387.142	1.972
328.327	1.922
267.192	1.871
208.871	1.821

Calibration Curve



Calibrated By: Connor H.
Date and Time: 6/24/2022 3:30 PM

Signature: _____

Specifications

Automated Strain Transducer Calibration System (ASTCS)

ASTCS Serial Number:	BDI CAL 0001
ASTCS Software Version Number:	2.0.1
ASTCS Independant Verification Date:	12/14/2020 3:47 PM
Transducer Gage Length:	5.25 inches (133.3 mm)
Full Scale Displacement Range:	-0.0000, +0.0062 (inches)
Method for Applying Displacement:	Precision Stepper Motor Connected to Linear Stage
Excitation Voltage for Calibration:	2.5 VDC
Displacement Measurements:	Dual Precision LVDTs, Output Averaged
Displacement Certification:	NIST 274437-07
Linearity Verification Technique:	Linear Correlation Coefficient < 0.9996
Repeatability Verification Technique:	Standard Deviation < 0.5% of mean

ASTCS System Check

Reference Strain Transducer:	5695
Reference General Gage Factor:	317.00 με/mV/V
LVDT #1 Sensitivity (inches/volt):	0.0055
LVDT #2 Sensitivity (inches/volt):	0.0055
System Temperature Status:	Passed
Date/Time of Last System Check:	6/17/2022 9:27 AM

Strain Transducer Connections

Red:	Excitation +
Black:	Excitation -
Green:	Signal +
White:	Signal -
Grey/Bare:	Shield

NIST Reference:

The manufacturer certifies that the supplied ASTCS instrument meets or exceeds published specifications at the time of manufacturing and has been verified using standards and instruments whose accuracies are traceable to the National Institute of Standards and Technology (NIST), an accepted value of a natural physical constant or a ratio calibration technique. Sensor calibrations performed by this instrument are certified by the owner of the ASTCS and are in accordance with the owner's quality assurance program. Measurements and information provided on this report are valid at the time of calibration only.

740 S PIERCE AVE, UNIT 15
LOUISVILLE, CO 80027
+1.303.494.3230

BDITEST.COM

Certificate of Calibration

Serial Number: ASTa1249

Transducer Model: BDI AST350-6
General Gage Factor (με/mV/V$_{exc}$): 1120.4
Initial Offset Voltage (mV/V$_{exc}$): 0.085

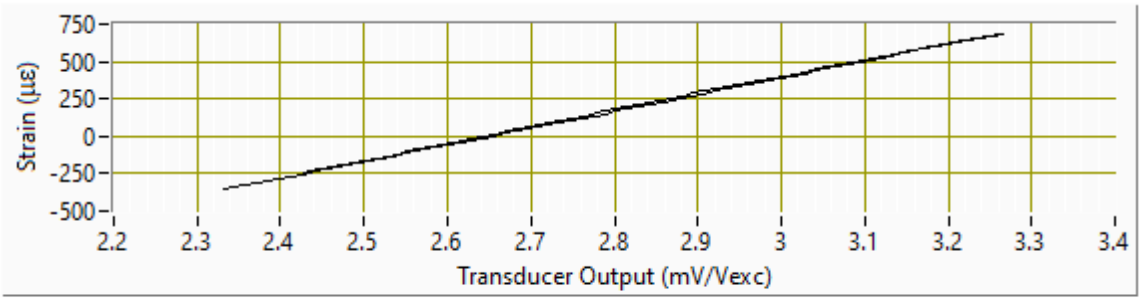
Temperature (C): 25.4
Mean Linear Correlation Coefficient [LCC]: 0.99986
LCC Standard Deviation: 2.216E-5

Table 1: Representative Calibration Data

Strain (micro-strain)	Transducer Output (mV/Vexc.)
-355.601	2.332
-298.329	2.385
-237.120	2.442
-177.372	2.493
-116.328	2.549
-58.312	2.603
2.823	2.656
61.481	2.708
121.942	2.762
181.252	2.814
241.840	2.870
300.454	2.920
361.249	2.973
420.184	3.028
480.415	3.081
540.619	3.132

Strain (micro-strain)	Transducer Output (mV/Vexc.)
600.189	3.187
661.281	3.239
672.911	3.248
614.372	3.195
553.022	3.137
494.774	3.085
433.794	3.030
375.439	2.976
315.210	2.923
256.699	2.869
196.367	2.815
136.672	2.766
77.475	2.710
17.456	2.657
-41.664	2.606
-101.897	2.553

Calibration Curve



Calibrated By: Connor H.
Date and Time: 6/24/2022 3:14 PM

Signature: _____

Specifications

Automated Strain Transducer Calibration System (ASTCS)

ASTCS Serial Number:	BDI CAL 0001
ASTCS Software Version Number:	2.0.1
ASTCS Independant Verification Date:	12/14/2020 3:47 PM
Transducer Gage Length:	5.25 inches (133.3 mm)
Full Scale Displacement Range:	-0.0000, +0.0062 (inches)
Method for Applying Displacement:	Precision Stepper Motor Connected to Linear Stage
Excitation Voltage for Calibration:	2.5 VDC
Displacement Measurements:	Dual Precision LVDTs, Output Averaged
Displacement Certification:	NIST 274437-07
Linearity Verification Technique:	Linear Correlation Coefficient < 0.9996
Repeatability Verification Technique:	Standard Deviation < 0.5% of mean

ASTCS System Check

Reference Strain Transducer:	5695
Reference General Gage Factor:	317.00 με/mV/V
LVDT #1 Sensitivity (inches/volt):	0.0055
LVDT #2 Sensitivity (inches/volt):	0.0055
System Temperature Status:	Passed
Date/Time of Last System Check:	6/17/2022 9:27 AM

Strain Transducer Connections

Red:	Excitation +
Black:	Excitation -
Green:	Signal +
White:	Signal -
Grey/Bare:	Shield

NIST Reference:

The manufacturer certifies that the supplied ASTCS instrument meets or exceeds published specifications at the time of manufacturing and has been verified using standards and instruments whose accuracies are traceable to the National Institute of Standards and Technology (NIST), an accepted value of a natural physical constant or a ratio calibration technique. Sensor calibrations performed by this instrument are certified by the owner of the ASTCS and are in accordance with the owner's quality assurance program. Measurements and information provided on this report are valid at the time of calibration only.

740 S PIERCE AVE, UNIT 15
LOUISVILLE, CO 80027
+1.303.494.3230

BDITEST.COM

Certificate of Calibration

Serial Number: ASTa1250

Transducer Model: BDI AST350-6
General Gage Factor (με/mV/V$_{exc}$): 1137.6
Initial Offset Voltage (mV/V$_{exc}$): -0.735

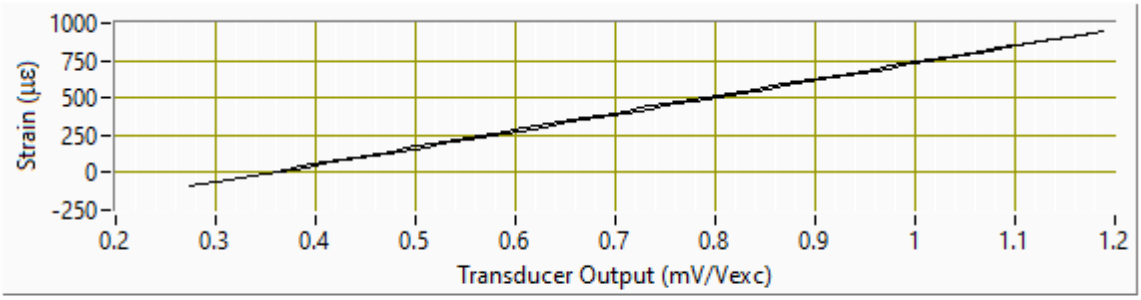
Temperature (C): 25.8
Mean Linear Correlation Coefficient [LCC]: 0.99979
LCC Standard Deviation: 1.812E-5

Table 1: Representative Calibration Data

Strain (micro-strain)	Transducer Output (mV/Vexc.)
-93.005	0.275
-37.530	0.325
22.543	0.379
82.052	0.430
143.134	0.486
202.118	0.539
262.662	0.591
321.804	0.643
382.606	0.697
442.246	0.749
502.868	0.804
562.089	0.853
622.255	0.906
681.873	0.960
741.507	1.012
802.191	1.062

Strain (micro-strain)	Transducer Output (mV/Vexc.)
862.089	1.116
922.098	1.167
923.457	1.165
863.087	1.114
803.152	1.055
743.071	1.003
683.049	0.950
622.734	0.896
562.897	0.842
503.427	0.791
444.541	0.737
383.509	0.685
325.467	0.634
264.323	0.578
206.369	0.530
145.054	0.477

Calibration Curve



Calibrated By: Connor H.
Date and Time: 6/24/2022 3:46 PM

Signature: _____

Specifications

Automated Strain Transducer Calibration System (ASTCS)

ASTCS Serial Number:	BDI CAL 0001
ASTCS Software Version Number:	2.0.1
ASTCS Independant Verification Date:	12/14/2020 3:47 PM
Transducer Gage Length:	5.25 inches (133.3 mm)
Full Scale Displacement Range:	-0.0000, +0.0062 (inches)
Method for Applying Displacement:	Precision Stepper Motor Connected to Linear Stage
Excitation Voltage for Calibration:	2.5 VDC
Displacement Measurements:	Dual Precision LVDTs, Output Averaged
Displacement Certification:	NIST 274437-07
Linearity Verification Technique:	Linear Correlation Coefficient < 0.9996
Repeatability Verification Technique:	Standard Deviation < 0.5% of mean

ASTCS System Check

Reference Strain Transducer:	5695
Reference General Gage Factor:	317.00 με/mV/V
LVDT #1 Sensitivity (inches/volt):	0.0055
LVDT #2 Sensitivity (inches/volt):	0.0055
System Temperature Status:	Passed
Date/Time of Last System Check:	6/17/2022 9:27 AM

Strain Transducer Connections

Red:	Excitation +
Black:	Excitation -
Green:	Signal +
White:	Signal -
Grey/Bare:	Shield

NIST Reference:

The manufacturer certifies that the supplied ASTCS instrument meets or exceeds published specifications at the time of manufacturing and has been verified using standards and instruments whose accuracies are traceable to the National Institute of Standards and Technology (NIST), an accepted value of a natural physical constant or a ratio calibration technique. Sensor calibrations performed by this instrument are certified by the owner of the ASTCS and are in accordance with the owner's quality assurance program. Measurements and information provided on this report are valid at the time of calibration only.

740 S PIERCE AVE, UNIT 15
LOUISVILLE, CO 80027
+1.303.494.3230

BDITEST.COM

Certificate of Calibration

Serial Number: ASTa1252

Transducer Model: BDI AST350-6
General Gage Factor (με/mV/V$_{exc}$): 1071.3
Initial Offset Voltage (mV/V$_{exc}$): 0.170

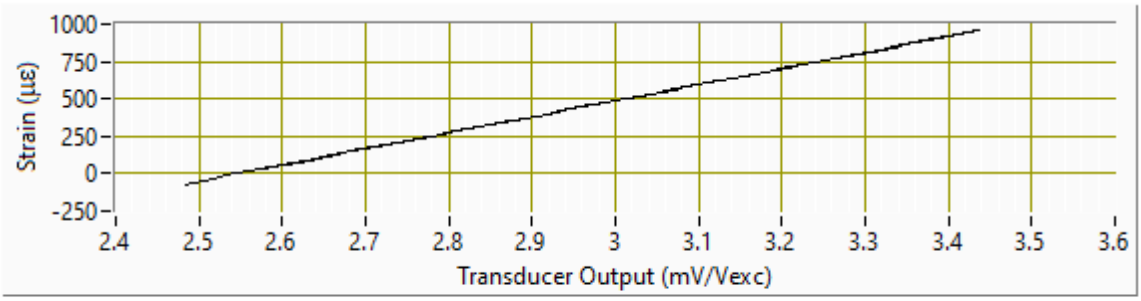
Temperature (C): 24.8
Mean Linear Correlation Coefficient [LCC]: 0.99997
LCC Standard Deviation: 5.434E-6

Table 1: Representative Calibration Data

Strain (micro-strain)	Transducer Output (mV/Vexc.)
-69.987	2.483
-14.727	2.531
44.909	2.587
103.119	2.642
163.257	2.694
220.743	2.750
281.434	2.808
339.387	2.862
400.389	2.918
458.285	2.972
518.919	3.029
576.876	3.085
636.892	3.141
695.852	3.194
755.714	3.252
815.148	3.306

Strain (micro-strain)	Transducer Output (mV/Vexc.)
874.781	3.357
933.735	3.412
949.022	3.426
890.729	3.377
830.156	3.322
772.880	3.266
712.170	3.211
653.887	3.156
593.572	3.099
535.526	3.045
475.971	2.988
417.204	2.933
357.729	2.880
298.487	2.824
239.749	2.767
180.026	2.714

Calibration Curve



Calibrated By: Connor H.
Date and Time: 6/24/2022 2:27 PM

Signature: _____

Specifications

Automated Strain Transducer Calibration System (ASTCS)

ASTCS Serial Number:	BDI CAL 0001
ASTCS Software Version Number:	2.0.1
ASTCS Independant Verification Date:	12/14/2020 3:47 PM
Transducer Gage Length:	5.25 inches (133.3 mm)
Full Scale Displacement Range:	-0.0000, +0.0062 (inches)
Method for Applying Displacement:	Precision Stepper Motor Connected to Linear Stage
Excitation Voltage for Calibration:	2.5 VDC
Displacement Measurements:	Dual Precision LVDTs, Output Averaged
Displacement Certification:	NIST 274437-07
Linearity Verification Technique:	Linear Correlation Coefficient < 0.9996
Repeatability Verification Technique:	Standard Deviation < 0.5% of mean

ASTCS System Check

Reference Strain Transducer:	5695
Reference General Gage Factor:	317.00 με/mV/V
LVDT #1 Sensitivity (inches/volt):	0.0055
LVDT #2 Sensitivity (inches/volt):	0.0055
System Temperature Status:	Passed
Date/Time of Last System Check:	6/17/2022 9:27 AM

Strain Transducer Connections

Red:	Excitation +
Black:	Excitation -
Green:	Signal +
White:	Signal -
Grey/Bare:	Shield

NIST Reference:

The manufacturer certifies that the supplied ASTCS instrument meets or exceeds published specifications at the time of manufacturing and has been verified using standards and instruments whose accuracies are traceable to the National Institute of Standards and Technology (NIST), an accepted value of a natural physical constant or a ratio calibration technique. Sensor calibrations performed by this instrument are certified by the owner of the ASTCS and are in accordance with the owner's quality assurance program. Measurements and information provided on this report are valid at the time of calibration only.

740 S PIERCE AVE, UNIT 15
LOUISVILLE, CO 80027
+1.303.494.3230

BDITEST.COM

Certificate of Calibration

Serial Number: ASTa1254

Transducer Model: BDI AST350-6
General Gage Factor (με/mV/V$_{exc}$): 1065.8
Initial Offset Voltage (mV/V$_{exc}$): -0.220

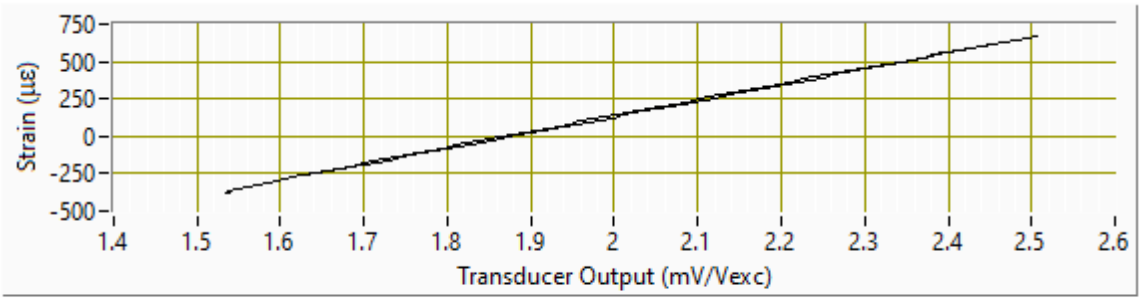
Temperature (C): 25.6
Mean Linear Correlation Coefficient [LCC]: 0.99987
LCC Standard Deviation: 2.324E-5

Table 1: Representative Calibration Data

Strain (micro-strain)	Transducer Output (mV/Vexc.)
-378.398	1.538
-363.283	1.536
-306.771	1.584
-247.276	1.643
-188.457	1.700
-126.876	1.758
-68.555	1.814
-7.953	1.871
50.548	1.927
110.431	1.985
168.644	2.037
228.963	2.095
288.471	2.152
348.765	2.207
408.814	2.263
468.138	2.318

Strain (micro-strain)	Transducer Output (mV/Vexc.)
528.019	2.372
586.559	2.429
647.542	2.482
661.251	2.495
602.847	2.442
542.917	2.383
484.773	2.328
424.453	2.270
365.941	2.212
305.356	2.156
246.011	2.101
186.369	2.043
127.985	1.989
69.552	1.934
9.747	1.879
-48.500	1.825

Calibration Curve



Calibrated By: Connor H.
Date and Time: 6/24/2022 3:27 PM

Signature: _____

Specifications

Automated Strain Transducer Calibration System (ASTCS)

ASTCS Serial Number:	BDI CAL 0001
ASTCS Software Version Number:	2.0.1
ASTCS Independant Verification Date:	12/14/2020 3:47 PM
Transducer Gage Length:	5.25 inches (133.3 mm)
Full Scale Displacement Range:	-0.0000, +0.0062 (inches)
Method for Applying Displacement:	Precision Stepper Motor Connected to Linear Stage
Excitation Voltage for Calibration:	2.5 VDC
Displacement Measurements:	Dual Precision LVDTs, Output Averaged
Displacement Certification:	NIST 274437-07
Linearity Verification Technique:	Linear Correlation Coefficient < 0.9996
Repeatability Verification Technique:	Standard Deviation < 0.5% of mean

ASTCS System Check

Reference Strain Transducer:	5695
Reference General Gage Factor:	317.00 με/mV/V
LVDT #1 Sensitivity (inches/volt):	0.0055
LVDT #2 Sensitivity (inches/volt):	0.0055
System Temperature Status:	Passed
Date/Time of Last System Check:	6/17/2022 9:27 AM

Strain Transducer Connections

Red:	Excitation +
Black:	Excitation -
Green:	Signal +
White:	Signal -
Grey/Bare:	Shield

NIST Reference:

The manufacturer certifies that the supplied ASTCS instrument meets or exceeds published specifications at the time of manufacturing and has been verified using standards and instruments whose accuracies are traceable to the National Institute of Standards and Technology (NIST), an accepted value of a natural physical constant or a ratio calibration technique. Sensor calibrations performed by this instrument are certified by the owner of the ASTCS and are in accordance with the owner's quality assurance program. Measurements and information provided on this report are valid at the time of calibration only.

740 S PIERCE AVE, UNIT 15
LOUISVILLE, CO 80027
+1.303.494.3230

BDITEST.COM

Certificate of Calibration

Serial Number: **ASTa1257**

Transducer Model: BDI AST350-6

General Gage Factor (με/mV/V$_{exc}$): 1123.9

Initial Offset Voltage (mV/V$_{exc}$): -0.182

Temperature (C): 25.9

Mean Linear Correlation Coefficient [LCC]: 0.99989

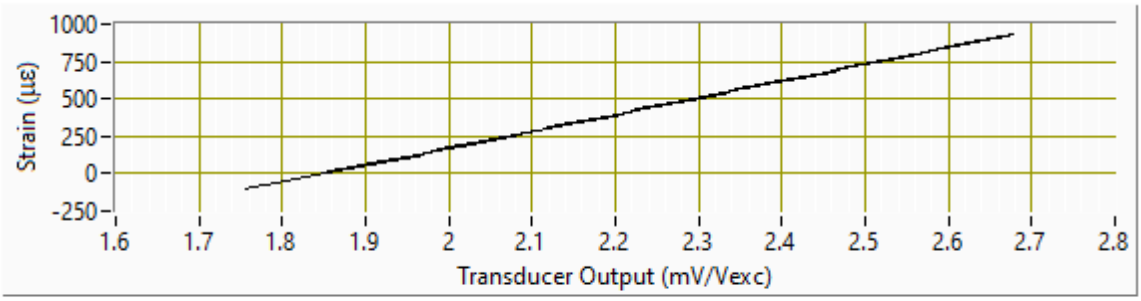
LCC Standard Deviation: 6.012E-6

Table 1: Representative Calibration Data

Strain (micro-strain)	Transducer Output (mV/Vexc.)
-102.458	1.755
-47.902	1.805
12.277	1.857
70.583	1.907
131.055	1.963
189.814	2.015
250.374	2.067
309.288	2.121
370.595	2.175
429.536	2.227
489.161	2.282
548.366	2.332
608.006	2.386
667.553	2.441
728.012	2.494
787.383	2.546

Strain (micro-strain)	Transducer Output (mV/Vexc.)
846.653	2.601
905.694	2.652
908.877	2.658
849.037	2.609
790.145	2.552
729.428	2.501
669.217	2.449
609.406	2.394
550.317	2.342
490.691	2.290
432.373	2.237
371.957	2.186
313.028	2.132
252.413	2.076
194.049	2.028
133.292	1.975

Calibration Curve



Calibrated By: Connor H.

Signature: _____

Date and Time: 6/24/2022 3:58 PM

Specifications

Automated Strain Transducer Calibration System (ASTCS)

ASTCS Serial Number:	BDI CAL 0001
ASTCS Software Version Number:	2.0.1
ASTCS Independant Verification Date:	12/14/2020 3:47 PM
Transducer Gage Length:	5.25 inches (133.3 mm)
Full Scale Displacement Range:	-0.0000, +0.0062 (inches)
Method for Applying Displacement:	Precision Stepper Motor Connected to Linear Stage
Excitation Voltage for Calibration:	2.5 VDC
Displacement Measurements:	Dual Precision LVDTs, Output Averaged
Displacement Certification:	NIST 274437-07
Linearity Verification Technique:	Linear Correlation Coefficient < 0.9996
Repeatability Verification Technique:	Standard Deviation < 0.5% of mean

ASTCS System Check

Reference Strain Transducer:	5695
Reference General Gage Factor:	317.00 με/mV/V
LVDT #1 Sensitivity (inches/volt):	0.0055
LVDT #2 Sensitivity (inches/volt):	0.0055
System Temperature Status:	Passed
Date/Time of Last System Check:	6/17/2022 9:27 AM

Strain Transducer Connections

Red:	Excitation +
Black:	Excitation -
Green:	Signal +
White:	Signal -
Grey/Bare:	Shield

NIST Reference:

The manufacturer certifies that the supplied ASTCS instrument meets or exceeds published specifications at the time of manufacturing and has been verified using standards and instruments whose accuracies are traceable to the National Institute of Standards and Technology (NIST), an accepted value of a natural physical constant or a ratio calibration technique. Sensor calibrations performed by this instrument are certified by the owner of the ASTCS and are in accordance with the owner's quality assurance program. Measurements and information provided on this report are valid at the time of calibration only.

740 S PIERCE AVE, UNIT 15
LOUISVILLE, CO 80027
+1.303.494.3230

BDITEST.COM

Certificate of Calibration

Serial Number: **VAS1000**

Transducer Model: BDI VAST350

General Gage Factor (με/mV/V$_{exc}$): 703.6

Initial Offset Voltage (mV/V$_{exc}$): -0.952

Temperature (C): 24.3

Mean Linear Correlation Coefficient [LCC]: 0.99997

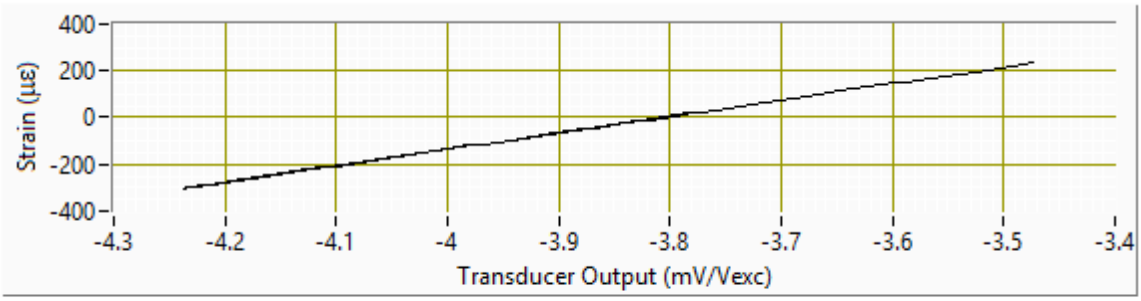
LCC Standard Deviation: 2.476E-5

Table 1: Representative Calibration Data

Strain (micro-strain)	Transducer Output (mV/Vexc.)
235.133	-3.474
215.016	-3.503
188.529	-3.539
163.034	-3.577
138.201	-3.610
113.360	-3.647
89.317	-3.677
64.981	-3.714
40.834	-3.747
17.605	-3.783
-5.783	-3.815
-28.560	-3.848
-51.326	-3.878
-74.043	-3.913
-96.931	-3.943
-120.308	-3.980

Strain (micro-strain)	Transducer Output (mV/Vexc.)
-143.600	-4.010
-167.303	-4.045
-191.204	-4.077
-214.674	-4.114
-238.941	-4.148
-262.966	-4.182
-286.667	-4.214
-302.149	-4.237
-284.592	-4.211
-260.388	-4.177
-235.230	-4.142
-210.606	-4.108
-186.366	-4.070
-161.606	-4.036
-136.339	-3.998
-111.936	-3.967

Calibration Curve



Calibrated By: Connor H.

Signature: _____

Date and Time: 1/21/2021 11:31 AM

Specifications

Automated Strain Transducer Calibration System (ASTCS)

ASTCS Serial Number:	BDI CAL 0001
ASTCS Software Version Number:	2.0.1
ASTCS Independant Verification Date:	12/14/2020 3:47 PM
Transducer Gage Length:	7.50 inches (190.5 mm)
Full Scale Displacement Range:	-0.0000, +-0.0062(inches)
Method for Applying Displacement:	Precision Stepper Motor Connected to Linear Stage
Excitation Voltage for Calibration:	2.5 VDC
Displacement Measurements:	Dual Precision LVDTs, Output Averaged
Displacement Certification:	NIST 274437-07
Linearity Verification Technique:	Linear Correlation Coefficient < 0.9996
Repeatability Verification Technique:	Standard Deviation < 0.5% of mean

ASTCS System Check

Reference Strain Transducer:	5695
Reference General Gage Factor:	317.00 με/mV/V
LVDT #1 Sensitivity (inches/volt):	0.0055
LVDT #2 Sensitivity (inches/volt):	0.0055
System Temperature Status:	Passed
Date/Time of Last System Check:	1/20/2021 3:26 PM

Strain Transducer Connections

Red:	Excitation +
Black:	Excitation -
Green:	Signal +
White:	Signal -
Grey/Bare:	Shield

NIST Reference:

The manufacturer certifies that the supplied ASTCS instrument meets or exceeds published specifications at the time of manufacturing and has been verified using standards and instruments whose accuracies are traceable to the National Institute of Standards and Technology (NIST), an accepted value of a natural physical constant or a ratio calibration technique. Sensor calibrations performed by this instrument are certified by the owner of the ASTCS and are in accordance with the owner's quality assurance program. Measurements and information provided on this report are valid at the time of calibration only.

740 S PIERCE AVE, UNIT 15
LOUISVILLE, CO 80027
+1.303.494.3230

BDITEST.COM

Certificate of Calibration

Serial Number: **VAS1001**

Transducer Model: BDI VAST350
General Gage Factor (με/mV/V$_{exc}$): 745.0
Initial Offset Voltage (mV/V$_{exc}$): -0.951

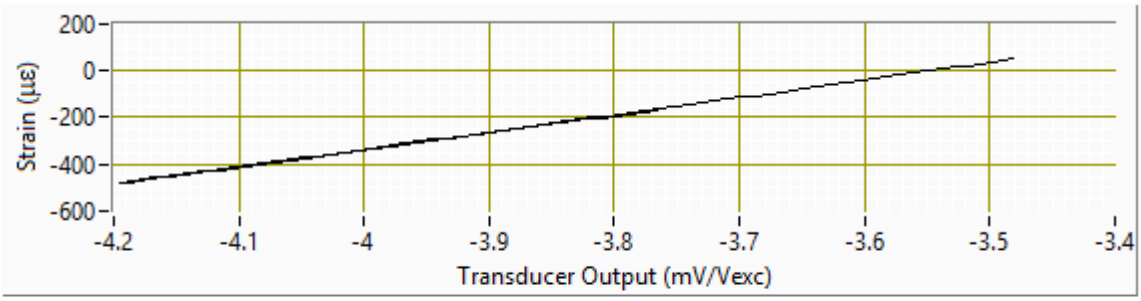
Temperature (C): 24.3
Mean Linear Correlation Coefficient [LCC]: 0.99988
LCC Standard Deviation: 1.987E-5

Table 1: Representative Calibration Data

Strain (micro-strain)	Transducer Output (mV/Vexc.)
51.589	-3.481
31.654	-3.508
6.717	-3.537
-17.689	-3.572
-42.248	-3.603
-66.441	-3.638
-89.956	-3.666
-113.674	-3.699
-137.385	-3.729
-160.860	-3.764
-184.198	-3.795
-207.258	-3.827
-231.061	-3.856
-254.526	-3.890
-278.435	-3.920
-302.374	-3.956

Strain (micro-strain)	Transducer Output (mV/Vexc.)
-325.263	-3.985
-348.740	-4.017
-371.798	-4.047
-395.484	-4.080
-419.359	-4.113
-441.837	-4.145
-466.166	-4.175
-481.168	-4.195
-463.201	-4.170
-439.465	-4.139
-415.851	-4.105
-389.663	-4.071
-365.747	-4.036
-341.674	-4.003
-315.707	-3.967
-291.333	-3.935

Calibration Curve



Calibrated By: Connor H.
Date and Time: 1/21/2021 11:41 AM

Signature: _____

Specifications

Automated Strain Transducer Calibration System (ASTCS)

ASTCS Serial Number:	BDI CAL 0001
ASTCS Software Version Number:	2.0.1
ASTCS Independant Verification Date:	12/14/2020 3:47 PM
Transducer Gage Length:	7.50 inches (190.5 mm)
Full Scale Displacement Range:	-0.0000, +-0.0062(inches)
Method for Applying Displacement:	Precision Stepper Motor Connected to Linear Stage
Excitation Voltage for Calibration:	2.5 VDC
Displacement Measurements:	Dual Precision LVDTs, Output Averaged
Displacement Certification:	NIST 274437-07
Linearity Verification Technique:	Linear Correlation Coefficient < 0.9996
Repeatability Verification Technique:	Standard Deviation < 0.5% of mean

ASTCS System Check

Reference Strain Transducer:	5695
Reference General Gage Factor:	317.00 με/mV/V
LVDT #1 Sensitivity (inches/volt):	0.0055
LVDT #2 Sensitivity (inches/volt):	0.0055
System Temperature Status:	Passed
Date/Time of Last System Check:	1/20/2021 3:26 PM

Strain Transducer Connections

Red:	Excitation +
Black:	Excitation -
Green:	Signal +
White:	Signal -
Grey/Bare:	Shield

NIST Reference:

The manufacturer certifies that the supplied ASTCS instrument meets or exceeds published specifications at the time of manufacturing and has been verified using standards and instruments whose accuracies are traceable to the National Institute of Standards and Technology (NIST), an accepted value of a natural physical constant or a ratio calibration technique. Sensor calibrations performed by this instrument are certified by the owner of the ASTCS and are in accordance with the owner's quality assurance program. Measurements and information provided on this report are valid at the time of calibration only.

740 S PIERCE AVE, UNIT 15
LOUISVILLE, CO 80027
+1.303.494.3230

BDITEST.COM

Certificate of Calibration

Serial Number: **VAS1002**

Transducer Model: BDI VAST350
General Gage Factor (με/mV/V$_{exc}$): 799.6
Initial Offset Voltage (mV/V$_{exc}$): -0.990

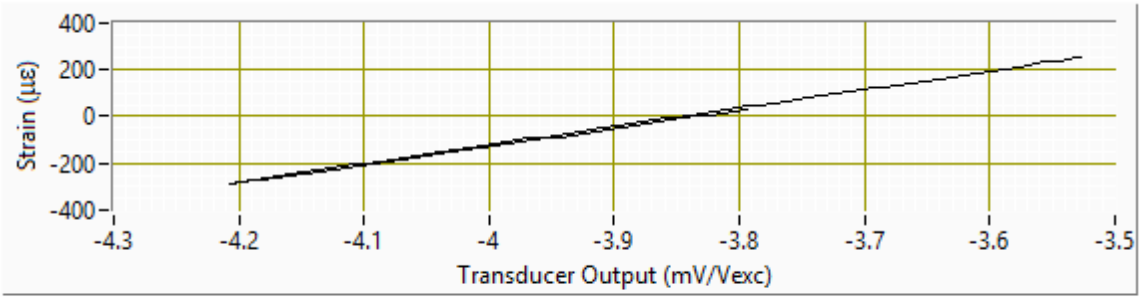
Temperature (C): 24.4
Mean Linear Correlation Coefficient [LCC]: 0.99963
LCC Standard Deviation: 6.156E-6

Table 1: Representative Calibration Data

Strain (micro-strain)	Transducer Output (mV/Vexc.)
256.256	-3.529
256.368	-3.527
240.027	-3.545
214.502	-3.575
187.364	-3.611
162.640	-3.640
137.302	-3.673
113.130	-3.702
89.997	-3.734
66.618	-3.763
43.720	-3.792
20.649	-3.819
-1.260	-3.850
-23.658	-3.877
-46.858	-3.909
-70.182	-3.935

Strain (micro-strain)	Transducer Output (mV/Vexc.)
-94.194	-3.967
-117.679	-3.995
-141.388	-4.028
-165.848	-4.057
-189.879	-4.088
-214.092	-4.116
-238.232	-4.148
-262.472	-4.177
-285.190	-4.208
-275.185	-4.189
-250.988	-4.159
-226.524	-4.124
-201.628	-4.092
-176.287	-4.059
-152.079	-4.030
-127.017	-3.995

Calibration Curve



Calibrated By: Connor H.
Date and Time: 1/21/2021 11:55 AM

Signature: _____

Specifications

Automated Strain Transducer Calibration System (ASTCS)

ASTCS Serial Number:	BDI CAL 0001
ASTCS Software Version Number:	2.0.1
ASTCS Independant Verification Date:	12/14/2020 3:47 PM
Transducer Gage Length:	7.50 inches (190.5 mm)
Full Scale Displacement Range:	-0.0000, +-0.0062(inches)
Method for Applying Displacement:	Precision Stepper Motor Connected to Linear Stage
Excitation Voltage for Calibration:	2.5 VDC
Displacement Measurements:	Dual Precision LVDTs, Output Averaged
Displacement Certification:	NIST 274437-07
Linearity Verification Technique:	Linear Correlation Coefficient < 0.9996
Repeatability Verification Technique:	Standard Deviation < 0.5% of mean

ASTCS System Check

Reference Strain Transducer:	5695
Reference General Gage Factor:	317.00 με/mV/V
LVDT #1 Sensitivity (inches/volt):	0.0055
LVDT #2 Sensitivity (inches/volt):	0.0055
System Temperature Status:	Passed
Date/Time of Last System Check:	1/20/2021 3:26 PM

Strain Transducer Connections

Red:	Excitation +
Black:	Excitation -
Green:	Signal +
White:	Signal -
Grey/Bare:	Shield

NIST Reference:

The manufacturer certifies that the supplied ASTCS instrument meets or exceeds published specifications at the time of manufacturing and has been verified using standards and instruments whose accuracies are traceable to the National Institute of Standards and Technology (NIST), an accepted value of a natural physical constant or a ratio calibration technique. Sensor calibrations performed by this instrument are certified by the owner of the ASTCS and are in accordance with the owner's quality assurance program. Measurements and information provided on this report are valid at the time of calibration only.

740 S PIERCE AVE, UNIT 15
LOUISVILLE, CO 80027
+1.303.494.3230

BDITEST.COM

Certificate of Calibration

Serial Number: **VAST1239**

Transducer Model: BDI VAST350

General Gage Factor (με/mV/V$_{exc}$): 1044.0

Initial Offset Voltage (mV/V$_{exc}$): -0.591

Temperature (C): 25.2

Mean Linear Correlation Coefficient [LCC]: 0.99809

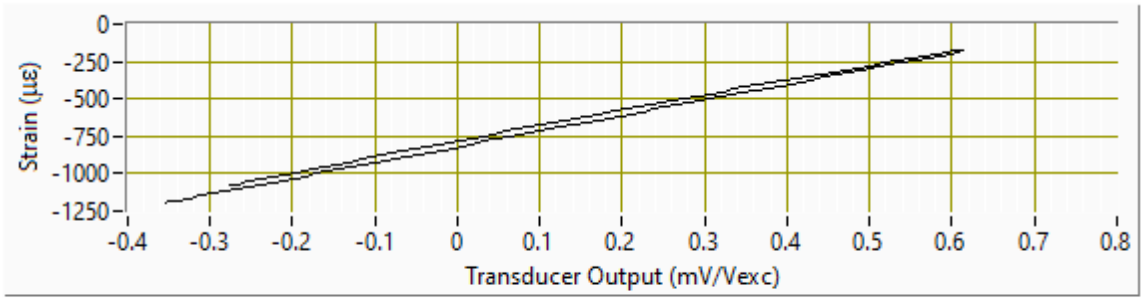
LCC Standard Deviation: 3.959E-5

Table 1: Representative Calibration Data

Strain (micro-strain)	Transducer Output (mV/Vexc.)
-1198.520	-0.353
-1176.642	-0.338
-1118.547	-0.281
-1057.014	-0.224
-1001.179	-0.171
-941.753	-0.113
-885.351	-0.062
-828.454	-0.005
-770.480	0.047
-714.535	0.099
-654.729	0.157
-599.744	0.211
-539.677	0.266
-486.173	0.319
-426.158	0.378
-371.653	0.430

Strain (micro-strain)	Transducer Output (mV/Vexc.)
-312.247	0.489
-256.462	0.539
-198.844	0.598
-189.024	0.595
-246.433	0.533
-304.429	0.472
-364.634	0.411
-421.420	0.349
-482.068	0.292
-538.568	0.234
-600.087	0.171
-656.904	0.117
-718.723	0.058
-774.413	0.005
-835.326	-0.051
-891.345	-0.104

Calibration Curve



Calibrated By: Connor H.

Signature: _____

Date and Time: 8/30/2022 3:56 PM

Specifications

Automated Strain Transducer Calibration System (ASTCS)

ASTCS Serial Number:	BDI CAL 0001
ASTCS Software Version Number:	2.0.1
ASTCS Independant Verification Date:	8/30/2022 2:17 PM
Transducer Gage Length:	5.00 inches (127.0 mm)
Full Scale Displacement Range:	-0.0000, +0.0062 (inches)
Method for Applying Displacement:	Precision Stepper Motor Connected to Linear Stage
Excitation Voltage for Calibration:	2.5 VDC
Displacement Measurements:	Dual Precision LVDTs, Output Averaged
Displacement Certification:	NIST 274437-07
Linearity Verification Technique:	Linear Correlation Coefficient < 0.9996
Repeatability Verification Technique:	Standard Deviation < 0.5% of mean

ASTCS System Check

Reference Strain Transducer:	5695
Reference General Gage Factor:	317.00 με/mV/V
LVDT #1 Sensitivity (inches/volt):	0.0055
LVDT #2 Sensitivity (inches/volt):	0.0054
System Temperature Status:	Passed
Date/Time of Last System Check:	8/30/2022 2:26 PM

Strain Transducer Connections

Red:	Excitation +
Black:	Excitation -
Green:	Signal +
White:	Signal -
Grey/Bare:	Shield

NIST Reference:

The manufacturer certifies that the supplied ASTCS instrument meets or exceeds published specifications at the time of manufacturing and has been verified using standards and instruments whose accuracies are traceable to the National Institute of Standards and Technology (NIST), an accepted value of a natural physical constant or a ratio calibration technique. Sensor calibrations performed by this instrument are certified by the owner of the ASTCS and are in accordance with the owner's quality assurance program. Measurements and information provided on this report are valid at the time of calibration only.

QUALITY CONTROL FABRICATION AND HOOK-UP SHEET

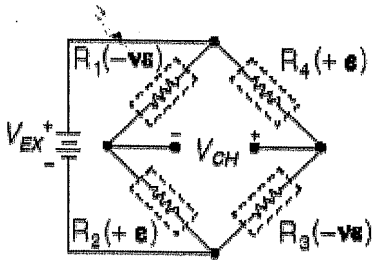
VAST350
VERTICAL ASPHALT STRAIN TRANSDUCER

Gage ID: VAS1000

Lead Length: 25ft

NOTE: MANUAL READINGS TAKEN USING VISHAY P-3500. GF = 2.00 BALANCE = 500

FABRICATION



GAGE RESISTANCE : 351/354

INITIAL READING AFTER WIRING GAGE : −6003

SHORT TO SHIELD : ok

TENSION = Increase IN READING

READING AFTER J-COAT : −6010

READING AFTER ALL PROTECTION : −6016

(after butyl rubber and heat shrink)

DATE : 8/31/22 WHO : dm

SHORT TO SHIELD : ok

COMMENTS: _____

COLOR	BRIDGE	P-3500
Red	V_{EX}+	P+
Black	V_{EX}-	P-
White	V_{CH}-	S-
Green	V_{CH}+	S+

CALIBRATION

EXCITATION : 5V CAL FACTOR : 703.6 ue/mV/V OTHER : _____

DATE : 8/31/22 WHO : dm

FINAL READING AFTER CALIBRATION AND DIPPING : −6025

INSTALLATION

NOTE: MANUAL READINGS TAKEN USING VISHAY P-3500. GF = 2.00 BALANCE = 500

LOCATION : _____ X:_____ Y:_____ Z:_____

DATE : _____ READING : _____ EVENT : _____

DATE : _____ READING : _____ EVENT : _____

HOOKUP TO SYSTEM

SPU : _____ CHANNEL : _____

DATE : _____ READING : _____ EVENT : _____

QUALITY CONTROL FABRICATION AND HOOK-UP SHEET

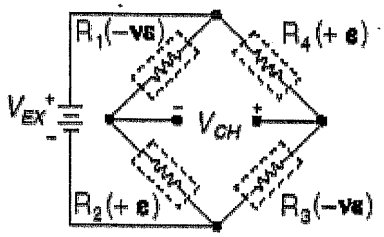
VAST350
VERTICAL ASPHALT STRAIN TRANSDUCER

Gage ID: VAS1001

Lead Length: 25ft

NOTE: MANUAL READINGS TAKEN USING VISHAY P-3500. GF = 2.00 BALANCE = 500

FABRICATION



COLOR	BRIDGE	P-3500
Red	V_{EX}+	P+
Black	V_{EX}-	P-
White	V_{CH}-	S-
Green	V_{CH}+	S+

GAGE RESISTANCE : 351/354

INITIAL READING AFTER WIRING GAGE : -6000

SHORT TO SHIELD : OK

TENSION = Increase IN READING

READING AFTER J-COAT : -6010

READING AFTER ALL PROTECTION : -6017

(after butyl rubber and heat shrink)

DATE : 8/31/22 WHO : CPM

SHORT TO SHIELD : OK

COMMENTS: _____

CALIBRATION

EXCITATION : 5V CAL FACTOR : 745 ue/mV/V OTHER : _____

DATE : 8/31/22 WHO : CPM

FINAL READING AFTER CALIBRATION AND DIPPING : -6022

INSTALLATION

NOTE: MANUAL READINGS TAKEN USING VISHAY P-3500. GF = 2.00 BALANCE = 500

LOCATION : _____ X:_____ Y:_____ Z:_____

DATE : _____ READING : _____ EVENT : _____

DATE : _____ READING : _____ EVENT : _____

HOOKUP TO SYSTEM

SPU : _____ CHANNEL : _____

DATE : _____ READING : _____ EVENT : _____

QUALITY CONTROL FABRICATION AND HOOK-UP SHEET

VAST350
VERTICAL ASPHALT STRAIN TRANSDUCER

Gage ID: VAS 1002

Lead Length: _____

NOTE: MANUAL READINGS TAKEN USING VISHAY P-3500. GF = 2.00 BALANCE = 500

FABRICATION

GAGE RESISTANCE : 351/354

INITIAL READING AFTER WIRING GAGE : -6201

SHORT TO SHIELD : ok

TENSION = Increase IN READING

READING AFTER J-COAT : -6234

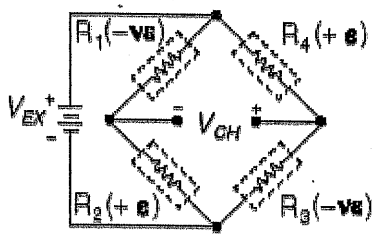
READING AFTER ALL PROTECTION : -6257

(after butyl rubber and heat shrink)

DATE : 8/31/22 WHO : JM

SHORT TO SHIELD : ok

COMMENTS: _____



COLOR	BRIDGE	P-3500
Red	V_{EX}+	P+
Black	V_{EX}-	P-
White	V_{CH}-	S-
Green	V_{CH}+	S+

CALIBRATION

EXCITATION : 5V CAL FACTOR : 799.6 ue/mV/V OTHER : _____

DATE : 8/31/22 WHO : JM

FINAL READING AFTER CALIBRATION AND DIPPING : -6284

INSTALLATION

NOTE: MANUAL READINGS TAKEN USING VISHAY P-3500. GF = 2.00 BALANCE = 500

LOCATION : _____ X:_____ Y:_____ Z:_____

DATE : _____ READING : _____ EVENT : _____

DATE : _____ READING : _____ EVENT : _____

HOOKUP TO SYSTEM

SPU : _____ CHANNEL : _____

DATE : _____ READING : _____ EVENT : _____

QUALITY CONTROL FABRICATION AND HOOK-UP SHEET

VAST350
VERTICAL ASPHALT STRAIN TRANSDUCER

Gage ID: VAST 1239

Lead Length: _____

NOTE: MANUAL READINGS TAKEN USING VISHAY P-3500. GF = 2.00 BALANCE = 500

FABRICATION

GAGE RESISTANCE : 986/987

INITIAL READING AFTER WIRING GAGE : -4002

SHORT TO SHIELD : Ok

TENSION = increase IN READING

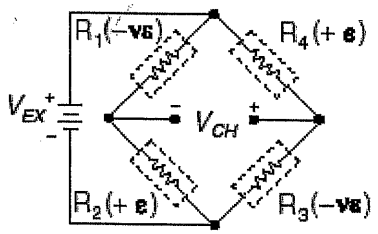
READING AFTER J-COAT : -4100

READING AFTER ALL PROTECTION : -4150
(after butyl rubber and heat shrink)

DATE : 8/30/22 WHO : CPM

SHORT TO SHIELD : OK

COMMENTS: _____



COLOR	BRIDGE	P-3500
Red	V_{EX}+	P+
Black	V_{EX}-	P-
White	V_{CH}-	S-
Green	V_{CH}+	S+

CALIBRATION

EXCITATION : 5V CAL FACTOR : 1044 ue/mV/V OTHER : _____

DATE : 8/30/22 WHO : CPM

FINAL READING AFTER CALIBRATION AND DIPPING : -4184

INSTALLATION

NOTE: MANUAL READINGS TAKEN USING VISHAY P-3500. GF = 2.00 BALANCE = 500

LOCATION : _____ X: _____ Y: _____ Z: _____

DATE : _____ READING : _____ EVENT : _____

DATE : _____ READING : _____ EVENT : _____

HOOKUP TO SYSTEM

SPU : _____ CHANNEL : _____

DATE : _____ READING : _____ EVENT : _____

QUALITY CONTROL FABRICATION AND HOOK-UP SHEET

BDI RAW DATA. REAL TIME. RESULTS.

DYNAMIC AST

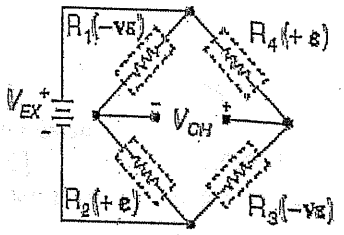
ASPHALT STRAIN GAGE 6X8"

Gage ID: AST41234

Lead Length: 10m

NOTE: MANUAL READINGS TAKEN USING VISHAY P-3500. GF = 2.00 BALANCE = 500

FABRICATION



GAGE RESISTANCE: 1031 / 1023

INITIAL READING AFTER WIRING GAGE: -3690

SHORT TO SHIELD: OK

TENSION = Increase IN READING

READING AFTER J-COAT: -3754

READING AFTER ALL PROTECTION: -4356
(after butyl rubber and heat shrink)

DATE: 6/24/22 WHO: DM

SHORT TO SHIELD: OK

COMMENTS:

COLOR	BRIDGE	P-3500
Red	V_{EX+}	P+
Black	V_{EX-}	P-
White	V_{CH-}	S-
Green	V_{CH+}	S+

CALIBRATION

EXCITATION: 2.5V CAL FACTOR: 1035.9 ue/mV/V OTHER:

DATE: 6/24/22 WHO: DM

FINAL READING AFTER CALIBRATION AND DIPPING: -4350

INSTALLATION

NOTE: MANUAL READINGS TAKEN USING VISHAY P-3500. GF = 2.00 BALANCE = 500

LOCATION: X: Y: Z:

DATE: READING: EVENT:

HOOKUP TO SYSTEM

SPU: CHANNEL:

DATE: READING: EVENT:

QUALITY CONTROL FABRICATION AND HOOK-UP SHEET

BDI RAW DATA. REFINED RESULTS.

DYNAMIC AST

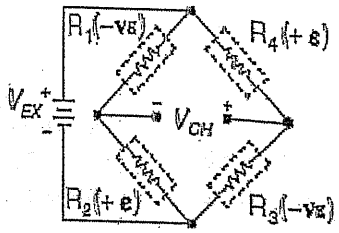
ASPHALT STRAIN GAGE 6X8"

Gage ID: Asta 1241

Lead Length: 10m

NOTE: MANUAL READINGS TAKEN USING VISHAY P-3500. GF = 2.00 BALANCE = 500

FABRICATION



GAGE RESISTANCE : 1024 | 1013

INITIAL READING AFTER WIRING GAGE : -2514

SHORT TO SHIELD : ok

TENSION = Increase IN READING

READING AFTER J-COAT : -2580

READING AFTER ALL PROTECTION : -2980
(after butyl rubber and heat shrink)

DATE : 6/24/22 WHO : DM

SHORT TO SHIELD : ok

COMMENTS:

COLOR	BRIDGE	P-3500
Red	V_{EX}+	P+
Black	V_{EX}-	P-
White	V_{CH}-	S-
Green	V_{CH}+	S+

CALIBRATION

EXCITATION : 2.5v CAL FACTOR : 1159.3 ue/mV/V OTHER :

DATE : 6/24/22 WHO : DM

FINAL READING AFTER CALIBRATION AND DIPPING : -2939

INSTALLATION

NOTE: MANUAL READINGS TAKEN USING VISHAY P-3500. GF = 2.00 BALANCE = 500

LOCATION : X: Y: Z:

DATE : READING : EVENT :

HOOKUP TO SYSTEM

SPU : CHANNEL :

DATE : READING : EVENT :

QUALITY CONTROL FABRICATION AND HOOK-UP SHEET

BDI RAW DATA. REFINED RESULTS.

DYNAMIC AST

ASPHALT STRAIN GAGE 6X8"

Gage ID: AST1243

Lead Length: 10m

NOTE: MANUAL READINGS TAKEN USING VISHAY P-3500. GF = 2.00 BALANCE = 500

FABRICATION

GAGE RESISTANCE: 1128 / 1116

INITIAL READING AFTER WIRING GAGE: -1700

SHORT TO SHIELD: ok

TENSION = Increase IN READING

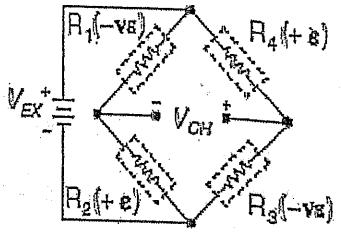
READING AFTER J-COAT: -1772

READING AFTER ALL PROTECTION: -2160
(after butyl rubber and heat shrink)

DATE: 6/24/22 WHO: JM

SHORT TO SHIELD: ok

COMMENTS:



COLOR	BRIDGE	P-3500
Red	V_{EX+}	P+
Black	V_{EX-}	P-
White	V_{CH-}	S-
Green	V_{CH+}	S+

CALIBRATION

EXCITATION: 2.5v CAL FACTOR: 1171.2 ue/mV/V OTHER:

DATE: 6/24/22 WHO: JM

FINAL READING AFTER CALIBRATION AND DIPPING: -2183

INSTALLATION

NOTE: MANUAL READINGS TAKEN USING VISHAY P-3500. GF = 2.00 BALANCE = 500

LOCATION: X: Y: Z:

DATE: READING: EVENT:

HOOKUP TO SYSTEM

SPU: CHANNEL:

DATE: READING: EVENT:

QUALITY CONTROL FABRICATION AND HOOK-UP SHEET

BDI RAW DATA. REFINED RESULTS.

DYNAMIC AST

ASPHALT STRAIN GAGE 6X8"

Gage ID: Asta2149

Lead Length: 10m

NOTE: MANUAL READINGS TAKEN USING VISHAY P-3500. GF = 2.00 BALANCE = 500

FABRICATION

GAGE RESISTANCE : 1141/1127

INITIAL READING AFTER WIRING GAGE : -377

SHORT TO SHIELD : ok

TENSION = Increase IN READING

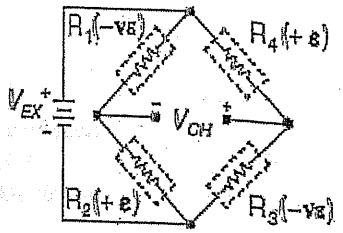
READING AFTER J-COAT : -438

READING AFTER ALL PROTECTION : -647
(after butyl rubber and heat shrink)

DATE : 6/24/22 WHO : am

SHORT TO SHIELD : ok

COMMENTS:



COLOR	BRIDGE	P-3500
Red	V_{EX+}	P+
Black	V_{EX-}	P-
White	V_{CH-}	S-
Green	V_{CH+}	S+

CALIBRATION

EXCITATION : 2.5V CAL FACTOR : 1120.4 ue/mV/V OTHER :

DATE : 6/24/22 WHO : am

FINAL READING AFTER CALIBRATION AND DIPPING : -776

INSTALLATION

NOTE: MANUAL READINGS TAKEN USING VISHAY P-3500. GF = 2.00 BALANCE = 500

LOCATION : X: Y: Z:

DATE : READING : EVENT :

HOOKUP TO SYSTEM

SPU : CHANNEL :

DATE : READING : EVENT :

QUALITY CONTROL FABRICATION AND HOOK-UP SHEET

BDI
RAW DATA. REFINED RESULTS.

DYNAMIC AST

ASPHALT STRAIN GAGE 6X8"

Gage ID: ASTa 1250

Lead Length: 10m

NOTE: MANUAL READINGS TAKEN USING VISHAY P-3500. GF = 2.00 BALANCE = 500

FABRICATION

GAGE RESISTANCE : 1137 / 1125

INITIAL READING AFTER WIRING GAGE : -4165

SHORT TO SHIELD : ok

TENSION = Increase IN READING

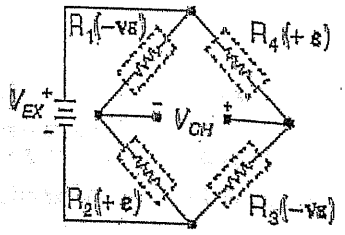
READING AFTER J-COAT : -4163

READING AFTER ALL PROTECTION : -4134
(after butyl rubber and heat shrink)

DATE : 6/24/22 WHO : CBM

SHORT TO SHIELD : ok

COMMENTS:



COLOR	BRIDGE	P-3500
Red	V_{EX+}	P+
Black	V_{EX-}	P-
White	V_{CH-}	S-
Green	V_{CH+}	S+

CALIBRATION

EXCITATION : 2.5V CAL FACTOR : 1137.6 ue/mV/V OTHER :

DATE : 6/24/22 WHO : CBM

FINAL READING AFTER CALIBRATION AND DIPPING : -4884

INSTALLATION

NOTE: MANUAL READINGS TAKEN USING VISHAY P-3500. GF = 2.00 BALANCE = 500

LOCATION : X: Y: Z:

DATE : READING : EVENT :

HOOKUP TO SYSTEM

SPU : CHANNEL :

DATE : READING : EVENT :

QUALITY CONTROL FABRICATION AND HOOK-UP SHEET

BDI RAW DATA. REPORTABLE RESULTS.

DYNAMIC AST

ASPHALT STRAIN GAGE 6X8"

Gage ID: Asta252

Lead Length: 10m

NOTE: MANUAL READINGS TAKEN USING VISHAY P-3500. GF = 2.00 BALANCE = 500

FABRICATION

GAGE RESISTANCE : 1075 / 1065

INITIAL READING AFTER WIRING GAGE : +40

SHORT TO SHIELD : ok

TENSION = Increase IN READING

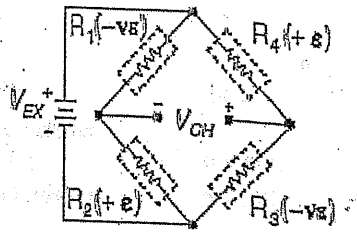
READING AFTER J-COAT : -55

READING AFTER ALL PROTECTION : -202
(after butyl rubber and heat shrink)

DATE : 6/24/22 WHO : CDM

SHORT TO SHIELD : ok

COMMENTS:



COLOR	BRIDGE	P-3500
Red	V_{EX+}	P+
Black	V_{EX-}	P-
White	V_{CH-}	S-
Green	V_{CH+}	S+

CALIBRATION

EXCITATION : 2.5v CAL FACTOR : 1071.3 ue/mV/V OTHER :

DATE : 6/24/22 WHO : CDM

FINAL READING AFTER CALIBRATION AND DIPPING : -333

INSTALLATION

NOTE: MANUAL READINGS TAKEN USING VISHAY P-3500. GF = 2.00 BALANCE = 500

LOCATION : X: Y: Z:

DATE : READING : EVENT :

HOOKUP TO SYSTEM

SPU : CHANNEL :

DATE : READING : EVENT :

QUALITY CONTROL FABRICATION AND HOOK-UP SHEET

BDI RAW DATA. REFINED RESULTS.

DYNAMIC AST

ASPHALT STRAIN GAGE 6X8"

Gage ID: ASTa 1254

Lead Length: 10m

NOTE: MANUAL READINGS TAKEN USING VISHAY P-3500. GF = 2.00 BALANCE = 500

FABRICATION

GAGE RESISTANCE : 1073 / 1059

INITIAL READING AFTER WIRING GAGE : -1709

SHORT TO SHIELD : OK

TENSION = Increase IN READING

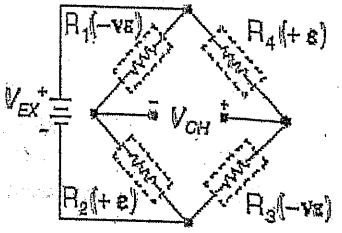
READING AFTER J-COAT : -1740

READING AFTER ALL PROTECTION : -2202
(after butyl rubber and heat shrink)

DATE : 6/24/22 WHO : DM

SHORT TO SHIELD : OK

COMMENTS:



COLOR	BRIDGE	P-3500
Red	V_{EX}+	P+
Black	V_{EX}-	P-
White	V_{CH}-	S-
Green	V_{CH}+	S+

CALIBRATION

EXCITATION : 2.5V CAL FACTOR : 1065.8 ue/mV/V OTHER :

DATE : 6/24/22 WHO : DM

FINAL READING AFTER CALIBRATION AND DIPPING : -2148

INSTALLATION

NOTE: MANUAL READINGS TAKEN USING VISHAY P-3500. GF = 2.00 BALANCE = 500

LOCATION : X: Y: Z:

DATE : READING : EVENT :

HOOKUP TO SYSTEM

SPU : CHANNEL :

DATE : READING : EVENT :

QUALITY CONTROL FABRICATION AND HOOK-UP SHEET

BDI RAW DATA. REFINED RESULTS.

DYNAMIC AST

ASPHALT STRAIN GAGE 6X8"

Gage ID: ASTa1257

Lead Length: 10m

NOTE: MANUAL READINGS TAKEN USING VISHAY P-3500. GF = 2.00 BALANCE = 500

FABRICATION

GAGE RESISTANCE: 1056 / 1047

INITIAL READING AFTER WIRING GAGE: -1605

SHORT TO SHIELD: ok

TENSION = Increase IN READING

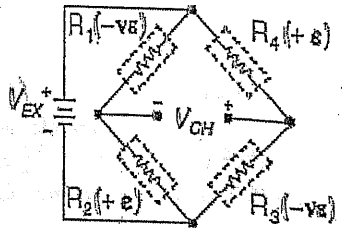
READING AFTER J-COAT: -1685

READING AFTER ALL PROTECTION: -2020
(after butyl rubber and heat shrink)

DATE: 6/24/22 WHO: dm

SHORT TO SHIELD: ok

COMMENTS:



COLOR	BRIDGE	P-3500
Red	V_{EX+}	P+
Black	V_{EX-}	P-
White	V_{CH-}	S-
Green	V_{CH+}	S+

CALIBRATION

EXCITATION: 2.5v CAL FACTOR: 1123.9 ue/mV/V OTHER:

DATE: 6/24/22 WHO: dm

FINAL READING AFTER CALIBRATION AND DIPPING: -209

INSTALLATION

NOTE: MANUAL READINGS TAKEN USING VISHAY P-3500. GF = 2.00 BALANCE = 500

LOCATION: X: Y: Z:

DATE: READING: EVENT:

HOOKUP TO SYSTEM

SPU: CHANNEL:

DATE: READING: EVENT:

Appendix B

Schematics of DAC Setup

BDI PROPRIETARY AND CONFIDENTIAL

NOTES:

REVISION HISTORY				
REV	DATE	DESCRIPTION	ECO	NAME
A	7/29/13	INITIAL RELEASE		T. Faber
B	9/1/20	Wiring, Electrical, Cabinet Details		N.Frey
C	9/6/21	Update Power Distribution		N.Frey

Waterloo Pavement Monitoring Cabinet Design

IFC # 001

Job No.: Waterloo
PM: S.Smith
Designer: N.Frey

	NAME	DATE
DRAWN		
CHECKED		
APPROVED		
MANUFACTURE		
MATERIAL		
FINISH		
COMMENTS		

BDI
RAIN DATA

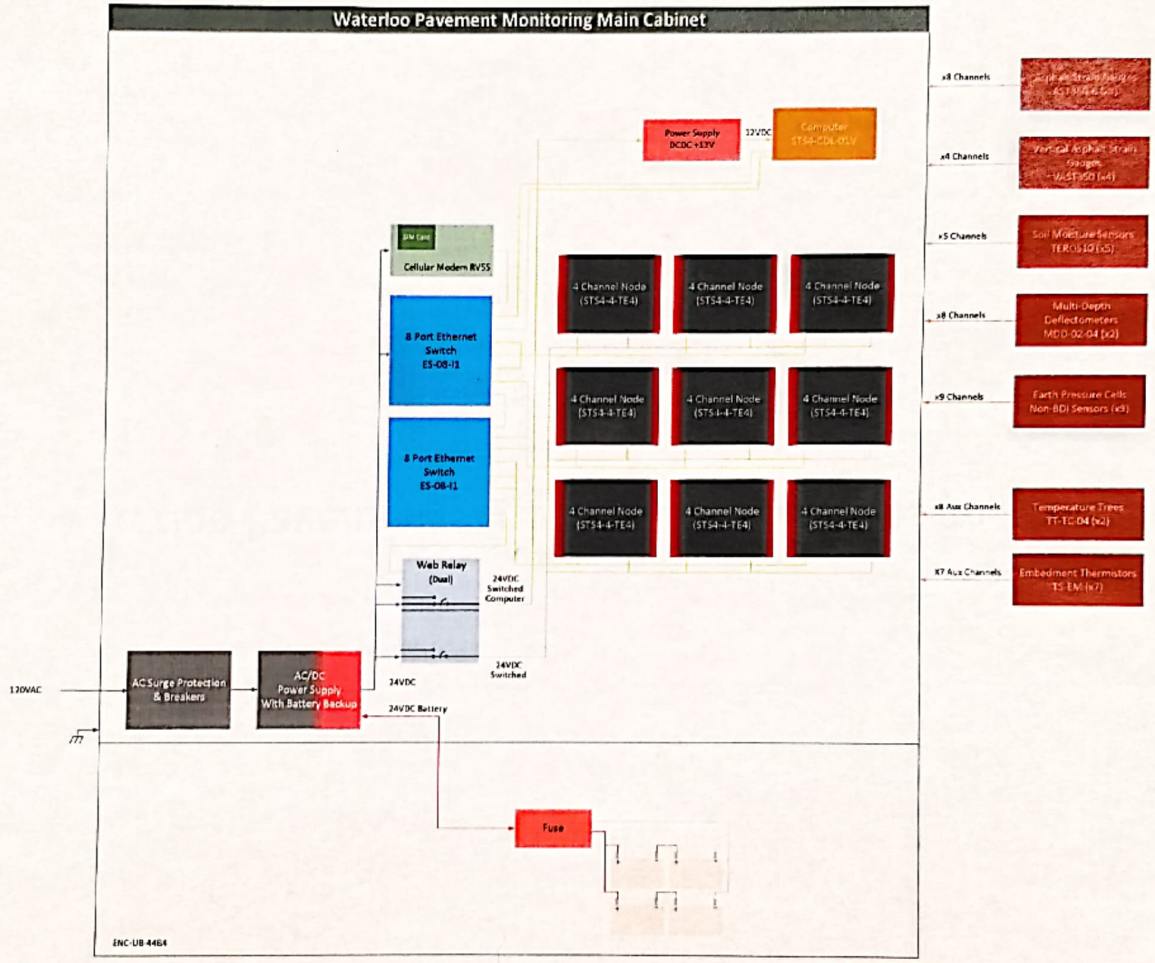
Pavement Monitoring Project
Waterloo University

PMP-WATERLOO | C

SIZE: D | DO NOT SCALE | SHEET 1 OF 5

BDI PROPRIETARY AND CONFIDENTIAL

NOTES:



IFC # 001

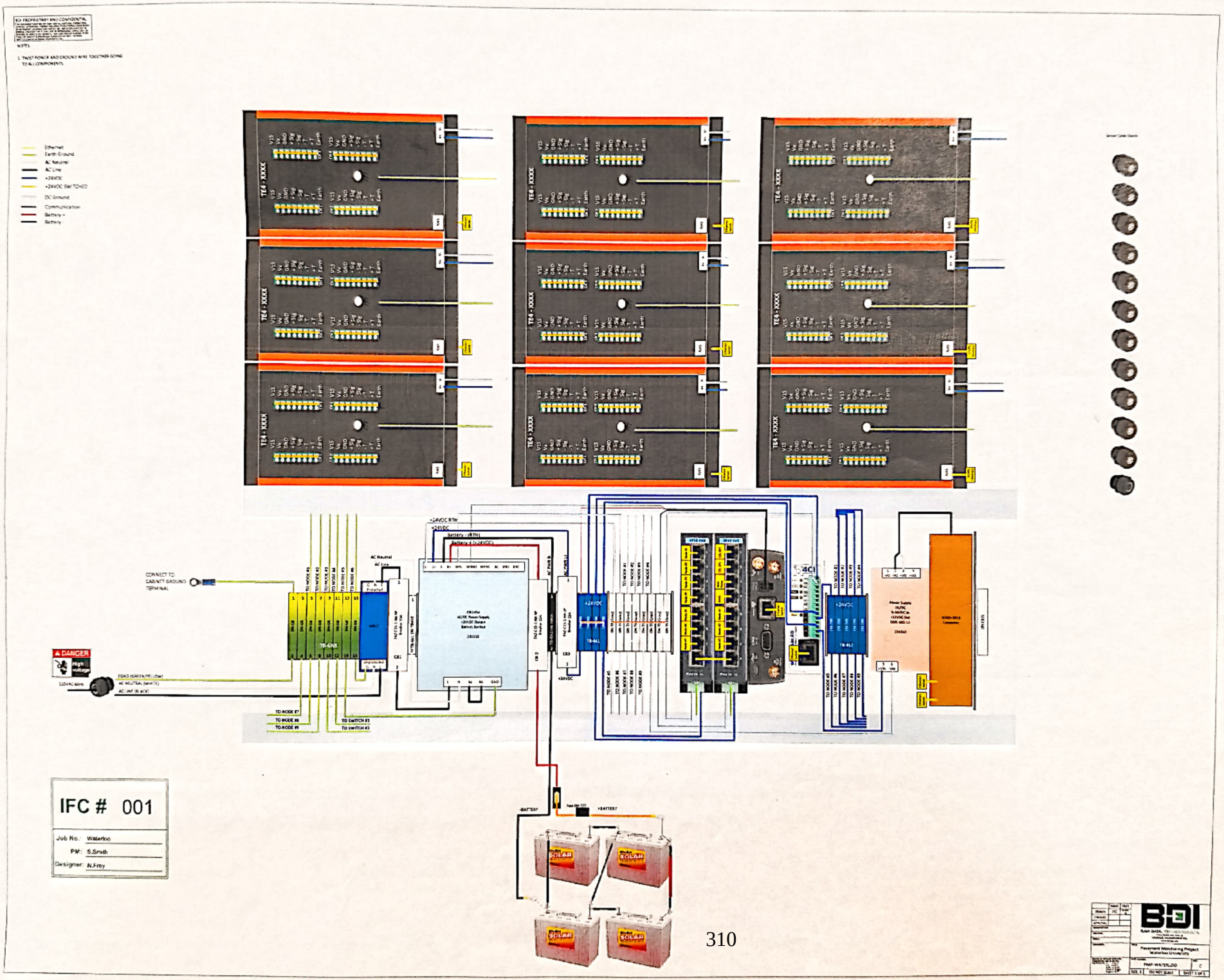
Job No.	Waterloo
PM	S.Smith
Designer	N.Frey

BDI
RAW DATA. REFINED RESULTS.

Pavement Monitoring Project
Waterloo University

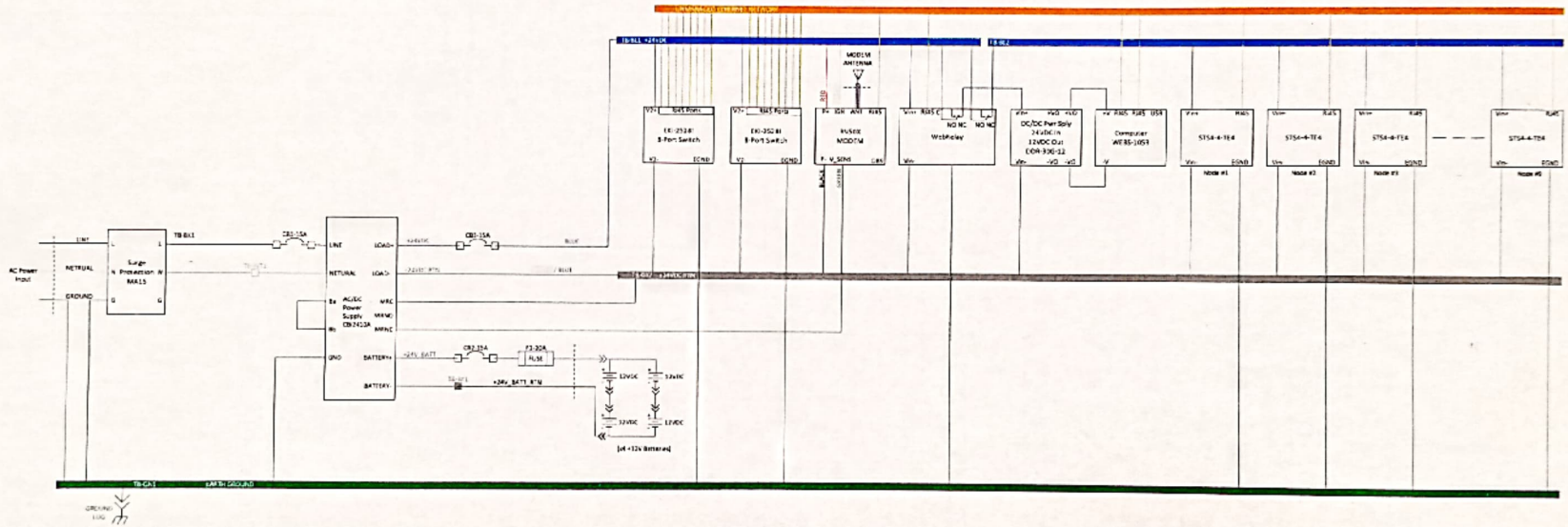
PMP-WATERLOO | C

SIZE: D | DO NOT SCALE | SHEET 1 OF 1


Ethernet
Earth Ground
AC Neutral
AC Line
+24VDC
+24VDC SWITCHED
DC Ground
Communication
Battery +
Battery -
TE4 - XXXX
CONNECT TO CABINET GROUND TERMINAL
DANGER
High Voltage
+24VDC RTN
+24VDC
Battery - (RTN)
Battery + (+24VDC)
TB-GND
TB-ALL
TB-ALT
TO MODE #1
TO MODE #2
TO MODE #3
TO MODE #4
TO MODE #5
TO MODE #6
TO MODE #7
TO MODE #8
TO MODE #9
TO SWITCH #1
TO SWITCH #2
TO SWITCH #3
-BATTERY
+BATTERY
SOLAR
IFC # 001
Job No.: Waterloo
PM: S.Smith
Designer: N.Frey
Pavement Monitoring Project
Waterloo University
PMP-WATERLOO

BDI PROPRIETARY AND CONFIDENTIAL

NOTES:



University of Waterloo
Electrical Schematic

IFC # 001

Job No.: Waterloo
PM: S.Smith
Designer: N.Frey

BDI
RAW DATA. REFINED RESULTS.

Pavement Monitoring Project
Waterloo University

PMP-WATERLOO

SIZE: D | DO NOT SCALE | SHEET 4 OF 5

BDI PROPRIETARY AND CONFIDENTIAL

NOTES:

1. Actual cabinet height, electronic compartment, and battery compartment heights are dependent on selected cabinet and battery compartment size
2. All Dimension are referenced to the top back corner of the cabinet.
3. Drawing shows standard position for all possible holes to be drilled. Which holes are drilled and what size holes are drilled is provide on a separate document or using the drill template provided with this document.

NOT ALL HOLES ARE REQUIRED TO BE DRILLED OUT

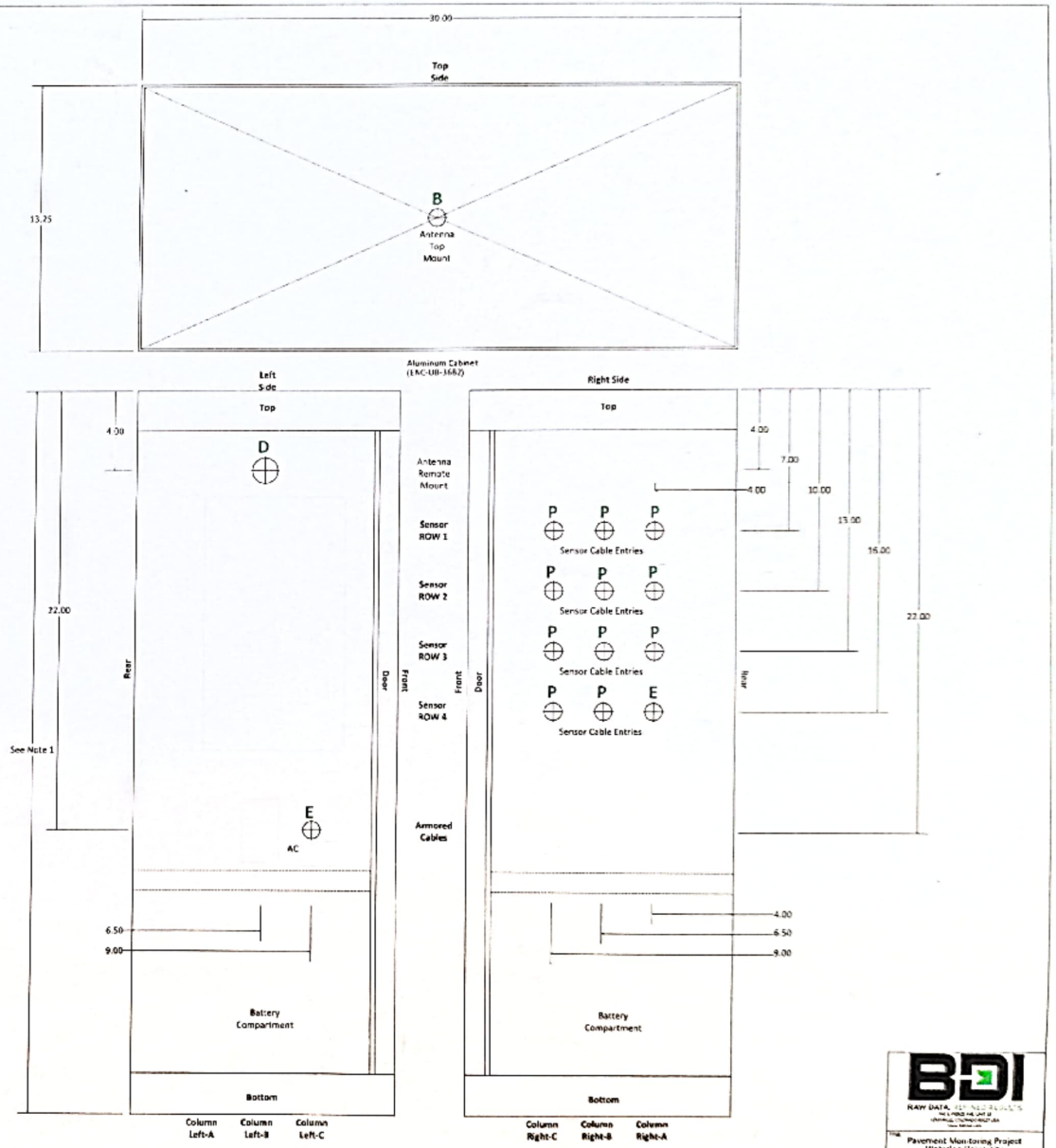
4. Holes for the vent and power input are provided on the left side of the cabinet.
5. Holes for an external antenna, cable grips for sensor cables, and armored cable entries are located on the right side of the cabinet
6. Hole for attached antenna is located on the top of the cabinet.
7. Holes for external antenna are always the top row on the right side of the cabinet
8. Holes for the armored cables and power are always the bottom row of their respective side of the cabinet.
   Subtract 8" if a 13.5" tall backplane is used and add 8" if a 29.5" tall backplane is used.
9. Identification of each hole is specified by a row and column identifier.

Drill	Description	QTY	Part Number		Thread Size	Thread Dia	Drill Size
A	Antenna Top Mount - Type 1	0					¾" [0.750"]
B	Antenna Top Mount - Type 2	1					1" [1.00"]
C	Kit, Bulkhead Nut Washer O-Ring & SMA Cables	0		232710/232670	1/4x36	0.24"	¼" [0.250"]
D	Polycarb/Acrylic	1		202150/202360	M32x1.5mm	1.26"	1 5/16" [1.312"]
E	Cord Grip, Single 0.12-0.26" OD Black Nylon, 1/4" Knockout	2	CG1-12-26-34	302340	1/4 NPT	0.54"	9/16" [0.5625"]
F	Cord Grip, Single 0.27-0.37" OD Black Nylon, 1/2" Knockout	0	CG1-27-37-12	278470	1/2 NPT	0.84"	7/8" [0.875"]
G	Cord Grip, Single 0.24-0.47" OD Black Nylon, 1/2" Knockout	0	CG1-24-47-12	279690	1/2 NPT	0.84"	7/8" [0.875"]
H	Cord Grip, Single 0.39-0.55" OD Black Nylon 3/4" Knockout	0	CG1-39-55-12	285460	1/2 NPT	0.84"	7/8" [0.875"]
I	Cord Grip, Single 0.55-0.63" OD Black Nylon 3/4" Knockout	0	CG1-55-63-34	285150	3/4 NPT	1.05"	1-1/16" [1.0625"]
J	Cord Grip, Single 0.63-0.71" OD Black Nylon 3/4" Knockout	0	CG1-63-71-34	295340	3/4 NPT	1.05"	1-1/16" [1.0625"]
K	Cord Grip, Dual 0.12-0.17" OD Wire Black Nylon 1/2" Knockout	0	CG2-12-17-12	228890	1/2 NPT	0.84"	7/8" [0.875"]
L	Cord Grip, Dual 0.16-0.2" OD Wire Black Nylon 1/2" Knockout	0	CG2-16-20-12	228860	1/2 NPT	0.84"	7/8" [0.875"]
M	Cord Grip, Dual 0.2-0.24" OD Wire Black Nylon 1/2" Knockout	0	CG2-20-24-12	294190	1/2 NPT	0.84"	7/8" [0.875"]
N	Cord Grip, Dual 0.27-0.31" OD Wire Black Nylon 3/4" Knockout	0	CG2-27-31-34	294140	3/4 NPT	1.05"	1-1/16" [1.0625"]
O	Cord Grip, Triple 0.24-0.28" OD Wire Black Nylon 3/4" Knockout	0	CG3-24-28-34	N/A	3/4 NPT	1.05"	1-1/16" [1.0625"]
P	Cord Grip, Quad 0.16-0.2" OD Wire Black Nylon 3/4" Knockout	11	CG4-16-20-34	228190	3/4 NPT	1.05"	1-1/16" [1.0625"]
Q	Cord Grip, Quad 0.2-0.24" OD Wire Black Nylon 3/4" Knockout	0	CG4-20-24-34	282620	3/4 NPT	1.05"	1-1/16" [1.0625"]
R	Cord Grip, Quad 0.81-0.85" OD Wire Black Nylon 1" Knockout	0	CG4-81-85-1	228270	1 NPT	1.32"	1-3/8" [1.375"]
S	Cord Grip, Hex 0.22-0.26" OD Wire Black Nylon 1" Knockout	0	CG6-22-26-1	232630	1 NPT	1.32"	1-3/8" [1.375"]

For Reference Only

.187" Diameter - Strain gages	(IC-30-187 - RED)
.250" Diameter - Cable Fees and biaxial ace ermeters/tilt	(IC-04-250 - Green)
.300" Diameter - Triaxial accelerometers/tilt	(IC-04-300 - Blue)
.315" Diameter - ACT84	(IC-06-315 - Black)

Hole Drill Template – Fill in each area with required hole drill size.
Refer to Cord Grip size chart as a reference.



Dual Node Datalogger Cabinet Drill Out Diagram

IFC #	001
Job No.:	Waterloo
PM:	S.Smith
Designer:	N.Frey

BDI RAW DATA, BEYOND RESULTS

Pavement Monitoring Project Waterloo University

PMP-WATERLOO | C

SIZE: D | DO NOT SCALE | SHEET 5 OF 5

Location	SensorName	Wire Color	Terminal Connection
TE4-0341-0-CHAN-1	VAS1000	n/a	V15
		red	Vx
		black	GND
		green	Sig+
		white	Sig-
		n/a	T+
		n/a	T-
		drain	shield
TE4-0341-0-CHAN-2	VAS1001	n/a	V15
		red	Vx
		black	GND
		green	Sig+
		white	Sig-
		n/a	T+
		n/a	T-
		drain	shield
TE4-0341-0-CHAN-3	VAS1002	n/a	V15
		red	Vx
		black	GND
		green	Sig+
		white	Sig-
		n/a	T+
		n/a	T-
		drain	shield
TE4-0341-0-CHAN-4	VAST1239	n/a	V15
		red	Vx
		black	GND
		green	Sig+
		white	Sig-
		n/a	T+
		n/a	T-
		drain	shield
TE4-0343-0-CHAN-1	ASTa1239	n/a	V15
		red	Vx
		black	GND
		green	Sig+
		white	Sig-
		n/a	T+
		n/a	T-
		drain	shield
TE4-0343-0-CHAN-2	ASTa1241	n/a	V15
		red	Vx
		black	GND
		green	Sig+
		white	Sig-

		n/a	T+
		n/a	T-
		drain	shield
TE4-0343-0-CHAN-3	ASTa1243	n/a	V15
		red	Vx
		black	GND
		green	Sig+
		white	Sig-
		n/a	T+
		n/a	T-
		drain	shield
TE4-0343-0-CHAN-4	ASTa1249	n/a	V15
		red	Vx
		black	GND
		green	Sig+
		white	Sig-
		n/a	T+
		n/a	T-
		drain	shield
TE4-0345-0-CHAN-1	ASTa1250	n/a	V15
		red	Vx
		black	GND
		green	Sig+
		white	Sig-
		n/a	T+
		n/a	T-
		drain	shield
TE4-0345-0-CHAN-2	ASTa1252	n/a	V15
		red	Vx
		black	GND
		green	Sig+
		white	Sig-
		n/a	T+
		n/a	T-
		drain	shield
TE4-0345-0-CHAN-3	ASTa1254	n/a	V15
		red	Vx
		black	GND
		green	Sig+
		white	Sig-
		n/a	T+
		n/a	T-
		drain	shield
TE4-0345-0-CHAN-4	ASTa1257	n/a	V15
		red	Vx
		black	GND

		green	Sig+
		white	Sig-
		n/a	T+
		n/a	T-
		drain	shield
TE4-0332-0-CHAN-1	TP1151769	red	V15
		n/a	Vx
		jumper to Sig-	GND
		black / resistor to Sig -	Sig+
		resistor to Sig + / jumper to GND	Sig-
		green	T+
		white	T-
		drain	shield
TE4-0332-0-CHAN-2	TP1152497	red	V15
		n/a	Vx
		jumper to Sig-	GND
		black / resistor to Sig -	Sig+
		resistor to Sig + / jumper to GND	Sig-
		green	T+
		white	T-
		drain	shield
TE4-0332-0-CHAN-3	TP1317162	red	V15
		n/a	Vx
		jumper to Sig-	GND
		black / resistor to Sig -	Sig+
		resistor to Sig + / jumper to GND	Sig-
		green	T+
		white	T-
		drain	shield
TE4-0332-0-CHAN-4	TP1152501	red	V15
		n/a	Vx
		jumper to Sig-	GND
		black / resistor to Sig -	Sig+
		resistor to Sig + / jumper to GND	Sig-
		green	T+
		white	T-
		drain	shield
TE4-0331-0-CHAN-1	TP11563165	red	V15
		n/a	Vx
		jumper to Sig-	GND
		black / resistor to Sig -	Sig+
		resistor to Sig + / jumper to GND	Sig-
		green	T+
		white	T-
		drain	shield
TE4-0331-0-CHAN-2	TP1152499	red	V15

		n/a	Vx
		jumper to Sig-	GND
		black / resistor to Sig -	Sig+
		resistor to Sig + / jumper to GND	Sig-
		green	T+
		white	T-
		drain	shield
TE4-0331-0-CHAN-3	TP1152500	red	V15
		n/a	Vx
		jumper to Sig-	GND
		black / resistor to Sig -	Sig+
		resistor to Sig + / jumper to GND	Sig-
		green	T+
		white	T-
		drain	shield
TE4-0331-0-CHAN-4	TEROS10_1	n/a	V15
		brown	Vx
		bare	GND
		orange	Sig+
		jumper to GND	Sig-
		red	T+
		black	T-
		n/a	shield
TE4-0333-0-CHAN-1	TEROS10_2	n/a	V15
		brown	Vx
		bare	GND
		orange	Sig+
		jumper to GND	Sig-
		red	T+
		black	T-
		n/a	shield
TE4-0333-0-CHAN-2	TEROS10_3	n/a	V15
		brown	Vx
		bare	GND
		orange	Sig+
		jumper to GND	Sig-
		red	T+
		black	T-
		n/a	shield
TE4-0333-0-CHAN-3	TEROS10_4	n/a	V15
		brown	Vx
		bare	GND
		orange	Sig+
		jumper to GND	Sig-
		red	T+
		black	T-

		n/a	shield
TE4-0333-0-CHAN-4	TEROS10_5	n/a	V15
		brown	Vx
		bare	GND
		orange	Sig+
		jumper to GND	Sig-
		red	T+
		black	T-
		n/a	shield
TE4-0330-0-CHAN-1	MDD-001_ML1	n/a	V15
		red	Vx
		black	GND
		green	Sig+
		white	Sig-
		n/a	T+
		n/a	T-
		n/a	shield
TE4-0330-0-CHAN-2	MDD-001_ML2	n/a	V15
		red	Vx
		black	GND
		green	Sig+
		white	Sig-
		n/a	T+
		n/a	T-
		n/a	shield
TE4-0330-0-CHAN-3	MDD-001_ML3	n/a	V15
		red	Vx
		black	GND
		green	Sig+
		white	Sig-
		n/a	T+
		n/a	T-
		n/a	shield
TE4-0330-0-CHAN-4	MDD-001_ML4	n/a	V15
		red	Vx
		black	GND
		green	Sig+
		white	Sig-
		n/a	T+
		n/a	T-
		n/a	shield
TE4-0334-0-CHAN-1	MDD-002_ML1	n/a	V15
		red	Vx
		black	GND
		green	Sig+
		white	Sig-

		n/a	T+
		n/a	T-
		n/a	shield
TE4-0334-0-CHAN-2	MDD-002_ML2	n/a	V15
		red	Vx
		black	GND
		green	Sig+
		white	Sig-
		n/a	T+
		n/a	T-
		n/a	shield
TE4-0334-0-CHAN-3	MDD-002_ML3	n/a	V15
		red	Vx
		black	GND
		green	Sig+
		white	Sig-
		n/a	T+
		n/a	T-
		n/a	shield
TE4-0334-0-CHAN-4	MDD-002_ML4	n/a	V15
		red	Vx
		black	GND
		green	Sig+
		white	Sig-
		n/a	T+
		n/a	T-
		n/a	shield
TE4-0328-0-CHAN-1	TP1153137	red	V15
		n/a	Vx
		jumper to Sig-	GND
		black / resistor to Sig -	Sig+
		resistor to Sig + / jumper to GND	Sig-
		green	T+
		white	T-
		drain	shield
TE4-0328-0-CHAN-2	TP1317164	red	V15
		n/a	Vx
		jumper to Sig-	GND
		black / resistor to Sig -	Sig+
		resistor to Sig + / jumper to GND	Sig-
		green	T+
		white	T-
		drain	shield
TE4-0328-0-CHAN-3	EMPTY	n/a	V15
		n/a	Vx
		n/a	GND

		n/a	Sig+
		n/a	Sig-
		n/a	T+
		n/a	T-
		n/a	shield
TE4-0328-0-CHAN-4	EMPTY	n/a	V15
		n/a	Vx
		n/a	GND
		n/a	Sig+
		n/a	Sig-
		n/a	T+
		n/a	T-
		n/a	shield

BDI PROPRIETARY AND CONFIDENTIAL
THIS DOCUMENT TOGETHER WITH ANY AND ALL ADDITIONS, CORRECTIONS, CHANGES, ALTERATIONS THEREOF INCLUDING ITS ELECTRONIC COUNTERPART IS THE PROPERTY OF BRIDGE DIAGNOSTICS, INC. AND IS FURNISHED ON THE EXPRESS CONDITION THAT IT SHALL NOT BE REPRODUCED, COPIED, LENT, OR DISPOSED OF DIRECTLY OR INDIRECTLY, NOR USED FOR ANY PURPOSE OTHER THAN FOR WHICH IT IS SPECIFICALLY FURNISHED WITHOUT THE PRIOR WRITTEN CONSENT OF BRIDGE DIAGNOSTICS, INC.

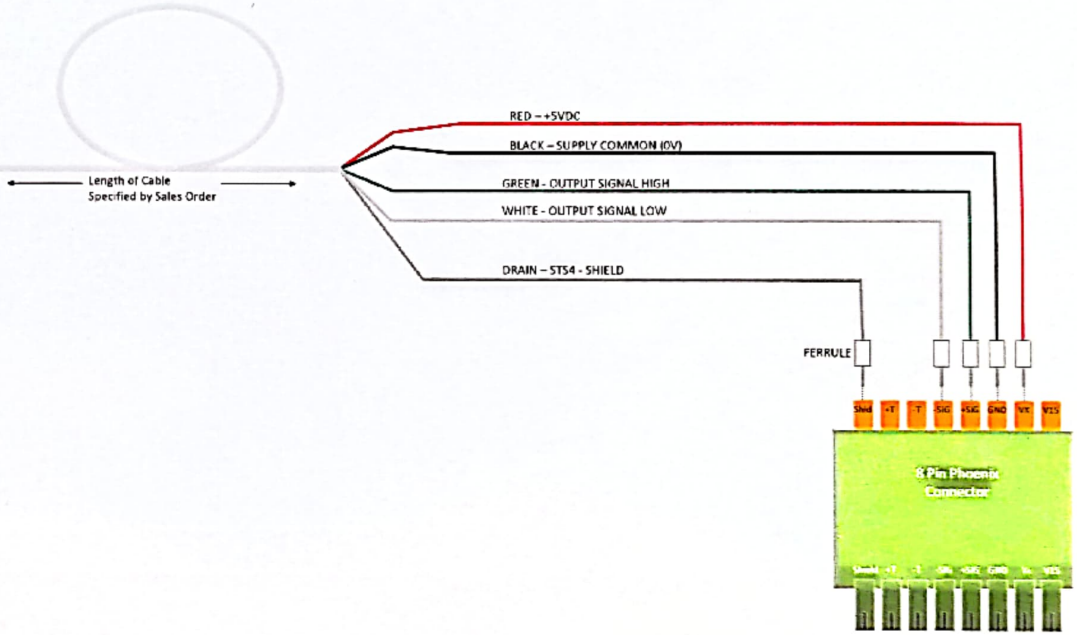
REVISION HISTORY				
REV	DATE	DESCRIPTION	ECO	NAME
A	07/13/22	INITIAL RELEASE		T. Cilke

NOTES:

WIRING TABLE FOR AST350-6 OR AST350-8 ASPHALT STRAIN GAGE

RED	+5VDC POWER
BLACK	GND (SUPPLY COMMON 0V)
GREEN	+SIG (OUTPUT SIGNAL HIGH)
WHITE	-SIG (OUTPUT SIGNAL LOW)
DRAIN – SHIELD	SHIELD - SHIELD CONNECTION





	NAME	DATE
DRAWN	JTC	07/3/22
CHECKED		
APPROVAL		
MANUFACTURE:		
MATERIAL:		
FINISH:		
COMMENTS:		

UNLESS OTHERWISE SPECIFIED:
DIMENSIONS ARE IN INCHES
TOLERANCES: X +/- 0.5
X.X +/- 0.1
X.XX +/- 0.03
X.XXX +/- 0.005
Angle +/- 0.5°

BDI
RAW DATA. REFINED RESULTS.
740 S. PIERCE AVE. UNIT 15
LOUISVILLE, COLORADO 80027 USA
www.bditest.com

TITLE:
ASSY, SENSOR ASPHALT STRAIN GAGE
6 or 8 inch

PART NUMBER:	REV:
AST350-X	A

SIZE: B	DO NOT SCALE	SHEET 1 OF 1

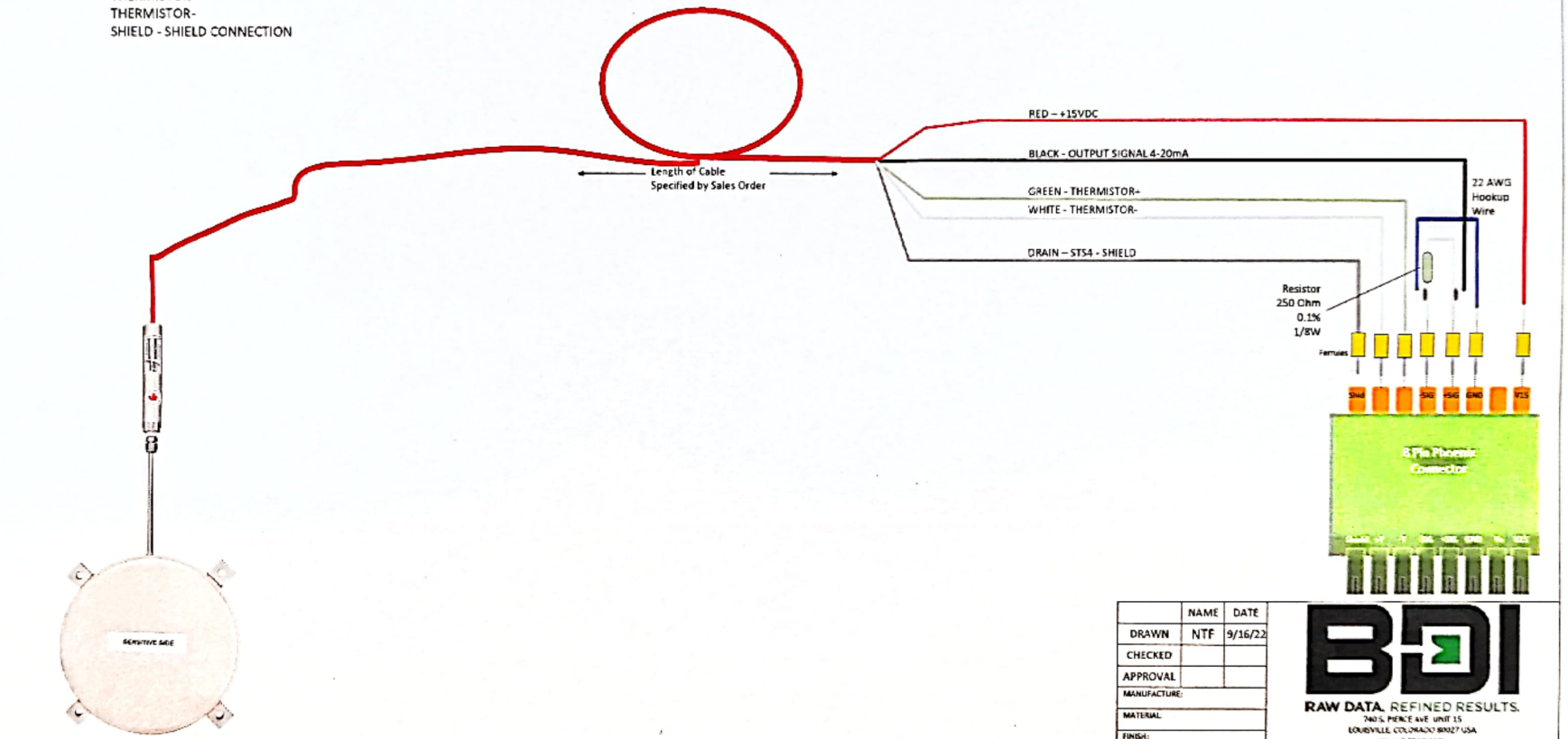
BDI PROPRIETARY AND CONFIDENTIAL
THIS DOCUMENT TOGETHER WITH ANY AND ALL ADDITIONS, CORRECTIONS, CHANGES, ALTERATIONS THEREOF INCLUDING ITS ELECTRONIC COUNTERPART IS THE PROPERTY OF BRIDGE DIAGNOSTICS, INC. AND IS FURNISHED ON THE EXPRESS CONDITION THAT IT SHALL NOT BE REPRODUCED, COPIED, LENT, OR DISPOSED OF DIRECTLY OR INDIRECTLY, NOR USED FOR ANY PURPOSE OTHER THAN FOR WHICH IT IS SPECIFICALLY FURNISHED WITHOUT THE PRIOR WRITTEN CONSENT OF BRIDGE DIAGNOSTICS, INC.

REVISION HISTORY				
REV	DATE	DESCRIPTION	ECO	NAME
A	9/16/22	INITIAL RELEASE		N.Frey

NOTES:

WIRING TABLE

RED	+15VDC POWER
JUMPER	GND (SUPPLY COMMON 0V)
BLACK/250ohm	SIGNAL +
250ohm/JUMPER	SIGNAL-
GREEN	THERMISTOR+
WHITE	THERMISTOR-
DRAIN – SHIELD	SHIELD - SHIELD CONNECTION



RST-LPTPC09-S-Q EARTH PRESSURE SENSOR

	NAME	DATE
DRAWN	NTF	9/16/22
CHECKED		
APPROVAL		
MANUFACTURE:		
MATERIAL:		
FINISH:		
COMMENTS:		

UNLESS OTHERWISE SPECIFIED:
DIMENSIONS ARE IN INCHES
TOLERANCES: X +/- 0.5
XX +/- 0.1
XXX +/- 0.03
XXXX +/- 0.005
Angle +/- 0.5°

BDI
RAW DATA. REFINED RESULTS.
7405 PIERCE AVE UNIT 15
LOUISVILLE, COLORADO 80027 USA
www.bditest.com

TITLE: ASSY, SENSOR EARTH PRESSURE CELL

PART NUMBER: RST-LPTPC09-S-Q
REV: A

SIZE: B | DO NOT SCALE | SHEET 1 OF 1

Appendix C
Data Cleaning Scripts

Data Cleaning Scripts

Table of Contents for Code

Excel VBA Scripts for Data Processing 324
- Convert Timestamps 324
- Convert Sensor Name HighSpeed 325
- Delete Columns by Header HighSpeed 326
- Add Timestamp Highspeed 328
- AutoFill Col A HighSpeed 329
- Delete Columns A and B HighSpeed 329
- Sort Columns Alphabetically HighSpeed 331
- AutoSave Active Sheet 331
- Delete Column by Header Decimated 332
- Convert Sensor Name Decimated 334
- Add Moisture Effect 336
- Delete Columns that have MDD 337
- Delete the Random Columns at the end of Decimated Worksheets 337
- Sort Columns Alphabetically Decimated 338
- Add Timestamp Columns Decimated 338
- Run the Scripts 340

Python Scripts for Data Processing 341

R Scripts for Data Processing 347
- Multiple Temperature Sensor Plotter (TEMP-01 AND TEMP-02) 347
- Multiple Temperature Sensor Plotter (with TEMP-02 only) 350
- Multiple Temperature Sensor Plotter (with TEMP-02 only) 353
- AND by month X-axis 353
- Temperature Plotter using TEMPS-02 only + Ambient Temperature 358
- Multiple Temperature Sensor Plotter (with TEMP-02 restricted) AND by month X-axis + Ambient Temperature 362
- Moisture Trend Plotter 368
- Moisture Trend Plotter + Precipitation Plotter 371
- Trend Strain Plotter + Ambient Temperature 374
- Trend Pressure Plotter + Ambient Temperature 377
- High Speed Strain Plotter + Ambient (not filtered) 381
- High Speed Strain Plotter + Ambient (filtered) 385
- High Speed Pressure Plotter + Ambient 388

Excel VBA Scripts for Data Processing

Convert Timestamps

```
Sub AAConvertTimestampHighSpeed()
    Dim originalTimestamp As String
    Dim convertedTimestamp As String

    ' Specify the cell containing the original timestamp
    originalTimestamp = Range("O2").Value

    ' Change the cell format to "yyy-mm-dd h:mm"
    Range("O2").NumberFormat = "yyyy-mm-dd h:mm"

    ' Convert the timestamp format
    convertedTimestamp = Format(CDate(Left(originalTimestamp,
Len(originalTimestamp) - 4)), "yyyy-mm-dd h:mm")

    ' Update the cell with the converted timestamp
    Range("O2").Value = convertedTimestamp
End Sub

Sub AAConvertTimestampDecimated()
    Dim originalTimestamp As String
    Dim convertedTimestamp As String

    ' Specify the cell containing the original timestamp
    originalTimestamp = Range("P2").Value

    ' Change the cell format to "yyy-mm-dd h:mm"
    Range("P2").NumberFormat = "yyyy-mm-dd h:mm"

    ' Convert the timestamp format
    convertedTimestamp = Format(CDate(Left(originalTimestamp,
Len(originalTimestamp) - 4)), "yyyy-mm-dd h:mm")

    ' Update the cell with the converted timestamp
    Range("P2").Value = convertedTimestamp
End Sub
```

Convert Sensor Name HighSpeed

```
Sub ConvertSensorNamesHighSpeed()
    Dim ws As Worksheet
    Dim cell As Range
    Dim sensorNames As Variant
    Dim convertedNames As Variant
    Dim i As Long

    ' Set the active worksheet
    Set ws = ActiveSheet

    ' Define the sensor names and their corresponding converted names
    sensorNames = Array("ASTa1257", "ASTa1243", "ASTa1239", "ASTa1249",
"ASTa1250", "ASTa1252", "ASTa1241", "ASTa1254", _
                        "VAS1002", "VAS1001", "VAS1000", "VAST1239",
"TEROS10_1", "TEROS10_2", "TEROS10_3", "TEROS10_4", _
                        "TEROS10_5", "TP1152500", "TP1151769", "TP1153165",
"TP1152501", "TP1152499", "TP1153137", _
                        "TP1317164", "TP1317162")

    convertedNames = Array("AS-LO-R-1", "AS-LO-L-2", "AS-TR-R-3", "AS-TR-
L-4", "AS-TR-R-5", "AS-TR-L-6", "AS-LO-R-7", _
                           "AS-LO-L-8", "VAS-R-1", "VAS-L-2", "VAS-R-3",
"VAS-L-4", "MOI-BA-1", "MOI-SB-2", "MOI-SB-3", _
                           "MOI-SB-4", "MOI-SG-5", "PC-BA-R-1", "PC-BA-L-
2", "PC-SB-R-3", "PC-SB-L-4", "PC-BA-R-5", _
                           "PC-BA-L-6", "PC-SG-R-7", "PC-SG-L-8")

    ' Loop through the first row of the active worksheet
    For Each cell In ws.Range("1:1")
        ' Check if the cell value matches any of the sensor names
        For i = LBound(sensorNames) To UBound(sensorNames)
            If cell.Value = sensorNames(i) Then
                ' If a match is found, replace the cell value with the
corresponding converted name
                cell.Value = convertedNames(i)
                Exit For
            End If
        Next i
    Next cell

    MsgBox "Sensor names converted successfully!", vbInformation
End Sub
```

Delete Columns by Header HighSpeed

```
Sub DeleteColumnsByHeaderHighSpeed()
    Dim ws As Worksheet
    Dim headerArray As Variant
    Dim header As Range
    Dim col As Range
    Dim deleteColumns As Range
    Dim deleteColumn As Range
    Dim i As Long

    ' Set the active worksheet as the target worksheet
    Set ws = ActiveSheet

    ' Define the headers to search for
    headerArray = Array("TP1152497", "EMPTY", "ASTa1249_Temperature",
"ASTa1257_Temperature", "ASTa1241_Temperature", _
                        "ASTa1252_Temperature", "ASTa1239_Temperature",
"ASTa1250_Temperature", "ASTa1243_Temperature", _
                        "ASTa1254_Temperature", "TEROS10_4_Temperature",
"TEROS10_1_Temperature", "TEROS10_5_Temperature", _
                        "TEROS10_2_Temperature", "VAS1001_Temperature",
"VAST1239_Temperature", "TEROS10_3_Temperature", _
                        "VAS1000_Temperature", "VAS1002_Temperature",
"TP1151769_Temperature", "TP1152497_Temperature", _
                        "TP1152499_Temperature", "TP1152500_Temperature",
"TP1152501_Temperature", "TP1153137_Temperature", _
                        "TP1153165_Temperature", "TP1317162_Temperature",
"TP1317164_Temperature")

    ' Loop through each header in the array
    For i = LBound(headerArray) To UBound(headerArray)
        ' Find the header in the first row of the worksheet
        Set header = ws.Rows(1).Find(headerArray(i), LookIn:=xlValues,
LookAt:=xlWhole)

        ' If the header is found, add the corresponding column to the
deleteColumns range
        If Not header Is Nothing Then
            If deleteColumns Is Nothing Then
                Set deleteColumns = header.EntireColumn
            Else
                Set deleteColumns = Union(deleteColumns,
header.EntireColumn)
            End If
        End If
    Next i

    ' If there are columns to be deleted, prompt the user for confirmation
    If Not deleteColumns Is Nothing Then
```

```
        If MsgBox("Are you sure you want to delete the specified
columns?", vbYesNo + vbQuestion) = vbYes Then
            ' Delete the columns
            deleteColumns.Delete
            MsgBox "Columns deleted successfully.", vbInformation
        Else
            MsgBox "Operation cancelled by user.", vbInformation
        End If
    Else
        MsgBox "No matching columns found.", vbInformation
    End If
End Sub
```

Add Timestamp Highspeed

```
Sub AddTimestampColumn()
    Dim ws As Worksheet
    Dim timestampSheet As Worksheet
    Dim timestampCell As Range
    Dim lastRow As Long
    Dim formula As String

    ' Add new column between columns A and B
    Columns("B:B").Insert Shift:=xlToRight

    ' Set the header in cell B1
    Range("B1").Value = "Timestamp"

    ' Find sheet with "Waterloo" in the name in the active workbook
    For Each ws In ActiveWorkbook.Worksheets
        If InStr(1, ws.Name, "Waterloo", vbTextCompare) > 0 Then
            Set timestampSheet = ws
            Exit For
        End If
    Next ws

    ' Check if "Waterloo" sheet was found
    If Not timestampSheet Is Nothing Then
        ' Find the timestamp cell O2 on the "Waterloo" sheet
        Set timestampCell = timestampSheet.Range("O2")

        ' Get the last row in column A of the active sheet
        lastRow = ActiveSheet.Cells(Rows.Count, 1).End(xlUp).Row

        ' Set the formula in column B starting from B2
        formula = "=" & timestampSheet.Name & "!$O$2+A2/86400"
        ActiveSheet.Range("B2:B" & lastRow).formula = formula

        ' Format the timestamps in column B as yyyy-mm-dd h:mm
        ActiveSheet.Range("B2:B" & lastRow).NumberFormat = "yyyy-mm-dd
h:mm"

        ' Autofit the width of column B to fit the contents
        ActiveSheet.Columns("B:B").AutoFit
    Else
        MsgBox "Sheet with 'Waterloo' in the name not found!"
    End If
End Sub
```

AutoFill Col A HighSpeed

```
Sub autofill_ColA()
    Dim lastRow As Long

    lastRow = Cells(Rows.Count, "A").End(xlUp).Row
    Range("A2:A4").AutoFill Destination:=Range("A2:A" & lastRow)
End Sub
```

Delete Columns A and B HighSpeed

```
Sub DeleteColumnsAandB()
    Dim ws As Worksheet
    Dim lastRow As Long
    Dim lastCol As Long
    Dim col As Long
    Dim maxCount As Long
    Dim maxCol As Long

    ' Set the active worksheet
    Set ws = ActiveSheet

    ' Find the last row in column A
    lastRow = ws.Cells(ws.Rows.Count, "A").End(xlUp).Row

    ' Find the last column with values starting from column C
    lastCol = ws.Cells(1, ws.Columns.Count).End(xlToLeft).Column

    ' Loop through each column from column C to the last column
    For col = 3 To lastCol
        ' Count the number of non-empty cells in the column
        Count = Application.WorksheetFunction.CountA(ws.Columns(col))

        ' Check if the current count is greater than the maximum count
        If Count > maxCount Then
            maxCount = Count
            maxCol = col
        End If
    Next col

    ' Find the last row in the column with the maximum count
    lastRowMax = ws.Cells(ws.Rows.Count, maxCol).End(xlUp).Row

    ' Calculate the row to delete in columns A and B
    deleteRow = lastRowMax + 1

    ' Delete the contents in columns A and B from the bottom up to the
calculated row
    If deleteRow <= lastRow Then
        ws.Range("A" & deleteRow & ":B" & lastRow).ClearContents
    End If
```

```
End Sub
```

Sort Columns Alphabetically HighSpeed

```
Sub sort_columns_alphabetically_high_speed()
    Dim lastColumn As Long
    Dim lastRow As Long
    Dim ws As Worksheet

    Set ws = ActiveSheet
    lastColumn = ws.Cells(1, ws.Columns.Count).End(xlToLeft).Column
    lastRow = ws.Cells(ws.Rows.Count, "C").End(xlUp).Row

    ws.Sort.SortFields.Clear
    ws.Sort.SortFields.Add2 Key:=ws.Range("C1:BK1"),
SortOn:=xlSortOnValues, Order:=xlAscending, DataOption:=xlSortNormal

    With ws.Sort
        .SetRange ws.Range("C1", ws.Cells(lastRow, lastColumn))
        .header = xlGuess
        .MatchCase = False
        .Orientation = xlLeftToRight
        .SortMethod = xlPinYin
        .Apply
    End With
End Sub
```

AutoSave Active Sheet

```
Sub AutoSaveActiveSheet()
    ' Disable screen updates and alerts to avoid interruptions
    Application.ScreenUpdating = False
    Application.DisplayAlerts = False

    ' Save the active worksheet
    ActiveWorkbook.Save

    ' Enable screen updates and alerts
    Application.ScreenUpdating = True
    Application.DisplayAlerts = True
End Sub
```

Delete Column by Header Decimated

```
Sub DeleteColumnsByHeaderDecimated()
    Dim ws As Worksheet
    Dim headerArray As Variant
    Dim header As Range
    Dim col As Range
    Dim deleteColumns As Range
    Dim deleteColumn As Range
    Dim i As Long

    ' Check if the "Sensors" sheet exists in the active workbook
    Set ws = ActiveWorkbook.ActiveSheet

    ' Define the headers to search for
    headerArray = Array("TP1152497", "ASTa1243_Temperature",
"ASTa1254_Temperature", "VAS1000_Temperature", _
                        "VAS1002_Temperature", "TP1151769_Temperature",
"TP1152497_Temperature", "TP1152499_Temperature", _
                        "TP1152500_Temperature", "TP1152501_Temperature",
"TP1153137_Temperature", "TP1153165_Temperature", _
                        "TP1317162_Temperature", "TP1317164_Temperature")

    ' Loop through each header in the array
    For i = LBound(headerArray) To UBound(headerArray)
        ' Loop through each column in the first row of the worksheet
        For Each col In ws.Rows(1).SpecialCells(xlCellTypeConstants)
            ' Check if the header contains the specified text
            If InStr(1, col.Value, headerArray(i), vbTextCompare) <> 0
Then
                ' Add the column to the deleteColumns range
                If deleteColumns Is Nothing Then
                    Set deleteColumns = col.EntireColumn
                Else
                    Set deleteColumns = Union(deleteColumns,
col.EntireColumn)
                End If
            End If
        Next col
    Next i

    ' If there are columns to be deleted, prompt the user for confirmation
    If Not deleteColumns Is Nothing Then
        If MsgBox("Are you sure you want to delete the specified
columns?", vbYesNo + vbQuestion) = vbYes Then
            ' Delete the columns
            deleteColumns.Delete
            MsgBox "Columns deleted successfully.", vbInformation
        Else
            MsgBox "Operation cancelled by user.", vbInformation
        End If
```

```
    Else
        MsgBox "No matching columns found.", vbInformation
    End If
End Sub
```

Convert Sensor Name Decimated

```
Sub ConvertSensorNamesDecimated()
    Dim ws As Worksheet
    Dim cell As Range
    Dim sensorNames As Variant
    Dim convertedNames As Variant
    Dim i As Long

    ' Set the worksheet
    Set ws = ActiveWorkbook.ActiveSheet

    ' Define the sensor names and their corresponding converted names
    sensorNames = Array("ASTa1249_Temperature", "ASTa1257_Temperature",
"ASTa1241_Temperature", "ASTa1252_Temperature", _
                        "ASTa1239_Temperature", "ASTa1250_Temperature",
"TEROS10_4_Temperature", "TEROS10_1_Temperature", _
                        "TEROS10_5_Temperature", "TEROS10_2_Temperature",
"VAS1001_Temperature", "VAST1239_Temperature", _
                        "TEROS10_3_Temperature")

    convertedNames = Array("TEMPS-02-1", "TEMPS-01-1", "TEMPS-02-2",
"TEMPS-01-2", "TEMPS-02-3", "TEMPS-01-3", "TM-BA-01", _
                           "TM-BA-02", "TM-SB-03", "TM-SB-04", "TM-SB-05",
"TM-SG-06", "TM-SG-07")

    ' Loop through the first row of the worksheet
    For Each cell In ws.Range("1:1")
        ' Check if the cell value contains any of the sensor names
        For i = LBound(sensorNames) To UBound(sensorNames)
            If InStr(1, cell.Value, sensorNames(i), vbTextCompare) > 0
Then
                ' If a match is found, replace the sensor name within the
cell value
                cell.Value = Replace(cell.Value, sensorNames(i),
convertedNames(i), , , vbTextCompare)
                Exit For
            End If
        Next i
    Next cell

' Define the second set of sensor names and their converted names
sensorNames = Array("ASTa1257", "ASTa1243", "ASTa1239", "ASTa1249",
"ASTa1250", "ASTa1252", "ASTa1241", "ASTa1254", _
                    "VAS1002", "VAS1001", "VAS1000", "VAST1239",
"TEROS10_1", "TEROS10_2", "TEROS10_3", "TEROS10_4", _
                    "TEROS10_5", "TP1152500", "TP1151769", "TP1153165",
"TP1152501", "TP1152499", "TP1153137", _
                    "TP1317164", "TP1317162")
```

```
convertedNames = Array("AS-LO-R-1", "AS-LO-L-2", "AS-TR-R-3", "AS-TR-L-4",
"AS-TR-R-5", "AS-TR-L-6", "AS-LO-R-7", _
                       "AS-LO-L-8", "VAS-R-1", "VAS-L-2", "VAS-R-3", "VAS-
L-4", "MOI-BA-1", "MOI-SB-2", "MOI-SB-3", _
                       "MOI-SB-4", "MOI-SG-5", "PC-BA-R-1", "PC-BA-L-2",
"PC-SB-R-3", "PC-SB-L-4", "PC-BA-R-5", _
                       "PC-BA-L-6", "PC-SG-R-7", "PC-SG-L-8")

' Loop through the first row of the worksheet to replace the second set of
names
For Each cell In ws.Range("1:1")
    ' Check if the cell value contains any of the sensor names
    For i = LBound(sensorNames) To UBound(sensorNames)
        If InStr(1, cell.Value, sensorNames(i), vbTextCompare) > 0 Then
            ' If a match is found, replace the sensor name within the cell
value
            cell.Value = Replace(cell.Value, sensorNames(i),
convertedNames(i), , , vbTextCompare)
            Exit For
        End If
    Next i
Next cell

End Sub
```

Add Moisture Effect

```
Sub add_moisture_efficient()
    Dim ws As Worksheet
    Dim lastCol As Long, i As Long, j As Long
    Dim newColCount As Long
    Dim equation As String

    ' Set the worksheet
    Set ws = ActiveSheet

    ' Get the last column in the header row (Row 1)
    lastCol = ws.Cells(1, ws.Columns.Count).End(xlToLeft).Column

    ' Loop through the header row to find columns with "MOI" in their
header
    For i = lastCol To 1 Step -1
        If InStr(1, ws.Cells(1, i).Value, "MOI", vbTextCompare) > 0 Then
            ' Add a new column to the right of the current column
            ws.Columns(i + 1).Insert

            ' Add the equation to the second row of the new column
            equation = "=(0.0000000004824*(RC[-1])^3)-(0.000002278*(RC[-
1])^2)+(0.003898*RC[-1])-2.154"
            ws.Cells(2, i + 1).FormulaR1C1 = equation

            ' Fill the formula down the column for all relevant cells
            ws.Cells(2, i + 1).AutoFill Destination:=ws.Range(ws.Cells(2,
i + 1), ws.Cells(ws.Cells(ws.Rows.Count, i).End(xlUp).Row, i + 1))

            ' Set the new header name for the newly added column
            ws.Cells(1, i + 1).Value = ws.Cells(1, i).Value

            ' Increment the new column count
            newColCount = newColCount + 1
        End If
    Next i

    ' Copy and paste the whole active worksheet as values
    ws.Cells.Copy
    ws.Cells.PasteSpecial xlPasteValues

    ' Clear the clipboard
    Application.CutCopyMode = False

        Range( _

"AA:AA,AC:AC,AE:AE,AG:AG,AI:AI,AK:AK,AM:AM,AO:AO,AQ:AQ,AS:AS,AU:AU,AW:AW,A
Y:AY,BA:BA,BC:BC" _
        ).Select
    Range("BC1").Activate
```

```
    Selection.Delete Shift:=xlToLeft
    Range("AU21").Select

End Sub
```

Delete Columns that have MDD

```
Sub DeleteColumnsWithMDD()
    Dim ws As Worksheet
    Set ws = ActiveSheet ' The active worksheet

    Dim lastColumn As Long
    lastColumn = ws.Cells(1, ws.Columns.Count).End(xlToLeft).Column

    Dim i As Long
    For i = lastColumn To 1 Step -1
        If InStr(1, ws.Cells(1, i).Value, "MDD", vbTextCompare) > 0 Then
            ws.Columns(i).Delete
        End If
    Next i
End Sub
```

Delete the Random Columns at the end of Decimated Worksheets

```
Sub DeleteColumnsDecimatedActiveWorksheet()
    Dim ws As Worksheet
    Set ws = ActiveSheet

    Application.ScreenUpdating = False
    ws.Range("EH:FP").Delete Shift:=xlToLeft
    Application.ScreenUpdating = True
End Sub
```

Sort Columns Alphabetically Decimated

```
Sub sort_columns_alphabetically_decimated()
    Dim lastColumn As Long
    Dim ws As Worksheet

    Set ws = ActiveSheet
    lastColumn = ws.Cells(1, ws.Columns.Count).End(xlToLeft).Column

    ws.Sort.SortFields.Clear
    ws.Sort.SortFields.Add2 Key:=ws.Range("C1:ED1"),
SortOn:=xlSortOnValues, Order:=xlAscending, DataOption:=xlSortNormal

    With ws.Sort
        .SetRange ws.Range("C1", ws.Cells(ws.Rows.Count, lastColumn))
        .header = xlGuess
        .MatchCase = False
        .Orientation = xlLeftToRight
        .SortMethod = xlPinYin
        .Apply
    End With
End Sub
```

Add Timestamp Columns Decimated

```
Sub AddTimestampColumnDec()
    Dim ws As Worksheet
    Dim timestampSheet As Worksheet
    Dim timestampCell As Range
    Dim lastRow As Long
    Dim formula As String

    ' Add new column between columns A and B
    Columns("B:B").Insert Shift:=xlToRight

    ' Set the header in cell B1
    Range("B1").Value = "Timestamp"

    ' Find sheet with "Waterloo" in the name in the active workbook
    For Each ws In ActiveWorkbook.Worksheets
        If InStr(1, ws.Name, "Waterloo", vbTextCompare) > 0 Then
            Set timestampSheet = ws
            Exit For
        End If
    Next ws

    ' Check if "Waterloo" sheet was found
    If Not timestampSheet Is Nothing Then
        ' Find the timestamp cell P2 on the "Waterloo" sheet
        Set timestampCell = timestampSheet.Range("P2")
```

```
        ' Get the last row in column A of the active sheet
        lastRow = ActiveSheet.Cells(Rows.Count, 1).End(xlUp).Row

        ' Set the formula in column B starting from B2
        formula = "=" & timestampSheet.Name & "!$P$2+A2/86400"
        ActiveSheet.Range("B2:B" & lastRow).formula = formula

        ' Format the timestamps in column B as yyyy-mm-dd h:mm
        ActiveSheet.Range("B2:B" & lastRow).NumberFormat = "yyyy-mm-dd
h:mm"

        ' Autofit the width of column B to fit the contents
        ActiveSheet.Columns("B:B").AutoFit
    Else
        MsgBox "Sheet with 'Waterloo' in the name not found!"
    End If
End Sub
```

Run the Scripts

```
Sub AARunHighSpeed()
    ConvertSensorNamesHighSpeed
    AddTimestampColumn
    autofill_ColA
    DeleteColumnsByHeaderHighSpeed
    sort_columns_alphabetically_high_speed
    DeleteColumnsAandB
    DeleteColumnsWithMDD
    AutoSaveActiveSheet
End Sub

Sub AARunDecimated()
    DeleteColumnsDecimatedActiveWorksheet
    DeleteColumnsByHeaderDecimated
    ConvertSensorNamesDecimated
    AddTimestampColumnDec
    sort_columns_alphabetically_decimated
    DeleteColumnsWithMDD
    AutoSaveActiveSheet
End Sub
```

Python Scripts for Data Processing

Python excel_extractor_trend_data_to_one_excel_sheet.py

```
import os
import openpyxl
from openpyxl.utils import get_column_letter
from openpyxl.workbook.workbook import Workbook
from tkinter import Tk
from tkinter.filedialog import askopenfilenames


def extract_data_from_workbook(workbook_path):
    wb = openpyxl.load_workbook(workbook_path, data_only=True)  # Load
workbook with data only (no formulas)
    sheet = wb['TrendData']
    data = []
    max_row = sheet.max_row
    max_col = sheet.max_column

    # Extract data rows (excluding headers)
    for row_idx in range(2, max_row + 1):
        row_data = [sheet[get_column_letter(col_idx) + str(row_idx)].value
for col_idx in range(1, max_col + 1)]
        data.append(row_data)

    return data


# Open file dialog to select Excel workbooks
root = Tk()
root.withdraw()
root.update()
selected_files = askopenfilenames(title='Select Excel workbooks',
filetypes=[('Excel files', '*.xlsx *.xls')])

if not selected_files:
    print("No files selected.")
    exit()

# Extract data from each workbook
output_data = []
header_extracted = False
for file in selected_files:
    workbook_path = os.path.abspath(file)
    extracted_data = extract_data_from_workbook(workbook_path)
```

```
    output_data.extend(extracted_data)

    # Extract headers from the first workbook only
    if not header_extracted:
        header_extracted = True
        wb = openpyxl.load_workbook(workbook_path)
        sheet = wb['TrendData']
        headers = [sheet[get_column_letter(col_idx) + '1'].value for
col_idx in range(1, sheet.max_column + 1)]
        output_data.insert(0, headers)

# Create a new workbook and save extracted data
output_workbook = Workbook()
output_sheet = output_workbook.active

# Write the data to the output worksheet
for row_idx, row_data in enumerate(output_data, start=1):
    for col_idx, cell_value in enumerate(row_data, start=1):
        cell = output_sheet.cell(row=row_idx, column=col_idx)
        if col_idx == 2:  # Column B (timestamps)
            if cell.data_type == 'f':  # Check if cell contains a formula
                cell.value = cell.value  # Retrieve the displayed value
instead of the formula
            else:
                cell.value = cell_value
        else:
            cell.value = cell_value

output_folder = os.path.dirname(selected_files[0])
output_file = os.path.join(output_folder, "output.xlsx")
output_workbook.save(output_file)

print(f"Data extracted from {len(selected_files)} workbook(s) and saved to
'{output_file}'.")
```

```
python convert_tdms_to_csv_timepropissue.py

import os
import nptdms
import csv
from tkinter import Tk
from tkinter.filedialog import askopenfilenames

# Open a file dialog for the user to select TDMS files
Tk().withdraw()
tdms_file_paths = askopenfilenames(title='Select TDMS files',
filetypes=[('TDMS Files', '*.tdms')])

# Iterate over the selected files
for tdms_file_path in tdms_file_paths:
    folder_path = os.path.dirname(tdms_file_path)

    # Generate the CSV file name
    csv_file_name = os.path.splitext(os.path.basename(tdms_file_path))[0]
+ '.csv'
    csv_file_path = os.path.join(folder_path, csv_file_name)

    # Open the TDMS file
    tdms_file = nptdms.TdmsFile.read(tdms_file_path)

    # Extract the data from the TDMS file
    data = []
    for group in tdms_file.groups():
        for channel in group.channels():
            try:
                time_track = channel.time_track()
            except KeyError:
                time_track = None

            if time_track:
                values = channel[:]
                for i, val in enumerate(values):
                    data.append((group.name, channel.name, time_track[i],
val))
            else:
                values = channel[:]
                for val in values:
                    data.append((group.name, channel.name, None, val))

    # Save the data as CSV
    with open(csv_file_path, 'w', newline='') as csv_file:
        writer = csv.writer(csv_file)
```

```
        writer.writerow(['Group', 'Channel', 'Time', 'Value'])  # Header
row
        for entry in data:
            writer.writerow(entry)

    print('Conversion completed. CSV file saved at:', csv_file_path)


importandprocesscsv (find max and min value for each sensor)

import csv
import os
from tkinter import Tk
from tkinter.filedialog import askopenfilenames

# Open file dialog to select multiple input files
Tk().withdraw()
input_files = askopenfilenames(title='Select Input Files',
filetypes=[('CSV Files', '*.csv')])

# Process each input file
for input_file_path in input_files:
    # Extract the directory path of the input file
    input_dir = os.path.dirname(input_file_path)

    # Open the input file and skip the header row
    with open(input_file_path, 'r') as file:
        reader = csv.reader(file)
        next(reader)  # Skip the header row

        # Initialize variables
        current_sensor = None
        max_value = None
        min_value = None

        # Process each row in the file
        for row in reader:
            channel = row[0].split(',')[0]  # Extract the channel name
            sensor = row[1].split(',')[0]  # Extract the sensor name
            value = float(row[3])  # Extract the value as a float

            # Check if the sensor has changed
            if sensor != current_sensor:
                # Output the previous sensor's data (if available)
                if current_sensor is not None:
                    output_row = [current_sensor, max_value, min_value]
```

```
                    print(output_row)  # Print the row (for testing
purposes)

                # Reset variables for the new sensor
                current_sensor = sensor
                max_value = value
                min_value = value
            else:
                # Update the maximum and minimum values for the current
sensor
                max_value = max(max_value, value)
                min_value = min(min_value, value)

        # Output the last sensor's data
        if current_sensor is not None:
            output_row = [current_sensor, max_value, min_value]
            print(output_row)  # Print the row (for testing purposes)

    # Extract the input file name and construct the output file path in
the same directory
    input_file_name = os.path.basename(input_file_path)
    output_file_path = os.path.join(input_dir, 'output_' +
input_file_name)

    # Create a new CSV file for the output
    with open(output_file_path, 'w', newline='') as file:
        writer = csv.writer(file)

        # Write the header row
        writer.writerow(['Name', 'Max Value', 'Min Value'])

        # Write the sensor data rows
        with open(input_file_path, 'r') as input_file:
            reader = csv.reader(input_file)
            next(reader)  # Skip the header row

            for row in reader:
                channel = row[0].split(',')[0]  # Extract the channel name
                sensor = row[1].split(',')[0]  # Extract the sensor name

                # Check if the sensor has changed
                if sensor != current_sensor:
                    # Output the previous sensor's data (if available)
                    if current_sensor is not None:
                        output_row = [current_sensor, max_value,
min_value]
                        writer.writerow(output_row)
```

```
                    # Reset variables for the new sensor
                    current_sensor = sensor
                    max_value = None
                    min_value = None

                # Update the maximum and minimum values for the current
sensor
                value = float(row[3])  # Extract the value as a float
                max_value = value if max_value is None else max(max_value,
value)
                min_value = value if min_value is None else min(min_value,
value)

            # Output the last sensor's data
            if current_sensor is not None:
                output_row = [current_sensor, max_value, min_value]
                writer.writerow(output_row)
```

R Scripts for Data Processing

Multiple Temperature Sensor Plotter (TEMP-01 AND TEMP-02)

File name of Code: multi_temp_plotter_temp01temp02

```
# Load required libraries
library(readxl)
library(ggplot2)
library(cowplot)
library(tidyr)
library(dplyr)

# Function to generate temperature chart for a specific layer
generate_layer_temperature_chart <- function(data, layer_name,
chart_title, y_axis_range) {
  # Reshape data into tidy format
  tidy_data <- data %>%
    pivot_longer(cols = starts_with(layer_name), names_to = "Sensor",
values_to = "Temperature")

  # Create the temperature chart with a separate legend
  layer_chart <- ggplot(data = tidy_data, aes(x = Timestamp, y =
Temperature, color = Sensor)) +
    geom_line() +
    labs(title = chart_title, y = "Layer Temp (°C)", x = "Timestamp") +
    ylim(y_axis_range) +  # Set y-axis range
    theme_minimal() +
    theme(legend.position = "right")  # Set legend position to right

  return(layer_chart)
}

# Set the directory containing your input Excel files
input_directory <- choose.dir()

# Get a list of all Excel files in the directory
excel_files <- list.files(input_directory, pattern = "*.xlsx", full.names
= TRUE)

# Initialize an empty list to store data frames
all_data <- list()

# Loop through each Excel file and read the data
for (file_path in excel_files) {
  data <- read_excel(file_path)

  # Convert non-numeric values to NA with error handling
  tryCatch({
    data <- data %>%
      mutate(across(starts_with("TEMPS-"), as.numeric))
  }, warning = function(w) {
```

```
    message("Warning: Some non-numeric values could not be converted to
NA.")
  })

  all_data <- append(all_data, list(data))
}

# Combine all data frames into one
combined_data <- bind_rows(all_data)

# Determine the maximum and minimum temperature values from all columns
with "TM-" AND "TEMPS-"
max_temp_value <- combined_data %>%
  select(starts_with(c("TM-", "TEMPS-"))) %>%
  na.omit() %>%
  max(na.rm = TRUE)

min_temp_value <- combined_data %>%
  select(starts_with(c("TM-", "TEMPS-"))) %>%
  na.omit() %>%
  min(na.rm = TRUE)

# Set the y-axis range for all charts with margins
margin_upper <- 10  # You can adjust this margin as needed for the upper
bound
margin_lower <- 10  # You can adjust this margin as needed for the lower
bound
y_axis_range <- c(floor(min_temp_value) - margin_lower,
ceiling(max_temp_value) + margin_upper)

# Generate temperature charts for each layer
subgrade_chart <- generate_layer_temperature_chart(combined_data, "TM-SG",
"Subgrade Layer Temperatures", y_axis_range)
subbase_chart <- generate_layer_temperature_chart(combined_data, "TM-SB",
"Subbase Layer Temperatures", y_axis_range)
base_chart <- generate_layer_temperature_chart(combined_data, "TM-BA",
"Base Layer Temperatures", y_axis_range)

# Combine TEMPS-01 and TEMPS-02 sensors for HMA chart
sensor_columns <- c("TEMPS-01-1", "TEMPS-01-2", "TEMPS-01-3", "TEMPS-02-
1", "TEMPS-02-2", "TEMPS-02-3")
hma_temps_combined <- combined_data %>%
  dplyr::select(Timestamp, all_of(sensor_columns)) %>%
  pivot_longer(cols = -Timestamp, names_to = "Sensor", values_to =
"Temperature")

hma_chart <- ggplot(data = hma_temps_combined, aes(x = Timestamp, y =
Temperature, color = Sensor)) +
  geom_line() +
  labs(title = "HMA Layer Temperatures", y = "Layer Temp (°C)", x =
"Timestamp") +
  ylim(y_axis_range) +  # Set y-axis range
  theme_minimal() +
  theme(legend.position = "right")  # Set legend position to right
```

```
# Combine all the generated charts into a single stacked chart
stacked_charts <- plot_grid(hma_chart, base_chart, subbase_chart,
subgrade_chart,
                            ncol = 1, align = "v")

# Display the stacked temperature charts
print(stacked_charts)
```

Multiple Temperature Sensor Plotter (with TEMP-02 only)

```
File name of Code: multi_temp_plotter_temp02

# Load required libraries
library(readxl)
library(ggplot2)
library(cowplot)
library(tidyr)
library(dplyr)

# Function to generate temperature chart for a specific layer
generate_layer_temperature_chart <- function(data, layer_name,
chart_title, y_axis_range) {
  # Reshape data into tidy format
  tidy_data <- data %>%
    pivot_longer(cols = starts_with(layer_name), names_to = "Sensor",
values_to = "Temperature")

  # Create the temperature chart with a separate legend
  layer_chart <- ggplot(data = tidy_data, aes(x = Timestamp, y =
Temperature, color = Sensor)) +
    geom_line() +
    labs(title = chart_title, y = "Layer Temp (°C)", x = "Timestamp") +
    ylim(y_axis_range) +  # Set y-axis range
    theme_minimal() +
    theme(legend.position = "right")  # Set legend position to right

  return(layer_chart)
}

# Set the directory containing your input Excel files
input_directory <- choose.dir()

# Get a list of all Excel files in the directory
excel_files <- list.files(input_directory, pattern = "*.xlsx", full.names
= TRUE)

# Initialize an empty list to store data frames
all_data <- list()

# Loop through each Excel file and read the data
for (file_path in excel_files) {
  data <- read_excel(file_path)

  # Convert non-numeric values to NA with error handling
  tryCatch({
    data <- data %>%
      mutate(across(starts_with("TEMPS-"), as.numeric))
  }, warning = function(w) {
    message("Warning: Some non-numeric values could not be converted to
NA.")
  })
```

```
  all_data <- append(all_data, list(data))
}

# Combine all data frames into one
combined_data <- bind_rows(all_data)

# Determine the maximum and minimum temperature values from all columns
with "TM-" AND "TEMPS-"
max_temp_value <- combined_data %>%
  select(starts_with(c("TM-"))) %>%
  na.omit() %>%
  max(na.rm = TRUE)

min_temp_value <- combined_data %>%
  select(starts_with(c("TM-"))) %>%
  na.omit() %>%
  min(na.rm = TRUE)

# Set the y-axis range for all charts with margins
margin_upper <- 5  # You can adjust this margin as needed for the upper
bound
margin_lower <- 5  # You can adjust this margin as needed for the lower
bound
y_axis_range <- c(floor(min_temp_value) - margin_lower,
ceiling(max_temp_value) + margin_upper)

# Generate temperature charts for each layer with the common y-axis range
subgrade_chart <- generate_layer_temperature_chart(combined_data, "TM-SG",
"Subgrade Layer Temperatures", y_axis_range)
subbase_chart <- generate_layer_temperature_chart(combined_data, "TM-SB",
"Subbase Layer Temperatures", y_axis_range)
base_chart <- generate_layer_temperature_chart(combined_data, "TM-BA",
"Base Layer Temperatures", y_axis_range)

# Combine TEMPS-02 sensors for HMA chart, exclude TEMPS-01
sensor_columns <- c("TEMPS-02-1", "TEMPS-02-2", "TEMPS-02-3")
hma_temps_combined <- combined_data %>%
  dplyr::select(Timestamp, all_of(sensor_columns)) %>%
  pivot_longer(cols = -Timestamp, names_to = "Sensor", values_to =
"Temperature")

# Generate temperature chart for HMA with the common y-axis range
hma_chart <- ggplot(data = hma_temps_combined, aes(x = Timestamp, y =
Temperature, color = Sensor)) +
  geom_line() +
  labs(title = "HMA Layer Temperatures", y = "Layer Temp (°C)", x =
"Timestamp") +
  ylim(y_axis_range) +  # Set y-axis range
  theme_minimal() +
  theme(legend.position = "right")

# Combine all the generated charts into a single stacked chart
```

```
stacked_charts <- plot_grid(hma_chart, base_chart, subbase_chart,
subgrade_chart,
                            ncol = 1, align = "v")

# Display the stacked temperature charts
print(stacked_charts)
```

Multiple Temperature Sensor Plotter (with TEMP-02 only)
AND by month X-axis

File name of Code: multi_temp_plotte_remp02_bymonthxaxis

```
# Load required libraries
library(readxl)
library(ggplot2)
library(cowplot)
library(tidyr)
library(dplyr)

# Calculate breaks based on the data range
timestamp_range <- range(combined_data$Timestamp)
time_interval <- difftime(timestamp_range[2], timestamp_range[1], units =
"days")
breaks <- ifelse(time_interval <= 31, "1 day", "1 month")

# Function to generate temperature chart for a specific layer
generate_layer_temperature_chart <- function(data, layer_name,
chart_title, y_axis_range) {
  tidy_data <- data %>%
    pivot_longer(cols = starts_with(layer_name), names_to = "Sensor",
values_to = "Temperature")

  layer_chart <- ggplot(data = tidy_data, aes(x = Timestamp, y =
Temperature, color = Sensor)) +
    geom_line() +
    labs(title = chart_title, y = "Layer Temp (°C)", x = "Timestamp") +
    ylim(y_axis_range) +
    scale_x_datetime(date_breaks = breaks, date_labels = "%b %Y") +
    theme_minimal() +
    theme(legend.position = "right")

  return(layer_chart)
}

# Set the directory containing your input Excel files
input_directory <- choose.dir()

# Get a list of all Excel files in the directory
excel_files <- list.files(input_directory, pattern = "*.xlsx", full.names
= TRUE)

# Initialize an empty list to store data frames
all_data <- list()

# Loop through each Excel file and read the data
for (file_path in excel_files) {
  data <- read_excel(file_path)

  # Convert non-numeric values to NA with error handling
```

```
  tryCatch({
    data <- data %>%
      mutate(across(starts_with("TEMPS-"), as.numeric))
  }, warning = function(w) {
    message("Warning: Some non-numeric values could not be converted to
NA.")
  })

  all_data <- append(all_data, list(data))
}

# Combine all data frames into one
combined_data <- bind_rows(all_data)

# Determine the maximum and minimum temperature values from all columns
with "TM-" AND "TEMPS-"
max_temp_value <- combined_data %>%
  select(starts_with(c("TM-"))) %>%
  na.omit() %>%
  max(na.rm = TRUE)

min_temp_value <- combined_data %>%
  select(starts_with(c("TM-"))) %>%
  na.omit() %>%
  min(na.rm = TRUE)

# Set the y-axis range for all charts with margins
margin_upper <- 5  # You can adjust this margin as needed for the upper
bound
margin_lower <- 5  # You can adjust this margin as needed for the lower
bound
y_axis_range <- c(floor(min_temp_value) - margin_lower,
ceiling(max_temp_value) + margin_upper)

# Generate temperature charts for each layer with the common y-axis range
subgrade_chart <- generate_layer_temperature_chart(combined_data, "TM-SG",
"Subgrade Layer Temperatures", y_axis_range)
subbase_chart <- generate_layer_temperature_chart(combined_data, "TM-SB",
"Subbase Layer Temperatures", y_axis_range)
base_chart <- generate_layer_temperature_chart(combined_data, "TM-BA",
"Base Layer Temperatures", y_axis_range)

# Combine TEMPS-02 sensors for HMA chart, exclude TEMPS-01
sensor_columns <- c("TEMPS-02-1", "TEMPS-02-2", "TEMPS-02-3")
hma_temps_combined <- combined_data %>%
  dplyr::select(Timestamp, all_of(sensor_columns)) %>%
  pivot_longer(cols = -Timestamp, names_to = "Sensor", values_to =
"Temperature")

# Generate temperature chart for HMA with the common y-axis range
hma_chart <- ggplot(data = hma_temps_combined, aes(x = Timestamp, y =
Temperature, color = Sensor)) +
  geom_line() +
```

```
  labs(title = "HMA Layer Temperatures", y = "Layer Temp (°C)", x =
"Timestamp") +
  ylim(y_axis_range) +
  scale_x_datetime(date_breaks = breaks, date_labels = "%b %Y") +  # Use
the same breaks logic as the other charts
  theme_minimal() +
  theme(legend.position = "right")

# Combine all the generated charts into a single stacked chart
stacked_charts <- plot_grid(hma_chart, base_chart, subbase_chart,
subgrade_chart,
                            ncol = 1, align = "v")

# Display the stacked temperature charts
print(stacked_charts)
```

OR

Columns Selection for Temperature Range Calculation:

- In the new code, when calculating the maximum and minimum temperature values (**max_temp_value** and **min_temp_value**), you are selecting columns starting with "TM-" and "TEMPS-02" instead of "TM-" and "TEMPS-".

This one is useful to see since after a while the TEMPS-02-3 sensor goes bad so then the data is skewed. This code shows the skewed TEMPS-02 data while the previous one does not.

```
# Load required libraries
library(readxl)
library(ggplot2)
library(cowplot)
library(tidyr)
library(dplyr)

# Calculate breaks based on the data range
timestamp_range <- range(combined_data$Timestamp)
time_interval <- difftime(timestamp_range[2], timestamp_range[1], units =
"days")
breaks <- ifelse(time_interval <= 31, "1 day", "1 month")

# Function to generate temperature chart for a specific layer
generate_layer_temperature_chart <- function(data, layer_name,
chart_title, y_axis_range) {
  tidy_data <- data %>%
    pivot_longer(cols = starts_with(layer_name), names_to = "Sensor",
values_to = "Temperature")

  layer_chart <- ggplot(data = tidy_data, aes(x = Timestamp, y =
Temperature, color = Sensor)) +
    geom_line() +
```

```
    labs(title = chart_title, y = "Layer Temp (°C)", x = "Timestamp") +
    ylim(y_axis_range) +
    scale_x_datetime(date_breaks = breaks, date_labels = "%b %Y") +
    theme_minimal() +
    theme(legend.position = "right")

  return(layer_chart)
}

# Set the directory containing your input Excel files
input_directory <- choose.dir()

# Get a list of all Excel files in the directory
excel_files <- list.files(input_directory, pattern = "*.xlsx", full.names
= TRUE)

# Initialize an empty list to store data frames
all_data <- list()

# Loop through each Excel file and read the data
for (file_path in excel_files) {
  data <- read_excel(file_path)

  # Convert non-numeric values to NA with error handling
  tryCatch({
    data <- data %>%
      mutate(across(starts_with("TEMPS-"), as.numeric))
  }, warning = function(w) {
    message("Warning: Some non-numeric values could not be converted to
NA.")
  })

  all_data <- append(all_data, list(data))
}

# Combine all data frames into one
combined_data <- bind_rows(all_data)

# Determine the maximum and minimum temperature values from all columns
with "TM-" AND "TEMPS-"
max_temp_value <- combined_data %>%
  select(starts_with(c("TM-", "TEMPS-02"))) %>%
  na.omit() %>%
  max(na.rm = TRUE)

min_temp_value <- combined_data %>%
  select(starts_with(c("TM-", "TEMPS-02"))) %>%
  na.omit() %>%
  min(na.rm = TRUE)

# Set the y-axis range for all charts with margins
margin_upper <- 5  # You can adjust this margin as needed for the upper
bound
```

```
margin_lower <- 5  # You can adjust this margin as needed for the lower
bound
y_axis_range <- c(floor(min_temp_value) - margin_lower,
ceiling(max_temp_value) + margin_upper)

# Generate temperature charts for each layer with the common y-axis range
subgrade_chart <- generate_layer_temperature_chart(combined_data, "TM-SG",
"Subgrade Layer Temperatures", y_axis_range)
subbase_chart <- generate_layer_temperature_chart(combined_data, "TM-SB",
"Subbase Layer Temperatures", y_axis_range)
base_chart <- generate_layer_temperature_chart(combined_data, "TM-BA",
"Base Layer Temperatures", y_axis_range)

# Combine TEMPS-02 sensors for HMA chart, exclude TEMPS-01
sensor_columns <- c("TEMPS-02-1", "TEMPS-02-2", "TEMPS-02-3")
hma_temps_combined <- combined_data %>%
  dplyr::select(Timestamp, all_of(sensor_columns)) %>%
  pivot_longer(cols = -Timestamp, names_to = "Sensor", values_to =
"Temperature")

# Generate temperature chart for HMA with the common y-axis range
hma_chart <- ggplot(data = hma_temps_combined, aes(x = Timestamp, y =
Temperature, color = Sensor)) +
  geom_line() +
  labs(title = "HMA Layer Temperatures", y = "Layer Temp (°C)", x =
"Timestamp") +
  ylim(y_axis_range) +
  scale_x_datetime(date_breaks = breaks, date_labels = "%b %Y") +  # Use
the same breaks logic as the other charts
  theme_minimal() +
  theme(legend.position = "right")

# Combine all the generated charts into a single stacked chart
stacked_charts <- plot_grid(hma_chart, base_chart, subbase_chart,
subgrade_chart,
                            ncol = 1, align = "v")

# Display the stacked temperature charts
print(stacked_charts)
```

Temperature Plotter using TEMPS-02 only + Ambient Temperature

File name of Code: multi_temp_plotte_rtemp02_ambienttemp

```
# Load required libraries
library(readxl)
library(ggplot2)
library(cowplot)
library(tidyr)
library(dplyr)

# Function to generate temperature chart for a specific layer
generate_layer_temperature_chart <- function(data, layer_name,
chart_title, y_axis_range) {
  # Reshape data into tidy format
  tidy_data <- data %>%
    pivot_longer(cols = starts_with(layer_name), names_to = "Sensor",
values_to = "Temperature")

  # Create the temperature chart with a separate legend
  layer_chart <- ggplot(data = tidy_data, aes(x = Timestamp, y =
Temperature, color = Sensor)) +
    geom_line() +
    labs(title = chart_title, y = "Layer Temp (°C)", x = "Timestamp") +
    ylim(y_axis_range) +  # Set y-axis range
    theme_minimal() +
    theme(legend.position = "right")  # Set legend position to right

  return(layer_chart)
}

# Set the directory containing temperature input Excel files
temperature_directory <- choose.dir()

# Get a list of all Excel files in the temperature directory
temperature_files <- list.files(temperature_directory, pattern = "*.xlsx",
full.names = TRUE)

# Initialize an empty list to store temperature data frames
all_data <- list()

# Loop through each Excel file and read the data
for (file_path in temperature_files) {
  data <- read_excel(file_path)

  # Convert non-numeric values to NA with error handling
  tryCatch({
    data <- data %>%
      mutate(across(starts_with("TEMPS-"), as.numeric))
```

```
  }, warning = function(w) {
    message("Warning: Some non-numeric values could not be converted to
NA.")
  })

  all_data <- append(all_data, list(data))
}

# Combine all temperature data frames into one
combined_data <- bind_rows(all_data)

# Determine the maximum and minimum temperature values from all columns
with "TM-" AND "TEMPS-"
max_temp_value <- combined_data %>%
  select(starts_with(c("TM-"))) %>%
  na.omit() %>%
  max(na.rm = TRUE)

min_temp_value <- combined_data %>%
  select(starts_with(c("TM-"))) %>%
  na.omit() %>%
  min(na.rm = TRUE)

# Set the y-axis range for all charts with margins
margin_upper <- 5  # You can adjust this margin as needed for the upper
bound
margin_lower <- 5  # You can adjust this margin as needed for the lower
bound
y_axis_range <- c(floor(min_temp_value) - margin_lower,
ceiling(max_temp_value) + margin_upper)

# Generate temperature charts for each layer with the common y-axis range
subgrade_chart <- generate_layer_temperature_chart(combined_data, "TM-SG",
"Subgrade Layer Temperatures", y_axis_range)
subbase_chart <- generate_layer_temperature_chart(combined_data, "TM-SB",
"Subbase Layer Temperatures", y_axis_range)
base_chart <- generate_layer_temperature_chart(combined_data, "TM-BA",
"Base Layer Temperatures", y_axis_range)

# Combine TEMPS-02 sensors for HMA chart, exclude TEMPS-01
sensor_columns <- c("TEMPS-02-1", "TEMPS-02-2", "TEMPS-02-3")
hma_temps_combined <- combined_data %>%
  dplyr::select(Timestamp, all_of(sensor_columns)) %>%
  pivot_longer(cols = -Timestamp, names_to = "Sensor", values_to =
"Temperature")

# Generate temperature chart for HMA with the common y-axis range
hma_chart <- ggplot(data = hma_temps_combined, aes(x = Timestamp, y =
Temperature, color = Sensor)) +
  geom_line() +
```

```
  labs(title = "HMA Layer Temperatures", y = "Layer Temp (°C)", x =
"Timestamp") +
  ylim(y_axis_range) +  # Set y-axis range
  theme_minimal() +
  theme(legend.position = "right")

# Prompt user to select directory for ambient temperature data
ambient_directory <- choose.dir()

# Get a list of all Excel files in the ambient temperature directory
ambient_files <- list.files(ambient_directory, pattern = "*.xlsx",
full.names = TRUE)

# Initialize an empty list to store ambient temperature data frames
ambient_data <- list()

# Loop through each Excel file and read the ambient temperature data
for (file_path in ambient_files) {
  ambient_temp_data <- read_excel(file_path)

  # Assuming the columns are named "Timestamp" and "Ambient Temperature
(°C)", adjust if needed
  ambient_temp_data <- ambient_temp_data %>%
    mutate(Ambient_Temperature = as.numeric(`Ambient Temperature (°C)`))

  ambient_data <- append(ambient_data, list(ambient_temp_data))
}

# Combine all ambient temperature data frames into one
combined_ambient_data <- bind_rows(ambient_data)

# Generate ambient temperature chart with its own y-axis range and legend
ambient_chart <- ggplot(data = combined_ambient_data, aes(x = Timestamp, y
= Ambient_Temperature, color = "Ambient")) +
  geom_line(na.rm = TRUE) +  # Ignore missing values
  labs(title = "Ambient Temperature", y = "Ambient Temp (°C)", x =
"Timestamp") +
  ylim(c(min(combined_ambient_data$Ambient_Temperature, na.rm = TRUE) - 2,
         max(combined_ambient_data$Ambient_Temperature, na.rm = TRUE) +
2)) +  # Set y-axis range
  scale_color_manual(values = "blue", name = "Legend") +  # Set color and
legend label
  theme_minimal() +
  theme(legend.position = "right")

# Combine all the charts into a single stacked chart
stacked_charts <- plot_grid(hma_chart, base_chart, subbase_chart,
subgrade_chart, ambient_chart,
                            ncol = 1, align = "v")
```

```
# Display the stacked temperature charts
print(stacked_charts)
```

Multiple Temperature Sensor Plotter (with TEMP-02 restricted) AND by month X-axis + Ambient Temperature

File name of Code: multi_temp_plotte_remp02_bymonthxaxis_ambienttemp

```
# Load required libraries
1. library(readxl)
library(ggplot2)
library(cowplot)
library(tidyr)
library(dplyr)

# Calculate breaks based on the data range
timestamp_range <- range(combined_data$Timestamp)
time_interval <- difftime(timestamp_range[2], timestamp_range[1], units =
"days")
breaks <- ifelse(time_interval <= 31, "1 day", "1 month")

# Function to generate temperature chart for a specific layer
generate_layer_temperature_chart <- function(data, layer_name,
chart_title, y_axis_range) {
  tidy_data <- data %>%
    pivot_longer(cols = starts_with(layer_name), names_to = "Sensor",
values_to = "Temperature")

  layer_chart <- ggplot(data = tidy_data, aes(x = Timestamp, y =
Temperature, color = Sensor)) +
    geom_line() +
    labs(title = chart_title, y = "Layer Temp (°C)", x = "Timestamp") +
    ylim(y_axis_range) +
    scale_x_datetime(date_breaks = breaks, date_labels = "%b %Y") +
    theme_minimal() +
    theme(legend.position = "right")

  return(layer_chart)
}

# Set the directory containing your input Excel files
input_directory <- choose.dir()

# Get a list of all Excel files in the directory
excel_files <- list.files(input_directory, pattern = "*.xlsx", full.names
= TRUE)

# Initialize an empty list to store data frames
all_data <- list()

# Loop through each Excel file and read the data
for (file_path in excel_files) {
  data <- read_excel(file_path)
```

```
  # Convert non-numeric values to NA with error handling
  tryCatch({
    data <- data %>%
      mutate(across(starts_with("TEMPS-"), as.numeric))
  }, warning = function(w) {
    message("Warning: Some non-numeric values could not be converted to
NA.")
  })

  all_data <- append(all_data, list(data))
}

# Combine all data frames into one
combined_data <- bind_rows(all_data)

# Determine the maximum and minimum temperature values from all columns
with "TM-" AND "TEMPS-"
max_temp_value <- combined_data %>%
  select(starts_with(c("TM-"))) %>%
  na.omit() %>%
  max(na.rm = TRUE)

min_temp_value <- combined_data %>%
  select(starts_with(c("TM-"))) %>%
  na.omit() %>%
  min(na.rm = TRUE)

# Set the y-axis range for all charts with margins
margin_upper <- 5  # You can adjust this margin as needed for the upper
bound
margin_lower <- 5  # You can adjust this margin as needed for the lower
bound
y_axis_range <- c(floor(min_temp_value) - margin_lower,
ceiling(max_temp_value) + margin_upper)

# Generate temperature charts for each layer with the common y-axis range
subgrade_chart <- generate_layer_temperature_chart(combined_data, "TM-SG",
"Subgrade Layer Temperatures", y_axis_range)
subbase_chart <- generate_layer_temperature_chart(combined_data, "TM-SB",
"Subbase Layer Temperatures", y_axis_range)
base_chart <- generate_layer_temperature_chart(combined_data, "TM-BA",
"Base Layer Temperatures", y_axis_range)

# Combine TEMPS-02 sensors for HMA chart, exclude TEMPS-01
sensor_columns <- c("TEMPS-02-1", "TEMPS-02-2", "TEMPS-02-3")
hma_temps_combined <- combined_data %>%
  dplyr::select(Timestamp, all_of(sensor_columns)) %>%
  pivot_longer(cols = -Timestamp, names_to = "Sensor", values_to =
"Temperature")
```

```
# Generate temperature chart for HMA with the common y-axis range
hma_chart <- ggplot(data = hma_temps_combined, aes(x = Timestamp, y =
Temperature, color = Sensor)) +
  geom_line() +
  labs(title = "HMA Layer Temperatures", y = "Layer Temp (°C)", x =
"Timestamp") +
  ylim(y_axis_range) +
  scale_x_datetime(date_breaks = breaks, date_labels = "%b %Y") +  # Use
the same breaks logic as the other charts
  theme_minimal() +
  theme(legend.position = "right")

# Prompt user to select directory for ambient temperature data
ambient_directory <- choose.dir()

# Get a list of all Excel files in the ambient temperature directory
ambient_files <- list.files(ambient_directory, pattern = "*.xlsx",
full.names = TRUE)

# Initialize an empty list to store ambient temperature data frames
ambient_data <- list()

# Loop through each Excel file and read the ambient temperature data
for (file_path in ambient_files) {
  ambient_temp_data <- read_excel(file_path)

  # Assuming the columns are named "Timestamp" and "Ambient Temperature
(°C)", adjust if needed
  ambient_temp_data <- ambient_temp_data %>%
    mutate(Ambient_Temperature = as.numeric(`Ambient Temperature (°C)`))

  ambient_data <- append(ambient_data, list(ambient_temp_data))
}

# Combine all ambient temperature data frames into one
combined_ambient_data <- bind_rows(ambient_data)

# Generate ambient temperature chart with the same breaks as other charts
ambient_chart <- ggplot(data = combined_ambient_data, aes(x = Timestamp, y
= Ambient_Temperature, color = "Ambient")) +
  geom_line(na.rm = TRUE) +  # Ignore missing values
  labs(title = "Ambient Temperature", y = "Ambient Temp (°C)", x =
"Timestamp") +
  ylim(c(min(combined_ambient_data$Ambient_Temperature, na.rm = TRUE) - 2,
         max(combined_ambient_data$Ambient_Temperature, na.rm = TRUE) +
2)) +  # Set y-axis range
  scale_x_datetime(date_breaks = breaks, date_labels = "%b %Y") +  # Use
the same breaks logic as the other charts
```

```
  scale_color_manual(values = "blue", name = "Legend") +  # Set color and
legend label
  theme_minimal() +
  theme(legend.position = "right")

# Combine all the charts into a single stacked chart
stacked_charts <- plot_grid(hma_chart, base_chart, subbase_chart,
subgrade_chart, ambient_chart,
                            ncol = 1, align = "v")

# Display the stacked temperature charts
print(stacked_charts)
```

OR

```
File name for Code:
multi_temp_plot_temp02_bymonthxaxis_ambienttemp_includesfulltemp02

# Load required libraries
library(readxl)
library(ggplot2)
library(cowplot)
library(tidyr)
library(dplyr)

# Calculate breaks based on the data range
timestamp_range <- range(combined_data$Timestamp)
time_interval <- difftime(timestamp_range[2], timestamp_range[1], units =
"days")
breaks <- ifelse(time_interval <= 31, "1 day", "1 month")

# Function to generate temperature chart for a specific layer
generate_layer_temperature_chart <- function(data, layer_name,
chart_title, y_axis_range) {
  tidy_data <- data %>%
    pivot_longer(cols = starts_with(layer_name), names_to = "Sensor",
values_to = "Temperature")

  layer_chart <- ggplot(data = tidy_data, aes(x = Timestamp, y =
Temperature, color = Sensor)) +
    geom_line() +
    labs(title = chart_title, y = "Layer Temp (°C)", x = "Timestamp") +
    ylim(y_axis_range) +
    scale_x_datetime(date_breaks = breaks, date_labels = "%b %Y") +
    theme_minimal() +
    theme(legend.position = "right")

  return(layer_chart)
}
```

```
# Set the directory containing your input Excel files
input_directory <- choose.dir()

# Get a list of all Excel files in the directory
excel_files <- list.files(input_directory, pattern = "*.xlsx", full.names
= TRUE)

# Initialize an empty list to store data frames
all_data <- list()

# Loop through each Excel file and read the data
for (file_path in excel_files) {
  data <- read_excel(file_path)

  # Convert non-numeric values to NA with error handling
  tryCatch({
    data <- data %>%
      mutate(across(starts_with("TEMPS-"), as.numeric))
  }, warning = function(w) {
    message("Warning: Some non-numeric values could not be converted to
NA.")
  })

  all_data <- append(all_data, list(data))
}

# Combine all data frames into one
combined_data <- bind_rows(all_data)

# Determine the maximum and minimum temperature values from all columns
with "TM-" AND "TEMPS-"
max_temp_value <- combined_data %>%
  select(starts_with(c("TM-", "TEMPS-02"))) %>%
  na.omit() %>%
  max(na.rm = TRUE)

min_temp_value <- combined_data %>%
  select(starts_with(c("TM-", "TEMPS-02"))) %>%
  na.omit() %>%
  min(na.rm = TRUE)

# Set the y-axis range for all charts with margins
margin_upper <- 5  # You can adjust this margin as needed for the upper
bound
margin_lower <- 5  # You can adjust this margin as needed for the lower
bound
y_axis_range <- c(floor(min_temp_value) - margin_lower,
ceiling(max_temp_value) + margin_upper)
```

```
# Generate temperature charts for each layer with the common y-axis range
subgrade_chart <- generate_layer_temperature_chart(combined_data, "TM-SG",
"Subgrade Layer Temperatures", y_axis_range)
subbase_chart <- generate_layer_temperature_chart(combined_data, "TM-SB",
"Subbase Layer Temperatures", y_axis_range)
base_chart <- generate_layer_temperature_chart(combined_data, "TM-BA",
"Base Layer Temperatures", y_axis_range)

# Combine TEMPS-02 sensors for HMA chart, exclude TEMPS-01
sensor_columns <- c("TEMPS-02-1", "TEMPS-02-2", "TEMPS-02-3")
hma_temps_combined <- combined_data %>%
  dplyr::select(Timestamp, all_of(sensor_columns)) %>%
  pivot_longer(cols = -Timestamp, names_to = "Sensor", values_to =
"Temperature")

# Generate temperature chart for HMA with the common y-axis range
hma_chart <- ggplot(data = hma_temps_combined, aes(x = Timestamp, y =
Temperature, color = Sensor)) +
  geom_line() +
  labs(title = "HMA Layer Temperatures", y = "Layer Temp (°C)", x =
"Timestamp") +
  ylim(y_axis_range) +
  scale_x_datetime(date_breaks = breaks, date_labels = "%b %Y") +  # Use
the same breaks logic as the other charts
  theme_minimal() +
  theme(legend.position = "right")

# Prompt user to select directory for ambient temperature data
ambient_directory <- choose.dir()

# Get a list of all Excel files in the ambient temperature directory
ambient_files <- list.files(ambient_directory, pattern = "*.xlsx",
full.names = TRUE)

# Initialize an empty list to store ambient temperature data frames
ambient_data <- list()

# Loop through each Excel file and read the ambient temperature data
for (file_path in ambient_files) {
  ambient_temp_data <- read_excel(file_path)

  # Assuming the columns are named "Timestamp" and "Ambient Temperature
(°C)", adjust if needed
  ambient_temp_data <- ambient_temp_data %>%
    mutate(Ambient_Temperature = as.numeric(`Ambient Temperature (°C)`))

  ambient_data <- append(ambient_data, list(ambient_temp_data))
}

# Combine all ambient temperature data frames into one
```

```
combined_ambient_data <- bind_rows(ambient_data)

# Generate ambient temperature chart with the same breaks as other charts
ambient_chart <- ggplot(data = combined_ambient_data, aes(x = Timestamp, y
= Ambient_Temperature, color = "Ambient")) +
  geom_line(na.rm = TRUE) +  # Ignore missing values
  labs(title = "Ambient Temperature", y = "Ambient Temp (°C)", x =
"Timestamp") +
  ylim(c(min(combined_ambient_data$Ambient_Temperature, na.rm = TRUE) - 2,
         max(combined_ambient_data$Ambient_Temperature, na.rm = TRUE) +
2)) +  # Set y-axis range
  scale_x_datetime(date_breaks = breaks, date_labels = "%b %Y") +  # Use
the same breaks logic as the other charts
  scale_color_manual(values = "blue", name = "Legend") +  # Set color and
legend label
  theme_minimal() +
  theme(legend.position = "right")

# Combine all the charts into a single stacked chart
stacked_charts <- plot_grid(hma_chart, base_chart, subbase_chart,
subgrade_chart, ambient_chart,
                            ncol = 1, align = "v")

# Display the stacked temperature charts
print(stacked_charts)
```

Moisture Trend Plotter

```
File name of Code: moisture_plotter_all sensors

# Load required libraries
library(readxl)
library(ggplot2)
library(cowplot)
library(tidyr)
library(dplyr)

# Function to generate moisture chart for a specific layer
generate_layer_moisture_chart <- function(data, layer_name, chart_title,
y_axis_range) {
  tidy_data <- data %>%
    pivot_longer(cols = starts_with(layer_name), names_to = "Sensor",
values_to = "Moisture") %>%
    filter(grepl("_Average", Sensor))  # Select only columns with
"_Average" suffix
```

```
  moisture_chart <- ggplot(data = tidy_data, aes(x = Timestamp, y =
Moisture, color = Sensor)) +
    geom_line() +
    labs(title = chart_title, y = "Layer Moisture (m3/m3)", x =
"Timestamp") +
    ylim(y_axis_range) +
    theme_minimal() +
    theme(legend.position = "right")

  return(moisture_chart)
}

# Set the directory containing your input Excel files
input_directory <- choose.dir()

# Get a list of all Excel files in the directory
excel_files <- list.files(input_directory, pattern = "*.xlsx", full.names
= TRUE)

# Initialize an empty list to store data frames
all_data <- list()

# Loop through each Excel file and read the data
for (file_path in excel_files) {
  data <- read_excel(file_path)

  # Convert non-numeric values to NA with error handling
  tryCatch({
    data <- data %>%
      mutate(across(starts_with("MOI-"), as.numeric))
  }, warning = function(w) {
    message("Warning: Some non-numeric values could not be converted to
NA.")
  })

  all_data <- append(all_data, list(data))
}

# Combine all data frames into one
combined_data <- bind_rows(all_data)

# Determine the maximum and minimum moisture values from all columns with
"MOI-BA", "MOI-SB", "MOI-SG"
max_moisture_value <- combined_data %>%
```

```
  select(starts_with(c("MOI-BA", "MOI-SB", "MOI-SG"))) %>%
  na.omit() %>%
  max(na.rm = TRUE)

min_moisture_value <- combined_data %>%
  select(starts_with(c("MOI-BA", "MOI-SB", "MOI-SG"))) %>%
  na.omit() %>%
  min(na.rm = TRUE)

# Print diagnostic information
cat("min_moisture_value:", min_moisture_value, "\n")
cat("max_moisture_value:", max_moisture_value, "\n")

# Set the y-axis range for all charts with margins
margin_upper <- 0.05  # You can adjust this margin as needed for the upper
bound
margin_lower <- 0.05  # You can adjust this margin as needed for the lower
bound
y_axis_range <- c(max(0, floor(min_moisture_value) - margin_lower),
min(0.5, ceiling(max_moisture_value) + margin_upper))

# Generate moisture charts for each layer
subgrade_chart <- generate_layer_moisture_chart(combined_data, "MOI-SG",
"Subgrade Layer Moisture", y_axis_range)
subbase_chart <- generate_layer_moisture_chart(combined_data, "MOI-SB",
"Subbase Layer Moisture", y_axis_range)
base_chart <- generate_layer_moisture_chart(combined_data, "MOI-BA", "Base
Layer Moisture", y_axis_range)

# Combine all the generated charts into a single stacked chart
stacked_moisture_charts <- plot_grid(base_chart, subbase_chart,
subgrade_chart,
                                     ncol = 1, align = "v")

# Display the stacked moisture charts
print(stacked_moisture_charts)
```

Moisture Trend Plotter + Precipitation Plotter

```
library(readxl)
library(ggplot2)
library(cowplot)
library(tidyr)
library(dplyr)

# Function to generate moisture chart for a specific layer
generate_layer_moisture_chart <- function(data, layer_name, chart_title,
y_axis_range) {
  tidy_data <- data %>%
    pivot_longer(cols = starts_with(layer_name), names_to = "Sensor",
values_to = "Moisture") %>%
    filter(grepl("_Average", Sensor))  # Select only columns with
"_Average" suffix

  moisture_chart <- ggplot(data = tidy_data, aes(x = Timestamp, y =
Moisture, color = Sensor)) +
    geom_line() +
    labs(title = chart_title, y = "Layer Moisture (m3/m3)", x =
"Timestamp") +
    ylim(y_axis_range) +
    theme_minimal() +
    theme(legend.position = "right")

  return(moisture_chart)
}

# Function to generate precipitation bar chart
generate_precipitation_chart <- function(precip_data, chart_title) {
  precipitation_chart <- ggplot(data = precip_data, aes(x = Timestamp, y =
`Total Precipitation (mm)`, fill = "Precipitation")) +
    geom_bar(stat = "identity") +
    scale_fill_manual(values = c("Precipitation" = "blue")) +  # Set fill
color manually
    labs(title = chart_title, y = "Total Precipitation (mm)", x =
"Timestamp", fill = "") +  # Set legend title
    theme_minimal() +
    theme(legend.position = "right")

  return(precipitation_chart)
}

# Set the directory containing your input Excel files for moisture data
moisture_input_directory <- choose.dir()

# Set the directory containing your input Excel file for precipitation
data
precipitation_input_directory <- choose.dir()
```

```
# Get a list of all Excel files for moisture data in the directory
moisture_excel_files <- list.files(moisture_input_directory, pattern =
"*.xlsx", full.names = TRUE)

# Get the Excel file for precipitation data
precipitation_excel_file <- list.files(precipitation_input_directory,
pattern = "*.xlsx", full.names = TRUE)[1]

# Initialize an empty list to store moisture data frames
all_moisture_data <- list()

# Loop through each moisture Excel file and read the data
for (moisture_file_path in moisture_excel_files) {
  moisture_data <- read_excel(moisture_file_path)

  # Convert non-numeric values to NA with error handling
  tryCatch({
    moisture_data <- moisture_data %>%
      mutate(across(starts_with("MOI-"), as.numeric))
  }, warning = function(w) {
    message("Warning: Some non-numeric values could not be converted to
NA.")
  })

  all_moisture_data <- append(all_moisture_data, list(moisture_data))
}

# Combine all moisture data frames into one
combined_moisture_data <- bind_rows(all_moisture_data)

# Read precipitation data
precipitation_data <- read_excel(precipitation_excel_file)

# Determine the maximum and minimum moisture values from all columns with
"MOI-BA", "MOI-SB", "MOI-SG"
max_moisture_value <- combined_moisture_data %>%
  select(starts_with(c("MOI-BA", "MOI-SB", "MOI-SG"))) %>%
  na.omit() %>%
  max(na.rm = TRUE)

min_moisture_value <- combined_moisture_data %>%
  select(starts_with(c("MOI-BA", "MOI-SB", "MOI-SG"))) %>%
  na.omit() %>%
  min(na.rm = TRUE)

# Print diagnostic information
cat("min_moisture_value:", min_moisture_value, "\n")
cat("max_moisture_value:", max_moisture_value, "\n")

# Set the y-axis range for all moisture charts with margins
```

```
margin_upper <- 0.05  # You can adjust this margin as needed for the upper
bound
margin_lower <- 0.05  # You can adjust this margin as needed for the lower
bound
y_axis_range <- c(max(0, floor(min_moisture_value) - margin_lower),
min(0.5, ceiling(max_moisture_value) + margin_upper))

# Generate moisture charts for each layer
subgrade_chart <- generate_layer_moisture_chart(combined_moisture_data,
"MOI-SG", "Subgrade Layer Moisture", y_axis_range)
subbase_chart <- generate_layer_moisture_chart(combined_moisture_data,
"MOI-SB", "Subbase Layer Moisture", y_axis_range)
base_chart <- generate_layer_moisture_chart(combined_moisture_data, "MOI-
BA", "Base Layer Moisture", y_axis_range)

# Generate precipitation chart
precipitation_chart <- generate_precipitation_chart(precipitation_data,
"Precipitation")

# Combine all the generated charts into a single stacked chart
stacked_charts <- plot_grid(base_chart, subbase_chart, subgrade_chart,
precipitation_chart,
                            ncol = 1, align = "v", axis = "tb")

# Display the stacked charts
print(stacked_charts)
```

Trend Strain Plotter + Ambient Temperature

```
File for Code name : multi_strain_plotter_trend_withambienttemp

# Load required libraries
library(readxl)
library(ggplot2)
library(cowplot)
library(tidyr)
library(dplyr)

# Calculate breaks based on the data range
timestamp_range <- range(combined_data$Timestamp)
time_interval <- difftime(timestamp_range[2], timestamp_range[1], units =
"days")
breaks <- ifelse(time_interval <= 31, "1 day", "1 month")

# Function to generate strain chart for a specific layer
generate_layer_strain_chart <- function(data, layer_name, chart_title,
y_axis_range) {
  tidy_data <- data %>%
    pivot_longer(cols = matches(paste0("^", layer_name, "-\\d+_Average")),
                 names_to = "Sensor", values_to = "Strain")

  layer_chart <- ggplot(data = tidy_data, aes(x = Timestamp, y = Strain,
color = Sensor)) +
    geom_line() +
    labs(title = chart_title, y = "Strain (με)", x = "Timestamp") +
    ylim(y_axis_range) +
    scale_x_datetime(date_breaks = breaks, date_labels = "%b %Y") +
    theme_minimal() +
    theme(legend.position = "right")

  return(layer_chart)
}

# Set the directory containing your input Excel files
input_directory <- choose.dir()

# Get a list of all Excel files in the directory
excel_files <- list.files(input_directory, pattern = "*.xlsx", full.names
= TRUE)

# Initialize an empty list to store data frames
all_data <- list()

# Loop through each Excel file and read the data
for (file_path in excel_files) {
  data <- read_excel(file_path)

  # Convert non-numeric values to NA with error handling
  tryCatch({
    data <- data %>%
      mutate(across(matches("^AS-"), as.numeric))
```

```
  }, warning = function(w) {
    message("Warning: Some non-numeric values could not be converted to
NA.")
  })

  all_data <- append(all_data, list(data))
}

# Combine all data frames into one
combined_data <- bind_rows(all_data)

# Determine the maximum and minimum strain values from all columns with
"AS-"
max_strain_value <- combined_data %>%
  select(starts_with(c("AS-LO-R", "AS-TR-R", "AS-LO-L", "AS-TR-L"))) %>%
  na.omit() %>%
  max(na.rm = TRUE)

min_strain_value <- combined_data %>%
  select(starts_with(c("AS-LO-R", "AS-TR-R", "AS-LO-L", "AS-TR-L"))) %>%
  na.omit() %>%
  min(na.rm = TRUE)

# Set the y-axis range for all charts with margins
margin_upper <- 5  # You can adjust this margin as needed for the upper
bound
margin_lower <- 5  # You can adjust this margin as needed for the lower
bound
y_axis_range <- c(floor(min_strain_value) - margin_lower,
ceiling(max_strain_value) + margin_upper)

# Generate strain charts for each layer with the common y-axis range
right_longitudinal_strain_chart <-
generate_layer_strain_chart(combined_data, "AS-LO-R", "Right Longitudinal
Strain", y_axis_range)
right_transverse_strain_chart <-
generate_layer_strain_chart(combined_data, "AS-TR-R", "Right Transverse
Strain", y_axis_range)
left_longitudinal_strain_chart <-
generate_layer_strain_chart(combined_data, "AS-LO-L", "Left Longitudinal
Strain", y_axis_range)
left_transverse_strain_chart <- generate_layer_strain_chart(combined_data,
"AS-TR-L", "Left Transverse Strain", y_axis_range)

# Prompt user to select directory for ambient temperature data
ambient_directory <- choose.dir()

# Get a list of all Excel files in the ambient temperature directory
ambient_files <- list.files(ambient_directory, pattern = "*.xlsx",
full.names = TRUE)

# Initialize an empty list to store ambient temperature data frames
ambient_data <- list()
```

```
# Loop through each Excel file and read the ambient temperature data
for (file_path in ambient_files) {
  ambient_temp_data <- read_excel(file_path)

  # Assuming the columns are named "Timestamp" and "Ambient Temperature
(°C)", adjust if needed
  ambient_temp_data <- ambient_temp_data %>%
    mutate(Ambient_Temperature = as.numeric(`Ambient Temperature (°C)`))

  ambient_data <- append(ambient_data, list(ambient_temp_data))
}

# Combine all ambient temperature data frames into one
combined_ambient_data <- bind_rows(ambient_data)

# Generate ambient temperature chart with the same breaks as other charts
ambient_chart <- ggplot(data = combined_ambient_data, aes(x = Timestamp, y
= Ambient_Temperature, color = "Ambient")) +
  geom_line(na.rm = TRUE) +  # Ignore missing values
  labs(title = "Ambient Temperature", y = "Ambient Temp (°C)", x =
"Timestamp") +
  ylim(c(min(combined_ambient_data$Ambient_Temperature, na.rm = TRUE) - 2,
         max(combined_ambient_data$Ambient_Temperature, na.rm = TRUE) +
2)) +  # Set y-axis range
  scale_x_datetime(date_breaks = breaks, date_labels = "%b %Y") +  # Use
the same breaks logic as the other charts
  scale_color_manual(values = "blue", name = "Legend") +  # Set color and
legend label
  theme_minimal() +
  theme(legend.position = "right")

# Combine all the charts into a single stacked chart
stacked_charts <- plot_grid(right_longitudinal_strain_chart,
right_transverse_strain_chart,
                            left_longitudinal_strain_chart,
left_transverse_strain_chart, ambient_chart,
                            ncol = 1, align = "v")

# Display the stacked strain charts
print(stacked_charts)
```

Trend Pressure Plotter + Ambient Temperature

File for Code name : multi_pressure_plotter_trend_withambienttemp

Note: you have to manually set the y-axis parameters in this one.

```
# Load required libraries
library(readxl)
library(ggplot2)
library(cowplot)
library(tidyr)
library(dplyr)

# Set the directory containing your input Excel files for pressure sensors
pressure_input_directory <- choose.dir()

# Get a list of all Excel files for pressure sensors in the directory
pressure_excel_files <- list.files(pressure_input_directory, pattern =
"*.xlsx", full.names = TRUE)

# Initialize an empty list to store pressure sensor data frames
all_pressure_data <- list()

# Loop through each Excel file for pressure sensors and read the data
for (pressure_file_path in pressure_excel_files) {
  pressure_data <- read_excel(pressure_file_path)

  # Assuming the columns are named "Timestamp", "PC-BA-R-1_Average", "PC-
BA-R-5_Average", etc.
  # Adjust the column names if needed
  pressure_data <- pressure_data %>%
    mutate(across(starts_with("PC-"), as.numeric))

  all_pressure_data <- append(all_pressure_data, list(pressure_data))
}

# Combine all pressure sensor data frames into one
combined_pressure_data <- bind_rows(all_pressure_data)

# Set the desired y-axis range
min_y_axis_value <- 0  # Replace with your desired minimum value
max_y_axis_value <- 200  # Replace with your desired maximum value
```

```
# Set the y-axis range for all pressure sensor charts with user-defined
values
y_axis_range_pressure <- c(min_y_axis_value, max_y_axis_value)

# Function to generate pressure chart for a specific layer with filtering
generate_layer_pressure_chart <- function(data, layer_name, chart_title,
y_axis_range) {
  tidy_data <- data %>%
    pivot_longer(cols = matches(paste0("^", layer_name, "-\\d+_Average")),
                 names_to = "Sensor", values_to = "Pressure")

  # Convert pressure from MPa to kPa
  tidy_data$Pressure <- tidy_data$Pressure * 1000

  # Filter data between 50000 kPa and 0 kPa
  tidy_data <- filter(tidy_data, Pressure >= 0, Pressure <= 5000)

  layer_chart <- ggplot(data = tidy_data, aes(x = Timestamp, y = Pressure,
color = Sensor)) +
    geom_line() +
    labs(title = chart_title, y = "Layer Pressure (kPa)", x = "Timestamp")
+
    ylim(y_axis_range) +  # Use the specified y-axis range
    scale_x_datetime(date_breaks = breaks, date_labels = "%b %Y") +
    theme_minimal() +
    theme(legend.position = "right")

  return(layer_chart)
}

# Generate pressure charts for each layer with the common y-axis range and
filtering
base_right_lane_pressure_chart <-
generate_layer_pressure_chart(combined_pressure_data, "PC-BA-R", "Base
Right Lane", y_axis_range_pressure)
base_left_lane_pressure_chart <-
generate_layer_pressure_chart(combined_pressure_data, "PC-BA-L", "Base
Left Lane", y_axis_range_pressure)
subbase_right_lane_pressure_chart <-
generate_layer_pressure_chart(combined_pressure_data, "PC-SB-R", "Subbase
Right Lane", y_axis_range_pressure)
subbase_left_lane_pressure_chart <-
generate_layer_pressure_chart(combined_pressure_data, "PC-SB-L", "Subbase
Left Lane", y_axis_range_pressure)
```

```
subgrade_right_lane_pressure_chart <-
generate_layer_pressure_chart(combined_pressure_data, "PC-SG-R", "Subgrade
Right Lane", y_axis_range_pressure)
subgrade_left_lane_pressure_chart <-
generate_layer_pressure_chart(combined_pressure_data, "PC-SG-L", "Subgrade
Left Lane", y_axis_range_pressure)

# Prompt user to select directory for ambient temperature data
ambient_directory <- choose.dir()

# Get a list of all Excel files in the ambient temperature directory
ambient_files <- list.files(ambient_directory, pattern = "*.xlsx",
full.names = TRUE)

# Initialize an empty list to store ambient temperature data frames
ambient_data <- list()

# Loop through each Excel file and read the ambient temperature data
for (file_path in ambient_files) {
  ambient_temp_data <- read_excel(file_path)

  # Assuming the columns are named "Timestamp" and "Ambient Temperature
(°C)", adjust if needed
  ambient_temp_data <- ambient_temp_data %>%
    mutate(Ambient_Temperature = as.numeric(`Ambient Temperature (°C)`))

  ambient_data <- append(ambient_data, list(ambient_temp_data))
}

# Combine all ambient temperature data frames into one
combined_ambient_data <- bind_rows(ambient_data)

# Generate ambient temperature chart with the same breaks as other charts
ambient_chart <- ggplot(data = combined_ambient_data, aes(x = Timestamp, y
= Ambient_Temperature, color = "Ambient")) +
  geom_line(na.rm = TRUE) +  # Ignore missing values
  labs(title = "Ambient Temperature", y = "Ambient Temp (°C)", x =
"Timestamp") +
  ylim(c(min(combined_ambient_data$Ambient_Temperature, na.rm = TRUE) - 2,
         max(combined_ambient_data$Ambient_Temperature, na.rm = TRUE) +
2)) +  # Set y-axis range
  scale_x_datetime(date_breaks = breaks, date_labels = "%b %Y") +  # Use
the same breaks logic as the other charts
  scale_color_manual(values = "blue", name = "Legend") +  # Set color and
legend label
```

```
  theme_minimal() +
  theme(legend.position = "right")

# Display the stacked pressure charts
stacked_charts <- plot_grid(base_right_lane_pressure_chart,
base_left_lane_pressure_chart,
                            subbase_right_lane_pressure_chart,
subbase_left_lane_pressure_chart,
                            subgrade_right_lane_pressure_chart,
subgrade_left_lane_pressure_chart,
                            ambient_chart,
                            ncol = 1, align = "v")

print(stacked_charts)
```

High Speed Strain Plotter + Ambient (not filtered)

```
# Load required libraries
library(readxl)
library(ggplot2)
library(cowplot)
library(tidyr)
library(dplyr)

# Function to generate temperature chart for a specific layer
generate_layer_temperature_chart <- function(data, layer_name,
chart_title, y_axis_range) {
  # Reshape data into tidy format
  tidy_data <- data %>%
    pivot_longer(cols = starts_with(layer_name), names_to = "Sensor",
values_to = "Temperature")

  # Create the temperature chart with a separate legend
  layer_chart <- ggplot(data = tidy_data, aes(x = Timestamp, y =
Temperature, color = Sensor)) +
    geom_line() +
    labs(title = chart_title, y = "Strain", x = "Timestamp") +
    ylim(y_axis_range) +  # Set y-axis range
    theme_minimal() +
    theme(legend.position = "right")  # Set legend position to right

  return(layer_chart)
}

# Set the directory containing strain input Excel files
strain_directory <- choose.dir()

# Get a list of all Excel files in the strain directory
strain_files <- list.files(strain_directory, pattern = "*.xlsx",
full.names = TRUE)

# Initialize an empty list to store strain data frames
all_data <- list()

# Loop through each Excel file and read the data
for (file_path in strain_files) {
  message("Processing file:", file_path)  # Displaying the file being
processed
  data <- read_excel(file_path)
```

```
  # Convert non-numeric values to NA with error handling
  tryCatch({
    data <- data %>%
      mutate(across(starts_with("AS-"), as.numeric))
  }, warning = function(w) {
    message("Warning: Some non-numeric values could not be converted to
NA.")
  })

  all_data <- append(all_data, list(data))
}

# Combine all strain data frames into one
combined_data <- bind_rows(all_data)

# Determine the maximum and minimum strain values from all columns with
"AS-"
max_strain_value <- combined_data %>%
  select(starts_with(c("AS-"))) %>%
  na.omit() %>%
  max(na.rm = TRUE)

min_strain_value <- combined_data %>%
  select(starts_with(c("AS-"))) %>%
  na.omit() %>%
  min(na.rm = TRUE)

# Set the y-axis range for all charts with margins
margin_upper <- 5  # You can adjust this margin as needed for the upper
bound
margin_lower <- 5  # You can adjust this margin as needed for the lower
bound
y_axis_range <- c(floor(min_strain_value) - margin_lower,
ceiling(max_strain_value) + margin_upper)

# Generate strain charts for each layer with the common y-axis range
right_longitudinal_strain_chart <-
generate_layer_temperature_chart(combined_data, c("AS-LO-R-1", "AS-LO-R-
7"), "Right, Longitudinal Strain", y_axis_range)
right_transverse_strain_chart <-
generate_layer_temperature_chart(combined_data, c("AS-TR-R-3", "AS-TR-R-
5"), "Right, Transverse Strain", y_axis_range)
left_longitudinal_strain_chart <-
generate_layer_temperature_chart(combined_data, c("AS-LO-L-2", "AS-LO-L-
8"), "Left, Longitudinal Strain", y_axis_range)
```

```
left_transverse_strain_chart <-
generate_layer_temperature_chart(combined_data, c("AS-TR-L-4", "AS-TR-L-
6"), "Left, Transverse Strain", y_axis_range)

# Prompt user to select directory for ambient temperature data
ambient_directory <- choose.dir()

# Get a list of all Excel files in the ambient temperature directory
ambient_files <- list.files(ambient_directory, pattern = "*.xlsx",
full.names = TRUE)

# Initialize an empty list to store ambient temperature data frames
ambient_data <- list()

# Loop through each Excel file and read the ambient temperature data
for (file_path in ambient_files) {
  message("Processing file:", file_path)  # Displaying the file being
processed
  ambient_temp_data <- read_excel(file_path)

  # Assuming the columns are named "Timestamp" and "Ambient Temperature
(°C)", adjust if needed
  ambient_temp_data <- ambient_temp_data %>%
    mutate(Ambient_Temperature = as.numeric(`Ambient Temperature (°C)`))

  ambient_data <- append(ambient_data, list(ambient_temp_data))
}

# Combine all ambient temperature data frames into one
combined_ambient_data <- bind_rows(ambient_data)

# Generate ambient temperature chart with its own y-axis range and legend
ambient_chart <- ggplot(data = combined_ambient_data, aes(x = Timestamp, y
= Ambient_Temperature, color = "Ambient")) +
  geom_line(na.rm = TRUE) +  # Ignore missing values
  labs(title = "Ambient Temperature", y = "Temperature (°C)", x =
"Timestamp") +
  ylim(c(min(combined_ambient_data$Ambient_Temperature, na.rm = TRUE) - 2,
         max(combined_ambient_data$Ambient_Temperature, na.rm = TRUE) +
2)) +  # Set y-axis range
  scale_color_manual(values = "blue", name = "Legend") +  # Set color and
legend label
  theme_minimal() +
  theme(legend.position = "right")
```

```
# Combine all charts into a single stacked chart
stacked_charts <- plot_grid(right_longitudinal_strain_chart,
right_transverse_strain_chart, left_longitudinal_strain_chart,
left_transverse_strain_chart, ambient_chart,
                            ncol = 1, align = "v")

# Display the stacked charts
print(stacked_charts)
```

High Speed Strain Plotter + Ambient (filtered)

```
# Load required libraries
library(readxl)
library(ggplot2)
library(cowplot)
library(tidyr)
library(dplyr)

# Function to generate strain chart for a specific layer with a filtered
range
generate_layer_strain_chart <- function(data, layer_name, chart_title,
y_axis_range) {
  # Reshape data into tidy format
  tidy_data <- data %>%
    pivot_longer(cols = starts_with(layer_name), names_to = "Sensor",
values_to = "Strain")

  # Create the strain chart with a separate legend
  layer_chart <- ggplot(data = tidy_data, aes(x = Timestamp, y = Strain,
color = Sensor)) +
    geom_line() +
    labs(title = chart_title, y = "Strain", x = "Timestamp") +
    ylim(y_axis_range) +  # Set y-axis range
    theme_minimal() +
    theme(legend.position = "right")  # Set legend position to right

  return(layer_chart)
}

# Set the directory containing strain input Excel files
strain_directory <- choose.dir()

# Get a list of all Excel files in the strain directory
strain_files <- list.files(strain_directory, pattern = "*.xlsx",
full.names = TRUE)

# Initialize an empty list to store strain data frames
all_data <- list()

# Loop through each Excel file and read the data
for (file_path in strain_files) {
  message("Processing file:", file_path)  # Displaying the file being
processed
  data <- read_excel(file_path)

  # Convert non-numeric values to NA with error handling
  tryCatch({
    data <- data %>%
      mutate(across(starts_with("AS-"), as.numeric))
```

```
  }, warning = function(w) {
    message("Warning: Some non-numeric values could not be converted to
NA.")
  })

  all_data <- append(all_data, list(data))
}

# Combine all strain data frames into one
combined_data <- bind_rows(all_data)

# Set the range for filtering strain data
strain_filter_min <- -6000
strain_filter_max <- 6000

# Generate strain charts for each layer with the filtered y-axis range
right_longitudinal_strain_chart <- generate_layer_strain_chart(
  combined_data,
  c("AS-LO-R-1", "AS-LO-R-7"),
  "Right, Longitudinal Strain",
  c(strain_filter_min, strain_filter_max)
)

right_transverse_strain_chart <- generate_layer_strain_chart(
  combined_data,
  c("AS-TR-R-3", "AS-TR-R-5"),
  "Right, Transverse Strain",
  c(strain_filter_min, strain_filter_max)
)

left_longitudinal_strain_chart <- generate_layer_strain_chart(
  combined_data,
  c("AS-LO-L-2", "AS-LO-L-8"),
  "Left, Longitudinal Strain",
  c(strain_filter_min, strain_filter_max)
)

left_transverse_strain_chart <- generate_layer_strain_chart(
  combined_data,
  c("AS-TR-L-4", "AS-TR-L-6"),
  "Left, Transverse Strain",
  c(strain_filter_min, strain_filter_max)
)

# Prompt user to select directory for ambient temperature data
ambient_directory <- choose.dir()

# Get a list of all Excel files in the ambient temperature directory
ambient_files <- list.files(ambient_directory, pattern = "*.xlsx",
full.names = TRUE)
```

```
# Initialize an empty list to store ambient temperature data frames
ambient_data <- list()

# Loop through each Excel file and read the ambient temperature data
for (file_path in ambient_files) {
  message("Processing file:", file_path)  # Displaying the file being
processed
  ambient_temp_data <- read_excel(file_path)

  # Assuming the columns are named "Timestamp" and "Ambient Temperature
(°C)", adjust if needed
  ambient_temp_data <- ambient_temp_data %>%
    mutate(Ambient_Temperature = as.numeric(`Ambient Temperature (°C)`))

  ambient_data <- append(ambient_data, list(ambient_temp_data))
}

# Combine all ambient temperature data frames into one
combined_ambient_data <- bind_rows(ambient_data)

# Generate ambient temperature chart with its own y-axis range and legend
ambient_chart <- ggplot(data = combined_ambient_data, aes(x = Timestamp, y
= Ambient_Temperature, color = "Ambient")) +
  geom_line(na.rm = TRUE) +  # Ignore missing values
  labs(title = "Ambient Temperature", y = "Temperature (°C)", x =
"Timestamp") +
  ylim(c(min(combined_ambient_data$Ambient_Temperature, na.rm = TRUE) - 2,
         max(combined_ambient_data$Ambient_Temperature, na.rm = TRUE) +
2)) +  # Set y-axis range
  scale_color_manual(values = "blue", name = "Legend") +  # Set color and
legend label
  theme_minimal() +
  theme(legend.position = "right")

# Combine all charts into a single stacked chart
stacked_charts <- plot_grid(right_longitudinal_strain_chart,
right_transverse_strain_chart, left_longitudinal_strain_chart,
left_transverse_strain_chart, ambient_chart,
                            ncol = 1, align = "v")

# Display the stacked charts
print(stacked_charts)
```

High Speed Pressure Plotter + Ambient

```
# Load required libraries
library(readxl)
library(ggplot2)
library(cowplot)
library(tidyr)
library(dplyr)

# Function to generate pressure chart for a specific layer
generate_layer_pressure_chart <- function(data, layer_name, chart_title,
y_axis_range) {
  # Reshape data into tidy format
  tidy_data <- data %>%
    pivot_longer(cols = starts_with(layer_name), names_to = "Sensor",
values_to = "Pressure")

  # Convert pressure to kilopascals
  tidy_data$Pressure <- tidy_data$Pressure * 1000

  # Create the pressure chart with a separate legend
  layer_chart <- ggplot(data = tidy_data, aes(x = Timestamp, y = Pressure,
color = Sensor)) +
    geom_line() +
    labs(title = chart_title, y = "Layer Pressure (kPa)", x = "Timestamp")
+
    ylim(y_axis_range) +  # Set y-axis range
    theme_minimal() +
    theme(legend.position = "right")  # Set legend position to right

  return(layer_chart)
}

# Set the directory containing pressure input Excel files
pressure_directory <- choose.dir()

# Get a list of all Excel files in the pressure directory
pressure_files <- list.files(pressure_directory, pattern = "*.xlsx",
full.names = TRUE)

# Initialize an empty list to store pressure data frames
all_pressure_data <- list()

# Loop through each Excel file and read the data
for (file_path in pressure_files) {
  message("Processing file:", file_path)  # Displaying the file being
processed
  data <- read_excel(file_path)

  # Convert non-numeric values to NA with error handling
  tryCatch({
```

```
    data <- data %>%
      mutate(across(starts_with("PC-"), ~.*1000, .names = "Pressure_PC-
{col}"))
  }, warning = function(w) {
    message("Warning: Some non-numeric values could not be converted to
NA.")
  })

  all_pressure_data <- append(all_pressure_data, list(data))
}

# Combine all pressure data frames into one
combined_pressure_data <- bind_rows(all_pressure_data)

# Set the desired y-axis range
min_y_axis_value <- 0  # Replace with your desired minimum value
max_y_axis_value <- 200  # Replace with your desired maximum value

# Generate pressure charts for each layer with the specified y-axis range
base_right_lane_pressure_chart <-
generate_layer_pressure_chart(combined_pressure_data, c("PC-BA-R-1", "PC-
BA-R-5"), "Base Right Array", c(min_y_axis_value, max_y_axis_value))
base_left_lane_pressure_chart <-
generate_layer_pressure_chart(combined_pressure_data, c("PC-BA-L-2", "PC-
BA-L-6"), "Base Left Array", c(min_y_axis_value, max_y_axis_value))
subbase_right_lane_pressure_chart <-
generate_layer_pressure_chart(combined_pressure_data, c("PC-SB-R-3"),
"Subbase Right Array", c(min_y_axis_value, max_y_axis_value))
subbase_left_lane_pressure_chart <-
generate_layer_pressure_chart(combined_pressure_data, c("PC-SB-L-4"),
"Subbase Left Array", c(min_y_axis_value, max_y_axis_value))
subgrade_right_lane_pressure_chart <-
generate_layer_pressure_chart(combined_pressure_data, c("PC-SG-R-7"),
"Subgrade Right Array", c(min_y_axis_value, max_y_axis_value))
subgrade_left_lane_pressure_chart <-
generate_layer_pressure_chart(combined_pressure_data, c("PC-SG-L-8"),
"Subgrade Left Array", c(min_y_axis_value, max_y_axis_value))

# Prompt user to select directory for ambient temperature data
ambient_directory <- choose.dir()

# Get a list of all Excel files in the ambient temperature directory
ambient_files <- list.files(ambient_directory, pattern = "*.xlsx",
full.names = TRUE)

# Initialize an empty list to store ambient temperature data frames
ambient_data <- list()

# Loop through each Excel file and read the ambient temperature data
for (file_path in ambient_files) {
```

```
  message("Processing file:", file_path)  # Displaying the file being
processed
  ambient_temp_data <- read_excel(file_path)

  # Assuming the columns are named "Timestamp" and "Ambient Temperature
(°C)", adjust if needed
  ambient_temp_data <- ambient_temp_data %>%
    mutate(Ambient_Temperature = as.numeric(`Ambient Temperature (°C)`))

  ambient_data <- append(ambient_data, list(ambient_temp_data))
}

# Combine all ambient temperature data frames into one
combined_ambient_data <- bind_rows(ambient_data)

# Generate ambient temperature chart with its own y-axis range and legend
ambient_chart <- ggplot(data = combined_ambient_data, aes(x = Timestamp, y
= Ambient_Temperature, color = "Ambient")) +
  geom_line(na.rm = TRUE) +  # Ignore missing values
  labs(title = "Ambient Temperature", y = "Temperature (°C)", x =
"Timestamp") +
  ylim(c(min(combined_ambient_data$Ambient_Temperature, na.rm = TRUE) - 2,
         max(combined_ambient_data$Ambient_Temperature, na.rm = TRUE) +
2)) +  # Set y-axis range
  scale_color_manual(values = "blue", name = "Legend") +  # Set color and
legend label
  theme_minimal() +
  theme(legend.position = "right")

# Combine all charts into a single stacked chart
stacked_charts <- plot_grid(base_right_lane_pressure_chart,
base_left_lane_pressure_chart,
                            subbase_right_lane_pressure_chart,
subbase_left_lane_pressure_chart,
                            subgrade_right_lane_pressure_chart,
subgrade_left_lane_pressure_chart,
                            ambient_chart,
                            ncol = 1, align = "v")

# Display the stacked charts
print(stacked_charts)
```